Understanding the Effect Rotating Sunspots have on their Magnetic Environment

Daniel Johnson

A thesis submitted in partial fulfilment
of the requirements for the degree of
Doctor of Philosophy

Jeremiah Horrocks Institute for Mathematics, Physics and Astronomy
University of Central Lancashire

February 2023

Declaration

Type of Award: Doctor of Philosophy

School: Physical Sciences and Computing

I declare that while registered as a candidate for the research degree, I have not been a registered candidate or enrolled student for another award of the University or other academic or professional institution.

I declare that no material contained in the thesis has been used in any other submission for an academic award and is solely my own work.

No proof-reading service was used in the compilation of this thesis.

Daniel Johnson

February 2023

Abstract

Sunspot rotation is a recognised mechanism for the injection of excess magnetic energy into the solar atmosphere, where that energy may be used to power eruptive events. This work aims to extend the current understanding of how sunspot rotation transfers energy from within the Sun into the magnetic fields in the solar atmosphere by carrying out numerical simulations of sunspot rotation. An idealised model to represent a simple sunspot is developed and used to identify the processes present during sunspot rotation, to determine how much energy sunspot rotation injects and to understand how each characteristic property of a sunspot contributes to the injection of magnetic energy. The investigation identifies a number of important properties of sunspot rotation. Specifically, the penumbra is found to be fundamentally important for the injection, storage and transport of magnetic energy. All simulations show that the majority of the excess magnetic energy injected by sunspot rotation, is located in the penumbra. The significance of this is that, in the model used, the penumbra represents a relatively small region and thus this finding highlights regions of high energy density may exist in the natural phenomenon. Secondly, a set of scaling laws are derived that give a numerical estimate of how the magnetic energy injected by rotating sunspots varies as the sunspots geometric, magnetic and rotational properties are varied. A general scaling law is derived based on the individual scaling relations. Finally we observe that the penumbral magnetic field expands as a consequence to rotation. This expansion is shown to play a fundamental role in the liberation of some of the injected magnetic energy introduced

into the penumbra. A number of avenues for the next steps in the investigation are identified, but the findings of this thesis are immediately relevant and may be used to estimate the amount of energy injected by a rotating sunspot using observational measurements as an input to the model.

Contents

Declaration **ii**

Abstract **iii**

Acknowledgements **xxxiii**

1 Introduction **1**

1.1 Space Weather 2

1.2 Active Regions and Sunspots 5

1.3 Sunspot Rotation 7

1.3.1 Measured and Simulated Sunspot Rotation 10

1.4 Sunspots 13

1.4.1 Sunspot Size 17

1.4.2 Magnetic Properties 18

1.4.3 Rotation Properties 22

1.5 Magnetohydrodynamics 23

1.5.1 The Resistive Magnetohydrodynamics Equations 23

1.6 Force-Free Magnetic Fields 28

1.7 Poynting's Theorem 30

1.7.1 Magnetohydrodynamic Poynting Theorem 33

1.8 Potential Magnetic Fields 35

1.8.1 Minimum Magnetic Energy 36
1.9 Outline of Thesis 38

2 Sunspot Model **42**
2.1 Deriving a Simplified Sunspot Model 44
2.1.1 Umbral Region 46
2.1.2 Penumbral Region 48
2.1.3 Constraining γ 50
2.2 Capturing the Penumbral Flux 51
2.3 Lare3D, Initialisation and Driving 54
2.3.1 Lare3D 54
2.4 Boundary Conditions 56
2.4.1 Upper Boundary Conditions 57
2.4.2 Side Boundary Conditions 58
2.4.3 Lower Boundary Conditions 59
2.4.4 The Driver 61
2.5 Initial Conditions 63
2.5.1 Potential Magnetic Field 64
2.5.2 Pressure Balance 67

3 Numerical Simulation of a Sunspot with a Penumbra **71**
3.1 Observed Evolution 72
3.2 Magnetic Field Evolution 72
3.3 Magnetic Field Strength 77
3.4 Current Density 81
3.5 Velocity 89
3.6 Density 95
3.7 Temperature 100

3.8 Chapter Summary 104

4 Evolution of the Penumbra **108**

4.1 Penumbral Field Identification 108

4.1.1 Testing the Grid Cells 112

4.1.2 Penumbral Volume 113

4.2 Separatrix Evolution 114

4.3 Twist 120

4.3.1 Alpha - Force-Free Parameter 121

4.3.2 Current Helicity 136

4.4 The Physical Importance of Twist and Current Helicity 143

5 The Dynamics and Energetics of Sunspot Rotation **147**

5.1 Dynamics 147

5.1.1 Lorentz Force 148

5.1.2 Thermal Pressure Gradient 159

5.1.3 Gravity 169

5.1.4 Total Acceleration 170

5.2 Energetics 173

5.2.1 Magnetic, Kinetic and Internal Energy 174

5.2.2 The Injection of Magnetic Energy from Sunspot Rotation . . . 178

6 A Parametric Investigation of Rotating Sunspots **188**

6.1 Introduction 188

6.1.1 An Ideal Magnetohydrodynamic Framework 190

6.1.2 The Methodology 190

6.1.3 Power-Law Fitting 191

6.2 Parametric Scaling Relations 195

6.2.1 Peak Umbral Field Strength- U_b 197

6.2.2 Sunspot Size - P_r . . . 215
6.2.3 Rotation Rate - ω . . . 225
6.2.4 Radii Ratio - $\psi \equiv \frac{Ur}{Pr}$ . . . 236
6.2.5 Penumbral Fractional Magnetic Field Strength - μ . . . 245
6.3 Combined Scaling Law . . . 256
6.4 Testing . . . 261

7 Summary and Future Work **268**
7.1 The Sunspot Model . . . 268
7.2 The Penumbra . . . 269
7.3 Scaling Laws . . . 271
7.4 Applicability of the Force-Free Assumption . . . 274
7.5 Connected Sunspots . . . 275
7.6 Resistive Effects . . . 284
7.7 Concluding Remarks . . . 286

A Base Simulation **289**

B Peak Umbral Field Strength - U_b **290**

C Radii Ratio - ψ **299**

D Sunspot Size - P_r **306**

E Peak Penumbral Field Strength - μ **309**

F Rotation Rate - ω **314**

G Gamma -γ **319**

H Lare3D Time-step **326**

List of Tables

6.1 A tabulated record of the simulations used throughout section 6.2.1 and their associated properties. 204
6.2 Table of coefficients for the data fits derived in this section. 212
6.3 A table of the simulations used to investigate the parameter P_r with $\psi = \frac{U_r}{P_r} = 0.5$ for all simulations. 217
6.4 Table of coefficients for the data fits derived in this section. 224
6.5 A tabulated record of the simulations used throughout section 6.2.3 and their associated properties. 229
6.6 Table of coefficients for the data fits derived in section 6.2.3. 236
6.7 A tabulated record of the simulations used throughout section 6.2.4 and their associated properties. 239
6.8 Table of coefficients for the data fits derived in this section. 245
6.9 A tabulated record of the simulations used throughout section 6.2.5 and their associated properties. 248
6.10 Table of coefficients for the data fits derived in section 6.2.5. 256

7.1 A tabulated record of the simulations used throughout to test the importance of the model parameter γ. 273

List of Figures

1.1 Three co-aligned images showing a sunspot (left), a magnetogram showing the normal component of the magnetic field's strength (middle) and an active region observed in 171Å (right). These images were created using helioviewer.org, with data collected by the SDO Pesnell et al. (2012); Lemen et al. (2012); Scherrer et al. (2012). . . . 6

1.2 This figure shows a HMI continuum (Pesnell et al., 2012; Scherrer et al., 2012; Schou et al., 2012) image of a sunspot from AR12158 and surrounding magnetic features and a quiver plot, over-plotted that indicates the direction of motion. The colour of the quivers indicates the magnitude of the velocity, red indicates greater speed and blue lesser. 12

1.3 A small regular sunspot. Image credit: Data collected with the SST in 2002 by Gran Scharmer and Kai Langhans, ISP. 15

1.4 A multi-line plot showing an averaged magnetic field profile as a function of radius for a magnetic field described in a cylindrical geometry. The curve that intersects the y-axis at 2500G represents B_z, the curve with the smallest magnitude at all radii represents B_ϕ and the remaining curve represents B_R. The two vertical dashed lines show the umbral radius (at $r = 0.4$) and the penumbral radius (at $r = 0.75$). Image credit: Keppens and Martinez Pillet (1996). 21

2.1 This figure shows an example cell of the numerical domain, showing the location of the variables within the grid cells. Image credit: Arber et al. (2001). 55
2.2 A line plot showing the temperature as a function of height profile used to initialise all simulations. 64
2.3 The initial, potential, magnetic field of simulation 1. The red and green field lines show the umbral magnetic field and the blue lines show the penumbral magnetic field. The yellow field lines show field lines that emerge through the photosphere at the umbral-penumbral interface. 66
2.4 A line plot showing the mass density as a function of height profile used to initialise all simulations. 70

3.1 This figure shows the evolution of the sunspot magnetic field, viewed from the side. The blue lines represent the penumbral magnetic field, the red and green lines represent the umbral magnetic field and the yellow lines represent field lines that originate from the umbra-penumbra boundary. The sub-figures, moving from top to bottom, show the magnetic field at times when it has been rotated by 0°, 30°, 45°, 60° and 75° by the driver respectively. 73
3.2 This figure shows the evolution of the sunspot magnetic field, viewed from the side. The blue lines represent the penumbral magnetic field, the red and green lines represent the umbral magnetic field and the yellow lines represent field lines that originate from the umbra-penumbra boundary. The sub-figures, moving from top to bottom, show the magnetic field at times when it has been rotated by 90°, 105°, 120°, 135° and 140° by the driver respectively. 74

3.3 This figure shows the absolute change of the sunspot magnetic field strength with respect to the initial potential field solution, in a slice through the centre of the sunspot. The top figure shows the initial potential magnetic field strength. Subsequent figures show the absolute magnetic field strength change at times when the driver has rotated the sunspot by 30°, 45°, 60° and 75° respectively. Each absolute change is calculated by subtracting the potential field solution from the magnetic field. The black contour represents the approximate location of the separatrix that divides the umbral and penumbral magnetic field regions, in a slice through the centre of the sunspot. The colour bars have units of Tesla (T). 78

3.4 This figure shows the absolute change of the sunspot magnetic field strength with respect to the initial potential field solution, in a slice through the centre of the sunspot. The figures show the absolute magnetic field strength change at times when the driver has rotated the sunspot by 90°, 105°, 120°, 135° and 140° respectively. Each absolute change is calculated by subtracting the potential field solution from the magnetic field. The black contour represents the approximate location of the separatrix that divides the umbral and penumbral magnetic field regions, in a slice through the centre of the sunspot. The colour bars have units of Tesla (T). 79

3.5 This figure shows the evolution of the magnitude of the current density during the simulation. The sub-figures, moving from top to bottom, show the magnitude of current density in a slice through the centre of the sunspot at times when the sunspot has been rotated by 30°, 45°, 60° and 75° by the driver respectively. The units of the colour bars are (Am^{-2}). 82

3.6 This figure shows the evolution of the magnitude of the current density during the simulation. The sub-figures, moving from top to bottom, show the magnitude of current density in a slice through the centre of the sunspot at times when the sunspot has been rotated by 90°, 105°, 120°, 135° and 140° by the driver respectively. The units of the colour bars are (Am^{-2}). 83

3.7 This figure shows the angle subtended by current density and the magnetic field vectors in a slice through the centre of the sunspot during the simulation. The sub-figures, moving from top to bottom, show the angle at times when the sunspot has been rotated by 30°, 45°, 60° and 75° by the driver respectively. The units of the colour bars are radians. 86

3.8 This figure shows the angle subtended by current density and the magnetic field vectors in a slice through the centre of the sunspot during the simulation. The sub-figures, moving from top to bottom, show the angle at times when the sunspot has been rotated by 90°, 105°, 120°, 135° and 140° respectively. The units of the colour bars are radians. 87

3.9 This figure shows the evolution of velocity during the lifetime of the simulation. The sub-figures, moving from top to bottom, show the velocity at times where the driver has rotated the sunspot by 30°, 45°, 60° and 75° respectively. The quivers show the normalised velocity in the plane of the slice, where each quiver is colour coded such that black indicates the slowest speed, white the fastest and green is intermediate. The background image shows the velocity normal to the plane of the slice, the colour bars have units of ms^{-1} and describe the background image. 90

3.10 This figure shows the evolution of velocity during the lifetime of the simulation. The sub-figures, moving from top to bottom, show the velocity at times where the driver has rotated the sunspot by 90°, 105°, 120°, 135° and 140° respectively. The quivers show the normalised velocity in the plane of the slice, where each quiver is colour coded such that black indicates the slowest speed, white the fastest and green is intermediate. The background image shows the velocity normal to the plane of the slice, the colour bars have units of ms^{-1} and describe the background image. 91

3.11 This figure shows the evolution of density in a slice through the centre of the sunspot during the lifetime of the simulation. The sub-figures, moving from top to bottom, show the density at times when the sunspot has been rotated by 0°, 30°, 45°, 60° and 75° by the driver respectively. The black contour represents the approximate location of the separatrix that divides the umbral and penumbral magnetic field regions, in a slice through the centre of the sunspot. The units of the colour bars are kgm^{-3}. 96

3.12 This figure shows the evolution of density in a slice through the centre of the sunspot during the lifetime of the simulation. The sub-figures, moving from top to bottom, show the density at times when the sunspot has been rotated by 90°, 105°, 120°, 135° and 140° by the driver respectively. The black contour represents the approximate location of the separatrix that divides the umbral and penumbral magnetic field regions, in a slice through the centre of the sunspot. The units of the colour bars are kgm^{-3}. 97

3.13 This figure shows the evolution of temperature in a slice through the centre of the sunspot during the lifetime of the simulation. The sub-figures, moving from top to bottom, show the temperature at times when the sunspot has been rotated by 0°, 30°, 45°, 60° and 75° by the driver respectively. The units of the colour bars are Kelvin (K). . 101

3.14 This figure shows the evolution of temperature in a slice through the centre of the sunspot during the lifetime of the simulation. The sub-figures, moving from top to bottom, show the temperature at times when the sunspot has been rotated by 90°, 105°, 120°, 135° and 140° by the driver respectively. The units of the colour bars are Kelvin (K).102

4.1 A line plot showing the volume of the penumbra throughout the simulation. 114

4.2 A line plot showing the volume of the umbra throughout the simulation.115

4.3 This figure shows the magnetic field and separatrix during the simulation. The separatrix is shown by the blue isosurface. The sub-figures, moving from top to bottom, show the this at times when the sunspot has been rotated by 0°, 30°, 45°, 60° and 75° by the driver respectively.117

4.4 This figure shows the magnetic field and separatrix during the simulation. The separatrix is shown by the blue isosurface. The sub-figures, moving from top to bottom, show this at times when the sunspot has been rotated by 90°, 105°, 120°, 135° and 140° by the driver respectively.118

4.5 This figure shows a streamline plot of the velocity projected onto a horizontal slice (where the vertical direction is the z-direction) at a height of 15.625Mm above the photosphere, at an arbitrary time during the simulation. This figure illustrates the characteristic horizontal flow pattern that develops within the domain, in response to the photospheric driving. The colours indicate the magnitude of the velocity, where red is assigned to the largest speed and blue the smallest speed. The colours are ordered blue, green, yellow then red. The colour coding is normalised and purely indicates relative speed. 119

4.6 This figure shows the distribution of α throughout the domain in a slice through the centre of the sunspot. The sub-figures, moving from top to bottom, show the this at times when the sunspot has been rotated by 0°, 30°, 45°, 60° and 75° by the driver respectively. The black contour represents the approximate location of the separatrix that divides the umbral and penumbral magnetic field regions, in a slice through the centre of the sunspot. The units of the colour bars are m^{-1}, but for compactness the colour bars are normalised by μ_0, meaning they each range from $-\mu_0(\mathrm{m}^{-1})$ to $\mu_0(\mathrm{m}^{-1})$. 123

4.7 This figure shows the distribution of α throughout the domain in a slice through the centre of the sunspot. The sub-figures, moving from top to bottom, show this at times when the sunspot has been rotated by 90°, 105°, 120°, 135° and 140° by the driver respectively. The black contour represents the approximate location of the separatrix that divides the umbral and penumbral magnetic field regions, in a slice through the centre of the sunspot. The units of the colour bars are m^{-1}, but for compactness the colour bars are normalised by μ_0, meaning they each range from $-\mu_0(\mathrm{m}^{-1})$ to $\mu_0(\mathrm{m}^{-1})$. 124

4.8 This figure shows the distribution of α in the penumbral and umbral regions. Specifically, the top figure shows a histogram of α in the penumbra, the middle shows the same in the umbra and the bottom sub-figure shows the magnetic field line and separatrix plot at the same time. The sunspot has been rotated by 30° in this figure. 127
4.9 This figure shows the distribution of α in the penumbral and umbral regions. Specifically, the top figure shows a histogram of α in the penumbra, the middle shows the same in the umbra and the bottom sub-figure shows the magnetic field line and separatrix plot at the same time. The sunspot has been rotated by 45° in this figure. 128
4.10 This figure shows the distribution of α in the penumbral and umbral regions. Specifically, the top figure shows a histogram of α in the penumbra, the middle shows the same in the umbra and the bottom sub-figure shows the magnetic field line and separatrix plot at the same time. The sunspot has been rotated by 60° in this figure. 129
4.11 This figure shows the distribution of α in the penumbral and umbral regions. Specifically, the top figure shows a histogram of α in the penumbra, the middle shows the same in the umbra and the bottom sub-figure shows the magnetic field line and separatrix plot at the same time. The sunspot has been rotated by 75° in this figure. 130
4.12 This figure shows the distribution of α in the penumbral and umbral regions. Specifically, the top figure shows a histogram of α in the penumbra, the middle shows the same in the umbra and the bottom sub-figure shows the magnetic field line and separatrix plot at the same time. The sunspot has been rotated by 80° in this figure. 131

4.13 This figure shows the distribution of α in the penumbral and umbral regions. Specifically, the top figure shows a histogram of α in the penumbra, the middle shows the same in the umbra and the bottom sub-figure shows the magnetic field line and separatrix plot at the same time. The sunspot has been rotated by 90° in this figure. 132
4.14 This figure shows the distribution of α in the penumbral and umbral regions. Specifically, the top figure shows a histogram of α in the penumbra, the middle shows the same in the umbra and the bottom sub-figure shows the magnetic field line and separatrix plot at the same time. The sunspot has been rotated by 120° in this figure. . . . 133
4.15 This figure shows the distribution of α in the penumbral and umbral regions. Specifically, the top figure shows a histogram of α in the penumbra, the middle shows the same in the umbra and the bottom sub-figure shows the magnetic field line and separatrix plot at the same time. The sunspot has been rotated by 135° in this figure. . . . 134
4.16 This figure shows the distribution of current helicity throughout the domain in a slice through the centre of the sunspot. The sub-figures, moving from top to bottom, show the this at times when the sunspot has been rotated by 0°, 30°, 45°, 60° and 75° by the driver respectively. The black contour represents the approximate location of the separatrix that divides the umbral and penumbral magnetic field regions, in a slice through the centre of the sunspot. The units of the colour bars are TAm^{-2}. 139

4.17 This figure shows the distribution of current helicity throughout the domain in a slice through the centre of the sunspot. The sub-figures, moving from top to bottom, show this at times when the sunspot has been rotated by 90°, 105°, 120°, 135° and 140° by the driver respectively. The black contour represents the approximate location of the separatrix that divides the umbral and penumbral magnetic field regions, in a slice through the centre of the sunspot. The units of the colour bars are TAm^{-2}. 140

4.18 Multiple line plots showing the total current helicity in the full domain (black), the penumbra (blue) and the umbra (red) as a function of rotation. 142

5.1 This figure shows the magnitude of the Lorentz force during the simulation in a slice through the centre of the sunspot. The sub-figures, moving from top to bottom, show this at times when the sunspot has been rotated by 30°, 45°, 60° and 75° by the driver respectively. The white contour represents the approximate location of the separatrix that divides the umbral and penumbral magnetic field regions, in a slice through the centre of the sunspot. The units of the colour bars are Nm^{-3}. 149

5.2 This figure shows the magnitude of the Lorentz force during the simulation in a slice through the centre of the sunspot. The sub-figures, moving from top to bottom, show this at times when the sunspot has been rotated by 90°, 105°, 120°, 135° and 140° by the driver respectively. The white contour represents the approximate location of the separatrix that divides the umbral and penumbral magnetic field regions, in a slice through the centre of the sunspot. The units of the colour bars are Nm^{-3}. 150

5.3 This figure shows the magnitude of the acceleration induced by the Lorentz force during the simulation in a slice through the centre of the sunspot. The sub-figures, moving from top to bottom, show this at times when the sunspot has been rotated by 30°, 45°, 60° and 75° by the driver respectively. The white contour represents the approximate location of the separatrix that divides the umbral and penumbral magnetic field regions, in a slice through the centre of the sunspot. The units of the colour bars is $m^{-2}s^{-2}$. 153

5.4 This figure shows the magnitude of the acceleration induced by the Lorentz force during the simulation in a slice through the centre of the sunspot. The sub-figures, moving from top to bottom, show this at times when the sunspot has been rotated by 90°, 105°, 120°, 135° and 140° by the driver respectively. The white contour represents the approximate location of the separatrix that divides the umbral and penumbral magnetic field regions, in a slice through the centre of the sunspot. The units of the colour bars is $m^{-2}s^{-2}$. 154

5.5 This figure shows the magnitude of the gradient of thermal pressure during the simulation in a slice through the centre of the sunspot. The sub-figures, moving from top to bottom, show this at times when the sunspot has been rotated by 30°, 45°, 60° and 75° by the driver respectively. The white contour represents the approximate location of the separatrix that divides the umbral and penumbral magnetic field regions, in a slice through the centre of the sunspot. The units of the colour bars are Nm^{-3}. 161

5.6 This figure shows the magnitude of the gradient of thermal pressure during the simulation in a slice through the centre of the sunspot. The sub-figures, moving from top to bottom, show this at times when the sunspot has been rotated by 90°, 105°, 120°, 135° and 140° by the driver respectively. The white contour represents the approximate location of the separatrix that divides the umbral and penumbral magnetic field regions, in a slice through the centre of the sunspot. The units of the colour bars are Nm^{-3}. 162

5.7 This figure shows the magnitude of the acceleration induced by the gradient of thermal pressure during the simulation in a slice through the centre of the sunspot. The sub-figures, moving from top to bottom, show this at times when the sunspot has been rotated by 30°, 45°, 60° and 75° by the driver respectively. The white contour represents the approximate location of the separatrix that divides the umbral and penumbral magnetic field regions, in a slice through the centre of the sunspot. The units of the colour bars is $m^{-2}s^{-2}$. 165

5.8 This figure shows the magnitude of the acceleration induced by the gradient of thermal pressure during the simulation in a slice through the centre of the sunspot. The sub-figures, moving from top to bottom, show this at times when the sunspot has been rotated by 90°, 105°, 120°, 135° and 140° by the driver respectively. The white contour represents the approximate location of the separatrix that divides the umbral and penumbral magnetic field regions, in a slice through the centre of the sunspot. The units of the colour bars is $m^{-2}s^{-2}$. . . 166

5.9 This figure shows the magnitude of the total acceleration induced by all forces during the simulation in a slice through the centre of the sunspot. The sub-figures, moving from top to bottom, show this at times when the sunspot has been rotated by 30°, 45°, 60° and 75° by the driver respectively. The white contour represents the approximate location of the separatrix that divides the umbral and penumbral magnetic field regions, in a slice through the centre of the sunspot. The units of the colour bars is $m^{-2}s^{-2}$. 171

5.10 This figure shows the magnitude of the total acceleration induced by all forces during the simulation in a slice through the centre of the sunspot. The sub-figures, moving from top to bottom, show this at times when the sunspot has been rotated by 90°, 105°, 120°, 135° and 140° by the driver respectively. The white contour represents the approximate location of the separatrix that divides the umbral and penumbral magnetic field regions, in a slice through the centre of the sunspot. The units of the colour bars is $m^{-2}s^{-2}$. 172

5.11 This figure shows the evolution of the dominant energies during the simulation. The top figure shows the evolution of the change of magnetic energy, the middle figure shows the evolution of the change of internal energy and the bottom figure shows evolution of the change of the kinetic energy (where ΔE_b, ΔE_ϵ and ΔE_{ke} represent the changes of magnetic, internal and kinetic energies respectively). In all cases the black line shows the domain total, the red line shows the umbral total and the blue line shows the penumbral total. 175

5.12 This figure shows the magnitude of the kinetic energy integrated over a grid cell during the simulation in a slice through the centre of the sunspot. The sub-figures, moving from top to bottom, show this at times when the sunspot has been rotated by 30°, 45°, 60° and 75° by the driver respectively. The black contour represents the approximate location of the separatrix that divides the umbral and penumbral magnetic field regions, in a slice through the centre of the sunspot. The units of the colour bars are Joules (J). 179

5.13 This figure shows the rate of change of the magnetic energy caused by the Lorentz force and velocity. The top figure shows this for the full domain, the middle figure for the penumbral region and the bottom figure for the umbral region. In all figures the black curves represent the total change of magnetic energy caused by the Lorentz force and velocity, the magenta and green lines show the total positive and negative change respectively. The blue line in the top figure shows the measured rate of change of the magnetic energy as measured over the whole domain (i.e. it includes the energy from the Poynting flux through the photosphere). 186

6.1 The power law fit for simulation number 1 (table 6.1). The solid-black curve shows the percentage change of the magnetic energy versus cumulative rotation and the dashed-red curve shows the power-law fit approximation. The blue shaded region between $\theta_1 = 70°$ and $\theta_2 = 130°$ defines the region where the power-law fit has been made. 194

6.2 This figure shows the percentage energy increase versus rotation for all the simulations in the batch which varies only peak umbral field strength (U_b) with $\mu = 0.5$. The figure uses logarithmic-logarithmic axes and therefore focuses mainly on the acceleration-phase of the simulations (which spans $0° - 32°$ for all simulations in this figure). The model properties and initial magnetic energy of each simulation shown in this figure are tabulated in table 6.1. 198

6.3 This figure shows the percentage energy increase versus rotation for all the simulations in the batch which varies only peak umbral field strength (U_b) with $\mu = 0.5$. This figure shows the same data as shown in figure 6.3, but focuses on the main-phase of the simulations. The x-axis ranges from $25° - 200°$ where the acceleration-phase of all the simulations shown ends at 32°, hence the majority of the acceleration-phase is omitted. The model properties and initial magnetic energy of each simulation shown in this figure are tabulated in table 6.1. . . 200

6.4 A plot showing the relationship between power-law fitting parameter, k, and independent sunspot model parameter, U_b. The red plus symbols depict the data-points for k tabulated in table 6.2 and the solid black line represents the interpolant described by equation 6.8. 206

6.5 A plot showing the relationship between power-law fitting parameter, a, and independent sunspot model parameter, U_b. The red plus symbols depict the data-points for a tabulated in table 6.2 and the solid black line represents the interpolant described by equation 6.9. 207

6.6 A plot showing the relationship between power-law fitting parameter, τ, and independent sunspot model parameter, U_b. The red plus symbols depict the data-points for τ derived as the product of column k and E_0 which are tabulated in table 6.2 and the solid black line represents the interpolant described by equation 6.12. 210

6.7 A contour plot of the injected magnetic energy as a function of peak umbral field strength (U_b) and rotation. Each contour label shows the numeric value of magnetic energy measured in joules. 213

6.8 A multi-line plot showing the percentage magnetic energy increase versus rotation curves for the simulations which vary penumbral radius (P_r) and the umbral radius (U_r) in proportion. 218

6.9 A plot showing the relationship between power-law fitting parameter, k, and independent sunspot model parameter, P_r. The red plus symbols depict the data-points for k tabulated in table 6.4 and the solid black line represents the interpolant described by equation 6.15. . . . 220

6.10 A plot showing the relationship between power-law fitting parameter, a, and independent sunspot model parameter, P_r. The red plus symbols depict the data-points for a tabulated in table 6.4 and the solid black line represents the interpolant described by equation 6.16. . . . 221

6.11 A plot showing the relationship between power-law fitting parameter, τ, and independent sunspot model parameter, P_r. The red plus symbols depict the data-points for τ derived using data tabulated in table 6.4 and the solid black line represents the interpolant described by equation 6.17. 222

6.12 A contour plot of the injected magnetic energy as a function of penumbral radius, P_r(Mm), and rotation. Each contour label shows the numeric value of magnetic energy measured in joules. 223

6.13 The percentage increase of magnetic energy versus rotation evolution for simulation number 3, a low peak field strength simulation from the U_b investigation. The solid-black curve shows the measured magnetic energy from the simulation data and the dashed-red curve the power-law approximation based on the, post-acceleration, main-phase of the simulation. 226

6.14 A collection of line plots each showing the evolution of the measured percentage increase of magnetic energy versus rotation, the legend shows the rotation rate of each simulation where the value is given in units of degrees per hour. 228

6.15 A plot showing the relationship between power-law fitting parameter, k, and independent sunspot model parameter, ω. The red plus symbols depict the data-points for k tabulated in table 6.6 and the solid black line represents the interpolant described by equation 6.19. . . . 231

6.16 A plot showing the relationship between power-law fitting parameter, a, and independent sunspot model parameter, ω. The red plus symbols depict the data-points for a tabulated in table 6.6 and the solid black line represents the interpolant described by equation 6.20. . . . 232

6.17 A plot showing the relationship between power-law fitting parameter, τ, and independent sunspot model parameter, ω. The red plus symbols depict the data-points for τ calculated using data tabulated in table 6.6 and the solid black line represents the interpolant described by equation 6.21. 233

6.18 A contour plot of the injected magnetic energy as a function of rotation rate, $\omega\,(^\circ\,\mathrm{hr}^{-}1)$ and rotation. Each contour label shows the numeric value of magnetic energy measured in joules. 235

6.19 A collection of line plots each showing the evolution of the measured percentage increase of magnetic energy versus rotation, the legend shows the ψ value of each simulation. 238
6.20 A plot showing the relationship between power-law fitting parameter, k, and independent sunspot model parameter, ψ. The red plus symbols depict the data-points for k tabulated in table 6.8 and the solid black line represents the interpolant described by equation 6.23. . . . 240
6.21 A plot showing the relationship between power-law fitting parameter, a, and independent sunspot model parameter, ψ. The red plus symbols depict the data-points for a tabulated in table 6.8 and the solid black line represents the interpolant described by equation 6.24. . . . 241
6.22 A plot showing the relationship between power-law fitting parameter, τ, and independent sunspot model parameter, ψ. The red plus symbols depict the data-points for τ calculated using data tabulated in table 6.8 and the solid black line represents the interpolant described by equation 6.25. 242
6.23 A contour plot of the injected magnetic energy as a function of ψ and rotation. Each contour label shows the numeric value of magnetic energy measured in joules. Top-right contours are 1.5×10^{24}j and 2×10^{24}j moving from the centre of the plot to the top-right corner respectively. 243
6.24 A collection of line plots showing the evolution of the measured percentage increase of magnetic energy versus rotation, for the simulations that vary the parameter μ. The legend shows the μ value of each simulation curve. 246

6.25 A plot showing the relationship between power-law fitting parameter, k, and independent sunspot model parameter, μ. The red plus symbols depict the data-points for k tabulated in table 6.10 and the solid black line represents the interpolant described by equation 6.27. . . . 250
6.26 A plot showing the relationship between power-law fitting parameter, a, and independent sunspot model parameter, μ. The red plus symbols depict the data-points for a tabulated in table 6.10 and the solid black line represents the interpolant described by equation 6.28. . . . 251
6.27 A plot showing the relationship between power-law fitting parameter, τ, and independent sunspot model parameter, μ. The red plus symbols depict the data-points for τ calculated using data tabulated in table 6.4 and the solid black line represents the interpolant described by equation 6.29. 252
6.28 A contour plot of the injected magnetic energy as a function of μ and rotation. Each contour label shows the numeric value of magnetic energy measured in joules. 254
6.29 This figure shows the magnetic energy versus rotation evolution for a simulated sunspot with $U_b = 1592$G, $\omega = 24°\text{hr}^{-1}$ and all other model parameters equal to those of simulation 1. The black curve shows the measured energy increase and the red dashed curve shows an approximation calculated using equation 6.38. 262
6.30 This figure shows the magnetic energy versus rotation evolution for a simulated sunspot with $U_b = 1838$G, $\omega = 24°\text{hr}^{-1}$ and all other model parameters equal to those of simulation 1. The black curve shows the measured energy increase and the red dashed curve shows an approximation calculated using equation 6.38. 263

6.31 This figure shows the magnetic energy versus rotation evolution for a simulated sunspot with U_b = 2600G, P_r = 15Mm and all other model parameters equal to those of simulation 1. The black curve shows the measured energy increase and the red dashed curve shows an approximation calculated using equation 6.38. 265

7.1 This figure shows the magnetic field of a tall sunspot simulation with the same simulation parameters as simulation 1. The upper domain of this simulation is static. The sunspot is shown at 135° rotation. . . 277

7.2 This figure shows the magnetic field of a tall sunspot simulation with a second sunspot on the top boundary, both sunspots use the same simulation parameters as simulation 1. The sunspot at the upper domain of this simulation is rotated similarly to the lower sunspot. The sunspots are shown at 135° rotation. 278

7.3 This figure shows the magnetic field of a tall sunspot simulation with a second sunspot on the top boundary, both sunspots use the same simulation parameters as simulation 1. The sunspot at the upper domain of this simulation is not rotated. The lower sunspot has rotated by 135°. 280

7.4 This figure shows the magnetic field of a tall sunspot simulation with a second sunspot on the top boundary, both sunspots use the same simulation parameters as simulation 1. The sunspot at the upper domain of this simulation is rotated oppositely to the lower sunspot. The sunspots are shown at 135° rotation. 281

7.5 A multi-line plot showing the excess magnetic energy versus rotation profile for the tall-domain sunspots discussed section 7.5. The black line shows the evolution of the counter rotating sunspot system, the red shows the evolution of the two sunspot system where only one is rotating, the blue curve shows the evolution of the connected similar rotating sunspots and the green curve shows the single sunspot evolution. 282

7.6 This figure shows the magnetic energy evolution of several identical rotating sunspot simulations with various background resistivities. The black line shows the evolution of simulation 1, the green line shows the evolution of a rotating sunspot where $\eta = 3e5\mu_0$, the orange curve shows the evolution of a rotating sunspot where $\eta = 3e6\mu_0$, the blue curve shows the same evolution where $\eta = 3e7\mu_0$ and the purple curve shows when $\eta = 1500$. 285

A.1 This figure shows the power-law fit for simulation number 1. 289

B.1 This figure shows the power-law fit for simulation number 3. 290

B.2 This figure shows the power-law fit for simulation number 4. 291

B.3 This figure shows the power-law fit for simulation number 5. 291

B.4 This figure shows the power-law fit for simulation number 6. 292

B.5 This figure shows the power-law fit for simulation number 7. 292

B.6 This figure shows the power-law fit for simulation number 8. 293

B.7 This figure shows the power-law fit for simulation number 9. 293

B.8 This figure shows the power-law fit for simulation number 10. 294

B.9 This figure shows the power-law fit for simulation number 11. 294

B.10 This figure shows the power-law fit for simulation number 12. 295

B.11 This figure shows the power-law fit for simulation number 13. 295

B.12 This figure shows the power-law fit for simulation number 14. 296

B.13 This figure shows the power-law fit for simulation number 15. 296
B.14 This figure shows the power-law fit for simulation number 16. 297
B.15 This figure shows the power-law fit for simulation number 17. 297
B.16 This figure shows the power-law fit for simulation number 18. 298
B.17 This figure shows the power-law fit for simulation number 19. 298

C.1 This figure shows the power-law fit for simulation number 33. 299
C.2 This figure shows the power-law fit for simulation number 34. 300
C.3 This figure shows the power-law fit for simulation number 35. 300
C.4 This figure shows the power-law fit for simulation number 36. 301
C.5 This figure shows the power-law fit for simulation number 37. 301
C.6 This figure shows the power-law fit for simulation number 38. 302
C.7 This figure shows the power-law fit for simulation number 39. 302
C.8 This figure shows the power-law fit for simulation number 40. 303
C.9 This figure shows the power-law fit for simulation number 41. 303
C.10 This figure shows the power-law fit for simulation number 42. 304
C.11 This figure shows the power-law fit for simulation number 43. 304
C.12 This figure shows the power-law fit for simulation number 44. 305

D.1 This figure shows the power-law fit for simulation number 20. 306
D.2 This figure shows the power-law fit for simulation number 21. 307
D.3 This figure shows the power-law fit for simulation number 22. 307
D.4 This figure shows the power-law fit for simulation number 23. 308
D.5 This figure shows the power-law fit for simulation number 24. 308

E.1 This figure shows the power-law fit for simulation number 45. 309
E.2 This figure shows the power-law fit for simulation number 46. 310
E.3 This figure shows the power-law fit for simulation number 47. 310
E.4 This figure shows the power-law fit for simulation number 48. 311

E.5 This figure shows the power-law fit for simulation number 49. 311
E.6 This figure shows the power-law fit for simulation number 50. 312
E.7 This figure shows the power-law fit for simulation number 51. 312
E.8 This figure shows the power-law fit for simulation number 52. 313
E.9 This figure shows the power-law fit for simulation number 53. 313

F.1 This figure shows the power-law fit for simulation number 25. 314
F.2 This figure shows the power-law fit for simulation number 26. 315
F.3 This figure shows the power-law fit for simulation number 27. 315
F.4 This figure shows the power-law fit for simulation number 28. 316
F.5 This figure shows the power-law fit for simulation number 29. 316
F.6 This figure shows the power-law fit for simulation number 30. 317
F.7 This figure shows the power-law fit for simulation number 31. 317
F.8 This figure shows the power-law fit for simulation number 32. 318

G.1 This figure shows the power-law fit for simulation number 54. 319
G.2 This figure shows the power-law fit for simulation number 55. 320
G.3 This figure shows the power-law fit for simulation number 56. 320
G.4 This figure shows the power-law fit for simulation number 57. 321
G.5 This figure shows the power-law fit for simulation number 58. 321
G.6 This figure shows the power-law fit for simulation number 59. 322
G.7 This figure shows the power-law fit for simulation number 60. 322
G.8 This figure shows the power-law fit for simulation number 61. 323
G.9 This figure shows the power-law fit for simulation number 62. 323
G.10 This figure shows the power-law fit for simulation number 63. 324
G.11 This figure shows the power-law fit for simulation number 64. 324
G.12 This figure shows the power-law fit for simulation number 65. 325
G.13 This figure shows the power-law fit for simulation number 66. 325

Acknowledgements

I would like to thank my supervisors, Daniel Brown and Gert Botha, for their constant support and patience during my PhD, without which the work in this thesis would surely not exist. I would also like to thank the solar physics research group within the Jeremiah Horrocks Institute, for the invaluable guidance they have provided throughout my PhD. I thank all members, staff and student, of the Jeremiah Horrocks Institute for their endless support during the creation of this thesis. Special thanks go to Gert Botha and Stéphane Régnier for providing the training and continued guidance that made the numerical work in this thesis possible, with additional thanks owed to Northumbria University's solar physics group for allowing me to use their computational resources to run most of the simulations presented in this thesis. I would like to thank the STFC for funding my PhD and wish to extend particular thanks to the two anonymous reviewers who supported my application for computational resources, which ultimately resulted in the DiRAC award that was used to produce many of the simulations in this thesis. Finally, I would like to thank my partner, Hayley for her endless support throughout my PhD.

Chapter 1

Introduction

Sunspots are relatively cool, and consequentially dark, regions of the photosphere that are permeated by strong magnetic fields. The magnetic flux within a sunspot originates from within the Sun, intersect the photosphere at the sunspot and can extend into the solar atmosphere. In this thesis we model and simulate idealised rotating sunspots, to better understand how they influence their magnetic environments. We do this because a significant amount of energy is required to explain the observed behaviour of the solar atmosphere (Withbroe and Noyes, 1977), in particular extreme solar eruptions require vast amounts of energy. Sunspot rotation is believed to be a mechanism that may contribute to the energy budget of extreme solar eruptions (Stenflo, 1969; Barnes and Sturrock, 1972; Santos et al., 2011; Török et al., 2013; Wang et al., 2022). Sunspot rotation, in the context of this work, concerns sunspots that rotate about their centres, examples are presented in Brown et al. (2003); Walker (2018); Grimes et al. (2020) and Brown and Walker (2021). Other studies investigate sunspot rotation defined as sunspots rotating around one another, as in Gerrard et al. (2003) and Yan et al. (2008), or sunspot rotation as a consequence of emerging flux, as in Sturrock et al. (2015b) and Sturrock and Hood (2016).

An additional aim of this investigation is to understand the importance of the

penumbra during sunspot rotation, because the penumbra has previously received little dedicated attention in comparative studies. More generally, we wish to understand how much energy a rotating sunspot produces during its lifetime based on its geometry, and identify the mechanisms by which this energy is created. At the time of writing, the work within this thesis is relevant to a number of outstanding scientific questions recognised internationally. The United Kingdom's Science and Technology Facilities Council (STFC) lists a number of outstanding scientific challenges deemed important to the current state of scientific progress. Of the STFC challenges (STFC, 2019), this work is relevant to the following, B:6 What are the processes that drive space weather?, B:1 How does the Sun and other stars work and what drives their variability? and B:2 What effects do the Sun and other stars have on their local environment? Hence, the findings of this work are recognised for their importance in the community, but specifically will contribute the a fuller understanding of the energy generation properties of sunspot rotation.

1.1 Space Weather

Space weather is a collective term associated with a number of phenomena that are correlated with solar activity. These phenomena originate from the Sun and can negatively impact modern life on the Earth (Eastwood et al., 2017). There are two main physical phenomena synonymous with the term space weather that sunspot rotation may be coupled with. These are coronal mass ejections and solar flares.

Coronal mass ejections are characterised by an expulsion of material, often at great velocity, from the Sun's corona. Typical speeds are in the range $200 - 3000\text{kms}^{-1}$ and total masses can be in excess of 10^{12}kg. Hence they carry vast amounts of kinetic energy away from the solar atmosphere. However, because the material transported by a coronal mass ejection originates from the magnetised, hot, solar atmosphere, large amounts of magnetic and internal energies stored in expelled

material are also transported away from the Sun by a coronal mass ejection. Coronal mass ejections can cause severe consequences if they encounter the Earth, a number of these consequences and their impacts are discussed by Eastwood et al. (2017). In summary, coronal mass ejections are recognised as a risk to modern life and are included (under space weather) in the government's national risk register.

The study of coronal mass ejections is a comprehensive topic and a proper description of the full complexity of phenomenon itself, the mechanisms which cause them and cataloguing and studying their general observed properties lies beyond of the scope of this investigation, but there is a wealth of literature devoted to these studies (Byrne et al., 2009; Howard, 2011; Howard and Tappin, 2009; Byrne, 2012, 2015; Harrison and Bewsher, 2007; Harrison et al., 2018; Gopalswamy et al., 2009, 2006; Usoskin, 2017; Pérez-Suárez et al., 2011; Materassi et al., 2011; Hutton and Morgan, 2017; Gonzalez et al., 1999). The important property of coronal mass ejections with respect to this investigation, is that they all carry energies away from the Sun's atmosphere. Coronal mass ejections occur regularly throughout the solar cycle (Gopalswamy et al., 2009), meaning that large expulsions of energy occur regularly. We observe the Sun's atmosphere remains highly energetic and thus, something must be contributing to the energy budget of coronal mass ejections. One such mechanism may be sunspot rotation.

Solar flares are the second phenomenon associated with the term space weather that sunspot rotation may be linked with (Yang, 2019). Solar flares are characterised by a sudden emission of electromagnetic energy that can be measured across the entire electromagnetic spectrum. Flares occur when free magnetic energy in the solar atmosphere is converted to kinetic and thermal energy via the process of magnetic reconnection (Priest, 2014). Thus, solar flares occur when there is excess magnetic energy to power them. They are classified in a number of ways, but a popular

classification system characterises the strength of a solar flare by the peak soft X-ray flux intensity, emitted by the flare, that is measured by the GOES satellites in the 1 to 8Å passband (Priest, 2014). Golub and Pasachoff (2010) explain that this classification system has five categories, A, B, C, M and X of which A represents the least energetic flares and X the most. The classification system uses a logarithmic scaling, for example a solar flare is designated as X-class if its measured peak soft X-ray intensity reaches $10^{-4}\mathrm{Wm}^{-2}$ (Golub and Pasachoff, 2010). It logically follows, that due to the logarithmic scaling, an M-class flare has a peak soft X-ray intensity of $10^{-5}\mathrm{Wm}^{-2}$. Similarly, C, B and A-class flares have peak intensities of $10^{-6}\mathrm{Wm}^{-2}$, $10^{-7}\mathrm{Wm}^{-2}$ and $10^{-8}\mathrm{Wm}^{-2}$ respectively. The classification system is further divided based on the actual measured peak intensity, for example if a peak intensity of $2 \times 10^{-5}\mathrm{Wm}^{-2}$ is measured the flare would be designated as M2. There is no classification above X-class, so a peak intensity of $200 \times 10^{-4}\mathrm{Wm}^{-2}$ would be denoted as X200 (however, this magnitude is one order larger than the largest measured solar flare on record). An X-class solar flare can release over 10^{25}J of energy that must be supplied to the solar atmosphere in some way. Sunspot rotation is one, of many, recognised mechanisms to provide some or all of this required energy (Zhang et al., 2007). Like CMEs, the study of solar flares is vast and there is a wealth of literature devoted to explaining the physics of flares (Alfven and Carlqvist, 1967; Hudson, 2011), cataloguing them (Sadykov et al., 2017) and understanding how they are produced (Schrijver, 2009). There also exists a vast amount of studies devoted to the investigation of specific events.

Solar flares and coronal mass ejections impose significant risk to civilisation and technology on Earth and in space, either directly or indirectly (Eastwood et al., 2017). To mitigate the impacts of space weather, a full understanding of how these phenomena are powered is fundamentally important. A more complete understanding will enable better prediction, which is currently the best means of protection

from the most severe instances of space weather.

This investigation recognises and aims to investigate the common themes present in many solar flare and coronal mass ejection studies, specifically that they are extremely energetic events that must be powered in some way. We investigate numerically the possible contribution to the energy budget of extreme space weather events made by sunspot rotation. Currently sunspot rotation is recognised as an important energisation mechanism, but this study addresses the specifics of how and why it is important, with the intent to develop a means to identify which sunspots are likely to be most linked to extreme space weather events.

1.2 Active Regions and Sunspots

Above a group of sunspots, the conglomeration of magnetic fields (and the plasma embedded within them) forms what are known as active regions. Active regions are associated with the emergence of magnetic flux through the photosphere from within the Sun and are assigned a unique identifying number if either a sunspot is present or a solar flare is produced (Phillips, 1992). A popular suggested mechanism for sunspot formation, is the rising of large magnetic flux tubes through the photosphere (Parker, 1955). Thus, the connection between active regions and sunspots is clear, an active region is rooted to some degree in sunspots and therefore the motion of sunspots may influence the magnetic field of an active region. Data from space based missions (Pesnell et al., 2012; Domingo et al., 1995) readily identifies sunspots as the foot-points of active regions that extend far into the corona. Active regions are the most common source regions of the most extreme space weather events, such as solar flares and coronal mass ejections as discussed previously. Figure 1.1 shows three aligned images, the left image is a continuum image that shows a sunspot (the largest relatively dark region), several smaller magnetic elements (the smaller dark entities around the sunspot) and the surrounding photosphere (the uniform lighter region

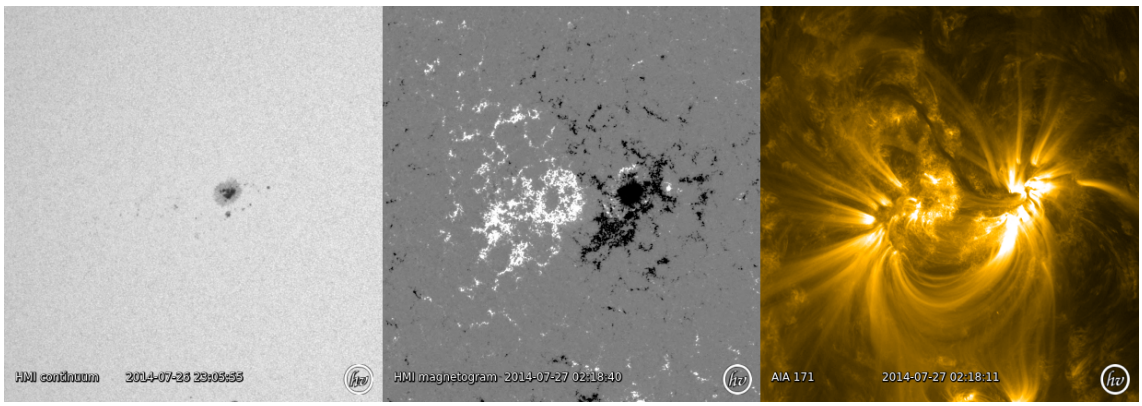

Figure 1.1: Three co-aligned images showing a sunspot (left), a magnetogram showing the normal component of the magnetic field's strength (middle) and an active region observed in 171Å (right). These images were created using helioviewer.org, with data collected by the SDO Pesnell et al. (2012); Lemen et al. (2012); Scherrer et al. (2012).

that forms most of the image). The central image of figure 1.1 is a magnetogram, it shows the distribution of the line-of-sight component of the magnetic field (i.e. the component of the magnetic field that points toward or away from the observer, which here is a space borne satellite located at the first Lagrange point). The magnetogram has a colour scale that ranges from black to white, via grey, where the black regions correspond to where the magnetic field points away from the observer (into the Sun), the white regions correspond to where the magnetic field points toward the observer (out of the Sun) and the grey regions correspond to where the field has lesser (if any) inclination toward or away from the observer. The image on the right of figure 1.1 shows the distribution of electromagnetic radiation, at a wavelength of 171Å, emitted from the solar atmosphere. This wavelength corresponds to a characteristic temperature of $10^{5.8}K$ (Lemen et al., 2012), which (in this particular example) highlights coronal material that traces the magnetic fields that are rooted in the sunspot and other magnetic elements. The curvilinear, bright, loop-like structures present in the right image of figure 1.1 are known as coronal loops.

It shows visually, the connection between sunspots, the magnetic flux which emerges from them and the scale of the active region they contribute to. An important point to make, is that the sunspot (left) appears to be the only dominant feature present and certainly is co-located with magnetic field protruding through the photosphere (middle). But the magnetogram (middle) shows that from a magnetic perspective the sunspot is far from isolated. The EIT 171Åimage (right) shows that the complexity introduced by the magnetogram extends into the third dimension and the connectivity of the magnetic field is very complicated.

1.3 Sunspot Rotation

Sunspot rotation was first observed at the beginning of the twentieth century by Evershed (1909) by means of spectral analysis, thus the study of sunspot rotation itself is neither new nor novel. However, the observed rotational motion of a sunspot alone, although scientifically interesting, does not provide any reason to assume it may be linked with extreme space weather. However, this first observation marks a seminal milestone in the history of our attempts to understand the importance of sunspot rotation.

It took approximately sixty more years after Evershed's first measurement, before the importance of sunspot rotation (in the context of the work presented in this thesis) was recognised. Stenflo (1969) and Barnes and Sturrock (1972) were the first to suggest that the rotational motion of a sunspot may transport energy from the interior of the Sun into the solar atmosphere. This extends the identification of sunspot rotation alone, as it implies that there may be consequences of sunspot rotation far from where the rotation itself is observed. Stenflo (1969) and Barnes and Sturrock (1972) established the causal mechanism which links sunspot rotation to space weather that is a sunspot seen to rotate at the photosphere may transfer energy via the magnetic field into the overlying solar atmosphere. This energy may

be stored and later released by a solar eruption. The introduction of this hypothesis into the literature marks the second key milestone in the history of sunspot rotation. Thus, the solar physics community, at that point, appreciates that sunspot rotation may be linked to the introduction of additional energy into the solar atmosphere. But, a full understanding linking rotating sunspots to the energisation of the solar atmosphere remained out of reach due to a lack of quality observational data.

The advent of the space era delivered a means to understand more quantitatively how rotating sunspots are linked to the energisation of the solar atmosphere. The development of high quality space borne observing instruments (e.g. the Solar Dynamics Observatory (SDO) (Pesnell et al., 2012) and the Solar and Heliospheric Observatory (SOHO) (Domingo et al., 1995)) provided the necessary data to show photospheric motions can lead to most extreme eruptive events (Somov et al., 2002), but has provided a wealth of observational data that can be used to investigate the natural rotation of sunspots. Consequently during the past several decades, multiple methods to measure sunspot rotation have been developed. The methods are diverse and include tracing penumbral features (Brown et al., 2003; Brown and Walker, 2021), magnetic features (Schuck, 2008; Chae and Sakurai, 2008) and umbral intensity profiles (Grimes et al., 2020) and more. Collectively, these studies and the many studies which use or develop from them (e.g. Vemareddy et al. (2012, 2016a); Vemareddy (2017); Zhang et al. (2007); Yan et al. (2008); Török et al. (2013); Botha et al. (2014); Tian and Alexander (2006); Zhu et al. (2012); Liu et al. (2016); Walker (2018); Grimes and Pintér (2022) and many more), have shown that sunspot rotation is most likely an important contributor to the magnetic energisation of the solar atmosphere. Furthermore, the measurement techniques provide a better appreciation for the characteristic properties of sunspot rotation, like rotation rate, duration and acceleration. The development of instruments to observe rotating sunspots and robust techniques to quantify their rotation, mark the next historical milestone in

the study of sunspot rotation.

We are in a new phase of the study of sunspot rotation. Now we not only acknowledge the link between sunspot rotation and energy generation but have a wealth of observational information and a range of literature to guide numerical work. With idealised numerical studies we can better quantify the importance of sunspot rotation by uncovering the coupling between the secular rotation of sunspots and energy generation. We do this so that we may use observations of rotating sunspots to predict extreme space weather events more accurately. Achievement of these goals will define the fourth milestone in the history of sunspot rotation studies.

The primary aim of this study is to make use of the wealth of computational resources that have become available to the scientific community, since the recognition of the importance of sunspot rotation by Stenflo (1969) and Barnes and Sturrock (1972), the development of techniques (e.g. Brown et al. (2003); Schuck (2008); Grimes et al. (2020)) and technologies to measure it (Pesnell et al., 2012; Domingo et al., 1995; Scherrer et al., 2012; Lemen et al., 2012). The work in this thesis is thus rooted in the numerical simulation and analysis of sunspot rotation using the Lare3D code (Arber et al., 2001).

But, we are hindered still by a subtle limitation imposed when studying a natural process like sunspot rotation. Because we wish to understand how rotating sunspots might generate magnetic energy according to their characteristic properties, we can not simulate rotating sunspots that match (to some level of agreement) examples that have been specifically observed. Because sunspots are somewhat unique, if we were to simulate a particular observed sunspot, we cannot be sure the outcome of such a simulation would be indicative for all sunspots, which would yield a very poor tool for extreme space weather prediction. Furthermore, when dealing with real rotating sunspot data, the connectivity of the sunspot to other magnetic features, and the secondary effects the rotation may have because of this, is likely to introduce

additional uncertainties.

1.3.1 Measured and Simulated Sunspot Rotation

The literature linking observations of rotating sunspots to energetic solar flares and CMEs is extensive (Brown et al., 2003; Tian and Alexander, 2006; Yan et al., 2008; Zhu et al., 2012; Zheng et al., 2016; Yan et al., 2012, 2018; Wang et al., 2018; Török et al., 2013; Li and Liu, 2015; Yang, 2019; Grimes et al., 2020; Grimes and Pintér, 2022) to the point that the importance of sunspot rotation must be recognised. Case studies of sunspot rotation are particularly popular as they highlight the potential for it to contribute to the largest X-class flares (Kazachenko et al., 2010; Vemareddy et al., 2012; Török et al., 2013; Vemareddy et al., 2016b), and conversely show that large flares may be able to induce rotation in sunspots (Bi et al., 2016; Liu et al., 2016), highlighting the connection between sunspot rotation and eruptive events extends to the most extreme scale. i.e. sunspot rotation is not a process that only contributes to small eruptions. Yan et al. (2008); Walker (2018) and Brown et al. (2003) performed statistical studies of rotating sunspots. Yan et al. (2008) identified that three types of sunspots are more strongly correlated with M and X-class flares, two correspond to sunspots with mutual rotation about each other (one of these being where one sunspot is also rotating individually). The third corresponds to two sunspots rotating about their axes in the same direction. They also found sunspot rotation that opposes the direction of differential rotation is more likely to produce highly energetic X-class flares. Walker (2018) reports that, on average, sunspot rotation injects more than enough energy to produce X-class flares with a surplus energy of 35%, implying that for smaller eruptions the energy injected by rotation may power multiple events. Collectively, the common theme within observational studies, highlights that the full relationship between sunspot rotation and extreme eruptive events is still not understood, but more importantly that the

physics of sunspot rotation is intricately convolved with other processes and solar features.

Data driven numerical simulation investigations that use real data, as an initial condition or driver, in order to reproduce some observed event have also been performed (Kazachenko et al., 2010; Santos et al., 2011). But they too convolve the effects of rotating sunspots, an evolving photosphere and also additional simulation assumptions. Numerical studies, that include rotating sunspots, that are far more idealised have also been performed, but typically neglect important features like the penumbra either for the sake of simplicity or to investigate far larger scales (e.g. Gerrard et al. (2003); Sturrock and Hood (2016)). A common theme present is the tendency to focus on the larger scale physics, typically either using observational data to drive numerical simulations with the intent of reproducing some violent eruptive event, or entirely numerical (simpler) models where a relatively simple set of connected sunspots are rotating (Sturrock et al., 2015b,a; Sturrock, 2016; Sturrock and Hood, 2016; Gerrard et al., 2003, 2001).

Figure 1.2 shows a HMI continuum image of a sunspot from AR12158 that was observed to rotate, and belonged to an active region that produced an X-class solar flare. The quiver plot projected on top of the image shows an indication of the motion at that time. The quivers are calculated using a, temporally smoothed, optical flow technique based on Horn and Schunck (1981). The colour of the quivers indicates the speed at a point. The important message illustrated by this figure is not the measurement one may make with this information (hence the magnitude of the quivers is omitted), but that sunspot rotation shows complexity at even the most reduced scale (i.e. the figure focuses on the sunspot and surrounding region only). Figure 1.2 shows rotation is clearly observed within the penumbra (upper portion most easily), but generally the motion within the sunspot is highly diverse and complex. Specifically, we see that counter-clockwise rotational motion is easily seen

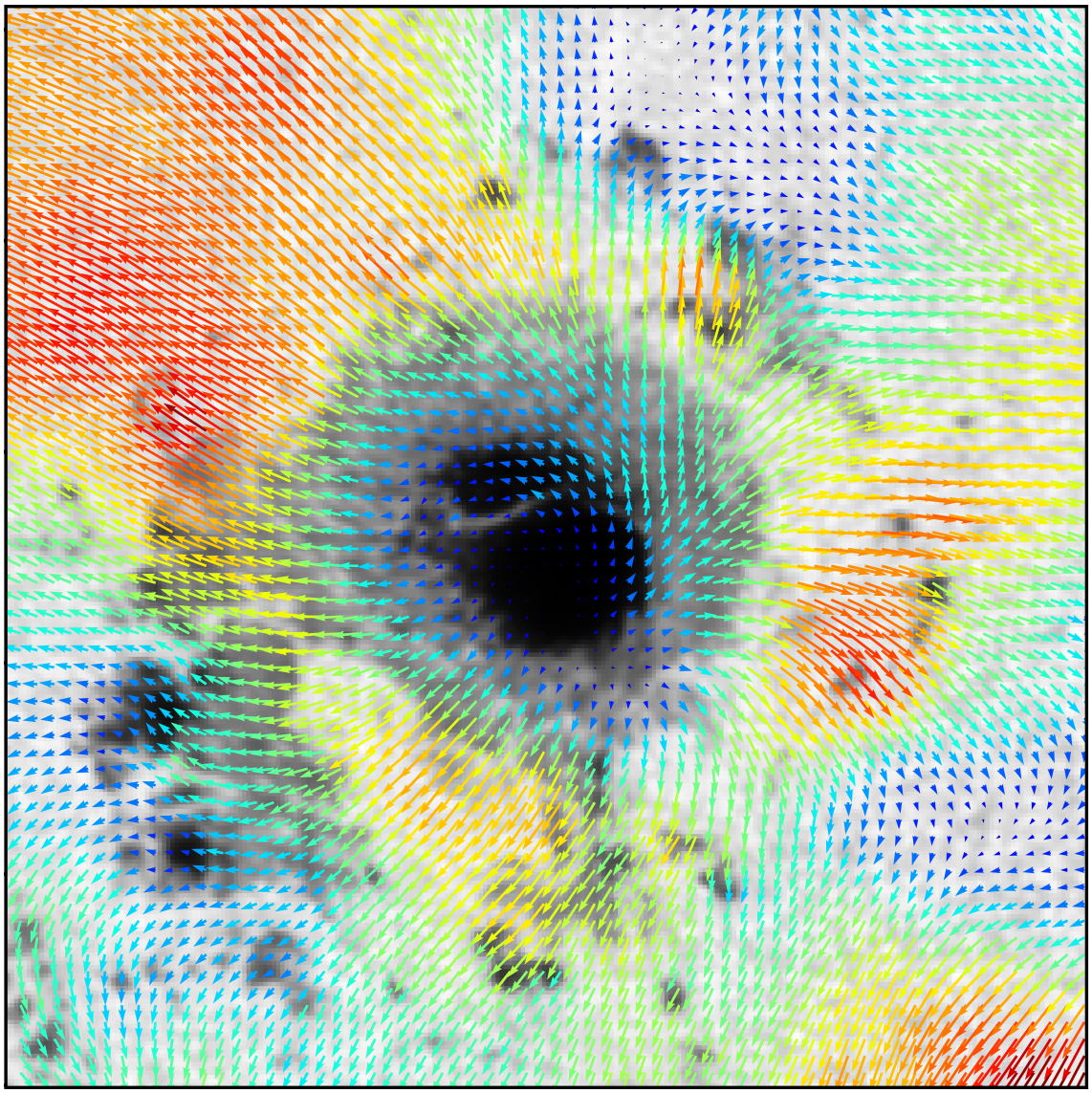

Figure 1.2: This figure shows a HMI continuum (Pesnell et al., 2012; Scherrer et al., 2012; Schou et al., 2012) image of a sunspot from AR12158 and surrounding magnetic features and a quiver plot, over-plotted that indicates the direction of motion. The colour of the quivers indicates the magnitude of the velocity, red indicates greater speed and blue lesser.

in the upper section of the penumbra but is far more difficult to discern elsewhere. In the lower-penumbra, strong divergent flows dominate and in the umbra the rotation is difficult to measure. Secondly, the complex nature shown by this figure grows as it shows magnetic elements in the vicinity of the sunspot that are likely connected in some way via the magnetic field. The motion of the photosphere outside the sunspot is highly chaotic and we see that magnetic elements move without order, and with a range of speeds. Thus, figure 1.2 highlights that even when focusing only on the sunspot and its immediate vicinity, the level of complexity is very high. The above discussion highlights the need to move away from trying to reproduce particular events, or to simulate sunspot rotation in as much detail as possible, because the level of disorder of even a reduced system (as shown by figure 1.2) is too great to meaningfully deconvolve the role of sunspot rotation.

Therefore, the approach adopted in this work is to acknowledge the inherent natural complexity of real rotating sunspot systems, but recognise that to understand sunspot rotation in a general sense we must use a model sunspot that is reduced to its most fundamental components. By developing a model that includes only the most fundamental properties, we may better identify the energy injection properties of real rotating sunspots. But of course, by following this approach we sacrifice a detailed description that may explain more accurately a given rotating sunspot's evolution.

1.4 Sunspots

To develop a meaningful model that can be used to simulate rotating sunspots, we first outline the fundamental properties of natural sunspots relevant to this investigation, so that the simulations in this investigation reflect something physically realistic. To do this we identify the key regions of sunspots but largely focus on the main features that we will use to construct a parametric sunspot model in chapter

2. Sunspots follow the 11-year solar activity cycle (Schwabe, 1844). At the start of the cycle sunspots tend to form at higher latitudes and near the end form closer to the solar equator (Carrington, 1858). Parker (1955) proposed that sunspots form when magnetic flux emerges through the solar surface, which we observe as sunspots (i.e. sunspots are where the flux tubes intersect the photosphere). This mechanism is widely accepted in the solar physics community and is itself a rich topic of research (Cheung and Isobe, 2014; Fan, 2001; Archontis and Hood, 2012a). However, we conclude that sunspots are magnetic structures (Hale, 1908; Hale et al., 1919) rooted within the interior of the Sun, where the magnetic fields alter the appearance of the photosphere.

Figure 1.3 shows an example sunspot. As shown, visually sunspots appear on the solar disk as regions of relatively reduced intensity, with respect to the surrounding photosphere. A sunspot appears dark because the magnetic field within it inhibits the transport of energies into the region (Thomas and Weiss, 2008; Priest, 2014), resulting in the sunspot being cooler than the surrounding photosphere, causing a reduction in intensity. However, this work aims to understand how rotating sunspots might increase magnetic energy in the solar atmosphere and so throughout the remainder of this work, we focus only on the magnetic field and not the cooling it induces. Figure 1.3 shows a dark central region (the umbra) and a slightly lighter outer region (the penumbra). For clarity, in figure 1.3 the umbra is the darkest region centred in the middle of the image, the background photosphere is the brightest region which extends to the boundaries of the figure and the penumbra is the intermediate intensity region between the umbra and background photosphere. These sizes and ratios of the umbral and penumbra are the geometric properties of a sunspot we include in the model. The example sunspot shown in figure 1.3 is presented because it is particularly representative of the sunspots we aim to approximate numerically. The desirable properties of this sunspot are that it is relatively

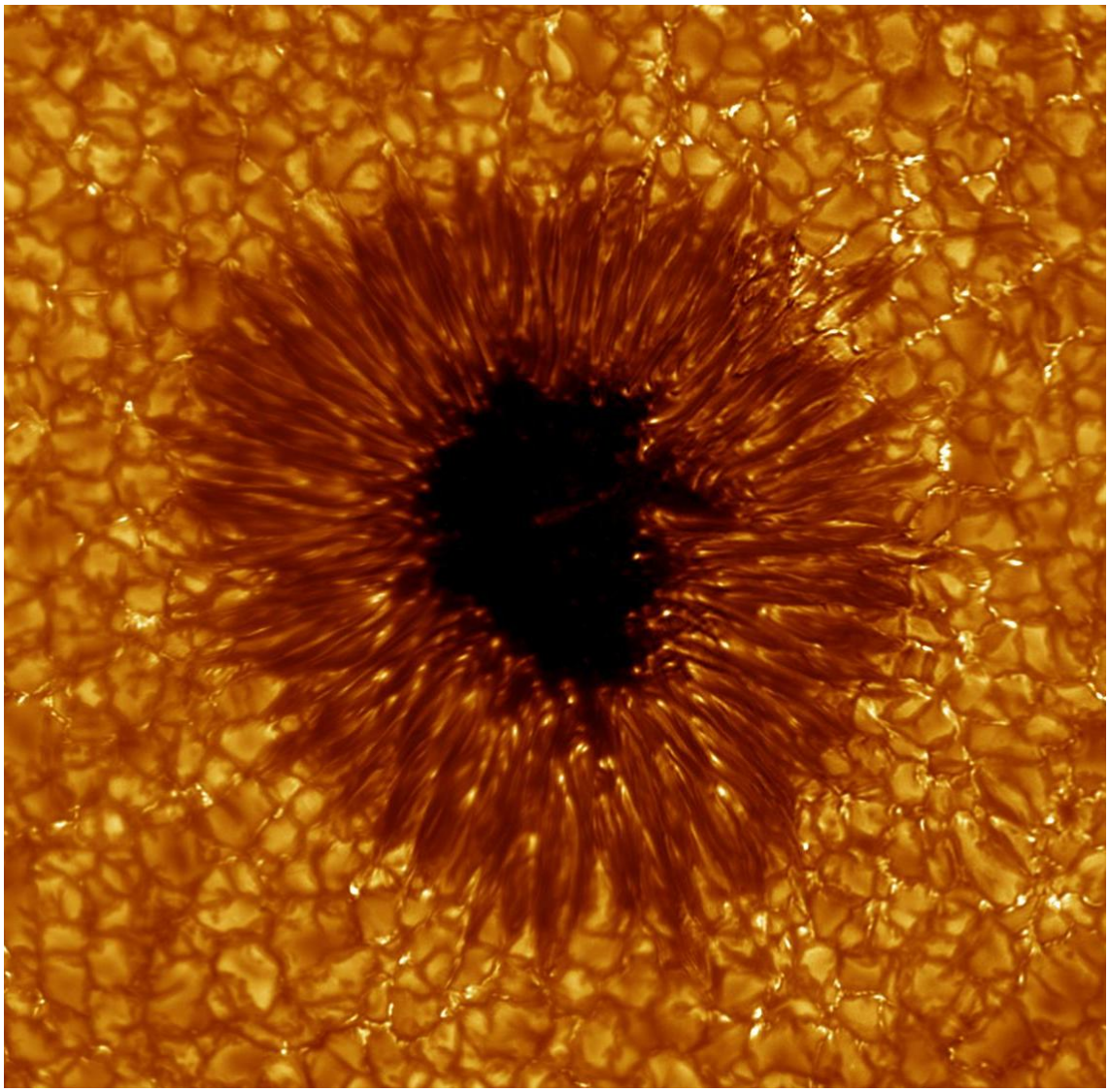

Figure 1.3: A small regular sunspot. Image credit: Data collected with the SST in 2002 by Gran Scharmer and Kai Langhans, ISP.

circular, has a single umbra, has no light-bridges or significant umbral dots (see Thomas and Weiss (2004, 2008); Solanki (2002, 2003) and Borrero and Ichimoto (2011) for explanation of these features) and has a rather uniform penumbra (uniform in width as it wraps the umbra).

The umbra, penumbra (geometrically and magnetically) and rotation of a sunspot are the only properties we use in this work, because all rotating sunspots should at least have these features. In general a sunspot may have other features in addition to the umbra and penumbra (like light-bridges, umbral dots or multiple umbra) that complicate the appearance and magnetic geometry of the sunspot, but it is not the intention of this investigation to study such complex examples.

We restrict our geometric description of a sunspot to the umbra and penumbra for two reasons. Firstly, because it is practically difficult to design a model to describe a general sunspot when some features are not always present. Hence a generalised model must focus on consistent features only. Secondly (and more importantly) we omit all but the most fundamental sunspot features because the intent of this investigation is to simulate relatively simple rotating sunspots. We do this so that we can understand sunspot rotation without the added complexity of secondary features near and/or within sunspots that may complicate the physics and misguide the our interpretation of the energy injection potential of sunspot rotation. Thus, we ensure that the simulations only include a sunspot composed of an umbra and penumbra and no other features commonly observed in or around sunspots. Initially, this approach may seem like an oversimplification, but it is taken so that the first results of this work lay a foundation on which more realistic configurations may be developed. We shall see in chapter 6 that even by varying only the fundamental properties of sunspots, the collection of simulations exhibit a significant range of complexity which would surely be increased should we include additional features, hence supporting the simplified approach taken.

In this work we shall simulate cylindrically symmetric rotating sunspots. We include an umbral and penumbral region, each with a magnetic field. A particular strength of this work is that we purposefully do not aim to replicate particular sunspots and instead simulate a highly varied range of simple rotating sunspots. Thus, we rely very little on observational studies of rotating sunspots and specifically what represents the most commonly observed sunspot. Each instance of the model developed in chapter 2 is sufficiently described given five basic quantities: the total radius (the outer penumbral radius), the umbral radius (where the umbra meets the penumbra), the peak magnetic field strength in the centre of the umbra, the peak penumbral magnetic field strength and the rotation rate. Thus, in the following sections we outline the literature values that give the observed range of these parameters, but again do not intend to identify or imply any preference for a given set of parameters. This is particularly relevant given the characteristics of sunspots may evolve during the solar cycle (Watson et al., 2011; Penn and MacDonald, 2007), and by remaining general we do not restrict the investigation to certain period of the Sun's activity cycle.

1.4.1 Sunspot Size

The size of a sunspot can vary significantly, the largest sunspots can reach 60Mm or more in diameter and the smallest approximately 3.5Mm (Solanki, 2003; Thomas and Weiss, 2008). Sunspots in excess of 60Mm are rare but have been observed (Newton, 1955). However, most fully formed sunspots are found to have diameters approximately $20-25$Mm (Tlatov and Pevtsov, 2014; Tlatov et al., 2019; Nagovitsyn et al., 2016; Bogdan et al., 1988; Solanki, 2003). Bogdan et al. (1988) (and many others) show that smaller sunspots are far more common than large.

In this work, due to numerical restrictions, we shall simulate sunspots with diameters in the range $10 - 35$Mm. This range does not span the entire range

of observed sunspots, but covers the most common sunspots well. This is generally supported (when allowing reasonable flexibility) by figure 5 in Nagovitsyn et al. (2016), figure 1 in Bogdan et al. (1988) and figures 1 and 2 in Tlatov et al. (2019), which show that by analysing this range we still capture much of the distribution.

Umbra to Penumbra Area Ratio

When observing physical sunspots, one may divide the umbra and penumbral components and analyse them individually for their relative contribution to the overall are of the sunspot, as in Antalova (1971). There are common themes present within the literature, but as is exhibited for overall sunspot size, there is a degree of variation shown. In this work we have the freedom not to be concerned with the precise "correct" umbral to penumbral area ratio because we shall push the model in chapter 6 to the point at which it begins to break down. In chapter 6, we shall vary the umbral area from being vastly dominated by the penumbral to being dominant. Thus, whilst there may be some agreed upon range of an appropriate umbral to penumbral ratio, we do not include it in this work to maintain generality.

1.4.2 Magnetic Properties

The magnetic properties of a sunspot are a defining feature that we wish to imitate well, but in an idealised way. The main properties required for modelling are the range of typical magnetic field strengths of sunspots and the general description of the magnetic field as a function of radius. Again, to maintain generality we take only the most crucial description.

Magnetic Field Strength

The magnetic field strength of a sunspot is of vital importance as a stronger magnetic field is able to contribute more significantly to the evolution of a plasma, as indicated by the magnetohydrodynamics equations in section 1.5. The model we derive in this work requires the definition of the peak umbral and penumbral magnetic field strengths, but we shall see in chapter 2 that via several assumptions an instance of the model sunspot is described given the peak umbral field strength only (the main assumption being the assumed ratio between the two). Tlatov and Pevtsov (2014) derives statistically that average field strength of fully formed sunspots is approximately 600G and Tlatov et al. (2019) finds that most sunspots have a maximum field strength in the range $1300 - 1400$G. However, many authors (including those listed above) find that there is a general observed correlation between sunspot size and magnetic field strength, specifically that the strongest fields are found within the largest sunspots (Ringnes and Jensen, 1960; Li et al., 2001b; Jin et al., 2006; Nagovitsyn et al., 2016). In this work we do not use the relationship between field strength and sunspot size directly, but acknowledge it here as it assists in the discussion of results in chapter 6.

The strongest magnetic fields in sunspots are reported in excess of 6000G (Livingston et al., 2006). This value is insightful because it provides a sensible order for strong sunspots for use in this investigation. However, in this work we simulate within in the range $500 - 15000$G to capture the commonly observed range of sunspot but also to explore the extremes of the model. Thus, the work in this thesis covers both the most extreme observed values of sunspot magnetic field strengths and the most common observed values.

CHAPTER 1

Magnetic Field Geometry

The sunspot model derived in chapter 2 has a good deal of flexibility, and can model a vast range of sunspot magnetic fields. However, there are several common themes presented in the literature that guide the design of the model. Here we outline the fundamental assumptions and impositions of the magnetic field geometry of the sunspots simulated in this thesis. However, we take use only the most fundamental observed properties to construct the sunspot model.

For the simple sunspots investigated in this work, the strongest magnetic field is typically found at the centre of a sunspot and the field strength decays monotonically with increasing distance from the centre (Keppens and Martinez Pillet, 1996; Solanki, 2002, 2003). The field in the centre of a sunspot is mostly perpendicular to the photosphere (Franz, 2012) and B_z (the component of the magnetic field that points normal to the photosphere) tends to become small at the outer penumbra boundary (Orozco Suarez et al., 2005; Keppens and Martinez Pillet, 1996; Solanki, 2002, 2003; Borrero and Ichimoto, 2011) implying the field becomes parallel to the solar surface. This description describes the global variation primarily, at smaller scales fine scale structure may become important (Solanki, 2002). Some of the penumbral magnetic field is believed to return to the photosphere near the penumbral boundary (Osherovich, 1980; Osherovich and Flaa, 1983) and more generally measurements of a significant return of the penumbral flux to the photosphere (locally at least) are reported (Franz, 2012; Osherovich and Garcia, 1989). Finally, Solanki (2002) highlights that the sharp transition observed at the umbral-penumbral boundary optically, is not manifest in the magnetic field which is found to vary smoothly.

Figure 1.4 shows a statistically derived average magnetic field description of a sunspot (Keppens and Martinez Pillet, 1996). This measurement captures the general description of a sunspot discussed above and is the archetype description

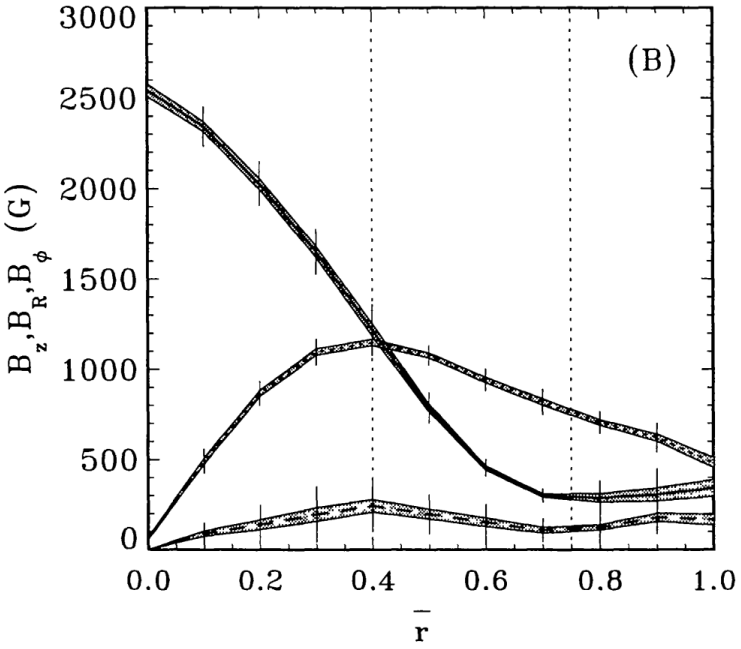

Figure 1.4: A multi-line plot showing an averaged magnetic field profile as a function of radius for a magnetic field described in a cylindrical geometry. The curve that intersects the y-axis at 2500G represents B_z, the curve with the smallest magnitude at all radii represents B_ϕ and the remaining curve represents B_R. The two vertical dashed lines show the umbral radius (at $r = 0.4$) and the penumbral radius (at $r = 0.75$). Image credit: Keppens and Martinez Pillet (1996).

we shall develop the sunspot model from. The figure shows that the B_z component is greatest in the centre of the sunspot and decays monotonically to its edge. The radial magnetic field increases from zero at the sunspot centre, but eventually decays also closer to the penumbral boundary. The profile in figure 1.4 is smooth due its statistical derivation, but similar measurements are presented in other works (Orozco Suarez et al., 2005; Joshi et al., 2017; Borrero and Ichimoto, 2011; Solanki, 2003).

In this investigation a simplified version (but very close) of the literature stated magnetic field properties are adopted for modelling purposes. Specifically that the magnetic field is primarily perpendicular to the photosphere at the centre of the sunspot. B_z decreases monotonically with increasing radius from the centre of the umbra and vanishes at the penumbral boundary. The remaining magnetic field components will be derived using a potential field solution given an imposed B_z description, thus are not motivated from the literature directly but are indirectly via B_z. We wish to inject the twist into all sunspots so all those in this work are initialised with $B_\phi = 0$. Solanki (2003) presents supports that regular isolated sunspots do not have significant twist ($< 20°$), implying that the assumption used here is justified.

Jurčák et al. (2018) find that there is a positive correlation between the inclination of the magnetic field and the size of the umbra. In chapter 6 we do not account for this scaling and vary each model parameter independently.

1.4.3 Rotation Properties

Finally, we address the observed rotation rates of sunspots. This property in a sense defines sunspot rotation. The literature concerning sunspot rotation is vast and it is not the intention of this work to identify any trends or statistical relationships present for rotating sunspots rotation rates. Here we merely wish to gauge the order

of rotation common in the literature, because the nature of this work is general and aims to derive an analytical definition for energy generation based on a set of properties including sunspot rotation. Typically, sunspot rotation tends to be recorded in the literature below $10°\text{hr}^{-1}$ (Brown et al., 2003; Walker, 2018; Brown and Walker, 2021; Vemareddy et al., 2012, 2016a) but far more extreme values of the order of tens of degrees per hour are also recorded (Bi et al., 2016; Liu et al., 2016; Grimes et al., 2020). In this work we simulate rotation rates in the range $2 - 96°\text{hr}^{-1}$, hence we operate in the physically meaningful parameter space.

1.5 Magnetohydrodynamics

This section introduces the theoretical framework and theorems used throughout this thesis. The theory in this section is standard magnetohydrodynamics and electromagnetism theory and can be found in a variety of literature sources. The material in this section has been composed of material taken from a number of standard texts including Boyd and Sanderson (1969); Jackson (1975); Priest and Forbes (2000); Gurnett and Bhattacharjee (2005); Golub and Pasachoff (2010); Priest (2014); Griffiths (2014) and Chen (2016).

1.5.1 The Resistive Magnetohydrodynamics Equations

The theory in this chapter begins with the resistive magnetohydrodynamics equations and therefore we assume that the magnetohydrodynamic (MHD hereafter) approximation is valid in our analysis and simulation of rotating sunspots. A fuller appreciation of the foundations of the magnetohydrodynamic framework requires a more rigorous derivation of these equations, using more general plasma theory, which is beyond the scope of this introduction. However, such derivations are present in the literature, specifically see chapter 3 of Boyd and Sanderson (1969), chapter 6 of

Gurnett and Bhattacharjee (2005), section 7.2 of Golub and Pasachoff (2010) and a motivation of the momentum equation is presented in chapter 3 of Chen (2016).

Chapter 2 of Priest (2014), presents a more fluid and electromagnetic fields focused derivation of the MHD equations and highlights some of the key assumptions under which the MHD approximation is valid. See Priest (2014) (pp.74-87) for a more rigorous derivation, here we outline the fundamental steps and assumptions made in deriving the MHD equations. Priest (2014) begins with the Maxwell equations (see Priest (2014) pp. (74-75), and more generally Jackson (1975) and Griffiths (2014)). Priest (2014) then states the first assumption imposed under the MHD assumption, specifically that "electromagnetic variations are non-relativistic" which means that the typical velocities under the standard resistive MHD assumption, must be small in comparison to the speed of light. The typical speeds present in rotating sunspots, which we shall simulate in this thesis, are far less than the speed of light, therefore thus far the MHD approximation is fit for purpose. Priest (2014) explains that because of this sub-relativistic velocity assumption, the displacement current must be small when compared to the current density and curl of the magnetic field in Amperes' law, and is therefore eliminated. Further to this they assume that the typical magnetic field strengths divided by the timescales over which they typically evolve is comparable to the typical electric field strengths divided by the typical length scales over which they exist. Specifically, equation 2.6 of Priest (2014) states,

$$\frac{E_0}{l_0} \approx \frac{B_0}{t_0}, \tag{1.1}$$

where E_0, B_0, l_0 and t_0 represent typical electric field strength, magnetic field strength, length scale and time scale respectively. Equation 1.1 is obtained by performing a dimensional analysis on Faradays Law (equation 1.6), using the typical electric field strength, magnetic field strength, length scale and time scale defined above as typical values. Equation 1.1 states that the magnitude of both sides of

Faraday's law have approximately the same magnitude. Equation 1.1, when supplemented by the sub-relativistic velocity assumption made above, can be used to show that the energy stored in the electric field is much smaller than that stored in the magnetic field. This result is given in Priest (2014) (pg 76), but is repeated below for clarity. If we multiply both sides of equation 1.1 by $l_0\sqrt{\mu_0\epsilon_0}/B_0$, where μ_0 and ϵ_0 are the permeability and permittivity of free space respectively and l_0 and B_0 maintain their previous meaning, equation 1.1 becomes,

$$\frac{E_0\sqrt{\mu_0\epsilon_0}}{B_0} = \frac{l_0\sqrt{\mu_0\epsilon_0}}{t_0}. \tag{1.2}$$

Classical electromagnetic theory states $c^{-2} = \mu_0\epsilon_0$, where c is the speed of light (Jackson, 1975; Griffiths, 2014). If we square both sides of equation 1.2 and substitute $c^{-2} = \mu_0\epsilon_0$ on the right hand side, we obtain,

$$\frac{E_0^2\epsilon_0}{B_0^2/\mu_0} = \frac{l_0^2}{c^2 t_0^2}. \tag{1.3}$$

Finally, if we define the typical velocity of the system (v_0) to be defined by $v_0 = l_0/t_0$ and recognise that the numerator and denominator of the left hand side of equation 1.3 are the electric and magnetic field energy densities respectively, we may conclude that,

$$\frac{E_e}{E_b} = \frac{v_0^2}{c^2}, \tag{1.4}$$

where E_e and E_b represent the electric and magnetic energies respectively. Because we have made the assumption that the typical velocities present are much less than the speed of light, we may transform equation 1.4 into an inequality by recognising that $v_0^2/c^2 \ll 1$, specifically.

$$\frac{E_e}{E_b} \ll 1. \tag{1.5}$$

Equation 1.5 states that when investigating the energy generation properties of a rotating sunspot in this work, we may assume that the magnetic energy is the primary form of electromagnetic energy that may be generated and stored in the

electromagnetic fields of a rotating sunspot. Priest (2014) continues by eliminating the electric field from Faraday's law,

$$\frac{\partial \mathbf{B}}{\partial t} = -\nabla \times \mathbf{E}, \tag{1.6}$$

by substituting $\mathbf{E}$ from Ohm's law (1.7) which is,

$$\eta \mathbf{j} = \mathbf{E} + \mathbf{v} \times \mathbf{B}, \tag{1.7}$$

to give the induction equation (after some use of vector identities and algebraic manipulation),

$$\frac{\partial \mathbf{B}}{\partial t} = \nabla \times (\mathbf{v} \times \mathbf{B}) + \eta \nabla^2 \mathbf{B}. \tag{1.8}$$

This is the first MHD equation and it describes how the magnetic field changes in time, in response to plasma flows (via the first term on the right hand side) and diffusive effects (via the second term on the right hand side). An important point to make at this time is that under an ideal MHD framework, we lose the second term as the resistivity is assumed to vanish.

The assumption of sub-relativistic characteristic velocities made previously, which introduced the ability to neglect the displacement current, Ampère's law,

$$\nabla \times \mathbf{B} = \mu_0 \mathbf{j} + \frac{1}{c^2} \frac{\partial \mathbf{E}}{\partial t}, \tag{1.9}$$

may be simplified to,

$$\nabla \times \mathbf{B} = \mu_0 \mathbf{j}. \tag{1.10}$$

Equation 1.10 states that under the MHD approximation, the current density is proportional to the circulation of the magnetic field. This identity will be used frequently throughout this work.

$$\frac{\partial \rho}{\partial t} = -\nabla \cdot (\rho \mathbf{v}) \,, \tag{1.11}$$

$$\frac{D\mathbf{v}}{Dt} = \frac{1}{\rho}\mathbf{j} \times \mathbf{B} - \frac{1}{\rho}\nabla P + \mathbf{g}, \tag{1.12}$$

$$\frac{\partial \mathbf{B}}{\partial t} = \nabla \times (\mathbf{v} \times \mathbf{B}) + \eta \nabla^2 \mathbf{B}, \tag{1.13}$$

$$\frac{D\epsilon}{Dt} = -\frac{P}{\rho}\nabla \cdot \mathbf{v} + \frac{\eta}{\rho} j^2, \tag{1.14}$$

with the additional constraints,

$$\nabla \cdot \mathbf{B} = 0, \tag{1.15}$$

$$P = \frac{\rho k_B T}{\mu_m}, \tag{1.16}$$

$$\epsilon = \frac{P}{\rho(\gamma - 1)} = \frac{k_B T}{\mu_m (\gamma - 1)}, \tag{1.17}$$

define the equations used in this work. Equations 1.11 to 1.14 are the resistive magnetohydrodynamic equations. Collectively they are a coupled set of equations that describe the evolution of a magnetised plasma. Specifically, equations 1.11 to 1.14 define how the mass density (ρ), the velocity ($\mathbf{v}$), the magnetic field ($\mathbf{B}$) and the internal energy density (ϵ) respectively evolve in time in response to the evolving properties of the plasma itself. Equation 1.15 states that a magnetic field has no sources or sinks. Equation 1.16 shows the equation of state used by all simulations in this work, this is the ideal gas equation. Equation 1.17 shows how the state variables are related to internal energy density. The variables γ and μ_m found in equations 1.16 and 1.17 represent the ratio of specific heats and the reduced mass respectively. All simulations discussed in this work set $\gamma = \frac{5}{3}$ and $\mu_m = 0.6\mathrm{m_p}$, where $\mathrm{m_p}$ represents the mass of a proton. These equations are used by the Lare3D code (Arber et al., 2001) to simulate sunspot rotation evolving under a magnetohydrodynamic description throughout this investigation. However, further discussion and use of these equations is deferred to the relevant sections where appropriate.

1.6 Force-Free Magnetic Fields

A particular interest when studying evolving magnetic fields in the solar corona is to determine how appropriate the use of force-free extrapolation methods (Grad and Rubin, 1958; Amari et al., 1999; Inhester and Wiegelmann, 2006; Wiegelmann and Sakurai, 2012; Wiegelmann et al., 2014) are for reproducing the observed evolution of such systems. It is common to use such methods to investigate the connectivity and structure of magnetic fields as well as to identify stored free magnetic energy (Régnier and Canfield, 2006; Régnier and Priest, 2007a,b; Aly, 1991; Sturrock, 1991), particularly involving sunspot rotation (Barnes and Sturrock, 1972). However, such methods use the photospheric magnetic field as a boundary condition and extrapolate magnetic fields through regions where the plasma beta does not support the force-free assumption (see Bourdin (2017) and references therein for motivation of this). In our investigation the applicability of the force-free assumption with respect to rotating sunspots can be analysed and will be discussed further where appropriate.

One may show that the force-free assumption can be reduced (after some assumptions, see Priest (2014)) to the condition that the Lorentz force must vanish everywhere within a magnetic volume. Specifically,

$$\mathbf{j} \times \mathbf{B} = \mathbf{0}, \tag{1.18}$$

which can only be true if $\mathbf{B} = \mathbf{0}$ (if there is no magnetic field there must be no current density via equation 1.10), if $\mathbf{j} = \mathbf{0}$ and $\mathbf{B} \neq \mathbf{0}$ (i.e. a potential magnetic field, which is at a minimum energy state (Woltjer, 1958)) or if $\mathbf{j} \parallel \mathbf{B}$ (which is a direct consequence of equation 1.18, as the cross product of two parallel vectors is zero). If there is current density, within a magnetic domain, that is aligned with the magnetic field, then the magnetic field imposes no force on the flow of the plasma.

From vector analysis, if the current density and magnetic field vectors are always aligned in a force-free magnetic field, then one must be a scalar multiple of the other.

Therefore using equation 1.10 we may write,

$$\mathbf{j} = \frac{1}{\mu_0}\left(\nabla \times \mathbf{B}\right) = \alpha(\mathbf{r})\mathbf{B} \tag{1.19}$$

where the $\alpha(\mathbf{r})$ represents a spatially dependent constant of proportionality between the current density and the magnetic field vector, where $\mathbf{r}$ represents an arbitrary position vector. We may isolate $\alpha(\mathbf{r})$ by taking the scalar product of equation 1.19 with the magnetic field, $\mathbf{B}$. This defines $\alpha(\mathbf{r})$ as,

$$\alpha(\mathbf{r}) = \frac{1}{\mu_0}\frac{(\nabla \times \mathbf{B}) \cdot \mathbf{B}}{B^2}, \tag{1.20}$$

where we are free to allow $\alpha(\mathbf{r})$ to absorb the permeability of free space constant.

The Lorentz force may be split further into components. The Lorentz force is defined as,

$$\mathbf{F_{Lf}} = \mathbf{j} \times \mathbf{B}, \tag{1.21}$$

which via equation 1.10 may be written as,

$$\mathbf{j} \times \mathbf{B} = \frac{1}{\mu_0}\left(\nabla \times \mathbf{B}\right) \times \mathbf{B}.$$

We may exploit the vector identity,

$$\nabla\left(\frac{1}{2}\mathbf{B} \cdot \mathbf{B}\right) = \mathbf{B} \times (\nabla \times \mathbf{B}) + (\mathbf{B} \cdot \nabla)\,\mathbf{B},$$

to define the Lorentz force alternatively as,

$$\mathbf{j} \times \mathbf{B} = \frac{1}{\mu_0}\left(\mathbf{B} \cdot \nabla\right)\mathbf{B} - \nabla\left(\frac{B^2}{2\mu_0}\right),$$

where we may define,

$$P_b = \frac{B^2}{2\mu_0}, \tag{1.22}$$

to be the magnetic pressure and where,

$$T_b = \frac{1}{\mu_0}\left(\mathbf{B} \cdot \nabla\right)\mathbf{B}, \tag{1.23}$$

is the magnetic tension force. The gradient of the magnetic pressure is what contributes to the Lorentz force, in that magnetic pressure behave similarly to thermal pressure in that the pressure gradient is what induces accelerations.

To be clear, just because a force-free magnetic field has zero Lorentz force does not imply that the magnetic field be devoid of any magnetic tensions or magnetic pressure gradients, although a configuration of this description would be force-free. Clearly, a force-free field is one where either the magnetic tension force balance the gradient of magnetic pressure or where we have a magnetic field where there is no magnetic tension or magnetic pressure gradients due to the magnetic field being uniform. A uniform magnetic field has no gradients and no tension force, due to a lack of curvature.

1.7 Poynting's Theorem

To better understand the electromagnetic energetics of the rotating sunspot system, we must understand how electromagnetic energy is stored, transported and generated. Here we discuss the relevant aspects of Poynting's theorem. The material in this section is primarily taken from Griffiths (2014) (pp. 360-364) and Priest (2014) (pg. 86) (various background theory from Jackson (1975)) but can be found as standard in most electromagnetism texts. Poynting's theorem defines the connection between the generation, storage and transport of electromagnetic energy. In this thesis, we are primarily interested with the magnetic field description of sunspot rotation, and thus focus our attention on understanding the properties of magnetic energy throughout the simulation. We will begin this development by focusing on the general form of Poynting's theorem by following Griffiths (2014), then we shall specialise the theorem for MHD electromagnetic fields.

Before we begin our discussion on Poynting's theorem, we highlight that we shall

use two vector identities throughout the discussion to follow, these are,

$$\frac{\partial\left(\mathbf{A}\cdot\mathbf{A}\right)}{\partial t}=2\mathbf{A}\cdot\frac{\partial\mathbf{A}}{\partial t}, \tag{1.24}$$

and,

$$\nabla\cdot\left(\mathbf{A}\times\mathbf{B}\right)=\mathbf{B}\cdot\left(\nabla\times\mathbf{A}\right)-\mathbf{A}\cdot\left(\nabla\times\mathbf{B}\right), \tag{1.25}$$

where in equations 1.24 and 1.25 both vectors, $\mathbf{A}$ and $\mathbf{B}$ are arbitrary three dimensional vectors and no physical significance (i.e. they do not represent the vector potential and magnetic induction).

In the remainder of this section, we first define the energy stored in electric and magnetic fields, then we establish how energy may enter or leave the electromagnetic system and conclude with how electromagnetic energies flow. The energy stored in an electric field is given by,

$$E_e=\frac{\varepsilon_0}{2}\iiint E^2\,dV. \tag{1.26}$$

Similarly, the energy stored within a magnetic field is given by,

$$E_b=\frac{1}{2\mu_0}\iiint B^2\,dV. \tag{1.27}$$

Therefore the energy density of an electromagnetic field is given by,

$$u=\frac{1}{2}\left(\varepsilon_0E^2+\frac{1}{\mu_0}B^2\right). \tag{1.28}$$

Equation 1.28 allows us to measure the amount of electromagnetic energy in a general field composed of both electric and magnetic fields, as a result of a distribution of charges and currents. Thus, we know how to measure the amount of stored electromagnetic energy.

Next we develop an understanding of how energy may be generated or used (i.e. lost from the electromagnetic energy budget, via conversion to some other form). It can be shown (Griffiths, 2014; Jackson, 1975) that, due to the Lorentz force, magnetic fields are incapable of doing work on moving charges (due to their

consequent force being perpendicular to the motion of the charge), but electric fields can do work and the work done by an electric field is given by,

$$\frac{dW}{dt} = \iiint \mathbf{E} \cdot \mathbf{j}\, dV. \tag{1.29}$$

Equation 1.29 defines the rate at which work is done in a volume. Therefore, the power per unit volume (by using Ampère's law) can be shown to be,

$$\mathbf{E} \cdot \mathbf{j} = \frac{1}{\mu_0}\mathbf{E} \cdot (\nabla \times \mathbf{B}) - \varepsilon_0 \mathbf{E} \cdot \frac{\partial \mathbf{E}}{\partial t},$$

which using equations 1.24, 1.25 and 1.6, reduces to,

$$\mathbf{E} \cdot \mathbf{j} = -\frac{1}{2}\frac{\partial}{\partial t}\left(\varepsilon_0 E^2 + \frac{1}{\mu_0}B^2\right) - \frac{1}{\mu_0}\nabla \cdot (\mathbf{E} \times \mathbf{B}). \tag{1.30}$$

If we define,

$$\mathbf{S} = \frac{1}{\mu_0}(\mathbf{E} \times \mathbf{B}), \tag{1.31}$$

and substitute equations 1.28 and 1.31 into equation 1.30, we retrieve,

$$\mathbf{E} \cdot \mathbf{j} = -\frac{\partial u}{\partial t} - \nabla \cdot \mathbf{S}. \tag{1.32}$$

Equation 1.32 indicates the means to define how electromagnetic energy flows. Because we already know the left hand side represents the power per unit volume of the electric field, the first term on the right hand side represents the rate of change of energy stored in the electric and magnetic fields per unit volume and thus the second (divergence) term on the right hand side represents the flow of energy per unit volume per unit time. This is a form of Poynting's theorem, one which we shall use throughout this thesis.

Following Griffiths (2014), we may go one further step to derive an alternate form of Poynting's theorem. By substituting equation 1.32 into equation 1.29, with some manipulation and application of the divergence theorem, we obtain the,

$$\frac{dW}{dt} = -\frac{d}{dt}\iiint u\, dV - \oiint \mathbf{S} \cdot d\mathbf{a}. \tag{1.33}$$

Equation 1.33 states that the rate at which work is done by the electromagnetic fields is equal to the negative of the change of total electromagnetic energy in the volume under consideration minus the Poynting vector integrated over the surface are of the surface which bounds the volume of interest. Equivalently, this says the gain (or loss) of total electromagnetic energy is equal to the energy introduced (or used) by the electric field plus (or minus) the electromagnetic energy which has entered (or left) the volume of interest. This form of Poynting's theorem will be used in the discussion of the domain setup, particularly the boundary conditions.

1.7.1 Magnetohydrodynamic Poynting Theorem

Because we use an MHD framework throughout this thesis, we must amend Poynting's theorem slightly for use with MHD simulation data. Throughout various chapters of this thesis, we will be primarily interested with the amount of energy generated by sunspot rotation, but also with where this energy forms, is stored and how it moves around the numerical domain. Therefore we shall primarily be interested in the form of Poynting's theorem given by equation 1.32, which after some rearrangement states,

$$\frac{\partial u}{\partial t} = -\left(\mathbf{E}\cdot\mathbf{j}\right) - \nabla\cdot\mathbf{S},$$

which says that the total electromagnetic energy at a point, remains constant unless there is work done by the electric field on the current density at the point or electromagnetic energy flows toward or away from the point. This statement is as valid for the classical electromagnetic field description as it is for an MHD one, but a consideration must be made because we are using an MHD framework. We saw previously that under the MHD assumption the energy stored within an electric field is much less than that stored within the magnetic (equation 1.5) as a consequence of the sub-relativistic velocity limitation. Thus, equation 1.28 becomes simply the magnetic field energy density (or equivalently the magnetic pressure). Therefore,

equation 1.32 under the MHD assumption becomes,

$$\frac{\partial}{\partial t}\left(\frac{B^2}{2\mu_0}\right) = -\left(\mathbf{E}\cdot\mathbf{j}\right) - \nabla\cdot\mathbf{S}. \tag{1.34}$$

Equation 1.34 states that the change in magnetic energy equals the energy lost (or gained) via work done by the electric field minus the flow of energy away (or toward) the point of interest. Equation 1.34 is only a slight amendment of the classical statement of Poynting's theorem, but the amendment is important as it removes the electric energy. Because of this, we lose a degree of freedom and any electromagnetic energy generated when we rotate the simulated model sunspots must flow into the magnetic field. We conclude this section with one final alteration to equation 1.34, we may recast the work done by the electric field $(\mathbf{E}\cdot\mathbf{j})$ using Ohm's law (equation 1.7), specifically by setting,

$$\mathbf{E}\cdot\mathbf{j} = \left(-\mathbf{v}\times\mathbf{B} + \frac{\mathbf{j}}{\sigma}\right)\cdot\mathbf{j}. \tag{1.35}$$

The expansion for $(\mathbf{E}\cdot\mathbf{j})$ in equation 1.35 may be substituted into equation 1.34, and with a vector identity we yield,

$$\frac{\partial}{\partial t}\left(\frac{B^2}{2\mu_0}\right) = -\frac{j^2}{\sigma} - \mathbf{v}\cdot\left(\mathbf{j}\times\mathbf{B}\right) - \nabla\cdot\mathbf{S}. \tag{1.36}$$

Equation 1.36 is particularly useful because it is a scalar equation, which we can use to understand the evolution of magnetic energy. The first term on the right hand side represents the electromagnetic energy converted to heat via Ohmic heating, under an ideal MHD framework this term vanishes. The second term on the right hand side is of greater interest, because it offers an avenue to introduce magnetic energy into the domain via the velocity. We shall see in subsequent chapters that the only thing we do to the simulated sunspots, is drive them with a velocity profile at the simulation domain boundary. We shall initialise all simulations with a potential magnetic field and so any perturbation by the driving velocity should introduce currents. We shall save further discussion of this for the appropriate chapter within

the main body of the thesis. We finalise this discussion by highlighting that the form of Poynting's theorem, presented by equation 1.36, indicates two possible avenues by which magnetic energy can enter the rotating sunspot simulation domains, either via collocated anti-parallel velocity and Lorentz forces (equation 1.21) or by the convergence of the Poynting vector (equation 1.31).

1.8 Potential Magnetic Fields

A magnetic field that has no currents is said to be potential, because it can be represented as the gradient of a scalar potential field. This is a standard result in classical electrodynamics and can be found in many standard texts, for example see Jackson (1975) (pg.192). Such a field exists at the minimum magnetic energy state. In this section we will discuss the relationship of a the scalar potential and the magnetic field, show that a potential field is a lower bound for the magnetic energy of a given system and outline how we may calculate a potential field (which will be continued in chapter 2).

A magnetic field under the MHD assumption must satisfy equations 1.15 and 1.10. If there are no currents in the field, equation 1.10 becomes,

$$\nabla \times \mathbf{B} = \mathbf{0}, \tag{1.37}$$

and because vector calculus shows us that the curl of any gradient must be zero, we may rewrite equation 1.37 as,

$$\nabla \times \nabla\psi = \mathbf{0}, \tag{1.38}$$

where ψ is a scalar field, commonly named the scalar potential. Thus, we have imposed that,

$$\mathbf{B} = \nabla\psi. \tag{1.39}$$

Because a magnetic field must always be source free, hence obey equation 1.15, we may insert 1.39 into equation 1.15 and yield that the Laplacian of the scalar

potential, specifically,

$$\nabla^2 \psi = 0. \tag{1.40}$$

In chapter 2, we shall discuss how one may solve equation 1.40 for a given set of boundary conditions to produce an initial magnetic field to initialise the simulations used throughout this thesis.

1.8.1 Minimum Magnetic Energy

It can be shown that for a given set of boundary conditions, where the normal component of the magnetic field is given, a potential magnetic field gives the minimum energy magnetic field configuration possible within a region (or for the purposes of this investigation, a numerical domain). Priest (2014) discusses this theorem in greater depth than we shall here, and in the following discussion we follow Priest (2014) and primarily reiterate the relevant material for our investigation presented there. Although we follow Priest (2014), the potential field minimum energy theorem is a general one that can be found throughout the literature.

A scalar potential solution in a region or domain, is unique if either ψ or the gradient of ψ normal to the boundary is imposed. Suppose we have a domain with a set of boundary conditions that yield a unique potential field solution, let that potential magnetic field solution be denoted $\mathbf{B_p}$. If we have a general magnetic field other than this potential field solution, we may use the principle of superposition to define it such that,

$$\mathbf{B} = \mathbf{B_p} + \mathbf{B}_\delta, \tag{1.41}$$

where $\mathbf{B}$ is the "other" general magnetic field and $\mathbf{B}_\delta$ represents the difference between the potential and general magnetic field. Because the potential solution is unique for given boundary conditions (as stated above) the boundary conditions for $\mathbf{B_p}$ and $\mathbf{B}$ must be the same. In practice, in the context of solar physics for example, this may be the boundary conditions of the magnetic field as observed on the solar

surface, where the potential solution above the surface and any other extrapolation (e.g. Régnier and Priest (2007b); Grad and Rubin (1958) and Barnes and Sturrock (1972)) must use the same photospheric magnetic field in the reconstruction of the field above. Because of this sharing of boundary conditions, we must impose that the normal component of $\mathbf{B}_\delta$ vanish at the boundaries.

Equation 1.27 states (with some rearrangement) that the total magnetic energy contained in a magnetic field is given by,

$$E_b = \iiint \frac{\mathbf{B} \cdot \mathbf{B}}{2\mu_0} \, dV,$$

which for the definition of $\mathbf{B}$ given by equation 1.41, becomes,

$$E_b = \iiint \frac{(\mathbf{B_P} + \mathbf{B}_\delta) \cdot (\mathbf{B_P} + \mathbf{B}_\delta)}{2\mu_0} \, dV,$$

which may be expanded to give,

$$E_b = \iiint \frac{B_P^2 + \mathbf{B}_\delta \cdot \mathbf{B_P} + B_\delta^2}{2\mu_0} \, dV. \tag{1.42}$$

We may show that the scalar product between the potential field ($\mathbf{B_p}$) and the additional magnetic field ($\mathbf{B}_\delta$), integrated over the volume of interest vanishes. We may write,

$$\iiint \mathbf{B_p} \cdot \mathbf{B}_\delta \, dV = \iiint \nabla\psi \cdot \mathbf{B}_\delta \, dV = \iiint \nabla \cdot (\psi \mathbf{B}_\delta) - \psi \left(\cancelto{0}{\nabla \cdot \mathbf{B}_\delta} \right) \, dV.$$

Finally, by applying the divergence theorem and recognising that by definition $\mathbf{B}_\delta$ vanishes at the boundary we yield,

$$\iiint \mathbf{B_p} \cdot \mathbf{B}_\delta \, dV = 0. \tag{1.43}$$

Equation 1.43 may be substituted into equation 1.42 to give,

$$E_b = \iiint \frac{B_P^2 + B_\delta^2}{2\mu_0} \, dV. \tag{1.44}$$

Equation 1.44 both shows that because of the way in which we define $\mathbf{B}$, the energy in that field is simply given by the sum of the energies of its component fields.

But more importantly, it shows that (as long as the fields are real) the magnetic energy of the general magnetic field ($\mathbf{B}$) must be greater than that of the potential field ($\mathbf{B_p}$) because for any non-zero additional field ($\mathbf{B}_\delta$) the energy will always be larger due to the squaring of the field strengths in equation 1.44. This proves that for domain with a set of boundary conditions, a scalar potential magnetic field has the minimum magnetic energy possible for the imposed boundary conditions. This theorem will be used frequently throughout this thesis and underpins many of the arguments made regarding the generation of magnetic energy.

1.9 Outline of Thesis

In this thesis, we numerically investigate how sunspots influence their magnetic environments when they rotate, with a particular focus on the magnetic energy generation properties of rotating sunspots. In chapter 2 we develop an analytical parametric model that describes an idealised sunspot magnetic field. The purpose is to develop a model, based on key observed properties of sunspots that is suitable for use in a simulation based investigation. The model focuses only on the most fundamental properties of sunspots and establishes a number of defining parameters, which can be tuned to alter a particular sunspots definition. A primary aspect of the model that maintains a persistent high level of importance throughout the thesis, is the inclusion of a dedicated penumbral magnetic field. In chapter 2 we also outline the key properties of the Lare3D (Arber et al., 2001) code, which provides the main body of results analysed in this thesis. We conclude chapter 2 by explaining the boundary conditions employed by the Lare3D code used to produce the collection of simulations in this work.

In chapter 3 we present the key evolutionary properties of the primary variables evolved by the resistive magnetohydrodynamic equations (equations 1.11 - 1.14) and some of the secondary variables like current density and temperature. The

main purpose of this chapter is to develop a foundational understanding of the evolutionary traits of a simulated model rotating sunspot. We find that most of the simulated sunspots throughout this work evolve similarly and thus the findings this chapter extend beyond the single simulation analysed there. In this chapter we shall see that the penumbra of the model sunspot evolves distinctly as compared the rest of the numerical domain.

In chapter 4 we build upon the general description of the simulated rotating sunspot evolution obtained in chapter 3, and focus further on the evolution of the region of the domain associated with the penumbral magnetic field. To do this, we develop a numerical method that identifies which cells of the domain belong to the penumbra, and which do not. This method is applied in several chapters of the thesis, but is first used directly in this chapter. Using this technique, we analyse the volume changes of the penumbra and investigate the distribution and magnitude of the geometrical twist of the magnetic field within the penumbral and umbral magnetic field regions. We correlate these findings with primary and secondary evolved properties of the MHD equations, presented in chapter 3. We conclude this chapter by analysing the current helicity and its relation to the twist, magnetic pressure and magnetic energy. This chapter is kept distinct from the work in chapter 3. This is done because, although many of the basic phenomena are present in other simulations present in the thesis, the specific analysis in this chapter is primarily quantitative, and thus the results are specific to the set of model parameters used to define the specific sunspot simulation investigated.

In chapter 5 we continue our analysis of a single rotating sunspot simulation and develop a quantitative analysis that is specific to the example simulation investigated. We specifically investigate the dynamics and energetics of a single rotating sunspot simulation, to better understand the key mechanisms responsible for the generation, storage and transport of magnetic energy, both in response to the driven

boundary conditions and due to the continued evolution within the domain. Thus, the findings are technically specific to the single simulation under investigation, but the characteristic mechanisms are broadly descriptive of the encompassing body of simulations presented throughout this thesis. We conclude this chapter by highlighting the importance of the, magnetically closed, penumbral field region for the potential contribution it may make to the energy budget of extreme space weather events.

In chapter 6 we focus all attention on understanding the magnetic energy generation potential of rotating sunspots, as described by the parametric model developed in chapter 2. We will establish and apply a method to link the magnetic energy generated and stored when a sunspot rotates, to each of the primary model parameters independently. This will yield a scaling relation linking each model parameter individually to the generation of magnetic energy. Doing this will allow us to understand the relative importance of the fundamental properties of natural rotating sunspots, but will secondarily provide the building blocks for a general description of rotating sunspots. We will conclude this chapter by combining the individual scaling laws into a single form, which takes as its arguments the model parameters from the sunspot model, such that one may use this to investigate observed rotating sunspots. We develop this single relation in such a way that we allow further development and the addition of new individual scaling relations. Thus, we shall end the discussion which connects the individual scaling relations with a brief motivation for how one may extend the current state of this piece of research.

In chapter 7 we will discuss potential avenues for future works that may be continued or developed, to extend and deepen the understanding of sunspot rotation developed throughout this thesis. This will include (but is not limited to) a discussion of the potential importance of connectivity, with some emphasis on the length scale of connectivity of the magnetic fields in rotating sunspots. Chapter 7 will also

conclude the thesis by summarising and reviewing the key findings.

Chapter 2

Sunspot Model

In this chapter we develop an analytical model to describe the B_z component of the magnetic field of an idealised sunspot at the photosphere. The model is based only on the most fundamental characteristic physical properties of observed sunspots, which are discussed in chapter 1. As highlighted in chapter 1, there are many properties and features a sunspot may have, but in this investigation we wish to understand generally how much energy a rotating sunspot might produce based on its defining features only. For this reason the model we develop in this chapter will include only the global magnetic field, the sizes of the umbra and penumbra and rotation rate. In addition we impose cylindrical symmetry, hence all sunspots modelled and simulated in this work are round on the photospheric plane.

It is not the intention of this work to reproduce a specific eruptive event associated with a given rotating sunspot, or to model sunspots that follow some observed scaling law (like peak magnetic field strength to size (Ringnes and Jensen, 1960)). Instead we wish to understand how any (simple) sunspot may evolve. However, in the pursuit to understand general sunspots we still take guidance from the literature reviewed in chapter 1. We do this to ensure that when simulating model sunspots, the investigation does not deviate and the result describes physically realistic sunspots. For example, exploiting the degrees of freedom of the model too

severely may result in an understanding of starspots, which is meaningful but not the focus of this work. In this investigation we simulate rotating sunspots with peak umbral magnetic field strengths in the range $500 - 15000$G (despite the strongest sunspots being around 6000G). The extended range is used to get a better fit, this is illustrated in section 6.2.1. The model sunspots in this work follow Keppens and Martinez Pillet (1996); Solanki (2002); Borrero and Ichimoto (2011) and employ a global magnetic field that reduces in strength with increasing distance from the centre of the umbra, and so the peak penumbral magnetic fields are modelled as a fraction of the peak umbral field strength in the range $0.2 - 0.8$. The size of the (round) sunspot is characterised by a maximum radius, in the model used in this work this is the penumbral radius (P_r). For numerical reasons, in this work we simulate sunspots with penumbral radii in the range $5 - 17.5$Mm. The umbral radius is defined such that it is always smaller than the penumbral and thus the umbral radius is given as a fraction of the penumbral radius, the range of fractional umbral radius simulated in this work is $0.2 - 0.8$. Finally, one cannot simulate sunspot rotation without some sense of a rotation rate, in this work we simulate sunspot rotation with rotation rates in the range $6 - 96^{\circ}\text{hr}^{-1}$. However, we find that the scaling law derived in section 6.2.3 suggests that smaller rotation rates are well approximated, but are not simulated due to numerical cost.

Finally, the sunspot magnetic field model is designed such that, when used to define the normal magnetic field component at the lower domain boundary (the photosphere), it yields a potential magnetic field solution where there are no field lines connecting the umbra and penumbra. Specifically, the potential field solutions (which are used to initialise each simulation) force the penumbral magnetic flux to enter and leave the domain through the photosphere (the lower domain boundary) and the umbral magnetic flux to enter through the photosphere and leave through the upper domain boundary. All simulations are initialised in this way so that if

at any point we observe field lines connecting the umbra and penumbra, we may assume that a reconnection event may have taken place.

2.1 Deriving a Simplified Sunspot Model

Sunspots exist with a variety of properties including size, shape and magnetic field. It would be difficult to find two truly identical sunspots in nature, but some single definition of a "typical" sunspot must be made if one hopes to numerically investigate sunspot rotation. Equivalently, it is also unlikely to find any example sunspot that displays perfect azimuthal symmetry. Nevertheless, to a crude approximation, single umbra sunspots typically appear circular (or more generally, elliptical) to a first approximation. The model sunspot used in this work imposes perfect symmetry in the azimuthal direction at the photosphere. Each sunspot investigated forms the lower boundary condition of a Cartesian numerical domain, and hence far from the sunspot the cylindrical symmetry of the magnetic field may break. All simulations will be initialised with a potential field for a given synthetic photospheric B_z distribution. The formalism adopted reduces the requirements of sunspot definition to one dimension; in a cylindrical coordinate system this is the radial direction.

Let $S(r)$ define a one-dimensional monotonic piecewise function that describes the normal magnetic field component (B_z) of a model sunspot as a function of radius, r. Within the domain, $S(r)$ is defined uniquely for the separate components that individually describe the umbra and penumbra of the sunspot, i.e. there are no radii shared by the umbra and penumbra. Certain impositions will be enforced on these functions such that $S(r)$ is continuous and smooth where the umbral and penumbral regions meet, and that $S(r)$ is maximum at $r = 0$ and decays monotonically, vanishing at $r = P_r$ where P_r is the penumbral radius.

To define a function that is able to be manipulated for the purposes of a numerical investigation, it proved convenient to define $S(r)$ to be a piecewise function that

individually defines the umbral and penumbral regions. Generally,

$$S(r) = f\left(U(r), P(r)\right), \tag{2.1}$$

where,

$$f = \begin{cases} U(r); & r \leq U_r, \\ P(r); & U_r < r \leq P_r, \\ 0; & P_r < r, \end{cases}$$

where U_r and P_r represent the radius of the umbra and penumbra respectively. Let,

$$U(r) = \alpha\left(\cos\left(\beta r\right) + 1\right)^{\gamma} + \varepsilon, \tag{2.2}$$

$$P(r) = \zeta\left(\cos\left(\eta r + \vartheta\right) + 1\right)^{\kappa} + \lambda, \tag{2.3}$$

where $\alpha, \beta, \gamma, \varepsilon, \zeta, \eta, \vartheta, \kappa$ and λ in equations 2.2 and 2.3 are constants to be determined. In addition to the imposition that $S(P_r) = 0$ it is also necessary to define $S(r)$ at $r = U_r$ such that the internal-endpoints of both $U(r)$ and $P(r)$ given by equations 2.2 and 2.3 connect to make $S(r)$ continuous over the interface between the umbra and penumbra. An additional constraint of smoothness across the umbral-penumbral boundary is also imposed to introduce sufficient conditions to solve the free variables in equations 2.2 and 2.3 but also to produce a more physical sunspot model where the magnetic field varies smoothly at the umbra-penumbra boundary.

To investigate sunspot rotation in a general sense, properties of observed sunspots ought to be able to be fed into the model description, such that the model has the flexibility to represent the range of sunspots found in nature (even if in a somewhat idealised sense). Common measured physical properties of sunspots include: magnetic field strength and orientation; size of both the umbra and penumbra (or sometimes area of each) and rotation rate (when considering rotating sunspots). Therefore, to determine the variables in equations 2.2 and 2.3 we may exploit the

desired properties of the to be modelled sunspot. These are: U_r, which is the umbral radius; P_r, which is the penumbral radius; U_b, which is the peak magnitude of B_z at the centre of the sunspot (at $r = 0$) and P_b which is the magnitude of B_z at the umbral radius. Equations 2.2 and 2.3 are solved individually as follows. Note the rotation rate (ω) does not contribute in any way to the sunspot model.

2.1.1 Umbral Region

The parameters α, β, γ and ε in equation 2.2 must be determined. For a given set of input parameters to the model (U_r, P_r, U_b and P_b) and by defining,

$$\mu = \frac{P_b}{U_b}, \tag{2.4}$$

the following set of constraints on $U(r)$ can be established;

$$\cos\left(\beta U_r\right) = \cos\left(\frac{\pi}{2}\right), \tag{2.5}$$

$$U(U_r) = P_b = \mu U_b \mid 0 \leq \mu \leq 1, \tag{2.6}$$

$$U(0) = U_b. \tag{2.7}$$

Equation 2.5 is obtained by imposing that at $r = U_r$ the argument of the cosine term in equation 2.2 is made equal to $\frac{\pi}{2}$. Therefore, the umbral portion of the sunspot profile is fundamentally the first quarter of a single-cycle cosine function. This remains in agreement with the requirement of monotonicity of the overall function, $S(r)$. Therefore equation 2.5 yields $\beta U_r = \frac{\pi}{2}$ and thus,

$$\beta = \frac{\pi}{2U_r}. \tag{2.8}$$

Evaluating equation 2.2 at $r = U_r$ and imposing conditions 2.6, 2.7 and 2.8 gives,

$$U(U_r) = \alpha\left(\cancel{\cos\left(\frac{\pi}{2}\right)}^{0} + 1\right)^{\gamma} + \varepsilon = \mu U_b = P_b,$$

$$\Rightarrow U(U_r) = \alpha 1^{\gamma} + \varepsilon = \mu U_b = P_b.$$

Therefore,

$$\alpha = \mu U_b - \varepsilon = P_b - \varepsilon. \tag{2.9}$$

Evaluating equation 2.2 at $r = 0$ gives,

$$U(0) = \alpha \left(\cancel{\cos(0)}^{1} + 1 \right)^{\gamma} + \varepsilon = U_b,$$
$$\Rightarrow U(0) = \alpha 2^{\gamma} + \varepsilon = U_b.$$

This yields the following second definition of α,

$$\alpha = \frac{U_b - \varepsilon}{2^{\gamma}}. \tag{2.10}$$

Equating equations 2.9 and 2.10 yields,

$$U_b - \varepsilon = 2^{\gamma} \left(\mu U_b - \varepsilon \right),$$
$$U_b = 2^{\gamma} \mu U_b - 2^{\gamma} \varepsilon + \varepsilon,$$

which gives,

$$\varepsilon = U_b \left(\frac{1 - \mu 2^{\gamma}}{1 - 2^{\gamma}} \right). \tag{2.11}$$

If γ is fixed by imposing that it may be considered an input parameter of the model (or constrained via some other conditions), equations 2.8 and 2.11 may be used with equation 2.9 to determine α;

$$\alpha = U_b \left(\frac{\mu - 1}{1 - 2^{\gamma}} \right). \tag{2.12}$$

Therefore inserting definitions 2.8, 2.11 and 2.12 into equation 2.2 gives the definition of the umbral B_z component as a function of radius,

$$U(r) = U_b \left(\frac{\mu - 1}{1 - 2^{\gamma}} \right) \left(\cos \left(\frac{\pi}{2U_r} r \right) + 1 \right)^{\gamma} + U_b \left(\frac{1 - \mu 2^{\gamma}}{1 - 2^{\gamma}} \right), \tag{2.13}$$

where for clarity, U_r, P_r, μ, and γ are input parameters to the model and hence may be varied between instances. One may observe a further constraint that $\gamma \neq 0$ else $U(r) \to \infty$.

2.1.2 Penumbral Region

Given the definition of the umbral region derived in section 2.1.1, a definition of the penumbral region may now be established. To define the model penumbra, equation 2.3 must be solved for $\zeta, \eta, \vartheta, \kappa$ and λ, given some boundary conditions that reflect the monotonic, smoothness and continuous properties of the overall function, $S(r)$.

To define the free variables in equation 2.3, the following constraints are imposed: $P(U_r) = \mu U_b = P_b$ (as per equation 2.4), $P(P_r) = 0$ and,

$$\left.\frac{dP}{dr}\right|_{r=U_r} = \left.\frac{dU}{dr}\right|_{r=U_r}. \tag{2.14}$$

Similar to the definition of the umbral region in section 2.1.1, to preserve the desired properties of the overall function $S(r)$, we impose the further constraints that the cosine term in equation 2.3 vanishes when $r = U_r$ and the same cosine term becomes -1 when $r = P_r$. It is trivial to show that $P(r)$ is maximum when $\cos(\eta r + \vartheta) = 0$ and minimum when $\cos(\eta r + \vartheta) = -1$, if $(\eta r + \vartheta) \in \left[\frac{\pi}{2}, \pi\right]$. If this range is honoured, and the minimum and maximum radii of the penumbral portion of $S(r)$ is $r = U_r$ and$r = P_r$ respectively, then the additional constraints are established;

$$\eta U_r + \vartheta = \frac{\pi}{2}, \tag{2.15}$$

$$\eta P_r + \vartheta = -1. \tag{2.16}$$

Solving equation 2.15 for η and substituting the subsequent result into equation 2.16, gives

$$\vartheta = \frac{\pi}{2(P_r - U_r)}, \tag{2.17}$$

and finally solving for η given 2.17, gives

$$\eta = \frac{\pi}{2}\frac{P_r - 2U_r}{P_r - U_r}. \tag{2.18}$$

Evaluating equation 2.3 at $r \in \{U_r, P_r\}$ gives,

$$P(U_r) = \zeta(1^\kappa) + \lambda = \mu U_b, \tag{2.19}$$

$$P(P_r) = 0 = \cancelto{0}{\zeta(0^\kappa)} + \lambda. \tag{2.20}$$

From equation 2.20, $\lambda = 0$. Given $\lambda = 0$, equation 2.19 simplifies to

$$\zeta = \mu U b. \tag{2.21}$$

Thus, all that remains to be determined is κ. The final constraint on 2.3 is that given by equation 2.14. Let, χ be defined as a constant which is equal to both sides of equation 2.14, i.e. it is the numerical value of the gradient of $U(r)$ and $P(r)$ at $r = U_r$. Specifically,

$$\chi = \left.\frac{dU(r)}{dr}\right|_{r=U_r} = \left.\frac{dP(r)}{dr}\right|_{r=U_r}. \tag{2.22}$$

Given $U(r)$, as defined in equation 2.2, $\frac{dU(r)}{dr}$ becomes,

$$\frac{dU(r)}{dr} = -\alpha\beta\gamma \left(\cos\left(\beta r\right) + 1\right)^{\gamma-1} \sin\left(\beta r\right),$$

which when evaluated at $r = U_r$ simplifies to,

$$\left.\frac{dU(r)}{dr}\right|_{r=U_r} = -\alpha\beta\gamma = \chi. \tag{2.23}$$

To define κ, the umbral radius given by equation 2.23 must be matched to an equal penumbral radius which means equation 2.3 must be differentiated with respect to r. This gives,

$$\frac{dP(r)}{dr} = -\zeta\kappa\eta \left(\cos\left(\eta r + \vartheta\right) + 1\right)^{\kappa-1} \sin\left(\eta r + \vartheta\right),$$

which when evaluated at $r = Ur$ becomes,

$$\left.\frac{dP(r)}{dr}\right|_{r=U_r} = -\zeta\kappa\eta = \chi. \tag{2.24}$$

Thus, equating equations 2.23 and 2.24 retrieves the following definition of κ,

$$\kappa = \frac{\alpha\beta\gamma}{\zeta\eta}, \tag{2.25}$$

for some choice of γ. Therefore for a given choice of γ, the function described by equation 2.3 that defines the penumbral region, when combined with the derived definitions of the penumbral region variables (equations 2.17, 2.18, 2.20, 2.21 and 2.25), becomes

$$P(r) = \mu U_b \left(\cos\left(\frac{\pi}{2}\left(\frac{P_r - 2U_r}{P_r - U_r}\right) r + \frac{\pi}{2(P_r - U_r)}\right) + 1\right)^{\frac{\alpha\beta\gamma}{\zeta\eta}}. \tag{2.26}$$

2.1.3 Constraining γ

In section 2.1.1, γ is defined as a constant parameter that is treated as an input of the model. However, due to the implications of the connectivity and smoothness of the function at the umbra-penumbra intersection (equation 2.14), γ may be further understood beyond merely the requirement that $\gamma \neq 0$. The definition of χ is such that it is the numerical value of a gradient (see equation 2.22), but this definition was borne of the attempt to define $P(r)$. χ from the point of view of the umbral region may be used to better understand, the currently free variable, γ.

Equation 2.23 highlights the relationship between γ and χ. Substituting the definitions of the already established variables given by equations 2.8 and 2.12, gives a definition for γ in terms of any desired gradient, χ,

$$\gamma = -\frac{\chi}{\alpha\beta} = \frac{-\chi}{U_b\left(\frac{\mu-1}{1-2^{\gamma}}\right)\frac{\pi}{2U_r}}. \tag{2.27}$$

This relationship is particularly convenient, as it further generalised the sunspot model by introducing an additional level of control. However, what equation 2.27 really does is show that γ, for a given choice of other sunspot parameters, acts to control the gradient at the umbra-penumbra intersection. If only γ is changed for a model sunspot, then the overall physical impact to the sunspot is to alter the ratio of flux in the umbral and penumbral regions.

In section 2.1.1, equation (2.13) showed that $\gamma \neq 0$ else $U(r) \to \infty$ and hence $S(r) \to \infty$. Equation 2.27 shows that this implies that $\chi \neq 0$, which makes sense because if this were not true the function would not decrease with increasing radius (let alone do so monotonically). Given one of the desired properties of $S(r)$ is that it should decrease monotonically with radius, χ may be constrained further by imposing it be negative. With the addition that $\chi \neq 0$, this produces to the condition

$$\chi < 0. \tag{2.28}$$

When simulating model sunspots, γ should be altered rather than χ, because it is γ that appears in the definition of the model sunspot and therefore it is it that should be understood. Once a scaling law for γ is established, equation 2.27 may be used see how this influences the gradient. However, this is left for future investigation but is discussed in chapter 7.

2.2 Capturing the Penumbral Flux

As discussed in chapter 1, there are both theoretical (Osherovich, 1980) and observational (Franz, 2012) motivations to assume that the penumbral magnetic field closes locally on the photosphere. However, a simplified model, such as that used in this work, cannot hope to reproduce the complex penumbral structure that is observed in nature (as shown in figure 1.3). However, numerical simulation works have shown that the penumbral structure is reproducible numerically (Rempel et al., 2009; Rempel, 2010, 2011, 2012), but doing so requires simulation resolutions greater than those used in this work (in addition to a magnetoconvective processes). Thus, capturing the fine scale structure of the penumbra is beyond the scope (and objectives) of this investigation.

The primary interest of this work concerns the global description of the magnetic field. Therefore, in this investigation we impose that the penumbral field emerge from the penumbra of the sunspot and re-enter the photosphere in an idealised opposite polarity annulus that envelopes the penumbra. This method has the benefit of ensuring that the umbral and penumbral regions of the model sunspot are distinct. Furthermore, this approach contributes to the model's accuracy in representing something indicative of a physical sunspot, where the penumbral magnetic field closes locally (albeit here in an idealised manner). Therefore, in this model, the penumbral magnetic field is defined to be of different connectivity than the umbral magnetic field.

Alternatively, in a typical sunspot, the magnetic field in the centre of the umbra is predominantly perpendicular to the solar surface (Borrero and Ichimoto, 2011; Solanki, 2003; Keppens and Martinez Pillet, 1996; Thomas and Weiss, 2008) and becomes increasingly parallel with increasing distance from the centre of the sunspot. Thus, whether or not all of the penumbral magnetic field is captured locally (and all the umbral field not) in nature, the idealised model presented here is of physical interest still, as one might expect the outer field of a sunspot to be captured more easily given its increased inclination and relatively weak field strength. If one so wished, they may relax the definition of umbra and penumbra used here and instead use the terms open and closed field regions.

To capture the penumbral flux locally, an opposite polarity annulus is imposed around each model sunspot investigated in this study. So that the annulus itself does not become a dominant magnetic feature of the domain, it is defined such that its magnetic field strength is approximately an order of magnitude less than the average penumbral magnetic field. Secondly owing to the requirement of the annulus to capture the penumbral flux, all annuli are designed so that,

$$\Phi_p = \Phi_n = \int f(r)A(r)dr, \tag{2.29}$$

where Φ_n and Φ_p represent the total magnetic flux of the negative annulus and the penumbra respectively, $f(r)$ represents the magnitude of B_z as a function of radius in the annulus and $A(r)$ is the area of an infinitesimal annulus at as a function of radius. We impose,

$$f(r) = \begin{cases} \frac{\kappa}{2}\left(\cos\left(\beta_1 r + \delta_1\right) + 1\right) \; ; \; r_3 \leq r \leq r_4, \\ \kappa \; ; \; r_4 < r < r_5, \\ \frac{\kappa}{2}\left(\cos\left(\beta_2 r + \delta_2\right) + 1\right) \; ; \; r_5 \leq r \leq r_6, \end{cases} \tag{2.30}$$

where κ is a constant that scales Φ_n to balance equation 2.29. β_1, β_2, δ_1 and δ_2 are variables to be determined and $r_3 - r_6$ represent the radii that define the borders

of the three regions of the annulus. We begin labelling at three to highlight that there are two other radii associated with the sunspot, U_r and P_r. Equation 2.30 shows that the central region of the negative annulus is constant. All simulations in this work have a much larger central region and thus are approximately regions of uniform magnetic field strength. Using some algebraic manipulation and calculus, the unknown variables of equation 2.30 can be defined,

$$\begin{aligned}\beta_1 &= \frac{\pi}{r_4 - r_3},\\ \delta_1 &= \frac{\pi r_4}{r_3 - r_4},\\ \beta_2 &= \frac{\pi}{r_5 - r_6},\\ \delta_2 &= \frac{\pi r_5}{r_6 - r_5}.\end{aligned}$$

and κ is given by,

$$\kappa = \frac{\Phi_p}{\frac{\pi}{2}\left(\frac{4}{\pi^2}\left(\left(r_4 - r_3\right)^2 - \left(r_5 - r_6\right)^2\right) + \left(r_6^2 + r_6 + r_5^2 + r_5\right) - \left(r_4^2 + r_4 + r_3^2 + r_3\right)\right)}. \tag{2.31}$$

Thus, the negative annulus represents a region of primarily uniform magnetic field, with exception to the boundaries of the annulus where the magnetic field strength decays smoothly to zero. The negative annulus B_z distribution given by equation 2.30 in addition to an instance of the sunspot model, defines fully the distribution of B_z on the photosphere. The B_x and B_y components are determined in the same way as they are for the main sunspot region, in that they are a product of a potential field extrapolation given the definition of B_z at the photosphere.

2.3 Lare3D, Initialisation and Driving

2.3.1 Lare3D

The simulations in this work are produced using the Lare3d code (Arber et al., 2001). The code is mature, well used (Gerrard et al., 2001; Haynes et al., 2008; Archontis and Hood, 2012b; Gerrard et al., 2001, 2003; Gordovskyy et al., 2014; Hood et al., 2009; Arber et al., 2007; Leake and Arber, 2006) and continues to be updated and refined. This work uses Lare3D version 3.4.1. The code is written in Fortran 90, is parallelised with MPI and has been used for technically similar studies (Sturrock et al., 2015b; Sturrock and Hood, 2016; Sturrock et al., 2015a; Sturrock, 2016; Gerrard et al., 2003). Lare3D was designed to solve the resistive MHD equations and accurately simulate shocks. To capture shocks accurately Lare3D employs both background and shock viscosity. However, in this investigation we are not interested in shock physics and in all simulations we endeavour to simulate gentle motions, e.g. the model sunspots are accelerated gently to full rotation speed. Therefore we use Lare3D for its ability to solve the resistive MHD equations. Lare3D is a predictor-corrector time-stepping code that evolves an initial system by numerically approximating the state of the system at a time (controlled by the CFL condition (Courant et al., 1928)). The code first evolves the MHD variables (the magnetic field, velocity, mass density and internal energy density) using a Lagrangian step. This step is able to distort the numerical grid, so Lare3D remaps the variables to a uniform grid (an Eulerian step).

The Lare3D Numerical Grid

Lare3D uses a staggered grid, meaning the MHD variables are not cospatial. Figure 2.1 shows an example of a Lare3D grid cell. The mass and internal energy densities are stored at the centre of each cell. All components of velocity are stored at the

corner of the cell and the magnetic field components are stored at the centre of individual cell faces, as shown by figure 2.1. This information will be used when describing the boundary and initial conditions below.

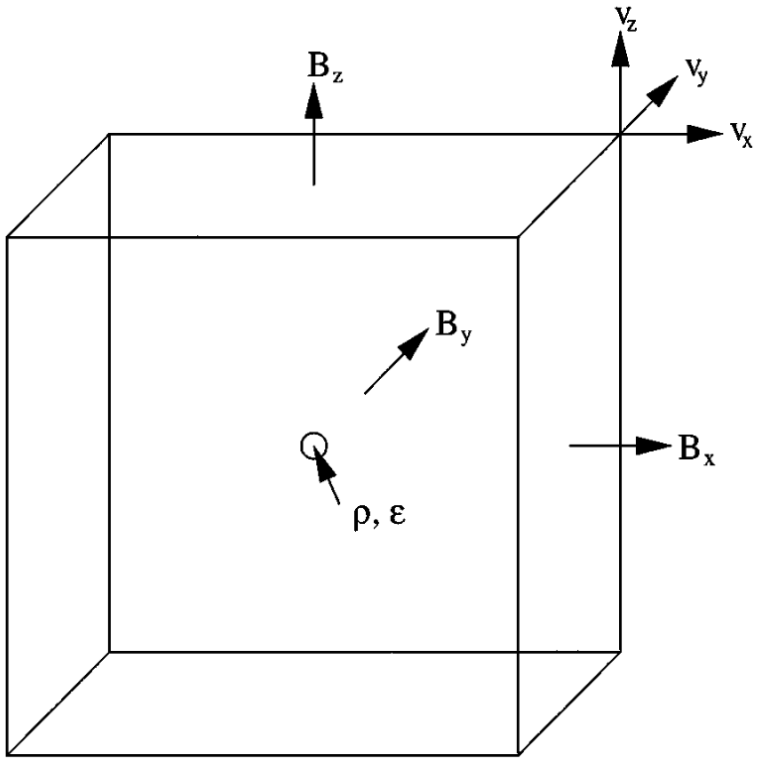

Figure 2.1: This figure shows an example cell of the numerical domain, showing the location of the variables within the grid cells. Image credit: Arber et al. (2001).

The Lare3D Time-Step

Because Lare3D solves the MHD equations which are hyperbolic, the CFL condition (Courant et al., 1928) is imposed to make the numerical scheme stable. The CFL condition limits the step-size of a numerical scheme to maintain stability, using the characteristics of the solution and information of the grid. Further explanation of the CFL condition can be found in Morton and Mayers (2005) (pg. 89) and the way that the CFL condition is imposed in Lare3D is shown in appendix H. The primary imposition of the CFL condition on this work is that it limits the time-step

of the code, and if not managed sufficiently the numerical expense of the simulations becomes exacerbated. Lare3D defines the time-step based on the conditions of the state variables and the grid, in addition to some corrections based on the numerical scheme and additional physics packages one may use.

Lare3D uses a time-step for each the Lagrangian and remap steps. It is found that the Lagrangian time-step was the most limiting to this investigation. The Lagrangian CFL limited time-step of Lare3D, is defined as a combination of the effective speeds from viscous pressure (for the background and artificial viscosities used by the code) and the fast mode wave speed, in combination with the smallest length scale of the grid. In this investigation, suitable resolution requirements fix the smallest grid size, but otherwise the contribution from the fast mode wave speed is found to be the dominant term in Lare3D CFL condition. Specifically the Alfvén speed component dominates over all else. The Alfvén speed is given by,

$$v_A^2 = \frac{B^2}{\mu_0 \rho}, \tag{2.32}$$

where v_A is the Alfvén speed, B is the magnetic field strength, ρ is the mass density and μ_0 is the vacuum permeability (Alfven, 1942). It is found that the strong magnetic fields of the model sunspots significantly limit the time-step of the simulations. However, testing showed that the mass density could be enhanced enough to regain control over the simulation time-step, without significantly altering the evolution of the magnetic field enough to cast doubt on the findings of this investigation. This will be discussed further in the latter sections of this chapter.

2.4 Boundary Conditions

The simulations that are discussed throughout this thesis employ a variety of numerical boundary conditions. In this section we explain the three types of boundary conditions used throughout this work. The different boundary conditions correspond

to the three unique boundaries used for the simulated model sunspots, namely, the upper-boundary, the side-boundaries and the lower-boundary. Each simulations discussed in this work use identical boundary conditions, unless stated otherwise in the relevant discussion. Lare3D requires the definition of all simulation primary variables in two layers of ghost-cells at each boundary. In each of the following sections we discuss the definition of the primary simulation variables at the domain boundary and in the two ghost-cell layers at the given boundary. The primary simulation variables (i.e. those evolved by the Lare3D code) are: the magnetic field ($\mathbf{B}$), the velocity ($\mathbf{v}$), the density (ρ) and the specific energy density (ε). When discussing the boundaries, we require a means to identify formally where we are referring to in the numerical grid. Let us define that each simulation is composed of a number of cells (see 2.3.1) and in the x, y and z-directions there are nx, ny and nz cells respectively. For example, this means that we may say the uppermost cell of the domain is found at $z = nz$, and therefore the first ghost-cell at the top of the domain is found at $z = nz + 1$. Following this convention allows us to minimise confusion due to the staggered grid used by Lare3D. In all circumstances, in the following discussion when we refer to a variable given at a particular location, we refer to the value of the variable in the given cell referenced by the location, i.e. $\rho(z = nz)$ is not collocated with $v_z(z = nz)$ but they do both refer to the respective parameters of the same cell.

2.4.1 Upper Boundary Conditions

The upper-boundary of the domain uses open-like boundary conditions. The purpose of this choice of boundary condition, is to minimise the effects of this boundary on the solution of the simulation by allowing material to leave freely and to allow the magnetic field to rotate without restriction.

At the upper boundary, we impose that at all times, the magnetic field leaves normal to the domain and continues to be normal in the ghost cells, thus the magnetic field at the upper boundary and ghost-cells is defined by,

$$\begin{aligned} \mathbf{B} \perp \hat{\mathbf{n}}|_{z \geq nz} &= \mathbf{0}, \\ B_x|_{z \geq nz} = B_y|_{z \geq nz} &= 0, \\ \nabla B_z \cdot \hat{\mathbf{n}}|_{z \geq nz} &= 0, \end{aligned}$$

where $\hat{\mathbf{n}}$ represents a unit normal vector that is perpendicular to the upper domain boundary. The velocity at the upper domain boundary is defined such that it is constant across the boundary. Specifically, maintaining the previous definition of $\hat{\mathbf{n}}$, the upper-boundary boundary conditions for velocity are,

$$\nabla \mathbf{v} \cdot \hat{\mathbf{n}}|_{z=nz} = \mathbf{0}.$$

This states that at the upper domain boundary, all components of velocity are held constant across the boundary. We also impose that the velocity remain constant in the ghost-cells at the top of the domain. We do this so that the upper-boundary does not impose any resistance on the magnetic field of the rotating sunspots. Finally, we define that both density and internal energy density remain constant across the domain boundary in the same manner as each component of velocity. Specifically,

$$\begin{aligned} \nabla \rho \cdot \hat{\mathbf{n}}|_{z=nz} &= 0, \\ \nabla \varepsilon \cdot \hat{\mathbf{n}}|_{z=nz} &= 0. \end{aligned}$$

We also maintain that both ρ and ε remain constant in the upper ghost-cells.

2.4.2 Side Boundary Conditions

All four side boundaries of the domain employ the same style of boundary condition, these are slippery-mirror boundary conditions. The purpose of this type of boundary condition being used is so that we do not lose magnetic flux through the side

boundaries of the domain and there is as little as possible resistance to the rotation of the sunspot imposed by the side boundaries. The magnetic field component boundary conditions at the side boundaries are as follows,

$$\mathbf{B} \cdot \hat{\mathbf{n}}|_{\tau \forall z} = 0,$$

where $\hat{\mathbf{n}}$ is a unit normal vector that is perpendicular a given side domain boundary and τ represents $(x, y) \in \{(0, 0), (nx, 0), (0, ny), (nx, ny)\}$. The reason we refer to this boundary condition as a mirror style condition is because in the ghost-cells at the side boundaries the magnetic field is defined such that it the mirror image. Thus, the magnetic field components in the ghost-cells are defined as such. Similarly, the velocity at all of the side boundaries follows the condition,

$$\mathbf{v} \cdot \hat{\mathbf{n}}|_{\tau \forall z} = 0,$$

where τ and $\hat{\mathbf{n}}$ retain their previous meaning. Again velocity is defined such that the velocity components in the ghost-cells are the mirror image of those in the domain at equal distance from the boundary. Finally, both density and internal energy density are again mirror image across the boundary. This can be written as,

$$\nabla \rho \cdot \hat{\mathbf{n}}|_{\tau} = 0,$$
$$\nabla \varepsilon \cdot \hat{\mathbf{n}}|_{\tau} = 0.$$

2.4.3 Lower Boundary Conditions

The lower boundary of the domain is where each instance of the magnetic field of the sunspot is defined according to the model derived in section 2.1 and where the sunspot rotation is induced. Therefore, the lower boundary conditions are unique for each simulation based on the particular definition of the sunspot being simulated. However, the normal magnetic field is always given by an instance of equations 2.13 and 2.26, for some set of model parameters (which are explained in detail in section

2.1). Thus

$$B_z|_{z=0} = S(r),$$

where $S(r)$ is given by equation 2.1. The remaining magnetic field components (B_x and B_y) are determined by solving for a potential field in the domain, where the upper and side domain boundary conditions are given above and the lower boundary condition is the B_z defined by the instance of model sunspot. At all times during all simulations, we maintain that the magnetic field in the lower ghost cells does not evolve and remains in the potential state. Due to the staggered grid (see section 2.3.1) and the potential field boundary conditions in the ghost cells, B_z is maintained constant at the lower boundary but B_x and B_y are not defined there, so strictly at the boundary these components may change, but half way into the first ghost cell all magnetic field components are constant in time. Hence the lower boundary imposes that,

$$\mathbf{B}|_{z<0} = \nabla\psi,$$

where ψ is the scalar potential field solution that the simulation is initialised with.

The density and internal energy density are held constant at all times in the lower ghost cells and so at the boundary, via interpolation, may evolve slightly. We may write,

$$\rho|_{z<0} = \rho_0,$$
$$\varepsilon|_{z<0} = \varepsilon_0.$$

The values of ρ_0 and ε_0 are defined as part of the pressure balance initialisation (see section 2.5.2).

Finally, the velocity at the lower boundary condition is dependent on the particular instance of sunspot being modelled, but we consistently impose that,

$$v_z|_{z\leq 0} = 0.$$

This means that there are no quantities advected into the domain by velocity. This is enforced so that we may better recognise a rotating sunspot's contribution to magnetic energy by isolating the sunspot from external factors as much as possible.

2.4.4 The Driver

The remaining velocity components (v_x and v_y) are determined uniquely for a given set of model sunspot parameters. Specifically the velocity driver, for a given sunspot, is a function of three of the model parameters: the umbral radius (U_r), the penumbral radius (P_r) and the rotation rate (ω). Because all model sunspots have cylindrical symmetry, we impose a cylindrically symmetric driver on the magnetically defined sunspot. Thus, for clarity we first illustrate the driver using cylindrical coordinates and then convert to Cartesian.

We drive all sunspots with a rotation profile motivated by the findings of Botha et al. (2008), who numerically simulate sunspot rotation and measure that the natural rotation of a sunspot is akin to a Rankine vortex. Specifically, Botha et al. (2008) find that the strongest magnetic field (the umbral region in this thesis) rotates as a solid body and the surrounding material forms a free vortex. However, Botha et al. (2008) rotated their numerical domain and observed this rotation profile form, in this work we wish to drive the sunspot and include more stringently defined magnetic regions in the domain. So with respect to the sunspot defined in this work, we impose that the umbral magnetic field region rotate solidly (in agreement with Botha et al. (2008)) and the penumbral region gradually decay with increasing radius. But because we are unable to fit a true free vortex in our simulation domain, we impose that penumbral driver decay more quickly in the radial direction than a free vortex would. This is principally done so that we can fit in the negative annulus which captures the penumbral field magnetic flux, without having this region experience rotation as well.

Thus, in cylindrical coordinates, as a function of radius, the azimuthal component of velocity is defined as,

$$v_\theta(r) = \begin{cases} \omega r \,;\, r \leq U_r, \\ \frac{\omega U_r}{2}\left(1 + \cos\left(\pi \frac{r - U_r}{P_r - U_r}\right)\right) \,;\, U_r < r \leq P_r, \\ 0 \,;\, P_r < r, \end{cases} \tag{2.33}$$

where r is the radial distance of a point, with respect to the centre of the umbra. Equation 2.33 represents the rotation profile associated with a given rotation rate (ω), but does not describe the acceleration phase. However, we may define the v_x and v_y boundary conditions that drive the sunspot after the acceleration phase using these results and define this as v_{xm} and v_{ym} where the m subscript denotes maximum (i.e. the maximum values of velocity reached at the end of the acceleration phase),

$$v_{xm}(\mathbf{c}) = -v_\theta \cos\left(\frac{\pi}{2} - \theta\right), \tag{2.34}$$

$$v_{ym}(\mathbf{c}) = v_\theta \sin\left(\frac{\pi}{2} - \theta\right), \tag{2.35}$$

where $\mathbf{c}$ represents a position vector on the photosphere and θ is the angle subtended by the vector that connects $\mathbf{c}$ to the centre of the sunspot, and the $\theta = 0$ line in cylindrical coordinates. We may define the velocity boundary conditions during the acceleration phase in terms of equations 2.34 and 2.35. During the acceleration phase, we gently accelerate all simulated sunspots from rest to the full rotation rate using a sinusoid, primarily to ensure smoothness of the driving at all times. Thus, the general velocity boundary conditions are given by,

$$v_x(\mathbf{c}) = A(t) v_{xm}(\mathbf{c}),$$

$$v_y(\mathbf{c}) = A(t) v_{ym}(\mathbf{c}),$$

where $A(t)$ represents a scaling amplitude that is a function of time and is defined

as,

$$A(t) = \begin{cases} 0\,;\, t < t_0, \\ \frac{1}{2}\left(\sin\left(-\frac{\pi}{2} + \pi\frac{(t-t_0)}{\delta}\right) + 1\right)\,;\, t_0 \leq t \leq t_0 + \delta, \\ 1\,;\, t_0 + \delta < t. \end{cases} \tag{2.36}$$

Thus, the lower domain boundary conditions for the x and y-components of velocity are defined collectively by equations 2.33, 2.34, 2.35 and 2.36 and at all times throughout the lower ghost cells and at the photosphere we impose $v_z = 0$. These boundary conditions for velocity are imposed in all ghost cells and at the photosphere.

2.5 Initial Conditions

All simulations evolve with the boundary conditions described in section 2.4, but in addition all primary variables must be initialised throughout the domain, at the start of each simulation. The numerical domain is initialised as stationary, thus all velocity components are zero. The internal energy density is initialised using the Val-C model temperature profile. Specifically the temperature data tabulated in the third column of table 26 in Avrett and Loeser (2008) provides this information (the height information is found in the same table). The temperature is then interpolated onto the equally spaced grid of our numerical domain. As stated in chapter 1, for simplicity we do not include the relatively cool properties of natural sunspots in the simulations in this work, so the Val-C temperature profile is imposed purely as a function of height.

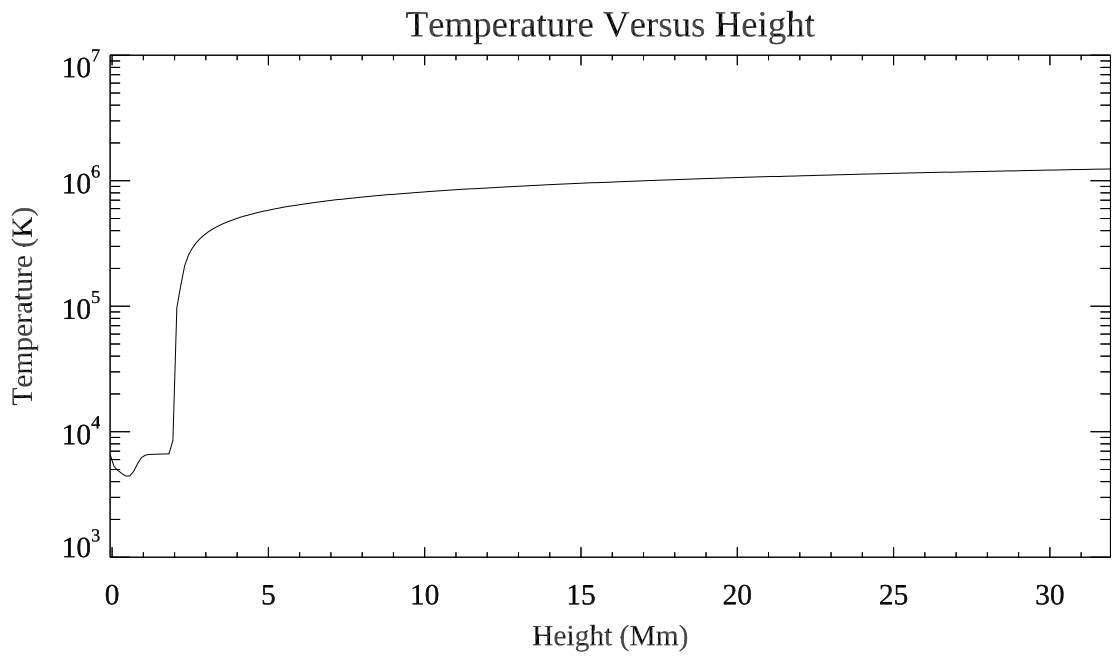

Figure 2.2: A line plot showing the temperature as a function of height profile used to initialise all simulations.

All simulations in the main body of this work have a physical domain height ranging from 0Mm at the photosphere to 32Mm at the upper domain boundary, with 256-cells in the z-direction. Figure 2.2 shows the resultant temperature versus height profile used to initialise all simulations in this work (unless stated otherwise).

2.5.1 Potential Magnetic Field

The magnetic field in the domain is initialised with a potential field solution (see section 1.8). This means that the initial magnetic field is free of current everywhere and can be written as,

$$\mathbf{B} = \nabla\psi,$$

where ψ is a scalar field that must obey equation 1.40. For a given set of boundary conditions where the magnetic field (or gradient of the scalar potential) normal to

each boundary is given, a unique solution to equation 1.40 exists and can be solved for numerically.

Equation 1.40 is an elliptic second order partial differential equation and there are numerous numerical methods for solving such equations (Saad, 2003; Burden and Faires, 2010; Garcia, 2015; Strang, 2021; Morton and Mayers, 2005). Here, we solve equation 1.40 using an iterative relaxation method, the method used belongs to a family of traditional (well established) techniques including the Jacobi and Gauss-Seidel schemes (Strang, 2021). We specifically use the method of successive over relaxation (SOR) (Young, 1954), which is a common finite difference method that solves elliptic PDEs (like 1.40) by approximating the Laplacian using the method of finite differences (Burden and Faires, 2010). Doing this recasts equation 1.40 as a linear system, $\mathbf{Ax} = \mathbf{b}$. Qualitatively, the SOR method uses the definition of the photospheric normal magnetic field component (B_z) to iteratively calculate more accurate approximations of the true the scalar potential, throughout the domain. It is easily shown that the solution of equation 1.40, when recast as a linear system, demands that each value of ψ, at a given grid point, be a weighted average of the neighbouring grid point's ψ values. The solution converges when each cell's ψ value is the average of the neighbouring cells (with weighting). Technically, full convergence occurs only after infinite iterations, but given a suitable error threshold a practical the converging series is curtailed prematurely and the solution is accurate to a predetermined accuracy.

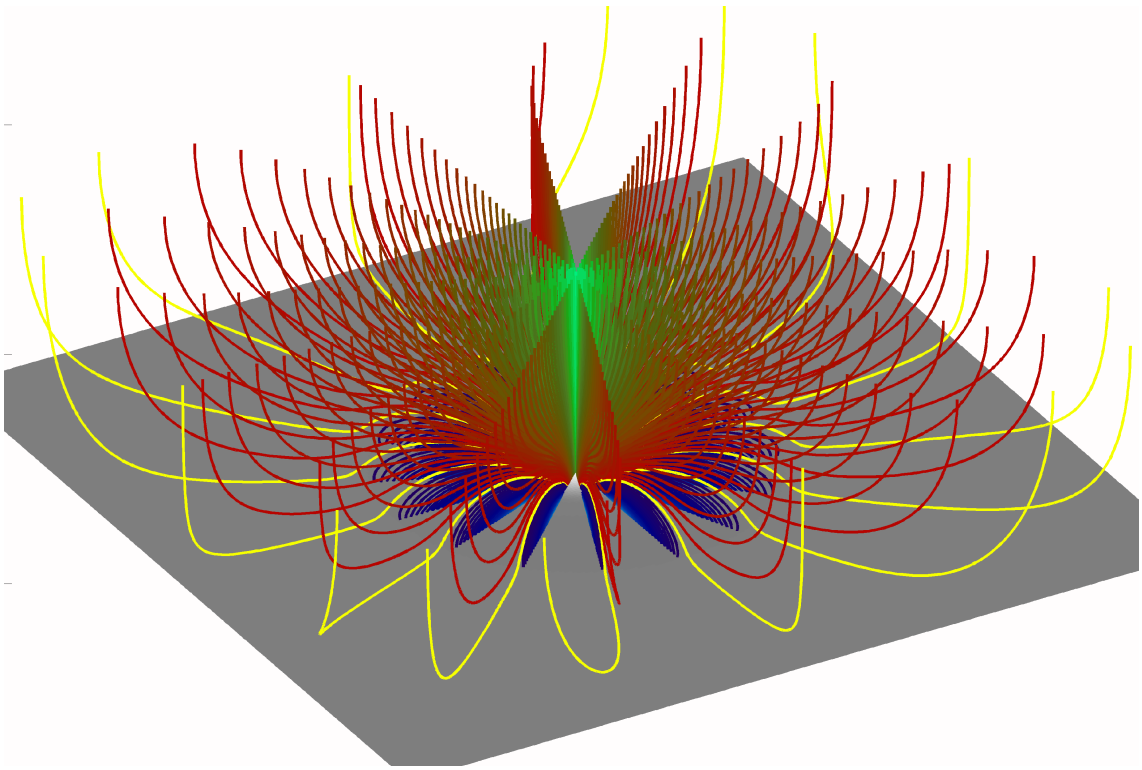

Figure 2.3: The initial, potential, magnetic field of simulation 1. The red and green field lines show the umbral magnetic field and the blue lines show the penumbral magnetic field. The yellow field lines show field lines that emerge through the photosphere at the umbral-penumbral interface.

Testing found the desired level of convergence can be reached more quickly by preconditioning the SOR method; specifically by initialising each layer (in height) of the domain with the net flux of the model sunspot being solved. This preconditioning step is found to reduce the time necessary to develop physically appropriate magnetic field strengths, and instead the solver simply must redistribute an initial estimate (primarily locally). Figure 2.3 shows a potential field solution obtained numerically using the method explained above.

The procedure described in this section is used to initialise all magnetic fields for any given instance of the sunspot model developed previously in this chapter.

Specifically, for any given photospheric definition of B_z, the magnetic field throughout the domain is defined uniquely.

2.5.2 Pressure Balance

We initialise the domain with a Val-C temperature profile (Avrett and Loeser, 2008) as explained previously in this section. The simulations include gravity and thus we must define the mass density such that the thermal pressure gradient (given by the mass density and internal energy density) balances the acceleration force imposed by gravity on the mass. We do this so that the initial domain is static, but also so that there are no accelerations present in the initial solution, hence ensuring all changes to the sunspots are a consequence of the imposed rotation only. To do this we begin with the momentum equation (equation 1.12), which we repeat for convenience,

$$\frac{D\mathbf{v}}{Dt} = \frac{1}{\rho}\mathbf{j} \times \mathbf{B} - \frac{1}{\rho}\nabla P - \mathbf{g},$$

where all variables maintain the meaning they were assigned in chapter 1. Our intention is to initialise all simulations with no velocity or acceleration and thus the left hand side of equation 1.12 vanishes. We impose that all simulations are initialised with a potential magnetic field, which by definition have no currents, hence the Lorentz force vanishes from equation 1.12. We have a temperature distribution and would like the domain to have mass and gravity, thus we cannot simplify equation 1.12 further. Equation 1.12 becomes,

$$\frac{1}{\rho}\nabla P = -\mathbf{g}. \tag{2.37}$$

To define an initial density distribution that does not introduce acceleration, we must define it such that it satisfies equation 2.37. Lare3D imposes gravity at the same location as velocity (see section 2.3.1) and both density and internal energy density are defined at cell centre. Because the temperature profile is a function of

height only, we may first simplify equation 2.37 to,

$$\frac{1}{\rho}\frac{\partial P}{\partial z} = -g. \tag{2.38}$$

Using the method of finite differences (Burden and Faires, 2010) (and substituting the definition of pressure using equation 1.16) it can be shown that equation 2.38 can be written as,

$$\rho(z+1) = \rho(z)\left(\frac{2(\gamma-1)\varepsilon(z) - g(z)h_z}{2(\gamma-1)\varepsilon(z+1) + g(z)h_z}\right), \tag{2.39}$$

where z represents a cell's z-coordinate (hence, not the same height for all variables, i.e. gravity is defined at the vertex) and h_z represents the distance between two cell centres in the z-direction, all other variables maintain their usual meaning and are located according to the Lare3D grid cell definition (see figure 2.1). Equation 2.39 expresses a means to calculate the density at a given height numerically, based on the definition of temperature, gravity and density from the cell below. By imposing a value of density at the photosphere we use equation 2.39 to define density throughout the domain.

All simulations in this thesis use a Val-C temperature profile that represents the quiet Sun atmosphere so that we can be sure that the rotation alone introduces any complexities that develop. But for density, we follow Maltby et al. (1986) and aim to replicate a density profile that is closer to what is suggested appropriate for a sunspot. However, we do not follow any specific table from Maltby et al. (1986) for density explicitly. Testing showed that the combination of simulation resolution, temperature in the lower chromosphere, magnetic field strength and the suggested true photospheric density (Maltby et al., 1986) of a sunspot resulted in a far too small simulation time-step. This is because the Alfvén speed increases either with increasing magnetic field strength or reducing density and this is a defining component of the CFL condition used by Lare3D (as explained previously). The root of the problem is shown by equation 2.39 which shows that the simulation

resolution and temperature influence how quickly mass density must reduce in the z-direction to maintain numerical pressure balance. Numerical expense limits the resolution we may use, but the solar atmosphere is characterised by its temperature, so it is clear an optimal solution does not exist. The consequence we find is that density drops too quickly in the lower chromosphere, where temperature is minimum, and if a physical density is used for the boundary condition we find a large Alfvén speed develops. This causes the simulations to run far too slowly to meaningfully carryout the investigations in this work.

The solution adopted is to increase the density at the photosphere until a suitable time-step is achieved. The density is thus overly large in the low-chromosphere. However, the primary interest of this work is to understand the magnetic properties of rotating sunspots and the magnetic energy produced by them. Thus, to improve the simulation time-step, we may also reduce the magnetic field strength, but this would certainly trivialise the overall investigation, so we elect to alter density. The density is primarily too large in the lower chromosphere but is reasonably defined elsewhere. Testing shows that the kinetic energy scales with increased density, but generally the magnetic energy (after the acceleration-phase) is less sensitive to changes in the density. The approach taken is imperfect, but provides a suitable compromise between simulation cost (given this investigation relies on so many) and accuracy.

Figure 2.4 shows the result of the pressure balance procedure explained above and thus the density profile used to initialise all simulations in this thesis (unless stated otherwise). Note that the density profile is smooth but contains the characteristic rapid decay with height observed at the transition region.

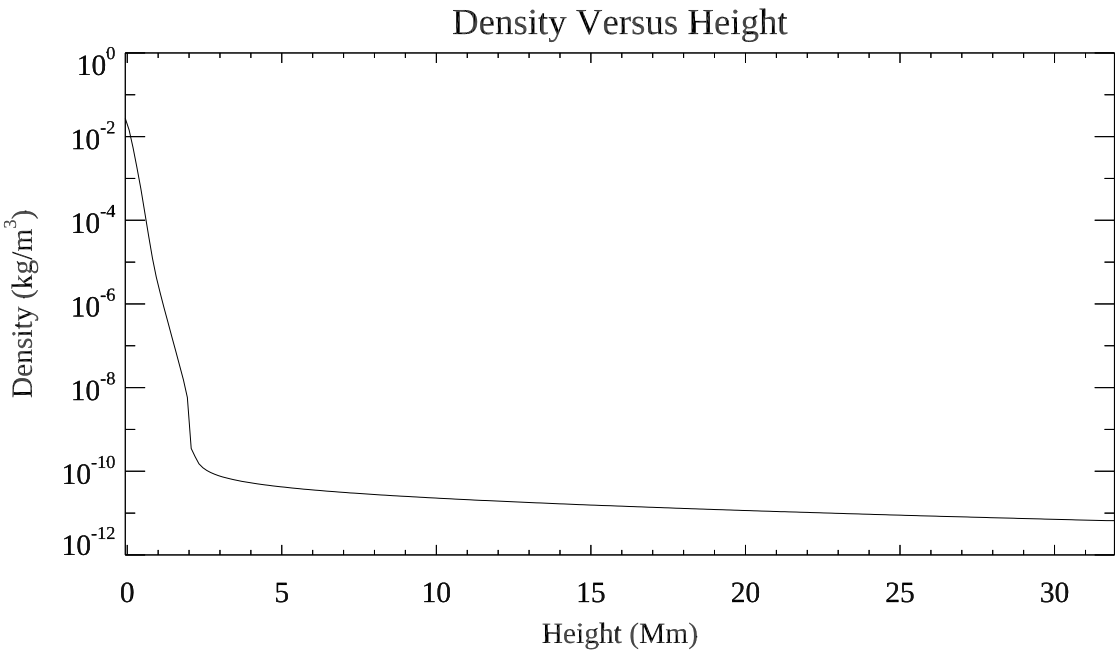

Figure 2.4: A line plot showing the mass density as a function of height profile used to initialise all simulations.

Chapter 3

Numerical Simulation of a Sunspot with a Penumbra

In this chapter we analyse the evolution of a single simulated rotating sunspot in detail. We do this to develop an understanding of how a simulated rotating model sunspot influences its magnetic environment as it is driven. Identifying and understanding the fundamental physical processes present in the single simulation, will assist with the interpretation of scaling relations in chapter 6, as we find there that all the simulated sunspots for this model (in a reasonable parameter space) evolve similarly. In this chapter, we identify the dominant characteristics of the simulation. The sunspot simulation analysed here is simulation 1, whose model parameters (see chapter 2) are $U_b = 1300\text{G}$, $\mu = 0.5$, $U_r = 5\text{Mm}$, $P_r = 10\text{Mm}$, $\omega = 48^\circ\text{hr}^{-1}$ and $\gamma = 1$. The specifics of the simulation initialisation and driving can be found in sections 2.5 and 2.4 respectively. The simulation discussed here is chosen because it is the one to which all other simulations scale in chapter 6, meaning all other simulations in this thesis can be considered a perturbed version of the one discussed in this chapter.

3.1 Observed Evolution

To investigate rotating sunspots, we drive a model sunspot (simulation 1 of table 6.1) with a rotation profile adapted from Botha et al. (2008) and observe the resulting changes within the numerical domain. All simulations in this thesis are initialised with a potential magnetic field and have no action taken upon them other than the imposition of a rotational velocity field at the lower simulation boundary. This means that measured changes to any magnetic-based property of the sunspot must be a consequence of the photospheric driving. The simulation investigated in this chapter is chosen because it represents something akin to an average sunspot, albeit rotating quicker than observations suggest it should (Brown et al., 2003; Brown and Walker, 2021; Zhu et al., 2012) for numerical efficiency. However, simulation 1 is particularly suitable for investigation here because is displays (to some degree) all of the key behaviours present within the larger collection of simulations. Thus, by investigating simulation 1, we may better appreciate and understand the findings of chapter 6.

3.2 Magnetic Field Evolution

Given the primary interest of this investigation is with the magnetic field environment of the sunspot, we will first consider the evolution of the magnetic field structure throughout the lifetime of the simulation. Figures 3.1 and 3.2 show how the magnetic field of the sunspot evolves (viewed from the side) throughout the simulation. The sunspot rotates in response to the imposed driving at the photosphere, which increases monotonically from no driving to a constant rotation rate (see section 2.4.4). Each panel in figures 3.1 and 3.2 show the sunspot at different points in the simulation, when the umbral region has been rotated by various amounts by the driver. The panels in figures 3.1 and 3.2 are arranged chronologically (and hence

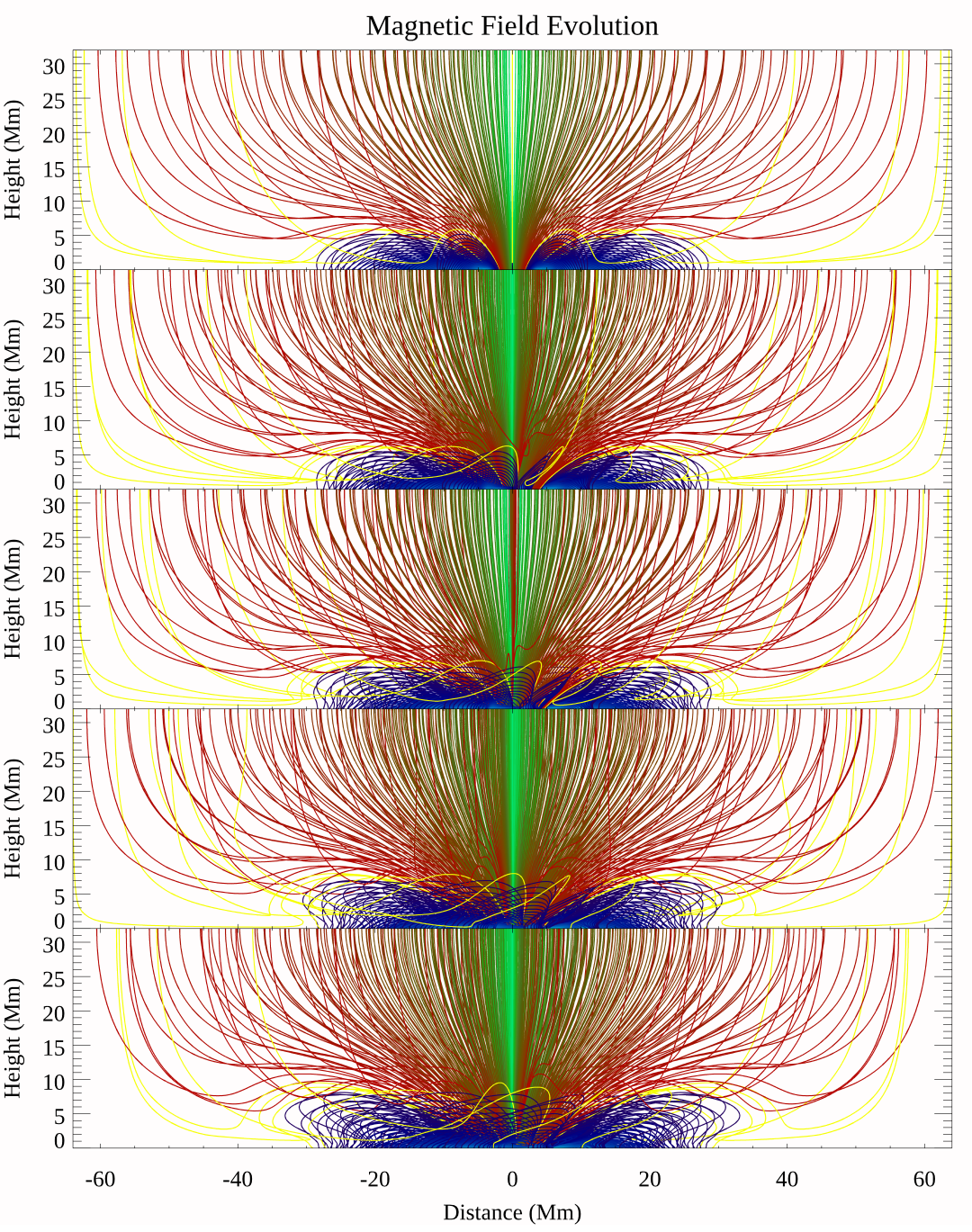

Figure 3.1: This figure shows the evolution of the sunspot magnetic field, viewed from the side. The blue lines represent the penumbral magnetic field, the red and green lines represent the umbral magnetic field and the yellow lines represent field lines that originate from the umbra-penumbra boundary. The sub-figures, moving from top to bottom, show the magnetic field at times when it has been rotated by 0°, 30°, 45°, 60° and 75° by the driver respectively.

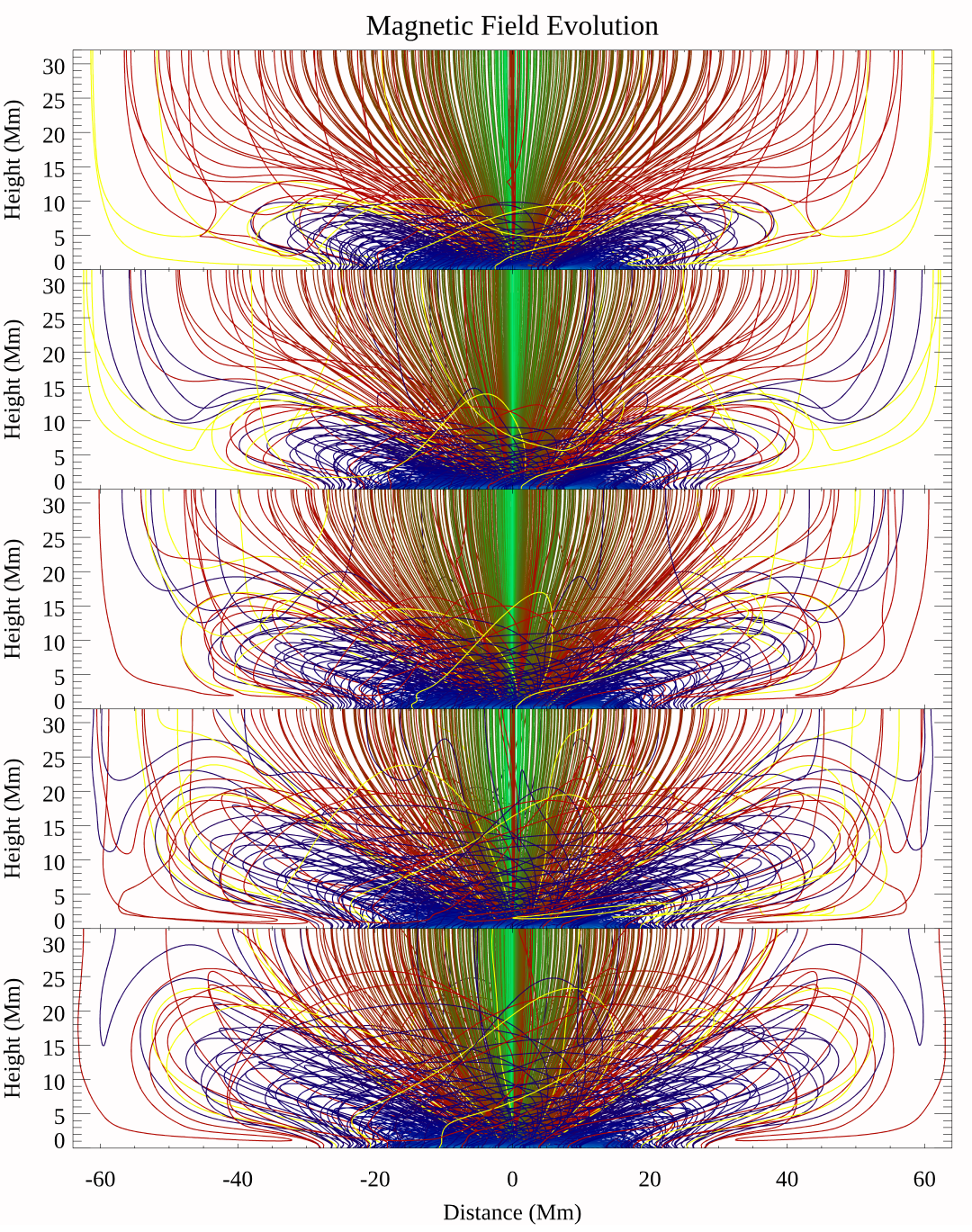

Figure 3.2: This figure shows the evolution of the sunspot magnetic field, viewed from the side. The blue lines represent the penumbral magnetic field, the red and green lines represent the umbral magnetic field and the yellow lines represent field lines that originate from the umbra-penumbra boundary. The sub-figures, moving from top to bottom, show the magnetic field at times when it has been rotated by 90°, 105°, 120°, 135° and 140° by the driver respectively.

are also in order of rotation, given the nature of the driver) beginning with the first panel in figure 3.1 and ending with the final panel in figure 3.2. The specific amount of rotation that has occurred in each panel is stated in the figure captions. The yellow magnetic field lines (present in all panels of figures 3.1 and 3.2) are those which originate at radii where the umbra and penumbra meet (on the photosphere). These field lines are coloured yellow to indicate that they should not be strictly associated with either the umbral or penumbral magnetic fields. This approach was deemed necessary because the yellow field lines are found to alternate between which region they appear to belong to. Testing found that this was solely due to the finite precision of which magnetic field lines are able to be traced (see section 4.1) and not because of (numerical) magnetic reconnection.

We observe that, generally, the state of the field is significantly perturbed from the initial potential field configuration by the end of the simulation, however, the observed perturbation is persistently greater for the penumbral field with increasing rotation. Because motion is induced where the magnetic field lines emerge from the model sunspot (see chapter 2) on the photosphere, the magnetic field is expected to be rearranged due to the plasma and magnetic field coupling. But the rearrangement is likely in one manner for the closed-penumbral field and another for the open-umbral field (which is free to relax). Indeed we observe that at all stages shown by figures 3.1 and 3.2 the blue-penumbral field lines and the red-green-umbral field lines evolve differently, as the sunspot is driven at the photosphere. We see that during the simulation the penumbral magnetic field becomes increasingly complex, but also that it expands (and eventually hits the top of the numerical domain in the final subplot of figure 3.2). Comparatively the umbral magnetic field remains far more relaxed throughout the simulation, with some change to structure as the penumbral region expands (likely in response).

The final observation we make is that although we are only performing a qualitative analysis here, we do not observe any obvious large-scale reconnection events between the two regions of different connectivity (the penumbral and umbral magnetic fields). Given the model has two differently connected regions, by design, we may expect that (or be unsurprised) if a change of connectivity were to occur in the vicinity of the separatrix which divides the two regions. We do observe what appears to be some, blue, penumbral field lines becoming untethered from the photosphere in figure 3.2, however, this may be a consequence of the finite accuracy of the field line tracing used for the diagnostic, as the penumbral field which appears to become free is near the separatrix and therefore a finite stepping method (as in the Runge-Kutta used) may simply take a step which begins in the penumbral region and steps into the umbral via the finite step-size used. This is most likely to occur near the separatrix. At this time we shall assume that the untethered blue penumbral field lines are actually a numerical issue contained in the diagnostic used to make the figure and not a physical change of connectivity brought on by magnetic reconnection. The simulation analysed here is evolved under the ideal MHD equations (equations 1.11-1.14) with $\eta = 0$. Thus, magnetic reconnection should not be physically present, although numerical effects may be.

We shall see further support that the observed change of connectivity is a plotting issue in chapter 5, where we analyse the magnetic energy in the domain; we shall see there is no clear reflection of magnetic energy reduction in the domain as one might expect if there is some true magnetic reconnection. This all implies that the sunspot primarily evolves under an ideal MHD description and resistive effects are minimal in this simulation. And secondly that the process of rotating the sunspot and its energisation appear to be stable processes. We will see in later chapters that this stability is preserved even in the presence of true resistive physics, and therefore is an interesting property of the model employed in this investigation.

3.3 Magnetic Field Strength

Given we observe that the closed penumbral magnetic field expands and the open umbral field does not, we may naturally assume that each region's properties during their evolution is not the same. There is likely something introduced and stored in the penumbral region (uniquely or in greater amount) as compared to the umbral region to fuel the expansion. Because we initialise the simulation at a minimum magnetic energy (potential) state, the logical property to first investigate is the magnetic energy, which is equivalent to the total magnetic pressure. To measure this we simply analyse the square of the magnetic field strength. Any change of the magnetic field strength in space must accompany a change in local magnetic pressure, as if the absolute magnitude of the magnetic field increases then so must the square of the field strength.

Figures 3.3 and 3.4 show the relative change in the local magnetic field strength as compared to the initial potential field solution (which is shown in top sub-figure of figure 3.3). These figures are constructed by taking the magnetic field at a given cumulative rotation, calculating the magnitude of this field at the centre of each cell, and then subtracting initial potential field solution from this. These figures highlight that although there is in general complex behaviour in the domain, the net influence of the rotation is to increase the magnetic field strength in the domain. We observe this more so than anywhere else near the photosphere where the penumbral field emerges from the sunspot. A quantitative analysis of this will be presented in chapter 5, here we merely focus on the primary observed characteristics of the sunspot evolution.

We must highlight here not all changes to the evolving magnetic field increased the magnitude of the magnetic field everywhere. There are regions where the field strength decreased, in these regions the local magnetic energies and pressures must decrease, however, only small field strength decreases are observed (e.g. reductions

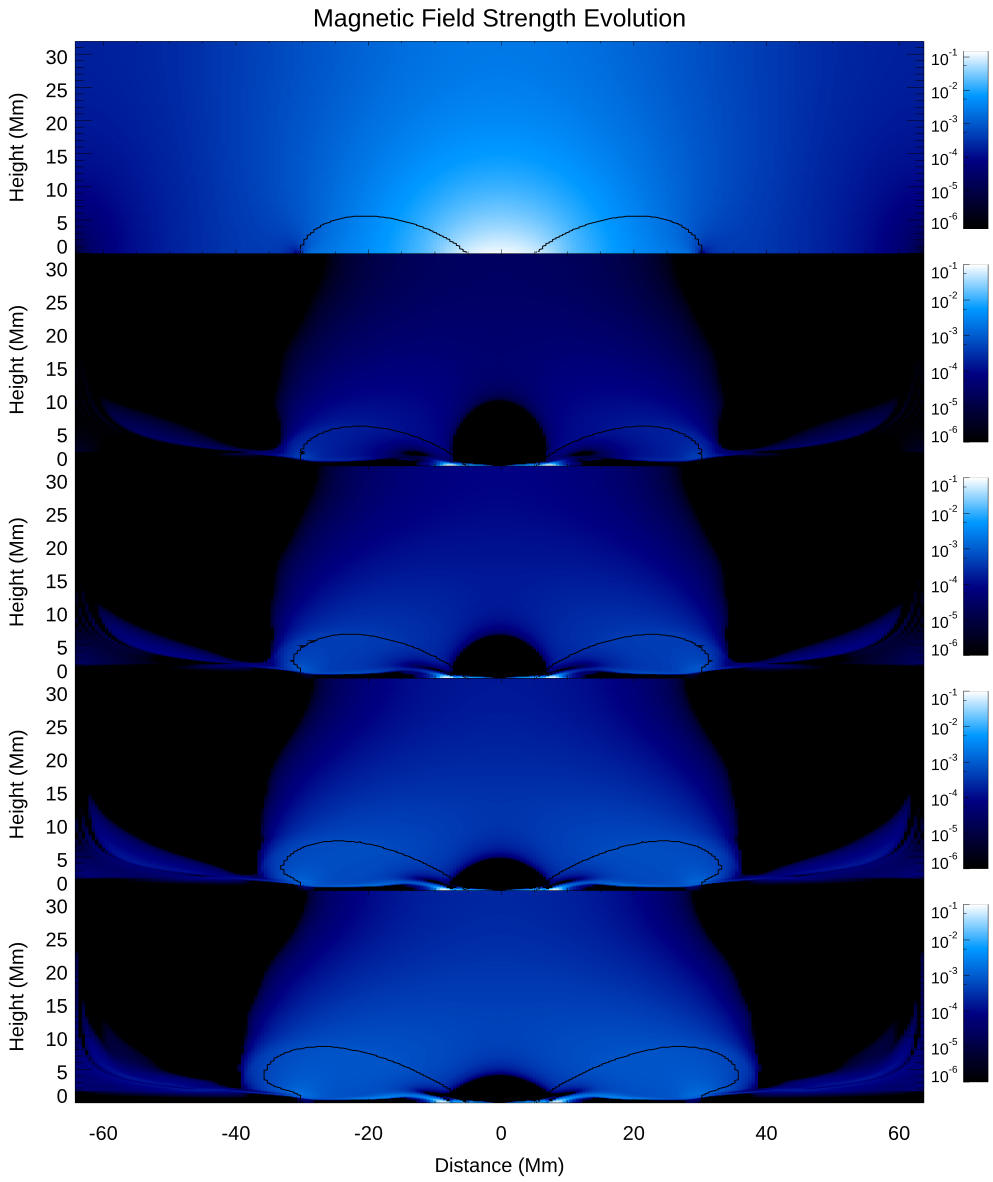

Figure 3.3: This figure shows the absolute change of the sunspot magnetic field strength with respect to the initial potential field solution, in a slice through the centre of the sunspot. The top figure shows the initial potential magnetic field strength. Subsequent figures show the absolute magnetic field strength change at times when the driver has rotated the sunspot by 30°, 45°, 60° and 75° respectively. Each absolute change is calculated by subtracting the potential field solution from the magnetic field. The black contour represents the approximate location of the separatrix that divides the umbral and penumbral magnetic field regions, in a slice through the centre of the sunspot. The colour bars have units of Tesla (T).

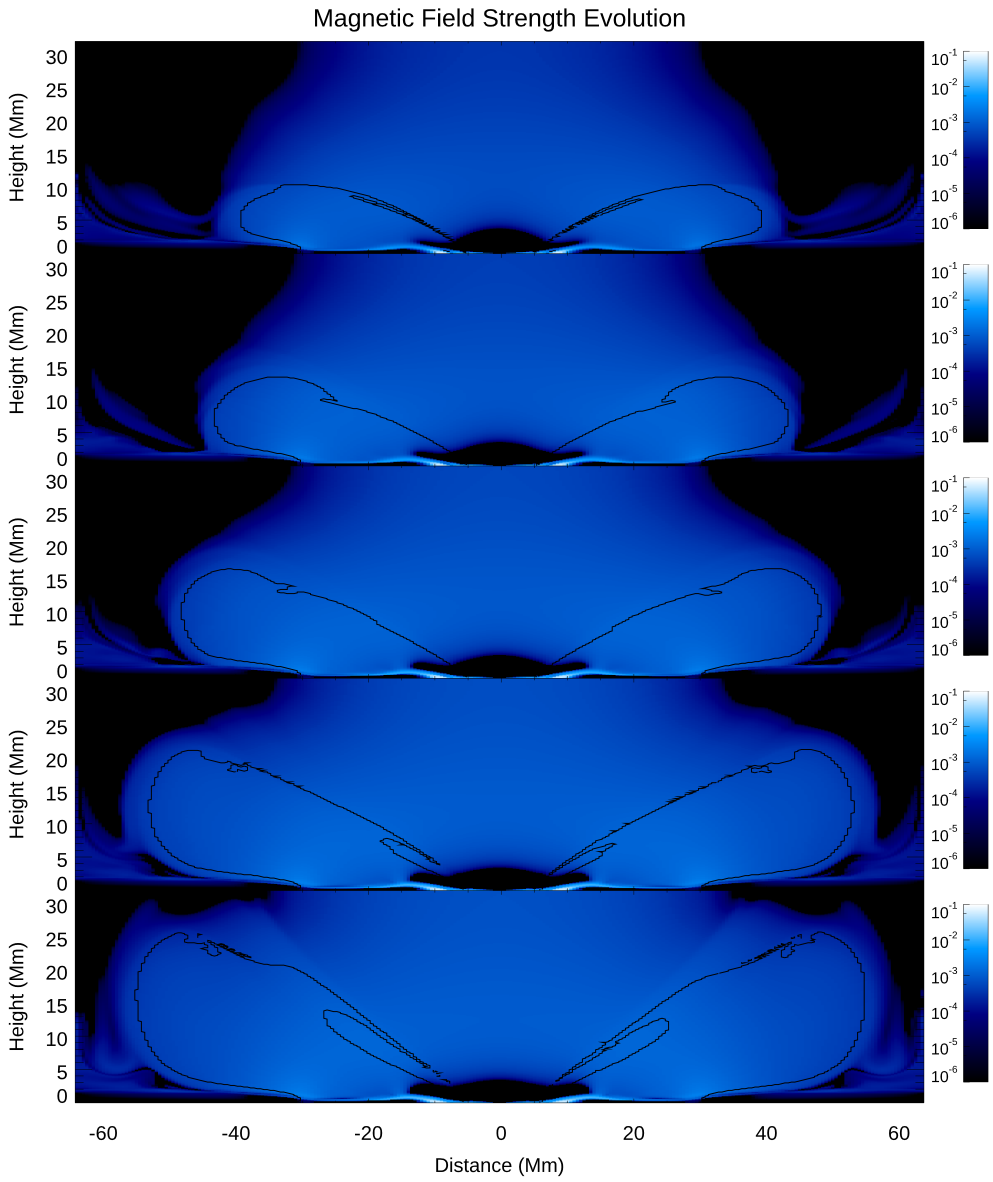

Figure 3.4: This figure shows the absolute change of the sunspot magnetic field strength with respect to the initial potential field solution, in a slice through the centre of the sunspot. The figures show the absolute magnetic field strength change at times when the driver has rotated the sunspot by 90°, 105°, 120°, 135° and 140° respectively. Each absolute change is calculated by subtracting the potential field solution from the magnetic field. The black contour represents the approximate location of the separatrix that divides the umbral and penumbral magnetic field regions, in a slice through the centre of the sunspot. The colour bars have units of Tesla (T).

of $\mathcal{O}(10G)$). The first of these regions is near the side-boundaries, where the small reductions measured, explained by figures 3.1 and 3.2 where we observe that the expanding penumbra forces the umbral field near the side-boundaries toward the z-axis of the sunspot, hence partially depleting the side boundaries of magnetic flux. Although our understanding is currently incomplete, we observe that overall the magnetic field strength is generally in excess of the initial potential field solution in most of the domain throughout the simulation and only small reductions are measured as compared to relatively strong increases of field strength. This is easily verified qualitatively, as we see in figures 3.3 and 3.4 that there is approximately as much black as there is blue, where because of the logarithmic scaling, the blue is orders of magnitude stronger.

Finally, although the penumbra is clearly the dominant region where the strongest induced magnetic fields form, we also see that small slabs of enhanced magnetic field strength form near the photosphere in the umbral field region. These features are present in figures 3.3 and 3.4 throughout the evolution of the sunspot, but do evolve slightly throughout the simulation. The features are observed within the first few, lowest, cells of the domain and seem to increase in height with increasing distance from the centre of the sunspot. These magnetic field strength enhancements may be caused directly by the velocity of the driver at the photosphere, which is the only thing introduced that also increases with radius within the umbra. Because the umbra rotates as a solid body and the magnetic field strength generally decreases with increasing radius; the observed radially dependent strengthened magnetic field may be a consequence of the combined effects of an increasing perturbation and decreasing Alfvén speed with radius. This would mean that the strong (slowly perturbed) magnetic field in the middle of the umbra has sufficient field strength and time to respond to the driver, but the relatively weak (more strongly perturbed) magnetic field in the outer umbra may not. The enhanced magnetic field with increasing

radius may then simply be a consequence of the compression of the field lines due to the rotational motion, which after some point the magnetic field becomes strong enough to resist further change.

3.4 Current Density

Thus, far we have observed that as the sunspot is driven, the penumbral magnetic field becomes increasingly twisted and because of this driving the closed-penumbral field expands. We see that the magnetic field within the penumbral region generally increases in strength by several hundred Gauss in the most extreme. By the nature of the driver, we are introducing some degree of twist or circulation into the magnetic field. An important property of the domain is the current density (especially in the context of solar MHD theory). The current density in MHD theory is defined equation 1.10. Given we initialise the domain with a potential field, any perturbation from the potential state in a closed region (given our constant photospheric boundary conditions) must introduce currents. But, given the upper boundary conditions are allowed to evolve with the system, we cannot be sure that the initial potential field solution for the umbral region is the same throughout the evolution of the simulation even though the photospheric umbra does not change. Therefore, we may expect currents in the penumbra but we may also accept that currents are likely to form in the open umbral field to some degree; albeit weaker due to the sustained relaxation of the umbral field as suggested by figures 3.1 and 3.2.

The influence of the current density will be discussed in subsequent sections and chapters; here we focus on identifying where in the domain dominant currents form. By doing so, we are able to develop an understanding of which parts of the domain are likely to host forces which may influence the evolution of the sunspot and where we may expect magnetic reconnection in the physical systems the simulations in this work represent.

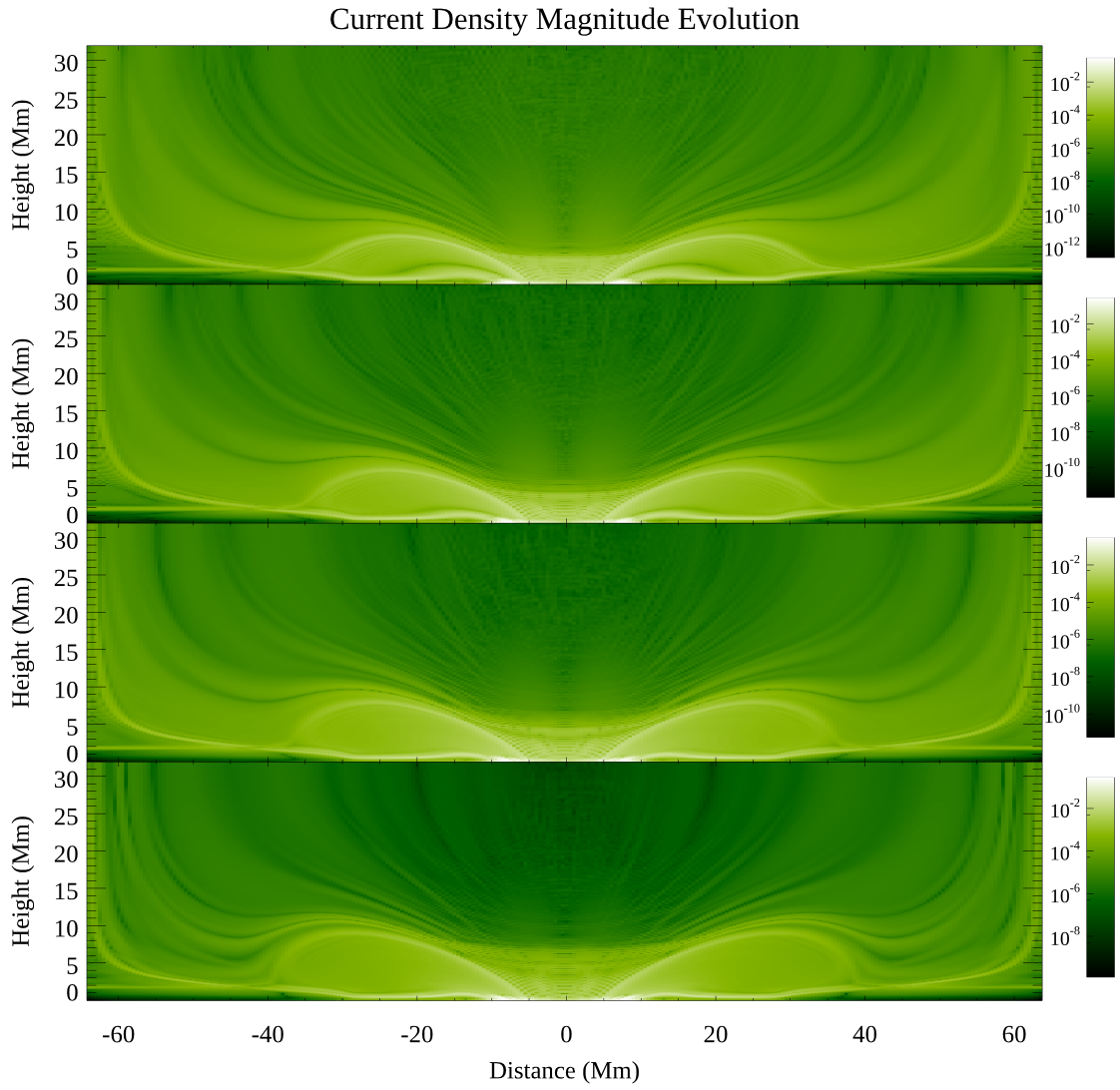

Figure 3.5: This figure shows the evolution of the magnitude of the current density during the simulation. The sub-figures, moving from top to bottom, show the magnitude of current density in a slice through the centre of the sunspot at times when the sunspot has been rotated by 30°, 45°, 60° and 75° by the driver respectively. The units of the colour bars are (Am^{-2}).

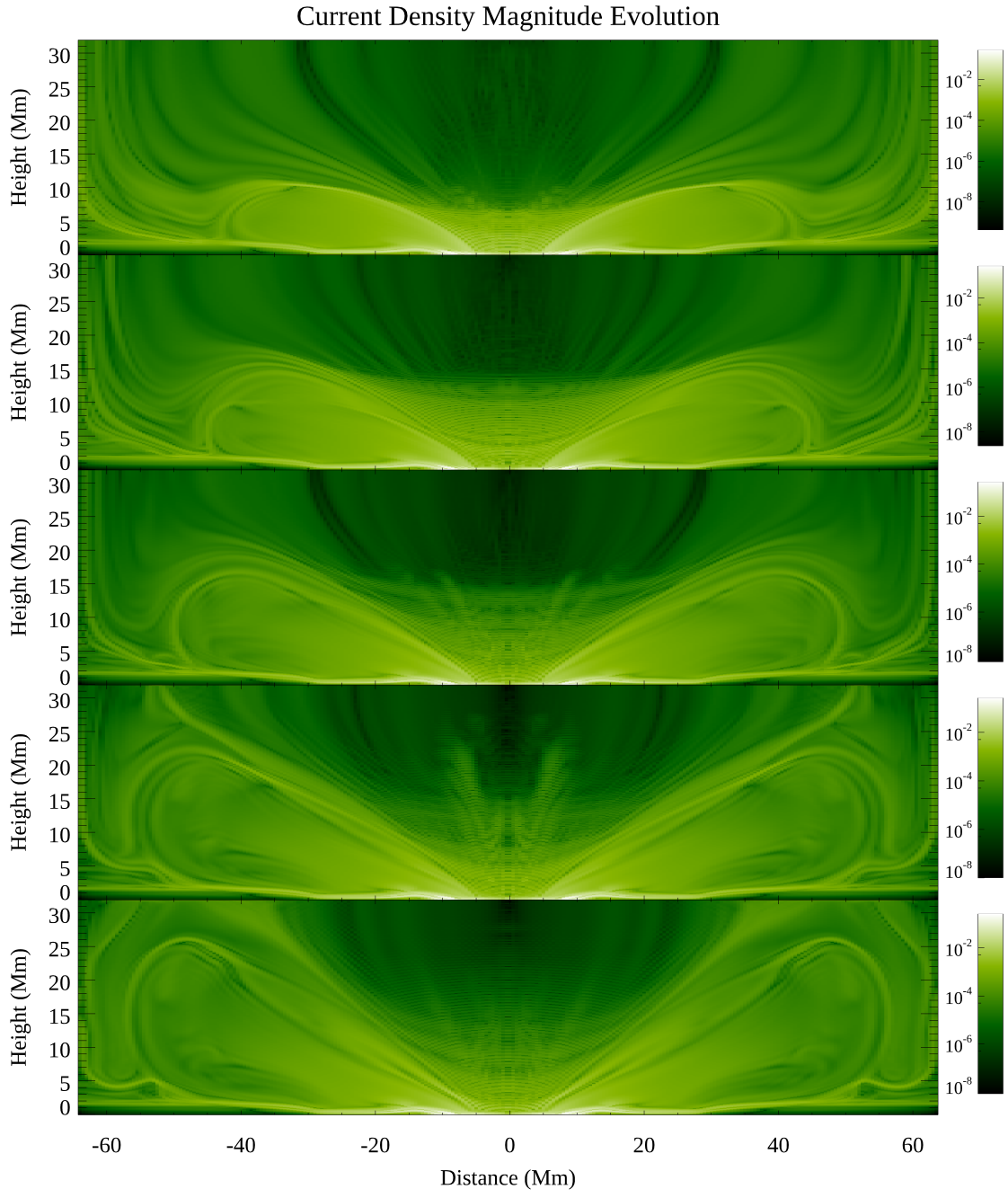

Figure 3.6: This figure shows the evolution of the magnitude of the current density during the simulation. The sub-figures, moving from top to bottom, show the magnitude of current density in a slice through the centre of the sunspot at times when the sunspot has been rotated by 90°, 105°, 120°, 135° and 140° by the driver respectively. The units of the colour bars are (Am^{-2}).

Figures 3.5 and 3.6 show how the magnitude of the current density evolves throughout the simulation. We do not include the initial domain because a potential field does not support currents, and thus has zero-current everywhere. This means all currents present, have formed as a consequence of the photospheric driving. Figures 3.5 and 3.6 show that as the sunspot is driven, currents develop throughout the entire domain to some degree. We see that the strongest currents develop in the lower-chromospheric/upper-photospheric atmosphere directly above where the penumbral magnetic field emerges from the sunspot. These regions are in exact alignment with the strongest induced magnetic field strengths, shown in figures 3.3 and 3.4. Therefore, this location not only develops and stores strong magnetic fields, but it also hosts the strongest currents in the domain.

Shifting focus away from the strongest currents, we see that generally the currents within the penumbra are somewhat stronger than those in the umbral magnetic field throughout the volume. It seems that the current density in the penumbra tends to be more consistent throughout the simulation whereas the strength of current in the umbral field is highly location and time dependent. Perhaps most interestingly, we observe relatively strong current sheets at the interface between the penumbral and umbral regions, this is likely a manifestation of the differing connectivity of the magnetic field across this interface (this will be further investigated in chapter 5).

As the sunspot is rotated, the strongest currents are observed to develop quickly, but it seems that the weaker currents are generally strengthened with increased rotation, implying that the strongest currents within the domain are achieved when rotational motion is introduced but the weaker currents tend to strengthen in correlation with the cumulative amount of twist (or perhaps as a result of the expanding penumbra).

Finally we observe that as the penumbra expands, the current sheet at the separatrix seems to move with the expanding penumbral volume. This is potentially

important because we may expect that if magnetic reconnection were to occur, it should do so within a current sheet in the vicinity of the separatrix where the connectivity of the magnetic field changes. Although we do not observe any magnetic reconnection events during the lifetime of this simulation, a knowledge of the alignment between the separatrix and current sheets is insightful, as magnetic reconnection may become more prevalent if the sunspot model used here were introduced into a domain with additional magnetic features.

Figures 3.7 and 3.8 show the angle subtended by the magnetic field and the current density vectors at various stages of the simulation. Specifically the angle is defined as,

$$\theta = \arccos\left(\frac{|\mathbf{j}\cdot\mathbf{B}|}{|\mathbf{j}|\,|\mathbf{B}|}\right) \tag{3.1}$$

We shall see in chapter 5 that the penumbra is the region where the majority of the magnetic energy introduced by the rotation of the sunspot is stored (as already suggested by figures 3.3 and 3.4), thus understanding how the penumbral magnetic field evolves is of importance. Figures 3.7 and 3.8 show that throughout the evolution of the sunspot, the angle subtended by the magnetic field and the current density is dominantly π (radians) throughout the majority of the penumbra but is 0 (radians) in the penumbra in the lower atmosphere, below the transition region at $\approx$ 2Mm. We also observe relatively thin regions of perpendicular current which separate much larger regions of dominantly parallel (or anti-parallel) current. The main physical interested in the inclination of the current density with respect to the magnetic field is that the cross product of current density with magnetic field gives the Lorentz force, which is able to alter the trajectory of a plasma flow. Therefore, any location in the domain where the current density and magnetic field are measured to be parallel must have a vanishing Lorentz force regardless of the magnitude of either the magnetic field or current density. We see that very few regions of the domain have purely parallel (or anti-parallel) currents, but generally most of the currents

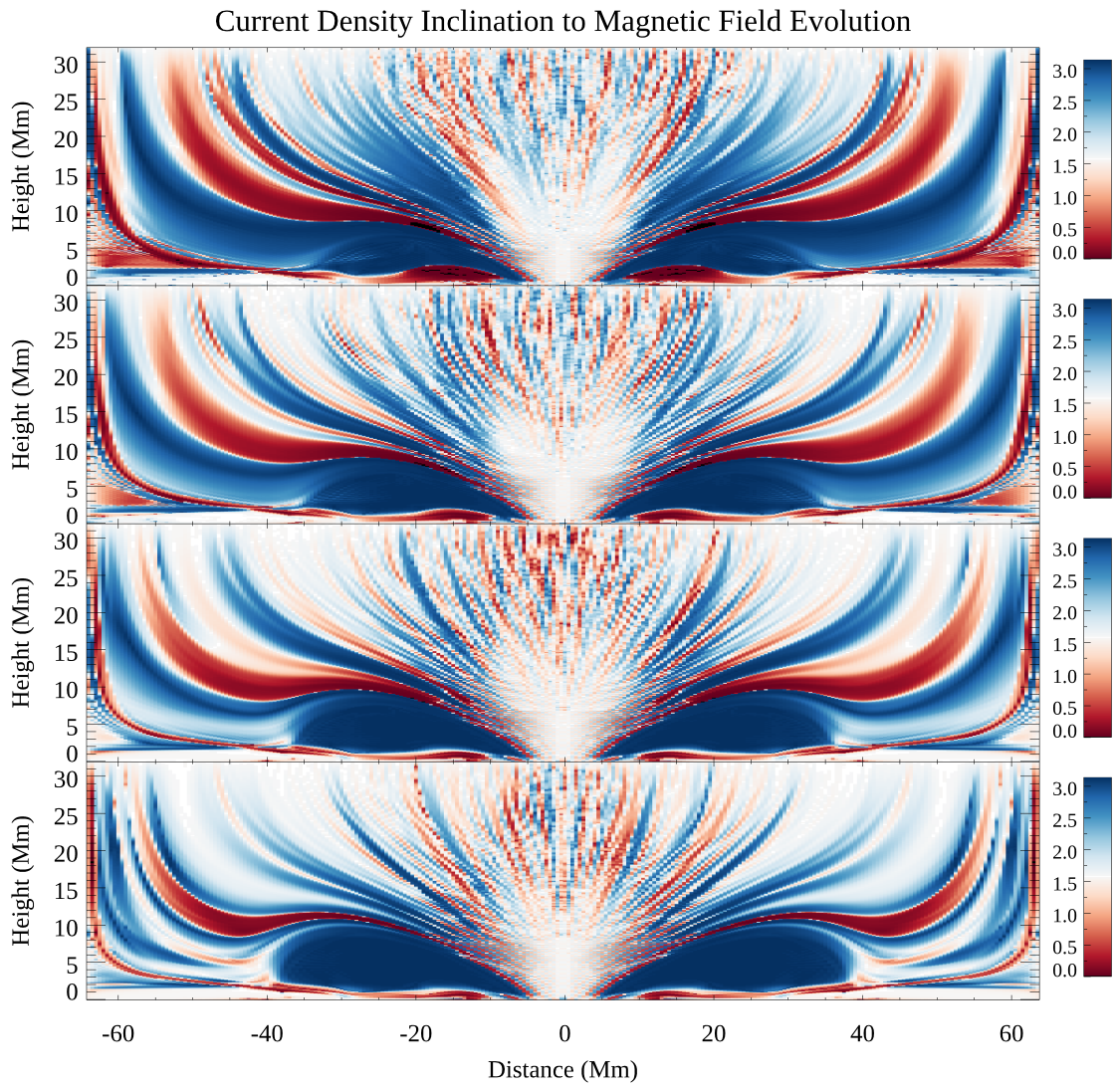

Figure 3.7: This figure shows the angle subtended by current density and the magnetic field vectors in a slice through the centre of the sunspot during the simulation. The sub-figures, moving from top to bottom, show the angle at times when the sunspot has been rotated by 30°, 45°, 60° and 75° by the driver respectively. The units of the colour bars are radians.

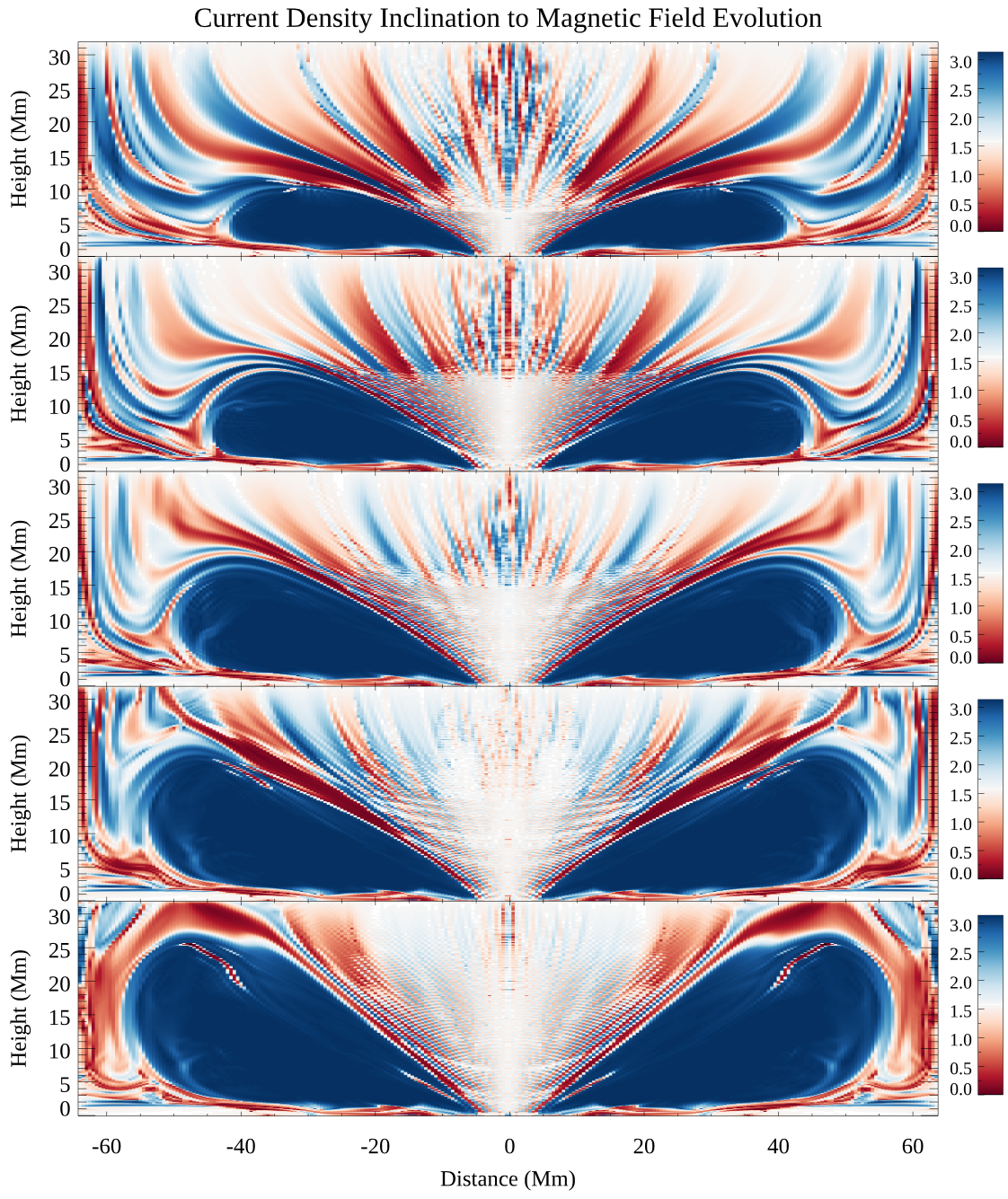

Figure 3.8: This figure shows the angle subtended by current density and the magnetic field vectors in a slice through the centre of the sunspot during the simulation. The sub-figures, moving from top to bottom, show the angle at times when the sunspot has been rotated by 90°, 105°, 120°, 135° and 140° respectively. The units of the colour bars are radians.

have a dominant parallel component. Thus, in these regions there may be Lorentz forces, but one may expect them to be small.

The regions where perpendicular current is observed are of physical importance, because of the Lorentz force, but are also more difficult to analyse. The additional difficulty of analysis arises because the Lorentz force vanishes where $\mathbf{j} \times \mathbf{B} = 0$, regardless of the strength of either the magnetic field or current density, but this is not true for perpendicular currents (or currents with a perpendicular component). A fuller understanding of the Lorentz force is physically meaningful to this investigation, but is not a primary observed quantity, therefore further discussion is deferred to a dedicated investigation of the Lorentz force in chapter 5. We may conclude that the white and intermediate colour regions (where perpendicular currents are identified) in figures 3.7 and 3.8 must represent where any significant Lorentz forces must be.

Finally we observe that the behaviour of the inclination of the current density with respect to the magnetic field in the umbral field region is far more complex than in the penumbra. Figures 3.7 and 3.8 show that, generally, there are alternating regions of parallel and anti-parallel currents present. Given the full three dimensional geometry of the domain we may expect this pattern to revolve around the sunspots central axis, and what we see in these figures is a slice through shells of alternating direction currents. Caution must be taken when analysing the angle of currents in the umbral field as figures 3.5 and 3.6 show the strength of the currents in this region are typically weak and figures 3.3 and 3.4 indicate that where there are strong currents in the umbral field (near the bottom-corners of the domain), we generally find that the strength of the magnetic field is weak. This culminates in low expectation that the forces present in the umbral field would significantly influence the evolution of the sunspot via the Lorentz force due to the lack of magnetic field strength at these locations and in fact the main finding of this diagnostic is that

the penumbra (where we measure strong currents and magnetic fields) is found to evolve in a state close to force-free.

3.5 Velocity

The magnetic properties of the domain are directly influential for the generation and storage of magnetic energy and are the primary focus of this investigation. But, given we initialise the simulation with a static domain and then introduce rotational motion at the lower boundary, we also investigate the velocities present within the domain. Figures 3.9 and 3.10 show the velocity of a slice taken through the centre of the sunspot, given the simulation is initialised at rest we omit a 0° sub-plot. The background image shows the y-component of velocity, of which the magnitude is given by the colour-bar in each sub-figure; this component represents rotational motion. The quiver plots over-plotted on each sub-figure represent the x and z-components of velocity, where the shade of the quiver represents the magnitude of the velocity of those components. We are predominantly interested in the characteristic flows present within the key regions of the domain and the stages of the simulation the flows are present. We divide the discussion into two parts, we shall first analyse the flows in the umbral field and then the penumbral field.

Figure 3.9 shows the velocity evolution during the early stages of the simulation, where relatively little expansion of the penumbra has occurred. In the umbral region we observe that as one moves away from the central axis of the sunspot, toward the domain side-boundaries, the velocity in the y-direction (the direction of rotation in the slice taken) increases with increasing distance from the centre of the sunspot at all heights as might be expected as one moves away from the axis of rotation, except for the bottom-corners of the domain. The magnetic field strength is weakest in the bottom-corners, as indicated by figure 3.3, thus the plasma beta conditions may simply suit a plasma dominated motion (we will investigate this in chapter 5). We

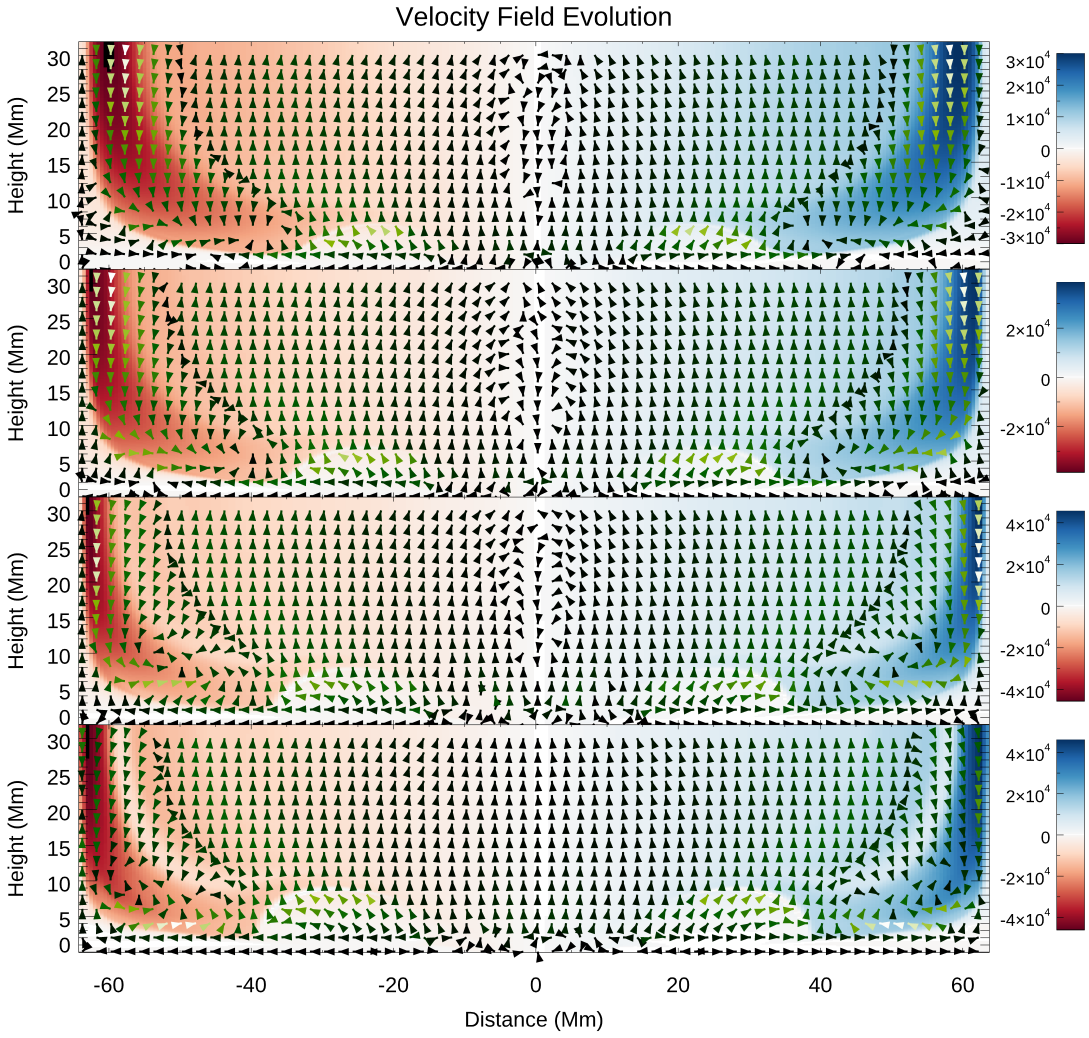

Figure 3.9: This figure shows the evolution of velocity during the lifetime of the simulation. The sub-figures, moving from top to bottom, show the velocity at times where the driver has rotated the sunspot by 30°, 45°, 60° and 75° respectively. The quivers show the normalised velocity in the plane of the slice, where each quiver is colour coded such that black indicates the slowest speed, white the fastest and green is intermediate. The background image shows the velocity normal to the plane of the slice, the colour bars have units of ms^{-1} and describe the background image.

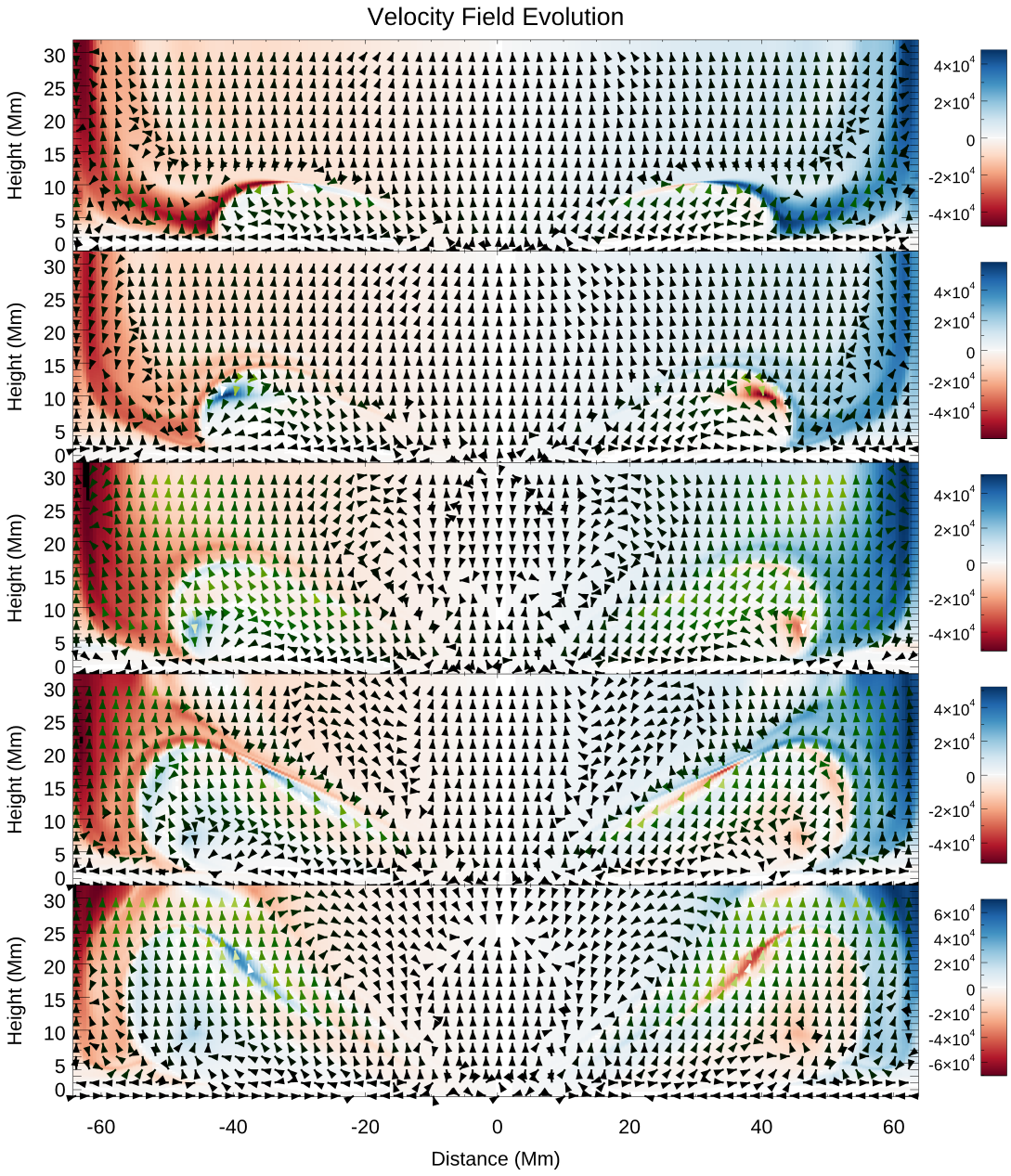

Figure 3.10: This figure shows the evolution of velocity during the lifetime of the simulation. The sub-figures, moving from top to bottom, show the velocity at times where the driver has rotated the sunspot by 90°, 105°, 120°, 135° and 140° respectively. The quivers show the normalised velocity in the plane of the slice, where each quiver is colour coded such that black indicates the slowest speed, white the fastest and green is intermediate. The background image shows the velocity normal to the plane of the slice, the colour bars have units of ms^{-1} and describe the background image.

observe that in the umbral region there are down-flows originating from the upper boundary that form near the sides of the domain. These down-flows are likely a consequence of the increasing rotation, which drags the umbral magnetic field at the side boundaries towards the centre of the domain and with them the initial mass near the side boundaries. Hence, the down flows are likely a response of the upper boundary conditions, to a depletion of the material directly beneath. We note here that these flows are not observed to meaningfully influence the magnetically dominant regions of the domain.

We observe that most of the umbral region, away from the side boundaries, exhibits a persistent, slow, upward flow at all heights with a drift of material toward the central axis of the sunspot. Finally in the centre of the umbral region, along the main axis of the sunspot, we observe that there is initially some, slow, complex motion which dissipates. This is likely at the noise level and therefore the importance of these flows may be over-implied in this figure.

Figure 3.10 shows the same velocity field diagnostic as figure 3.9, for the latter part of the simulation. The umbral field region in this figure begins at 90° with the central region continuing to show a slow persistent up-flow, with the rotational background trend still present. We observe that the down-flows initially near the side-boundaries have vanished for all rotation values in this figure, strengthening the argument that they were a result of the initial movement of the magnetic field from the side-boundaries. Figure 3.10 shows that as the penumbra continues to rise, the geometry of the flows within the umbral region develop increasing complexity but generally the complex flows are of small magnitude. By 120° we observe at coronal heights, within the central umbral region, the formation of flows directed toward the centre of the sunspot, directly above the expanding penumbra. This may be a consequence of the rising penumbra displacing the overlying umbral field and the material within that field. However, the magnitude of these flows is small and thus

limited interpretation of these features is encouraged. Finally, figure 3.10 shows relatively fast up-flows above the highest part of the penumbral region forming at 120° and persisting throughout the remainder of the simulation. This implies that as the penumbra gets close to the top of the domain, its vertical velocity accelerates. This will be investigated in a broader context in subsequent sections.

We now move onto analysing the flows present within the penumbral region. We have seen that the penumbra grows as the sunspot as driven, and that it hosts the strongest magnetic fields and currents and therefore the largest magnetic energy density and magnetic pressure. Therefore, understanding how the penumbra expands is key to understanding how stored magnetic energy is transported, how the introduced magnetic pressure drives the expansion, how the motion of the penumbral field alters the current density near the separatrix and how the energised penumbral field relaxes in response to the induced photospheric motion.

Figures 3.9 and 3.10 show that throughout the simulation, the flows within the penumbral region are far more steady and ordered than those in the umbral region. Furthermore, we see that the rotational motion is generally small within the penumbra, as compared to the enveloping umbral region, with some complexity forming at 90° and developing beyond. An interesting feature of the relatively slowly rotating penumbra, is that the slow rotation seems to extend slightly beyond the measured extent of the penumbral region. This region of the umbra appears to be a shear layer where the domain moves from the umbral regime to the penumbral. Within this shear layer, we observe that the non-rotational motion (the quivers) seems to interpolate the motion within the penumbral and umbral regions, as one would expect in a shearing layer. The observed differences between the flow characteristics of the penumbral and umbral regions, is a direct consequence of the tethered nature of the penumbra. Specifically, the tethering restricts the rotational motion (as indicated by the whiter penumbra in the background images), but more significantly the very

presence of the tethering is responsible for the penumbral expansion, via the storing of induced strong magnetic field strengths (and hence pressure) in the penumbral field, which inevitably fuels the expansion. In summary, the tethering causes the expansion and therefore the non-rotational flows present within the penumbra are a result of the expansion itself.

Focusing further on the non-rotational motion within the penumbra, we observe that the motion is similar regardless of the stage of the simulation. We find generally that there is consistent motion directed away from the centre of the sunspot at all times. In addition to this outward flow, there is also an upward component which seems to diminish below the transition region. Most interestingly, we observe that the fastest motion is measured near the separatrix. This shows that although the penumbra is driven at the photosphere, the consequential fastest expansion primarily occurs where the penumbra is highest in the domain and far from the centre of the sunspot.

Despite the misalignment of the introduced penumbral field strength (and hence magnetic pressure) and expansion of the penumbra, the expansion exhibited makes physical sense. We may compare figures 3.3 and 3.9 to see that the planar motion tends to point directly away from where the strongest induced magnetic fields in the penumbra are found. This indicates that the penumbra expands in the direction of the induced magnetic pressure gradient. The reason the fastest expansion is high in the penumbra, far from the sunspot centre, is likely a consequence of the initialised domain; simply that this region is where the most tenuous plasma (because of the height) and the weakest magnetic field strength (because of the distance from sunspot centre) is found. Therefore, despite the magnetic pressure being primarily injected close to the sunspot, the magnetic field in the penumbra will expand more readily where it is easiest for it to do so.

Figure 3.7 implies that, in the penumbra, the Lorentz force is always small

(because of the highly parallel nature of the current density and magnetic field vectors), meaning that the magnetic pressure gradient and magnetic tension are relatively balanced throughout the expansion. For this to be achieved, the generated magnetic pressure ought to be introduced at a rate sufficiently small enough for the penumbral magnetic field as a whole to respond (such that the field lines gain the required curvature to balance the new magnetic pressure gradient). Thus, although still somewhat speculative, the collective measurements presented in this section suggest that the penumbral magnetic field responds quickly to the driver and evolves as a single body (at least during the early stages). If the previous speculation is correct, the introduction of additional magnetic pressure near the sunspot centre and the penumbral expansion being quickest far from the centre, is not something unreasonable if the penumbra is considered a single magnetic entity.

3.6 Density

We now investigate the evolution of density in the numerical domain. By investigating the density we develop the first half of an understanding of how the plasma pressure influences the evolution of the sunspot. The second half will be presented in section 3.7 where we analyse the evolution of the temperature, hence collectively describing thermal pressure (see equation 1.16). Figures 3.11 and 3.12 show the density in the domain during the evolution of the model sunspot. The initial domain is stratified (see section 2.5) as indicated by the $\theta = 0°$ subplot of figure 3.11. The most significant changes to the density are observed (most easily) in the corona. Focusing first on the penumbral region, we observe that as the penumbra expands the plasma within becomes increasingly more tenuous. The density decrease appears to occur quasi-uniformly throughout the penumbra between $0° - 75°$. After this time, significant variations of the density are found in the penumbra. At $90°$ we observe the formation of a relatively low-density region near the separatrix, in the

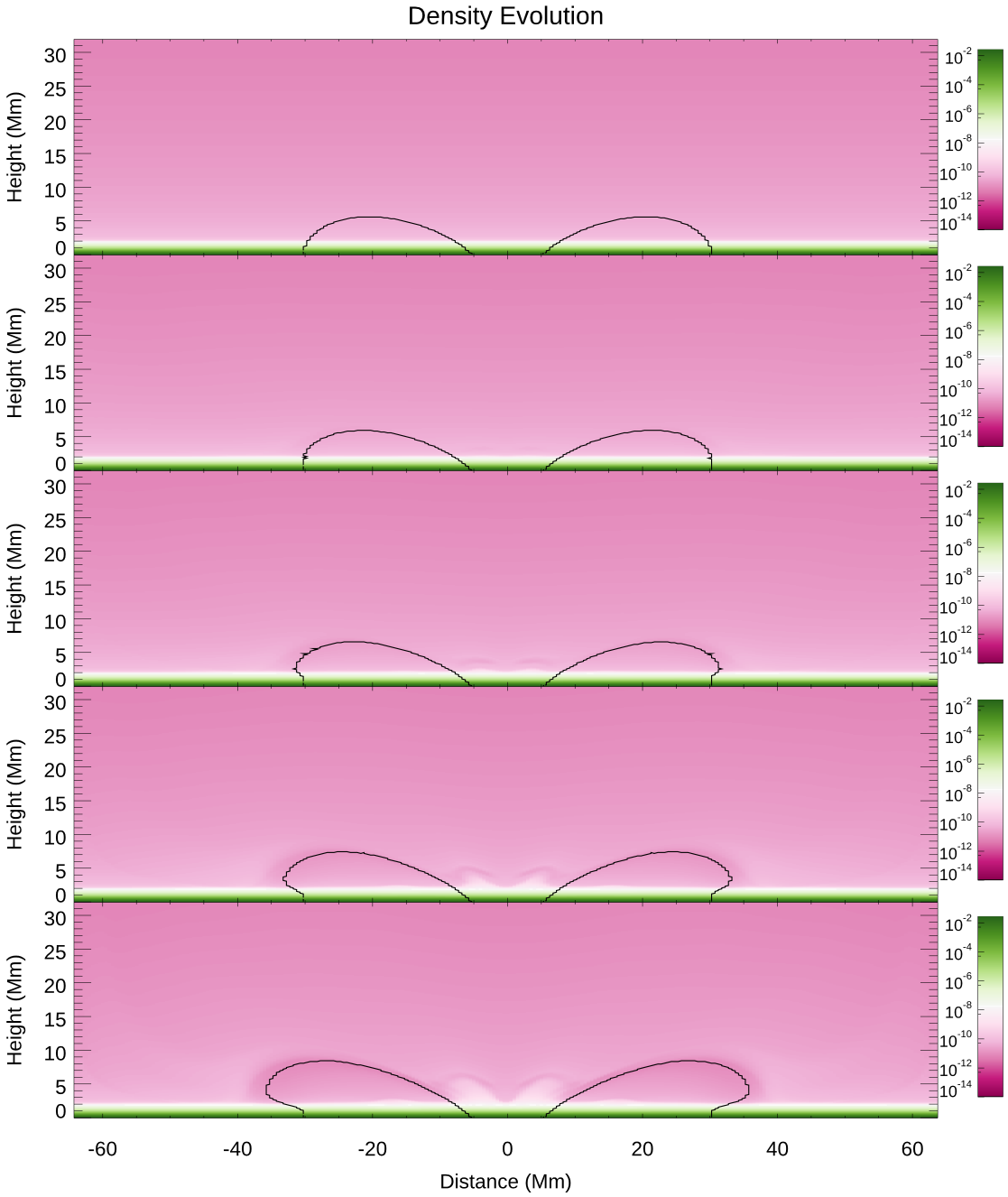

Figure 3.11: This figure shows the evolution of density in a slice through the centre of the sunspot during the lifetime of the simulation. The sub-figures, moving from top to bottom, show the density at times when the sunspot has been rotated by 0°, 30°, 45°, 60° and 75° by the driver respectively. The black contour represents the approximate location of the separatrix that divides the umbral and penumbral magnetic field regions, in a slice through the centre of the sunspot. The units of the colour bars are kgm^{-3}.

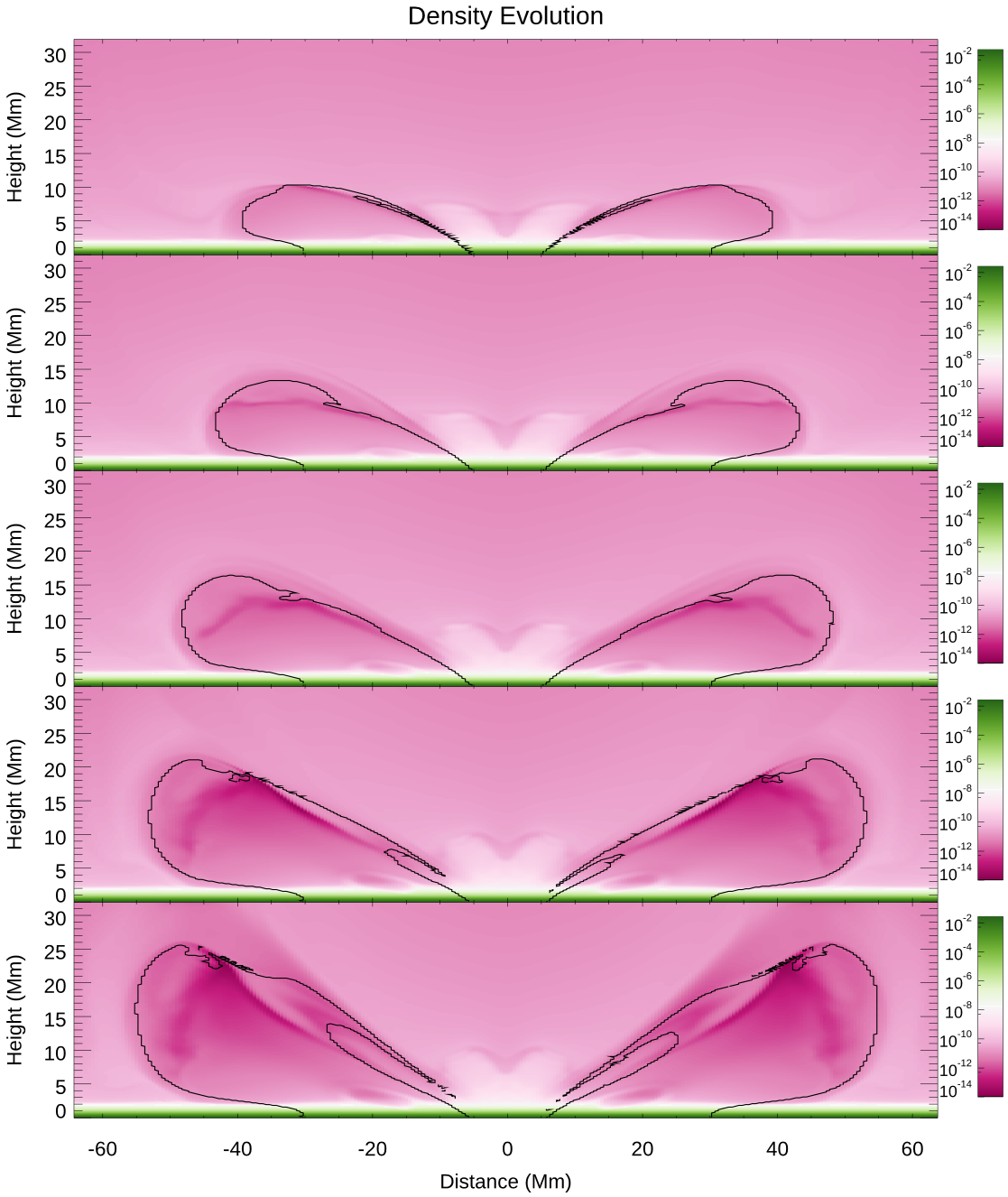

Figure 3.12: This figure shows the evolution of density in a slice through the centre of the sunspot during the lifetime of the simulation. The sub-figures, moving from top to bottom, show the density at times when the sunspot has been rotated by 90°, 105°, 120°, 135° and 140° by the driver respectively. The black contour represents the approximate location of the separatrix that divides the umbral and penumbral magnetic field regions, in a slice through the centre of the sunspot. The units of the colour bars are kgm^{-3}.

penumbral. As the sunspot is driven further, this low-density region grows in size, to the point that the penumbral density is significantly reduced by several orders of magnitude towards the end of the simulation.

As the penumbra expands, the low-density region which begins near the separatrix is shown to protrude further into the penumbra, after which the region is observed to become less dense and grow. The measurement of the density reduction itself is expected; the penumbra is closed and has an initial amount of mass that should be conserved during the expansion. Hence, as the volume of the region increases, the average density must decrease. What remains unclear, is why the tenuous layer first forms at the separatrix (at 90° in the selected times) far from the strongest induced magnetic fields within the penumbra (see figures 3.3 and 3.4).

Figure 3.10 shows that where the relatively tenuous region forms near the separatrix, at 90°, there is a measured velocity in the direction of rotation which opposes the direction of the driver (i.e. in the background image, we observe red regions on the side of the sunspot that was previously all blue, and vice-versa). Both this and new regions of rotational motion form and develop in complexity within the penumbra as the simulation proceeds. Generally, there is no clear one-to-one correlation shown between the regions of counter rotation and density reduction after the initial phase at 90°, but generally it seems that where the most extreme perturbations of the penumbral density are observed there is some motion either in the rotation or counter-rotation directions. Two possible explanations are, firstly the observed protrusion of the tenuous region (which forms at 90°) into the central region of the penumbra, with the replenishing of the material near the separatrix as this happens, may be a consequence of the non-rotational flow pattern within the penumbra. It may be that as the penumbra expands (which occurs in the upper penumbra, far from the sunspot centre most readily) the non-rotational flows are

introducing additional mass into the region near the separatrix, replenishing the material and counteracting the density reduction caused by the expansion. Secondly, it may be that the low-density region which forms at 90° forms at the separatrix because at this time this is the region of the penumbra which is expanding most quickly as shown by the velocity field at this time in figure 3.10. However, this also means that more material may be advected into this region at this time. To analyse this one would have to analyse the nature of the flow as well as the mass flux.

These competing explanations highlight further the two types of flow present within the domain, namely those which move magnetic field and plasma together and those which move material along magnetic fields.

Diverting our focus to density changes in the umbral region, we observe in figures 3.11 and 3.12 that there is only one significant feature within the umbral region. This feature is the "double-bump" which forms at the base of the umbral field region. This region develops gradually during the simulation and represents an increase of density in the region, several orders of magnitude greater than the ambient plasma density. Once again the velocity diagnostics of section 3.5 provide explanation. Figures 3.9 and 3.10 show that during the simulation there exists persistent up-flows within the umbral magnetic field region. These up-flows, accompanied by our understanding of the initial domain, indicate that these regions form when mass is transferred upward from the dense sub-transition region heights. This must be the case, firstly because the flows which transport the material are measured and secondly because the density through any vertical cut of this region remains stratified, and there is simply insufficient material above to produce this feature. Now we understand how this feature formed, we may address the question of why it forms at all. Figures 3.3 and 3.4 show that at the base of the umbral magnetic field region there are two slabs of increased magnetic field strength present throughout the simulation, which vanish at the centre of the umbra and generally decrease in

thickness with decreasing distance from the centre of the umbra, eventually vanishing at the centre. This implies that as the sunspot is driven, additional magnetic field strength is induced at the photospheric and low-chromospheric umbral field region. This additional field must increase the magnetic pressure in this region, and this magnetic pressure increase may drive the upward flowing velocity profile observed. This idea is consistent with the observed structure of the double-bump feature, because the size of the increased magnetic field strength region diminishes with reduced radius as does the density feature, as indicated by the central depression. To investigate this further would require analysing the mass flux within the domain, rather than simply the density and velocity characteristics presented here, and also the pressure gradients formed by the magnetic and gas pressures.

3.7 Temperature

We now investigate the temperature, which via the equation of state equates to internal energy density. Temperature and density (section 3.6) define the gas pressure, whose gradient is able to induce motion within the plasma. Therefore in this section we will identify the primary characteristics of temperature in the domain, but also compare these characteristics to corresponding density, to identify the primary regions where gas pressure may influence the evolution of the sunspot.

We first analyse how the temperature evolves within the penumbral magnetic field region. Figures 3.13 and 3.14 show the evolution of temperature during the simulation. Figure 3.13 shows that temperature evolves similarly to density between the start of the simulation and 75°. Specifically we observe that within the penumbral magnetic field region, the temperature is found to decrease as the sunspot is driven and the distribution of temperature is smooth in the early stages of the simulation. At 60° we see that cold plasma is starting to flow upward into the corona, shown by the small blue protrusions at the top of the transition region between

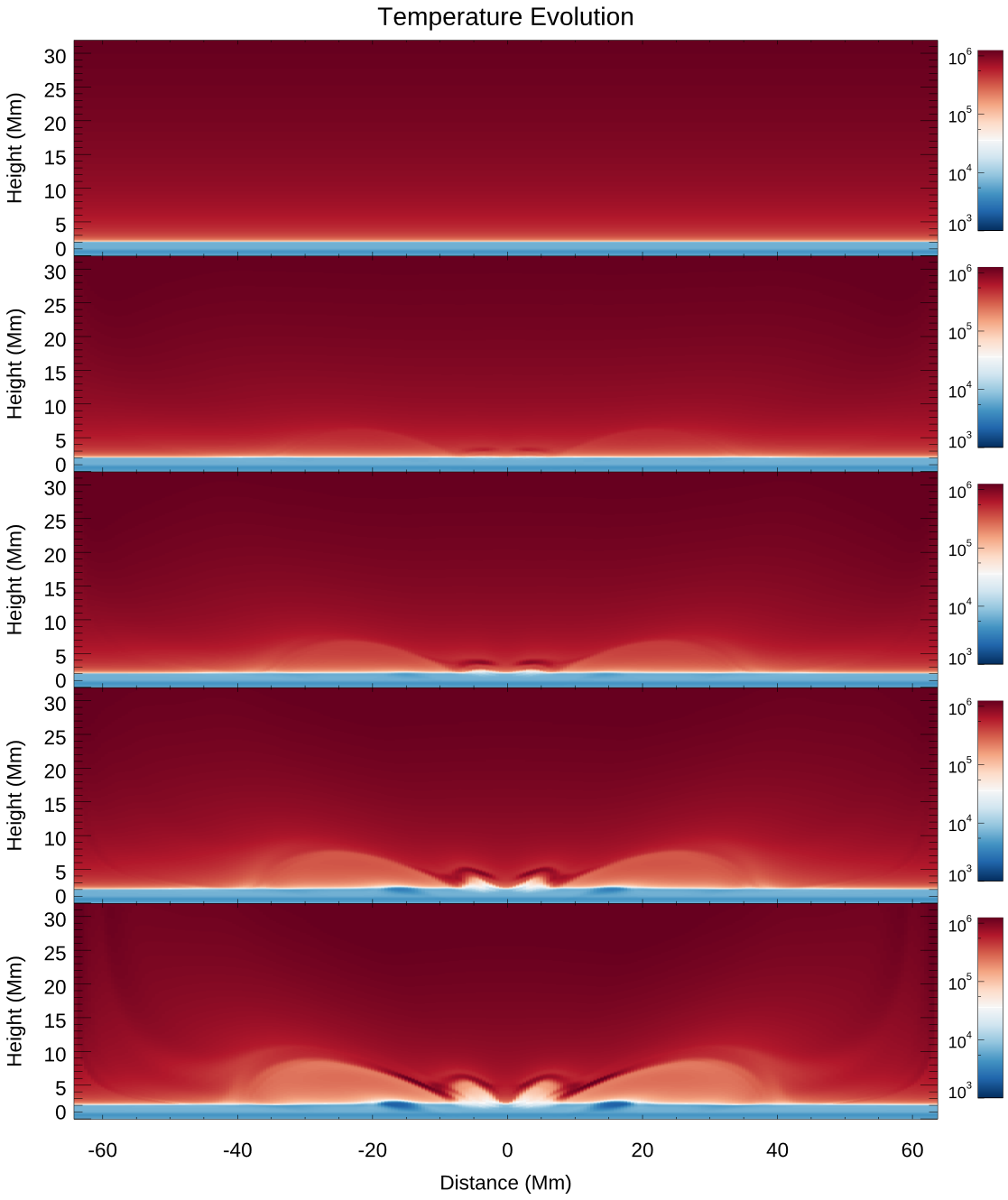

Figure 3.13: This figure shows the evolution of temperature in a slice through the centre of the sunspot during the lifetime of the simulation. The sub-figures, moving from top to bottom, show the temperature at times when the sunspot has been rotated by 0°, 30°, 45°, 60° and 75° by the driver respectively. The units of the colour bars are Kelvin (K).

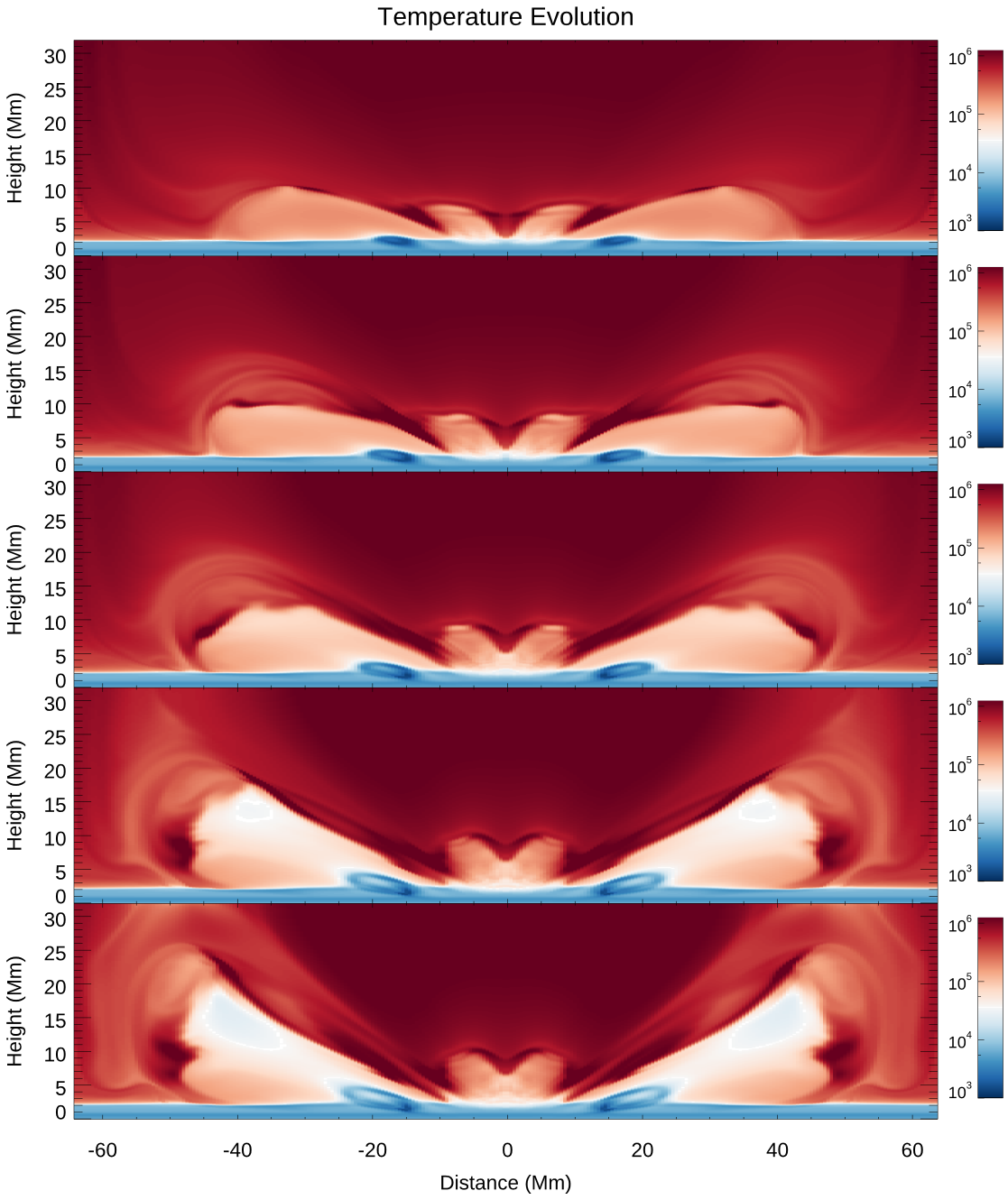

Figure 3.14: This figure shows the evolution of temperature in a slice through the centre of the sunspot during the lifetime of the simulation. The sub-figures, moving from top to bottom, show the temperature at times when the sunspot has been rotated by 90°, 105°, 120°, 135° and 140° by the driver respectively. The units of the colour bars are Kelvin (K).

$\sim 12.5 - 20$Mm from the sunspot centre. This feature is also found in the density (although the corresponding density figure does not show it as clearly as figure 3.13). These small regions, being cold and dense, accompany non-rotational flows shown by figure 3.9 which indicate that these regions form due to chromospheric and transition region material flowing into the overlying corona. Figure 3.14 shows that these relatively cold, dense regions continue to develop throughout the simulation; however, by 105° the centre of these regions becomes hotter and (as indicated by figure 3.12) more tenuous. Therefore in the latter stages of the simulation this region has a hot tenuous core and a relatively dense cool exterior.

The temperature evolution within the rest of the penumbra seems to evolve in an "equal but opposite" manner to the density. Figure 3.14 shows that, generally, the temperature in the penumbra is lesser than that in the surrounding umbral field region, but there is an increasing level of complexity in the distribution of temperature which evolves in the same manner as found and discussed for the density in section 3.6. Comparing figures 3.14 and 3.12 we see that where there are relatively hot regions, there is a measured relative decrease in density. This finding implies that as the sunspot is driven the density and pressure evolve in a manner which acts to minimise thermal pressure gradients via the redistribution of material and thermal energy.

Focusing on the umbral magnetic field region, we see that there is only one main feature that forms within the umbral region, this is the same feature identified in section 3.6 for the density, namely the "double-bump" feature at the base of the umbral magnetic field region. The analysis presented in section 3.6 applies also to the description of the temperature evolution. However, we may now supplement the findings of section 3.6, with the identification of transition region and chromospheric temperature material in this feature (similarly to that explanation postulated for the density in this region). In conclusion, the idea that this region forms when transition

region and chromospheric material flows upwards is the most sensible explanation for the formation of this region. This is supported by analyses of the evolution of the magnetic field strength, the velocity, the density and temperature.

3.8 Chapter Summary

In this chapter we have analysed the general observed behaviour of a single simulated rotating sunspot, with the intention of identifying the primary evolutionary characteristics of the state variables of the system as the sunspot is driven. Because this thesis focuses on the connection between rotating sunspots and their magnetic environments, in addition to analysing the primary variables evolved by the magnetohydrodynamics equations, we also analysed the current density in this chapter. The primary finding of this chapter is that as the sunspot is driven at the photosphere, the umbral and penumbral magnetic field regions evolve distinctly due to the difference of connectivity of the magnetic fields in each region.

We observe that as the sunspot is rotated, the penumbral magnetic field lines develop increasing complexity with additional rotation. The penumbral region is found to increase in size and eventually (at $\sim 145^{\circ}$) reach the top of the numerical domain. Whilst the penumbra rises it displaces the overlying umbral magnetic field, forcing the umbral field away from the sides of the numerical domain and toward the central, azimuthal, axis of the sunspot. In doing this the magnetic field strength within the umbral region is slightly strengthened, however, the increase is relatively small (although the volume of the increased magnetic field strength region is large which may have cumulative effects on the magnetic energy increase within this region). There is an overwhelming bias to where the most significant increase of magnetic energy is found, and this is at the very bottom of the domain near the photosphere. We see that there are both greater strength induced magnetic fields but also more regions of intense field strength in the penumbra as compared to

the umbra. However, intense magnetic field is induced at the base of the umbral region, just above the photosphere. The structure of this induced umbral magnetic field is slab like, with the height of the slab vanishing in the centre of the sunspot and increasing with radius up to the end of the umbra. The form of the umbral magnetic feature implies that the cause is the rotational velocity, which is the only thing introduced into the domain and also increases with radius.

We find that the strongest currents form within the penumbral region, primarily where the penumbral field emerges from the sunspot, where the differential rotation is applied. The strong currents in the penumbra are aligned with the strongest induced magnetic fields. There are also relatively strong currents at the base of the umbral field region (also where we observe increased magnetic field strength) but the currents here are weaker than the penumbral currents; interestingly weaker than the magnetic field comparison between the umbral and penumbral magnetic field strength would suggest. We also find relatively strong currents form at the separatrix and move with the expanding penumbra. We see that, generally, the current within the penumbra decreases with distance from the part of the photosphere where its magnetic field is rooted, implying simply that the drop off of magnetic field strength as one moves further from the sunspot scales the magnitude of the current density. We see that generally the current density in the umbral magnetic field is relatively weak, especially so in the field found near the central axis of the sunspot. There are relatively strong currents near the domain side-boundaries and at the base of the corona outside the sunspot, but these currents form where the magnetic field is very weak and thus cannot induce significant Lorentz forces and hence are assumed inconsequential for the evolution of the sunspots magnetic environment.

The nature of the currents present within the domain are found to be distinct in the umbra and penumbra. In the umbral magnetic field there are observed regular variations of parallel and anti-parallel currents, divided by regions of perpendicular

current. These perpendicular currents are found where the current density is weakest and seem to define the borders of neighbouring regions of primarily parallel and anti-parallel currents. Therefore, the consequences to the motion of the plasma from the perpendicular currents is expected to be minimal. These findings form the basis for an investigation of the Lorentz force in chapter 5. The main characteristics of the current density in the penumbral region is that once current systems have formed, they remain primarily parallel to the magnetic field and like the umbral scenario, the perpendicular currents seem to form where the current density magnitude is weakest. The primary finding is that the penumbra evolves whilst maintaining minimal Lorentz forces, implying that at all times the magnetic pressure gradients generated are balanced (for the most part) by the magnetic tension of the field lines themselves. Even as the penumbra grows it remains in this minimum Lorentz force state, implying that the magnetic field strength is sufficient in the penumbra at all times to quickly dissipate the perturbations introduced by the constant driving throughout the volume. There appear to be both parallel and anti-parallel currents within the penumbra, where the anti-parallel currents are primarily below the transition region and where the parallel currents occupy most of the penumbra.

The imposition of rotation at the photosphere is found to induce rotation motion throughout the domain, i.e. far from the driver as a consequence of the magnetic field and plasma coupling. The most significant motion is found in the penumbra, which is found to show lesser rotational motion than the umbral region and hosts far more consistent flow geometries. The penumbra expands most quickly at the portion of the separatrix which is both high in the atmosphere and far from the sunspot centre. The velocities found within the penumbra tend to point away from the strong induced magnetic field and current locations.

The density and temperature are primarily found to evolve within the penumbral region only (although as the penumbra rises there is some feedback seen in the

umbral field region). As the penumbra expands the density within it is found to decrease on average, as expected for a closed increasing volume. The decrease of density is found to be relatively uniform until regions of the penumbra are found to rotate counter to the direction of the driver, at which point non-uniformity is introduced. This non-uniformity develops throughout the remainder of the simulation. The temperature seems to evolve oppositely, but in a mirror fashion to the density. Specifically we see that both temperature and density are advected from low in the domain to greater heights, but at any given time in a region where there is neighbouring high and low density we see the opposite low and high temperature structure. This indicates that the temperature and density evolve together, perhaps to maintain thermal pressure balance (this will be investigated further in chapter 5). It seems that the density is the primary state variable which is evolved by the expansion of the closed penumbral field, and the temperature may evolve to maintain a stable pressure.

Chapter 4

Evolution of the Penumbra

4.1 Penumbral Field Identification

A primary goal of this work is to better understand how magnetic energy is injected by sunspot rotation (e.g. chapter 6). More generally, we wish understand the key physical processes present within rotating sunspots. Because magnetic energy is proportional to the square of the magnetic field strength (equation 1.27), to fully understand how the sunspot generates magnetic energy, where it stores it and how it may be transported and released, we must be able to differentiate which magnetic field belongs to the penumbra and which belongs to the umbra. Throughout this thesis, we repeatedly observe that many properties of the simulation domain exhibit unique behaviour in the umbral and penumbral magnetic field regions. By developing a means to identify the penumbral magnetic field (and conversely the umbral magnetic field), we will be able to segregate the many properties measured in chapters 3, 5 and this one to better understand their evolution and contribution to the rotating sunspot. We first discuss the general approach taken and then develop the numerical scheme used.

To identify the penumbral magnetic field, we define a new diagnostic that takes

the magnetic field at a time in a simulation, and returns the locations of the numerical grid occupied by the penumbral magnetic field. The method builds upon the imposed nature of the penumbral magnetic field, specifically that it both enters and leaves the domain through the lower boundary (the photosphere). There ought to be a separatrix enveloping the closed penumbral region (blue field lines in figures 3.1 and 3.2). The Lare3D code divides the domain into a number of cells (see section 2.3.1 and Arber et al. (2001) for further details) each of which we shall define to be either umbral or penumbral. We shall classify the cells as penumbral or umbral by identifying where the separatrix is and thus classifying which side of it each cell in the numerical domain belongs. This approach relies identifying the separatrix using knowledge that the penumbral magnetic field enters and leaves the domain through the bottom domain boundary. It is extremely unlikely that the cells at the separatrix will entirely umbral or penumbral, but for computational expense reasons, we shall classify them as such in the hope that the error is small compared to the number of cells identified correctly. This will obviously be true when the surface area of the separatrix is small when compared to the volume of the penumbral region (this is generally true). The method was found to be rather computationally expensive (especially when considering the number of simulations and simulation snapshots that make up the entire project) so was tuned to optimise performance rather than accuracy. However, further adaptations could be made to better define the separatrix. The method works starting at the bottom of the domain and moving upward iteratively after all the penumbral cells at a given height of the domain are identified.

The initialisation steps of the method are as follows; first, we create a three dimensional array (initialised with zeros) of equal size and shape as the numerical grid of the simulation. We shall call this the mask array and its purpose is to contain the information that defines which cells are penumbral and which are umbral.

Secondly, we identify where at the lower boundary (the photosphere, see chapter 2) there is non-zero magnetic field in the z-direction (i.e. where $B_z \neq 0$ at $z = 0$Mm). This will occur within the model sunspot and in the negative annulus surrounding the sunspot. We next, designate the cells of the mask that have collocated cells in the simulation snapshot that are directly above the non-zero B_z photosphere, as having a value of one. From this point any cell labelled with a one will be identified as penumbral and if left as zero, umbral. Next, we find where there are cells identified as penumbral in the mask array, neighbouring those identified as umbral; part of the separatrix must exist between these cells if the initial distribution of ones and zeros is correct. The cells identified as penumbral that neighbour umbral (and umbral that neighbour penumbral) are then tested (explanation of testing to follow in section 4.1.1) to see if they are indeed identified correctly. If so they are left unaltered, if not they are given their proper classification. This process is repeated until all the cells at the lowest layer of the domain (and hence mask array) are correctly identified as either umbral or penumbral.

The next phase of the process has two main stages: first, we initialise the next layer (in the z-direction) of the mask array, by copying the penumbral cells identified in the layer below directly to the cells above. Then, we grow and shrink the given layer (fixed z value) of penumbral cells by testing the cells at the interface between umbral and penumbral identified cells, until the cells at the interface are all identified correctly. The process of "copy penumbral cells from particular mask layers to the above layer, and refine" is repeated until such a height is reached that no new penumbral cells are identified.

The stages of the method so far, will result in a volume of cells which should be simply connected by the nature of the magnetic field being modelled and simulated. This technique is used because by only testing the cells at the edge of the already identified (temporary) region, the cells that fall within the bulk of the volume of the

penumbra are identified without having to be explicitly tested; i.e. there is a fill-in effect to this method up to this point.

However, this approach thus far is susceptible to a fundamental flaw. Because it tests at the edges until it reaches a height where no more cells are found, by starting at the assumed edge (from the copying process from layer below) and shrinking the layer until it vanished. At this "vanished" height, we will have tested all the cells and can be certain they are umbral. But it is not clear that the cells below this are definitely penumbral. This statement may not be clear at this point, but is easily explained via an example. Consider, for now, a system far simpler than the sunspot model, for example one where we know the shape of the separatrix. Let the separatrix take the shape of a simple hill (i.e. a negative quadratic polynomial). The method outlined above will begin at the base of the"hill", fill in the bottom bottom layer and grow upward iteratively. The circumference of the penumbral region will gradually shrink with height and taper off in size until at some height, no more "hill" is found. The method will have no issue with this, as the choice to only test the edges and then leave the cells within unchanged (effectively filling them in) will be appropriate. However, the method would be unsuitable if at the top of the fictitious "hill" there were a depression (e.g a negative quartic polynomial). This is because the method would, again, start at the extreme edges of the hill, copying upward and shrinking each layer, until a height where no more hill is found. But the depressed region would appear filled in because the void which defined it would fall within the extremes of the sides of the hill, i.e. the separatrix at that height in the xy-plane.

Therefore the final step of the method of identifying the penumbral region is to take the penumbral volume identified thus far, and perform the three-dimensional equivalent of the region growing/shrinking process used previously. Thus, the final step is to identify where the penumbral region meets the umbral, test all cells that

envelope this region, and grow and shrink the surface appropriately (in the full three-dimensions) until the solution converges. This small addition was found only to be rarely required in the larger context of the project and larger sample of simulations. The overall process is made more efficient by ensuring that any cells tested are not tested more than once.

An alternate method would have been to identify the lower layer of the mask using the photosphere as in the method explained, and then simply grow the region until the whole penumbral volume is defined, by testing the interface in all directions (rather than layer by layer in the z-direction). This would be a more accurate method, but would result in having to test vastly more cells. It was found that this approach was extremely detrimental to the computational cost of this diagnostic and was far too impractical for anything other than testing.

4.1.1 Testing the Grid Cells

In the preceding description of the method by which the penumbral field region is identified, we repeatedly stated that cells were "tested" but we intentionally made no effort to explain what is meant by this for clarity of the method explanation. The Lare3D code solves the resistive MHD equations in a time-stepping manner and offers ability to dump snapshots of the physical domain at a user defined cadence. This means that at particular times we have a full snapshot of the physical domain therefore when attempting to determine where the penumbral region of the domain is, we have access to the full description of the magnetic field in domain. To test a cell, we start at the centre of that cell and trace the magnetic field through the domain. Doing this traces the magnetic field line whose trajectory intersects the centre of the cell. If that field line traces to the top of the domain, we designate that cell as an umbral cell (and give it the numerical value zero) and if it traces to the photosphere we designate it as penumbral (and give it the numerical value one).

The fourth order Runge-Kutta method (Garcia, 2015; Burden and Faires, 2010) is used to trace the magnetic field through the domain and linear interpolation is used to approximate the magnetic field at any point deemed necessary within the domain.

An illustrative example of the quality of the penumbral identification code is shown in figures 4.3 and 4.4. These figures show the field lines of the umbral field (red and green field lines) at various times, each with a blue surface depicting the region where the penumbral field lines have been identified. Although seemingly simple looking in these example figures, this diagnostic is invaluable throughout the work performed in this thesis. It serves both as a direct diagnostic to show the evolution of the penumbra, but is also used as a mask to measure specifically the properties of interest in the penumbral and umbral regions independently.

4.1.2 Penumbral Volume

The first product of the penumbral identification method, is the direct measurement of the volume of the penumbra (and consequently the umbra), simply calculated as the number of cells identified an penumbral. We can easily convert this to true volume by multiplying this measurement by the volume of one grid cell. As the penumbra expands, its volume increases and consequently the volume of the domain occupied by the umbral magnetic field reduces. Figures 4.1 and 4.2 respectively show how the volume of the penumbral and umbral regions evolve. We observe that as the simulation proceeds, the penumbral volume increases monotonically, until the penumbra reaches the top boundary at which point volume is transferred from the penumbra to the umbra, as a consequence of the region identification method. Perhaps the most interesting feature of the penumbral volume evolution, is the observed increasing rate of expansion. This is likely a result of the ever decreasing magnetic field strength, with increasing height, of the umbral field (which the penumbra must displace) and the fact that at latter times the penumbra is

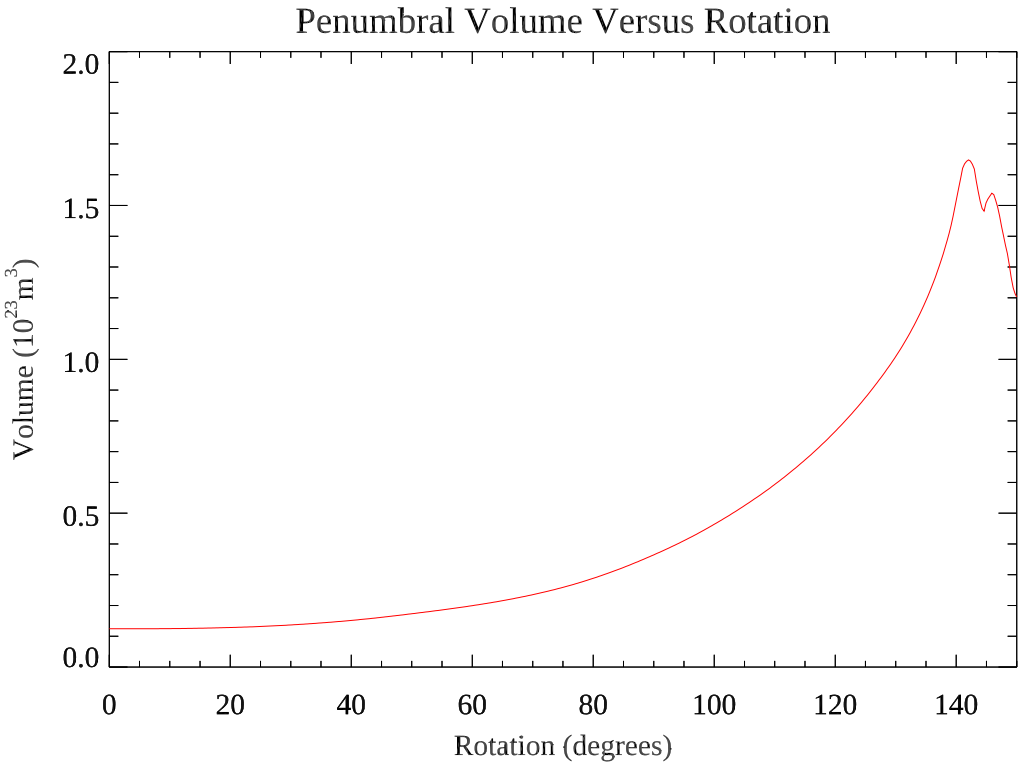

Figure 4.1: A line plot showing the volume of the penumbra throughout the simulation.

larger, meaning there is an ever increasing amount of penumbra which is expanding. Finally, we see clearly that the umbral volume mirrors the penumbral as the sum of the two volumes by definition must give the volume of the numerical domain.

4.2 Separatrix Evolution

In chapter 3, we saw that the closed penumbral magnetic field region grows as the sunspot is rotated. In this section we investigate the properties of the penumbral region expansion. Because the penumbral magnetic field is closed, and the umbral open, a separatrix must divide the two magnetic field regions. As the penumbra expands, the separatrix surface itself must move with it. Given a number of properties are found to exhibit unique behaviour at the separatrix (e.g. current density,

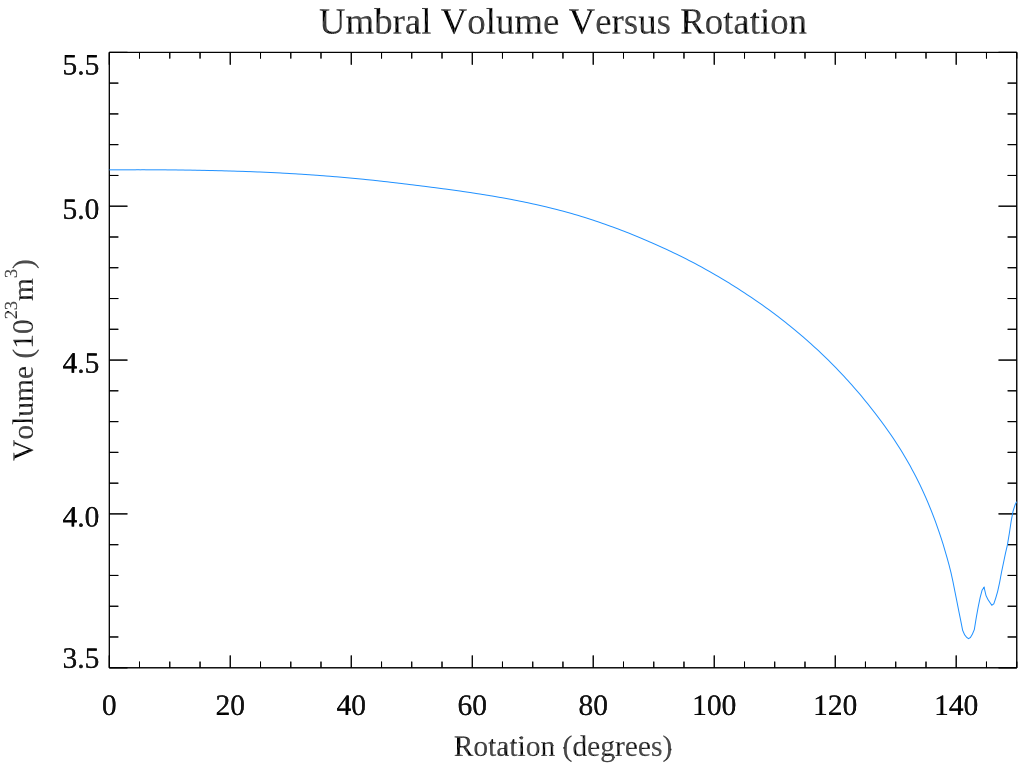

Figure 4.2: A line plot showing the volume of the umbra throughout the simulation.

temperature and density) and more generally within each region of magnetic connectivity, monitoring the evolution of the separatrix surface is important.

Figures 4.3 and 4.4 show that as the simulation progresses the separatrix surface expands with the penumbral region, but over time the surface develops kinks and folds and generally becomes more complex. As noted in chapter 3, we measure an increase of magnetic pressure (via magnetic field strength increase) in the penumbral region which likely drives the expansion of the penumbral region. However, it is not clear that the region of the simulation domain into which the penumbra expands is uniform and hence there is no guarantee that the penumbral region would expand uniformly. Figure 4.3 shows that the magnetic field lines which emanate from the umbra, spread and fill the domain (due to the initial potential solution). Therefore, where the umbral field lines touch (or come close to) the x and y-boundaries of the domain (as the sunspot rotates) there is likely to be some level of feedback from the side boundaries, which may impose some resistance. Figure 4.5 shows a streamline plot of the horizontal components of velocity (where height varies in the vertical direction). The intent of figure 4.5 is purely to illustrate the nature of flows in the azimuthal direction that form in response to the photospheric driving. There is no significance as to the time of the particular measurement presented in figure 4.5, other than it occurs after the initial acceleration of the sunspot from rest. Secondly, the height of the vertical slice is also arbitrary, but for reference is 15.625Mm from the bottom of the domain. We see that stagnation points in the direction of rotation form near the corners of the domain where the umbral field skims the walls and generally there is a slowing down as the sunspot structure rotates into a side-boundary and a speeding up as it leaves (the blue and green regions indicate this respectively). Clearly the sunspot umbral field experiences some differential resistance in the azimuthal direction as it rotates. The field lines which skim the side-boundaries are exactly those which envelope the separatrix (on

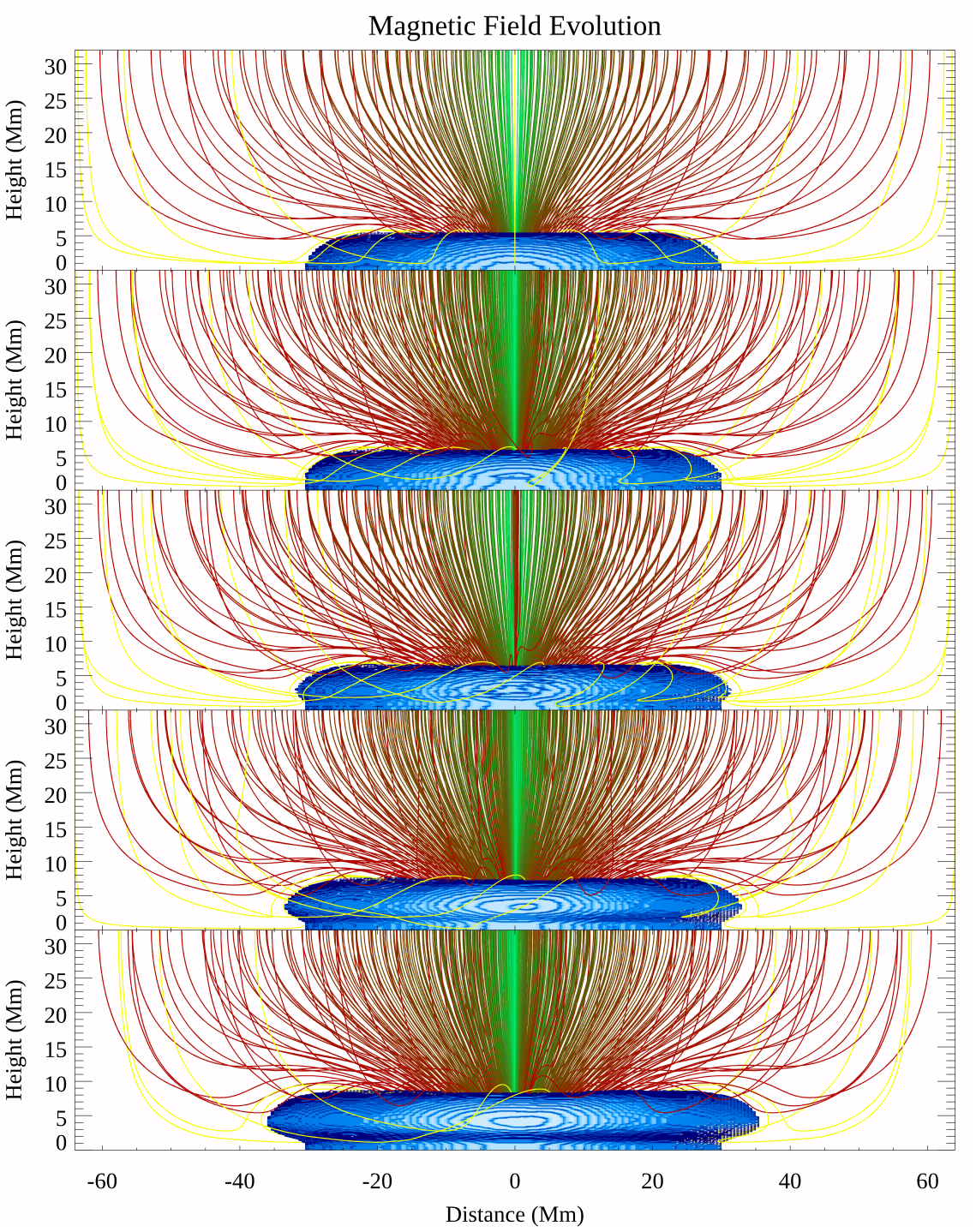

Figure 4.3: This figure shows the magnetic field and separatrix during the simulation. The separatrix is shown by the blue isosurface. The sub-figures, moving from top to bottom, show the this at times when the sunspot has been rotated by 0°, 30°, 45°, 60° and 75° by the driver respectively.

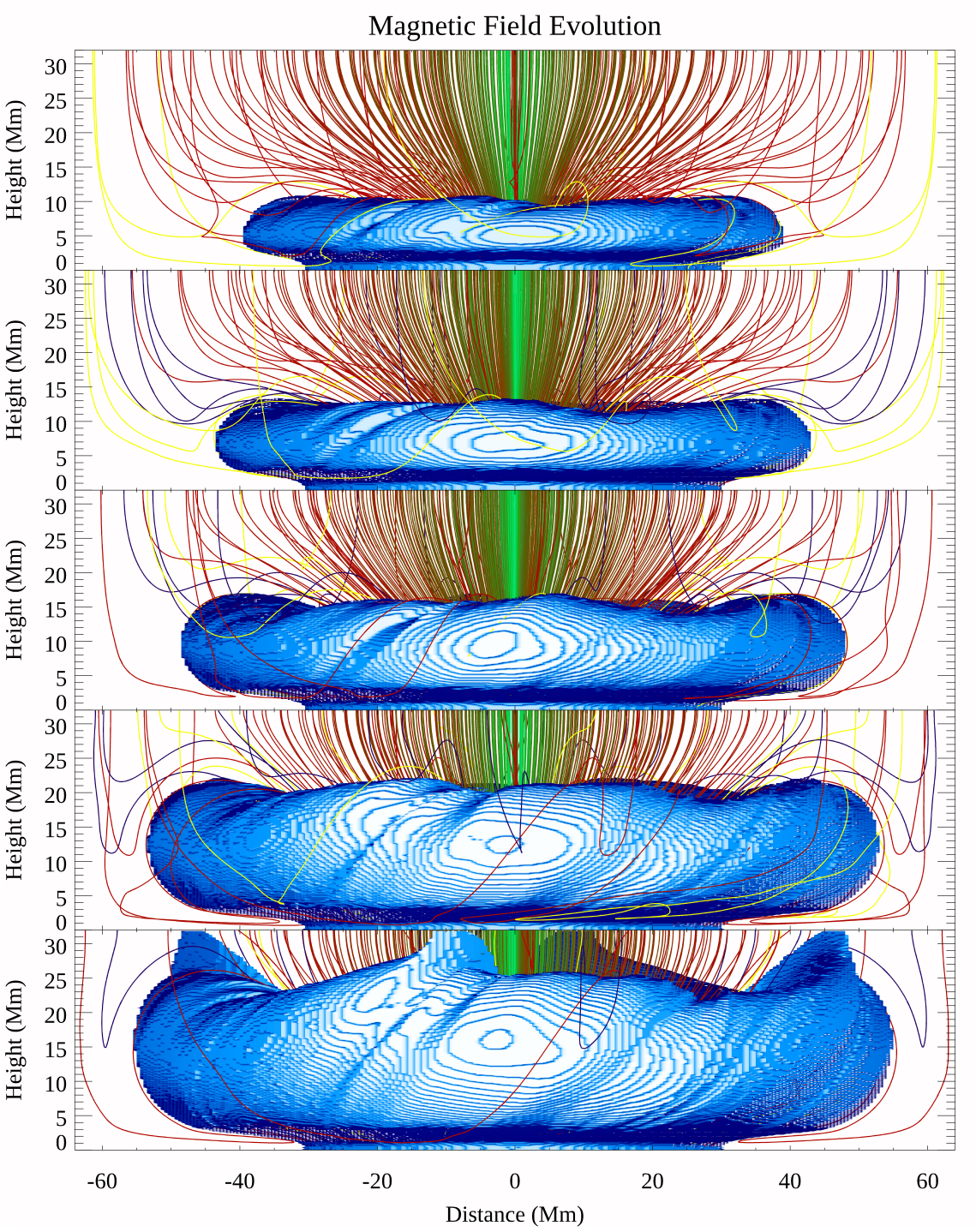

Figure 4.4: This figure shows the magnetic field and separatrix during the simulation. The separatrix is shown by the blue isosurface. The sub-figures, moving from top to bottom, show this at times when the sunspot has been rotated by 90°, 105°, 120°, 135° and 140° by the driver respectively.

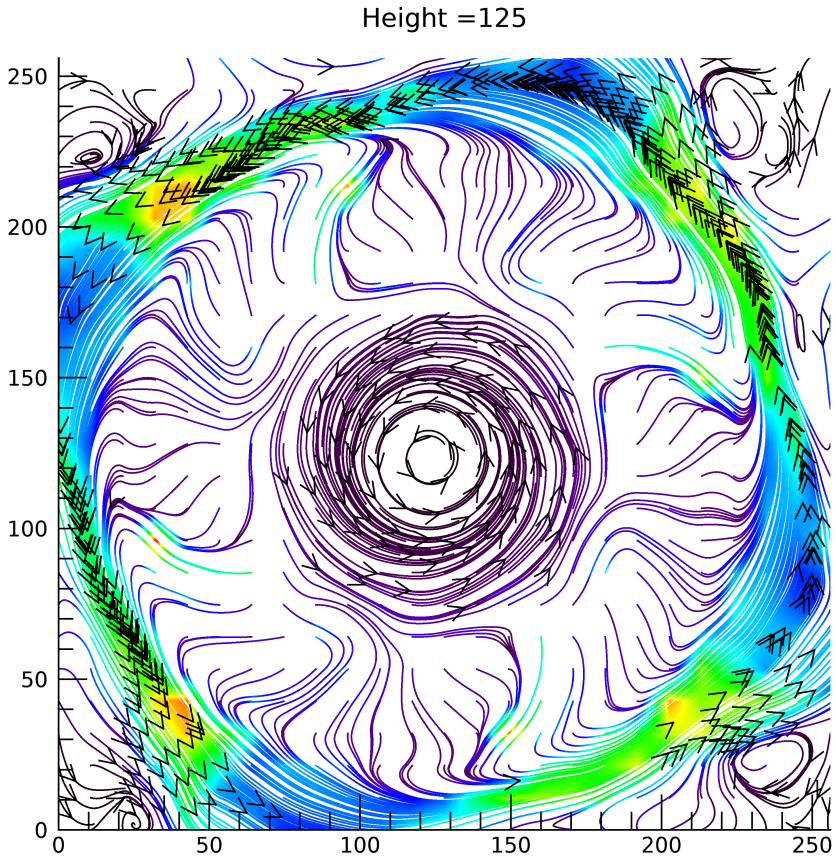

Figure 4.5: This figure shows a streamline plot of the velocity projected onto a horizontal slice (where the vertical direction is the z-direction) at a height of 15.625Mm above the photosphere, at an arbitrary time during the simulation. This figure illustrates the characteristic horizontal flow pattern that develops within the domain, in response to the photospheric driving. The colours indicate the magnitude of the velocity, where red is assigned to the largest speed and blue the smallest speed. The colours are ordered blue, green, yellow then red. The colour coding is normalised and purely indicates relative speed.

the umbral side) and therefore it is reasonable to assume that simply having a cylindrical mode sunspot in a square domain, would lead to an-isotropic expansion of the penumbra and consequently of the separatrix. The complex expansion of the separatrix could also be attributed to shearing at the interface between the penumbral and umbral regions; clearly in the early stages of the simulation the umbra and penumbra rotate in synchrony, but at latter stages the umbral region will continue to rotate freely but the penumbral region rotates slower. Again the differential resistance of the side-boundaries may influence any shearing forces.

The deformation of the separatrix is not found to significantly influence the evolution of the sunspot (or of the larger collection of simulations in general). We primarily see (in figures 4.3 and 4.4) that although the separatrix deforms, the expansion is symmetric in each quadrant of the domain (implying that the deformation is not due to numerical effects) and only at the very end of the simulation does the deformation influence the nature of the penumbral expansion (shown in the final sub-figure of figure 4.4 as four points simultaneously hit the top boundary). Other than at the very end, the disparity in expansion is relatively small compared to the overall side of the expanding structure.

4.3 Twist

In response to the photospheric driving, the penumbra increases in volume and stores magnetic energy, one may wonder what from the driving alone causes this increase in magnetic energy (and hence magnetic pressure) and penumbral volume. An obvious property that ought to be investigated is the twist of the magnetic field. Twist must be introduced by the driving boundary conditions because they employ rotational velocity fields, which will to some degree be stored in the penumbral magnetic field, given it is closed.

The magnetic helicity is a commonly used metric to measure twist, but we do

not investigate the magnetic helicity in this work because calculating it is a sizeable task in itself and there seems to be no best agreed upon method for doing so in the community. There are documented disparities of magnetic helicity measurements based on the method used to approximate it (Valori et al., 2016). Helicity may be a more physically desirable quantity to measure but the numerical domain we employ is not closed (via the umbral field) and therefore the conservation of helicity is not guaranteed.

4.3.1 Alpha - Force-Free Parameter

To analyse the twist of the magnetic field we first investigate the force-free parameter, α, where,

$$\alpha = \frac{(\nabla \times \mathbf{B}) \cdot \mathbf{B}}{B^2}. \tag{4.1}$$

By analysing the twist of the magnetic field, by approximating its circulation in the direction of itself, we get a scalar metric that is always definable and does not rely on closed systems like magnetic helicity to be physically meaningful. Using the penumbra identifying method (section 4.1), we may localise the measurement of α to the penumbral and umbral regions to measure twist independent. Given we know the umbral field is open and the penumbral closed, we may expect the distribution of alpha in these regions be distinct. The distribution of this twist proxy is meaningful and of physical interest from an energy (Nandy et al., 2003) and modelling (Grad and Rubin, 1958; Inhester and Wiegelmann, 2006; Wiegelmann and Sakurai, 2012; Régnier and Priest, 2007b; Régnier, 2013) perspective. The parameter, α, measures the geometrical twist of the magnetic field and removes the weighting of the magnetic field strength itself. This means that caution must be employed when interpreting the importance of twist defined this way where the magnetic field is very weak (i.e. near domain side boundaries). The curl of the magnetic field is proportional to the current density (equation 1.10) and therefore α is a measure of the current density in

the direction of the magnetic field, but normalised by the magnetic field and current strengths. Therefore, α amplifies in appearance the structures shown by the current density (see chapter 3).

Figures 4.6 and 4.7 show the evolution and distribution of α during the simulation. Generally, the magnitude of twist in the penumbral magnetic field is greater than that in the umbral field. The persistent untwisted nature of the umbral field region is an expected reflection of the open-like upper-boundary conditions (i.e. the umbral magnetic field should not store twist and is observed not to). The umbral field region does show enhanced twist near the side-boundaries, but as discussed previously the magnetic field strength at this location is vanishingly small and hence these features are not expected to meaningfully influence the magnetic properties of the sunspot during the simulation. We observe that in the umbral region, there is a strong band of twist near the separatrix with the same handedness as the twist measured within most of the penumbra. This feature is aligned with the current sheet identified in chapter 3 in figures 3.5 and 3.6 and is therefore likely the geometric measurement of the magnetic field circulation which produced these currents (see equation 1.10).

Figures 4.6 and 4.7 show that as the sunspot is driven, the penumbra develops twisted magnetic field with both positive and negative handedness. The positive handedness forms below the transition region (below 2Mm). A strong negative handed region of twist forms low in the atmosphere (from the second cell at 187.5Km) above where the penumbral field lines emerge from the model sunspot (between $\pm(5-10)$Mm). These regions are also in alignment with strong currents as highlighted in figures 3.5 and 3.6. The most interesting observation is that within most of the penumbral region, the magnitude and distribution of twist is relatively uniform (excluding the highly twisted regions previously discussed) during most of the simulation. This result is insightful because it suggests that the sunspot evolves

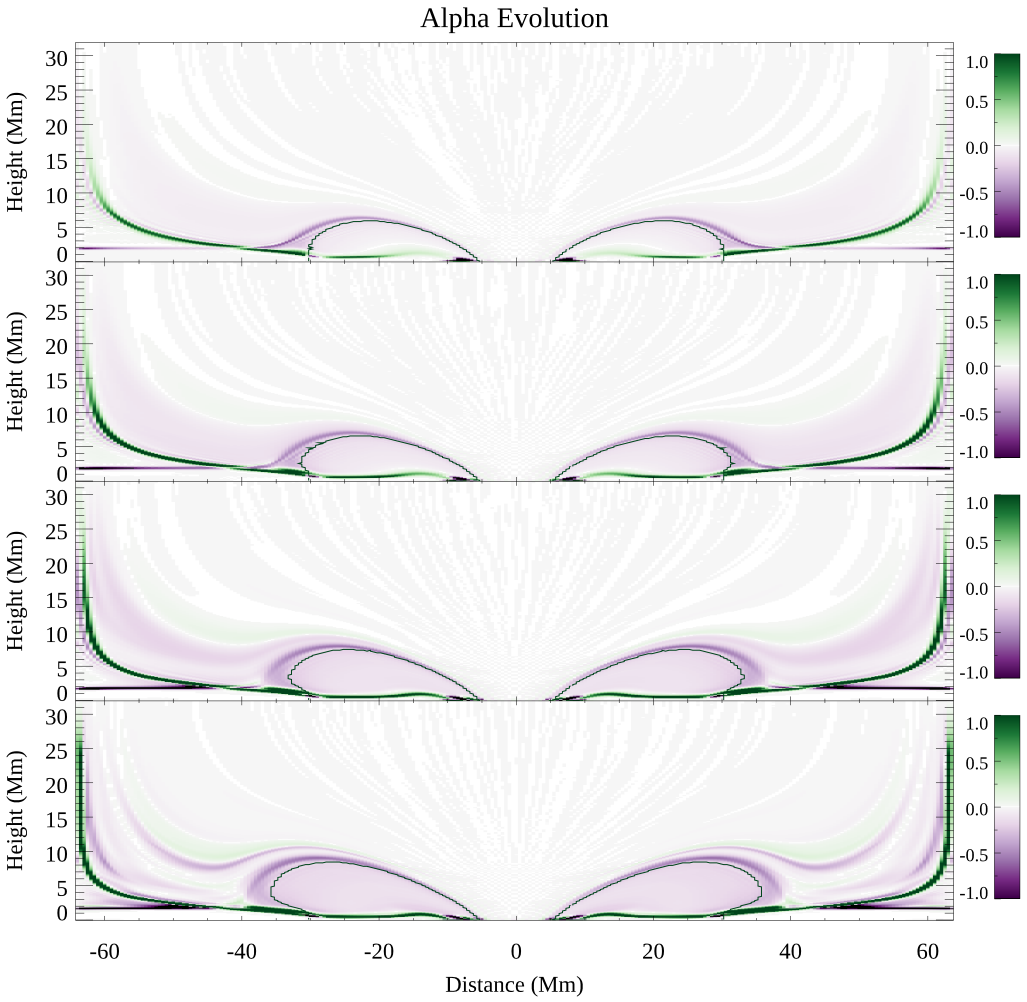

Figure 4.6: This figure shows the distribution of α throughout the domain in a slice through the centre of the sunspot. The sub-figures, moving from top to bottom, show the this at times when the sunspot has been rotated by 0°, 30°, 45°, 60° and 75° by the driver respectively. The black contour represents the approximate location of the separatrix that divides the umbral and penumbral magnetic field regions, in a slice through the centre of the sunspot. The units of the colour bars are m^{-1}, but for compactness the colour bars are normalised by μ_0, meaning they each range from $-\mu_0(\mathrm{m}^{-1})$ to $\mu_0(\mathrm{m}^{-1})$.

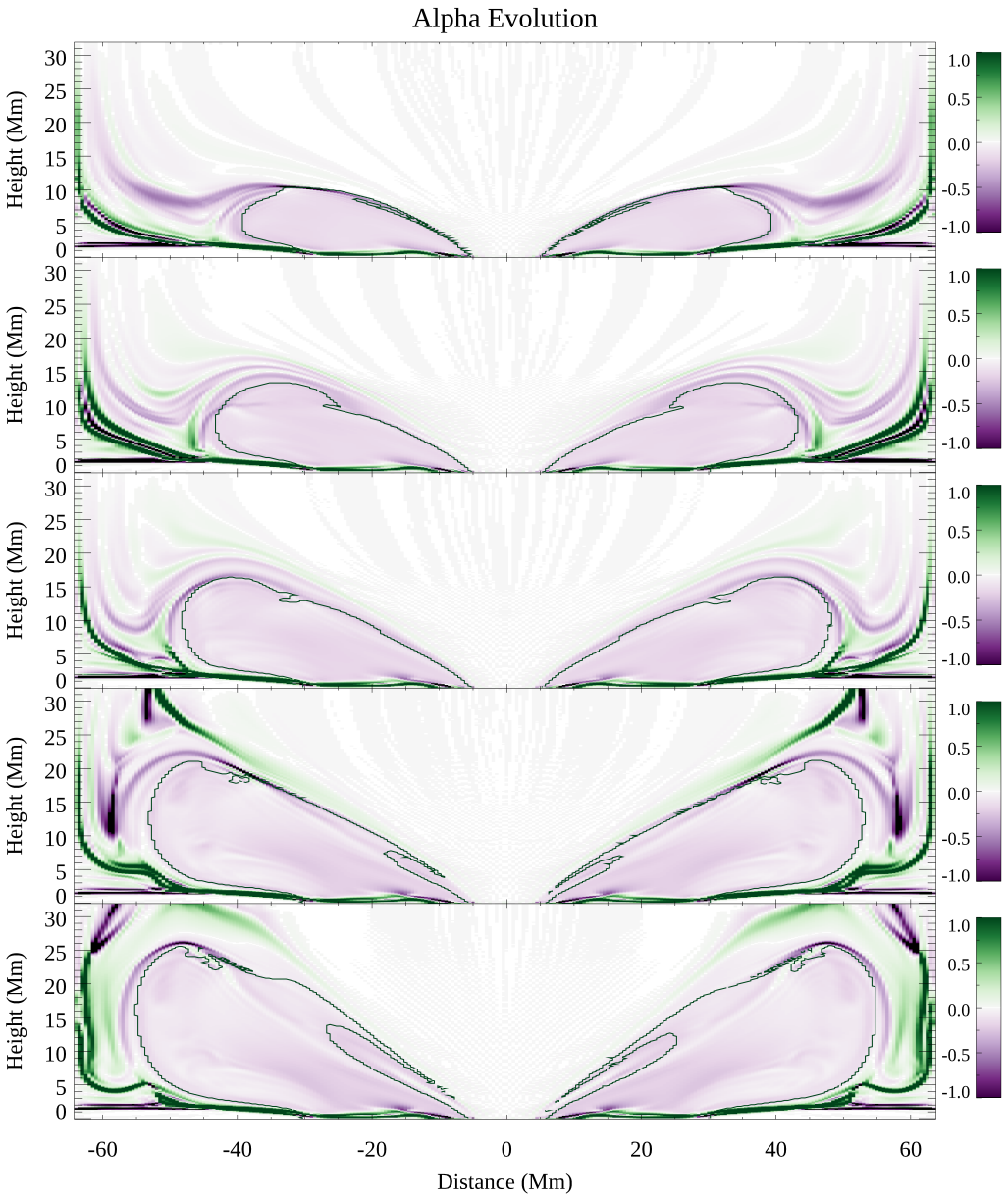

Figure 4.7: This figure shows the distribution of α throughout the domain in a slice through the centre of the sunspot. The sub-figures, moving from top to bottom, show this at times when the sunspot has been rotated by 90°, 105°, 120°, 135° and 140° by the driver respectively. The black contour represents the approximate location of the separatrix that divides the umbral and penumbral magnetic field regions, in a slice through the centre of the sunspot. The units of the colour bars are m^{-1}, but for compactness the colour bars are normalised by μ_0, meaning they each range from $-\mu_0(\mathrm{m}^{-1})$ to $\mu_0(\mathrm{m}^{-1})$.

in such a manner that the twist stored in its closed magnetic field distributes quickly and uniformly in response to the driver. This is particularly encouraging because it implies that the relatively fast rotation used for numerical cost saving has not introduced spurious results into the simulation. This finding also supports the results and discussion of section 3.4 in that where we observe the dominance of parallel current in the penumbra, we also see smooth distribution of α, suggesting that α in this region remains constant along magnetic field lines (which produce a force-free magnetic field). It is difficult to say this conclusively with only a series of two dimensional slice plots, but given the measurement of aligned current and magnetic field too, this seems to be a sensible explanation for what is observed. However, the measurement of α along magnetic field lines is possible via interpolation and field line tracing and is something that will be addressed in future works.

If the assumption that most of the penumbra in the corona is force-free (specifically the penumbra where we measure dominant parallel currents) and we assume that the slices shown in figures 4.6 and 4.7 are indicative of the full azimuthal range, we can conclude that most of the penumbra in these regions have similar α values. If true, this would mean that these large regions of the penumbra are near the linear force-free state and therefore we may expect them to be near a minimum magnetic energy state for a given net helicity (Priest, 2014). However, the picture becomes clouded when one considers that the top of the domain is open. Thus, there is some uncertainty with specifically which linear force-free state corresponds to the minimum. The penumbral region is a closed magnetic body, so one might assume that it has its own linear force-free state. The linear force-free field we might be measuring here, would therefore correspond to the minimum energy state associated with the net helicity introduced into the penumbral region by the driver. However, the umbral region is open, and should the appropriate conditions arise, the penumbral magnetic field may reconnect with the umbral field, at which point helicity would be

free to leave the system via the upper domain boundary. This would mean that the potential state (which is a linear force-free state, where $\alpha = 0$ everywhere) is actually the linear force-free field associated with the numerical domain. But clearly to achieve a potential field minimum energy state requires magnetic reconnection and simulation 1 is evolved under an ideal MHD regime (of course numerical resistivity can be, and most likely is to some extent, present).

Figures 4.8-4.15 each show histograms show the distribution of α at key times during the simulation, separately for the umbral and penumbral field regions, with a magnetic field line with separatrix surface plot included. In this analysis, we shall be primarily concerned with the distribution of α itself and are not concerned with the histogram count (the y-axes of each histogram). The range of the x-axes of all α histograms is limited to ± 0.5 as preliminary analysis found that the primary data structure is found within this range, where the statistical outliers can be an order of magnitude larger but are far less frequent. Figures 4.8-4.15 conclusively show that throughout the simulation the majority of the umbra remains untwisted, with a small broadening of the profile.

The remaining discussion focuses on the penumbra only. Figure 4.8 shows the first α-distribution that forms near the end of the acceleration phase. This structure contains a peak at $\alpha = 0$ indicating that there are still untwisted parts of the penumbral magnetic field. It also shows that the remaining penumbral region has both positive and negative handed twist, with a significant majority being negative. Figure 4.9 shows that far more of the penumbral region has developed negative twist, but there is still some regions that are untwisted. Some small structural changes have developed in the positive region (but remain relatively minor). The magnetic field with separatrix plot in this figure shows that the penumbra has begun to rise, the α-distribution for the penumbra shows a small peak developing at $\alpha = -0.2$ at the same time. This correlation alone is insufficient to offer an explanation, but we

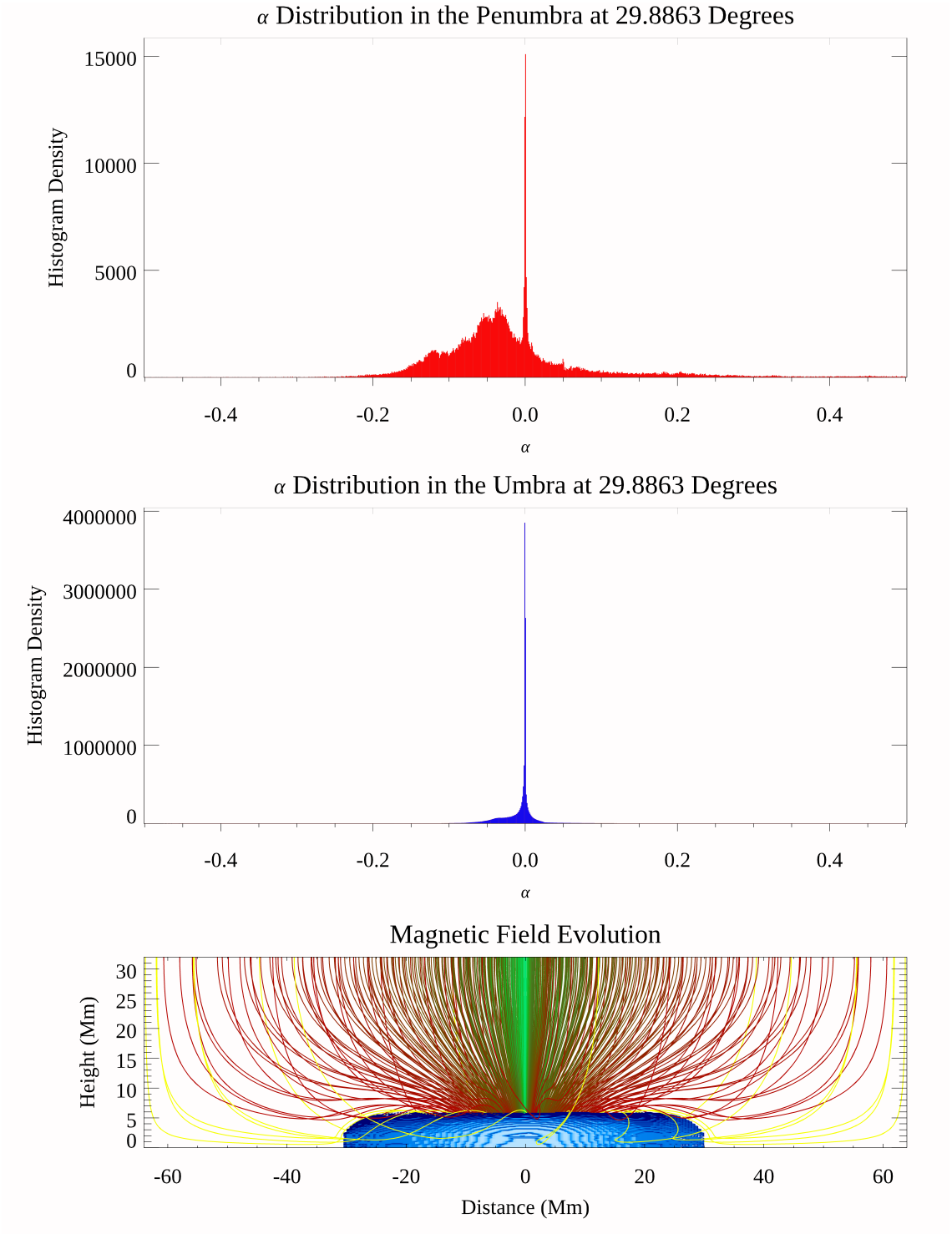

Figure 4.8: This figure shows the distribution of α in the penumbral and umbral regions. Specifically, the top figure shows a histogram of α in the penumbra, the middle shows the same in the umbra and the bottom sub-figure shows the magnetic field line and separatrix plot at the same time. The sunspot has been rotated by 30° in this figure.

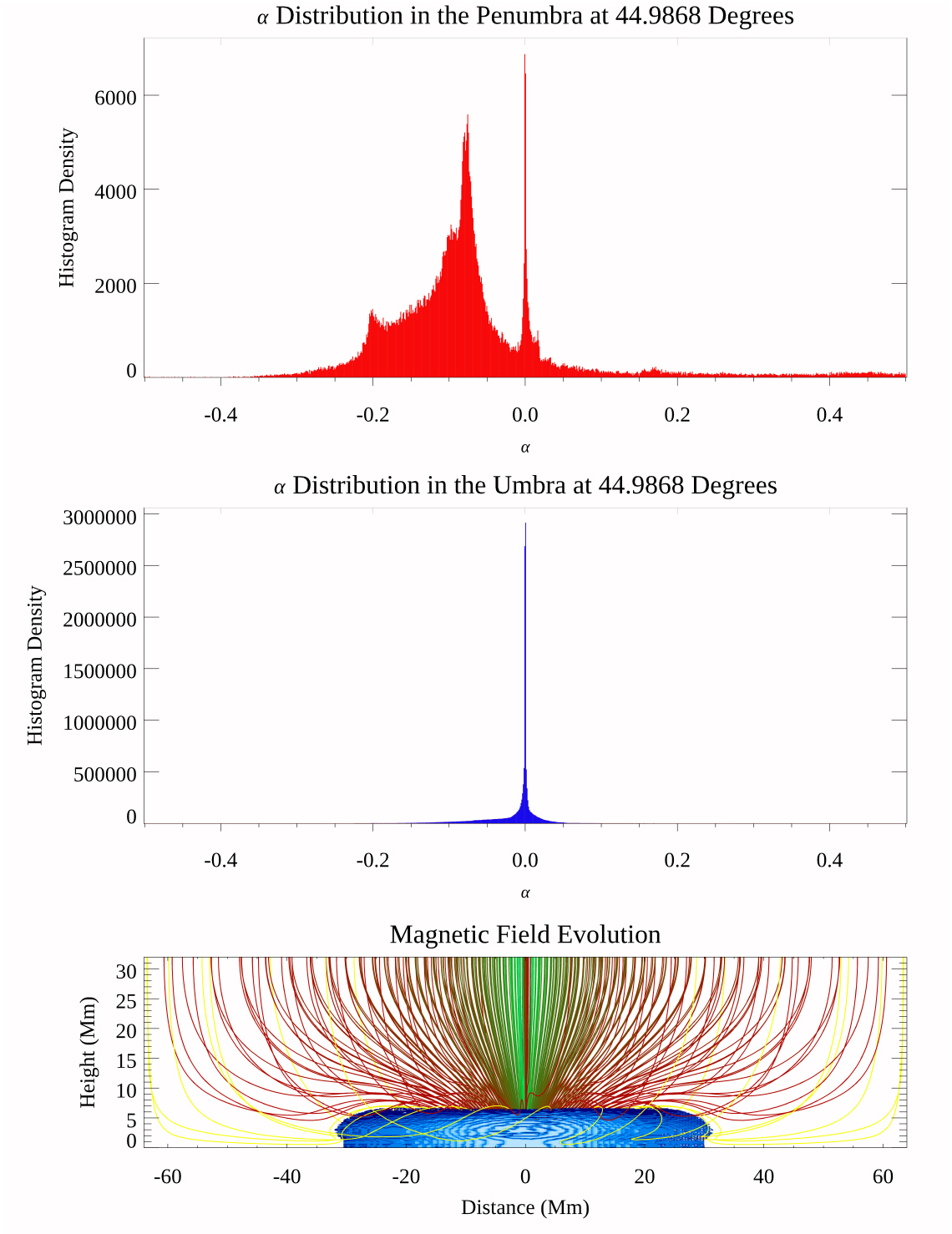

Figure 4.9: This figure shows the distribution of α in the penumbral and umbral regions. Specifically, the top figure shows a histogram of α in the penumbra, the middle shows the same in the umbra and the bottom sub-figure shows the magnetic field line and separatrix plot at the same time. The sunspot has been rotated by 45° in this figure.

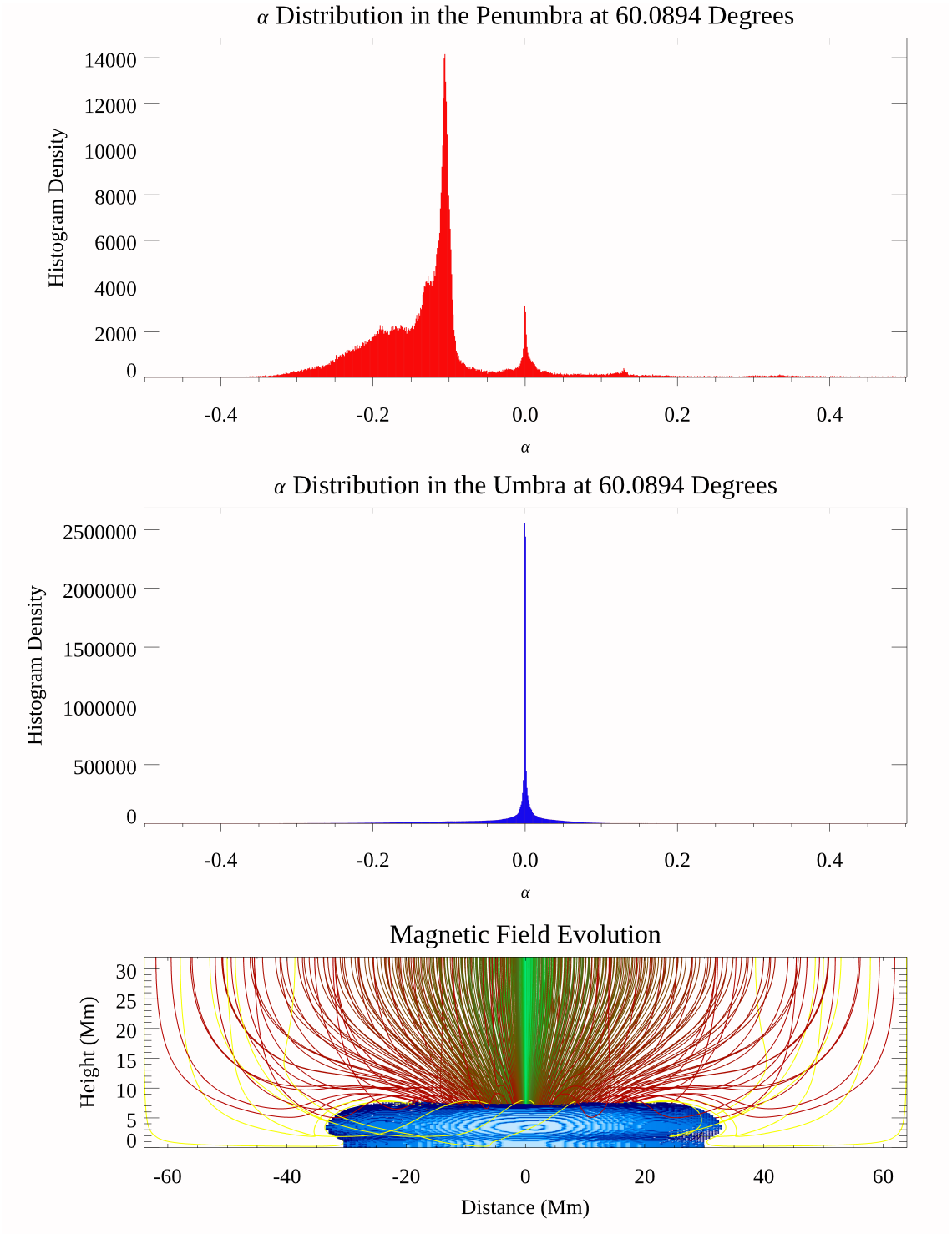

Figure 4.10: This figure shows the distribution of α in the penumbral and umbral regions. Specifically, the top figure shows a histogram of α in the penumbra, the middle shows the same in the umbra and the bottom sub-figure shows the magnetic field line and separatrix plot at the same time. The sunspot has been rotated by 60° in this figure.

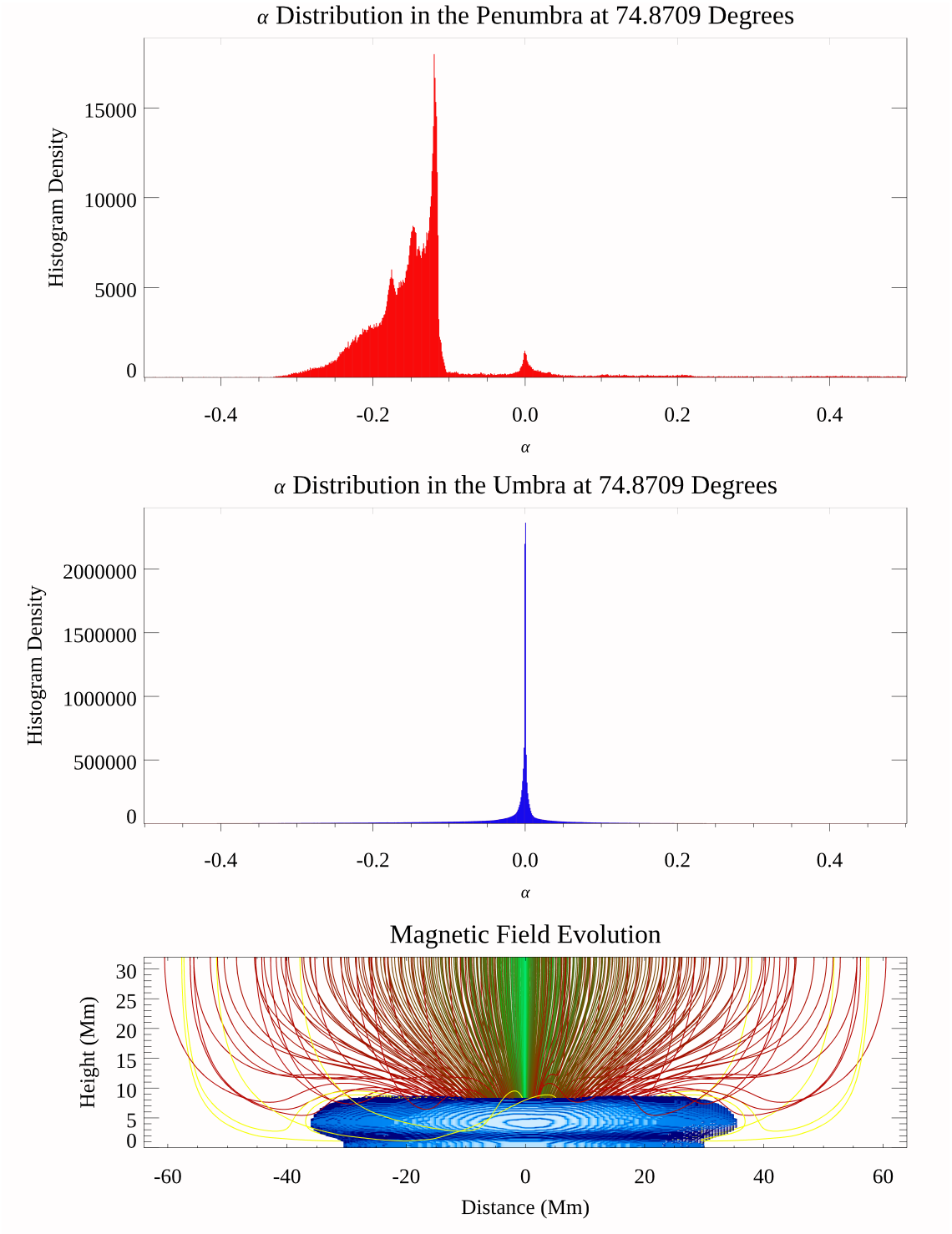

Figure 4.11: This figure shows the distribution of α in the penumbral and umbral regions. Specifically, the top figure shows a histogram of α in the penumbra, the middle shows the same in the umbra and the bottom sub-figure shows the magnetic field line and separatrix plot at the same time. The sunspot has been rotated by 75° in this figure.

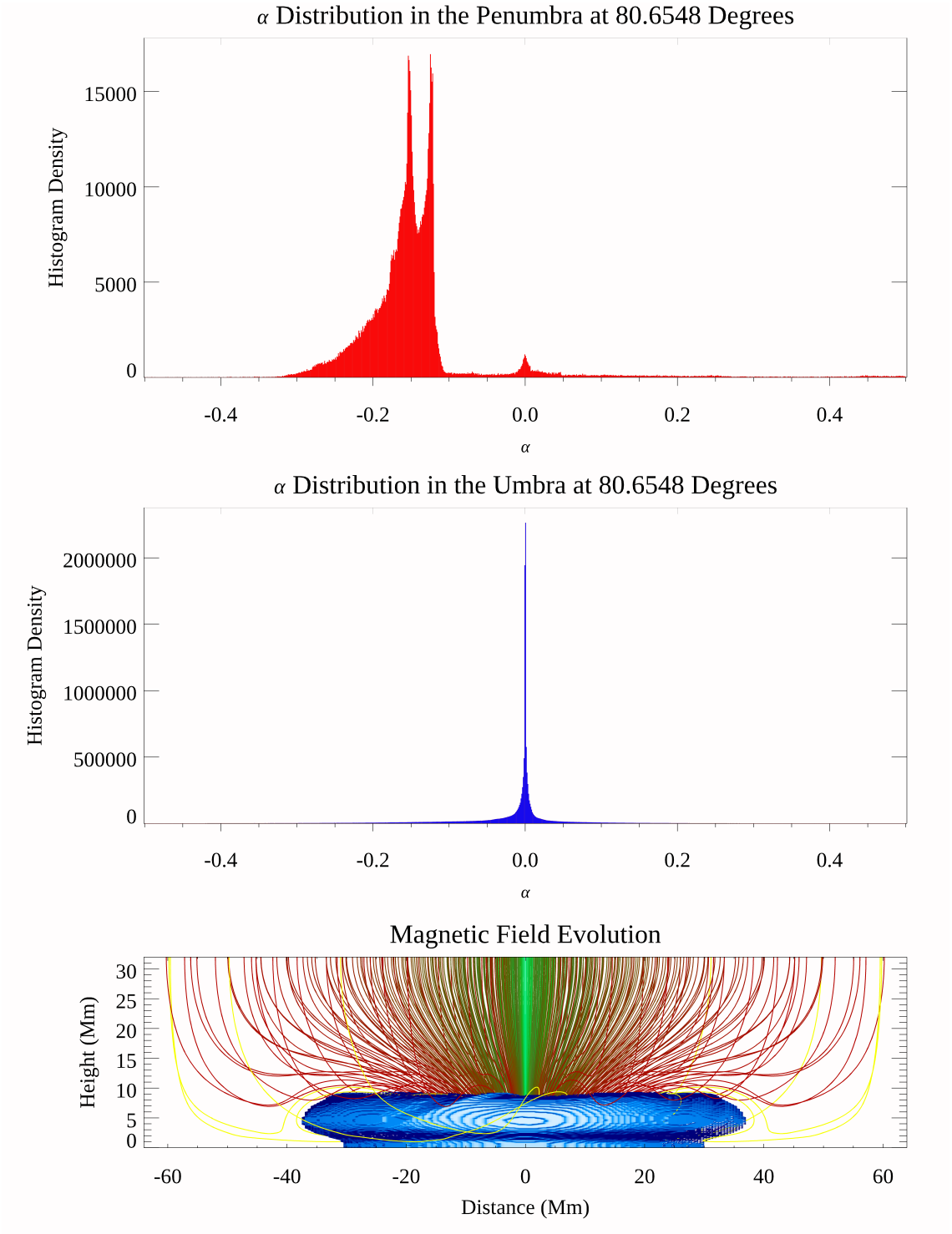

Figure 4.12: This figure shows the distribution of α in the penumbral and umbral regions. Specifically, the top figure shows a histogram of α in the penumbra, the middle shows the same in the umbra and the bottom sub-figure shows the magnetic field line and separatrix plot at the same time. The sunspot has been rotated by 80° in this figure.

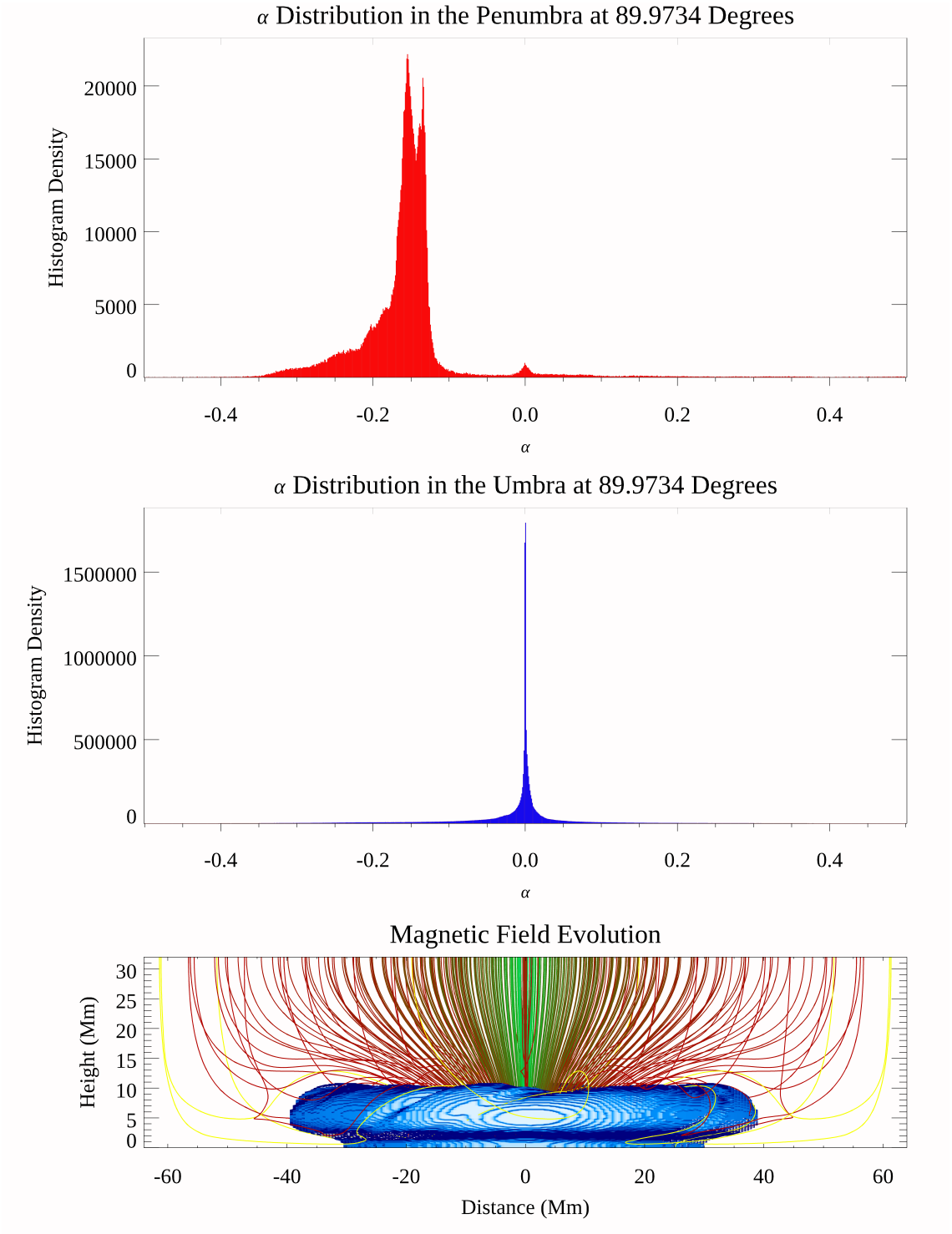

Figure 4.13: This figure shows the distribution of α in the penumbral and umbral regions. Specifically, the top figure shows a histogram of α in the penumbra, the middle shows the same in the umbra and the bottom sub-figure shows the magnetic field line and separatrix plot at the same time. The sunspot has been rotated by 90° in this figure.

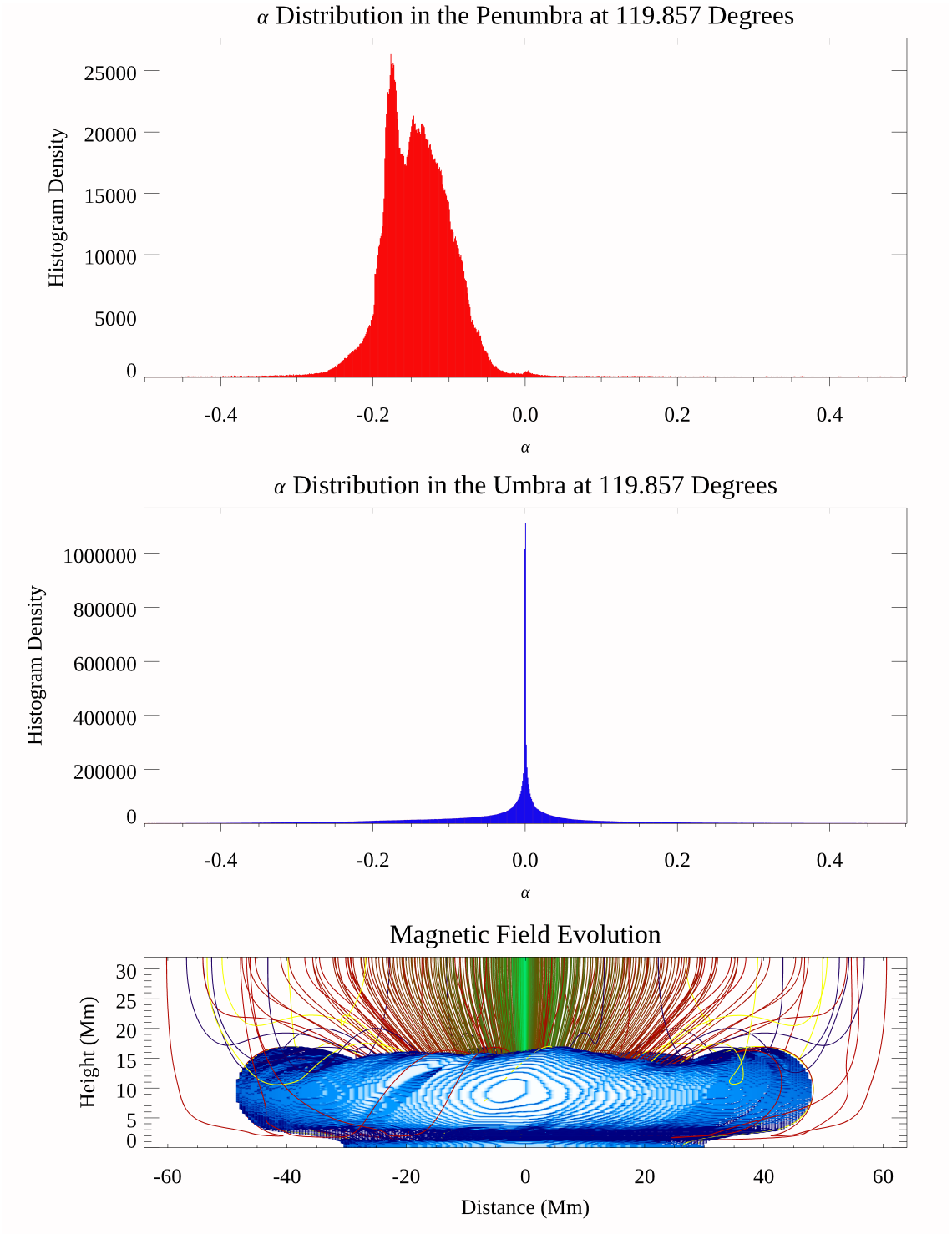

Figure 4.14: This figure shows the distribution of α in the penumbral and umbral regions. Specifically, the top figure shows a histogram of α in the penumbra, the middle shows the same in the umbra and the bottom sub-figure shows the magnetic field line and separatrix plot at the same time. The sunspot has been rotated by 120° in this figure.

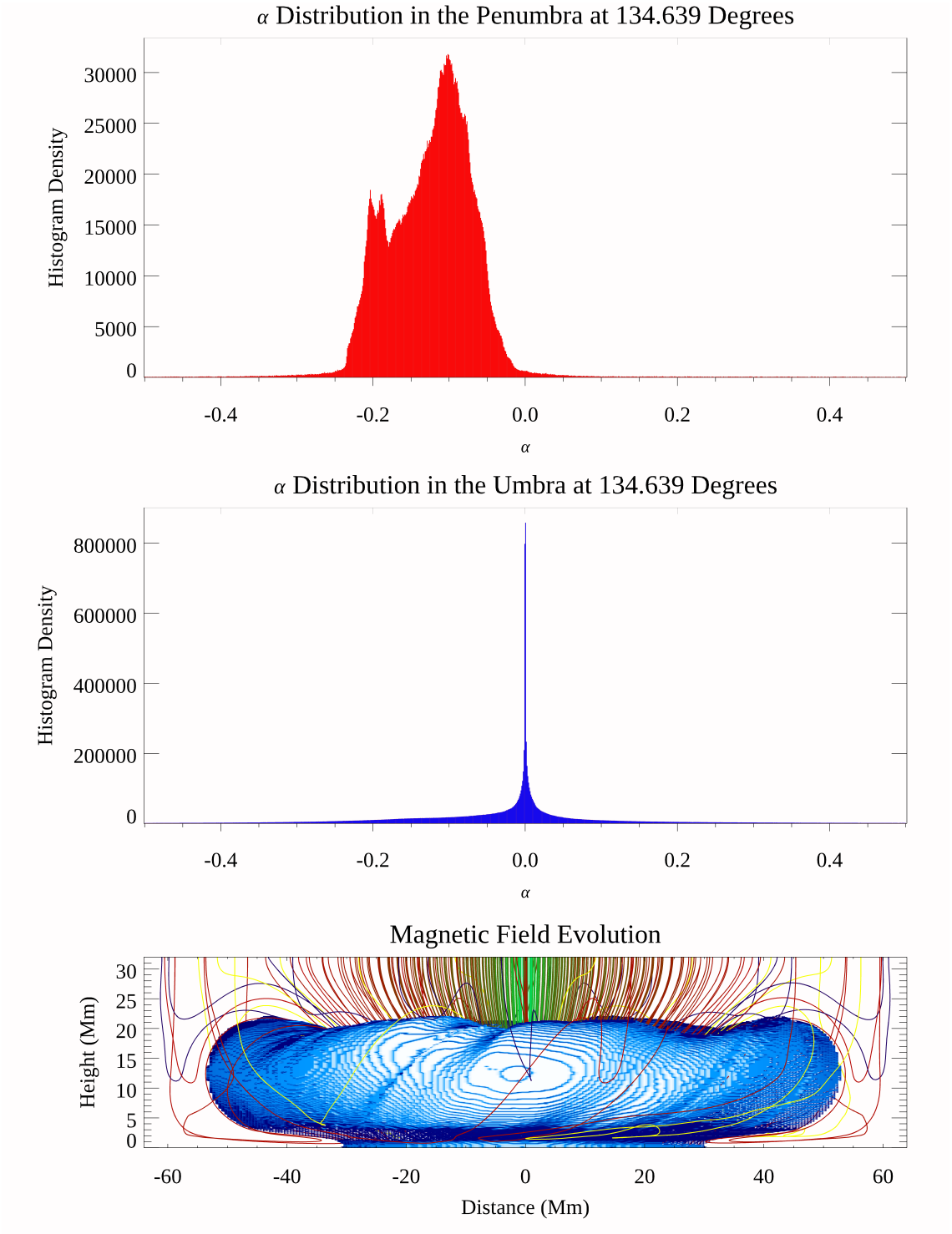

Figure 4.15: This figure shows the distribution of α in the penumbral and umbral regions. Specifically, the top figure shows a histogram of α in the penumbra, the middle shows the same in the umbra and the bottom sub-figure shows the magnetic field line and separatrix plot at the same time. The sunspot has been rotated by 135° in this figure.

shall see similar correlations in the subsequent discussion. Figure 4.10 shows that the amount of untwisted field has reduced further, the distribution of positive twist has maintained its structure, but generally the region between the peaks at $\alpha = -0.1$ and $\alpha = -0.2$ has filled out to the point that the peak at $\alpha = -0.2$ in the previous plot has become part of a flat region in figure 4.10. We see generally that the total amount of negative twist has increased significantly, with more strong (negative) twist having also developed. Figure 4.11 shows that the amount of untwisted field has continued to reduce, but the overall amount of negative twist has increased. We now see a clear depletion between $\alpha = 0.1$ and $\alpha = 0$ which in hindsight was developing in the previous figures. We now recognise a trend, the peak at $\alpha \approx -0.125$ has moved to this location from the right, this peak matches the values within the majority of the penumbral region. Collectively this peak and those in the previous figures analysed, agree with figure 4.6 where we see the twist in the penumbra strengthen in the early phase of the simulation. The penumbra has visibly continued to grow and several small peaks of larger magnitude (negative) twist have developed.

Figure 4.12 continues all the trends discussed above, however, a new feature forms at $\alpha \approx -0.15$. This new peak forms quickly and seems to appear at the precise moment the separatrix begins to develop folds. Figure 4.13 shows that the two peaks in figure 4.12 have begun to merge as the lower magnitude α value peak continues to develop and the peak value becomes increasingly negative. This figure also shows that the penumbra has begun to expand more significantly, with the folded separatrix maintaining its form. Figure 4.14 shows that the penumbral region has expanded significantly since the previous figure, and the double peak structure remains but has become much smoother. Most interestingly, as the penumbra has expanded the amount of large magnitude twist has diminished, i.e. most of the α values lie between -0.2 and 0, with a small wing extending to $\alpha = -0.25$. This implies

that the expansion of the penumbra has reduced the magnitude of the strongest twist. Finally figure 4.15 shows that the separatrix has enlarged significantly and the overall magnitude of the penumbral field twist has reduced since the previous time, there is now far more localisation of the twist between $\alpha = -0.25$ and $\alpha = 0$. What was the primary peak at $\alpha \approx -0.2$ has now become a minor peak with most of the distribution being concentrated around $\alpha = -0.1$.

Collectively these figures show that as the sunspot is driven, negative twist is introduced into the penumbral magnetic field. The distribution of twist seems to be highly correlated with the state of the separatrix and the penumbral volume. As folds begin to develop in the separatrix we observe additional strong twist values forming peaks in the distribution. As the penumbra expands the overall magnitude of twist generally decreases, however, smaller peaks of strong twist persist from their development until the end of the simulation. Most importantly though, is the observation that at all times there is a distribution of α values in the penumbral field region, indicating that the penumbra is certainly not in a linear force-free state as may have been inferred if only analysing figures 4.6 and 4.7. This is particularly encouraging as it directly shows that the system hosts not just magnetic energy, but free magnetic energy which may contribute to the powering of extreme space weather events.

4.3.2 Current Helicity

In section 4.3.1, we observed that the magnetic field in the penumbral region is in general in a persistent state of enhanced twist as compared to the umbral magnetic field. The increased proportion of twist in the penumbral region, as compared to the umbral region, highlights that the penumbral expansion may be linked with the increase of stored twist in penumbral region in combination with the relatively relaxed umbral magnetic field. This hypothesis has firm logical foundations, because

we initialise with an untwisted magnetic field (with a potential minimum energy magnetic field) and do nothing but drive the lower domain boundary (with a rotational profile), we must deviate the system from the unique potential field state and introduce magnetic energy and hence magnetic pressure. But, we must simultaneously introduce twist into the closed magnetic field via the continued driving, which we measured in section 4.3.1. Therefore, we may stipulate the increase in twist in the closed penumbral magnetic field must result in a magnetic energy increase, as the twist must cause a deviation from the potential field state we initialise with. If the twist is associated with increased magnetic energy, it must also be associated with increased magnetic pressure. The force-free parameter (α) was used in section 4.3.1 to investigate the distribution of geometrical twist present in the magnetic field throughout the domain and more specifically in the penumbral and umbral regions. But the force-free parameter (α) suffers in regions where the magnetic field vanishes as shown by equation 4.1 where there is a division by the square of the magnetic field strength. Ideally, we would like a second measure of the twist of the magnetic field that does not suffer from anomalous normalisation effects. Another metric for measuring the twist of a magnetic field is the current helicity density, which is defined as,

$$h_c = \iiint \mathbf{B} \cdot \mathbf{J} \, dV = \frac{1}{\mu_0} \iiint \mathbf{B} \cdot (\nabla \times \mathbf{B}) \, dV, \tag{4.2}$$

where $\mathbf{B}$ and $\mathbf{J}$ represent the magnetic field and the current density respectively and μ_0 is the permeability of free space. The current helicity, h_c, is typically used as a proxy for twist but is also used in conjunction with the magnetic helicity (Blackman, 2015; Ruiz Cobo and Puschmann, 2012; Tian and Alexander, 2006; Pevtsov, 2008). Unlike the magnetic helicity, the current helicity is not a quantity that is necessarily conserved under any MHD regime, which means we do not have to worry about its use with the upper boundary conditions of the numerical domain. The current helicity also has the added benefit of a relative ease of calculation as compared to

magnetic helicity, for which there are a plethora of techniques to approximate (Valori et al., 2016).

The current helicity, h_c, simply put is the sum over a region of the dot product of the current density and the magnetic field. By comparing equations 4.1 and 4.2 we observe that the kernel of the integral in equation 4.2 is equal to the numerator of the right hand side of equation 4.1. Therefore, the current helicity density is the product of the twist parameter (defined by equation 4.1) and twice the magnetic pressure (defined by equation 1.22). Thus, we may write,

$$h_c = \frac{1}{\mu_0} \iiint \mathbf{B} \cdot (\nabla \times \mathbf{B}) \, dV = \iiint \alpha \frac{B^2}{\mu_0} \, dV. \tag{4.3}$$

Therefore, we see that the current helicity in a volume is equal to the product of the geometrical twist of the magnetic field and twice the magnetic pressure, integrated over the volume. The current helicity density, $\alpha B^2 {\mu_0}^{-1}$, can be calculated in the penumbral and umbral regions independently, to give a second measure of the distribution of twist to compliment the findings of section 4.3.1 without the potential consequence of vanishingly weak magnetic fields and current densities introducing spurious results; here weak currents and field strengths force current helicity density to vanish, rather than blow up.

Figures 4.16 and 4.17 show that as the sunspot is driven, the current helicity density generally increases in magnitude until a point is reached where the strongest values tend to plateau. The most interesting, and physically meaningful, result contained within figures 4.16 and 4.17 shows itself most prominently when compared to figures 4.6 and 4.7. Figures 4.16 and 4.17 show that when the mask of B^2 is applied to the geometrical twist of the magnetic field we observe that the large regions of twist in the umbral field (as indicated by the force-free parameter, α) have all but vanished when the magnetic field strength is included. The striking part of this result is that our initial hypothesis that twist and magnetic energy (and magnetic pressure) are inevitably linked seems partially correct. Specifically, where

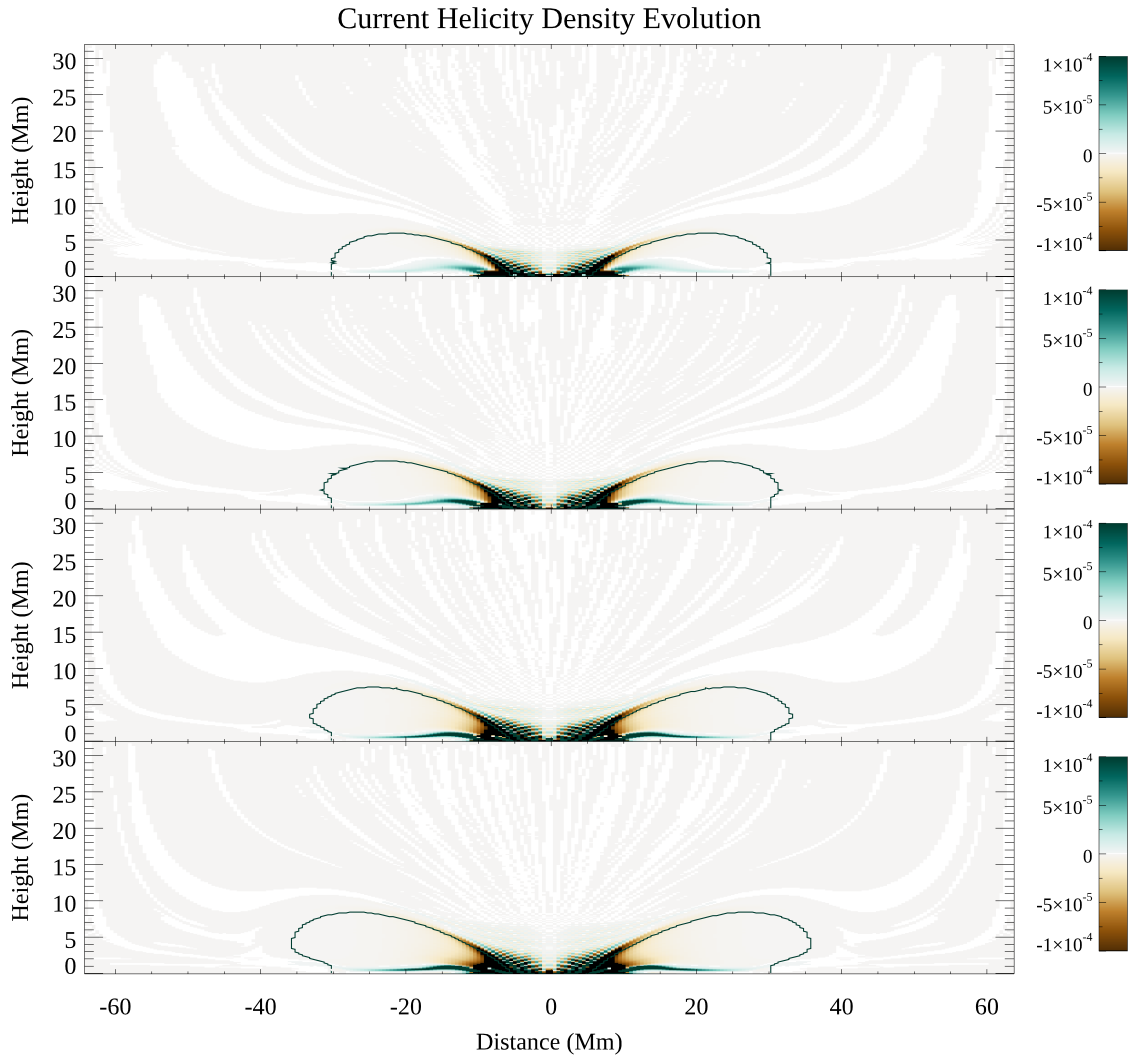

Figure 4.16: This figure shows the distribution of current helicity throughout the domain in a slice through the centre of the sunspot. The sub-figures, moving from top to bottom, show the this at times when the sunspot has been rotated by 0°, 30°, 45°, 60° and 75° by the driver respectively. The black contour represents the approximate location of the separatrix that divides the umbral and penumbral magnetic field regions, in a slice through the centre of the sunspot. The units of the colour bars are TAm^{-2}.

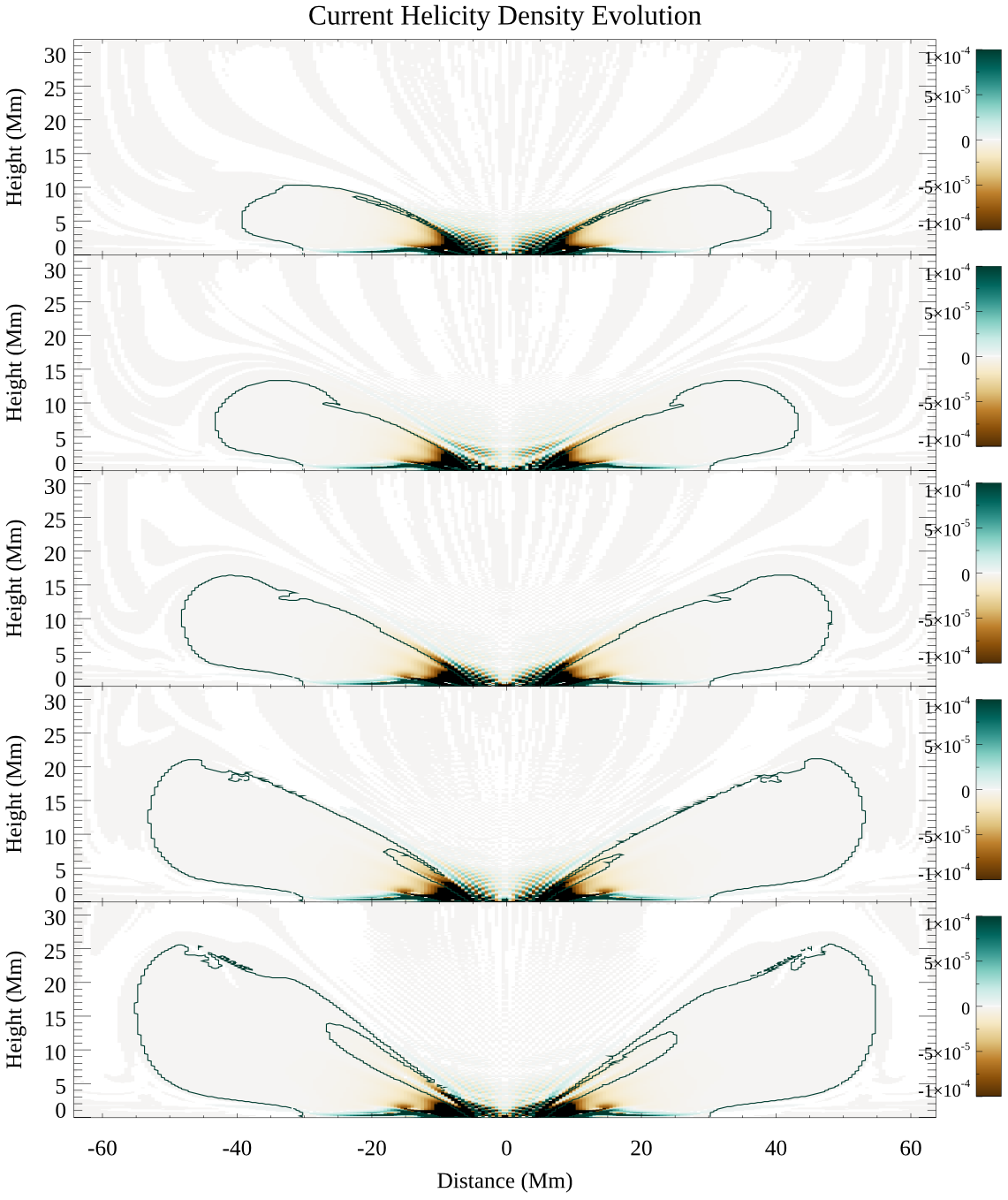

Figure 4.17: This figure shows the distribution of current helicity throughout the domain in a slice through the centre of the sunspot. The sub-figures, moving from top to bottom, show this at times when the sunspot has been rotated by 90°, 105°, 120°, 135° and 140° by the driver respectively. The black contour represents the approximate location of the separatrix that divides the umbral and penumbral magnetic field regions, in a slice through the centre of the sunspot. The units of the colour bars are TAm^{-2}.

we see the most strongly induced magnetic fields and currents (see chapter 3) we measure strong levels of current helicity, which implies that the geometric twist of the magnetic field is important in those locations. But we also see that not all locations that show large geometric twist (α) are associated with large magnetic energy and the current helicity offers a metric to identify the regions where both twist and magnetic energy are co-located. We may expect that from the perspective of this project, which wishes to understand the influence rotating sunspots have on their magnetic environments, the current helicity is more physically meaningful metric than the geometric twist (α) alone as it includes in its definition the magnetic energy density (magnetic pressure), and thus highlights the regions of importance in the domain. Finally, we see that there is an overwhelming dominance of current helicity in the penumbral field than the umbral. This is unsurprising, given we know that the penumbra stores twist and the umbra does not, despite the umbra having a generally stronger magnetic field.

We now transition from analysing the current helicity density to measuring the current helicity in the domain, and separately for the penumbral and umbral volumes. Figure 4.18 shows that as the simulation proceeds, the current helicity of the penumbral and umbral regions evolves in a coupled manner. The total current helicity increases in magnitude as the sunspot is accelerated from rest, then once full speed rotation is reached at $\sim 32°$, it begins to settle and eventually plateaus to a steady value. A key point to make at this time, is that we know the from the other chapters of this thesis that the current and twist in the umbral region is typically smaller in magnitude than those found in the penumbra. Figure 4.18 supports this finding, showing that the current helicity in the umbral region is always of lesser magnitude than in the penumbra. The size difference of the umbral and penumbral regions should also be considered. The umbral region has at all times a much larger volume (shown by figures 4.1 and 4.2) and so the average current helicity in the

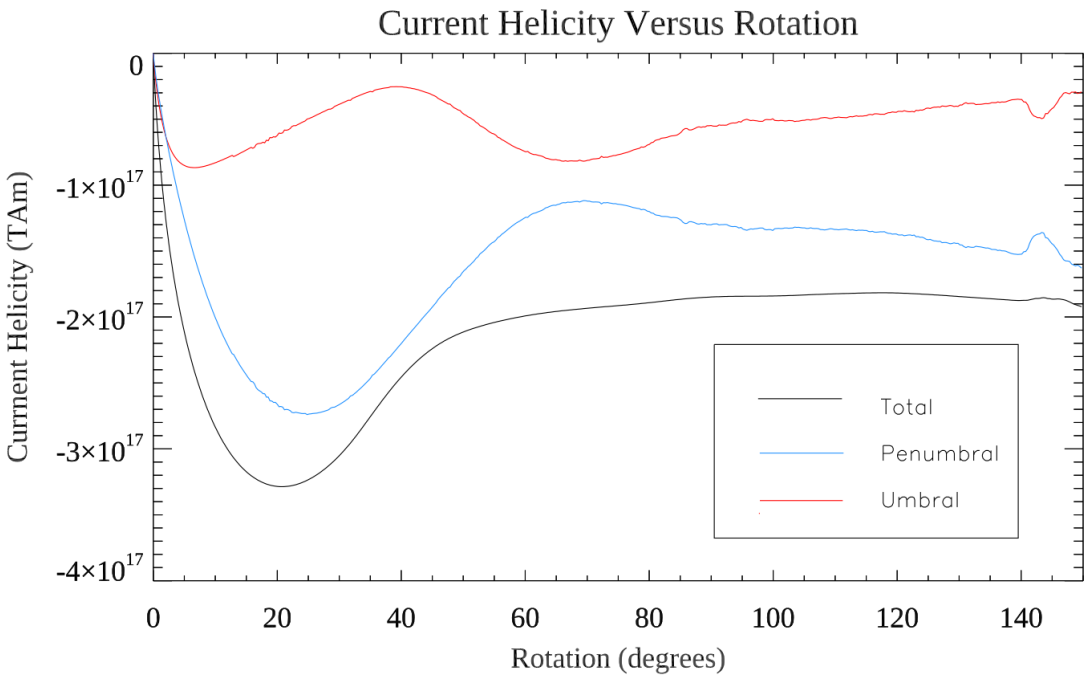

Figure 4.18: Multiple line plots showing the total current helicity in the full domain (black), the penumbra (blue) and the umbra (red) as a function of rotation.

penumbra vastly dominates that of the umbra. We also know from this section that the penumbra hosts positive and negative strong current helicities, which will to some degree cancel when integrating over the penumbral volume. Further analysis should consider normalisation of each curve by the instantaneous volume measurement. This would give the average current helicity density in each region and would highlight better the dominance of the penumbral field twist and current helicity.

During the acceleration phase ($0° < \theta < 32°$) the umbral and penumbral region current helicities evolve very differently, the penumbra clearly follows the trend of the total (unsurprising given it holds most of the twisted field and strong currents). During the main phase of the simulation the current helicity in each region seems to form a mirror image profile, this phase correlates with the penumbral expansion phase and because currents form near the separatrix, we must exercise caution in interpreting the physics of the current helicity of each region because the separation

method has limited accuracy. And so it may be that some error is introduced in the splitting of the current helicity measurement. This is supported given that the total value remains relatively constant during the expansion phase of the penumbra.

4.4 The Physical Importance of Twist and Current Helicity

In section 1.7.1, we derived the Poynting theorem for MHD and found that there are two physical mechanisms that may result in an increase (or more generally, a change) of the magnetic energy at a point. Equation 1.36 (Priest, 2014) states the theorem and is repeated here for clarity,

$$\frac{\partial}{\partial t}\left(\frac{B^2}{2\mu_0}\right) = -\frac{j^2}{\sigma} - \mathbf{v}\cdot(\mathbf{J}\times\mathbf{B}) - \nabla\cdot\mathbf{S}.$$

Equation 1.36 shows that, for simulation 1 which evolves under an ideal MHD regime, the only means to change the magnetic energy density at a point is either by the convergence of magnetic energy toward that point (which corresponds to the third term on the right hand side of equation 1.36) or if there is a collocated anti-parallel velocity and Lorentz force (which corresponds to the second term on the right hand side of equation 1.36). In chapter 2, we find that the simulation domain boundaries employ a variety of magnetic field conditions. The boundary conditions at the side and upper boundaries forbid the propagation of magnetic energy across them, which means $\mathbf{S}\cdot\hat{\mathbf{n}} = 0$ (where $\hat{\mathbf{n}}$ is a unit normal vector perpendicular to an upper or side boundary). This means that the upper and side boundaries are energetically closed for electromagnetic forms of energy. This is a powerful imposition, as it means that the Poynting vector (equation 1.31) must be perpendicular to the upper and side boundaries at all times. Thus, we cannot introduce magnetic energy into the domain through the upper or side boundaries, which means any magnetic energy (in excess to the initial potential field) found within the numerical domain

at any time must form within the domain in response to the driving imposed at the lower boundary, flow into the domain through the lower boundary or develop as a secondary consequence of some process induced by the driving.

As we have discussed, equation 1.36 is very insightful for understanding the generation of magnetic energy within the domain. However, we may develop equation 1.36 further to better understand the importance of twist (α) and current helicity for the generation of magnetic energy. Simulation 1 evolves under the ideal MHD equations and thus the first term on the right hand side vanishes, as there is no resistivity (although in practice, there is likely numerical resistivity). Thus, equation 1.36 first becomes,

$$\frac{\partial}{\partial t}\left(\frac{B^2}{2\mu_0}\right) = -\left(\mathbf{v}\cdot(\mathbf{J}\times\mathbf{B}) + \nabla\cdot\mathbf{S}\right). \tag{4.4}$$

Next we may recast $\mathbf{v}\cdot(\mathbf{J}\times\mathbf{B})$ in terms of the current helicity. To do this we must establish a relationship between the Lorentz force and current helicity. We may write,

$$|\mathbf{J}\cdot\mathbf{B}| = |\mathbf{J}|\,|\mathbf{B}|\,|\cos\theta|\,, \tag{4.5}$$

where θ is the angle subtending the current density and magnetic field. Secondly, we may write,

$$|\mathbf{J}\times\mathbf{B}| = |\mathbf{J}|\,|\mathbf{B}|\,|\sin\theta|\,. \tag{4.6}$$

If we square and add equations 4.5 and 4.6, we retrieve,

$$|\mathbf{J}\times\mathbf{B}| = \sqrt{J^2B^2 - |\mathbf{J}\cdot\mathbf{B}|^2}, \tag{4.7}$$

which expresses the magnitude of the Lorentz force in terms of the magnetic field strength, the current density magnitude and the magnitude of the current helicity. If we equate the magnitude of each side of equation 4.4 and recast the result as an inequality, we may write,

$$\left|\frac{\partial}{\partial t}\left(\frac{B^2}{2\mu_0}\right)\right| \leq |\mathbf{v}\cdot(\mathbf{J}\times\mathbf{B})| + |\nabla\cdot\mathbf{S}|\,. \tag{4.8}$$

If we define ψ to be the angle subtended by the velocity vector and the Lorentz force, we may write,

$$|\mathbf{v} \cdot (\mathbf{J} \times \mathbf{B})| = |v||\mathbf{J} \times \mathbf{B}| \, |\cos \psi| \, . \tag{4.9}$$

We may then substitute equation 4.7 into 4.9 and define,

$$|\mathbf{v} \cdot (\mathbf{J} \times \mathbf{B})| = |v| \sqrt{J^2 B^2 - |\mathbf{J} \cdot \mathbf{B}|^2} \, |\cos \psi| \, . \tag{4.10}$$

Then, by substituting equation 4.10 into 4.8 we yield,

$$\left| \frac{\partial}{\partial t} \left(\frac{B^2}{2\mu_0} \right) \right| \leq |v| \sqrt{J^2 B^2 - |\mathbf{J} \cdot \mathbf{B}|^2} \, |\cos \psi| + |\nabla \cdot \mathbf{S}| \, . \tag{4.11}$$

Equation 4.2 shows that the $|\mathbf{J} \cdot \mathbf{B}|$ term in equation 4.11 represents the current helicity density and further to this equation 4.3 indicates that we may write equation 4.11 in a final form,

$$\left| \frac{\partial}{\partial t} \left(\frac{B^2}{2\mu_0} \right) \right| \leq |v||B| \sqrt{J^2 - \frac{\alpha^2 B^2}{\mu_0^2}} \, |\cos \psi| + |\nabla \cdot \mathbf{S}| \, , \tag{4.12}$$

where α is defined by equation 4.1.

Collectively, equations 4.11 and 4.12 extend our previous discussion of how the magnetic energy at a point may evolve under the ideal MHD regime, as now we recognise that if $\psi \neq \frac{n\pi}{2}$ (where n is an odd integer) we may alter the total magnetic energy at a point if there is an imbalance between $J^2 B^2$ and $|\mathbf{J} \cdot \mathbf{B}|^2$ or J^2 and $\alpha^2 B^2 \mu_0^{-2}$. Given the Lare3D code (Arber et al., 2001) yields the velocity and magnetic field distributions, it is trivial to calculate the sign of $\mathbf{v} \cdot (\mathbf{J} \times \mathbf{B})$ (and similarly $\nabla \times \mathbf{S}$) so that it is clear if the twisting magnetic field is generating or diffusing magnetic energy from a point.

At the start of the simulation, we have a static potential magnetic field which is a global energy minimum which means that there is not any free magnetic energy to contribute to the divergence term in equations 4.11 and 4.12. Secondly, because we perturb the simulation away from a potential configuration, we must introduce currents to the domain. Both points illustrate that the first terms on the right hand

side of equations 4.11 and 4.12 are significant at least at the start of the simulation for the generation of magnetic energy in the initially energetically minimised domain, after this point the divergence term is free to redistribute any magnetic energies.

We shall continue this analysis in chapter 5 where we look more closely at the energetics of the simulated sunspot.

Chapter 5

The Dynamics and Energetics of Sunspot Rotation

5.1 Dynamics

In this section we investigate the dominant forces present within the numerical domain of simulation 1. We do this to better understand the evolution of the penumbra primarily, but also highlight potentially important features found in the umbral magnetic field region. The momentum equation (equation 1.12) dictates the evolution of motion within the system. Equation 1.12, repeated here for convenience,

$$\frac{D\mathbf{v}}{Dt} = \frac{1}{\rho}\mathbf{j} \times \mathbf{B} - \frac{1}{\rho}\nabla P - \mathbf{g},$$

states that the acceleration of a plasma element (in a reference frame moving with the plasma) is equal to the sum of forces acting on the mass of the plasma element. The left hand side of equation 1.12 shows the advective derivative acting on velocity, which defines the acceleration in a frame moving with the plasma. The right hand side of equation 1.12 is composed of the forces relevant to this investigation that are modelled by the Lare3D code. The first term on the right hand side represents the Lorentz force (equation 1.6) divided by the density. Similarly, the second term shows

the pressure gradient upon the density and the final term represents the acceleration due to gravity. All terms, on the right hand side of equation 1.12, if multiplied by density yield forces. Therefore in their present state each term represents the force per unit volume per unit mass, contribution from each respective force to the total acceleration.

In this section we shall investigate the distribution and magnitude of each of the acceleration terms on the right hand side of equation 1.12, to understand which forces dominate and to understand better the evolution of the sunspot. In each following section, we begin by analysing the distribution of the magnitude of a given force itself and then analyse the acceleration induced by the same force (by dividing the force by density).

5.1.1 Lorentz Force

Figures 5.1 and 5.2 show the distribution of the magnitude of the Lorentz force in a slice through the centre of the sunspot. Both figures show very consistent behaviour in both the umbral and penumbral regions individually, which persist throughout the entire simulation. Within the penumbra, we observe that near the start of the simulation the strongest Lorentz forces form in alignment with the strongest currents found within the penumbra identified in section 3.4, these locations are collocated with the perpendicular currents (with respect to the magnetic field) also identified in section 3.4. Given the definition of the Lorentz force, equation 1.6, these findings are in agreement with expectation. Figure 5.1 shows that the strongest currents in the domain have formed by 45° of rotation where the order is slightly in excess of $10^{-2}\mathrm{N/m}^3$.

Throughout the rest of the simulation the strongest Lorentz forces maintain the same order of magnitude, possibly implying some sort of equilibrium has been

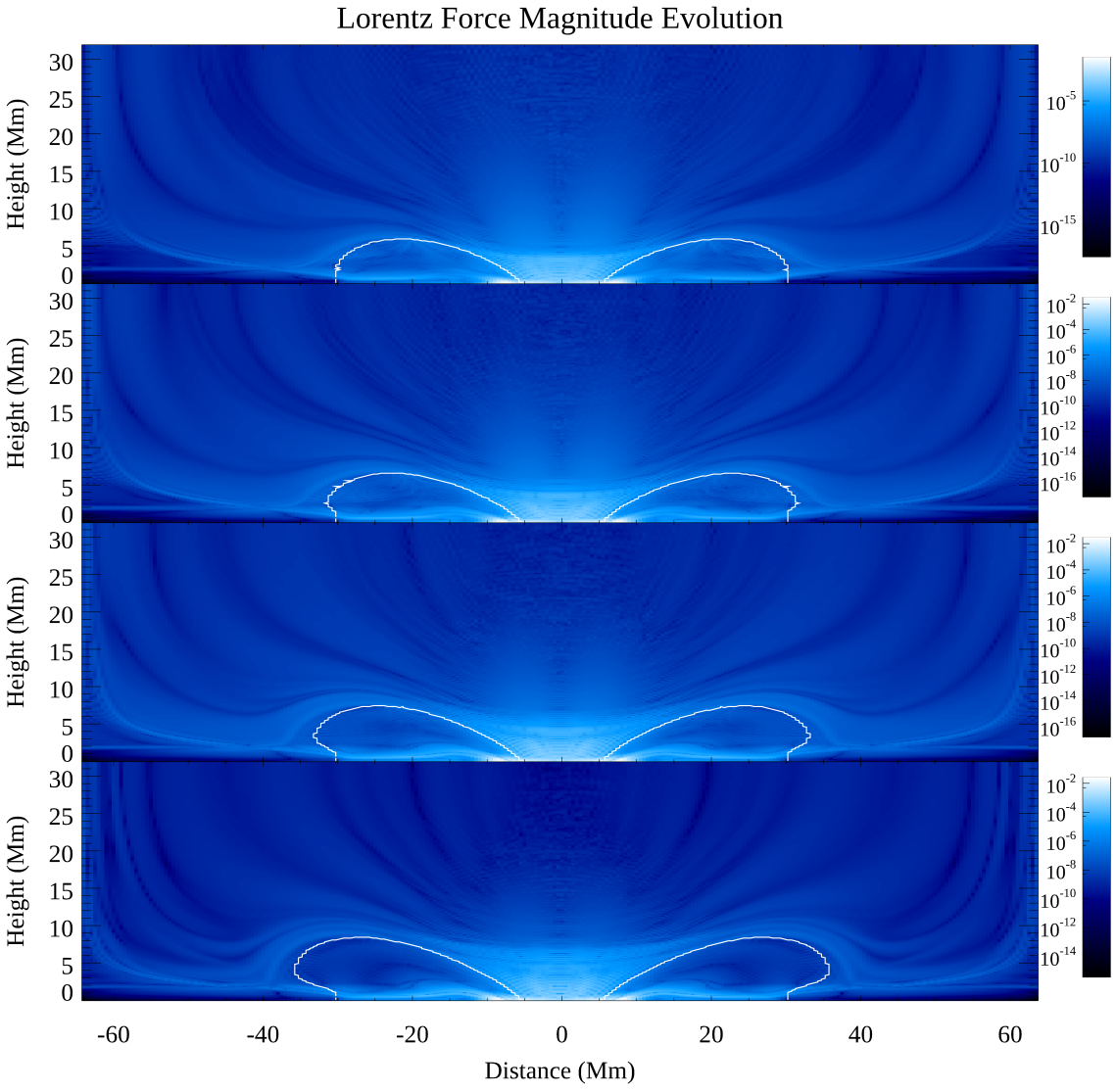

Figure 5.1: This figure shows the magnitude of the Lorentz force during the simulation in a slice through the centre of the sunspot. The sub-figures, moving from top to bottom, show this at times when the sunspot has been rotated by 30°, 45°, 60° and 75° by the driver respectively. The white contour represents the approximate location of the separatrix that divides the umbral and penumbral magnetic field regions, in a slice through the centre of the sunspot. The units of the colour bars are Nm^{-3}.

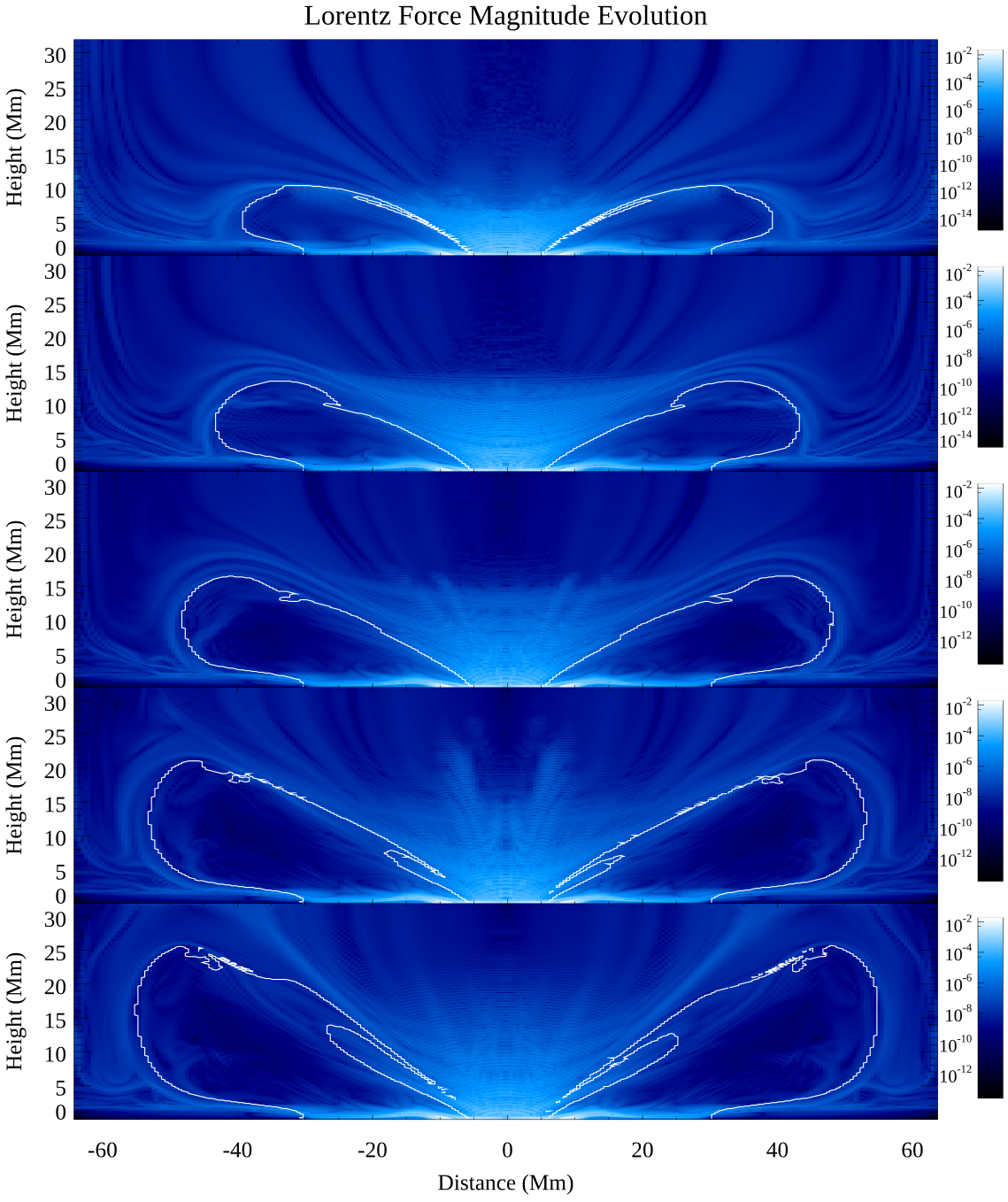

Figure 5.2: This figure shows the magnitude of the Lorentz force during the simulation in a slice through the centre of the sunspot. The sub-figures, moving from top to bottom, show this at times when the sunspot has been rotated by 90°, 105°, 120°, 135° and 140° by the driver respectively. The white contour represents the approximate location of the separatrix that divides the umbral and penumbral magnetic field regions, in a slice through the centre of the sunspot. The units of the colour bars are Nm^{-3}.

achieved between rotation and penumbral expansion. However, to attempt to understand if this is true would deviate our investigation, and thus is set aside for future investigation. In the remainder of the penumbral volume (i.e. most of the penumbra) we see that the Lorentz force is much smaller relative to the strong forces discussed above. This also directly supports the findings of section 3.4, where we observe that throughout most of the penumbra the current density is found to be enhanced and is primarily parallel to the magnetic field. Given the Lorentz force vanishes if $\mathbf{j} \parallel \mathbf{B}$, there is likely still some small perpendicular component of current density present within this region, given a finite Lorentz force is measured. The strong Lorentz force at the base of the penumbra and the large region of relatively small force throughout the rest of the penumbra, are both features which persist throughout the simulation.

In the umbral magnetic field region, we observe similar persistent behaviour of the Lorentz force during the simulation. We observe a region of strong Lorentz force at the base of the umbral field where the magnetic field emerges from the photosphere. This region also seems to reach its final magnitude by approximately 45° and generally remains at the same strength throughout the simulation. This region grows in height as the penumbral region expands. This finding is in agreement with those presented in section 3.4 where we observe the current density in this region to evolve in the same way. This implies that as the penumbra expands, the magnetic field lines in this region either become more twisted, or the magnetic field strength increases. Figure 3.4 shows that we measure an increase of magnetic field strength that may explain this, whereas figures 4.7 and 4.17 indicate that some twist has developed, but not clearly in the same manner as the current density and Lorentz forces in this region. This implies that it may be a combination of effects, but most likely because the magnetic field strength has increased here. We observe that this feature dissipates partially in height, near the end of the simulation. At this

stage of the simulation, the penumbra has displaced much of the overlying umbral field during its rise, thus this observation may be a manifestation of a relationship between the rising penumbra, the displacement of umbral magnetic field and the strengths of the current density and magnetic field in the low-atmosphere umbral magnetic field.

Further investigation of the dissipation of this feature should include taller numerical domains, as clearly there is some importance of the distance of the penumbra from the top of the domain which in nature would not occur. However, the presence of the development of currents, strengthening of the magnetic fields and resultant Lorentz force in this region seems consistent prior to the end of the simulation, and therefore seems physical. The second persistent key feature of the Lorentz force in the umbral field region, is the presence of thin layers of enhanced force near the separatrix, these are again well correlated with the presence of perpendicular currents (with respect to the magnetic field) shown in section 3.4. These features wax and wane slightly in their magnitude, but remain to some degree present throughout the simulation.

The Magnitude of Lorentz Force Induced Acceleration

Figures 5.3 and 5.4 show the distribution of the acceleration per unit volume caused by the Lorentz force in the domain, throughout the simulation. These figures are in stark contrast to the actual Lorentz force distributions shown in figures 5.1 and 5.2. The primary difference we observe is that, previously the strongest currents and magnetic fields (found near the photosphere) were both collocated with the strongest Lorentz forces, we see that there is no such correlation with acceleration. Figures 5.3 and 5.4 show that there exists a far more complex relationship between current density, the magnetic field and mass density than exists between current and magnetic field alone. Figures 5.3 and 5.4 show that the previous dominance of

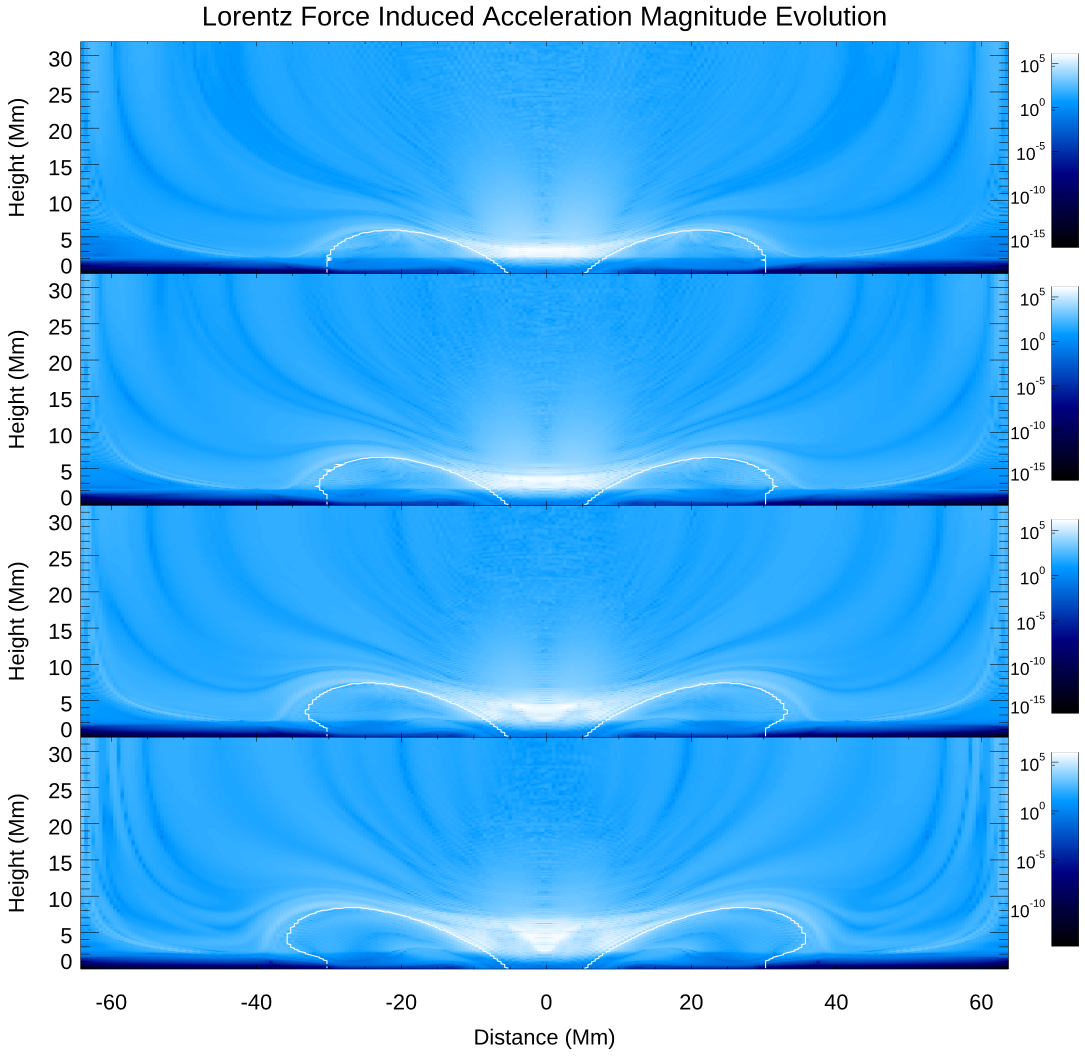

Figure 5.3: This figure shows the magnitude of the acceleration induced by the Lorentz force during the simulation in a slice through the centre of the sunspot. The sub-figures, moving from top to bottom, show this at times when the sunspot has been rotated by 30°, 45°, 60° and 75° by the driver respectively. The white contour represents the approximate location of the separatrix that divides the umbral and penumbral magnetic field regions, in a slice through the centre of the sunspot. The units of the colour bars is $m^{-2}s^{-2}$.

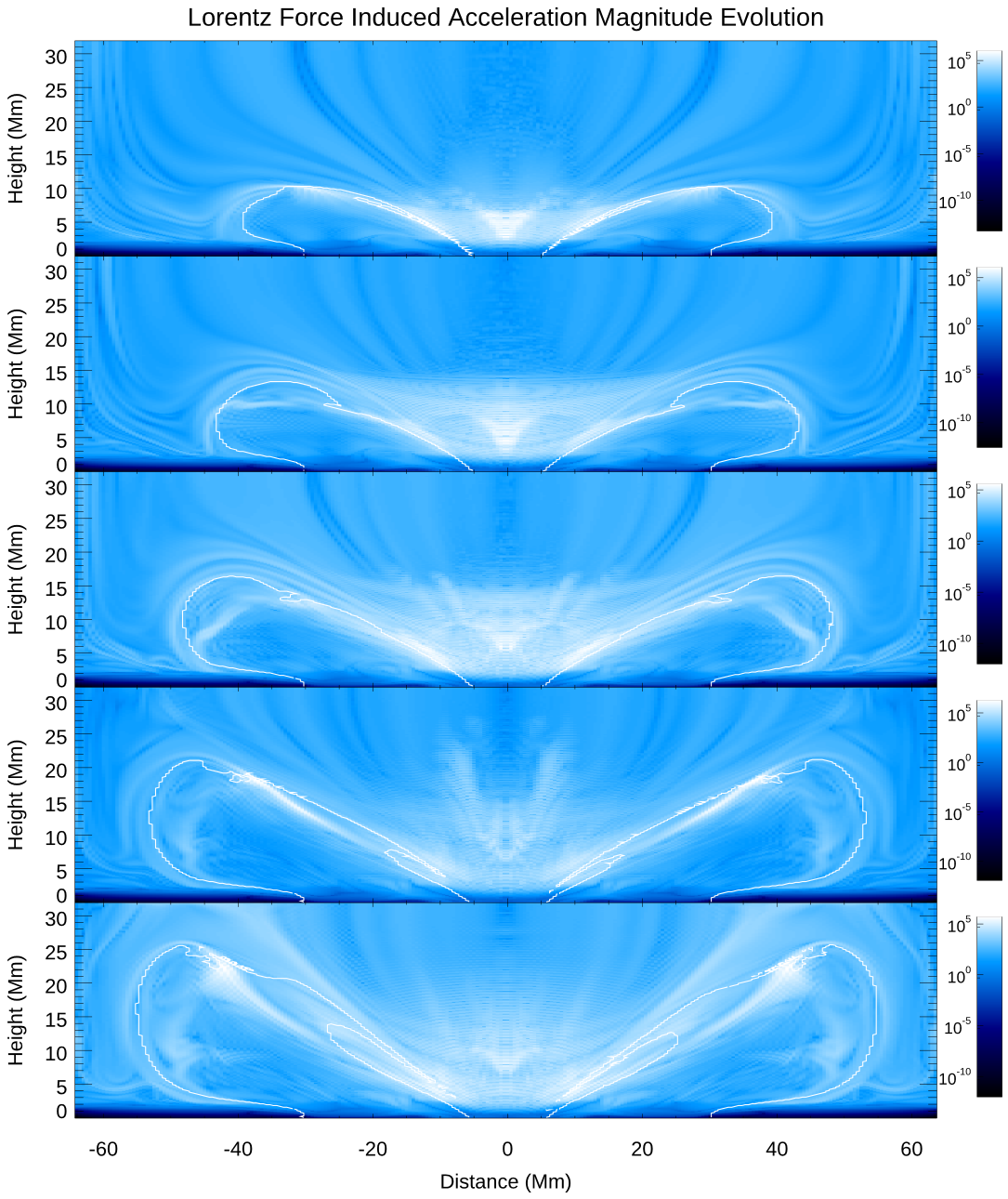

Figure 5.4: This figure shows the magnitude of the acceleration induced by the Lorentz force during the simulation in a slice through the centre of the sunspot. The sub-figures, moving from top to bottom, show this at times when the sunspot has been rotated by 90°, 105°, 120°, 135° and 140° by the driver respectively. The white contour represents the approximate location of the separatrix that divides the umbral and penumbral magnetic field regions, in a slice through the centre of the sunspot. The units of the colour bars is $\mathrm{m}^{-2}\mathrm{s}^{-2}$.

the strong currents and magnetic fields found in the low atmosphere, has vanished. This is the first indication throughout this investigation that the general dominance of the magnetic field strength at the bottom of the domain does not dominate the evolution of the sunspot, penumbra or umbra. Evidently, we may conclude that the mere presence of strong magnetic forces does not guarantee a large imposition on a given systems overall evolution.

Figures 5.3 and 5.4 show the impact of the Lorentz force, specifically they show that it is indeed impactful, as it is able to induce significant accelerations in the plasma (just not where one may expect given the findings of chapter 3). Figure 5.3 shows that the strongest accelerations induced by the Lorentz force are found in the low coronal umbral magnetic field, near the axis of rotation. Generally, the strongest accelerations are focused around the axis of rotation but extend radially to the separatrix. Unlike the Lorentz force itself, the maximum magnitude of the acceleration is presented in the first figure at only 30° of rotation in the central umbral field. Further investigation is required, but at this time the rotation rate of the sunspot has also reached its maximum and therefore the accelerations that are measured in this region may simply be caused by the Lorentz forces developed to maintain a steady rotation.

An interesting feature of this strong acceleration region is that it has finite thickness (in height) which clearly grows in the same way as did the general Lorentz force (figures 5.1 and 5.2) and current density (figures 3.5 and 3.6). The specific formation and consequences of this region need further investigation, which are beyond the scope of this work. However, within this region, we observe that the mass density structures that extend from the photosphere into the low-mid corona (identified in section 3.6) now play a functional role. The dense regions, via the increased mass within them, directly limit the net acceleration felt by the plasma as a consequence of the Lorentz force. The Lorentz force in the same region, does not show any

indication of feedback from the density.

A second key Lorentz force induced acceleration feature, present in the umbral magnetic field region, is the thin layers which are found near the separatrix (on the umbral side) throughout the duration of the simulation. These layers are found where we have previously identified currents (shown in figures 3.5) and 3.6) and are most likely manifestations of these currents on the Lorentz force. Generally, the two regions of Lorentz force induced acceleration discussed above are the primary ones present during the simulation. As the simulation proceeds, these features increase in complexity but generally maintain the same order of magnitude and location with respect to the expanding penumbra. The general lack of features in the upper corona is a direct consequence of the relatively weak and uniform magnetic field and small currents there.

Figures 5.3 and 5.4 show that unlike the umbral field, the penumbra evolves in a far more complex manner. The figures show that the penumbra's Lorentz force acceleration characteristics are in much higher contrast to the previous analyses of the magnetic field, current density and Lorentz force in the same region. Figures 3.3, 3.5 and 3.7 (and corresponding latter stage snapshot figures) show that in the penumbra we measure strong magnetic fields and currents (some of which are perpendicular to one another) in the low chromosphere and photosphere. Therefore one may expect that any significant accelerations caused by the Lorentz force should be primarily found in the low atmosphere, below the transition region, and the majority of the (coronal) penumbral volume should evolve in a force-free manner as implied by the dominance of parallel currents found in section 3.4. However, figures 3.5 and 3.6 show that there is generally an enhancement of current density in the penumbra relative to the surrounding umbral region, and although figures 3.7 and 3.8 imply that most of these currents are parallel (and hence induce no Lorentz force or acceleration on the plasma), figures 5.1 and 5.2 do show that there

is some small Lorentz force present. This indicates that no matter how dominant the parallel current is over the perpendicular current, the very presence of non-zero Lorentz force demands that there must be some perpendicular current.

The penumbral region shows two primary Lorentz force induced acceleration phases occur during this simulation. In the early stage, primarily shown by figure 5.1, we observe that there is relatively little acceleration induced within the penumbra, the most significant regions seem to be at the highest point within the penumbra, but are still vastly overshadowed by the umbral field region acceleration magnitudes. This pattern of behaviour persists (in these figures at least) until 90°, where we begin to see the development of relatively large acceleration within the penumbral volume, again still near where the separatrix is highest in the atmosphere. Figure 5.4 shows that, generally, the regions of most significant acceleration grow slightly as the penumbra expands, but always remain close to the separatrix and the maximum values maintain the same order of magnitude ($\mathcal{O}(10^5 \mathrm{m/s}^2)$) throughout the remainder of the simulation.

To explain the development of the relatively large Lorentz force induced accelerations in the penumbra at 90° and beyond, we look at the size and co-alignment of the Lorentz force and density during the second phase of the Lorentz force acceleration, as identified in the previous paragraph. Figure 5.2 shows that at 90° the Lorentz force, on the penumbral side of the highest point of the separatrix, is slightly enhanced with respect to the surrounding penumbra, but is generally of similar order as the forces present at previous times. This means that the Lorentz force is enhanced but alone does not explain why large accelerations have formed in the region at specifically this time in the simulation, as there were equivalently strong forces present previously in the same region. However, figure 3.12 shows at the same location, there is a local minimum of density which was not present previously. The density is observed to reduce by several orders of magnitude near the highest point

of the separatrix, where we see the strongest penumbral accelerations in figure 5.4. The observed evolution of the Lorentz force and density thus implies that Lorentz forces develop relatively quickly during the simulation but are generally enhanced and redistributed as the sunspot rotates. The Lorentz force alone is insufficient to induce significant acceleration, until a time when the density diminishes to such an extent that the Lorentz force becomes sufficient. With this collective information we may stipulate that the dominant penumbral accelerations are, by definition, a combination of density and the Lorentz force, but seem to be far more temporally correlated with specific densities rather than some specific strength Lorentz force.

From the first identification of significant penumbral Lorentz force induced acceleration at 90°, we see that the mechanism identified in the above discussion that links these accelerations to density reductions, continues to produce additional accelerations throughout the remainder of the simulation. Figure 5.4 shows that at 105° the Lorentz force induced accelerations have protruded deeper into the penumbra and have thus began to develop away from the highest point of the separatrix. Beyond 105°, regions of large acceleration continue to be present near the separatrix, and towards the end of the simulation ($\theta \geq 120°$) significant accelerations are found at the side boundaries of the separatrix as well as the top. Figure 3.12 shows (again) that all of these relatively large accelerations are spatially and temporally co-aligned with regions of local density reduction. Generally we observe that as the penumbra expands, the regions of low density increase in complexity and grow. The growth of the low density regions in correlation with the penumbral expansion makes sense, as the penumbra evolves ideally and thus as the penumbra expands the average density within it must decrease as the penumbral volume increases (see figure 4.1).

The observed behaviour of the Lorentz force induced accelerations raise a number of questions, but perhaps the most important one in the context of this thesis and more generally for sunspots, asks to what extent does the observed behaviour of

Lorentz force induced acceleration present itself for different sunspots? Because we have seen that the Lorentz forces are unable to induce significant motion until regions of a sufficiently low density are developed, we may wonder how a weaker or stronger magnetic field strength may change this. Given we have initialised with a standard quiet sun model atmosphere, any other sunspot of equal size would have the same initial density profile of the sunspot studied in this chapter. But if, say, the magnetic field strength was altered, the Lorentz forces ought to scale. If the magnetic field were slightly stronger, we may expect that the required density to induce motion may increase, i.e. the density reduction would not have to be relied on as much to induce the same motion. However, if we drastically increase the magnetic field strength we may further reduce the dependence on density to such a point that the magnitude of the Lorentz force becomes the dominant component in place of low-density. We make this hypothesis here, because in chapter 6 we will analyse the magnetic energy properties of geometrically identical sunspots with various magnetic field strengths where such scaling of Lorentz force induced accelerations may have influenced the evolution of the sunspots there. We conclude this discussion by foreshadowing the importance of accelerations induced by the Lorentz force. We shall see in section 5.2 that where the motion of the plasma is aligned with the Lorentz force, we must have a reduction to the local magnetic energy (and magnetic pressure). Therefore in this section, where we have highlighted significant accelerations induced by the Lorentz forces we must have identified regions where the magnetic field is attempting to either relax or is limiting further generation of magnetic energy into those regions.

5.1.2 Thermal Pressure Gradient

$$\mathbf{F_P} = \nabla P.$$

Pressure Gradient

We now investigate the magnitude and distribution of thermal pressure gradients. Figures 5.5 and 5.6 shows that during the simulation a relatively complex system of pressure gradients develop. We see that at 0° the pressure gradient is essentially structure-less and constant throughout the domain. We observe some artefacts of the finite difference method used to calculate the data in these figures, namely the bright line at the top of the transition region (most visible in the 0° figure). This is a consequence of the method used to calculate the gradient of pressure having a lower resolution than used by the Lare3D code itself to evolve the system. However, generally the order of the magnitudes discussed are in good agreement with the true values for latter times of the simulation, i.e. the sensitivity is dominant at the start of the simulation where the thermal pressure gradient is non-zero to balance gravity, prior to the development of Lorentz forces which may then contribute. We generally observe that as the simulation proceeds the artefact fades to a background value as far more larger dominant (physical) pressure gradients develop.

Figures 5.5 and 5.6 show that at all stages throughout the simulation the most significant pressure gradients are found below the transition region. This is most likely a direct consequence of the initialisation of density in the domain to be such that for a given temperature profile density is defined such that the resulting pressure gradient balances the force of gravity. This means that where there are large densities (such as below the transition region) there is always a relatively large gravitational force which must be balanced by either pressure gradients or Lorentz forces. Given we observe negligible Lorentz forces develop in the chromosphere and photosphere, outside the central region where the sunspot is defined, it must be that the pressure gradient must persist to act against gravity. This explains the persistent strong pressure gradient below the transition region. Once the sunspot begins to rotate the Lorentz forces which form low in the domain may contribute to the

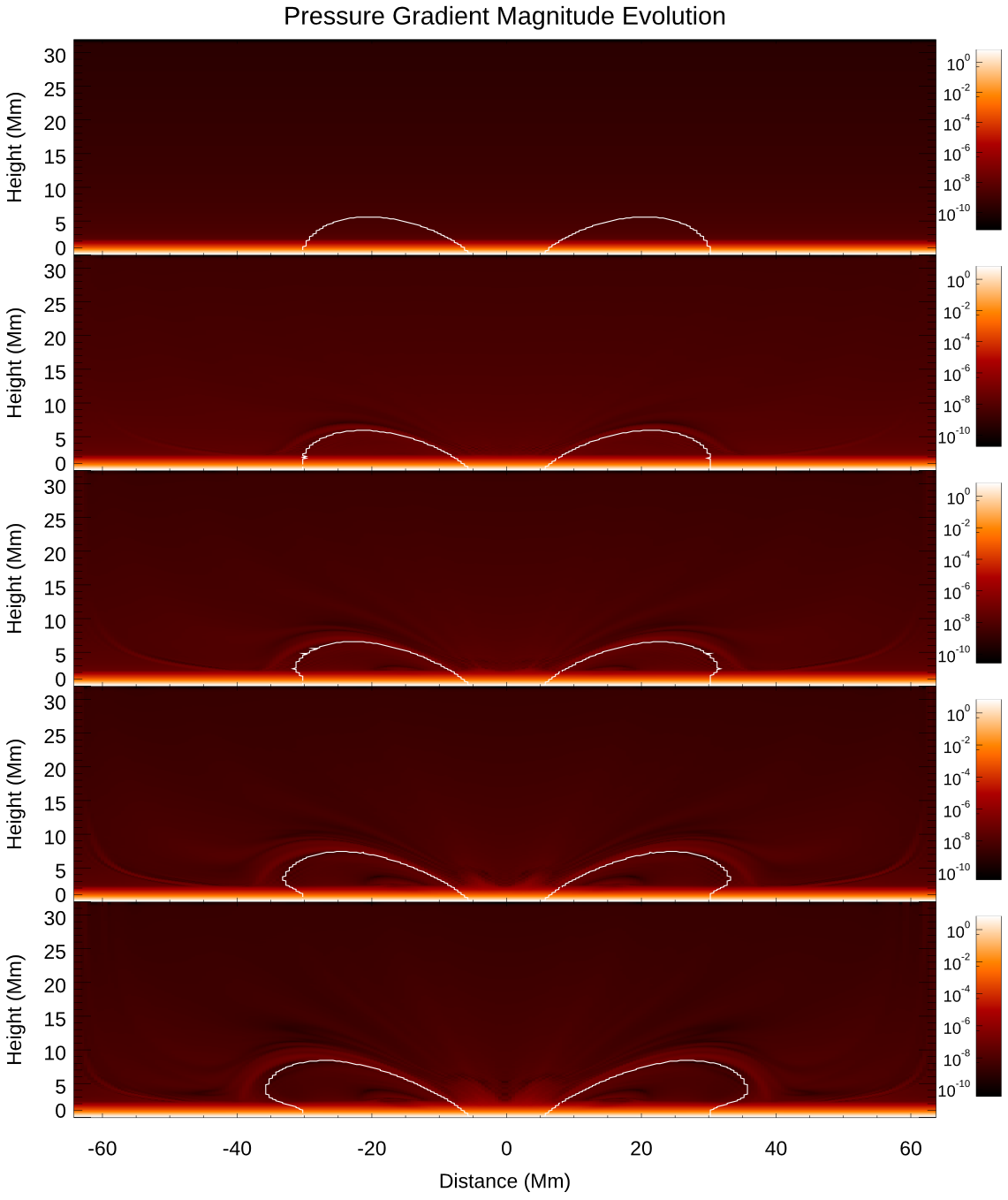

Figure 5.5: This figure shows the magnitude of the gradient of thermal pressure during the simulation in a slice through the centre of the sunspot. The sub-figures, moving from top to bottom, show this at times when the sunspot has been rotated by 30°, 45°, 60° and 75° by the driver respectively. The white contour represents the approximate location of the separatrix that divides the umbral and penumbral magnetic field regions, in a slice through the centre of the sunspot. The units of the colour bars are Nm^{-3}.

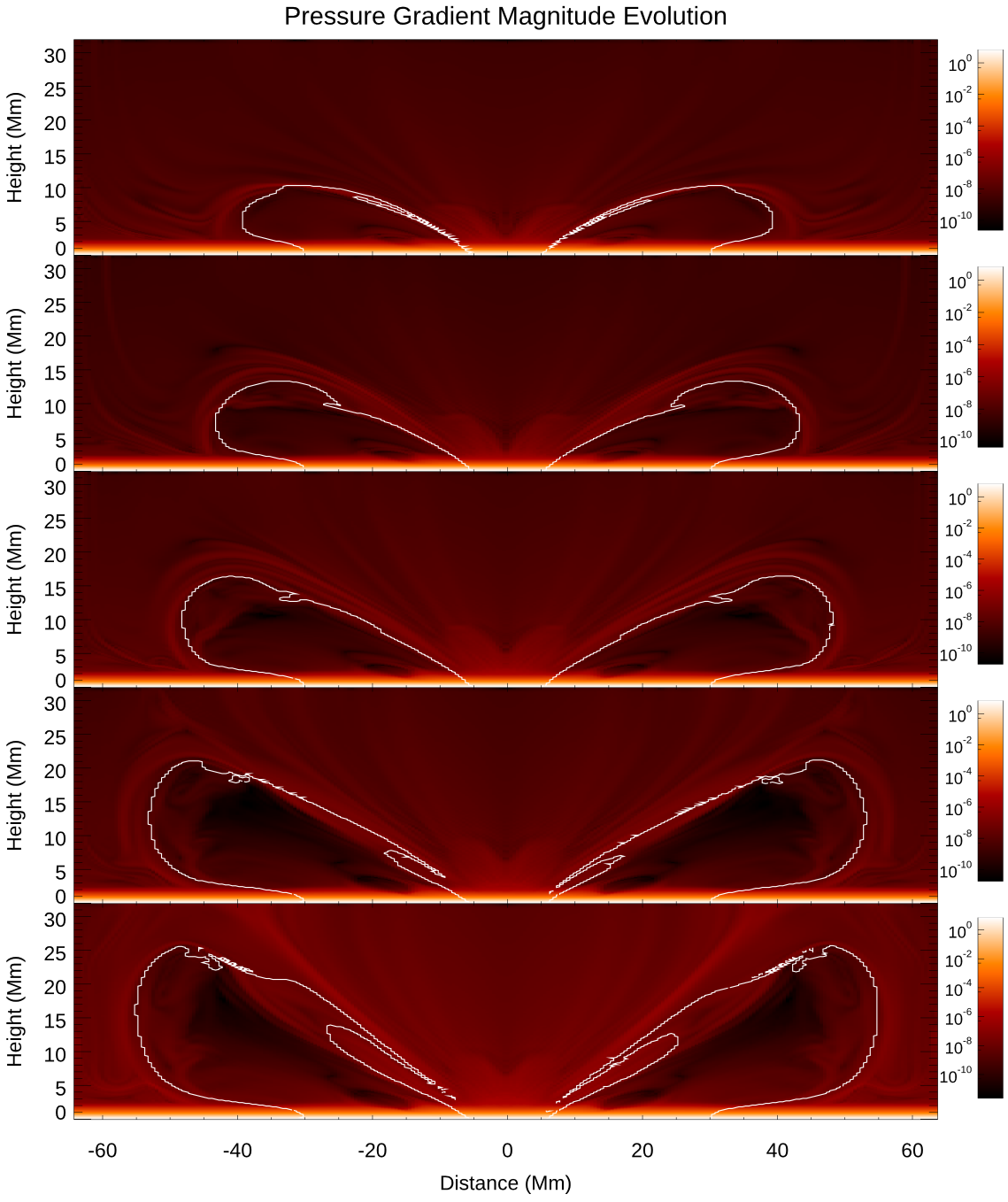

Figure 5.6: This figure shows the magnitude of the gradient of thermal pressure during the simulation in a slice through the centre of the sunspot. The sub-figures, moving from top to bottom, show this at times when the sunspot has been rotated by 90°, 105°, 120°, 135° and 140° by the driver respectively. The white contour represents the approximate location of the separatrix that divides the umbral and penumbral magnetic field regions, in a slice through the centre of the sunspot. The units of the colour bars are Nm^{-3}.

balance of gravity in addition to pressure gradients, but given the consistency of the dominant sub-transition region pressure gradient it seems likely that the pressure gradient is primarily balancing gravity.

Figures 5.5 and 5.6 show that the pressure gradient evolves similarly to the Lorentz force, specifically that between 0° and 75° there is relatively little development of features in the penumbra at this time. However, we do see the formation of pressure gradient on the umbral side of the separatrix where we observe the gentle formation of a band of enhanced pressure gradient which seems to envelope the penumbra. The size and strength of this region seem to correlate well with the growth of the penumbra and may be a consequence of the feedback imposed on the umbra as the penumbra expands. We also see that pressure gradients develop in the double-bump feature which is found above where the umbral field emerges from the photosphere. We saw in chapter 3 that these features are both cold and dense, and velocity field analysis suggests that the material within them originates from the chromosphere where the initial development of magnetic pressure at the base of the umbral field has forced the up-flow of material. Because we measure this structure to be cold and dense and it is found within the hot corona, pressure gradients to maintain this structure are expected given we observe it to be long-lived. Finally in the penumbra we see the development of bands of low pressure gradient, we first observe this at 60° centred at radii of $\pm$15Mm, at a height of approximately $2-3$Mm. This feature seems to grow in size during the remainder of the simulation.

Figure 5.6 shows that beyond 90° the pressure gradient enters a more complex evolutionary phase. Within the penumbra we observe that the regions of weakest pressure gradient grow and their extremes become increasingly weaker. Just as was observed for the Lorentz force, the pressure gradients within the penumbra are generally distributed quasi-uniformly until 90° where we see the strongest coronal

pressure gradients form near the separatrix. As the sunspot continues to rotate additional pressure gradients form deeper within the penumbra, but generally the overall location of these regions is still close to the separatrix. We see that the structures of weak pressure gradients that form (as identified at the end of the previous paragraph) continue to develop and by 105° is found between $\pm 15 - 20$Mm at a height range of $2 - 4$Mm. This feature continues to grow slightly throughout the rest of the simulation, but it has now become a single void of pressure gradient rather than the initial striation pattern. Figures 3.12 and 3.14 show the comparative density and temperature samples respectively. We observe that this feature is present and collocated in all three diagnostics. We see now that this feature is both tenuous and relatively cold as compared to the surrounding material. The temperature of this feature suggests that its origins are the sub-transition region, but its density does not. In fact its density is of the lowest found within the domain. This implies that this region does not form as a consequence of a movement of material alone (as was found for the central double-bump in the umbral field) but rather it forms because of the evolution of the system as a whole and not simply as a consequence of relatively few of the parameters.

Finally we see that the pressure gradients in general, after 90° of rotation show most variation in the penumbra and that this variation is extremely well correlated with the features identified in chapter 3 for the density and temperature, which given the definition of pressure (equation 1.16) is expected. The primary point of interest here is that in the penumbra the size of the pressure gradient is comparable to that of the Lorentz force, implying that there is a coupling between the two.

Pressure Gradient Induced Acceleration

Figures 5.7 and 5.8 show the distribution of acceleration induced by the pressure gradient throughout the simulation. These figures essentially show the consequence

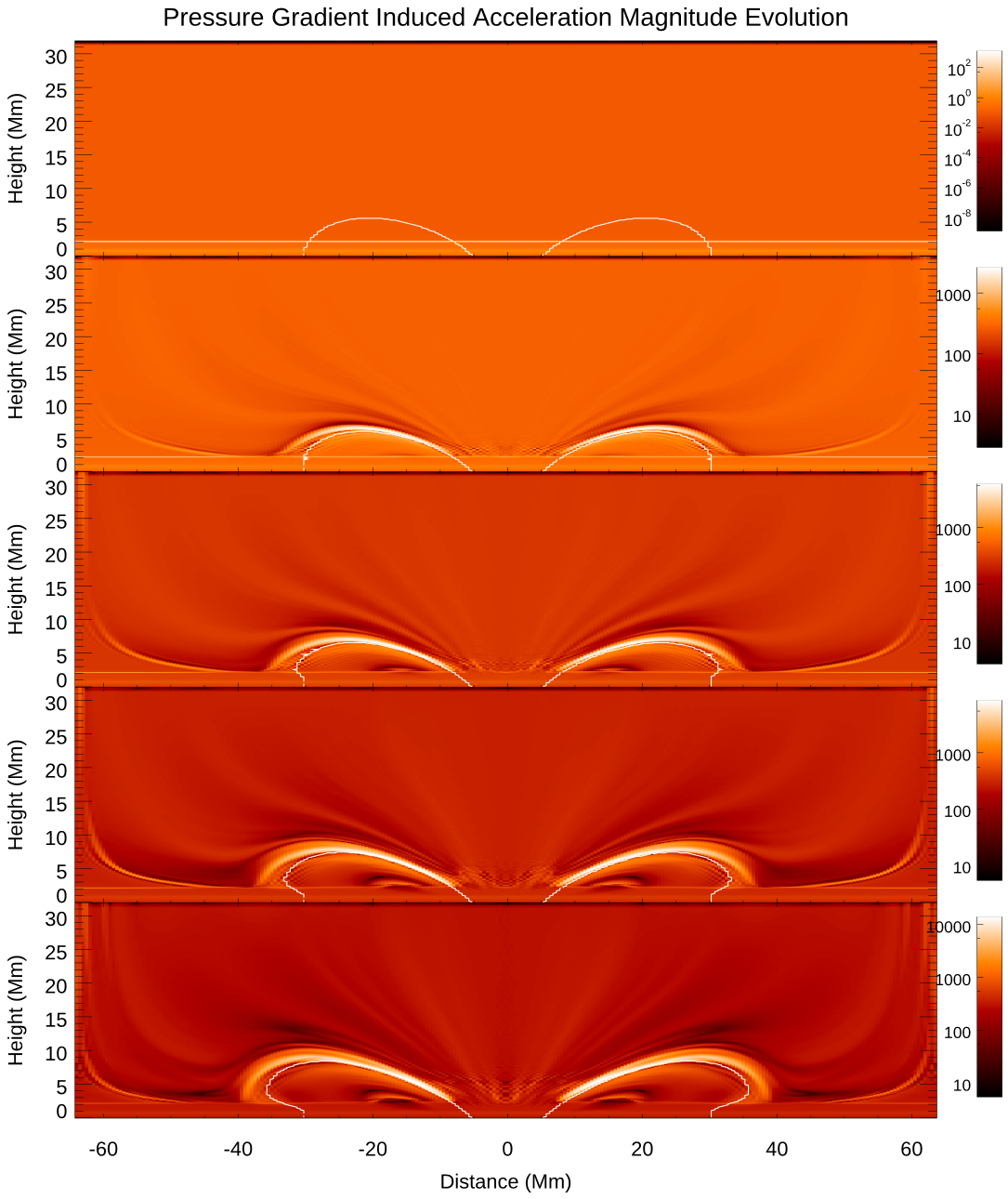

Figure 5.7: This figure shows the magnitude of the acceleration induced by the gradient of thermal pressure during the simulation in a slice through the centre of the sunspot. The sub-figures, moving from top to bottom, show this at times when the sunspot has been rotated by 30°, 45°, 60° and 75° by the driver respectively. The white contour represents the approximate location of the separatrix that divides the umbral and penumbral magnetic field regions, in a slice through the centre of the sunspot. The units of the colour bars is $\mathrm{m}^{-2}\mathrm{s}^{-2}$.

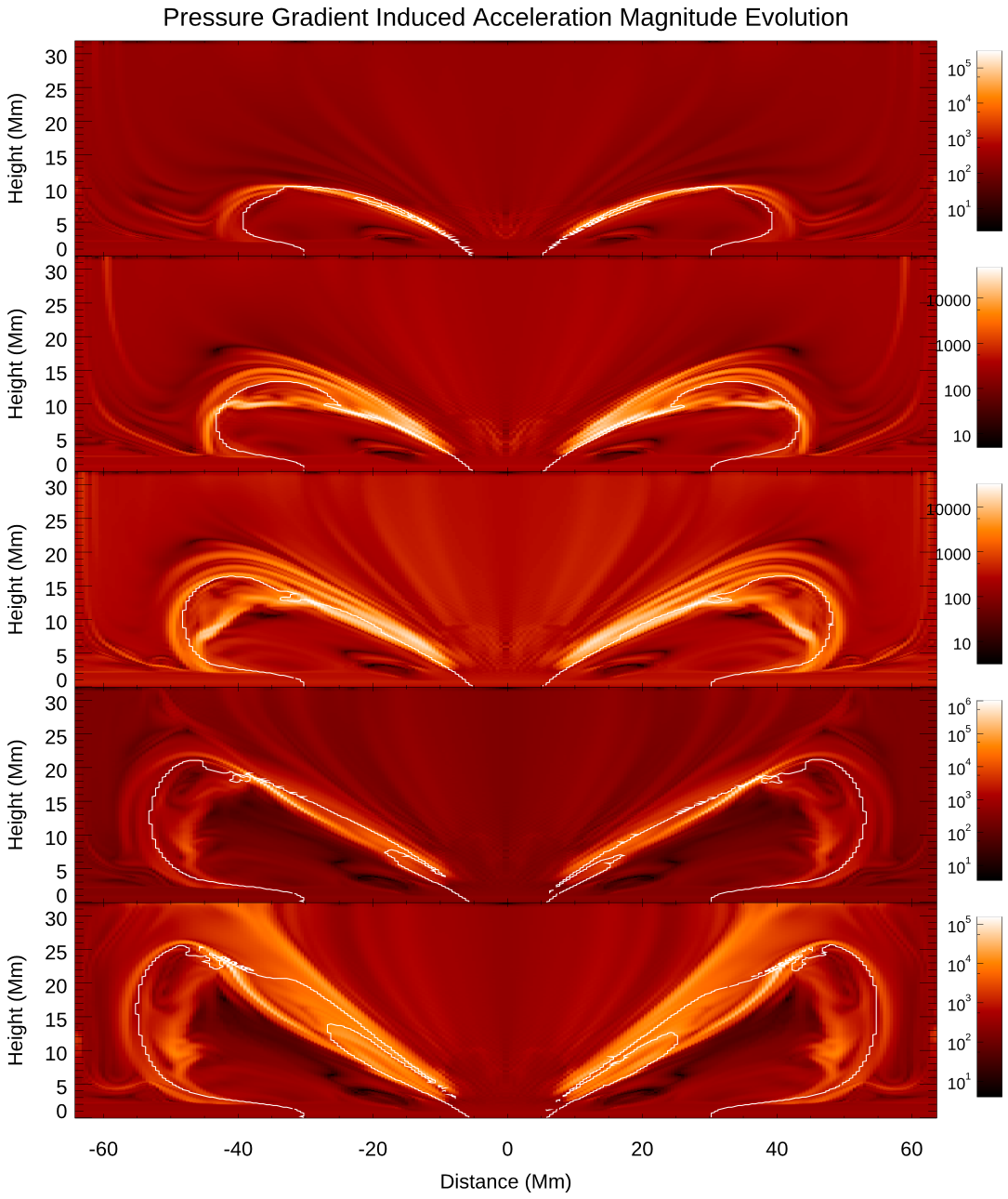

Figure 5.8: This figure shows the magnitude of the acceleration induced by the gradient of thermal pressure during the simulation in a slice through the centre of the sunspot. The sub-figures, moving from top to bottom, show this at times when the sunspot has been rotated by 90°, 105°, 120°, 135° and 140° by the driver respectively. The white contour represents the approximate location of the separatrix that divides the umbral and penumbral magnetic field regions, in a slice through the centre of the sunspot. The units of the colour bars is $m^{-2}s^{-2}$.

of the pressure gradient on the evolution of the plasma within the domain and thus show the distribution of the $\frac{\nabla P}{\rho}$ term in equation 1.12. Figure 5.7 shows that at 0° the pressure gradient induced acceleration throughout the domain is rather constant. This is because the domain is initialised with zero Lorentz force and thus the thermal pressure acceleration must balance gravity, therefore we have a pressure gradient here that balances gravity in the z-direction entirely. At subsequent stages when the Lorentz force has developed, there will be a combination of Lorentz force and pressure gradient balancing gravity. By comparing figures 5.3 and 5.7, we see that the accelerations caused by the Lorentz force are clearly in vast majority to those caused by pressure gradients in the early stage of the simulation. In this stage, the maximum pressure gradient is an order smaller than the Lorentz force. Second to this we also observe in figures 5.7 and 5.8 that the maximum pressure gradient acceleration grows far more slowly than the Lorentz force's, but reaches comparable values toward the end of the simulation. This indicates that during the early stage of the simulation the Lorentz force dominates and the momentum equation essentially reduces to,

$$\frac{D\mathbf{v}}{Dt} = \frac{1}{\rho}\mathbf{j} \times \mathbf{B},$$

but for latter stages the pressure gradient becomes important.

Figure 5.7 shows that between $0 - 75°$ there is only one region of significant pressure gradient induced acceleration and that is at the separatrix on the umbral side. This appears as a thin region of strong acceleration, first visible at 30° where it forms between the separatrix and thin region of very small acceleration (i.e. it is the white band beneath the black one). There is some interesting development within the penumbra, but rather the formation of layers of steady flow (i.e slow acceleration) which envelope sheets of far greater acceleration. These are visible first at 60° between $\pm 10 - 20$Mm at heights between $2 - 4$Mm and then grow with increasing

rotation. These region are associated with the cold tenuous plasma regions identified and analysed in the discussion of the pressure gradient itself. However, our primary interest is with where the accelerations induced by the pressure gradient is largest and therefore meaningfully contributes to the momentum equation and thus maintains that system evolve. However, given that the primary observation we can make of the cold tenuous material structures within the penumbra are that they do not meaningfully contribute to the momentum equation, we can take some freedom in not focusing further attention on them. Thus, we may conclude that until 75° we observe that the only main region of the domain that meaningfully contributes to the momentum equation is in the umbra above the expanding penumbra and this region grows steadily is size and maximum magnitude. Hence at least until 75°, accelerations caused by the Lorentz force dominate.

Figure 5.8 shows a far more complex phase of the simulation with respect to accelerations caused by thermal pressure gradients. We first note that the maximum scale of each figure shows that the size of the accelerations vary significantly and seemingly gain or lose as much as an order of magnitude between the successive plots. We must recall that what we are plotting in these ladder figures is a two-dimensional slice of a three-dimensional rotating structure, with a highly complex evolution, and thus further analysis of the maximum acceleration present throughout the entire domain is required before we can say something more about this. However, a consistent result is that beyond 90° the amount of material that shows large acceleration continues to grow. In a similar manner as was found for the Lorentz force induced acceleration, the pressure gradient induced acceleration within the penumbra first develops at 90° at the upper section of the separatrix and then increasingly protrudes further into the main body of the penumbra. Once again the comparison is easily made with figure 3.12 where we see once again that the greatest penumbral accelerations are associated with tenuous plasma. Unlike

the Lorentz force acceleration, the pressure gradient accelerations do not have any meaningful structure within the middle of the domain and all significant pressure induced acceleration is concentrated at all times near the separatrix. This result implies that the primary cause of the thermal pressure gradients is the expansion of the penumbra itself. This explanation is also supported by the gradual growth of the magnitude of the accelerations which is something we measure also for the penumbral volume (figure 4.1). In contrast the maximum acceleration caused by the Lorentz force was achieved in correlation with maximum rotation rate. But we do observe a similar growth around the separatrix which may imply that the Lorentz force accelerations are linked to two key mechanisms, rotation rate and penumbral expansion. We may develop this further by recognising that the pressure gradients and consequential acceleration seem to manifest in response to the penumbra expanding, however, given the closed magnetic nature of the region (and as we shall see its ability to store magnetic energy and hence pressure) it is likely magnetic pressure which causes the expansion. Hence, we may be observing one force causing the other, if this is true we may expect some degree of cancellation.

5.1.3 Gravity

In this work we employ a uniform gravity profile for most of the domain (see chapter 2) and thus an equivalent analysis for the gravitational force as was performed for the Lorentz and pressure gradient is not presented here. This is because such an analysis would essentially be a scaled discussion of the density evolution discussed in section 3.6. But with this in mind we may observe that the most relevant feature of the distribution of gravity forces is that as the penumbra expands it becomes less dense than the surrounding material and thus there are likely buoyancy forces present within the penumbra.

To understand the consequences of gravity is much simpler, the acceleration

induced by gravity always points downward with magnitude 274m/s^2 throughout the majority of the domain (i.e. not at the top of the box). By simply comparing the magnitude scales in figures 5.3, 5.4, 5.7 and 5.8 we see that accelerations due to gravity are smaller than those induced by the Lorentz force and thermal pressure gradient in the regions of interest we have discussed previously. However, we do observe that gravitational forces may be significant outside the sunspot (i.e. near the domain boundaries). In the remaining discussion the gravitational force will not be focused on but will be included in all calculations regarding total force and acceleration.

5.1.4 Total Acceleration

To conclude our discussion of the momentum equation, we now look at the total acceleration constructed by calculating the magnitude of the vector sum of the accelerations discussed in this section. This describes the left hand side of equation 1.12, i.e. it defines $\frac{D\mathbf{v}}{Dt}$. Figures 5.9 and 5.10 show the total acceleration caused by the superposition of the Lorentz, pressure gradient and gravitational forces. We have already discussed each component in some detail and it is not the purpose of this section to repeat those discussions here. Instead what we are primarily interested in here is identifying the global evolutionary properties of the sunspot and secondly to identify where the accelerations identified in the previous sections cancel with one another when we consider the total.

Unsurprisingly, the characteristics of the Lorentz force dominate the early stage ($0^\circ - 75^\circ$) of the total acceleration's evolution. Figure 5.9 shows that the umbral region between the two penumbral regions shows the most significant acceleration. As rotation increases to 75° this region grows in thickness, seemingly in correlation with the expansion of the penumbra, as did the Lorentz force. Figure 5.10 shows that this umbral region of strong acceleration continues to grow in size as the penumbra

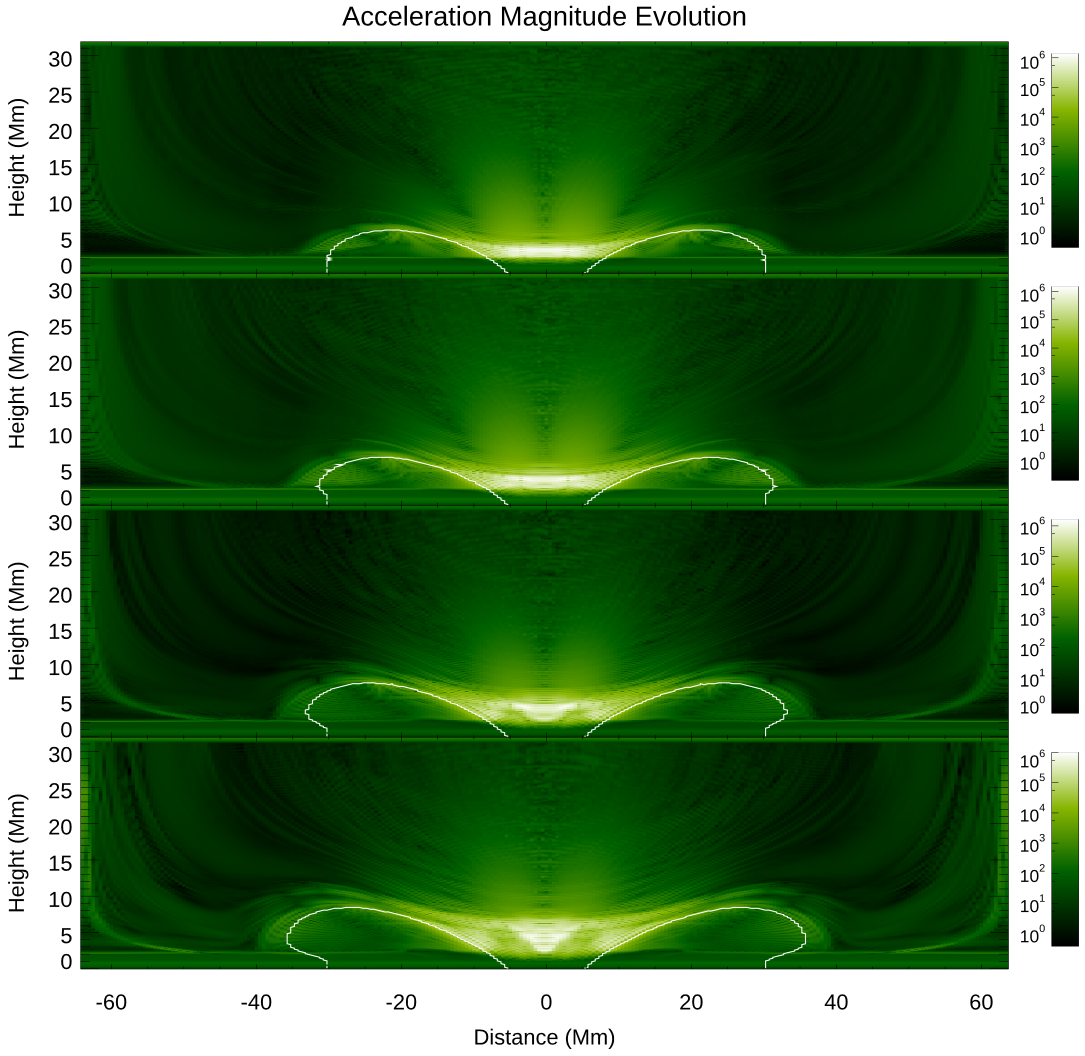

Figure 5.9: This figure shows the magnitude of the total acceleration induced by all forces during the simulation in a slice through the centre of the sunspot. The sub-figures, moving from top to bottom, show this at times when the sunspot has been rotated by 30°, 45°, 60° and 75° by the driver respectively. The white contour represents the approximate location of the separatrix that divides the umbral and penumbral magnetic field regions, in a slice through the centre of the sunspot. The units of the colour bars is $m^{-2}s^{-2}$.

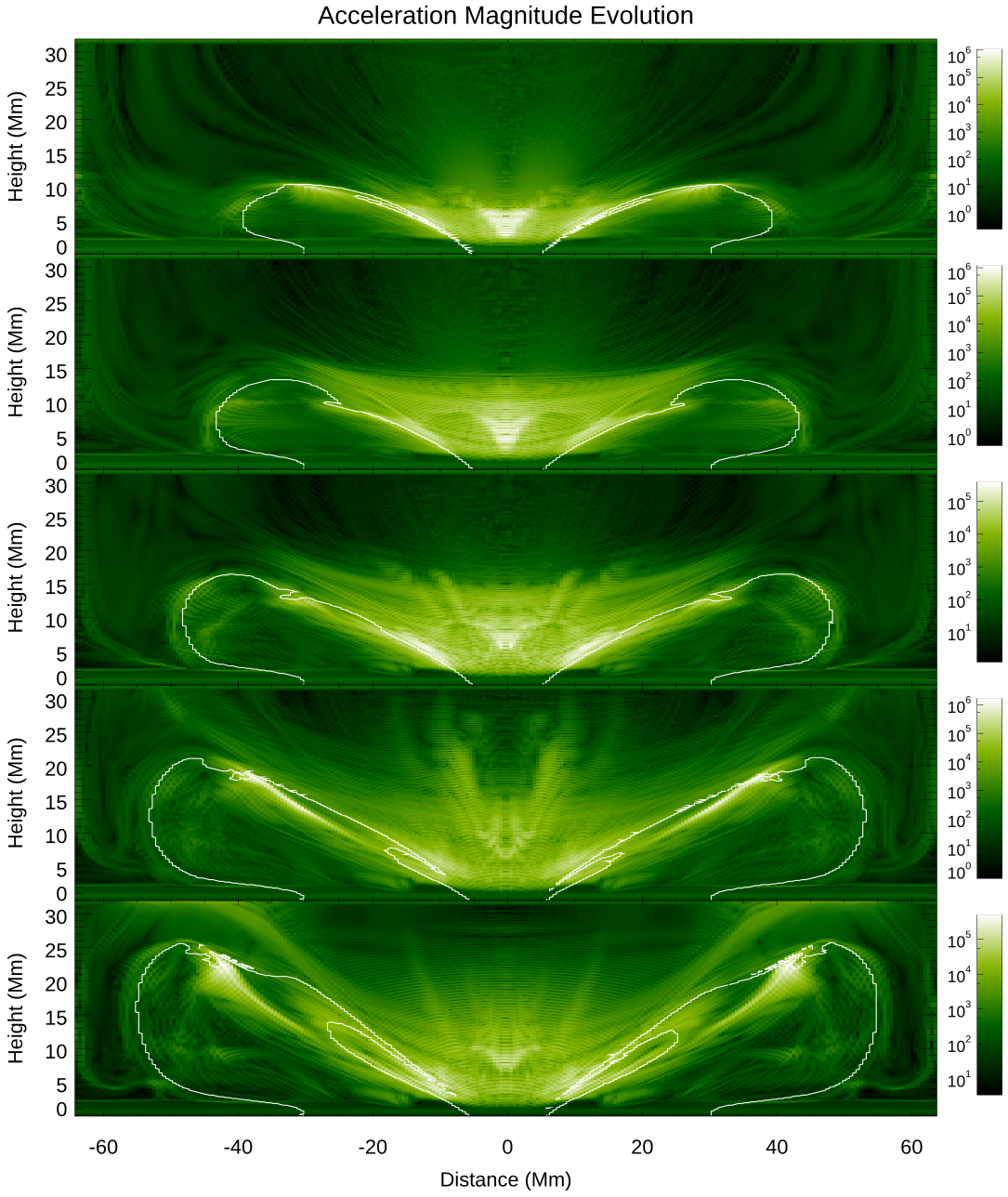

Figure 5.10: This figure shows the magnitude of the total acceleration induced by all forces during the simulation in a slice through the centre of the sunspot. The sub-figures, moving from top to bottom, show this at times when the sunspot has been rotated by 90°, 105°, 120°, 135° and 140° by the driver respectively. The white contour represents the approximate location of the separatrix that divides the umbral and penumbral magnetic field regions, in a slice through the centre of the sunspot. The units of the colour bars is $m^{-2}s^{-2}$.

expands, again as was found for the Lorentz force acceleration. The penumbral acceleration clearly follows both the findings of the previous sections, in that between $0° - 75°$ the acceleration in the penumbra is second to that in the umbra. Between $90° - 140°$, as before, we see that accelerations begin to develop within the penumbra, again initially near the separatrix at 90° and generally increasingly so within the core of the penumbra as rotation continues. Figure 5.10 shows a significant difference to both figures 5.4 and 5.8, where previously both the Lorentz and pressure gradient induced accelerations showed significant magnitude in the penumbra near the side boundaries of the separatrix. The feature we speak of here can be found, for example, in figures 5.4 and 5.8 at $\theta = 140°$, between $\pm 45 - 55$Mm from the rotational axis of the sunspot between heights of $3 - 25$Mm. Generally the acceleration contribution from the Lorentz force in this region seems to largely cancel with the accelerations from the pressure gradient. This is clearly shown by the darkening of the equivalent region in figure 5.10. What remains in the penumbra is that the most significant accelerations are focused near the upper region of the separatrix. This indicates that either, the growth of the penumbra toward the top of the domain is most aggressive at this region of the separatrix or that the interface between the umbra and penumbra influences the evolution of the sunspot significantly. But in either case we see that near the sides of the penumbral region, there are significant accelerations caused by forces, but they appear to form in equal and opposite pairs which yield little motion.

5.2 Energetics

We now investigate the primary motivation of this work, to understand how sunspot rotation and magnetic energy injection are linked. In this section we shall begin by investigating the overall evolution of magnetic, kinetic and internal energy within the numerical domain of simulation 1. Then we shall identify how the energies

are divided into the umbral and penumbral magnetic field regions where possible. We shall then focusing more deeply on magnetic energy and use several forms of Poynting's theorem to analyse the movement and generation of magnetic energy. We shall conclude this section with a brief discussion of how energy is transferred from the driver to the domain.

5.2.1 Magnetic, Kinetic and Internal Energy

Magnetic Energy

As the sunspot modelled by simulation 1 is rotated, we observe that the total magnetic energy within the domain increases. Figure 5.11 shows the evolution of the absolute change of the dominant energies (i.e. the initial energy of each term has been subtracted) during the simulation. Figure 5.11 shows that the magnetic energy within the domain increases by approximately 4×10^{23}J by the end of the end of the simulation (where the end phase of the simulation corresponds with the magnetic energy peak at approximately 140° rotation). For clarity, we reiterate that (as discussed in chapter 1) because we use a domain with an open boundary, we adopt the potential field as the linear force-free field that represents the minimum energy state for the rotating sunspot. This assumption is why we represent the measurement of magnetic energy in figure 5.11 to be the energy introduced into the initial potential field solution. The total energy of the domain is much larger.

We use the domain splitting technique developed in chapter 4 to differentiate the energy introduced into the umbral and penumbral fields respectively. Figure 5.11 shows that the amount of magnetic energy introduced into the domain during the evolution of the sunspot is primarily found (and possibly generated) in the penumbral region. This shows that the average magnetic pressure in this region has increased more so that it did in the umbral region and that the penumbra would appear to store the introduced energy far better. Given the umbral field is open at

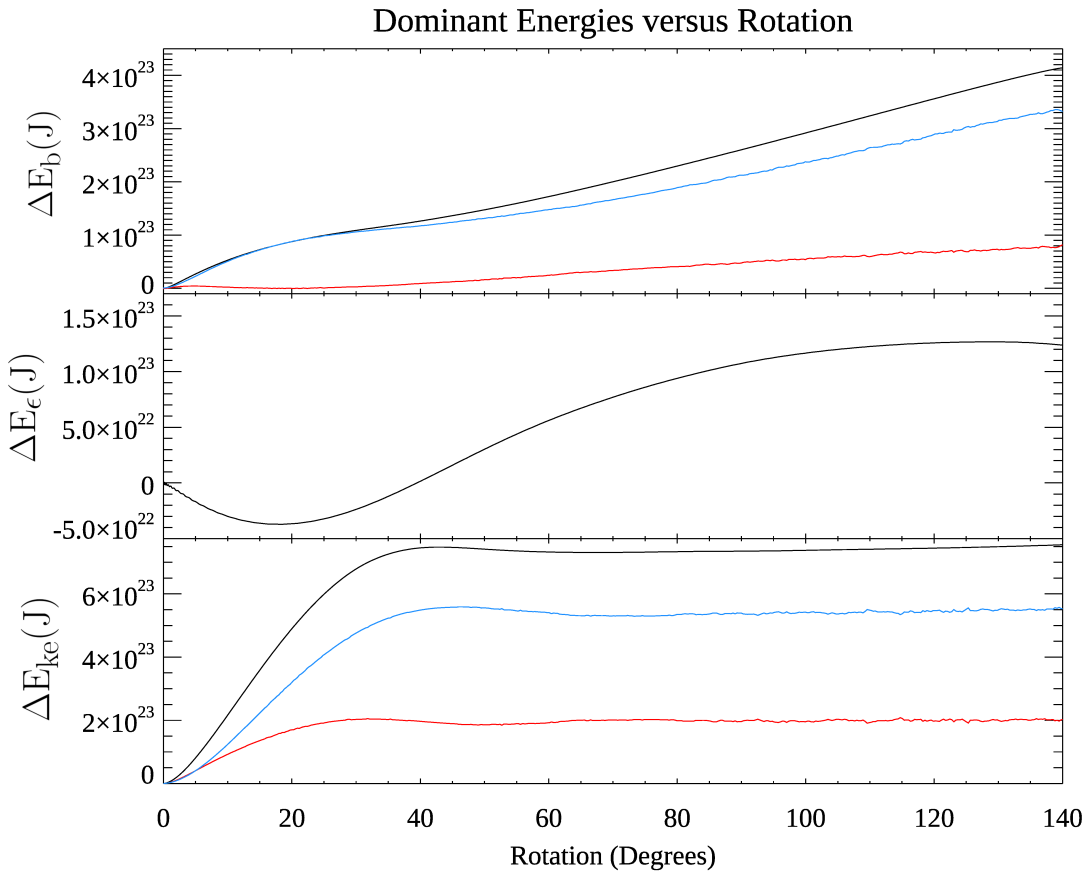

Figure 5.11: This figure shows the evolution of the dominant energies during the simulation. The top figure shows the evolution of the change of magnetic energy, the middle figure shows the evolution of the change of internal energy and the bottom figure shows evolution of the change of the kinetic energy (where ΔE_b, ΔE_ϵ and ΔE_{ke} represent the changes of magnetic, internal and kinetic energies respectively). In all cases the black line shows the domain total, the red line shows the umbral total and the blue line shows the penumbral total.

the top of the domain, this result is unsurprising. But we will see that the upper and side domain boundaries forbid magnetic energy itself to leave through them. Thus, the energy transferred into the umbral field must leave as some other form, most likely kinetic. We must note however that what is represented by figure 5.11 is the energy increase within the domain (and each region) and not the total magnetic energy. We find (but do not show) that the total magnetic energy within the umbra is at all times much larger than the penumbral magnetic energy. This is because the umbral field roots itself in the strongest magnetic field of the sunspots which dominate the magnetic energy of the domain.

An interesting feature that presents itself is that the umbral field seems like it is completely unable to store any additional magnetic energy (given it is free to relax this is reasonable) until approximately 50° of rotation has occurred. The origin of this additional energy is not clear, if it were due to the rotation of the sunspot (which is our only input to the simulation) then one may expect this effect to manifest itself immediately. A clue as to the origin of this additional umbral magnetic energy is presented in figures 4.1 and 4.2, where we clearly see that also at approximately 50° the penumbral volume begins to expand in a significant way. It seems that as the penumbral region expands, it displaces the overlying umbral field (shown by figures 3.1 and 3.2) and compresses it, and hence may introduce this additional magnetic energy in the umbral region. Therefore the additional quantity of magnetic energy in the umbral field is also possibly by proxy a product of the penumbral field regions ability to store energy and expand as a consequence.

In summary, figure 5.11 has highlighted that there is indeed evidence that magnetic energy is generated by sunspot rotation, but we see that there is a clear preference for this energy being stored in the penumbral field. The observation that the umbral and penumbral fields have different energetic properties is not to be unexpected, given the difference of connectivity of each and also the highly contrasting

nature of the properties in each of these regions identified in chapters 3, 4 and earlier in this chapter. We find that the distribution of magnetic energy is too smooth and is not well represented by the ladder plots which feature frequently throughout this thesis. Our means of analysis of the magnetic energy moving forward will be entirely quantitative, as the primary finding here shows that the penumbra is an important region for magnetic energy storage, regardless of how the magnetic energy is distributed within.

Kinetic Energy

Figure 5.11 also shows that the kinetic energy increases approximately linearly in correlation with the acceleration of the driver to full speed rotation. It then reaches a maximum at around 40° and eventually plateaus to a steady rate. This is in agreement with expectation as the primary influence we take on the numerical domain is to introduce motion at the lower boundary. Hence the kinetic energy ought to trace evolution of the lower boundary motion, which it is found to do. An interesting finding is that kinetic energy within the penumbra is found to be larger than that of the umbra, but still of the same order. This finding is somewhat surprising given the vast volume of the umbral field region, but is explained by the majority of the umbral field being composed of very tenuous plasma. The primary finding here is that, after the acceleration phase, the kinetic energy in both the umbral and penumbral magnetic field regions quickly tends to a constant value. This directly shows that the expansion of the penumbra, and consequential displacement of the umbra, is a smooth and steady process. If the penumbral expansion were an instability, we may expect a sudden increase at some point in one, or both, of the kinetic evolution curves. Interestingly, we see that the order of the kinetic energy introduced matches the order of the magnetic energy. Because we only induce motion which creates magnetic energy, we may expect that there must be a link between the kinetic and

magnetic energies (we shall discuss this further in section 5.2.2).

We conclude this section by briefly investigating the distribution of kinetic energy in the domain. Figure 5.12 shows a ladder plot which shows the distribution of kinetic energy between $30° - 75°$. The main purpose of showing this figure is to highlight that there is a clear localisation of kinetic energy where the sunspot is driven. This characteristic persists throughout the simulation. We observe that generally as the sunspot is rotated the kinetic energy within the coronal penumbra tends to decrease with further expansion. This can be seen if one compares a penumbral kinetic energy value at 75° at ±30Mm distance from the rotation axis and at 5Mm height. We see that at 75° the kinetic energy in the coronal (outer) penumbra has decreased, but generally that the region as a whole has grown in volume. However, as figure 5.11 shows, we can be certain that no matter the interplay between rotation, velocity, density and expansion the total kinetic energy in the region must remain constant (or rather is observed to remain constant).

5.2.2 The Injection of Magnetic Energy from Sunspot Rotation

We have observed that there seems to be sufficient evidence to support the statement that sunspot rotation is able increase the magnetic energy content of a sunspot. However, the simple relationship shown by figure 5.11 is very limited, and whilst it established a causal link between magnetic energy generation and sunspot rotation, it does not in any way differentiate where in the domain the magnetic energy is generated, stored or is being transported to. An investigation into the properties of magnetic energy would be incomplete without developing some understanding of the manner in which the magnetic energy flows. Poynting's theorem (see section 1.7.1) describes the generation, loss and transport of electromagnetic energy. There are several forms of Poynting's theorem we shall use in this section and are given by

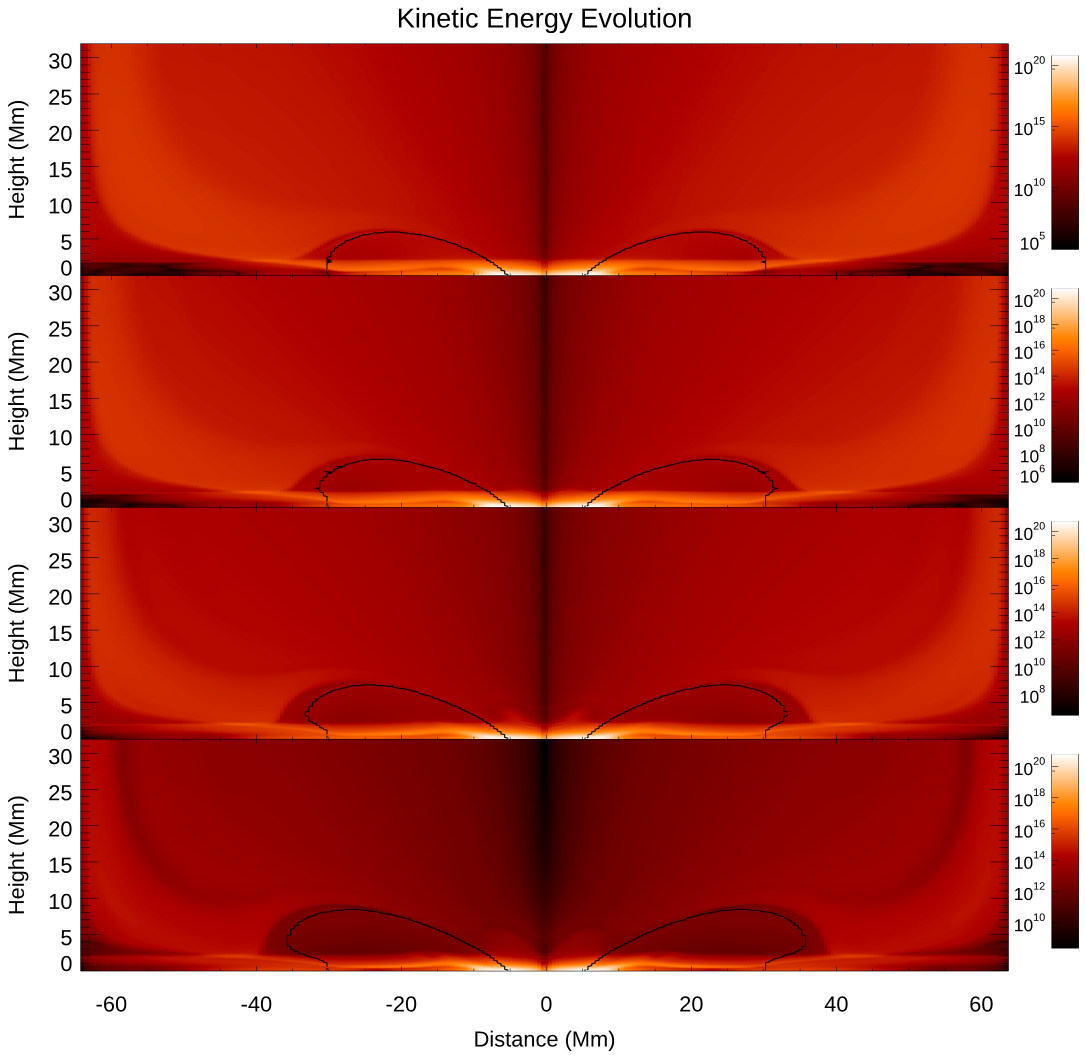

Figure 5.12: This figure shows the magnitude of the kinetic energy integrated over a grid cell during the simulation in a slice through the centre of the sunspot. The sub-figures, moving from top to bottom, show this at times when the sunspot has been rotated by 30°, 45°, 60° and 75° by the driver respectively. The black contour represents the approximate location of the separatrix that divides the umbral and penumbral magnetic field regions, in a slice through the centre of the sunspot. The units of the colour bars are Joules (J).

equations 1.34 and 1.36 and are repeated as follows,

$$\frac{\partial}{\partial t}\left(\frac{B^2}{2\mu_0}\right) = -\left(\mathbf{E}\cdot\mathbf{j}\right) - \nabla\cdot\mathbf{S},$$

$$\frac{\partial}{\partial t}\left(\frac{B^2}{2\mu_0}\right) = -\cancelto{0}{\frac{j^2}{\sigma}} - \mathbf{v}\cdot\left(\mathbf{j}\times\mathbf{B}\right) - \nabla\cdot\mathbf{S},$$

where the $\frac{j^2}{\sigma}$ term in equation 1.36 vanishes under the ideal MHD regime employed in simulation 1, because $\sigma \to \infty$. Collectively, equations 1.34 and 1.36 state that magnetic energy density at a point may increase or decrease if either the electric field does work on the current density or there is either a divergence or convergence of the Poynting vector at the point. The Poynting vector itself represents the movement of electromagnetic energy and thus the divergence of the Poynting vector simply describes the accumulation or diffusion of magnetic energy toward, or away from, a point respectively. Therefore in this section we shall analyse the movement of electromagnetic energy, but we will focus far more attention on the generation and loss of magnetic energy from the volume. Further explanation of the boundary conditions can be found in chapter 2, but next we focus on the boundary conditions relevant to the Poynting vector.

Upper Boundary

At the upper domain boundary we impose that the magnetic field leaves normal to the plane of the boundary, i.e,

$$\left(\mathbf{B}\times\hat{\mathbf{n}}\right)\big|_{z=top} = \mathbf{0},$$

where $\mathbf{B}$ and $\hat{\mathbf{n}}$ represent the magnetic field vector and a unit normal vector that points normal to the upper boundary respectively. Because the Poynting vector is proportional to the cross product of electric and magnetic fields ($\mathbf{S} = \frac{1}{\mu_0}\mathbf{E}\times\mathbf{B}$), the upper boundary conditions mean that no matter what the electric field is at the top boundary the Poynting vector must always be perpendicular to the boundary itself.

Hence electromagnetic energy cannot leave through the upper domain boundary. Hence,

$$(\mathbf{S} \cdot \hat{\mathbf{n}})|_{z=top} = 0, \tag{5.1}$$

Side Boundaries

At all side boundaries we impose that the magnetic field and velocity either vanish or are perpendicular to the boundary, i.e.,

$$(\mathbf{B} \cdot \hat{\mathbf{n}})|_{x,y=sides} = 0,$$
$$(\mathbf{v} \cdot \hat{\mathbf{n}})|_{x,y=sides} = 0.$$

where $\mathbf{B}$, $\mathbf{v}$ and $\hat{\mathbf{n}}$ represent the magnetic field and velocity vectors and a unit normal vector that points normal to the side boundaries respectively. Under ideal MHD regime the electric field is given by $\mathbf{E} = \mathbf{B} \times \mathbf{v}$ (i.e. Ohm's law with $\eta = 0$, see equation 1.7), which means that by definition of the Poynting vector (equation 1.31) the Poynting vector must be parallel (or anti-parallel) to the velocity vector under the ideal MHD assumption. This is easily shown as,

$$\mathbf{S} = \frac{1}{\mu_0}\mathbf{E} \times \mathbf{B},$$
$$\mathbf{S} = \frac{1}{\mu_0}(\mathbf{B} \times \mathbf{v}) \times \mathbf{B},$$

where it is easy to see that the $(\mathbf{B} \times \mathbf{v})$ must point perpendicular to both the magnetic field and velocity and thus when crossed with $\mathbf{B}$, the resulting vector is directed along $\mathbf{v}$. Because the velocity normal to the side boundaries vanishes, so must the Poynting vector, thus,

$$\mathbf{S} \parallel \mathbf{v}. \tag{5.2}$$

Therefore we find that the side boundaries of the domain are also impervious to electromagnetic energy.

Whilst this seems initially limiting (as we may get greater energisation of the solar atmosphere, as a result of sunspot rotation, if magnetic energy were allowed to flow

into the numerical domain through the upper or side boundaries) this result is very helpful for establishing a causal link between sunspot rotation and magnetic energy generation. As with this result we can derive a particular instance of Poynting's theorem that describes the generation of magnetic energy in the numerical domain of simulation 1. We begin with the point version of Poynting's theorem (equation 1.36) for an ideal MHD plasma, as below,

$$\frac{\partial}{\partial t}\left(\frac{B^2}{2\mu_0}\right) = -\mathbf{v}\cdot(\mathbf{j}\times\mathbf{B}) - \nabla\cdot\mathbf{S}, \tag{5.3}$$

where the work done by the electric field is given in the expanded form and the $\frac{j^2}{\sigma}$ term vanishes as a consequence of $\sigma \to \infty$ under the ideal MHD assumption. First we recognise that under the ideal MHD assumption $\mathbf{E}\cdot\mathbf{j} = -\mathbf{v}\cdot(\mathbf{j}\times\mathbf{B})$. This form is easier to interpret as it more clearly suggests the mechanism of energy conversion, specifically that magnetic energy can be generated at a point if there are collocated anti-directed velocities and Lorentz forces, and conversely dissipated where there exists parallel velocity and Lorentz forces.

Consider equation 5.3, it describes the change of magnetic energy density (magnetic pressure) at a point and states that it can be altered either when magnetic energy flows toward or away from that point, or when magnetic energy is converted to or from other forms of energy at that point. We have also seen that as the simulated sunspot rotates, magnetic energy is injected into the domain. However, we also observe that beneath this simple observation lies a more complex range of phenomena, specifically magnetic energy is stored primarily in the penumbral magnetic field, which expands and appears to consequently induce (move) magnetic energy in (into) the umbral field. This description, although simplified and severely abridged, still describes a very complex evolutionary interplay between various evolving magnetic field regions, the energies stored within them and the many properties investigated throughout in this and other chapters of this work. If we recall that our primary interest is to understand how magnetic energy is generated when a given sunspot

rotates, and recognise that at this point we have identified a number of interesting characteristics and mechanisms inherent to the model rotating sunspot, we may convince ourselves that we have succeeded and all that remains is to quantify the energy generation versus rotation characteristics of the model sunspot. However, presently we do not know how any of the model sunspot parameters, if changed, may influence this (perhaps sensitive) dynamic. For example, if we were to decrease the size of the penumbra and make the umbral field much stronger, would the penumbra still rise? Or if we scaled the magnetic field strength of the sunspot overall, would we observe the same fraction of induced magnetic energies in the open umbral field (with respect to the penumbral magnetic energy) or would it relax far more quickly due to the enhanced Alfvén speed? Although we shall see in chapter 6 that our problem appears to at least be well-posed (in that the total magnetic energy generation varies smoothly when any parameter is varied, implying a subsequent smooth variation of the mechanisms which lie beneath), we are still unable to answer with any confidence the questions asked above.

However, because we know (or shall know) from the work of chapter 6 that the magnetic energy varies smoothly as we vary the properties of the simulated rotating sunspots, we may expect that the general physics and mechanisms be similar (even if there is some shift in dominance). Secondly, we may make the rather sensible argument that it does not matter to a solar flare if the magnetic energy which creates it comes from a primary mechanism like the rotation of a sunspot, or a secondary one like the magnetic energy found in the umbral field as a consequence of the expanding penumbra. All energy within the domain, created by the sunspot's rotation (directly or secondarily) is useful if it is free. Finally, we know now that all of the magnetic energy, which is in surplus to the initial potential field energy, must truly form within the domain or flow into it through the lower boundary. Therefore we may still hope to understand sunspot rotation, in a sense that we can apply

the findings to sunspots which are different to that analysed in this chapter, by focusing less on the small scale physics and mechanisms and recognising that all of the magnetic energy found within the domain is a result of the driving of the sunspot and transition to attempting to understand the magnetic energy generation properties of the whole domain. By doing this we shall see that we may derive a far simpler description.

To do this, we convert the point form of Poynting's theorem shown by equation 5.3 into an integral form. Doing so will change our description from local energy density evolution to the total rate of change of magnetic energy within the domain. Thus, equation 5.3 becomes,

$$\iiint \frac{\partial}{\partial t}\left(\frac{B^2}{2\mu_0}\right) dV = \iiint -\mathbf{v}\cdot(\mathbf{j}\times\mathbf{B}) - \nabla\cdot\mathbf{S}\, dV,$$

where dV represents an infinitesimal volume element, expanding the right hand side, we yield,

$$\iiint \frac{\partial}{\partial t}\left(\frac{B^2}{2\mu_0}\right) dV = \iiint -\mathbf{v}\cdot(\mathbf{j}\times\mathbf{B})\, dV - \iiint \nabla\cdot\mathbf{S}\, dV.$$

We may now use Gauss' theorem to recast the integral of the divergence of the Poynting vector as a surface integral,

$$\iiint \frac{\partial}{\partial t}\left(\frac{B^2}{2\mu_0}\right) dV = \iiint -\mathbf{v}\cdot(\mathbf{j}\times\mathbf{B})\, dV - \iint \mathbf{S}\cdot\hat{\mathbf{n}}\, d\tau,$$

where $\hat{\mathbf{n}}$ is a unit normal vector that points perpendicular to the surface defined by τ. Finally we may recognise that the surface, τ, in question is in fact the boundaries of the numerical domain, where we previously established $\mathbf{S}\cdot\hat{\mathbf{n}} = 0$ on the upper and side boundaries. Thus, we retrieve the final form,

$$\iiint \frac{\partial}{\partial t}\left(\frac{B^2}{2\mu_0}\right) dV = \iiint -\mathbf{v}\cdot(\mathbf{j}\times\mathbf{B})\, dV + S_{phot}, \tag{5.4}$$

where S_{phot} represents the total Poynting flux flowing through the lower boundary. Equation 5.4 states that if we observe the total magnetic energy within the volume

to increase, that increase must come as a result of a net dominance of anti-parallel velocity and Lorentz forces or from magnetic energy entering the domain through the lower boundary. Conversely, equation 5.4 also explains that we may lose energy from the domain if there is a net dominance of parallel Lorentz forces and velocities (or again, through the lower boundary). We may now think back to the work of section 5.1 where we investigated the Lorentz force and accelerations induced by it. We can now recognise an acceleration induced by the Lorentz force will always be aligned with the Lorentz force itself, and hence given equation 5.4 we see this action represents the attempted relaxation of the magnetic field and reduction of magnetic energy. Clearly the energy resulting from acceleration by the Lorentz force is kinetic energy, hence this result represents the conversion mechanism between magnetic and kinetic energy. The strong accelerations we observe in figures 5.3 and 5.4 thus show relaxation of the magnetic field, and because we see there is an increase in the magnitude and amount of Lorentz force accelerations in the penumbra, during the latter stages of the simulation, we can conclude that as the penumbra expands and the average density within it reduces, the magnetic field is able to more freely relax. This result it particularly relevant in the coronal penumbral field.

We may expand equation 5.4 one final time to better understand the how the Lorentz force and velocity influence the energy generation properties in the penumbral and umbral magnetic field regions independently. We may write,

$$\iiint \frac{\partial}{\partial t}\left(\frac{B^2}{2\mu_0}\right) dV = \iiint_{Pen} -\mathbf{v}\cdot(\mathbf{j}\times\mathbf{B})\, dV + \iiint_{Umb} -\mathbf{v}\cdot(\mathbf{j}\times\mathbf{B})\, dV + S_{phot}, \quad (5.5)$$

where we have split the volume integral on the right hand side of equation 5.4 into its penumbral and umbral components, as denoted by the subscript "Pen" and "Umb" labels respectively.

Figure 5.13 shows that as the sunspot is rotated (after the acceleration phase) the rate of change of magnetic energy (caused by Lorentz forces and velocities) in the whole domain is positive (as indicated by the black line in the top sub-plot of

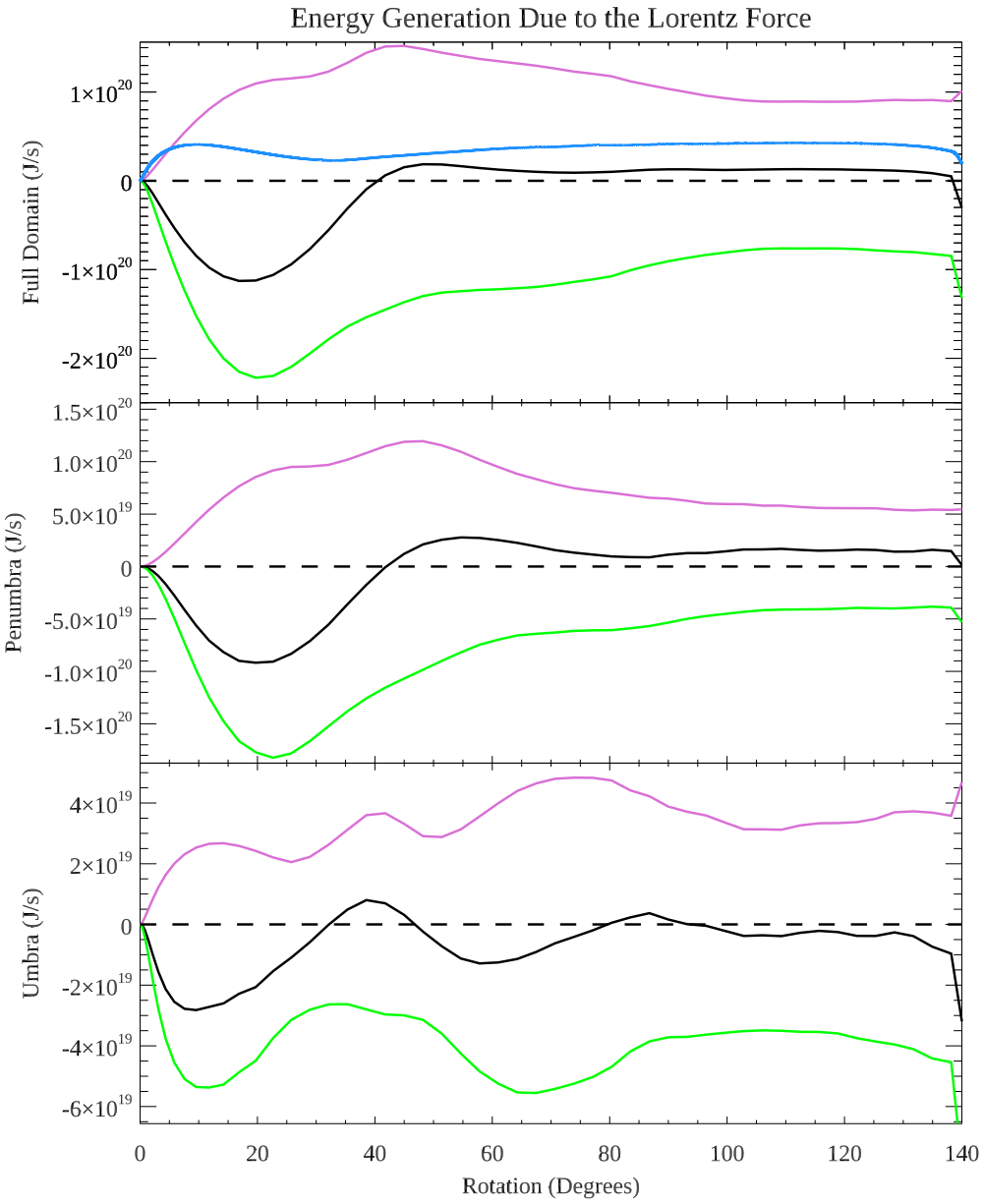

Figure 5.13: This figure shows the rate of change of the magnetic energy caused by the Lorentz force and velocity. The top figure shows this for the full domain, the middle figure for the penumbral region and the bottom figure for the umbral region. In all figures the black curves represent the total change of magnetic energy caused by the Lorentz force and velocity, the magenta and green lines show the total positive and negative change respectively. The blue line in the top figure shows the measured rate of change of the magnetic energy as measured over the whole domain (i.e. it includes the energy from the Poynting flux through the photosphere).

the figure). When compared to the measured rate of change of the magnetic energy (blue line in the same sub-figure) we see that the contribution from the anti-parallel Lorentz forces and velocity only contribute about one third of the total magnetic energy generation rate. Given the only action taken on the sunspot is its driving, we might expect that the lower domain boundary is providing the additional energy. What the discrepancy between the measured change (blue) and the total change due to $-\mathbf{v} \cdot (\mathbf{j} \times \mathbf{B})$ (black) must show is the energy that flows through the lower domain boundary via the Poynting flux, i.e. the contribution from S_{phot}.

We conclude this chapter by highlighting an important result shown in figure 5.13. Specifically, we observe that the penumbral field region is clearly responsible for the net positive average of the total magnetic energy increase. This is shown by the black line in the middle figure remaining positive during the main phase of the simulation whereas the umbral contribution fluctuates and is generally smaller. Finally, we stipulate that in the penumbra, the maximum positive contribution is approximately three times the net contribution. If we assume that the negative contribution is fully or partially a result of the penumbral expansion (as suggested in section 5.1) then we may see a significant increase in the penumbra's contribution to the magnetic energy if we restrict its expansion. Showing this requires further work and is deferred for future studies.

Chapter 6

A Parametric Investigation of Rotating Sunspots

6.1 Introduction

The overarching goal of this work is to gain a better understanding of the underlying physical processes responsible for the generation, storage and transport of magnetic energy that is induced by the rotation of a secular, regular sunspot. This means understanding how rotating sunspots influence their magnetic environments. In chapter 3 we undertake a broad analysis of the evolution of a single, numerically modelled, rotating sunspot. A key finding is that the sunspot is able to generate and store magnetic energy and transport it into the corona. However, in nature sunspots are observed with a wide range of properties, hence one cannot hope to understand the complex phenomenon of sunspot rotation (in a general sense) by studying a single sunspot only (as in chapter 3). In this chapter we build upon the findings of chapter 3 by widening the numerical investigation to include sunspots with varied properties, however, we focus our interests here to understanding only the magnetic energy characteristics of the sunspots.

CHAPTER 6

The idealised sunspot model (chapter 2) depends on a number of input parameters to sufficiently define a single instance of the model sunspot. Collectively the input parameters aim to reflect the most fundamental properties of real-world sunspots (size, shape, magnetic field strength etc.). In this chapter we analyse a collection of sunspot simulations across the parameter space, with the intent to determine the magnetic energy generation characteristics of each. By dividing the collection of simulations into groups which vary a common model parameter only, we can develop an understanding of how each model parameter contributes to the magnetic energy characteristics individually. This approach allows us to understand general sunspot rotation by simulating a finite number of rotating sunspots, by deriving scaling relations for each model parameter individually. With the individual scaling relations, we can compare and contrast each to better understand the dominant mechanisms for energy generation. Finally, we combine the individual scaling relations to form a single equation, which approximate how the magnetic energy of any model sunspot should evolve under rotation. However, we emphasise that this is an empirically derived equation and its form is not motivated by any physical processes. This is both a first and necessary step to understanding the real world phenomenon of sunspot rotation.

The sunspot model, described in chapter 2, simplifies the definition of a sunspot to relatively few parameters. These parameters are: the umbral radius (U_r), the peak field strength in the centre of the sunspot (U_b), the penumbral radius (P_r), the peak penumbral field strength (P_b), the rotation rate of the sunspot (ω) and the inclination of the normal magnetic field component (B_z) at the umbral-penumbral intersection (controlled by γ; see equation 2.27). These parameters are the fundamental ones which describe each sunspot simulation, but there are two derived parameters that are used in this chapter, namely: the ratio of peak penumbral to peak umbral field strength $\left(\mu \equiv \frac{P_b}{U_b}\right)$ and the ratio of umbral to penumbral radii $\left(\psi \equiv \frac{U_r}{P_r}\right)$. It was

found to be helpful to use these secondary, derived, properties in the scaling law derivations that follow.

6.1.1 An Ideal Magnetohydrodynamic Framework

The Lare3d code (Arber et al., 2001) allows the user to choose the physics that is modelled by the code. The main physics that can be altered that is relevant to this work, is: conductivity, hence are resistive effects physically included; thermal conductivity, which gives importance to temperature gradients (as in the solar atmosphere) and the degree of ionisation of the plasma, which is particularly important in the chromosphere (Leake, 2005; Leake and Arber, 2006; Arber et al., 2007; Yalim et al., 2020).

Ideal MHD is the basis regime chosen for this investigation, primarily because under it complex physical processes like magnetic reconnection and magnetic slippage are not physically present, which minimises magnetic energetic losses. Therefore, under the ideal MHD assumption the simulations should produce an estimate of the upper limit for energy storage to which more natural physical regimes may be compared retrospectively. Secondly, because there should not be any physical magnetic reconnection processes, the total magnetic energy evolution should be relatively smooth, we saw this to be the case in chapter 3 and generally find this to be true. A smooth evolution of the total magnetic energy proves to be particularly beneficial when establishing scaling relations in this chapter (i.e. it is easier to fit a function confidently using clean data rather than noisy).

6.1.2 The Methodology

The purpose of this chapter is to establish a relationship between a given model parameter and the generation of magnetic energy as the model sunspots rotate. For each parameter, there is a batch of simulations where only that single parameter

varies and all other parameters are equal to that of simulation 1. The approach to establishing a relationship between a given parameter and the amount of magnetic energy generated as a function of rotation is broken down into the following key stages:

1. For each simulation, in a batch which varies only one model parameter, determine the relationship between the percentage change of magnetic energy (with respect to the initial potential field) and cumulative rotation using a power-law fitting function.

2. Compare the power-law parameters of each simulation in the batch and determine if any relationship between the power-law parameters exists. If so, establish a functional relationship between the power-law parameters and the varied model parameter.

3. Combine the functional fits of both power-law parameters for a batch of simulations into a single expression, establishing a relationship between magnetic energy increase and rotation as a function of the changing model parameter under investigation.

The steps listed above outline the basic process and were determined to be suitable from experimentation, in that they produced the desired scaling relations. The specific meaning behind each step listed is explained further via example in the following sections. To make the comparison between properties of particular simulations clearer in the following discussion, a unique numeric identifier is given to each simulation (for example see the left-most column of table 6.1).

6.1.3 Power-Law Fitting

The first step to attaining a functional relationship between a model parameter, cumulative rotation and energy generation is to determine the energy generation

properties of each simulation individually. To do this we fit a power-law to each simulation's percentage magnetic energy versus rotation time-series, so that we may compare these power-law fits against one another. A power-law function was chosen because it was found to be the simplest form of fitting function that produced a measurably good fit to all the simulation data and provides good compromise between the accuracy of each fit and simplicity of the function itself. This allows comparison between the individual scaling relations (section 6.3).

A general power-law relationship has the form,

$$y = kx^a, \tag{6.1}$$

where k and a are constants, x is some independent variable and y is a variable dependent on x. In this investigation, the independent variable x in equation 6.1 is the angle of cumulative rotation (θ) of the umbral region. The dependent variable, y, becomes the percentage change in the magnetic energy, $\triangle E_b(\%)$. The reason for analysing the percentage change rather than the total change of magnetic energy is that the scale of the energy becomes normalised and this normalisation proved to be of significant importance when establishing scaling laws. The energies represented by the total collection of simulations varies significantly and those with the weakest magnetic fields (and hence magnetic energy) were found to fall within the noise-level of the fit of those with the strongest magnetic fields when the normalisation is not used. Therefore equation 6.1 becomes,

$$\triangle E_b(\%) = k\theta^a, \tag{6.2}$$

where the variables k and a in equation 6.2 must be determined for each simulation. This is done by taking the logarithm of equation 6.2, which gives,

$$\log\left(\triangle E_b(\%)\right) = \log\left(k\theta^a\right) = \log(k) + a\log(\theta).$$

Linear regression is used to find the best fit straight line to this data and yields a

slope equal to a and an intercept equal to $\log(k)$. Hence k and a are calculable from the simulation data directly. To do this we use standard χ^2 minimisation methods.

The process described above is repeated for each simulation and thus each simulation is assigned a k and a value. Each simulation is also assigned two angles, (θ_1 and θ_2) that define the data range within which the power-law fit is made. This step is performed out of necessity, as it was found that the magnitude and longevity of start-up effects vary between simulations (see chapters A-F for numerous illustrative examples of the range of the start-up effects). It was found to be important to begin the power-law fit after the dominant start-up effects have dissipated (thus defining θ_1). Under the ideal MHD regime we cannot have physical magnetic reconnection, meaning we are forced to end each simulation if and when the penumbral magnetic field of a given simulated sunspot, expands enough to reach the top of the domain. The reason we must end the simulation is due to the open-like boundary conditions invoked at the upper domain boundary. We find that when the closed penumbral magnetic field encounters the upper domain boundary, the boundary conditions induce an artificial magnetic reconnection-like event and the penumbral field lines that reach the upper domain break and become part of the open umbral magnetic field. This process is of course non-physical and consequently we endeavour to avoid using data from this phase of any simulation. This means that not only is there a final rotation value where the simulation data is physically meaningful, there is also a short period just prior to this end point where the solution may be influenced by the impending ending (thus defining θ_2).

Figure 6.1 shows an example of the power-law fitting process to one of the simulations under the ideal MHD regime (the simulation discussed in depth in chapters 3, 4 and 5). As shown, the power-law fit is in very good agreement with the simulation data between approximately 50° and 140°, but fails to produce a good fit far from this fitting range due to start-up and end effects (which we do not wish

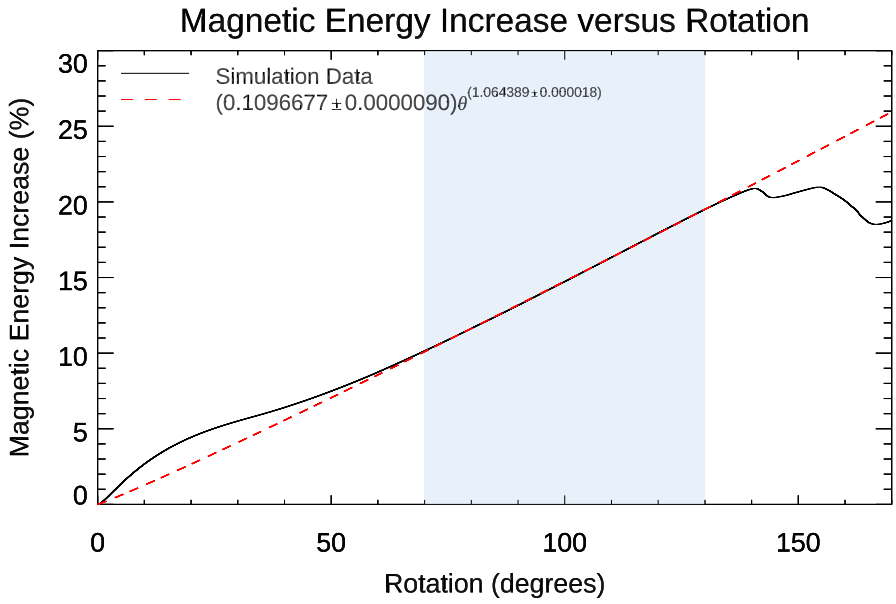

Figure 6.1: The power law fit for simulation number 1 (table 6.1). The solid-black curve shows the percentage change of the magnetic energy versus cumulative rotation and the dashed-red curve shows the power-law fit approximation. The blue shaded region between $\theta_1 = 70°$ and $\theta_2 = 130°$ defines the region where the power-law fit has been made.

to include in any derived scaling relation). Note that the region of good agreement extends somewhat beyond the data range where the power-law fit was made. When attempting a fit of this form using the entire data range, a lesser quality fit produced. This phenomenon illustrates the motivation for restricting the fitting to data within the range θ_1 and θ_2; i.e. in the region we shall refer to as the "main-phase" of the simulation going forward. The uncertainty of the k and a values is also calculated and used when comparing simulations in the same parameter batch, so that if at any point the power-law fitting begins to under-perform for a given simulation that simulations fitting parameters will be weighted appropriately in the final derivation of scaling laws.

Given the process of fitting is established, the next thing to do is to determine what k and a are for each of the simulations. The process of fitting all the simulations is divided into relevant sections for each model parameter under investigation in section 6.2. Focusing only on the simulations of current interest facilitates simpler analysis that better motivates the construction of each scaling law, because the nature of each scaling relation is found to have a unique degree of complexity.

6.2 Parametric Scaling Relations

For each of the model parameters investigated in this chapter, we follow the same general path to derive a scaling relation. First we take the batch of simulations that vary the parameter of interest and list their model properties in a table. We then identify defining features of the magnetic energy characteristics of the simulations in this table and discuss where appropriate. We shall discuss the values of power-law fitting parameters and identify the trends present between these fitting parameters and the individual model parameter under investigation. This will independently link the fitting parameters to the model property in question. Next, we approximate

a functional relationship between the model parameter and the power-law parameters; the emphasis is to find a good interpolant rather than an analytical expression with physical meaning. We then substitute the functional relationship, between the power-law parameters and the model parameter, into equation 6.2 to derive a description of the percentage magnetic energy change versus the model parameter. Finally, we convert from percentage increase of magnetic energy into Joules so that a meaningful quantification may be made as to the energy generation properties of rotating sunspots. Following this method we effectively remove the power-law parameters from the problem, leaving a relation between magnetic energy and the model parameter. Throughout this investigation the range of the model parameters will (mostly) encompass the range of physically observed properties of rotating sunspots, such that the functional forms fitted to the data will interpolate and not be used for extrapolation. This is an important consideration that must be understood, as it removes some of the rigidity for which functions to fit to the data. For example, if we intend to extrapolate well beyond the range of parameters tested then one may expect that a physically motivated fitting function should be used so that there is at least some physical expectation for any trends to continue beyond the fitting range. However, because we only wish to interpolate our data, we have the freedom to fit functions without reference to the underlying physical mechanisms. However, we maintain that where polynomial fits are used, the order of the fitting function should be no more than half the number of data points in the set of data being fit to.

We introduce an additional step when investigating the rotation rate parameter. Specifically, we test the scaling relation that is derived, to see if it is able to approximate a slowly rotating sunspot's magnetic energy evolution. The slowly rotating sunspot simulation that is tested is not used to derive the scaling relation. The reason we do this is because for numerical efficiency (specifically cost saving) we

drive the simulated sunspots in this work quickly, and by doing so alter the energy generation properties of the rotating sunspot (this will be shown in section 6.2.3). The reason the slowly rotating sunspot simulation is not included in derivation of the scaling relation itself, is because it was too computationally expensive to complete that simulation. Thus, by performing the additional testing, we show that the rotation rate scaling relation (and the final combined scaling relation) is capable of predicting the energy generation properties of sunspots rotating at natural rates and that we can account for the consequences of rotating the sunspots quickly.

The individual scaling relations derived in this chapter are subsequently combined and the predictive potential of the combined scaling relation will be tested. The testing will be performed on simulations where multiple model parameters are varied. The testing determines if the means by which we combine the individual scaling laws is valid and provides us with an estimate of the predictive capabilities and accuracy of the combined scaling relation.

6.2.1 Peak Umbral Field Strength- U_b

The batch of simulations which vary U_b and hold all others constant ($\mu = \frac{P_b}{U_b}$ is held constant rather than P_b) are analysed in this section. The peak umbral field strength, U_b, is a key parameter of the model sunspot which reflects the overall magnetic field strength of the umbral region and due to the definition of the sunspot model (chapter 2) it also scales the overall field strength of the entire sunspot (because $\mu = 0.5$ throughout this section). Therefore, the model sunspots analysed in this section are geometrically similar but differ in the magnitude of their magnetic field strengths.

The magnetic field strength is responsible for the magnetic energy itself and hence further motivates our choice to analyse the percentage energy increase over the true magnetic energy. Table 6.1 lists the simulations (and model parameters

of each) that are used in this section to derive a scaling law for the peak umbral field strength, U_b. Table 6.1 shows that the peak umbral field strengths studied in this section span a very broad range. The purpose of this is to ensure that this investigation covers the physical range of field strengths of observed sunspots and beyond.

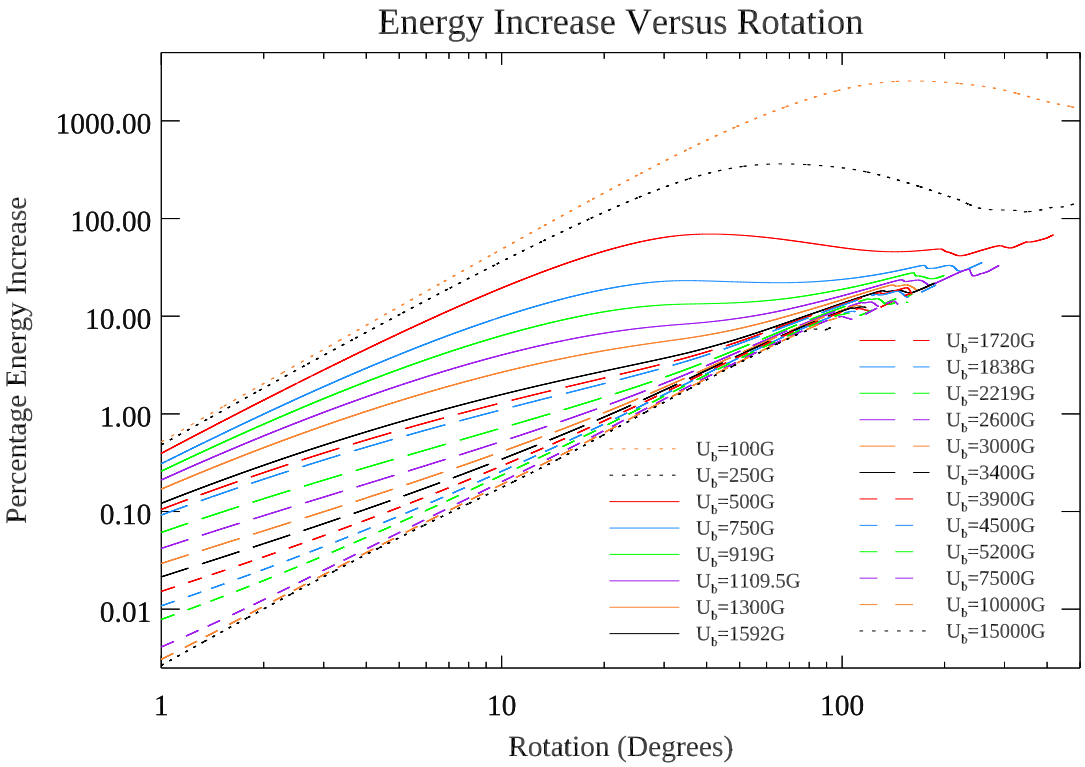

Figure 6.2: This figure shows the percentage energy increase versus rotation for all the simulations in the batch which varies only peak umbral field strength (U_b) with $\mu = 0.5$. The figure uses logarithmic-logarithmic axes and therefore focuses mainly on the acceleration-phase of the simulations (which spans $0° - 32°$ for all simulations in this figure). The model properties and initial magnetic energy of each simulation shown in this figure are tabulated in table 6.1.

Figures 6.2 and 6.3 each show the percentage change magnetic energy versus rotation properties of the collection of simulations considered in this section (i.e.

those which vary U_b only). Figure 6.2 shows the full range of data and figure 6.3 focuses on the main-phase of the simulations; i.e. it removes most of the early start-up phase which we do not consider when fitting power-laws. Although we aim to analyse the main-phase of each simulation only, it is important to understand what data we neglect in our investigation and why we must do this. Figure 6.2 shows that during the acceleration-phase ($0^\circ - 32^\circ$) most simulations display, to a greater or lesser extent, a different evolution of their respective percentage change magnetic energy than they do during the main-phase. The post acceleration-phase in each case displays a mix of main-phase and relaxation from the consequences of the start-up effects; the strongest field strength simulations show very little susceptibility to the start-up effects and evolve in what appears to be a more relaxed state. Furthermore, in the post acceleration-phase all simulation curves (at least begin to) converge in figure 6.2. Figure 6.2 shows that the weakest magnetic field strength simulations introduce a larger percentage increase of magnetic energy throughout, however, it is clear that the disparity is far more significant during the acceleration-phase. Figure 6.2 further shows that the strongest and weakest field strength simulations show power-law like behaviour during the acceleration-phase, whereas the intermittent field strength simulations evolve between the two limiting power-law-like curves. A fuller understanding of the acceleration phase is deferred to future work.

Figure 6.3 shows only the data we will consider in the following derivations of scaling relations (i.e. not all simulation data from figure 6.2 is present). The range of data shown spans 25° until each simulation ends (when the penumbra in each hits the top of the domain). The acceleration-phase ends at approximately 32° for all simulations considered in this batch therefore in the following discussion all fitting will focus on data after this point in all simulations respectively. Figure 6.3 shows the same monotonic style ordering as present in figure 6.2, specifically that (prior to the end of each simulation) the percentage change of magnetic energy of one

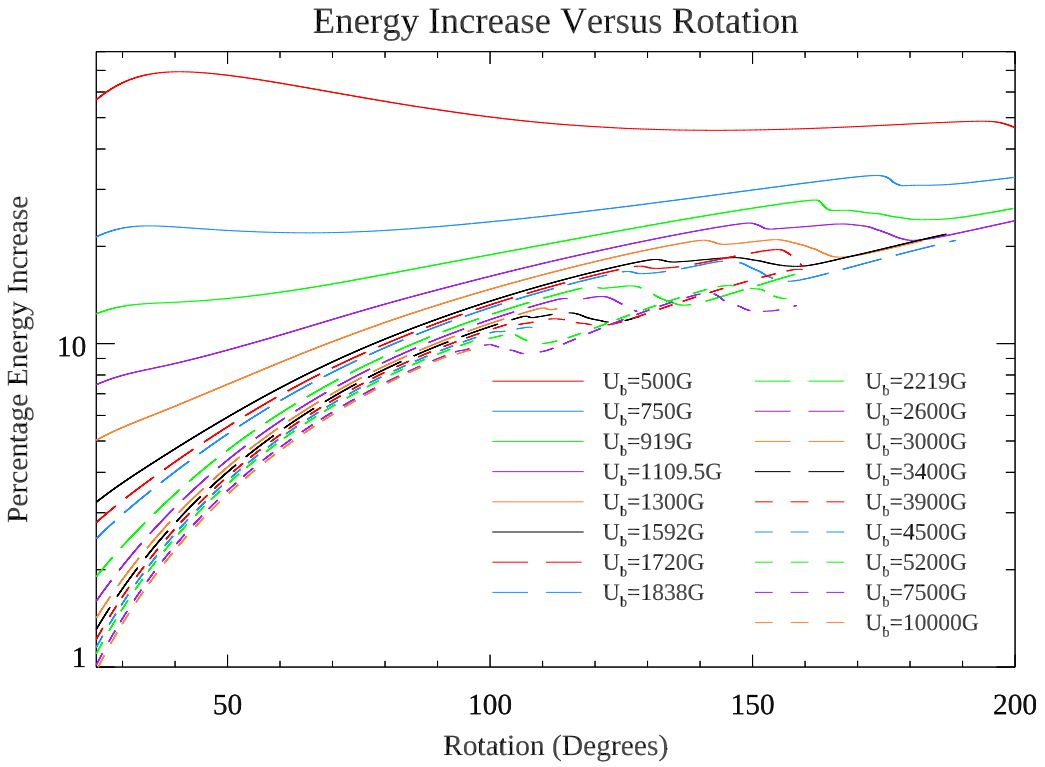

Figure 6.3: This figure shows the percentage energy increase versus rotation for all the simulations in the batch which varies only peak umbral field strength (U_b) with $\mu = 0.5$. This figure shows the same data as shown in figure 6.3, but focuses on the main-phase of the simulations. The x-axis ranges from $25° - 200°$ where the acceleration-phase of all the simulations shown ends at 32°, hence the majority of the acceleration-phase is omitted. The model properties and initial magnetic energy of each simulation shown in this figure are tabulated in table 6.1.

simulations evolution curve does not overlap with any other simulations curve. We see more clearly in figure 6.3 that the energy evolution curves begin to converge as the sunspot magnetic field strength increases during the main-phase. Generally, for all but the weakest sunspots simulated, the magnetic energy tended to increase by between $10\% - 20\%$ during each simulations lifetime. Secondly, the lifetime of the simulations (i.e. the time taken for the penumbra to rise and reach the top of the

numerical domain) is found to decrease by a factor of two between the weakest and strongest field strengths modelled respectively.

Although the sunspots show this monotonic style ordering for the percentage change of magnetic energy, the initial magnetic energy of each simulation scales quadratically with magnetic field strength; therefore, it is unlikely that this highly structured trend would be present if considering the net energy increase rather than percentage. This is one of the main advantages of considering the percentage change to link all the simulations in a batch. We shall see in the following discussion that once the true energy increase is considered, the energy evolution scaling becomes non-monotonic.

The remainder of this section develops a quantitative relationship between the model parameter U_b and the energy characteristics of the simulated model rotating sunspots in this section. Equation 6.2, in the context of this sections model parameter (U_b) becomes

$$\triangle E_b(\%) = k(U_b)\theta^{a(U_b)}. \tag{6.3}$$

Equation 6.3 illustrates the main task to achieve our goal; eliminate the k and a terms of equation 6.2 by establishing a functional dependence of each on the model parameter in question, U_b. Then substitute these forms into equation 6.3 and eliminate $k(U_b)$ and $a(U_b)$ entirely. Once achieved, we shall conclude the section by deriving a second scaling law for the true magnetic energy increase rather than the percentage increase. To do this we define another form of equation 6.2; specifically,

$$\triangle E_b(\mathrm{J}) = \tau(U_b)\theta^{a(U_b)}, \tag{6.4}$$

where $\tau(U_b)$ is given by,

$$\tau\left(U_b\right) = \frac{k\left(U_b\right) E_0\left(U_b\right)}{100}, \tag{6.5}$$

and where E_0 is the initial magnetic energy of a simulation domain where the sunspot in said domain has a particular value of U_b. Our goal is to fit the finite data from each

batch of simulations to derive continuous functions which represent $\tau(U_b)$, $k(U_b)$ and $a(U_b)$. We shall, in the exact same way, eliminate $\tau(U_b)$ by establishing a functional form for this parameter based on fitting the finite number of data points in table 6.1.

The primary goal of this work is to model the net magnetic energy increase but we also continue to study the percentage energy increase as this might uncover additional information about the underlying influence of each model parameter. For example, we shall see that U_b scales several aspects of the magnetic energy evolution, which we do not see as clearly when considering the true energy.

More importantly, the percentage energy increase route to total energy increase proved to be a necessary intermediate step for the derivation of meaningful scaling laws throughout this chapter. It was found that trying to perform the same analysis with the true magnetic energy data was difficult, because the range of energies varies so vastly between some simulations that the power-law fits became overly sensitive. The percentage energy increase route effectively normalised all the magnetic energy evolution data so that each simulations magnetic energy increase is of the same order of magnitude (for the vast majority). The reason we are able to convert back to true energy (as in equation 6.4) is primarily due to the definition of $a(U_b)$. Both $a(U_b)$ terms in equations 6.3 and 6.4 are the identical; specifically the $a(U_b)$ from the percentage magnetic energy increase is used also in the true energy increase equation (6.4), but crucially it is calculated using the percentage increase data. The method of determining the true energy increase reduces to using the (well-behaved and more accurately fitted) percentage magnetic energy increase data for $k(U_b)$ and multiplying each data-point by the simulations initial energy and fitting the resulting data with some function. For example, the parameter U_b scales the initial magnetic energy quadratically (because magnetic energy is proportional to the field strength squared) and therefore the function which fits the $k(U_b)$ data is multiplied by a

quadratic curve.

Alternate methods to derive the scaling relations may exist and should be explored in future studies. But, we follow the procedure described above because it gives, relatively simple, good scaling relations which we are able to use individually and in combination. In subsequent sections we follow the exact same approach as that is outlined in the previous discussion for model parameter U_b and, for the sake of brevity and clarity, we shall not repeat the current discussion.

	Model Parameters						Power-Law Fit Parameters						Initial Energy
Sim	$U_b(G)$	μ	$U_r(Mm)$	$P_r(Mm)$	$\omega^\circ \mathrm{hr}^{-1}$	γ	k	δk	a	δa	$\theta_1(^\circ)$	$\theta_2(^\circ)$	E_0(Joules)
1	1300	0.5	5.0	10.0	48	1	0.1096677	9.0E-6	1.064389	1.8E-5	70	130	1.9926e+24
2	250	0.5	5.0	10.0	48	1	-	-	-	-	-	-	7.3692e+22
3	500	0.5	5.0	10.0	48	1	9.1126	1.7E-3	0.319129	3.5E-5	170	190	2.9477e+23
4	750	0.5	5.0	10.0	48	1	0.661703	9.2E-5	0.760326	2.7E-5	150	170	6.6323e+23
5	919	0.5	5.0	10.0	48	1	0.337693	2.5E-5	0.868710	1.5E-5	120	150	9.9580e+23
6	1109.5	0.5	5.0	10.0	48	1	0.1681787	2.7E-6	0.9903554	3.4E-6	120	130	1.4514e+24
7	1592	0.5	5.0	10.0	48	1	0.0507495	1.1E-6	1.2131406	5.1E-6	70	90	2.9890e+24
8	1720	0.5	5.0	10.0	48	1	0.03850469	9.3E-7	1.2681505	5.6E-6	60	90	3.4871e+24
9	1838	0.5	5.0	10.0	48	1	0.0311287	1.6E-6	1.310614	1.2E-5	60	90	3.9832e+24
10	2219	0.5	5.0	10.0	48	1	0.01738790	3.6E-7	1.4307044	5.1E-6	45	75	5.8057e+24
11	2600	0.5	5.0	10.0	48	1	0.01154338	1.1e-7	1.5171902	2.4e-6	45	60	7.9705e+24
12	3000	0.5	5.0	10.0	48	1	0.008550639	6.6E-8	1.5812375	2.0E-6	40	50	1.0612e+25
13	3400	0.5	5.0	10.0	48	1	0.00688670	1.7E-7	1.6275922	6.7E-6	40	50	1.3630e+25
14	3900	0.5	5.0	10.0	48	1	0.005482155	7.6E-8	1.6781595	3.9E-6	30	45	1.7934e+25
15	4500	0.5	5.0	10.0	48	1	0.00495417	2.5E-7	1.696210	1.4E-5	40	50	2.3876e+25
16	5200	0.5	5.0	10.0	48	1	0.00398778	1.7E-7	1.74675	1.2E-5	30	45	3.1882e+25
17	7500	0.5	5.0	10.0	48	1	0.0036499	3.6E-7	1.755830	2.6E-5	35	55	6.6323e+25
18	10000	0.5	5.0	10.0	48	1	0.00345555	3.3E-7	1.762940	2.5E-5	40	55	1.1791e+26
19	15000	0.5	5.0	10.0	48	1	2.81606e-3	1.7e-7	1.810184	1.6e-5	40	50	2.6529e+26

Table 6.1: A tabulated record of the simulations used throughout section 6.2.1 and their associated properties.

Table 6.1 catalogues the simulations used in this section, though is a subset of the simulations used in this chapter. From table 6.1 we see that, when only varying U_b, the fitted coefficient k decreases with increasing U_b and that the fitted exponent, a, increases with increasing U_b. Table 6.1 also shows that what was deemed to be the "main" phase of the simulation (i.e. the data range within which the power-law function is fit) tended to occur sooner as U_b increased. The reason for this is twofold; first, the stronger magnetic field will inevitably scale the magnetic pressure in the penumbra, which we saw in chapter 3 to be the cause of the end of the simulation. If this growth is more rapid, then the simulation end is brought forward and this is what we measure in this batch of simulations. Figure 6.2 also shows that the stronger the magnetic field of the model sunspot, the smaller the impact of start-up effects. The combination of lesser start-up effects and the premature end to each simulation both with increasing U_b is physically justifiable, but nonetheless interesting given we are able to capture this with the scaling laws which are derived using power-laws fitted to these data ranges.

Figures 6.4 and 6.5 show graphically the relationship between the power-law fit parameters and the model parameter U_b. Figure 6.4 shows that as U_b increases the fit parameter (k) decreases in what appears to be some asymptotic manner, tending toward a constant value beyond $U_b \approx 5000G$. In a similar manner, figure 6.5 shows power-law parameter a seems to have opposite behaviour to that of parameter k, in that a increases with increasing U_b but also seems to plateau to a constant value beyond $U_b \approx 5000G$. Given the nature of the power-law as depicted by equation 6.3, if both k and a tend to a constant value each, beyond some value of the independent model parameter, then all sunspots beyond that threshold ought to behave similarly in their magnetic energy percentage increase versus rotation characteristics, or at least a function which approximates the trend of each parameter should reflect this. To understand the percentage magnetic energy increase as a

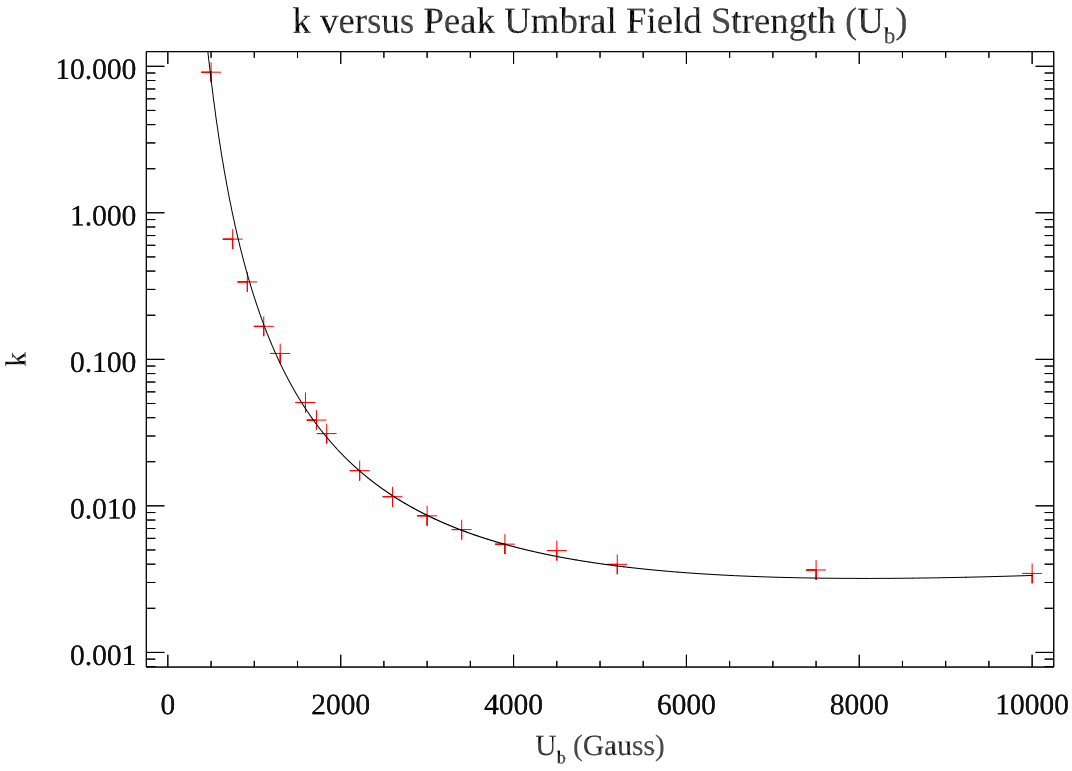

Figure 6.4: A plot showing the relationship between power-law fitting parameter, k, and independent sunspot model parameter, U_b. The red plus symbols depict the data-points for k tabulated in table 6.2 and the solid black line represents the interpolant described by equation 6.8.

function of the model parameter, U_b, only we must establish functional forms to act as an interpolant to define both k and a explicitly in terms of U_b. Figures 6.4 and 6.5 show there is clearly some functional relationship between the fitting parameters and the model parameter U_b. To do this we look to figures 6.4 and 6.5 and attempt to derive a function to fit the data in each. The peak umbral field strength parameter, U_b, proved to be the most challenging to accurately fit (hence why there are more simulations for this parameter). Many functions were tested (e.g. exponents, logarithms, polynomials, asymptotic functions; and then more of each with varying degrees of freedom) to approximate $k(U_b)$ and $a(U_b)$, but

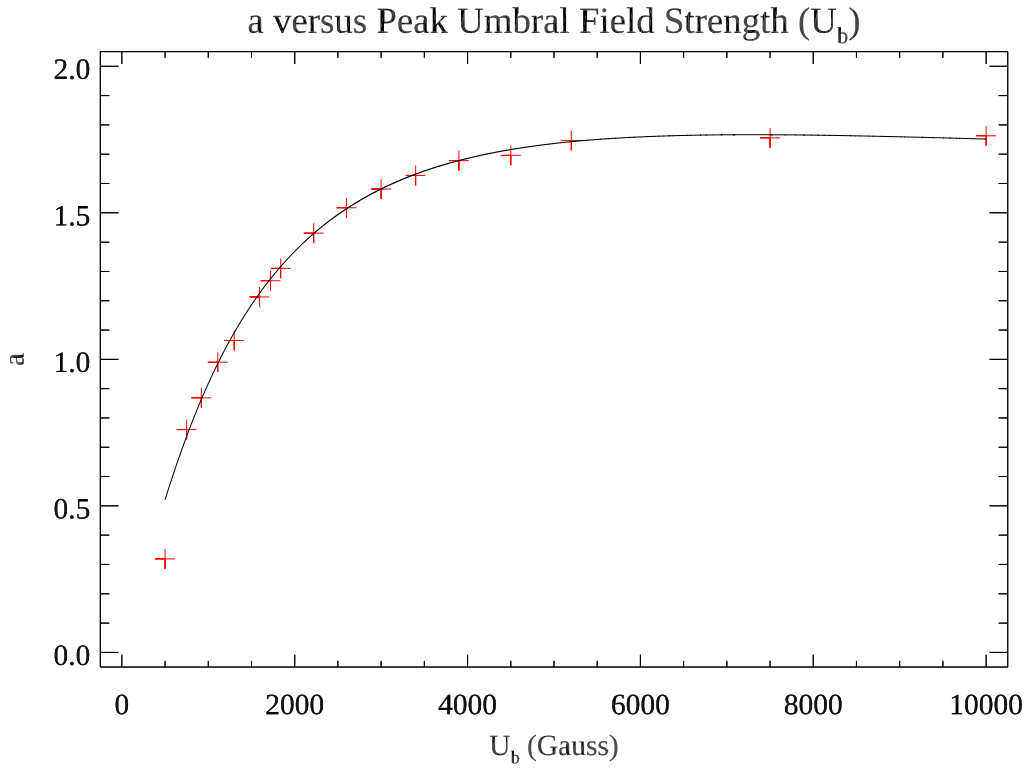

Figure 6.5: A plot showing the relationship between power-law fitting parameter, a, and independent sunspot model parameter, U_b. The red plus symbols depict the data-points for a tabulated in table 6.2 and the solid black line represents the interpolant described by equation 6.9.

the best agreement is found when fitting relatively low-order polynomial functions individually to $\ln k$ and $\ln a$ versus $\ln U_b$; the order of polynomial in best agreement with the data in each case produced functions of the form,

$$\ln k = c_1 + c_2 \ln U_b + c_3 \ln^2 U_b, \tag{6.6}$$

$$\ln a = c_4 + c_5 \ln U_b + c_6 \ln^2 U_b + c_7 \ln^3 U_b + c_8 \ln^4 U_b, \tag{6.7}$$

where $c_i \in \{c_j \,|\, j \in \mathbf{Z}, 1 \leq j \leq 8\}$ represent coefficients, which are consolidated into table 6.2 for convenience with respective uncertainties. With some algebraic manipulation of equations 6.6 and 6.7, we obtain the following definitions of $k(U_b)$

and $a(U_b)$ respectively,

$$k = \exp\left(\sum_{i=0}^{2} c_{i+1} \ln^i U_b\right) = \prod_{i=0}^{2} \exp\left(c_{i+1} \ln^i U_b\right), \tag{6.8}$$

$$a = \exp\left(\sum_{i=0}^{4} c_{i+4} \ln^i U_b\right) = \prod_{i=0}^{4} \exp\left(c_{i+4} \ln^i U_b\right). \tag{6.9}$$

In both equations 6.8 and 6.9 all coefficients (c_i) are again tabulated in table 6.2. The approximations represented by equations 6.8 and 6.9 are plotted on the power-law parameter data for $k(U_b)$ and $a(U_b)$ respectively in figures 6.4 and 6.5. These figures show that the agreement between the fit and the data in both cases is good and that the fitting functions do well in all regions of the U_b range. However, we do see that just beyond $U_b = 8000G$ both curves show a slight inflection implying a local minimum and maximum for $k(U_b)$ and $a(U_b)$ respectively. The data does not match this inflection and thus the fitting in this region should be interpreted with more caution; although, the size of the inflection in both cases is not very large and is essentially a result of non-linear polynomials attempting to approximate a relatively linear region of the data. Fortunately (as we shall see) when we derive the true energy increase form (equation 6.4) some of these limitations are softened by the introduction of non-linearity in the same region.

Combining equations 6.8, 6.9 and 6.3 gives us the desired scaling law expression where only the peak field strength, U_b, is varied; this equation is of the form,

$$\triangle E_b(\%) = \exp\left(\sum_{i=0}^{2} c_{i+1} \ln^i U_b\right) \theta^{\exp\left(\sum_{i=0}^{4} c_{i+4} \ln^i U_b\right)}, \tag{6.10}$$

where as previously, all coefficient values are given in table 6.2.

We stress that this is an empirical fit to the simulation results and the form of equation 6.10 is not intended to represent any underlying physical process. We must observe that in both attempts to fit functions to $k(U_b)$ and $a(U_b)$, the functional forms which were used have an arguably large number of free parameters, such that one may question to what degree are we over-fitting the data. To justify the

approach taken one should consider more deeply the motivation of what we are attempting to do with this work. In the grander scheme, beyond the scope of this thesis, this work aims to derive an expression from simulation data that could be used with observed sunspots to understand and predict their behaviour. Over-fitting the simulation data could therefore be detrimental if we intend to extrapolate beyond the range of the physical model sunspot properties. The typical peak (and typical statistical properties) magnetic field strength of sunspots is present within the literature (Tlatov and Pevtsov, 2014; Tlatov et al., 2019; Borrero and Ichimoto, 2011; Stix, 2002; Thomas and Weiss, 2004, 2008) and perhaps more importantly measurements of the strongest recorded magnetic field strengths are also present in the literature (Okamoto and Sakurai, 2018). The literature shows that the range of peak field strengths tested in this investigation extend well beyond the physical range of observed sunspots and hence the functional fits described by equations 6.8 and 6.9 can be expected to interpolate only. Hence given our fitting functions are smooth and suitably well behaved in the regions between any two data points, the limitations of the generous amount of freedom for the fitting functions is justified. If, however, the functions oscillated significantly between neighbouring data points, the validity of the fit would be questionable. A second point of caution must also be made; given one may fit a polynomial to any data-set given the polynomial is of degree one less than the number of data points, where polynomial fits are used in this chapter we will ensure that the order of the polynomial is at least half the number of data-points used to mitigate this over-fitting problem. In this example, a fourth-order polynomial is used to approximate $a(U_b)$ where the number of data points used is seventeen (hence the order of the fit is clearly less than half the number of points).

The final derivation to make is that of $\tau(U_b)$ as defined by equation 6.5. The τ data points can be calculated using the k and E_0 columns of table 6.1. Figure 6.6

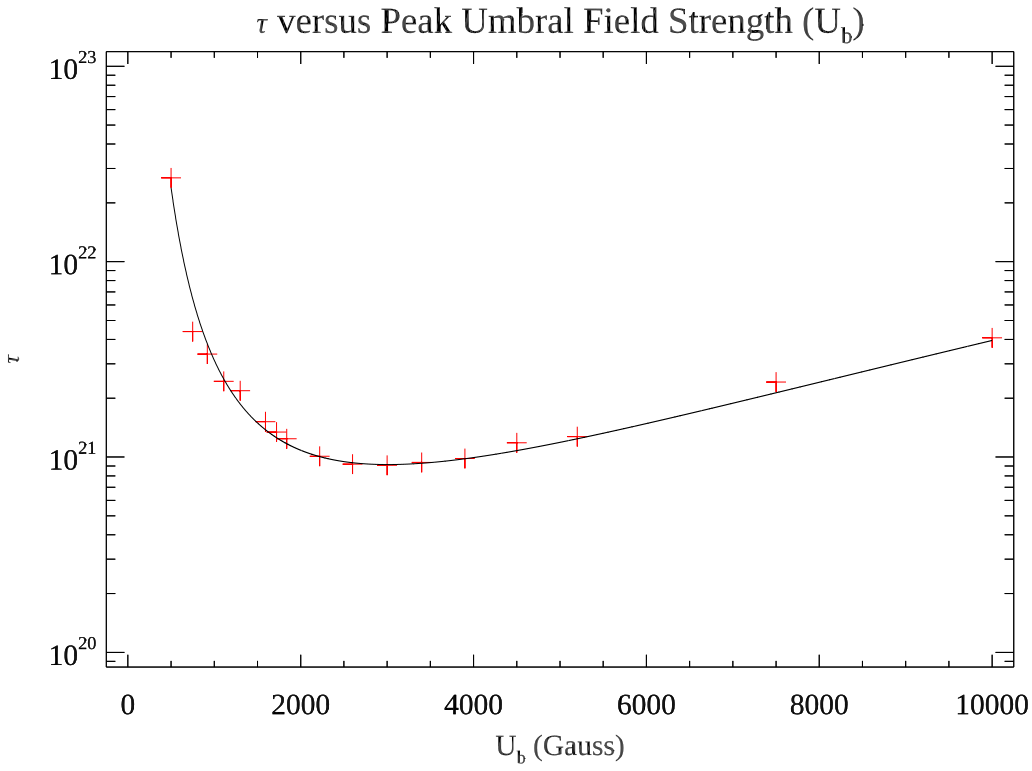

Figure 6.6: A plot showing the relationship between power-law fitting parameter, τ, and independent sunspot model parameter, U_b. The red plus symbols depict the data-points for τ derived as the product of column k and E_0 which are tabulated in table 6.2 and the solid black line represents the interpolant described by equation 6.12.

shows the $\tau(U_b)$ data-points plotted as a function of the peak umbral field strength (U_b) as red plus symbols; clearly the non-linear scaling of $E_0(U_b)$ has altered the monotonically decreasing $k(U_b)$ profile and has introduced a physical point of inflection in the data.

Given the task is to define an approximation function which can interpolate the $\tau(U_b)$ data-points and we know that $\tau(U_b)$ generally is a function of $k(U_b)$ (see equation 6.5), a logical choice of candidate fitting function is the same as that which was used to fit $k(U_b)$ given the only structural difference in the data is a result of a

quadratic scaling. In the same manner as the procedure followed for fitting $k(U_b)$, first we attempt to fit a second degree polynomial to the natural-logarithmically scaled data as described by,

$$\ln \tau = c_9 + c_{10} \ln U_b + c_{11} \ln^2 U_b. \tag{6.11}$$

Equation 6.11 is rearranged to give $\tau(U_b)$ as an explicit function of U_b as follows,

$$\tau = \exp\left(\sum_{i=0}^{2} c_{i+9} \ln^i U_b\right) = \prod_{i=0}^{2} \exp\left(c_{i+9} \ln^i U_b\right), \tag{6.12}$$

where $c_i \in \{c_j \,|\, j \in \mathbf{Z}, 9 \leq j \leq 11\}$ represent constant coefficients and are found in table 6.2. The solid-black line over-plotted on the $\tau(U_b)$ data represents the functional fit described by equation 6.12; clearly the level of agreement between the data and the fitted function is good and the relationship described by equation 6.12 not only interpolates the data well, but introduces a physically meaningful inflection in the relationship between $\tau(U_b)$ and U_b, the local minimum around $U_b = 3000G$ which is in excellent agreement with the trend suggested by the data-points.

Next we substitute the derived functional forms of $\tau(U_b)$ (equation 6.12) and $a(U_b)$ (equation 6.9) and eliminate both the corresponding terms in equation 6.4 to derive the true energy increase scaling relation as a function of the peak umbral field strength (U_b). This gives,

$$\triangle E_b(J) = \exp\left(\sum_{i=0}^{2} c_{i+9} \ln^i U_b\right) \theta^{\exp\left(\sum_{i=0}^{4} c_{i+4} \ln^i U_b\right)}, \tag{6.13}$$

or alternatively,

$$\triangle E_b(J) = \left(\prod_{i=0}^{2} \exp\left(c_{i+9} \ln^i U_b\right)\right) \theta^{\prod_{i=0}^{4} \exp\left(c_{i+4} \ln^i U_b\right)}, \tag{6.14}$$

where, again, $c_i \in \{c_j \,|\, j \in \mathbf{Z}, 9 \leq j \leq 11\}$ represent constant coefficients and are found in table 6.2.

Figure 6.7 shows a contour plot that connects peak umbral field strength (U_b), rotation and magnetic energy increase as dictated by equation 6.14. This plot has

Coefficient	Value	Uncertainty	Value
c_1	76.268231906637084	δc_1	0.0013147594708880096
c_2	-18.233942661012406	δc_2	0.00034226981217447792
c_3	1.0134805238349145	δc_3	2.2249858937671927e-05
c_4	17.770449876785278	δc_4	0.032351538957405175
c_5	-13.645062804222107	δc_5	0.016354823986659234
c_6	3.1955906748771667	δc_6	0.0030932837041895010
c_7	-0.29890487156808376	δc_7	0.00025941998683433440
c_8	0.0098554908763617277	δc_8	8.1396523311270170e-06
c_9	113.27521061571315	δc_9	0.0013147596788894577
c_{10}	-16.234174668090418	δc_{10}	0.00034226986293073921
c_{11}	1.0134956122637959	δc_{11}	2.2249861994645293e-05

Table 6.2: Table of coefficients for the data fits derived in this section.

four main, distinct regions of various physics. This top-left corner of this figure clearly shows that at relatively large values of U_b (say, $U_b > 4000G$), for small amounts of rotation (approximately $\theta < 100°$) that the contours in this figure are mostly vertical. This implies that the magnetic energy generation potential of rotating sunspots in this range, very clearly more heavily relies on rotation rather than overall magnetic field strength. This result is interesting as one may expect that stronger magnetic field sunspots might tend to be able to readily produce more free magnetic energy, however, in the limit of relatively small amounts of rotation this does not seem to be true (with the caveat that what we are interested in here is order of magnitude energy increases). The top-right region of figure 6.7 (where $U_b > 4000G$ and $\theta > 100°$) shows that as the amount of rotation increases the dominant importance on rotation along for the additional generation of magnetic energy begins to lessen and the overall umbral field strength begins to gain importance. The contours found in the top-right corner show that at such large rotations and umbral field strengths, the two properties become comparably important. The third important region of figure 6.7 is that where $U_b < 1000G$ and $0° \leq \theta \leq 200°$. In this

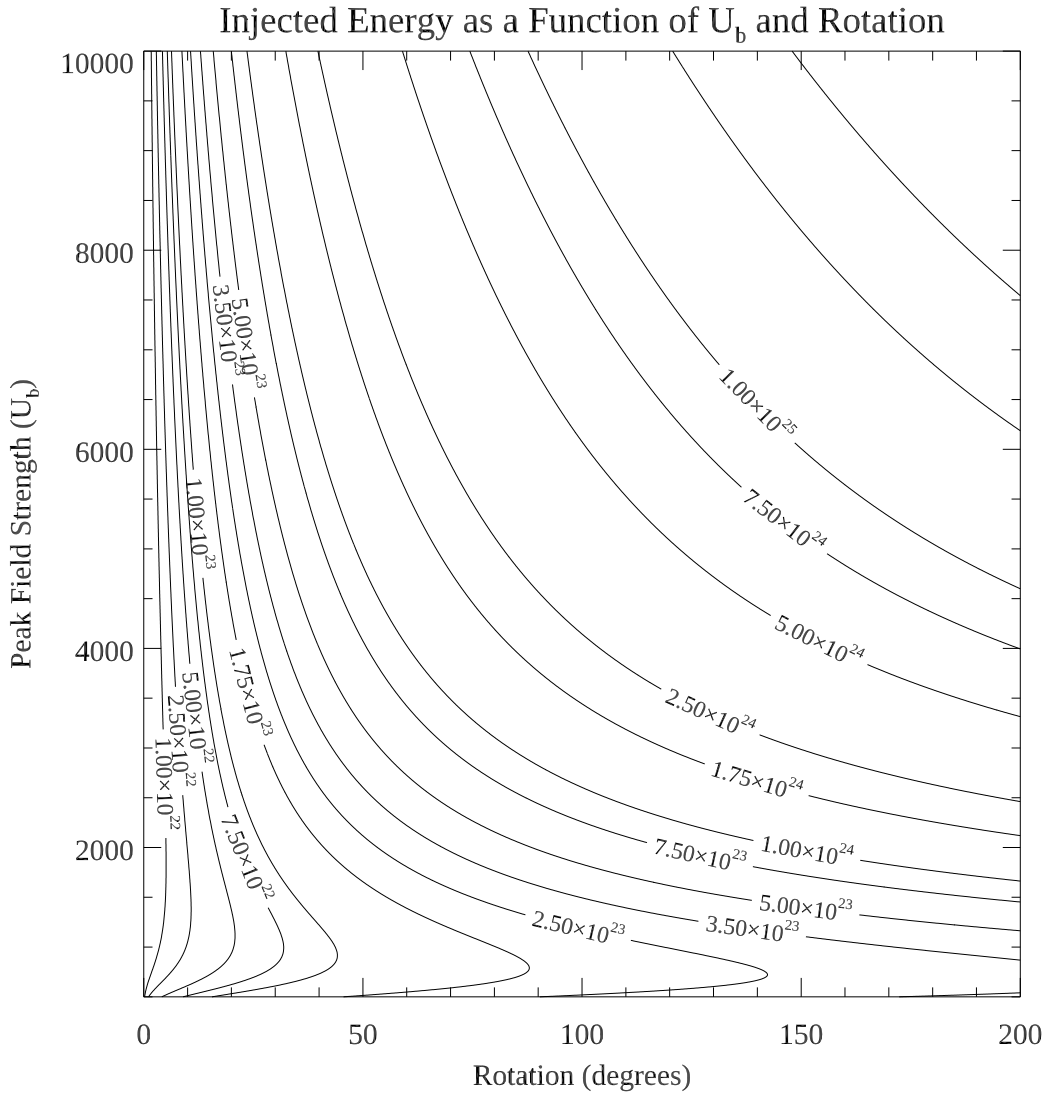

Figure 6.7: A contour plot of the injected magnetic energy as a function of peak umbral field strength (U_b) and rotation. Each contour label shows the numeric value of magnetic energy measured in joules.

region we see complex behaviour regarding any dominant importance of either the rotation or the peak umbral field strength. There seems to be an increase in the energy generation potential of rotating sunspots as the peak umbral field strength begins to vanish (i.e. where $U_b < 750G$). This may be because the Alfvén speed begins to vanish with the diminishing magnetic field strength and hence stresses in

the magnetic introduced by the rotation of the sunspot may be injected at a quicker rate than they are redistributed through the field, causing a build up. This additional magnetic energy generation effect could alternatively be caused by a poor fit of the fitting function to the data in this range. The $U_b = 500G$ data point in figures 6.5 and 6.6 respectively show that the fits to this simulation are over-approximated for parameter a and under-approximated for parameter τ; of the two parameters, a seems the most inaccurately represented and is almost double what its actual data point would suggest it ought to be. Given parameter a is the exponent of the rotation, it is reasonable to assume that by overestimating this exponent we artificially introduce additional importance to the rotation of the sunspot which may explain the increased magnetic energy generation in this range. However, the data point for $U_b = 750G$ is relatively well captured by the functional fits and hence from this point we shall encourage caution in interpreting predictions using this work for sunspots with peak umbral field strengths less than $750G$.

The fourth, and perhaps the most important, region of figure 6.7 is that where $1000G \leq U_b \leq 4000G$ and $0^\circ \leq \theta \leq 200^\circ$. This is the region where most real observed sunspots exist (however, there are a few recorded at high as $U_b \approx 6000G$). What we see in this range is a crossover of importance between rotational dominance and peak field strength dominance for the generation of additional magnetic energies. For the strongest magnetic fields, the peak umbral field strength (U_b) has lesser importance than for the weaker field strengths in general for all rotation value. For all field strengths in this region below approximately 50° of rotation the peak field strength is almost irrelevant as compared to the cumulative rotation, however, between $50^\circ < \theta < 100^\circ$ of rotation the importance of the peak umbral field strength begins to increase such that its importance is comparable to the net rotation. When θ becomes greater than 100° (in this field strength band) we see very clearly that we have transitioned almost completely to a regime where the net rotation has become

less significant and the primary means to increase the injected magnetic energy is to increase the peak umbral field strength (U_b). This region of figure 6.7 is of fundamental importance because it implies that, if true for real sunspots, there may be a limit to the order of magnitude of free magnetic energy one can introduce into a secular sunspot system (reached at a field strength dependent rotation value). If this is valid, then prediction of the potential dangers of rotating sunspots may be simplified and potential risk classification may be able to be based on a sunspots immediate magnetic field properties; i.e. small weak field sunspots may be considered very unlikely to produce x-class solar flares, but possibly somewhat likely to eventually produce a m-class flare for example.

A result of fundamental importance that is highlighted by figure 6.7 is that the problem of sunspot rotation must not simply be broken down into important geometrical, magnetic or rotational properties for some model sunspot, but we must also consider how much rotation has occurred. This is because the magnetic energy generation properties of a rotating sunspot not only rely on characteristic properties of a sunspot but the reliance on each property clearly evolves as the sunspot continues to rotate.

6.2.2 Sunspot Size - P_r

In this section we analyse the influence of the model parameter P_r, which represents the radius of a model sunspot. The batch of simulated model sunspots analysed in this section vary in their overall size, but the ratio of umbral to penumbral radii is maintained at $\psi = 0.5$, so the umbra scales in proportion to the sunspot. This means that total flux of the each model sunspot is scaled by varying the radius. A secondary influence on the evolution of magnetic energy, as a result of the varied radii of each sunspot, is the initial plasma properties in each key region of the sunspot (i.e. the umbral and penumbral regions). When the radius of the sunspot

is increased the potential magnetic field solution, which initialises each simulation, will inevitably trace different heights of the domain. We may expect larger natural sunspots to have closed penumbral magnetic fields which reach higher into the solar atmosphere.

The physical meaning of the parameter discussed in this section (the sunspot radius) is of obvious physical importance, as the size of a sunspot is a measurable property (Tlatov and Pevtsov, 2014; Tlatov et al., 2019) which we may use to relate the model presented in this work to observations of rotating sunspots. The overall size of a sunspot also relates to more commonly measured total area and total flux (in combination with field strength properties). However, in this section we shall derive a scaling relation in terms of the radii of the model sunspots. We chose the radius for two main reasons: firstly, it proved to give a simpler scaling relation and secondly, with a radius based scaling relation we may analytically derive scaling relations for sunspot area or total flux (with knowledge of our model magnetic field), if required.

	Model Parameters						Power-Law Fit Parameters						Initial Energy
Sim	$U_b(G)$	μ	$U_r(Mm)$	$P_r(Mm)$	$\omega^\circ \mathrm{hr}^{-1}$	γ	k	δk	a	δa	$\theta_1(^\circ)$	$\theta_2(^\circ)$	E_0(Joules)
20	1300	0.5	2.5	5.0	48	1	0.0602401	1.8e-6	1.2351285	6.3e-6	95	120	2.5782e+23
21	1300	0.5	3.75	7.5	48	1	0.0788598	1.3e-6	1.1602900	3.4e-6	110	120	8.5315e+23
1	1300	0.5	5.0	10.0	48	1	0.1096677	9.0e-6	1.064389	1.8e-5	70	130	1.9926e+24
22	1300	0.5	6.25	12.5	48	1	0.1756820	1.9e-6	0.9489328	2.4e-6	80	90	3.8305e+24
23	1300	0.5	7.5	15.0	48	1	0.3129006	2.3e-6	0.7998819	1.7e-6	75	80	6.5245e+24
24	1300	0.5	8.75	17.5	48	1	0.658042	6.9e-5	0.625098	2.6e-5	55	60	1.0177e+25

Table 6.3: A table of the simulations used to investigate the parameter P_r with $\psi = \frac{U_r}{P_r} = 0.5$ for all simulations.

Table 6.3 shows the simulation properties for the batch of simulations used to derive a scaling law for the sunspot radius, P_r. All parameters except P_r and U_r (which varies in proportion to P_r) take the simulation values of simulation 1. Figure 6.8 shows a multi-line plot of the percentage magnetic energy increase versus rotation for the batch of simulations tabulated in table 6.3. This shows that the amount of time for the penumbra to reach the top of the numerical domain increases as the sunspot radius reduces. The phenomenon is likely a consequence of the larger sunspot's penumbral magnetic fields initially reaching higher into the numerical domain, thus hence having lesser distance to travel before reaching the top of the domain.

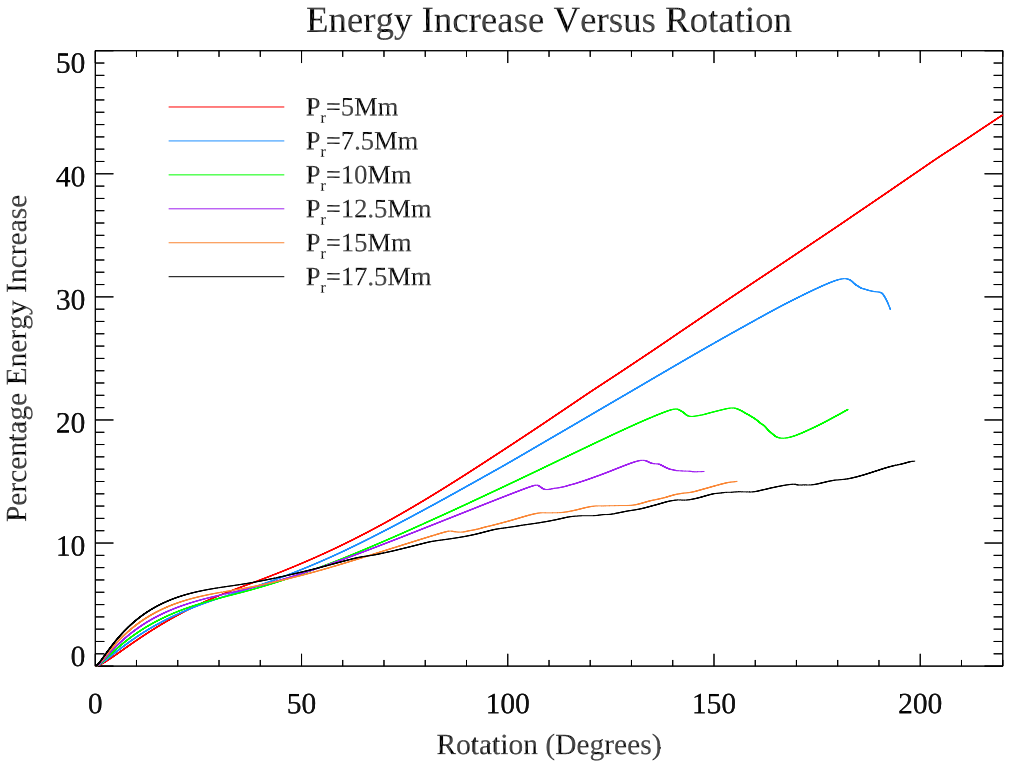

Figure 6.8: A multi-line plot showing the percentage magnetic energy increase versus rotation curves for the simulations which vary penumbral radius (P_r) and the umbral radius (U_r) in proportion.

Figure 6.8 shows that after the acceleration-phase ($\theta > 32°$) the percentage magnetic energy change tends to increase at very different rates. There is a clear monotonic relationship, where the smaller the sunspot the more the percentage change of magnetic energy and vice-verse for larger sunspots. This is confirmed by table 6.3 where we see that the power-law exponent (a) shows that the power-law description of percentage magnetic energy increase is super-linear for $P_r \leq 10Mm$ and sub-linear for $P_r > 10Mm$. This behaviour of the exponent parameter (a) explains the varied gradient characteristic shown in figure 6.8. Conversely, during the acceleration-phase ($\theta < 32°$) we observe the opposite behaviour to that seen during the main-phase of the simulations, specifically that the order of largest energy increase has changed to the largest sunspots having the greatest percentage magnetic energy increase. We do not intend to understand the specifics of the acceleration-phase in this work, but highlight several mechanisms that may explain the observed behaviour below.

Because we investigate sunspots with similar magnetic geometries in this section (and chapter 5 shows that the penumbra hosts most of the magnetic energy during the acceleration phase) we know that the larger sunspots have larger penumbral field regions, and therefore consequently the larger sunspots may induce greater start-up effects (due to having larger penumbra). Alternatively, the size of the start-up effects may be a result of the initial penumbral magnetic fields tracing different regions of the solar atmosphere. Hence, the accelerations caused by the Euler forces during the acceleration-phase may vary between sunspots because the regions being accelerated have different densities. Or finally, perhaps the variation is a manifestation of the driver, which for larger sunspots ramps down more gently from maximum rotation rate at the end of the umbral region to zero, just beyond the penumbral boundary. Irrespective of the cause, we are able to capture this effect in the power-law parameter fits and thus reflect them in our scaling relations.

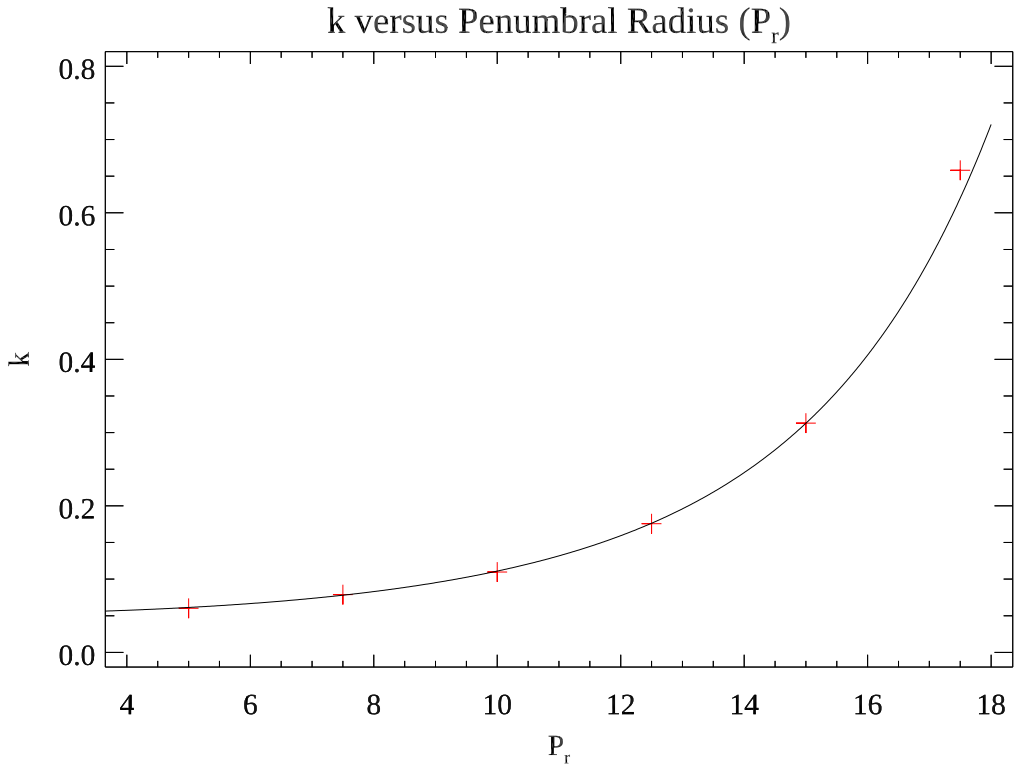

Figure 6.9: A plot showing the relationship between power-law fitting parameter, k, and independent sunspot model parameter, P_r. The red plus symbols depict the data-points for k tabulated in table 6.4 and the solid black line represents the interpolant described by equation 6.15.

Figures 6.9, 6.10 and 6.11 show, respectively, plots for k, a and τ versus P_r, where τ maintains the meaning it was given in section 6.2.1 but as a function of P_r rather than U_b. Figure 6.9 shows that as P_r is increased, k increases monotonically and non-linearly. Figure 6.10 shows that as P_r increases a decreases monotonically and non-linearly. Finally figure 6.11 shows that as P_r increases τ increases monotonically and non-linearly. We are able to fit the data in these figures with relatively simple fitting functions. We find that the forms given by equations 6.15, 6.16 and 6.17 fit the data in figures 6.9, 6.10 and 6.11 respectively where $d_i \in \{d_j \,|\, j \in \mathbf{Z}, 1 \leq j \leq 8\}$

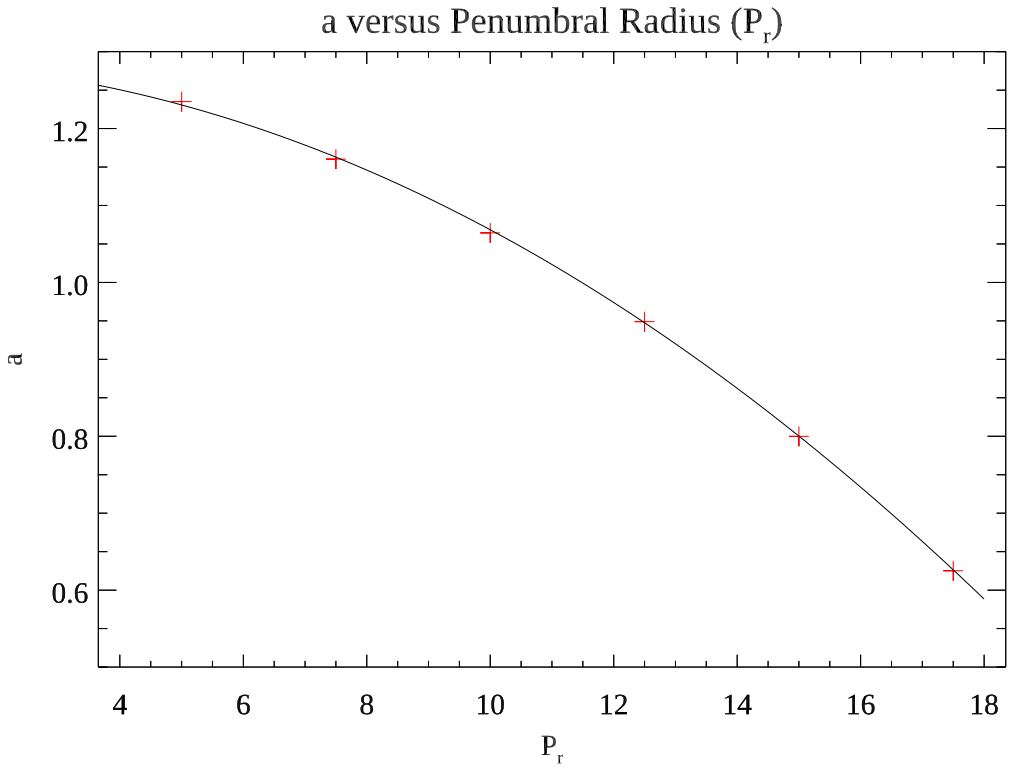

Figure 6.10: A plot showing the relationship between power-law fitting parameter, a, and independent sunspot model parameter, P_r. The red plus symbols depict the data-points for a tabulated in table 6.4 and the solid black line represents the interpolant described by equation 6.16.

represent constant-value coefficients and are tabulated in table 6.4.

$$k = e^{d_1 + d_2 P_r + d_3 P_r^2}, \tag{6.15}$$

$$a = d_4 + d_5 P_r + d_6 P_r^2, \tag{6.16}$$

$$\tau = e^{d_7 + d_8 P_r}. \tag{6.17}$$

Figures 6.9, 6.10 and 6.11 show that the fits to the data capture the general trends and for the most part the agreement between the fits and the data is excellent for all three parameters. Equations 6.15 and 6.16 show that the largest order polynomial fit to any of the data sets used in this section is two, which is clearly much smaller

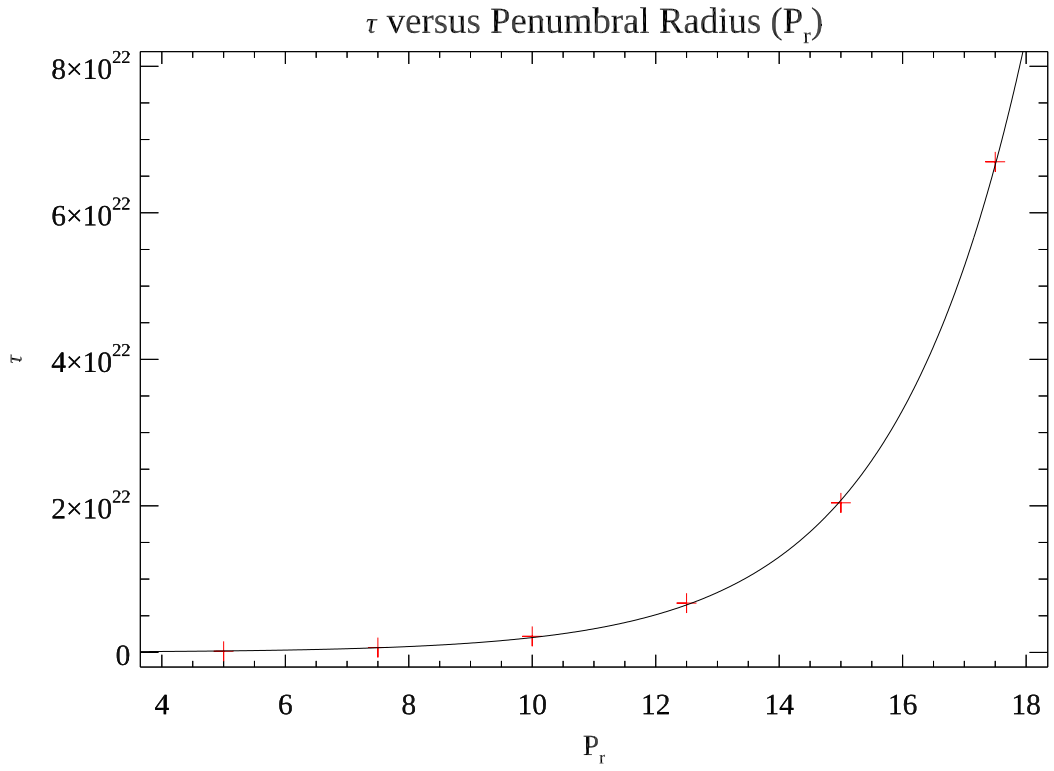

Figure 6.11: A plot showing the relationship between power-law fitting parameter, τ, and independent sunspot model parameter, P_r. The red plus symbols depict the data-points for τ derived using data tabulated in table 6.4 and the solid black line represents the interpolant described by equation 6.17.

than the number of points used and ought not to represent over-fitting. A point of interest here is that we are able to apply a functional form with fewer parameters for the true magnetic energy parameter (τ) than for the percentage magnetic energy parameter (k), without loss of quality of the fit. The fits to the data for a and τ yield an empirical equation for the energy increase versus rotation, as a function of penumbral radius. This is of the form,

$$\triangle E_b(J) = e^{d_7+d_8P_r}\theta^{d_4+d_5P_r+d_6P_r^2}, \tag{6.18}$$

where, again $d_i \in \{d_j \,|\, j \in \mathbf{Z}, 4 \leq j \leq 8\}$ in equation 6.18 represent constant-value coefficients and are tabulated in table 6.4.

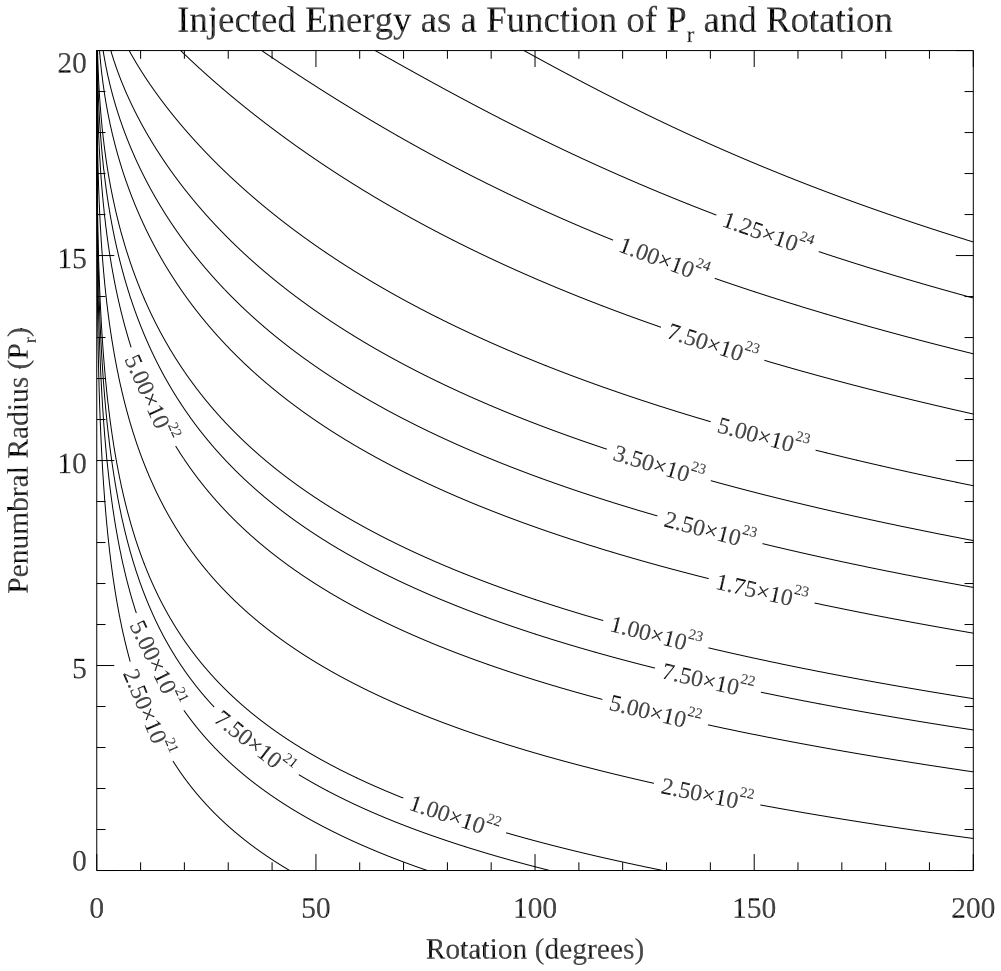

Figure 6.12: A contour plot of the injected magnetic energy as a function of penumbral radius, P_r(Mm), and rotation. Each contour label shows the numeric value of magnetic energy measured in joules.

Figure 6.12 shows a contour plot which highlights the behaviour of equation 6.18. It has two main regions of physical importance, first the left most portion of the figure (where $\theta < 30°$) shows the first region of physical importance. In this region we observe that the best means to increase magnetic energy is, primarily, to introduce rotation into the system regardless of sunspot size. This is highlighted by

the largely vertical nature of the contours in this region.

The second region of physical importance is where $\theta \geq 30$, in this region we see a complete regime change from that at low rotations. For relatively large amounts of rotation we see that the primary way to introduce significantly more magnetic energy is to increase the size of the model sunspots rather than try to gain additional energies from more rotation. However, rotation always acts to increase the magnetic energy of all the rotating sunspots.

This scaling law (equation 6.18) will gain more physical relevance when we combine it with the other scaling relations derived in this chapter. Specifically, with this and the scaling law derived for the overall sunspot magnetic field strength (U_b), given by equation 6.14, we can already perform meaningful analyses, as the overall size and magnetic field strength of a sunspot are both measurable features and together represent the total flux of a sunspot. In nature, the size of a sunspot and its magnetic field strength are typically correlated, the larger the sunspot the stronger the peak magnetic flux (Li et al., 2001a). Figure 6.12 shows that none of the sunspot sizes in our range are able to reach X-class flare energy requirements (around 10^{25} j) with the relatively weak peak umbral field strength used, but if we were to combine this scaling relation with the peak field strength scaling relation we would expect to see larger energies in an equivalent figure.

Coefficient	Value	Uncertainty	Value
d_1	-2.9414406645738040	δd_1	8.2290437784588135e-05
d_2	-0.014341048089690389	δd_2	1.6084230969543784e-05
d_3	0.0088638764187347618	δd_3	7.2852670959905018e-07
d_4	1.2869781210167730	δd_4	1.8079192694333740e-05
d_5	-0.00066157160472357646	δd_5	3.5655851358678892e-06
d_6	-0.0021193534082137866	δd_6	1.6224694552182560e-07
d_7	44.400029189107499	δd_7	2.5595554984845828e-05
d_8	0.46583018072843174	δd_8	1.9129219617678606e-06

Table 6.4: Table of coefficients for the data fits derived in this section.

6.2.3 Rotation Rate - ω

In this section we investigate the influence of a sunspot's rotation rate (ω) on the generation of magnetic energy. Rotation rate is a defining property of rotating sunspots and therefore is one of the most important parameters analysed in this work. In this investigation we measure rotation rate in degrees per hour for easier comparison to observational literature of rotating sunspots (Brown et al., 2003; Yan et al., 2008; Walker, 2018; Grimes et al., 2020). Typical observed values of sunspot rotation rates are in the range $0 - 10^{\circ}\,\mathrm{h}^{-1}$ (Brown et al., 2003; Walker, 2018; Brown and Walker, 2021) but larger values of tens of degrees per hour, for short intervals, are present within the literature (Grimes et al., 2020; Bi et al., 2016; Li and Liu, 2015).

Given that the investigation and scaling-laws in general are concerned with cumulative rotations, we may ask what may we expect by varying the rotation rate, other than simply varying when we reach a particular net rotation.

In chapter 5 we find that there are magnetic energies within the domain that are stored on relatively long time-scales and others which are not. The dynamically introduced magnetic energy we see in the simulations, is a consequence of being far from the force-free state; simply there may be additional magnetic energy due to forces on (and thus accelerations of) the plasma and coupled magnetic field. We observe various cases of this behaviour in several simulations in the wider study, but a clear example is where the start-up effects are more severe. Many examples of this are presented in the appendices.

Figure 6.13 shows a simulation with a relatively large start-up effect. For this simulation the acceleration-phase ends at 32° and clearly the impact of start-up are much longer lived. During the acceleration-phase the magnetic energy increases with additional rotation. After the acceleration-phase, we see that the magnetic energy in the system begins to decay until it tends to a new evolutionary profile

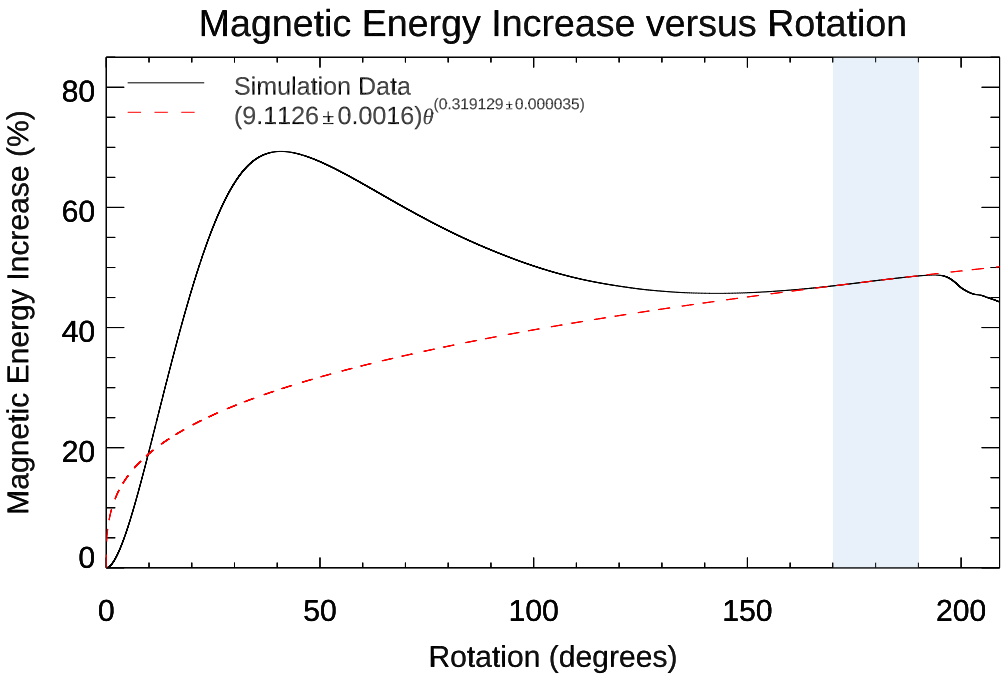

Figure 6.13: The percentage increase of magnetic energy versus rotation evolution for simulation number 3, a low peak field strength simulation from the U_b investigation. The solid-black curve shows the measured magnetic energy from the simulation data and the dashed-red curve the power-law approximation based on the, post-acceleration, main-phase of the simulation.

(approximated by the red-dashed curve). It is clear that some of the magnetic energy introduced into the domain during the acceleration-phase is stored, but a large portion is dynamic in nature and hence dissipates (or leaves through to upper boundary of the domain) after the acceleration-phase. If all the magnetic energy introduced by rotation in this system were stored, we would not expect to see a reduction in the magnetic energy, given all we are doing to the sunspot is rotating in one direction. Figure 6.13, and the discussion above, implies that there are energies which are present as a result of additional forces in the domain; during the acceleration-phase we have the contribution from the Euler force, which may be the dominant cause of this additional energy. However, during the main-phase of the

simulations, we rotate constantly and thus do not have this Euler force.

In this investigation we try to exclude start-up effected data as best we can, but given we drive the model sunspots we will perturb the systems further from a quasi-static force-free evolution as we reach greater rotation rates. At the quasi-static force-free limit we expect the Lorentz force to dominate the other forces and also to vanish (i.e. the gradient of magnetic pressure balances magnetic tension), at this limit we would not get contributions to the total magnetic energy from dynamic sources given the system is without net forces (it is at pseudo-rest).

Thus, as we drive each sunspot, and move away from the quasi-static limit, we may alter the importance of forces which may introduce additional (dynamic) magnetic energy and acknowledge that some of these forces may scale with increased rotation rate and hence their respective contribution to the dynamic magnetic energy may alter with rotation rate.

Figure 6.14 shows that as rotation rate is increased the amount of magnetic energy in the domain generally increases. For this model parameter (ω) all the sunspots which are driven have identical magnetic geometries and so each simulation starts from the same initial potential field, hence the percentage magnetic energy increase shown in figure 6.14 is simply a scaled version of the true magnetic energy increase. Each simulation's penumbra hits the top of the domain at approximately the same amount of rotation ($140^\circ < \theta < 145^\circ$); though the slowest rotating sunspots were too computationally expensive to allow to reach their natural ends, but we have no reason to expect the trend present to differ for these simulations.

If we make the assumption that the slowest rotating sunspots also have aligned end rotation values, then we may conclude that the cumulative rotation required for a model penumbra to expand and reach the top of the numerical domain is independent of rotation rate for physically reasonable values of ω.

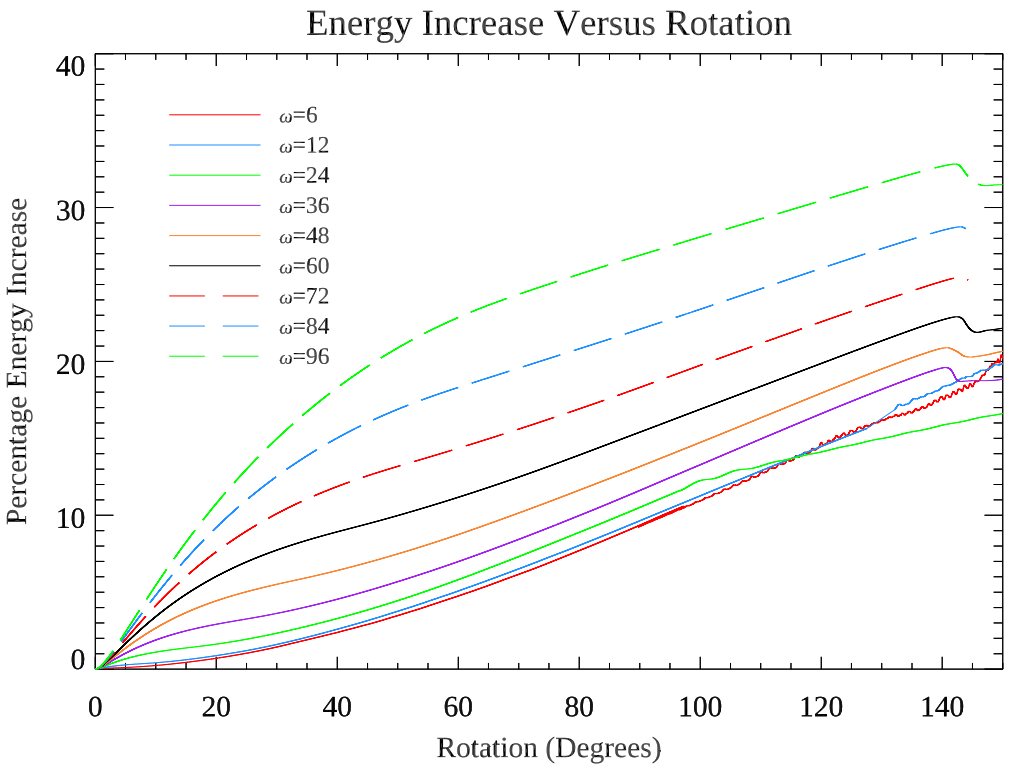

Figure 6.14: A collection of line plots each showing the evolution of the measured percentage increase of magnetic energy versus rotation, the legend shows the rotation rate of each simulation where the value is given in units of degrees per hour.

	Model Parameters						Power-Law Fit Parameters						Initial Energy
Sim	$U_b(G)$	μ	$U_r(Mm)$	$P_r(Mm)$	$\omega^\circ \mathrm{hr}^{-1}$	γ	k	δk	a	δa	$\theta_1(^\circ)$	$\theta_2(^\circ)$	E_0(Joules)
25	1300	0.5	5.0	10.0	6	1	4.23146e-3	2.6e-7	1.714628	1.6e-5	10	85	1.9926e+24
26	1300	0.5	5.0	10.0	12	1	8.2942e-3	1.4e-6	1.567389	3.8e-5	50	110	1.9926e+24
27	1300	0.5	5.0	10.0	24	1	1.43833e-2	1.4e-6	1.465987	2.3e-5	50	95	1.9926e+24
28	1300	0.5	5.0	10.0	36	1	3.68952e-2	2.3e-6	1.278152	1.4e-5	70	100	1.9926e+24
1	1300	0.5	5.0	10.0	48	1	0.1096677	9.0e-6	1.064389	1.8e-5	70	130	1.9926e+24
29	1300	0.5	5.0	10.0	60	1	2.79564e-1	1.8e-5	8.90491e-1	1.4e-5	100	120	1.9926e+24
30	1300	0.5	5.0	10.0	72	1	6.68256e-1	2.3e-5	7.351699e-1	7.4e-6	105	120	1.9926e+24
31	1300	0.5	5.0	10.0	84	1	1.442608	5.2e-5	0.6043803	7.5e-6	110	125	1.9926e+24
32	1300	0.5	5.0	10.0	96	1	3.50978	5.2e-4	4.51327e-1	3.1e-5	100	130	1.9926e+24

Table 6.5: A tabulated record of the simulations used throughout section 6.2.3 and their associated properties.

Table 6.5 shows the simulation parameter values used for the batch of simulations which are used to investigate the nature of the rotation rate of sunspots (ω). Varying the rotation rate also causes the acceleration profile to scale accordingly during the start-up phase, though the duration of the acceleration phase is maintained across all rotation rates. All other simulations that investigate other model parameters have the same acceleration properties. The acceleration-phase is chosen to be 100 simulation time-units (which is ≈ 4820 seconds) regardless of the final rotation rate. This means that the Euler force, which is only present during the acceleration-phase, will be diminished for slower rotating sunspots and strengthened for those that rotate more quickly. This is why the fitting ranges shown in table 6.5 vary so significantly. The data presented in table 6.5 is presented graphically in figures 6.15-6.17.

Table 6.5 highlights that individually the k and a parameters have a broad range of values, spanning multiple orders of magnitude. However, owing to the highly similar structure of the evolution of each simulation in this batch (figure 6.14), we find that we are able to fit relatively simple functions to both k and a versus ω, and given for this parameter all simulations have equal initial magnetic energies, we fit the same function to τ versus ω as we do for k (with scaled coefficients). We find that a versus ω is able to be fitted with a linear function, figure 6.16 shows that the linear fit captures the essence of the data-points throughout the entire ω range. We find that we are able to fit an exponential function to both k and τ versus ω, however, these fits both clearly better agree with the data for smaller rotation rates, but still comfortably capture the trend of the data. The $96°\text{hr}^{-1}$ data-point (for both k and τ) is the one which is in least agreement with the fitted curve, but still lies within $\sim 10\%$ error of the approximation.

However, $96°\,\text{h}^{-1}$ is well in excess of the fasted observed sunspot rotation rate, so some uncertainty here has minimal practical implications. It appears that there

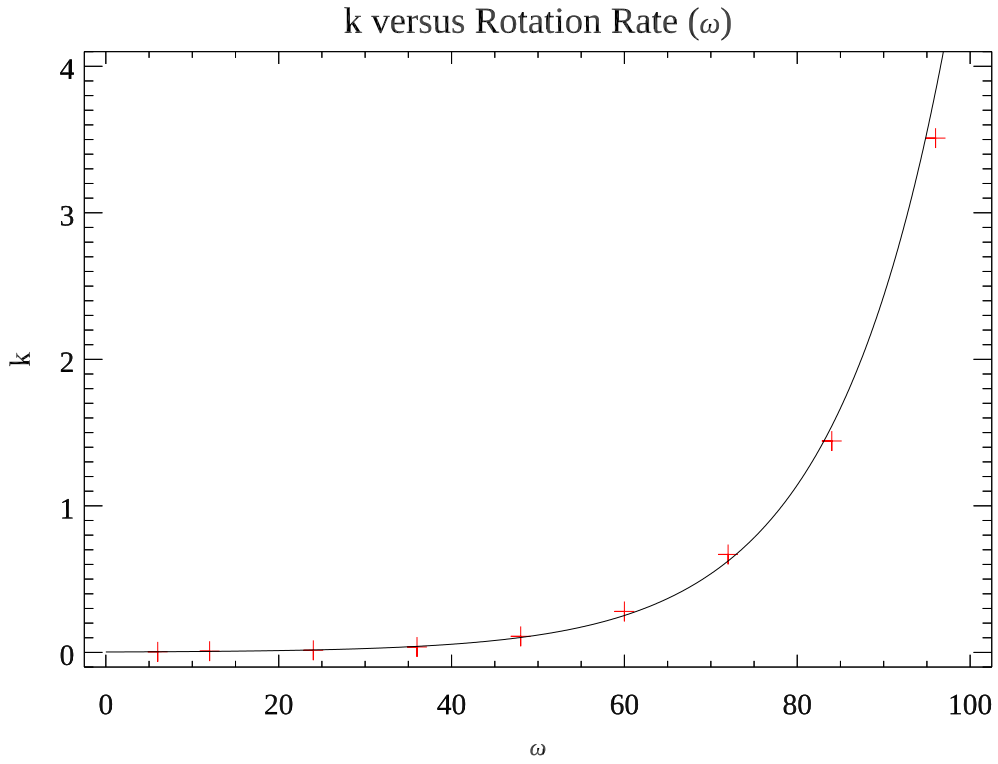

Figure 6.15: A plot showing the relationship between power-law fitting parameter, k, and independent sunspot model parameter, ω. The red plus symbols depict the data-points for k tabulated in table 6.6 and the solid black line represents the interpolant described by equation 6.19.

is an increasing agreement between the fitted function and the data-points as ω reduces, and hence one may assume greater safety extrapolating towards $\omega = 0$. The fitting functions are of the form,

$$k = e^{f_1 + f_2 \omega}, \tag{6.19}$$

$$a = f_3 + f_4 \omega, \tag{6.20}$$

$$\tau = e^{f_5 + f_6 \omega}, \tag{6.21}$$

where $f_i \in \{f_j \,|\, j \in \mathbf{Z}, 1 \leq j \leq 6\}$ in equations 6.19 - 6.21 represent constant coefficients which are tabulated and presented in table 6.6. A key result of these

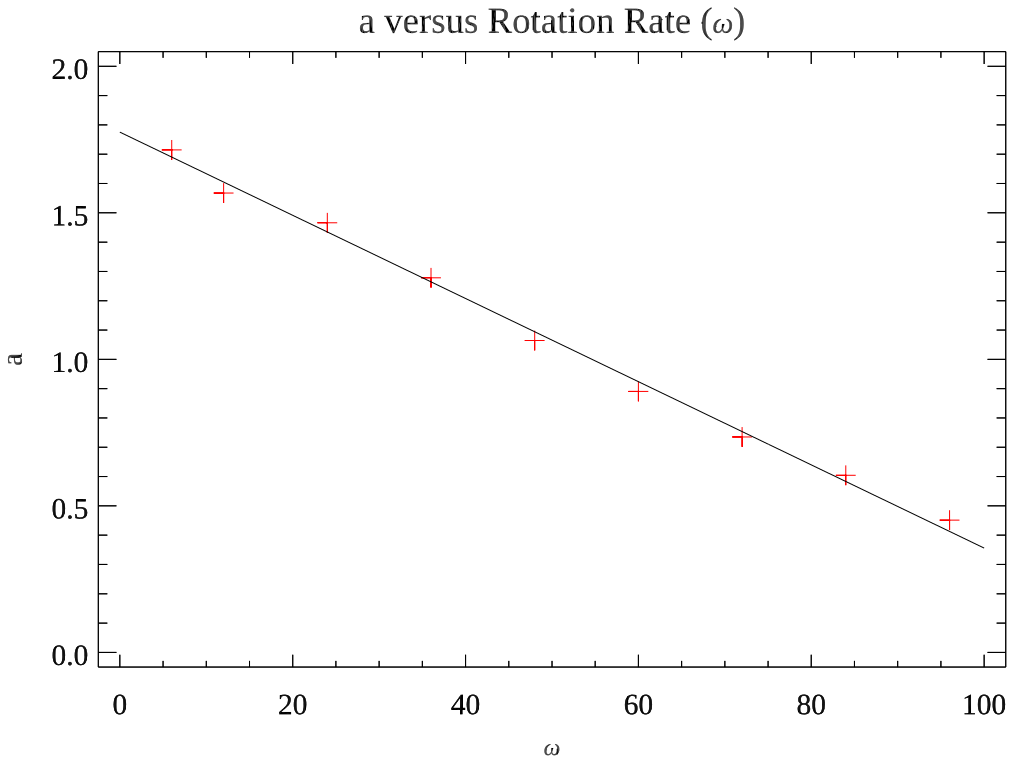

Figure 6.16: A plot showing the relationship between power-law fitting parameter, a, and independent sunspot model parameter, ω. The red plus symbols depict the data-points for a tabulated in table 6.6 and the solid black line represents the interpolant described by equation 6.20.

functional fits is evident in the specific values of the coefficients in table 6.6, we observe that any coefficient which is multiplied by ω in equations 6.19-6.21 is noticeably small in comparison to those which are not. A point of interest here is how large must ω be before it meaningfully alters the magnetic energy evolution. We observe that for the k and a power-law parameters, relatively large rotation rates are required to simply make the coefficient product with ω of the same order as the remaining coefficients, and for τ one would need an ω value of several hundred degrees per hour to make the product of $f_6\omega$ match f_5 in magnitude.

The weak scaling with ω is interesting for two main (related) reasons. Firstly, we

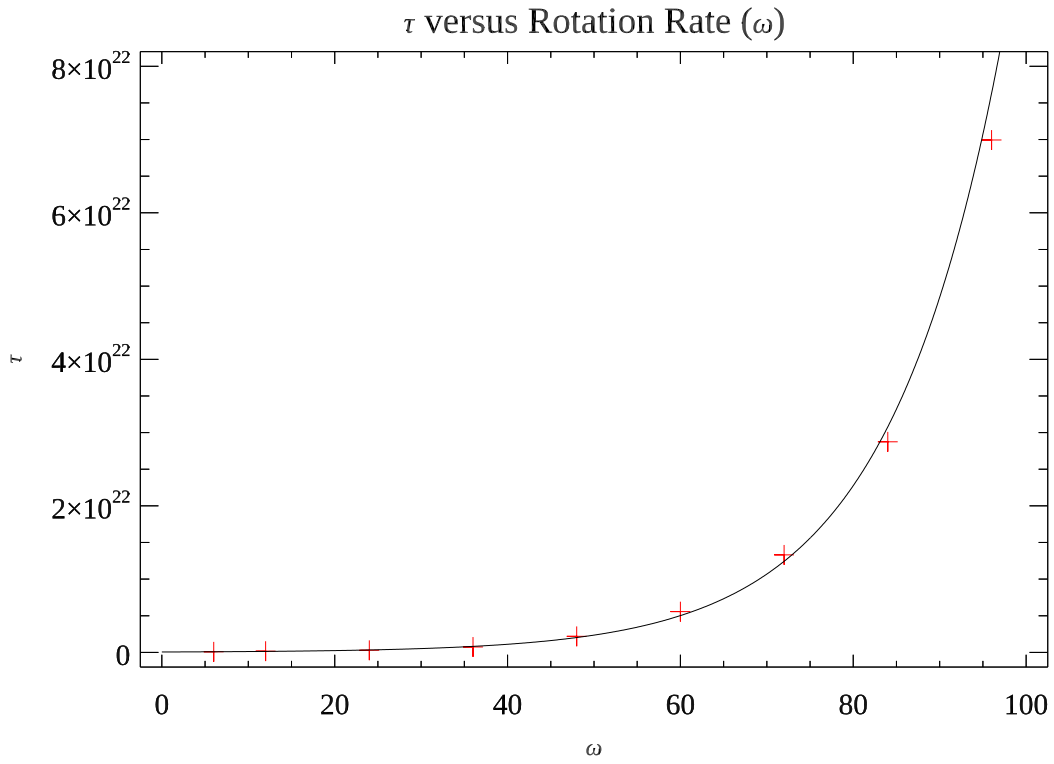

Figure 6.17: A plot showing the relationship between power-law fitting parameter, τ, and independent sunspot model parameter, ω. The red plus symbols depict the data-points for τ calculated using data tabulated in table 6.6 and the solid black line represents the interpolant described by equation 6.21.

may expect from this result that for more commonly observed, relatively modest, rotation rates $(0-10^{\circ}\,\mathrm{h}^{-1})$ the rotation rate itself plays very little role in the energy evolution of the system, and the cumulative amount of rotation is far more significant than how quickly it is achieved. We are able to derive an empirical equation to describe the energy introduced into the system as a function of the model parameter, ω. This gives,

$$\triangle E_b(J) = e^{f_5+f_6\omega}\theta^{f_3+f_4\omega}, \tag{6.22}$$

where $f_i \in \{f_j \,|\, j \in \mathbf{Z}, 1 \leq j \leq 6\}$ are presented in table 6.6. We see that in the

limit that ω vanishes, we are still left with a meaningful equation for the energy generation properties of rotating sunspots and that for rotating sunspots we may be able to use the ω vanishing limit to approximate a quasi-static evolutionary limit for a given rotating sunspot. This result may become much more powerful when combined with the other scaling relations, derived in this chapter, as it suggests a means to approximate as close to a force-free evolution as is possible for this model under the MHD framework, rather than a dedicated force-free approach. However, this is outside the aims of this investigation and is deferred for future studies.

Figure 6.18 shows a contour plot of the injected magnetic energy of the model rotating sunspots as a function of rotation and rotation rate as described by equation 6.22. This shows that the cumulative rotation is more important than the rotation rate (ω), as a mechanism for the injection of additional magnetic energy over all of rotation rate space. We observe that (as we saw for the scaling equations) for relatively small rotation rates ($\omega < 20°\text{hr}^{-1}$) that there is little additional energy to be gained by rotating the model sunspot more quickly. However, for the largest ω values, rotation rate is able to achieve between double and triple the amount of magnetic energy in the domain. In order to power large solar flares, we would need an order of magnitude or more difference between the quasi-static limit and the upper limit of $100°\text{hr}^{-1}$ (which already exceeds the largest reported observed rotation rates). This suggests that rotation rate is not a dominant parameter for scaling the net injected energy that may contribute to large flares. But sunspots that rotate more quickly will inject similar amounts of energy more quickly. However, if a natural rotating sunspot system has significant diffusive properties, i.e. η becomes large enough to contribute to the change of the magnetic field (as described by equation 1.13), then a more rapid injection of magnetic energy may become meaningful. However, in this work we do not observe such complexities.

Although we do not investigate the influence of parameters on one another in

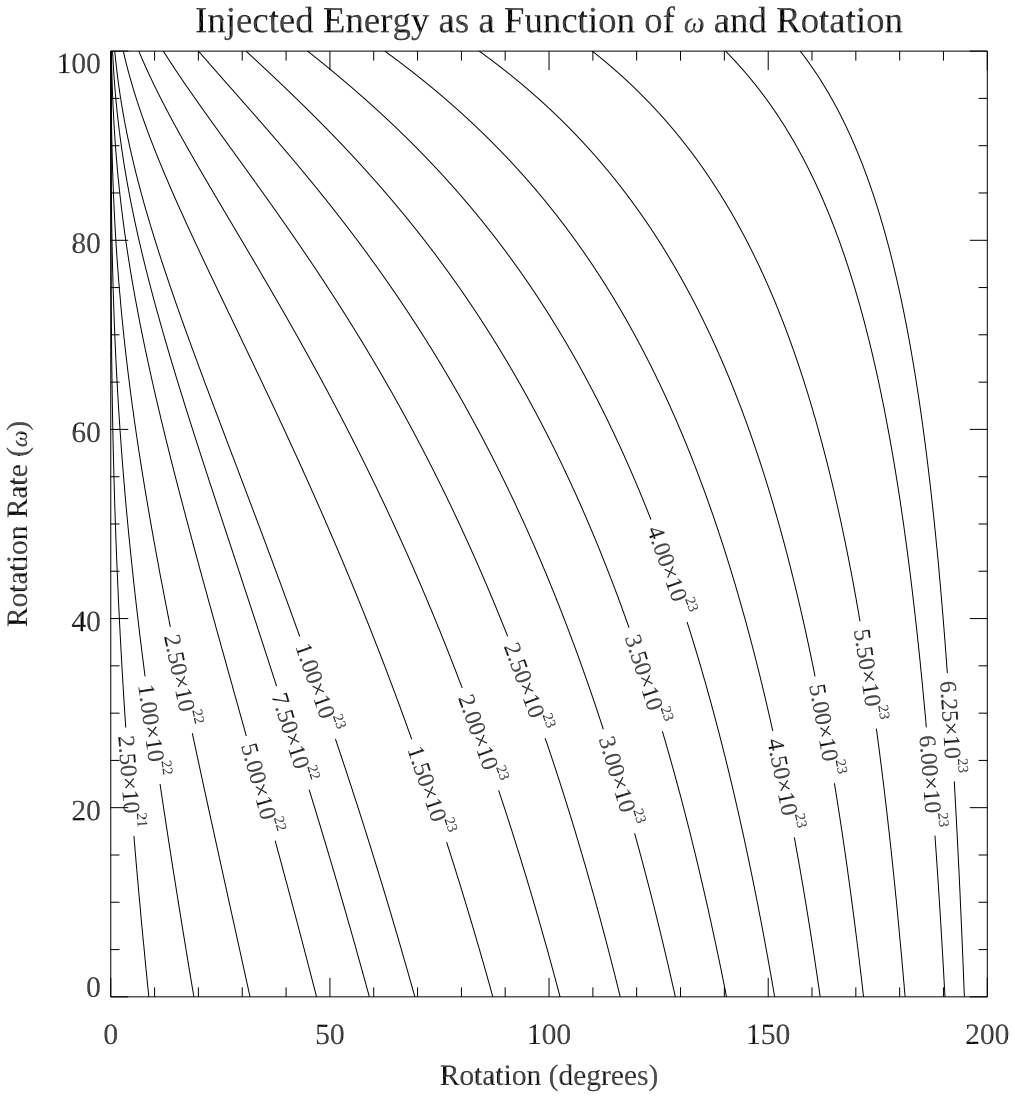

Figure 6.18: A contour plot of the injected magnetic energy as a function of rotation rate, $\omega\,(^\circ\,\mathrm{hr}^{-}1)$ and rotation. Each contour label shows the numeric value of magnetic energy measured in joules.

this work, we may speculate as to what we may see if we increased the magnetic field strength (U_b) such that X-class flare energies were present as contours in figure 6.18. Thus, if the magnetic field strength of the sunspots in this model parameter batch were fortified, then (as suggested by section 6.2.1) we might expect the magnetic energy and forces to dominate by a greater degree, and hence our sunspots ought

to evolve closer to the force-free limit. Thus, we would expect in the attempt to add more energy to meet X-class flare requirements, something which causes the magnetic energy to depend less on the rotation rate than it does presently. i.e. for stronger field strengths we would expect the contours in figure 6.18 to become increasingly vertical as the stronger field dominates non-magnetic forces more. We could also add more flux into the domain to reach X-class energies in the same way, but from an observational perspective, there is a correlation between total flux and sunspot radius (Li et al., 2001b), which suggests there is restrictions to doing this.

Finally, while figure 6.18 shows that there is little additional energy to be gained by rotating slightly faster, figure 5.11 suggests that additional magnetic energy is injected during the acceleration phase. Measured sunspot rotation profiles consistently show rotation rate variation (Brown et al., 2003; Walker, 2018; Brown and Walker, 2021; Grimes et al., 2020) and thus must exhibit some acceleration. Therefore there may be a secondary importance of the rotation rate in that it does not introduce large additional energies itself, but the associated acceleration may well correlate with increased energy production.

Coefficient	Value	Uncertainty	Value
f_1	-5.9137606866897539	δf_1	4.9056318131299874e-05
f_2	0.075584229593119973	δf_2	7.4358201292445476e-07
f_3	1.7753787113622366	δf_3	1.2100573199946674e-05
f_4	-0.014193176422497775	δf_4	1.7784588290079647e-07
f_5	45.432570852069887	δf_5	4.9056318131299874e-05
f_6	0.075584210130447360	δf_6	7.4358201292445476e-07

Table 6.6: Table of coefficients for the data fits derived in section 6.2.3.

6.2.4 Radii Ratio - $\psi \equiv \frac{Ur}{Pr}$

The next model parameter investigated, represents the ratio of umbral to penumbral radii $\psi \equiv \frac{U_r}{P_r}$, where U_r and P_r represent the umbral and penumbral radii

respectively. The simulations we shall use to investigate this parameter maintain a penumbral radius of 10Mm, and so variation of ψ translates to variation of U_r. This parameter is more than simply a consequence of the sunspot model we employ (chapter 2), it represents the amount of the sunspot which is umbra and which is penumbra, a measurement popular in the literature (typically given in terms of solar hemispheric area based units, e.g. see Tlatov and Pevtsov (2014); Tlatov et al. (2019)). The ψ parameter also represents how much of the flux which passes through the photosphere will be captured to form the penumbral magnetic field. Given chapter 3 shows that the penumbral region is the dominant region for stored energy, we may expect the ψ parameter to have some importance; although, we may not expect as much additional energy as we saw from more direct scaling parameters like U_b.

Figure 6.19 shows the collection of magnetic energy percentage increase versus rotation curves for the batch of simulations investigating the ψ parameter. The relationship between this parameter, rotation and magnetic energy injection appears more complicated than what we have seen for the previous parameters, in that there is no obvious ordering in magnitude of the curves and for the first time we see the curves intersecting significantly during the main-phase of the simulations. Table 6.7 shows the model parameters, power-law fitting values and initial magnetic energies associated with the simulations in this batch of parameters. As shown the values of the power-law fitting parameters do not vary as significantly between simulations as they do for other parameters investigated in this chapter. This explains the relatively similar evolutionary properties of the simulations as shown by figure 6.19. Figure 6.19 does show a general trend however, in that the smaller ψ becomes longer the simulations run before the penumbra reaches the top of the domain. This result seems somewhat counter-intuitive, in that we may expect a larger penumbral region (with lesser umbral region to overcome) to expand more freely and reach the top of the domain more quickly. But because we maintain all parameters other than ψ

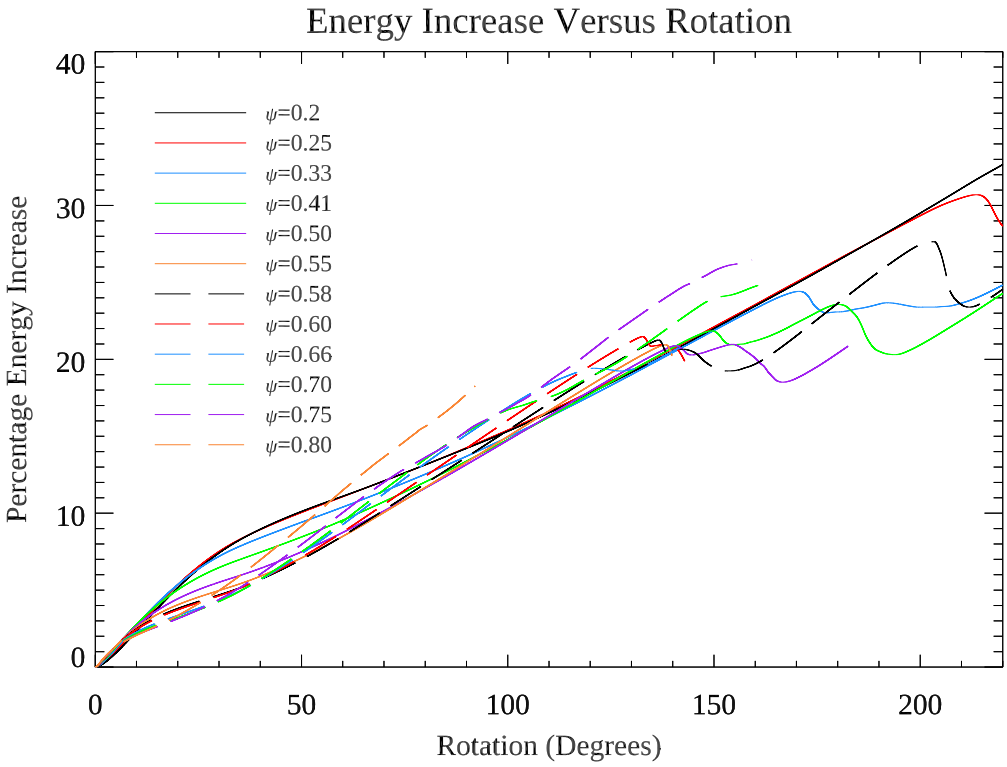

Figure 6.19: A collection of line plots each showing the evolution of the measured percentage increase of magnetic energy versus rotation, the legend shows the ψ value of each simulation.

for this testing, we may be altering some dominant driver or restricting force of the penumbral expansion. An obvious candidate may be that $\mu = 0.5$ for all simulations here and thus we are not simply altering only the size of the umbral and penumbral regions by varying ψ, we are also altering the ratio of flux associated with both regions and not in as simple a manner as we are for changing the umbral radius.

	Model Parameters						Power-Law Fit Parameters						Initial Energy
Sim	$U_b(G)$	μ	$U_r(Mm)$	$P_r(Mm)$	$\omega^\circ \mathrm{hr}^{-1}$	γ	k	δk	a	δa	$\theta_1(^\circ)$	$\theta_2(^\circ)$	E_0(Joules)
33	1300	0.5	2.0	10.0	48	1	1.05692e-1	2.6e-5	1.063031	4.7e-5	180	220	1.7623e+23
34	1300	0.5	$\frac{10}{4}$	10.0	48	1	0.1509745	9.0e-6	0.995038	1.2e-5	160	180	3.2589e+23
35	1300	0.5	3.0	10.0	48	1	1.66096e-1	2.0e-5	9.77772e-1	1.1e-5	140	150	5.3332e+23
36	1300	0.5	$\frac{10}{3}$	10.0	48	1	0.1603435	8.7e-6	0.981058	1.1e-5	130	150	7.0645e+23
37	1300	0.5	$\frac{50}{12}$	10.0	48	1	0.1331818	4.3e-6	1.0220103	6.8e-6	110	130	1.2610e+24
1	1300	0.5	5.0	10.0	48	1	0.1096677	9.0e-6	1.064389	1.8e-5	70	130	1.9926e+24
38	1300	0.5	5.5	10.0	48	1	0.0862550	2.1e-6	1.1198862	5.5e-6	80	90	2.5123e+24
39	1300	0.5	$\frac{70}{12}$	10.0	48	1	7.16720e-2	4.6e-6	1.166957	1.5e-5	65	85	2.8876e+24
40	1300	0.5	6.0	10.0	48	1	6.61840e-2	4.6e-6	1.194109	1.6e-5	65	85	3.0802e+24
41	1300	0.5	$\frac{20}{3}$	10.0	48	1	0.057194	1.6e-5	1.243153	6.5e-5	60	80	3.9135e+24
42	1300	0.5	7.0	10.0	48	1	0.0479791	3.9e-6	1.290429	2.0e-5	50	70	4.3645e+24
43	1300	0.5	$\frac{15}{2}$	10.0	48	1	0.0559522	4.8e-6	1.267570	2.2e-5	45	60	5.0659e+24
44	1300	0.5	8.0	10.0	48	1	6.90281e-2	6.8e-6	1.249283	2.5e-5	50	60	5.7825e+24

Table 6.7: A tabulated record of the simulations used throughout section 6.2.4 and their associated properties.

Using the power-law fitting parameters and initial magnetic energies presented in table 6.7 we may now approximate functional forms for k, a and τ versus ψ respectively, in the same manner as we have for other parameters.

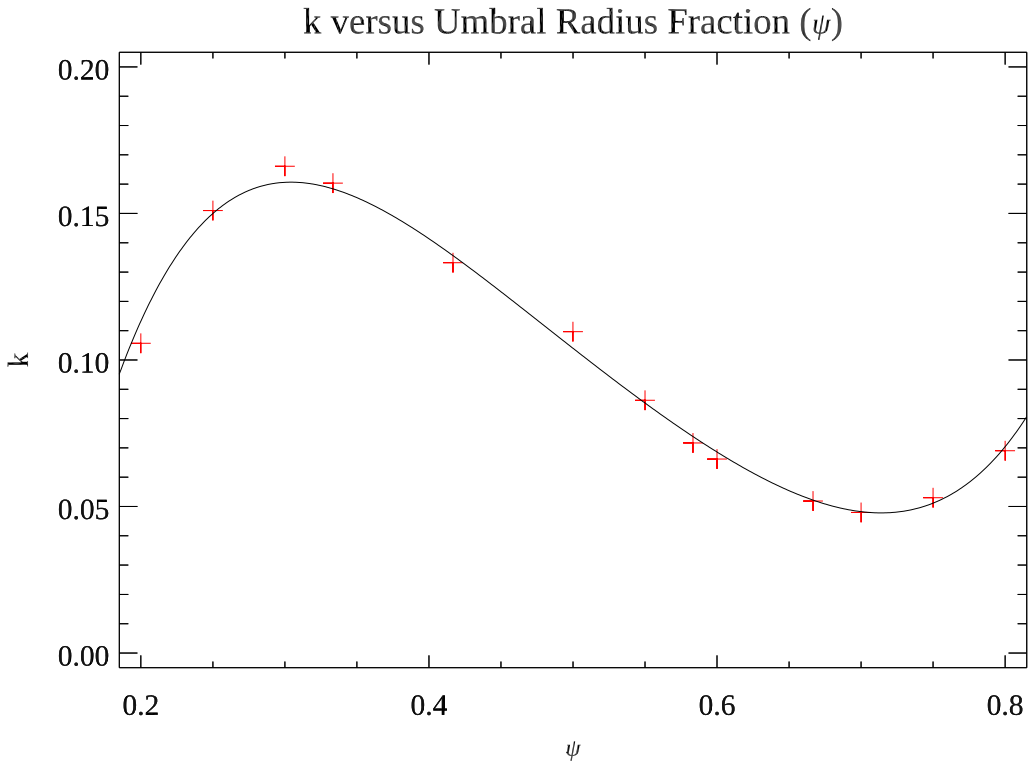

Figure 6.20: A plot showing the relationship between power-law fitting parameter, k, and independent sunspot model parameter, ψ. The red plus symbols depict the data-points for k tabulated in table 6.8 and the solid black line represents the interpolant described by equation 6.23.

Figures 6.20, 6.21 and 6.22 show the data and functional fits for k, a and τ versus ψ respectively. There is a more complex trend in the data in all cases compared to previous parameters, likely a consequence of the complicated variation of the penumbral and umbral region flux and general magnetic field geometry scaling. Despite the increased complexity, we can fit the trends present in these data sets. The specific forms found to best match the data in each case are given by the

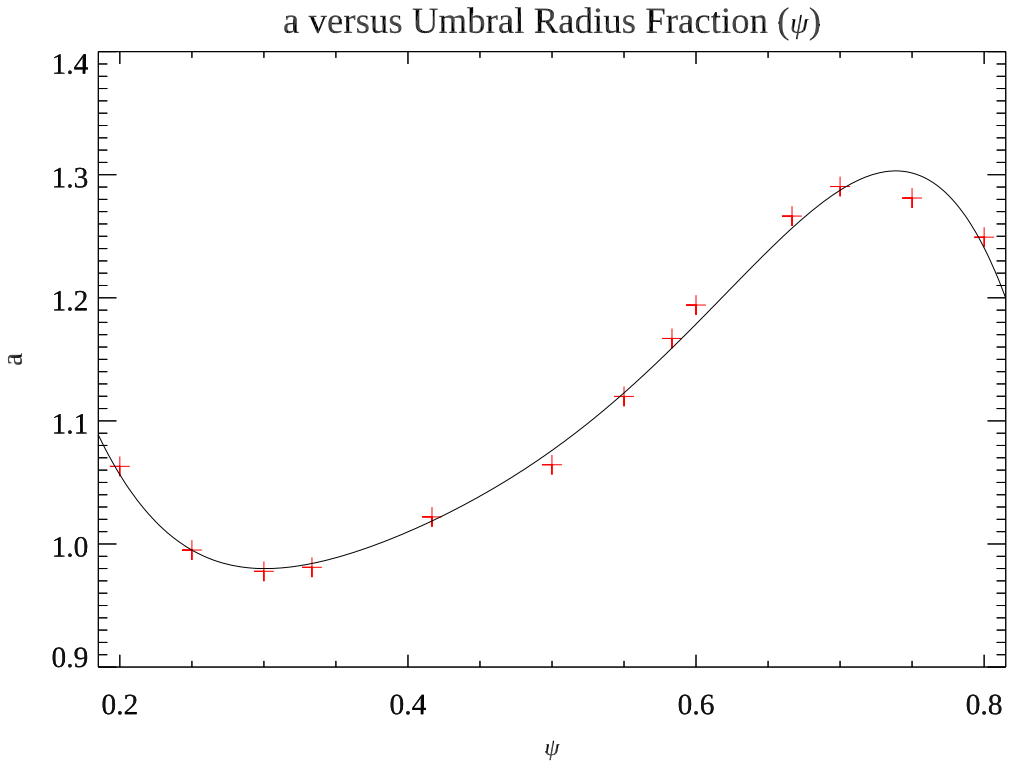

Figure 6.21: A plot showing the relationship between power-law fitting parameter, a, and independent sunspot model parameter, ψ. The red plus symbols depict the data-points for a tabulated in table 6.8 and the solid black line represents the interpolant described by equation 6.24.

following equations,

$$k = g_1 + g_2\psi + g_3\psi^2 + g_4\psi^3 + g_5\psi^4 + g_6\psi^5, \tag{6.23}$$

$$a = g_7 + g_8\psi + g_9\psi^2 + g_{10}\psi^3 + g_{11}\psi^4 + g_{12}\psi^5, \tag{6.24}$$

$$\tau = g_{13} + g_{14}\psi + g_{15}\psi^2 + g_{16}\psi^3 + g_{17}\psi^4 + g_{18}\psi^5, \tag{6.25}$$

where, in equations 6.23 - 6.25, $g_i \in \{g_j \,|\, j \in \mathbf{Z}, 1 \leq j \leq 18\}$ represent constant coefficients which are tabulated in table 6.8. It is clear that, despite the complicated behaviour of the power-law fitting parameters for this parameter, the functional fits generally do a good job representing the data whilst maintaining the maximum

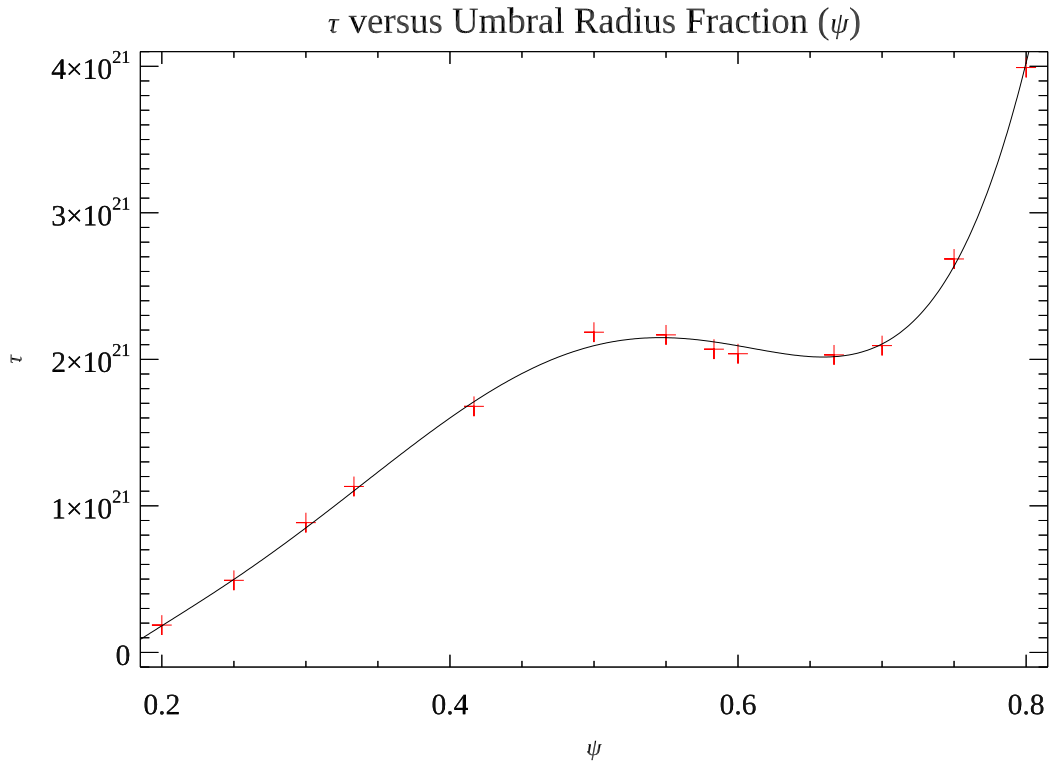

Figure 6.22: A plot showing the relationship between power-law fitting parameter, τ, and independent sunspot model parameter, ψ. The red plus symbols depict the data-points for τ calculated using data tabulated in table 6.8 and the solid black line represents the interpolant described by equation 6.25.

order of polynomial fits be less than or equal half the number of data points used to. A fuller understanding of what causes the complexity present in the data for this parameter (for all k, a and τ) is beyond the scope of this chapter and is deferred to future work in chapter 7.

We are now able to establish an equation that describes the magnetic energy increase as a function of ψ. This equation has the (more compact) form,

$$\triangle E_b(J) = \left(\sum_{i=0}^{5} g_{i+13} \psi^i \right) \theta^{\sum_{i=0}^{5} g_{i+7} \psi^i}, \tag{6.26}$$

where $g_i \in \{ g_j \,|\, j \in \mathbf{Z}, 1 \leq j \leq 18 \}$, again, represent constant coefficients which are tabulated in table 6.8.

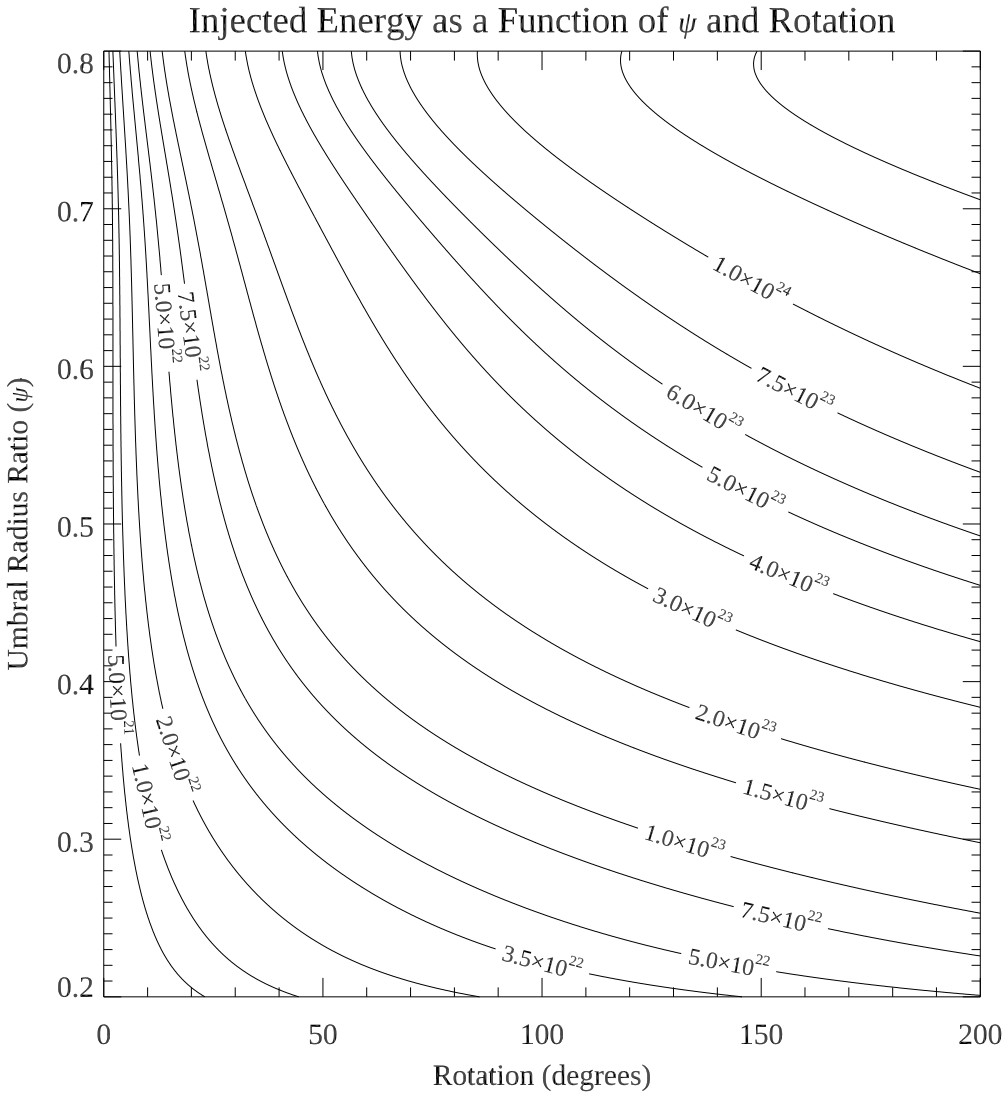

Figure 6.23: A contour plot of the injected magnetic energy as a function of ψ and rotation. Each contour label shows the numeric value of magnetic energy measured in joules. Top-right contours are 1.5×10^{24}J and 2×10^{24}J moving from the centre of the plot to the top-right corner respectively.

Figure 6.23 shows a contour plot relating the parameter ψ, the cumulative rotation of the sunspot and the energy introduced into the sunspot systems, based on equation 6.26. We see that there is a clear dependence on the rotation and parameter ψ for the amount of magnetic energy produced. The contour plot has three

primary regions where there is a trend present. The first region is located where $\theta < 50°$, in this region we observe that the primary way to increase the order of the magnetic energy of the system is to continue rotating the sunspots and that the parameter ψ plays relatively little role for the introduction of additional magnetic energy. The second region of interest is where $\psi < 0.35$ and where $\theta \geq 50°$, in this region we see that to introduce additional orders of magnetic energy into the system one is forced to increase ψ; additional rotation continues to increase the magnetic energy but at a much slower rate than at smaller rotation values. The final region is the remainder of the contour plot (i.e. where $\psi \geq 0.35$ and where $\theta \geq 50°$), in this region we see that there is a far greater balance between the importance of increasing ψ and additional rotation. One may expect that the order of energies present within figure 6.23 to scale to larger values if the sunspots in this batch had stronger magnetic field strengths or were larger, as suggested by sections 6.2.1 and 6.2.2. We shall return to this concept in section 6.3.

Coefficient	Value	Uncertainty	Value
g_1	-0.64574797928071348	δg_1	0.00056313639021683399
g_2	7.9243934103869833	δg_2	0.0062542656630910232
g_3	-29.345483005279675	δg_3	0.026429877774099074
g_4	52.273865945171565	δg_4	0.053466626242210012
g_5	-47.475348792038858	δg_5	0.052079098319834136
g_6	17.820504413219169	δg_6	0.019639601055007790
g_7	2.7603270013059955	δg_7	0.0010273408862521919
g_8	-19.687517907470465	δg_8	0.011625176664130196
g_9	85.117329088971019	δg_9	0.050384954294013268
g_{10}	-182.41622929647565	δg_{10}	0.10510190976869895
g_{11}	196.82706859335303	δg_{11}	0.10602140091596154
g_{12}	-83.825818020850420	δg_{12}	0.041524097745220263
g_{13}	-2.9256726043959409e+21	δg_{13}	3.0342494980778243e+20
g_{14}	3.9632301337335747e+22	δg_{14}	3.9723916658247221e+21
g_{15}	-2.2691765001180468e+23	δg_{15}	1.9829516227247197e+22
g_{16}	7.1699490186673929e+23	δg_{16}	4.7166154714453698e+22
g_{17}	-1.0313378304079310e+24	δg_{17}	5.3595547674191356e+22
g_{18}	5.3651740326556399e+23	δg_{18}	2.3338688976254679e+22

Table 6.8: Table of coefficients for the data fits derived in this section.

6.2.5 Penumbral Fractional Magnetic Field Strength - μ

In this section a scaling law is derived for the percentage magnetic energy change relative to the peak penumbral field strength (P_b) to peak umbral field strength (U_b) ratio, which we define as $\mu = \frac{P_b}{U_b}$. Figure 6.24 shows the percentage change magnetic energy versus rotation curves for the simulations considered in this section. There is a clear ordering present; specifically that as μ decreases in magnitude the percentage magnetic energy increase. This happens throughout the entire rotation rate range (i.e. the acceleration and main phases). Secondly we observe that as μ increases the amount of rotation/time required for the penumbral field to reach the top of the domain decreases. Hence, the stronger the penumbral magnetic field, the more

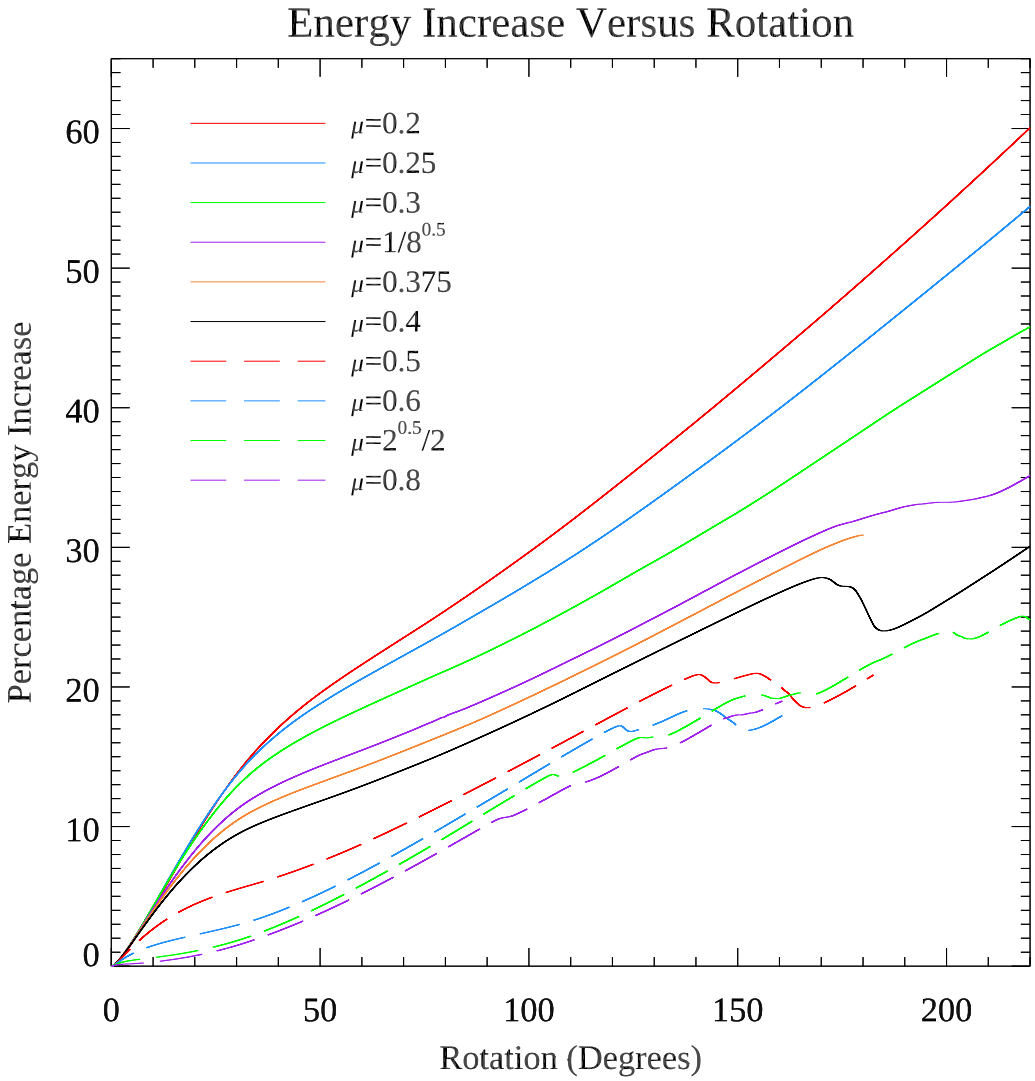

Figure 6.24: A collection of line plots showing the evolution of the measured percentage increase of magnetic energy versus rotation, for the simulations that vary the parameter μ. The legend shows the μ value of each simulation curve.

quickly the penumbra rises. Section 6.2.1 shows that magnetic energy (and thus the average magnetic pressure) scales with overall field strength, so we may expect this observed behaviour from the penumbral region. An interesting feature which must compliment this explanation is that, by increasing μ, we also increase the magnetic field strength in the outer umbral radii and so increase the flux in the umbra overall.

Figure 6.24 shows that there are three simulations ($\mu = 0.2$, $\mu = 0.25$ and $\mu = 0.3$) where the end of the simulation is not met. It was found that these simulations did not seem to exhibit the same sort of evolution of the penumbra as all other simulations in this investigation (chapter wide). The main difference is that the penumbra in these simulations does not rise in the same way as those in the other simulations. As μ decreases in size the simulations must run for longer and thus the sunspots must twist more for the penumbral magnetic field to reach the top of the domain. These "different" simulations seem to pass some critical threshold, where the penumbra is no longer able to rise and reach the top of the domain. The simulations with penumbra that do not seem to be able to rise, also display numerical reconnection effects (from qualitative analysis and comparison to more "well-behaved" simulations). This means that when using the results of this section, one must ensure that the expansion of the behaviour of the penumbra is properly considered.

	Model Parameters						Power-Law Fit Parameters						Initial Energy
Sim	$U_b(G)$	μ	$U_r(Mm)$	$P_r(Mm)$	$\omega^\circ \mathrm{hr}^{-1}$	γ	k	δk	a	δa	$\theta_1(^\circ)$	$\theta_2(^\circ)$	E_0(Joules)
1	1300	0.5	5.0	10.0	48	1	0.1096677	9.0e-6	1.064389	1.8e-5	70	130	1.9926e+24
45	1300	$\frac{1}{5}$	5.0	10.0	48	1	2.46907e-1	2.8e-5	1.018551	2.1e-5	200	220	8.536e+23
46	1300	$\frac{1}{4}$	5.0	10.0	48	1	1.79971e-1	1.0e-5	1.058669	1.0e-5	250	280	9.654e+23
47	1300	$\frac{3}{10}$	5.0	10.0	48	1	3.01731e-1	2.6e-5	9.33086e-1	1.6e-5	170	190	1.1002e+24
48	1300	$\frac{1}{2\sqrt{2}}$	5.0	10.0	48	1	4.41532e-1	5.6e-5	8.28912e-1	2.6e-5	120	160	1.2759e+24
49	1300	$\frac{75}{20}$	5.0	10.0	48	1	3.40316e-1	2.8E-05	8.71665e-1	1.6e-5	140	155	1.3570e+24
50	1300	$\frac{2}{5}$	5.0	10.0	48	1	3.441273e-1	2.9e-6	8.581218e-1	1.7e-6	120	150	1.4605e+24
51	1300	$\frac{6}{10}$	5.0	10.0	48	1	3.22897e-2	6.7e-6	1.312173	4.5e-5	90	110	2.7880e+24
52	1300	$\frac{\sqrt{2}}{2}$	5.0	10.0	48	1	1.01246e-2	1.7e-6	1.554871	3.9e-5	70	90	4.0996e+24
53	1300	$\frac{8}{10}$	5.0	10.0	48	1	3.77632e-3	7.7e-7	1.765260	5.1e-5	45	65	5.8484e+24

Table 6.9: A tabulated record of the simulations used throughout section 6.2.5 and their associated properties.

Table 6.9 shows the model properties, power-law fit parameters and initial magnetic energies for the simulations presented in this section. The power-law fitting parameters presented in table 6.9 highlight further that we must take caution with the interpretation of scaling laws in this section, but also that we must consider here what it is we intend to produce. We see clearly that the trends present for the fitting parameters as μ decreases breaks down for the three simulations with the smallest μ values. If we again look at the curves in figure 6.24 which represent those simulations which do not have rising penumbra ($\mu = 0.2$, $\mu = 0.25$ and $\mu = 0.3$), we see that these three curves display a subtle difference in their overall magnetic energy. Simulations with $\mu \geq \frac{1}{2\sqrt{2}}$ seem to have gradients which decrease as μ becomes smaller, the three smallest μ simulations apparently have gradients which tend to show the opposite behaviour. It may be that due to the combination of the constant rotation injecting and storing energy in the penumbra, and the penumbra for these examples being unable to expand (and partially relax) cause these systems physically store more energy.

For now we proceed by interpreting the two regions of parameter space separately with the exception that the $\mu = \frac{1}{2\sqrt{2}}$ simulation data is used in fitting functions to both regions. While this intermediate simulation has an end-phase, further inspection suggests that it shows signs of both regimes, therefore we treat this point as if it belongs to both ranges. In particular, while the penumbra reaches the top of the domain, it seems that only a smaller fraction of it extends to the top (at the point of first contact) than in other examples and the end of the simulation releases lesser magnetic energy for this simulation as compared to others.

To establish the scaling relations for the μ parameter, we again fit functions to the power-law fit data (from table 6.9) to derive a functional representation of the relationship between k, a and τ versus μ. Figures 6.25, 6.26 and 6.27 show the data for k, a and τ versus μ plotted respectively and in each case two functional fits

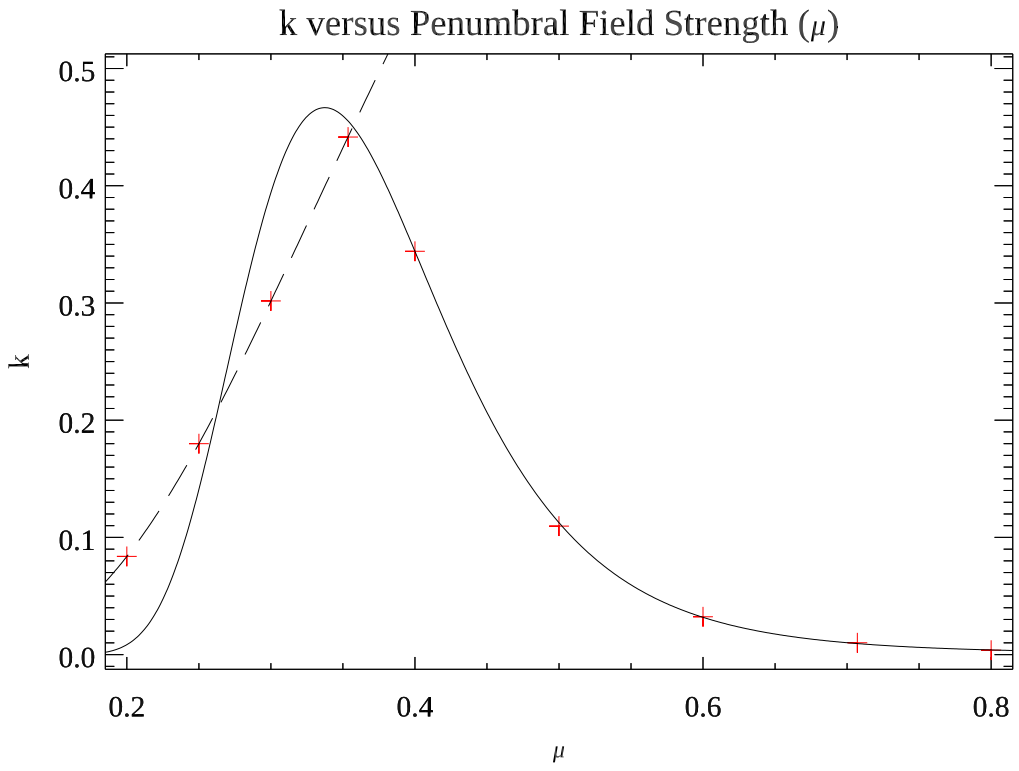

Figure 6.25: A plot showing the relationship between power-law fitting parameter, k, and independent sunspot model parameter, μ. The red plus symbols depict the data-points for k tabulated in table 6.10 and the solid black line represents the interpolant described by equation 6.27.

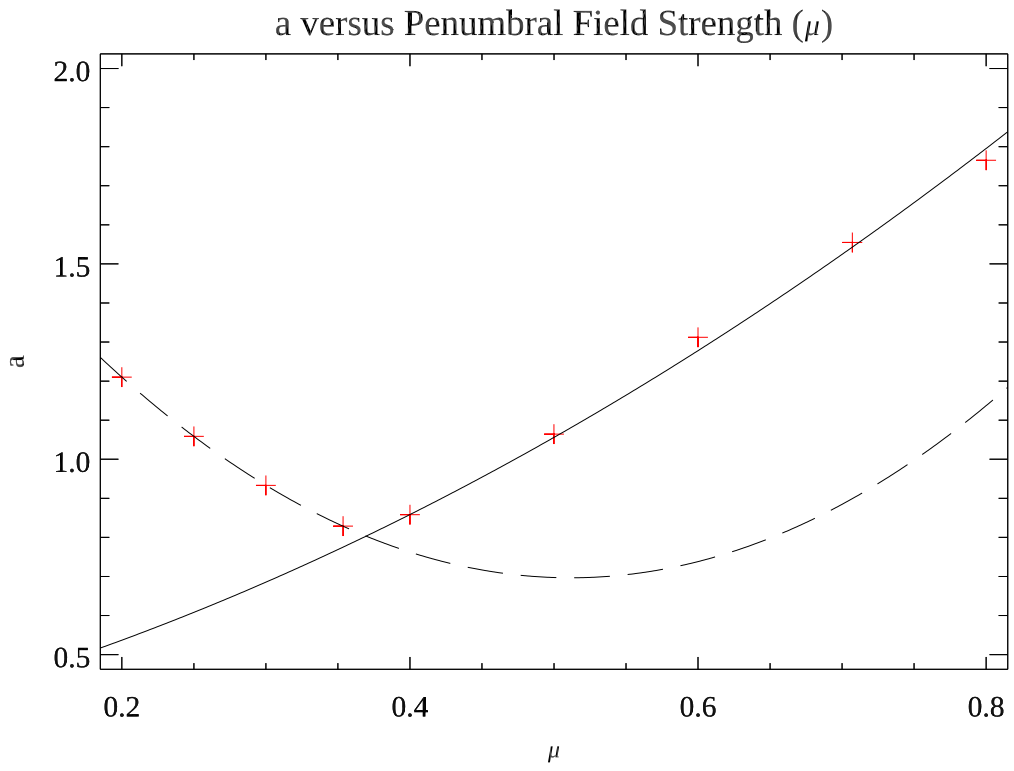

Figure 6.26: A plot showing the relationship between power-law fitting parameter, a, and independent sunspot model parameter, μ. The red plus symbols depict the data-points for a tabulated in table 6.10 and the solid black line represents the interpolant described by equation 6.28.

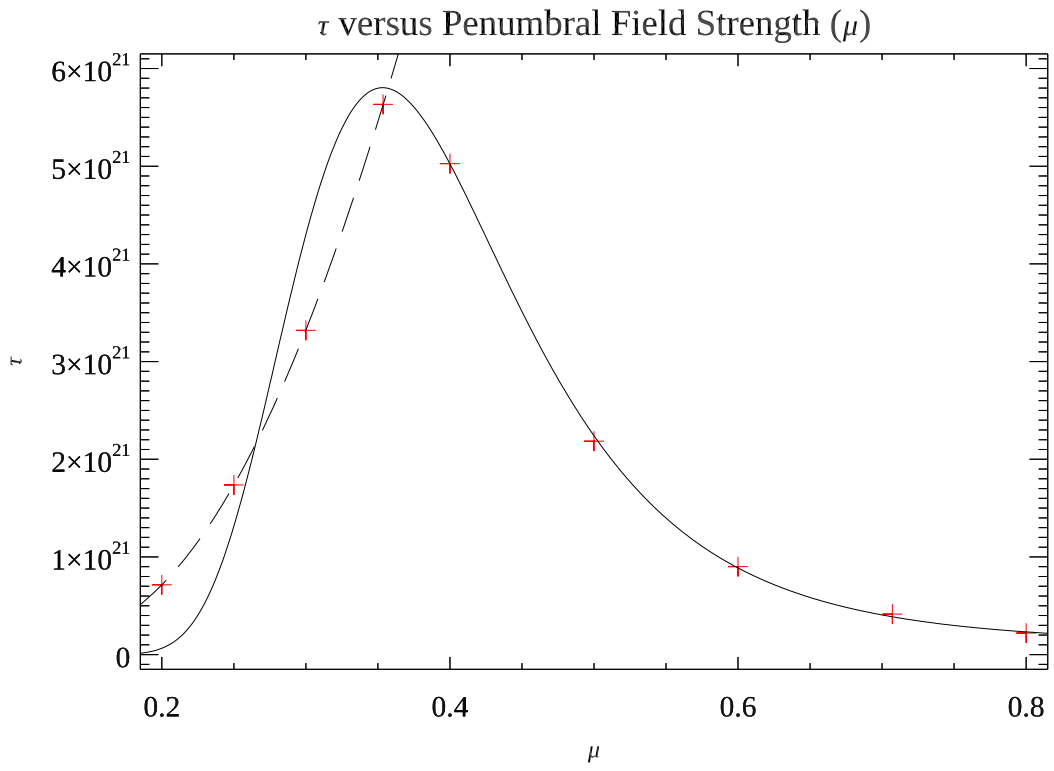

Figure 6.27: A plot showing the relationship between power-law fitting parameter, τ, and independent sunspot model parameter, μ. The red plus symbols depict the data-points for τ calculated using data tabulated in table 6.4 and the solid black line represents the interpolant described by equation 6.29.

corresponding to each of the distinct parameter ranges are over-plotted.

Note that in all examples the two μ regions meet at local extremum. As with all other parameters, many functional fits were tested and those which gave the best agreement were chosen for the final functional forms. The forms which appear in figures 6.25, 6.26 and 6.27, and hence those found to fit best are,

$$k = \begin{cases} \prod_{i=0}^{2} \exp\left(h_{i+1} \ln^i \mu\right); 0.2 \leq \mu \leq \frac{1}{2\sqrt{2}}, \\ \prod_{i=0}^{3} \exp\left(h_{i+4} \ln^i \mu\right); \frac{1}{2\sqrt{2}} < \mu \leq 0.8, \end{cases} \tag{6.27}$$

$$a = \begin{cases} h_8 + h_9\mu + h_{10}\mu^2; 0.2 \leq \mu \leq \frac{1}{2\sqrt{2}}, \\ h_{11} + h_{12}\mu + h_{13}\mu^2; \frac{1}{2\sqrt{2}} < \mu \leq 0.8, \end{cases} \tag{6.28}$$

$$\tau = \begin{cases} \prod_{i=0}^{2} \exp\left(h_{i+14} \ln^i \mu\right); 0.2 \leq \mu \leq \frac{1}{2\sqrt{2}}, \\ \prod_{i=0}^{3} \exp\left(h_{i+17} \ln^i \mu\right); \frac{1}{2\sqrt{2}} < \mu \leq 0.8, \end{cases} \tag{6.29}$$

where $h_i \in \{h_j \,|\, j \in \mathbf{Z}, 1 \leq j \leq 20\}$ represent constant valued coefficients which are tabulated in table 6.10. Despite the $\mu = \frac{1}{2\sqrt{2}}$ data-point being used in both μ ranges to establish the fit, it is clear that in the regime where the penumbra do not rise that the functional fits agree far better with this point. For this reason, in equations 6.27, 6.28 and 6.29, we now define that the non-rising penumbra form be used for the $\mu = \frac{1}{2\sqrt{2}}$ data points in all cases. A consequence of using the $\mu = \frac{1}{2\sqrt{2}}$ data points for both regimes, is that we may pollute the fitting to the regime where this point is less valid; for this reason equations 6.27, 6.28 and 6.29 reserve the rising-penumbra describing functional descriptions to be applied where $\mu > \frac{1}{2\sqrt{2}}$ only, but we still include the description over the full range of μ. The combined scaling law is given by,

$$\triangle E_b(J) = \begin{cases} \prod_{i=0}^{2} \exp\left(h_{i+14} \ln^i \mu\right) \theta^{\sum_{i=0}^{2} h_{i+8}\mu^i}; 0.2 \leq \mu \leq \frac{1}{2\sqrt{2}}, \\ \prod_{i=0}^{3} \exp\left(h_{i+17} \ln^i \mu\right) \theta^{\sum_{i=0}^{2} h_{i+11}\mu^i}; \frac{1}{2\sqrt{2}} < \mu \leq 0.8. \end{cases} \tag{6.30}$$

where $h_i \in \{h_j \mid j \in \mathbf{Z}, 1 \leq j \leq 20\}$, again, represent constant coefficients which are tabulated in table 6.8.

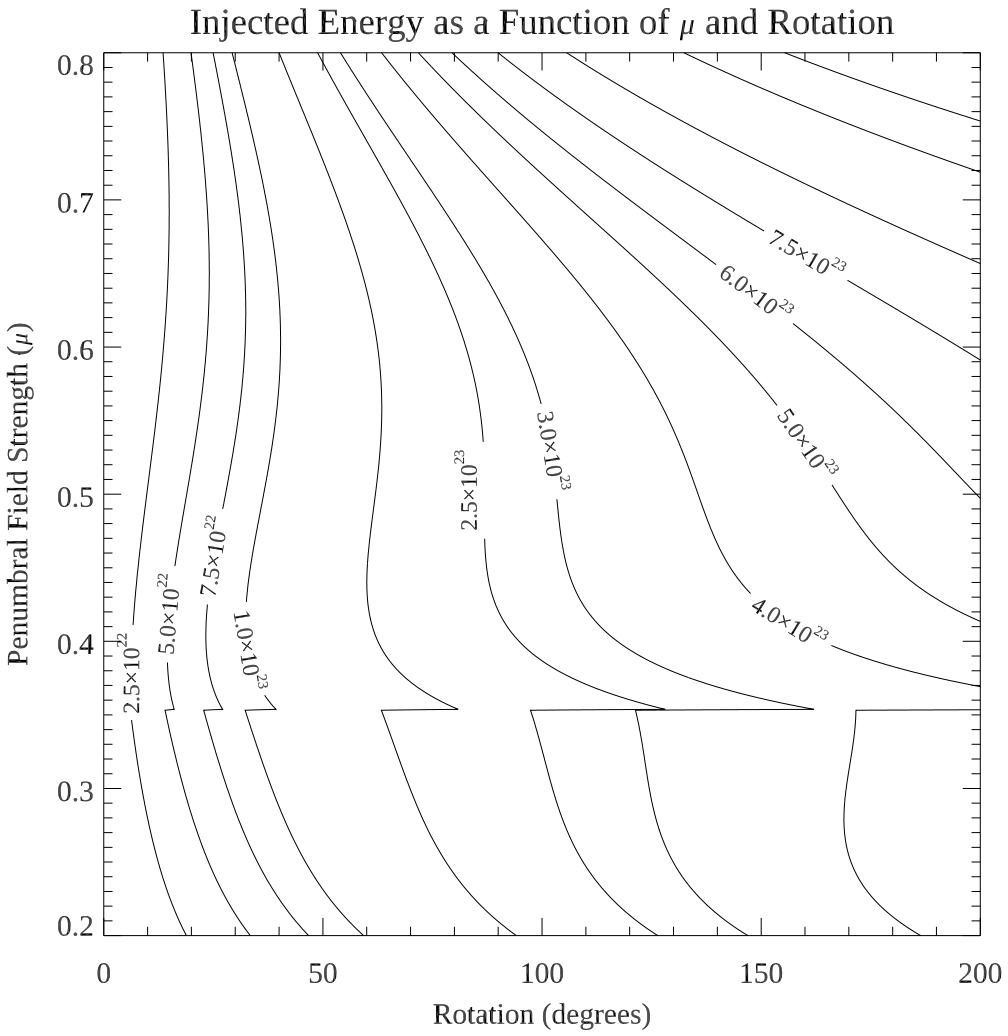

Figure 6.28: A contour plot of the injected magnetic energy as a function of μ and rotation. Each contour label shows the numeric value of magnetic energy measured in joules.

Figure 6.28 shows a contour plot of the relationship between μ, cumulative rotation and the injected magnetic energy, based on equation 6.30. As compared to the other contour plots in this chapter, this figure shows an obvious characteristic

property where $\mu = \frac{1}{2\sqrt{2}}$, in that there is a discontinuity in the isocontours. The discrepancy between the two key regions of the contour plot seems to grow with rotation. This discontinuity is a result of not imposing that the two functions smoothly connect at $\mu = \frac{1}{2\sqrt{2}}$, but given the two fits represent something physically different it is not clear that ensuring a smooth but piece-wise description across the entire μ range would be sensible. Figure 6.28 shows two primary behaviours throughout. For amounts of rotation below 100° we see that there is little additional energy gained for increasing μ, although the particular behaviour is somewhat dependent on rotation. The second region of interest appears in the top-right corner of the contour plot (approximately where $\mu > 0.6$ and $\theta > 100°$), where we see the importance of μ increasing. This additional importance generally occurs as smaller rotations for stronger μ (i.e. where $\mu = 0.6$ the isocontours at $\sim 100°$ become increasingly horizontal with additional rotation).

In the limit where μ vanishes (i.e., where the penumbra no longer rises), our model begins to more poorly represents a sunspot, because the penumbra begins to disappear. We may say that the model begins to define a pore in this limit, but it is not clear in the literature that pores behave in the same was as sunspots, or follow a comparable level of statistical behaviours (Keppens and Martinez Pillet, 1996).

Coefficient	Value	Uncertainty	Value
h_1	-0.24501600788607902	δh_1	0.0020983074748559044
h_2	-0.97935536652767041	δh_2	0.0031247288421166640
h_3	-1.4712582786914936	δh_3	0.0011506329338686672
h_4	-6.7357524033614027	δh_4	0.00079557467896919181
h_5	-3.9609358529269230	δh_5	0.0043301331138280337
h_6	7.8893703332869336	δh_6	0.0070372581350498717
h_7	5.9592475495010149	δh_7	0.0035705278718927091
h_8	2.0812402126105098	δh_8	0.00020842627394390613
h_9	-5.4137804550837245	δh_9	0.0015938575477510129
h_{10}	5.2919989961701503	δh_{10}	0.0029807589925900271
h_{11}	0.31338829375454225	δh_{11}	0.00017921284245841563
h_{12}	0.87306173162505729	δh_{12}	0.00070329838441233496
h_{13}	1.2241582347960502	δh_{13}	0.00064445962340904672
h_{14}	52.134737242740812	δh_{14}	0.0020983074748559044
h_{15}	0.91075426043244079	δh_{15}	0.0031247288421166640
h_{16}	-1.0229765683470760	δh_{16}	0.0011506329338686672
h_{17}	46.478803253034130	δh_{17}	0.00079557467896919181
h_{18}	0.087969087995588779	δh_{18}	0.0043301331138280337
h_{19}	10.237940106540918	δh_{19}	0.0070372581350498717
h_{20}	6.5322180632501841	δh_{20}	0.0035705278718927091

Table 6.10: Table of coefficients for the data fits derived in section 6.2.5.

6.3 Combined Scaling Law

In this section we build upon the magnetic energy scaling relations derived in sections 6.2.1 - 6.2.5 by combining the individual primary parameter scaling laws, into a single scaling law which may be applied to understand a sunspot with any combination of the model parameters. To combine the individual scaling laws derived in this chapter (equations 6.14, 6.18, 6.22, 6.26 and 6.30) we first recognise the true strength of the power-law fitting method that has been used in to derive each scaling law. Because we fit a power-law to each simulation used throughout this chapter, we know that a

power-law fit is an appropriate description of all the simulations under consideration. Therefore, we may impose that any generalised scaling relation should also be a power-law, albeit one with more free parameters.

There is no obvious meaningful way to best combine the individual scaling relations into a single form. One approach would be to start from the beginning and derive a general scaling relation, following the same approach used to derive the individual scaling-laws. i.e. one could use the power-law fit parameters of each simulation to uniquely derive an entirely new scaling relation that is a function of five model parameters (rather than of one as done previously). But this method requires some assumed functional form to represent what the general scaling law should look like to use as a basis, then the individual simulation information could be used to determine coefficients (in the same way as was done for the scaling laws in this chapter). When constructing the individual scaling laws, a significant amount of effort was devoted to finding the best functional forms to approximate each fit made in each section respectively. The individual scaling relations were intrinsically single parameter problems. This is not true for a generalised scaling relation, which in this case would be five-dimensional. Making any assumption of an appropriate functional form is therefore incredibly difficult. One could use the individual scaling relations as a guide as to what such a form may look like, however, there remains a key limitation. The individual scaling relations in this chapter are by their very nature individual, in that they do not offer any description of how one model parameter may influence another. Thus, they cannot be used to construct something general, as a truly general description should account for the variation of multiple parameters (i.e. cross-terms). A fully general scaling relation would be one where not only is there an established relationship between energy injection and each parameter, but also a description of the interplay between the model parameters themselves. For the five model parameters discussed in this chapter, an

average magnitude estimate of ten simulations are required to derive each scaling law. To derive a general scaling relation would require simulating every combination of model parameter. Specifically, we may write,

$$n = \bar{S}^P, \tag{6.31}$$

where n represents the number of simulations required to simulate every combination of parameters, $\bar{S}$ represents the average number of simulations required by each parameter individually and P represents the number of parameters. Thus, for the five-parameter scaling relation, $n = 100000$. Even this large number of simulations is likely an underestimate as we are assuming that the level of complexity of the fitting would not increase as more parameters are added (i.e. we maintain the assumption that $\bar{S} = 10$). Given the number of simulations used thus far is around fifty (using our simplification) and collectively required in excess of two-million CPU-hours of computational time to produce. The generalised approach is clearly physically impossible and becomes increasingly more so if one wishes to improve on the model and additional parameters.

Therefore the best option that makes the most of the derived scaling relations produced in this chapter, is to sacrifice some degree of accuracy and attempt to combine the individual forms as they are. A means to do this is suggested by the approach that has been taken. Specifically we have simulated a particular sunspot (simulation 1) and perturbed each parameter individually about this point in parameter space. Thus, the scaling relations produced thus far are eigenfunctions of a more general scaling relation about the parameter set of simulation 1, in the parameter-energy space. If we make the assumption that the eigenfunctions form an orthogonal basis (i.e. there are no cross-terms in the general scaling relation), or at least we assume the projections are small enough to be neglected, we can establish a means to combine individual scaling relations.

Following this logic, we now explain the process used to combine individual

scaling relations. If we can establish a means to join two single-parameter scaling relations, with the product being a third scaling relation, we may iteratively repeat the process and combine an arbitrary number of single parameter scaling relations. This procedure would also allow us to amend any general form obtained later to either include additional scaling relations or improve already existing components (i.e. if a better scaling relation is found for the μ parameter, the previous could be deconvolved from the general form and replaced).

To do this we must build upon the nature in which this investigation is conducted, in that all derived scaling relations include the data for simulation number 1. Because of this, we may impose that all the scaling relations should (to some accuracy) predict the behaviour of simulation 1 and thus we may use the values of the power-law fit parameters for this simulation to provide a sort of boundary condition. Consider first that we wish to join the rotation rate (ω) and sunspot size (P_r) scaling relations using the fact they must agree at simulation 1. Each scaling relation is a power-law and so must their product be, thus we may define,

$$\triangle E_b(J) = \tau_\omega \tau_{P_r} \tau_c \theta^{a_\omega + a_{P_r} + a_c}, \tag{6.32}$$

where the subscripts on the first two τ and a terms is to denote specifically which parameter they represent. The τ_c and a_c terms represent correction terms to be determined using the simulation 1 information. There are a number of routes one may follow to determine τ_c and a_c, but here we shall chose the simplest, specifically that we treat each term separately (i.e. the coefficient end exponent collective terms are analysed individually). Let τ_{ω_1}, a_{ω_1}, $\tau_{P_{r_1}}$ and $a_{P_{r_1}}$, denote the approximations of τ and a by the rotation rate (ω) and sunspot size (P_r) scaling relations respectively and let τ_1 and a_1 denote the true measured power-law fit parameters as found in table 6.1 (and others throughout the chapter). First to determine τ_c, we recognise that for equation 6.32 to be valid for simulation 1, the entire coefficient term, when

evaluated at simulation 1 ,must equal τ_1, hence $\tau_{\omega_1}\tau_{P_{r_1}}\tau_c = \tau_1$. Thus,

$$\tau_c = \frac{\tau_1}{\tau_{\omega_1}\tau_{P_{r_1}}}. \tag{6.33}$$

By making the exact same argument for the exponent term of equation 6.32, we find that exponent term must equal a_1, hence $a_{\omega_1} + a_{P_{r_1}} + a_c = a_1$. Thus,

$$a_c = a_1 - a_{\omega_1} - a_{P_{r_1}}, \tag{6.34}$$

where we see that we have been able to use the power-law parameter measurements for simulation 1 act as boundary conditions in this problem and provide a means to normalise the product of all individual scaling laws. This approach introduces some assumptions, most significantly it assumes that we are valid to combine the individual scaling laws in this way with the consequence being that we must assume that the scaling shown by one scaling relation also scales similarly in the presence of other altered parameters. This is not something we have the freedom to assume is correct, but we shall show that this approach does a suitable job when predicting magnetic energy evolution where multiple parameters are varied for a given simulated sunspot, with the stringent understanding of our primary interest being to estimate the order of the magnetic energy introduced by sunspot rotation.

Given a means to combine two scaling laws has been established, we may (somewhat trivially) construct a form of equations 6.33 and 6.34 for the more general case. Specifically, by following the same procedure, it is simple to see that the general case is defined by,

$$\triangle E_b(J) = \tau_{U_b}\tau_{P_r}\tau_\omega\tau_\psi\tau_\mu\tau_c\theta^{a_{U_b}+a_{P_r}+a_\omega+a_\psi+a_\mu+a_c}, \tag{6.35}$$

where, as before, all subscripts denote the model parameter each component represents, and the correction terms now become,

$$\tau_c = \frac{\tau_1}{\tau_{U_{b_1}}\tau_{P_{r_1}}\tau_{\omega_1}\tau_{\psi_1}\tau_{\mu_1}}, \tag{6.36}$$

and

$$a_c = a_1 - a_{U_{b_1}} - a_{P_{r_1}} - a_{\omega_1} - a_{\psi_1} - a_{\mu_1}, \tag{6.37}$$

where again all subscript 1 terms denote that the scaling law for that parameter is evaluated at the conditions imposed for simulation 1. With a method in place, we may now write the final function by substituting the relevant equations from each section in this chapter. Thus, the combined scaling relation has the form,

$$\triangle E_b(J) = \tau\left(U_b, P_r, \omega, \psi, \mu\right) \theta^{a(U_b, P_r, \omega, \psi, \mu)}, \tag{6.38}$$

where,

$$\begin{aligned}\tau\left(U_b, P_r, \omega, \psi, \mu\right) = &\left(\tau_c \sum_{j=0}^{5} g_{j+13}\psi^j\right) \exp\left(\sum_{i=0}^{3}\left(1-\mathcal{H}\left(i-2.5\right)\right)\left(c_{i+9}\ln^i U_b + \right.\right.\\ &\left.\left(1-\mathcal{H}\left(\mu-\frac{1}{2\sqrt{2}}\right)\right)h_{i+14}\ln^i\mu\right) + \left(1-\mathcal{H}\left(i-1.5\right)\right)\\ &\left.\left(d_{i+7}P_r^i + f_{i+5}\omega^i\right) + \mathcal{H}\left(\mu-\frac{1}{2\sqrt{2}}\right)h_{i+17}\ln^i\mu\right),\end{aligned} \tag{6.39}$$

and,

$$\begin{aligned}a\left(U_b, P_r, \omega, \psi, \mu\right) = &a_c + \exp\left(\sum_{k=0}^{4} c_{k+4}\ln^k U_b\right) + \sum_{m=0}^{5}\left(1-\mathcal{H}\left(m-1.5\right)\right)\\ &f_{m+3}\omega^m + g_{m+7}\psi^m + \left(1-\mathcal{H}\left(m-2.5\right)\right)\left(d_{m+4}P_r^m + \right.\\ &\left.\mathcal{H}\left(\mu-\frac{1}{2\sqrt{2}}\right)h_{m+11}\mu^m + \left(1-\mathcal{H}\left(\mu-\frac{1}{2\sqrt{2}}\right)\right)h_{m+8}\mu^m\right),\end{aligned} \tag{6.40}$$

where in both equations 6.39 and 6.40 $\mathcal{H}$ represents the Heaviside step function, τ_c and a_c are given by equations 6.36 and 6.37 respectively and, as mentioned throughout the chapter, all coefficients are presented in tables 6.2, 6.4, 6.6, 6.8 and 6.10.

6.4 Testing

In this section we perform some preliminary tests to assess the accuracy of equation 6.38 which aims to combine the individual scaling relations derived in section 6.3.

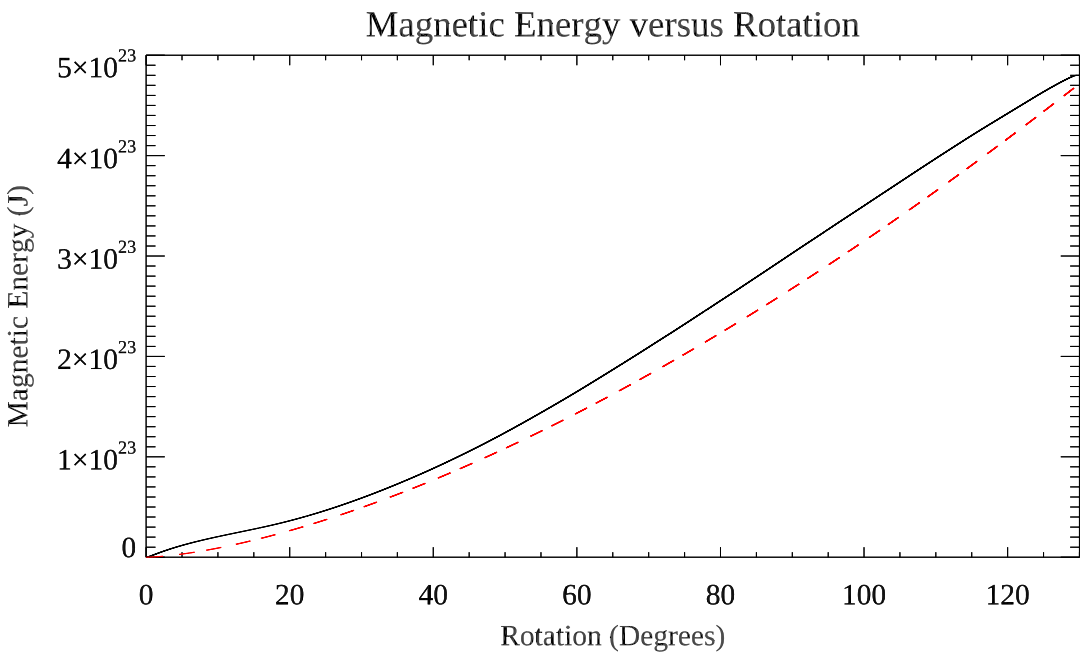

Figure 6.29: This figure shows the magnetic energy versus rotation evolution for a simulated sunspot with $U_b = 1592\text{G}$, $\omega = 24°\text{hr}^{-1}$ and all other model parameters equal to those of simulation 1. The black curve shows the measured energy increase and the red dashed curve shows an approximation calculated using equation 6.38.

We must note that the main effort of this work focuses on producing the individual scaling relations found in sections 6.2.1-6.2.5 and thus the majority of the sunspot rotation simulations produced have been intended for this use. A more rigorous testing of of equation 6.38 requires a great deal more simulations various combinations of parameters varied simultaneously. Due to the computational expense of running each individual simulation, and the large number of simulations required for the accurate derivation of the individual scaling laws, relatively few simulations that vary multiple model parameters have been run. But three simulations were able to be ran with the remaining resources and are discussed below.

Figures 6.29 and 6.30 show the magnetic energy versus rotation evolution for two simulations that vary both U_b and ω. Figure 6.29 shows the evolution of a

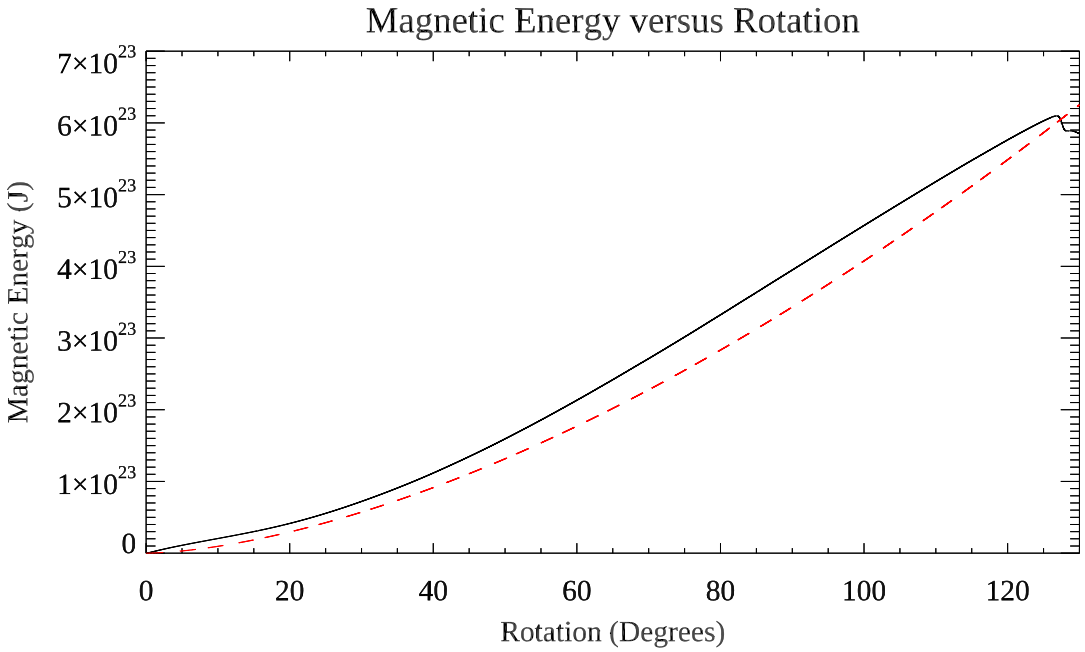

Figure 6.30: This figure shows the magnetic energy versus rotation evolution for a simulated sunspot with $U_b = 1838\text{G}$, $\omega = 24°\text{hr}^{-1}$ and all other model parameters equal to those of simulation 1. The black curve shows the measured energy increase and the red dashed curve shows an approximation calculated using equation 6.38.

sunspot with all the same model parameters as simulation 1 but with $U_b = 1592$G and $\omega = 24°\text{hr}^{-1}$. Figure 6.30 shows the evolution of a sunspot with all the same model parameters as simulation 1 but with $U_b = 1838$G and $\omega = 24°\text{hr}^{-1}$. Both figures imply that equation 6.38 does very well at approximating the magnetic energy introduced into the system when only magnetic field strength and rotation rate are varied. Neither the rotation rate or the magnetic field strength (U_b varied with $\mu = 0.5$) alter the geometry of the magnetic field. Overall both approximations are accurate within approximately 5% when considering only the magnetic energy introduced into the system. One could rather simply add the initial magnetic energy of each simulation onto each curve and use equation 6.38 to estimate the total evolution of magnetic energy versus rotation and would find that the percentage difference between the approximations and the measured curves would vanish (given the relatively large initial energy of each simulation compared to the introduced magnetic energy). We could have done this in section 6.3 by establishing another scaling relation between the initial magnetic energy of the domain and the model parameters. This would somewhat generalise the work of the present chapter by estimating the total magnetic energy evolution rather than simply the energy increase with respect to the initial potential field energy. However, in this study we are interested free magnetic energy and thus this is not done, but such an extension may be of relevance to more general studies of solar magnetic fields.

Figure 6.31 shows the magnetic energy versus rotation evolution for a rotating sunspot simulation where some of the sunspot model parameters have been varied in comparison to simulation 1. This figure shows that generally the approximation given by equation 6.38 does reasonably well at estimating the true evolution, but is of lesser agreement when compared figures 6.29 and 6.30. However, we see that the main source of difference is introduced during the acceleration phase ($\theta \leq 32°$), after which the estimate and measured values tend to increase with similar trend

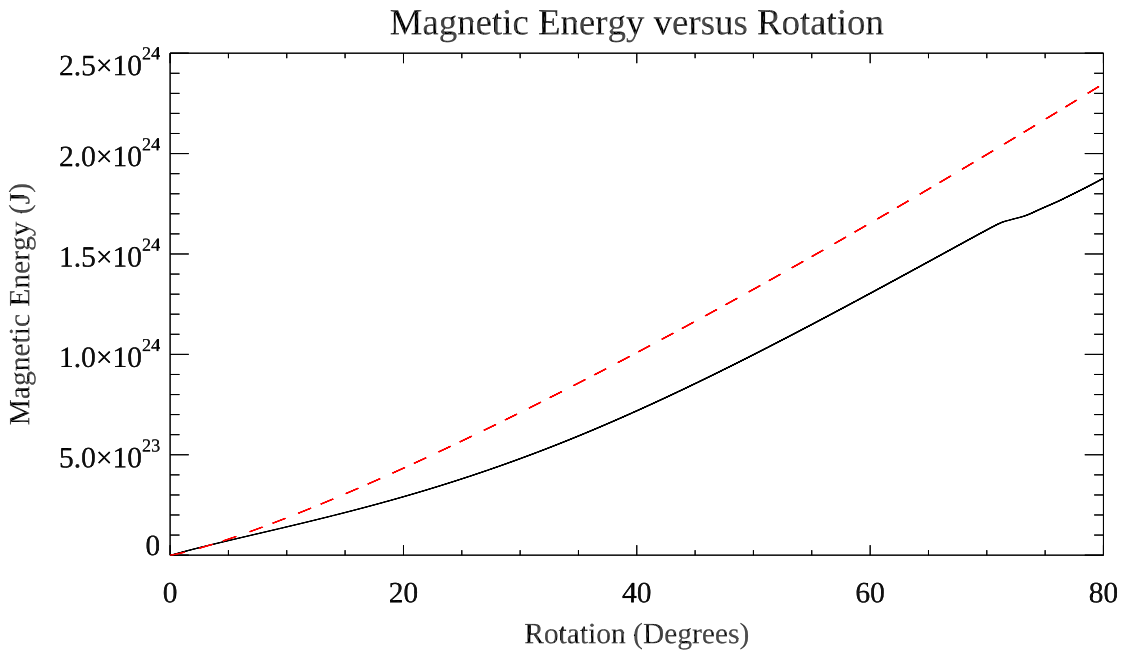

Figure 6.31: This figure shows the magnetic energy versus rotation evolution for a simulated sunspot with $U_b = 2600$G, $P_r = 15$Mm and all other model parameters equal to those of simulation 1. The black curve shows the measured energy increase and the red dashed curve shows an approximation calculated using equation 6.38.

(albeit offset). The largest difference is found near the end of the simulation at around $\theta = 70°$, but even here the disparity is only approximately 15%. Given that during main phase of the simulation the disparity of less than this, we may conclude that although this is not in as good agreement as the previous tests, equation 6.38 does indeed capture the characteristic evolution of this simulation well. We ought to recognise at this stage that when varying P_r in this instance, we also dramatically increase the magnetic field strength, thus the total flux of the simulated sunspot (with respect to simulation 1) is increased due to two alterations rather than only one at a time in sections 6.2.1 and 6.2.2. This implies it may be fruitful to further investigate how the model parameters alter the total flux of the model sunspots and perhaps further simulations could help explain the disparity observed in figure 6.31.

However, the level of agreement shown in figure 6.31 implies that the general physics is captured well by the individual (and combined) scaling laws derived in this chapter. Further refinement of the model may improve its predictive capabilities, but surely would only do so slightly. The primary purpose of this investigation is to produce a tool one may use to predict extreme space weather events, such events exhibit energy variations over orders of magnitude and having the ability to predict within a few percent what magnetic energy is produced by a rotating sunspot is far less useful than the estimating magnitude of energy injected. Note, the performance of equation 6.38 does have direct implications on the quality of the individual scaling laws derived in this chapter, as several assumptions are made when combining the individual scaling laws that may be the dominant sources of error. However, given the good performance displayed by equation 6.38 we may conclude that the manner in which the individual scaling laws are combined in section 6.3 is sufficient, however, further testing is required to confirm this.

In conclusion the preliminary tests that are able to be performed here indicate that equation 6.38 performs well under the worst level of agreement found, and very

well under the best. These preliminary tests suggest that equation 6.38 is accurate to approximately 10% or better for the majority of the main phase of the simulations investigated. However, further investigation is required to give a better estimate of error.

Chapter 7

Summary and Future Work

The intent of this investigation is to develop an understanding of how rotating sunspots transfer energy into the solar atmosphere and store it as magnetic energy, as a consequence of rotation. A number of subsidiary investigations were performed to develop this understanding and a summary of each key result is presented in the following discussion, and where appropriate a brief discussion of the potential means for future development is discussed.

7.1 The Sunspot Model

Although it is not a primary result that sheds light on sunspot rotation, the model that was developed to simulate rotating sunspots in chapter 2 is itself one of the most important products of this investigation. This is because it provided the means by which we could investigate sunspot rotation in a well-posed sense, by facilitating the smooth variation of each model parameter. Other analytic models are found within the literature (e.g. see Borrero and Ichimoto (2011); Stix (2002); Solanki (2003)) but they do not have the flexibility of the one developed in this thesis, which as we see is necessary to conduct meaningful simulation work.

Future iterations of the model should aim to include more freedom over the

definition of the magnetic field at the photosphere. Specifically, there is observational evidence that the B_z magnetic field component does not vanish at the outer radius of the penumbra, but rather it becomes small in comparison to the peak umbral field. This is shown directly in figure 1.4 and is presented in Keppens and Martinez Pillet (1996). We may include this additional flux simply by adding a constant to the current definition of B_z given by the model. This additional flux ought to surely introduce additional energy into the domain as in this thesis we see that the kinetic energy provided by the driver is transferred across the boundary by the magnetic field, thus we may expect that additional flux in the penumbra would enhance this process. We do not do this in this work because doing so would introduce an additional model parameter that would need to be understood, and it was the intent of this investigation to only include the most fundamental properties of sunspots and no others.

We may also wish to introduce fine-scale features into the model to see how things like penumbral filaments and an uncombed penumbra (details of fine-scale penumbral features can be found in Borrero and Ichimoto (2011); Solanki (2003); Thomas and Weiss (2004) and Thomas and Weiss (2008)) influence the injection and storage of magnetic energy in the penumbra. Given in this thesis we observe that the magnetic field that closes locally stores most of the magnetic energy, we might expect that using a more realistic magnetic field in the penumbra (some of which closes within the penumbra (Franz, 2012)) may shorten the range over which the magnetic fields close and increase the total energy stored.

7.2 The Penumbra

Throughout this work the penumbra has been identified as a key region that evolves uniquely to the open magnetic field during sunspot rotation. It is found to be important for the conversion of kinetic energy into magnetic (section 5.1), for the storage

of magnetic energy (section 5.2), is identified as a region where highly twisted magnetic fields develop (chapter 4) and a region of enhanced current density with an enveloping separatrix that may play an important role in magnetic reconnection processes (chapter 3). The primary message of this investigation is that the penumbra, or more generally the magnetic field that closes locally to the sunspot, is very important and must be included in any meaningful investigation of sunspot rotation.

As discussed elsewhere in this chapter, the importance of the penumbra highlighted throughout this thesis is likely a lower limit of its full importance. From a magnetic energy perspective, the penumbra is important because it is composed of closed magnetic field. We find that the field that closes on short scales and has the most amount of shear introduced into it is where most of the magnetic energy is stored. In a real sunspot, the penumbra has magnetic field that close over far shorter scales and flows that are far more complex than those used in this work. Thus, a real rotating sunspot's penumbra may host magnetic energy in excess of this measured in this work. Because we initialise with a potential magnetic field and drive gently, we may assume that our measurement of magnetic energy storage is a lower limit, or at least lesser than what may be observed in nature.

In chapter 6, we derived a set of scaling laws that quantify the relative importance of the fundamental properties of a sunspot for the injection of magnetic energy into the magnetic environment of a rotating sunspot. However, when we did this we considered the whole sunspot. A logical further development that is immediately possible using the data produced by this investigation, is to derive individual scaling relations for each of the model parameters contribution to the magnetic energy stored within the umbral and penumbral magnetic fields individually. Further testing with more realistic systems of connected sunspots would then be far easier to compare, as one would be able to determine the dominant changes introduced by the added connectivity. If we were to simulate rotating sunspots where the umbral magnetic

field of one connects to the umbral field of another, we would expect the largest change to be introduced into the umbral magnetic energy as it would too be able to store twist. However, we saw in chapter 5 that the expansion of the penumbra might have reduced the magnetic energy stored there significantly. As we shall discuss in section 7.5, when we introduce connectivity into the umbral field, the penumbra is observed to have greater difficulty expanding. The combination of effects requires significant further analysis, but clearly this work has laid the foundations upon which such an investigation may be developed.

7.3 Scaling Laws

In chapter 6 we investigated the relative contribution of the primary model parameters derived in chapter 2 to the injection of magnetic energy caused by sunspot rotation. Specifically, we derive a means to predict how much magnetic energy a rotating sunspot may inject into the solar atmosphere based only on its most fundamental geometric, magnetic and rotational properties. This particular project was one of the primary goals of this investigation and the results produced are of significant value for the prediction of eruptive events and extreme space weather.

We find that the peak magnetic field strength (U_b) was fundamentally the key parameter that scaled the injected magnetic energy most significantly. Most of the other parameters were of comparable importance with the exception of the rotation rate, ω. Thus, we see that, other than the expected importance of the magnetic field strength and rotation rate, all characteristic properties of a rotating sunspot contribute meaningfully to the magnetic energy it injects into the solar atmosphere. Interestingly, we find that the specific rotation rate of a rotating sunspot, has relatively little effect on the total energy that is injected into the magnetic field from the driver (in an order of magnitude sense). This is a valuable finding as it suggests that the magnetic energy that is produced by dynamic processes is second to stored

magnetic energy. However, we do find that for larger rotation rates more energy is injected, implying that the dynamic sources do play a role, just not a dominant one. Furthermore, the additional energy from dynamic sources is of sufficient order to produce lower classification solar flares and thus the dynamic energy may be an important contributor to the energy budget of frequently observed small scale solar flares.

Perhaps the most important finding provided by the general scaling law derived in chapter 6 is that the amount of magnetic energy injected into the solar atmosphere is very dependent on the geometry and magnetic properties of the sunspot that is rotating. This may seem obvious, but a common theme in the literature is that sunspot rotation is recognised to be important, where the findings of this work generally support that statement but develop it by adding that sunspot rotation may be important, depending on the particular sunspot that is rotating.

Various other sections in this chapter have commented on how one may develop the scaling relations further, and we shall not repeat those discussions here, but we may highlight what the immediate next steps should be. The current scaling relations only investigate the importance of five parameters, the peak magnetic field strength (U_b), the size of the sunspot (P_r), the peak penumbral field strength (P_b), the ratio of umbral to penumbral region size (ψ) and the rotation rate (ω). However, there are not only more properties of sunspots (or their surroundings) that one may wish to include in the combined scaling law, but there are also additional properties of the model investigated in this work that should first be included. There is an additional property of the model derived that is not included in chapter 6. This is the parameter that scales the gradient of the B_z component of the magnetic field in the radial direction, γ. A number of simulation that vary γ have been produced and their properties and results are presented in table 7.1.

	Model Parameters						Power-Law Fit Parameters						Initial Energy
Sim	$U_b(G)$	μ	$U_r(Mm)$	$P_r(Mm)$	$\omega(^\circ/hr)$	γ	k	δk	a	δa	$\theta_1(^\circ)$	$\theta_2(^\circ)$	E_0(Joules)
54	1300	0.5	5.0	10.0	48	-10	1.14958e-2	3.9e-6	1.627873	6.1e-5	270	290	2.0229e+24
55	1300	0.5	5.0	10.0	48	-7	6.64085e-3	8.2e-7	1.662606	2.2e-5	250	260	1.9777e+24
56	1300	0.5	5.0	10.0	48	-5	0.0219069	1.0e-6	1.4409349	8.4e-6	260	280	1.9319e+24
57	1300	0.5	5.0	10.0	48	-3	0.113356	1.0e-5	1.121544	1.8e-5	150	160	1.8820e+24
58	1300	0.5	5.0	10.0	48	-2	0.162439	1.3e-5	1.037144	1.6e-5	155	165	1.8663e+24
59	1300	0.5	5.0	10.0	48	-1	0.2497790	3.4e-6	0.9321325	2.8e-6	120	140	1.8692e+24
60	1300	0.5	5.0	10.0	48	-0.5	0.2322751	3.1e-6	0.9374209	2.8e-6	120	130	1.8821e+24
61	1300	0.5	5.0	10.0	48	10^{-5}	0.1921780	9.6e-6	0.966571	1.1e-5	100	120	1.9055e+24
62	1300	0.5	5.0	10.0	48	0.5	0.1439889	2.2e-6	1.0168041	3.2e-6	100	120	1.9416e+24
1	1300	0.5	5.0	10.0	48	1	0.1096677	9.0e-6	1.064389	1.8e-5	70	130	1.9926e+24
63	1300	0.5	5.0	10.0	48	2	0.0436509	2.2e-6	1.245323	1.1e-5	90	110	2.1466e+24
64	1300	0.5	5.0	10.0	48	5	0.006783055	8.3e-7	1.603291	2.8e-5	70	90	2.9471e+24
65	1300	0.5	5.0	10.0	48	7	0.00315676	9.1e-7	1.745790	6.8e-5	60	80	3.4030e+24
66	1300	0.5	5.0	10.0	48	10	0.001614909	6.0e-8	1.8810160	9.1e-6	55	65	3.6333e+24

Table 7.1: A tabulated record of the simulations used throughout to test the importance of the model parameter γ.

The same analyses performed for the other model parameters have been performed for this batch of simulations, but are not shown here. We find that γ displays a level of complexity far in excess of any other scaling law derived in this work. Because of this, we found great difficulty identifying suitable functional forms to fit to the data so that we could derive a meaningful scaling relation for γ. We find that like μ, γ shows a piece-wise scaling and the batch of simulations that investigate γ similarly include some where the penumbra does not rise. We do find a scaling relation for γ but choose not to include it in chapter 6 because it is of poor quality, and including it in the combined scaling relation would pollute the quality of its predictive capabilities.

Thus, not only should the immediate next steps to advance the general scaling law be to finalise the description of the γ parameter, we should also aim to investigate the conditions required to stop the penumbral magnetic field expanding. To do this we may wish to investigate further simulations that vary γ and μ to determine the critical values. We shall see evidence in section 7.5 that when we allow the umbral field to become closed, the penumbral expansion seems to be hindered. As shown, there are a number of possible directions for advancement, but first we should finalise and include the last elements of the model and then attempt to introduce other properties.

7.4 Applicability of the Force-Free Assumption

In chapter 3 we observed that the current density in most of the penumbra is found to be in excess of that in the open, umbral magnetic field. Because we initialise with a potential field, all currents found are created by the imposed rotation of the sunspot. We find that during most of simulation 1, the penumbral magnetic field shows that the parallel current density dominates the perpendicular current density. Specifically, we measure in figures 3.7 and 3.8 that in much of the penumbra, the

angle that subtends the magnetic field and current density is close to 180°. Analysis of the strength of the current density shows that the penumbra hosts most of the strong currents that form during the simulation, due to the closed nature of the penumbral magnetic field defined by the model used. These findings suggest that we may be able to exploit a force-free description of the magnetic field, to either measure real rotating sunspots or to use the force-free field assumption to quantify the free magnetic energy of our systems. However, in chapter 5 we find that the Lorentz force induces significant accelerations within the penumbra. This finding suggests that a force-free description may not be applicable. The contrast between the results implying a force-free system being appropriate and not, are exacerbated by the observation that specifically where we measure large accelerations caused by the Lorentz force is precisely where we identify the parallel current to be strongest. Thus, exactly where we may expect the Lorentz force to vanish is exactly where we find it to have the most impact to the solution of the simulation. Therefore we conclude that, although much of the current density observed in the penumbra is dominantly parallel to the magnetic field, the residual perpendicular current is sufficient to induce large accelerations in the domain. Thus, for most of the simulation a force-free description is not applicable and there seems to be no sensible way to identify where or when it may be, as the characteristic measurements one may make to identify the conditions for force-free applicability, identified here do not correspond to force-free evolution.

7.5 Connected Sunspots

An immediate extension of the model developed and used in this thesis, is to increase the range of the solar atmosphere that is represented by the model. Specifically, we may question what a more realistic magnetic configuration may do, say if we simulated the scale over which the umbral magnetic field should close. Secondly, we

may ask what influence on the magnetic energy might the connection of the rotating sunspot to another have. Furthermore, to better understand rotating sunspots within more realistic magnetic configurations, one ought to investigate how connected sunspot systems evolve if multiple sunspots are rotating. In this section we show a number of simulations where the preliminary work to answer these questions has been performed.

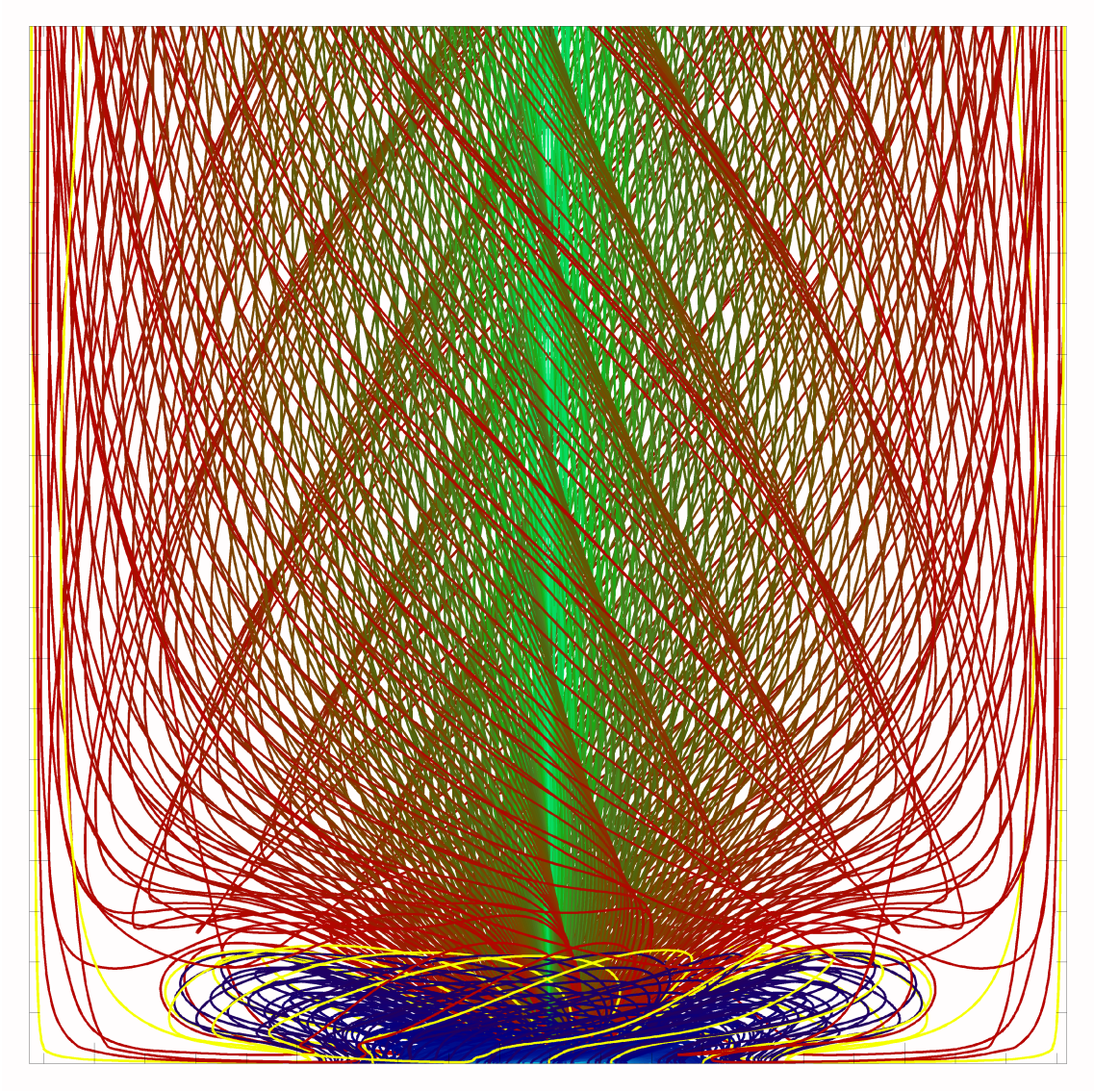

Figure 7.1: This figure shows the magnetic field of a tall sunspot simulation with the same simulation parameters as simulation 1. The upper domain of this simulation is static. The sunspot is shown at 135° rotation.

Figure 7.1 shows a single sunspot with model parameters equal to simulation 1 after 135° of rotation. In this example, however, the umbral field at the top of the domain has not been allowed to rotate and thus the umbral magnetic field has become twisted. Figure 3.2 shows that at this point the penumbra in simulation 1 had expanded significantly and was about to reach the top of the domain. But in

this example the penumbra has clearly begun to deform, but the expansion is not as great. The domain in this simulation is four times taller, but uses a similar initial atmosphere as simulation 1. Clearly the stored twist of the umbral field has had an influence on the expansion of the penumbra.

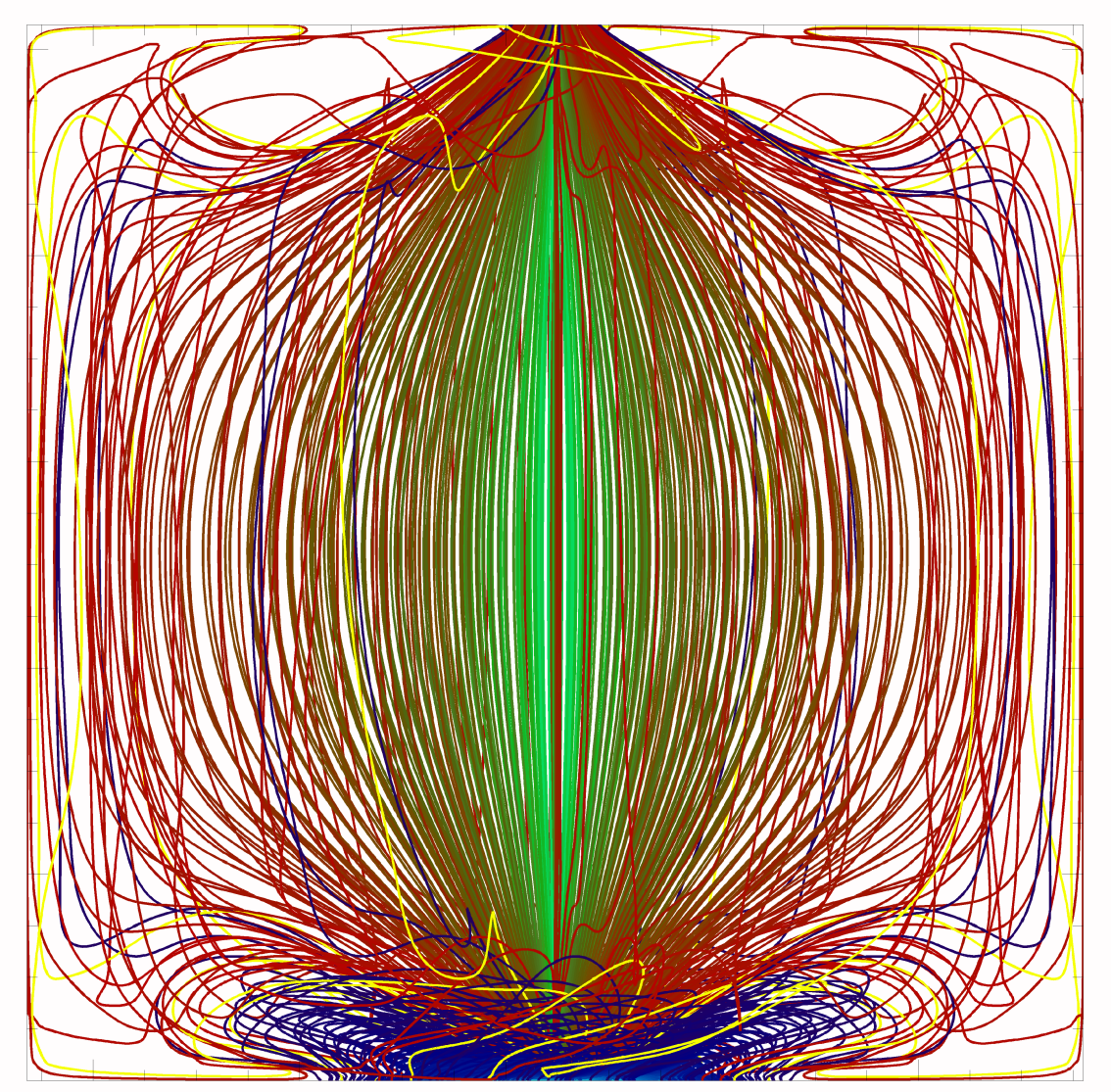

Figure 7.2: This figure shows the magnetic field of a tall sunspot simulation with a second sunspot on the top boundary, both sunspots use the same simulation parameters as simulation 1. The sunspot at the upper domain of this simulation is rotated similarly to the lower sunspot. The sunspots are shown at 135° rotation.

Figure 7.2 shows two connected sunspots that are rotating in the same direction (though if on the same plane it would be opposite). Each sunspot here uses the same model parameters as simulation 1 and a total of 135° of rotation has been introduced to each sunspot. In this example we see that the umbral field has no twist but the penumbra still has not risen as much as it did in simulation 1. This is interesting as it suggests that additional magnetic pressure introduced into the umbral field by the storage of twist is not the only means for restricting the expansion of the penumbra. Although further analysis is required, this result would suggest that for the penumbra to rise, the umbra must not twist (the importance of which is shown highlighted by figure 7.1) and the umbral field must be able to be displaced. The displacement of the umbral field is not possible due to the presence of the other sunspot at the top of the numerical domain.

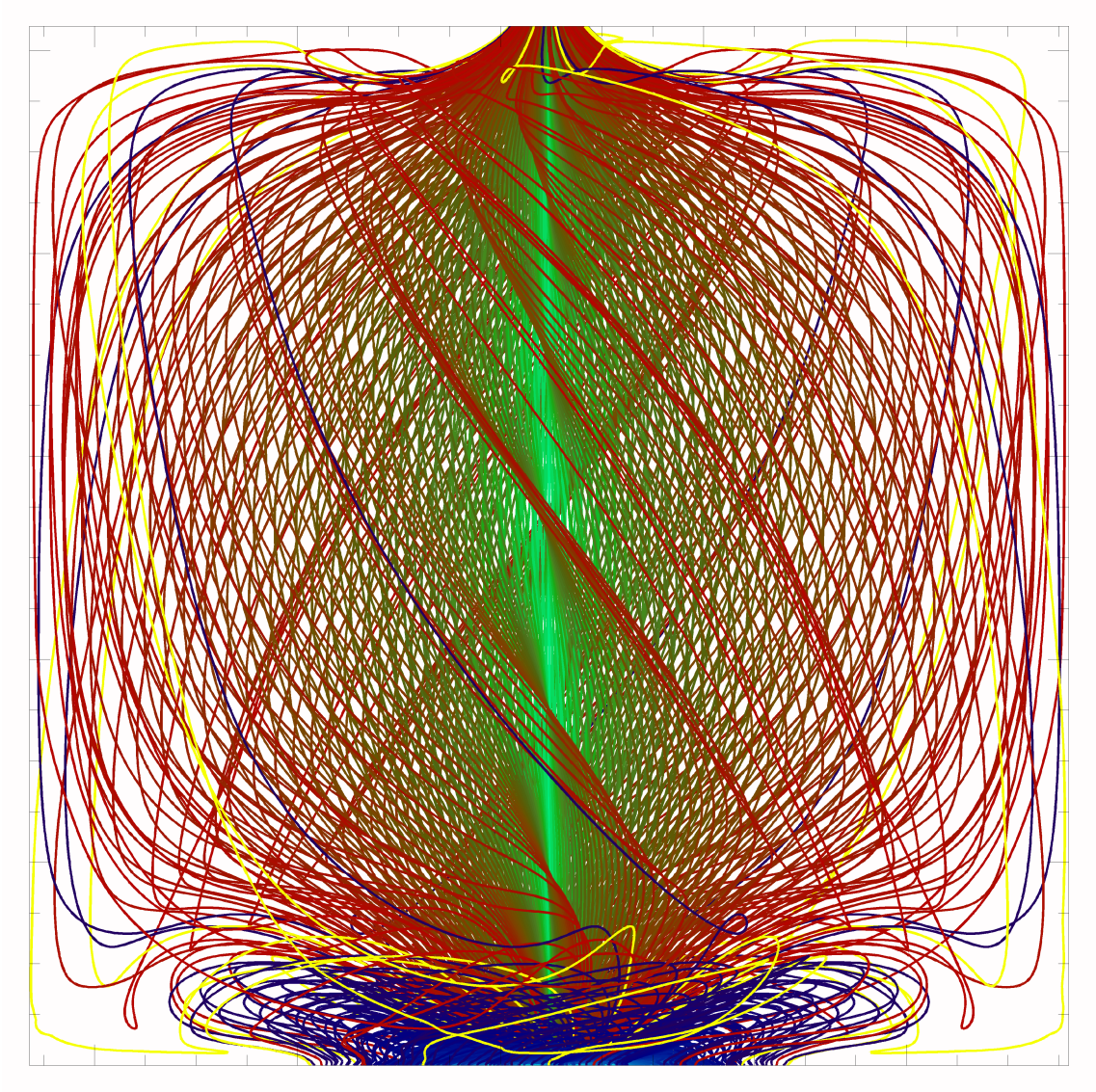

Figure 7.3: This figure shows the magnetic field of a tall sunspot simulation with a second sunspot on the top boundary, both sunspots use the same simulation parameters as simulation 1. The sunspot at the upper domain of this simulation is not rotated. The lower sunspot has rotated by 135°.

Figure 7.3 shows two connected sunspots where only the bottom sunspot is rotating. Again, each sunspot here uses the same model parameters as simulation 1 and a total of 135° of rotation has been introduced into the rotating sunspot. In this example we see that the umbral field twists but when compared to figure 7.1

the umbral field clearly spreads out in the mid-domain and accumulates again at the opposite sunspot. This concentration of umbral flux is found to introduce additional magnetic energy. We shall discuss this shortly.

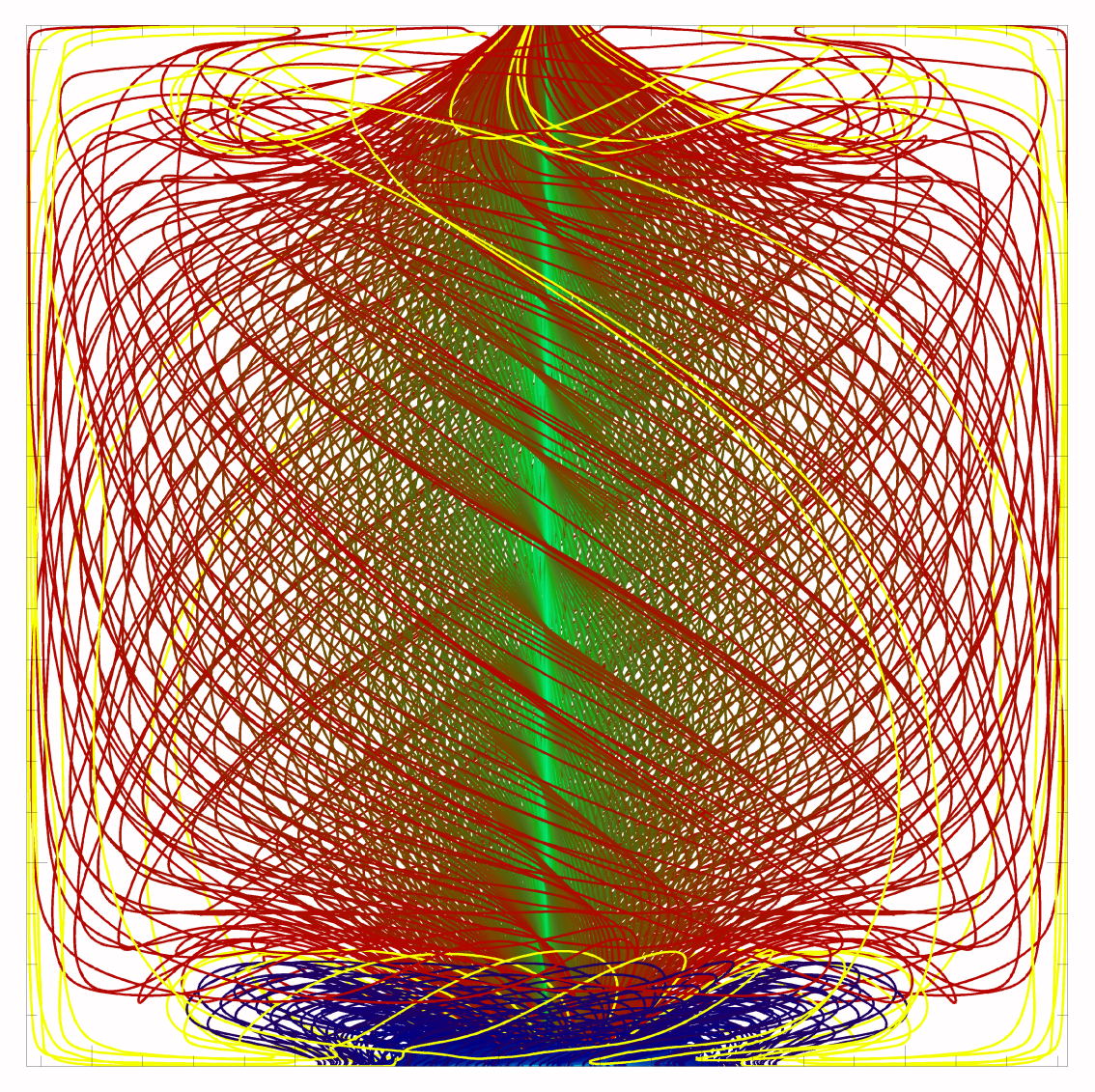

Figure 7.4: This figure shows the magnetic field of a tall sunspot simulation with a second sunspot on the top boundary, both sunspots use the same simulation parameters as simulation 1. The sunspot at the upper domain of this simulation is rotated oppositely to the lower sunspot. The sunspots are shown at 135° rotation.

Figure 7.4 shows two connected sunspots that are rotating in the opposite direction (though if on the same plane the rotation would be in the same direction). Each sunspot here uses the same model parameters as simulation 1 and a total of 135° of rotation has been introduced to each. In comparison to figure 7.2, the umbral field in this configuration is significantly twisted. Specifically this umbral field is twisted from both ends and so a total of 270° of rotation is stored within it. Clearly, once again the penumbra has not risen as it did in simulation 1 but seems to have expanded comparably to the other connected sunspot simulations shown previously.

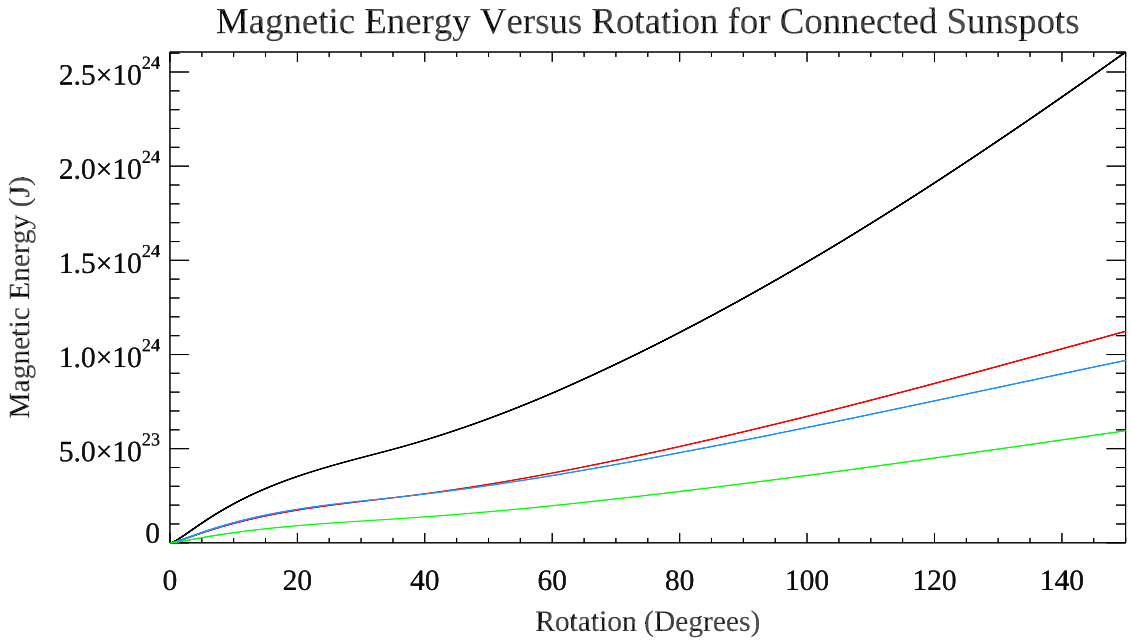

Figure 7.5: A multi-line plot showing the excess magnetic energy versus rotation profile for the tall-domain sunspots discussed section 7.5. The black line shows the evolution of the counter rotating sunspot system, the red shows the evolution of the two sunspot system where only one is rotating, the blue curve shows the evolution of the connected similar rotating sunspots and the green curve shows the single sunspot evolution.

Figure 7.5 shows the magnetic energy increase (with respect to each simulations

initial magnetic energy) versus rotation for each simulation presented above. Clearly we see that where we have two counter rotating sunspots, a vast dominance over all the other simulation energies is found. This is unsurprising as the most amount of twist is stored in that configuration. However, figure 7.5 shows that there is little difference between the evolutionary properties of excess magnetic energy of the similarly rotating connected sunspots and the connected sunspots where only one is rotating. This is perhaps the most enlightening result of this figure as it shows that even under a far more complex connected sunspot model, a single twisted penumbra and an umbral field each with 135° of stored twist induces a roughly equal amount of magnetic energy as two twisted penumbral regions each with 135° of stored twist, with no twist stored in the umbra. This directly shows that under our model, the penumbra is found to be as important as the umbral magnetic field for the development and storage of magnetic energy.

Finally, figure 7.5 shows that the additional magnetic energy introduced to the single sunspot, even with a twisted umbral field, is less than that of all other configurations tested. This is likely a result of the concentration imposed on the umbral magnetic field by having it connect to another sunspot. This result highlights that the next stages of this work should be to represent more appropriate conditions for the closing of the umbral magnetic field. This finding also suggests that should our scaling laws derived in chapter 6 include a connected umbral region, we should get additional energy from the stored twist in the umbral field but also we may double the energy of the system by connecting the each rotating sunspot to a partner. In summary, these results indicate that the additional magnetic energy introduced by rotation in the umbral field if stored, is approximately equal to that introduced by the penumbra, and secondly we may again double the estimated energy if we connect the rotating sunspot to a twin. Thus, we may generalise our model further by stating that for a more realistic system of connected sunspots, the estimate produced

by the scaling laws of chapter 6 may be 25% of the total. Given eruptive space weather events exist on scales over orders of magnitude, a factor of four introduces little concern for the validity of our scaling laws. But one may simply use the scaling laws derived in this thesis as a lower bound, and in practice take four times that energy estimate as the physically meaningful answer.

7.6 Resistive Effects

In this thesis we have simulated rotating sunspots that evolve under the ideal MHD regime. This may appear an oversimplification, but a justification of doing this is that under the ideal MHD regime magnetic reconnection should not be present as resistivity, η, is zero, however, numerical resistivity is always present. However, as part of the wider investigation of sunspot rotation undertaken here, we simulate a number of rotating sunspot that evolve under a full resistive MHD regime. The reason these findings are not presented in the main body of this thesis is because the investigation into resistivity produced one key result that may be summarised succinctly. Figure 7.6 shows five curves, each representing the total magnetic energy versus rotation evolution of a simulated rotating sunspot. The black line shows simulation 1 (i.e. an ideal MHD simulation) and the others show an identical rotating sunspot, with various values of imposed background resistivity. The only result shown by this figure is that as the resistivity increases the total magnetic energy introduced by rotation decreases. We find that the cause of this loss of magnetic energy is an increasing dominance of diffusive effects as η is increased. Specifically, the diffusive term in equation 1.13 dominates the advective term as resistivity is increased. The reason this result is presented as future work, is because the specific values of resistivity that were found to be necessary to see any difference with respect to the ideal MHD simulation are orders of magnitude greater than what is expected to be physical. For this reason we omit this finding from the main investigation

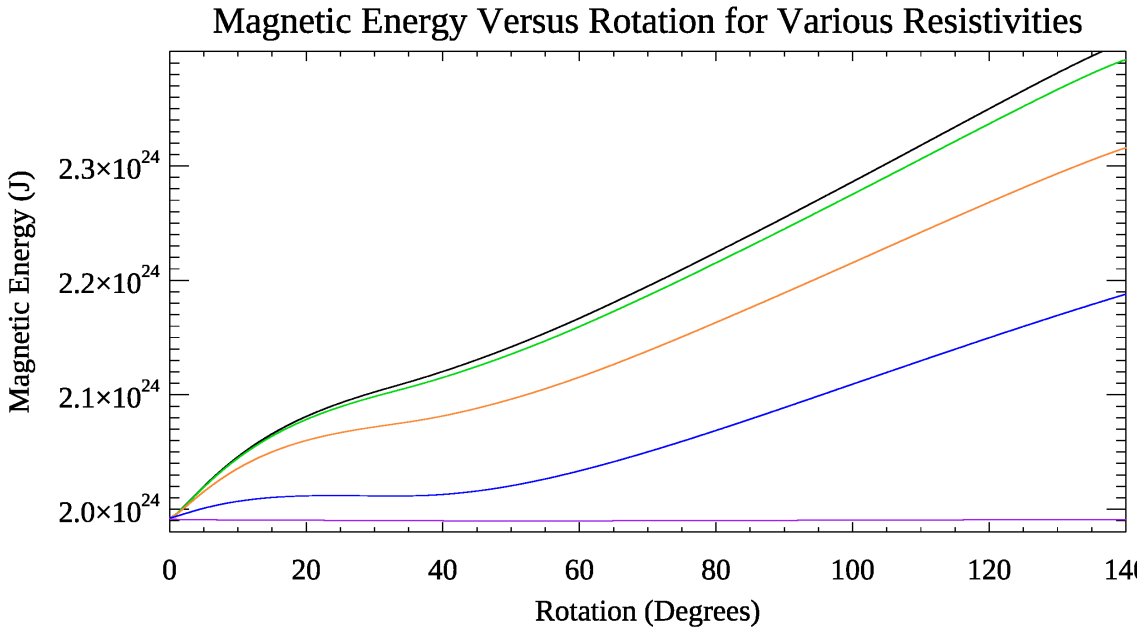

Figure 7.6: This figure shows the magnetic energy evolution of several identical rotating sunspot simulations with various background resistivities. The black line shows the evolution of simulation 1, the green line shows the evolution of a rotating sunspot where $\eta = 3e5\mu_0$, the orange curve shows the evolution of a rotating sunspot where $\eta = 3e6\mu_0$, the blue curve shows the same evolution where $\eta = 3e7\mu_0$ and the purple curve shows when $\eta = 1500$.

and leave further discussion of resistive effects for a time when we have a model we may expect to produce something other than diffusion. Specifically, we find that the rotating sunspots simulated in this thesis, evolve in such a way that the advective term in equation 1.13 always dominates.

Thus, resistive effects must be investigated for a more complete understanding of the physics of sunspot rotation, and what is presented in this work represents an upper limit of what a rotating sunspot may produce (form the perspective or resistivity). However, what we find in this thesis is that because we require such large nonphysical levels of resistivity to see any difference in the amount of magnetic energy injected, the rotating sunspot model that has been developed is shown to be inherently stable. Further analysis is required, but we may speculate that because we have simulated such a range of sunspots, with a variety of physical properties, we might have expected to see some magnetic reconnection if it were likely to occur. Thus, we conclude that the sunspot model developed in this work is stable to resistive effects and because we have developed the model such that it represents something physically meaningful, it is reasonable to assume that our findings imply that sunspot rotation itself is a stable mechanism for the injection of magnetic energy into the solar atmosphere.

Further work is definitely required to say more on this, but we recognise that the findings of this thesis suggest that an external trigger, possibly another magnetic entity close to the sunspot for it to reconnect with, are likely required to release the magnetic energy stored in the penumbral magnetic field.

7.7 Concluding Remarks

This thesis has investigated sunspot rotation numerically to extend the understanding of the coupling between rotating sunspots and the energisation of extreme space weather events. Numerical simulations of highly idealised rotating sunspots find

that sunspot rotation is able to introduce energies comparable to those required for large eruptive events, into the solar atmosphere in which large amounts are stored. Furthermore we find the amount of additional energy can be approximated accurately using the defining observed characteristic properties of rotating sunspots. This includes the geometric properties of the sunspot, its magnetic field properties and its rotation rate. All of these parameters are frequently measured and thus the findings of this thesis may be used to predict extreme eruptive events. Secondly, we find that the vast majority of magnetic energy introduced into the domain is stored in the penumbral magnetic field, or more abstractly in the magnetic field of the sunspot that closes locally, which we suggest is representative of the penumbra. This is particularly important as the closed field regions are far smaller than the typical scales of an active region. This result is significant because it suggests that not only can sunspot rotation power extreme eruptive events, but the magnetic energy that may be liberated, during an eruption, might be stored locally. Having large amounts of magnetic energy stored locally (as opposed to being spread over large distances) may result in greater amounts of it being converted to other forms of energy during a magnetic reconnection event. The previous statement is purely speculative, but is logically supported by the concept that magnetic reconnection occurs over a finite length-scale and thus has limited access to energies significantly far from the reconnection site.

Our findings thus not only imply that sunspot rotation can power eruptive events, but shows how the magnetic energy is introduced, where it is stored, how it is transported once stored, how it may be converted back to kinetic energy via powering expansion of the closed field and how much energy may be generated by a rotating sunspot based on the sunspots observable properties.

A secondary, but fundamentally important product of this work is the manner in which it is conducted. All simulations use a sunspot model that only contains

the most fundamental properties of a sunspot, meaning all simulations truly represent the physical processes associated with sunspot rotation, and only rotation. The approach adopted in this investigation is in contrast to many previous studies, which typically elect to investigate observed rotating sunspots or much larger systems of which a rotating sunspot is part of, either directly or by simulation using observational data as a boundary condition. The approach taken in this work thus deconvolves sunspot rotation from the other complex general motions, processes and features present on the photosphere and in the solar atmosphere, which must inevitably be captured and reflected in other works. Furthermore, future investigations may not only use the results of this investigation, but because of the approach used to derive and combine energy scaling relations, they may build on this work directly by introducing additional parameters into the model or additional physics.

Appendix A

Base Simulation

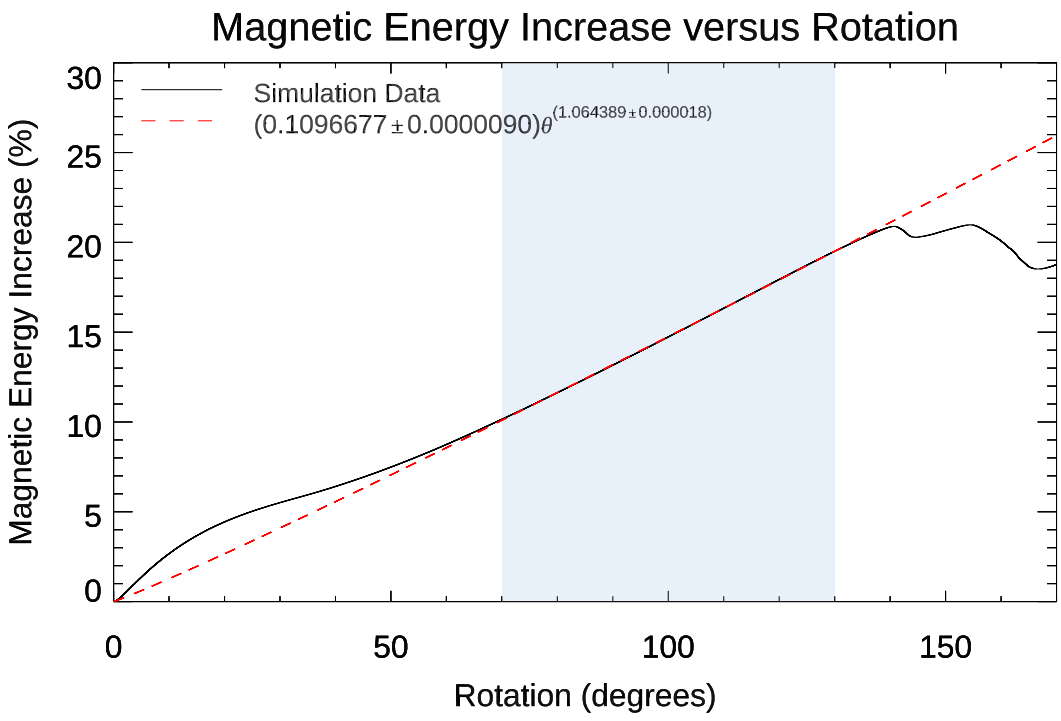

Figure A.1: This figure shows the power-law fit for simulation number 1.

Appendix B

Peak Umbral Field Strength - U_b

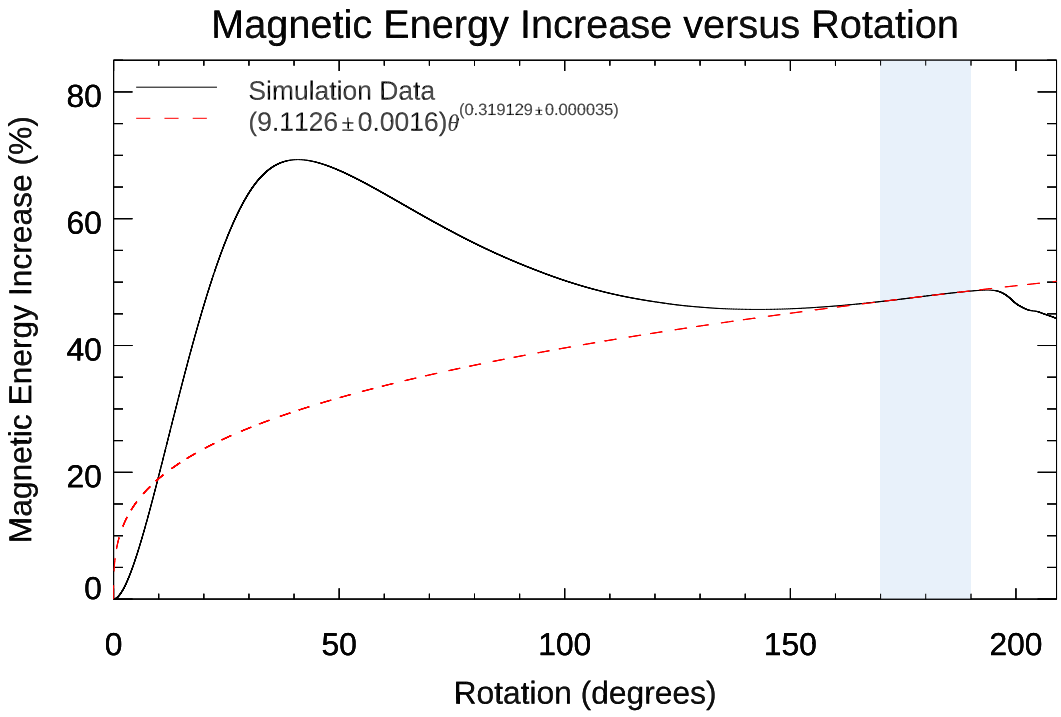

Figure B.1: This figure shows the power-law fit for simulation number 3.

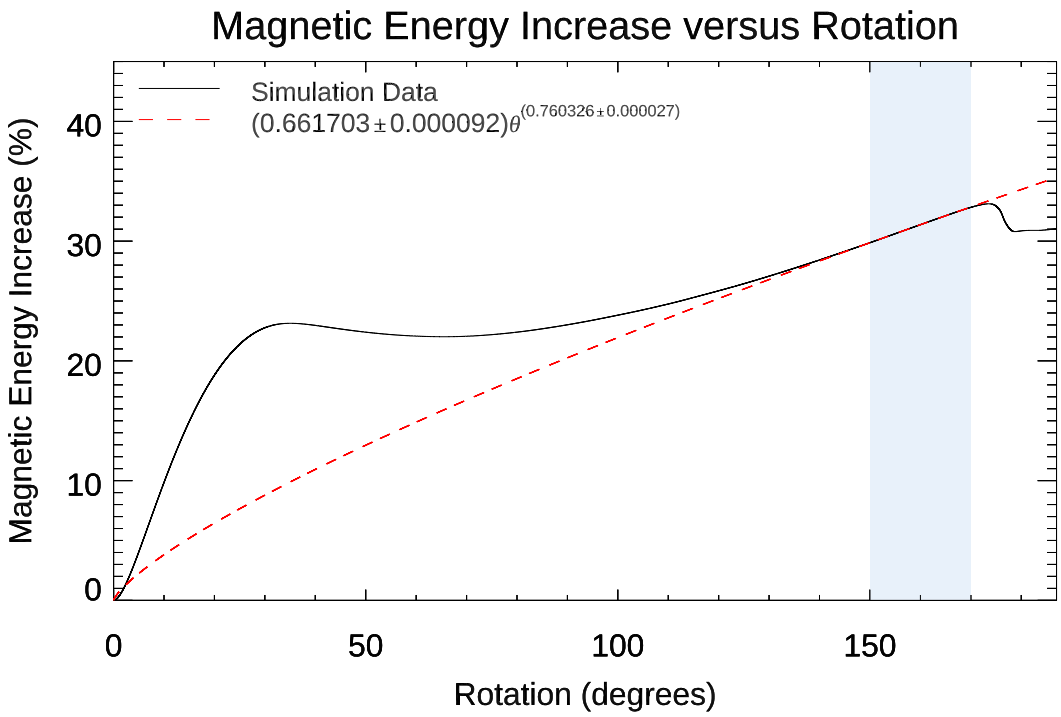

Figure B.2: This figure shows the power-law fit for simulation number 4.

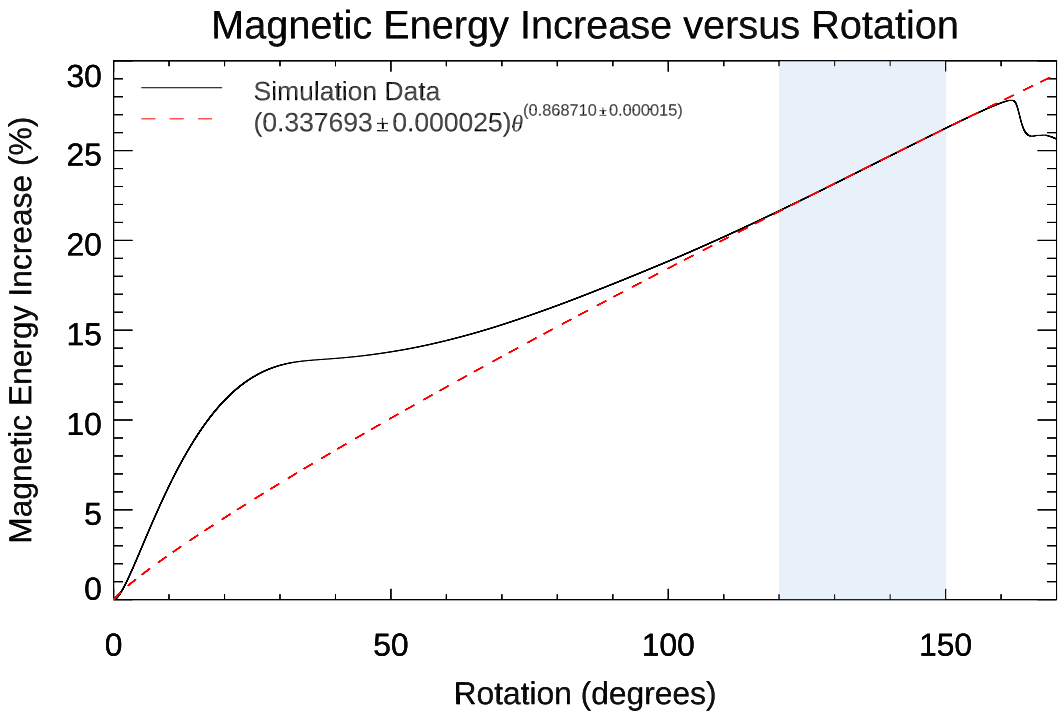

Figure B.3: This figure shows the power-law fit for simulation number 5.

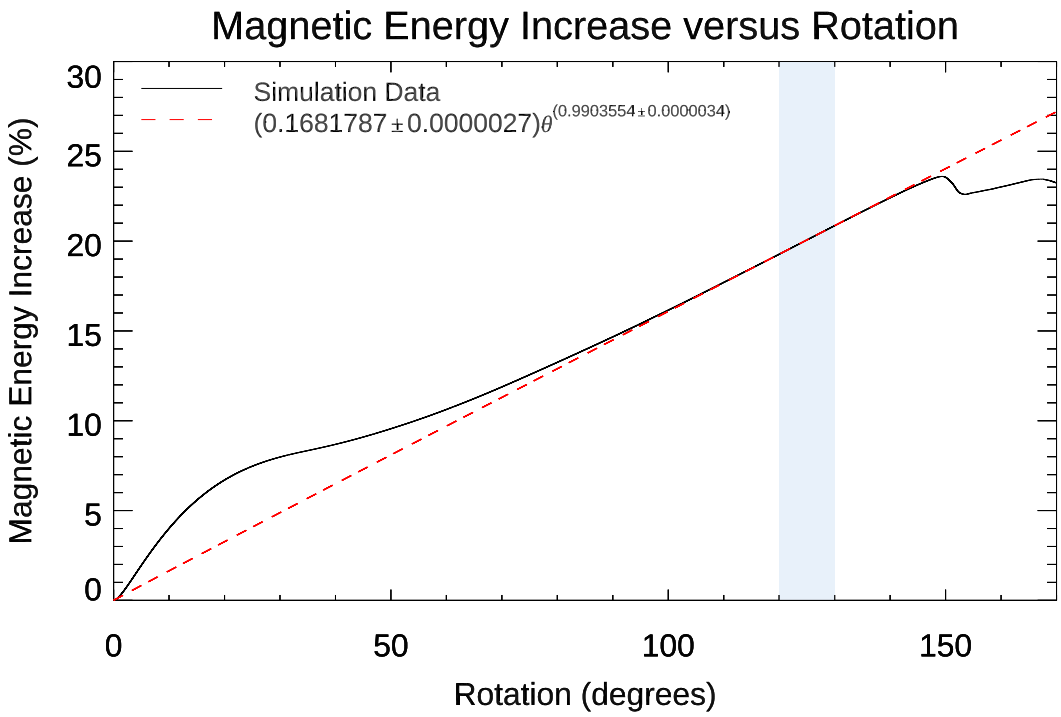

Figure B.4: This figure shows the power-law fit for simulation number 6.

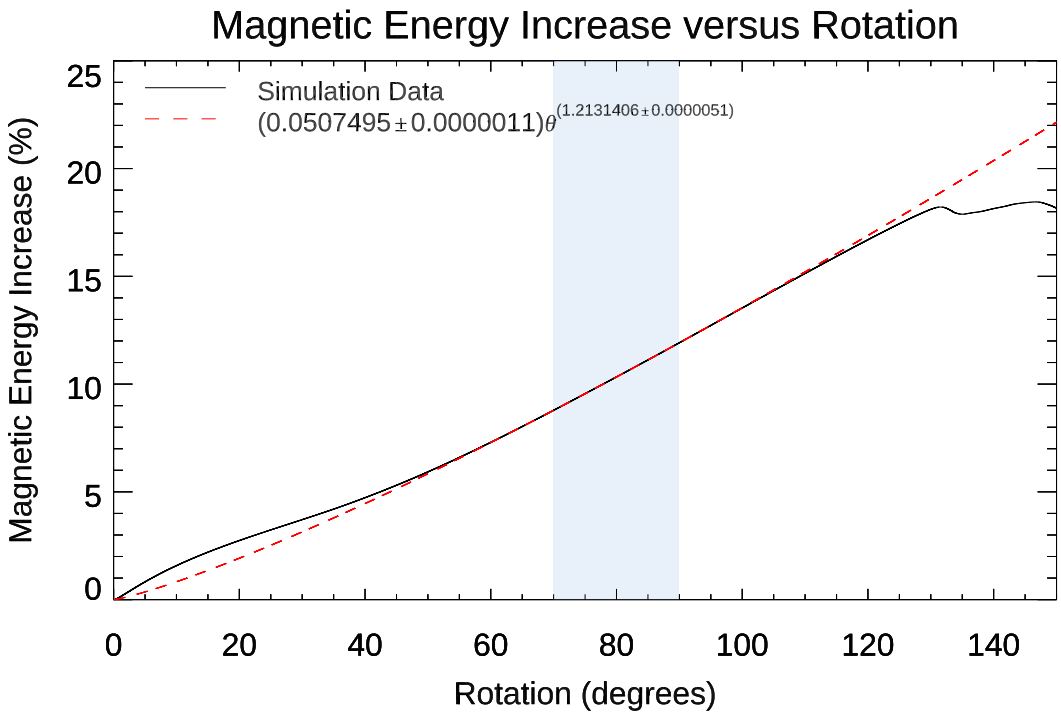

Figure B.5: This figure shows the power-law fit for simulation number 7.

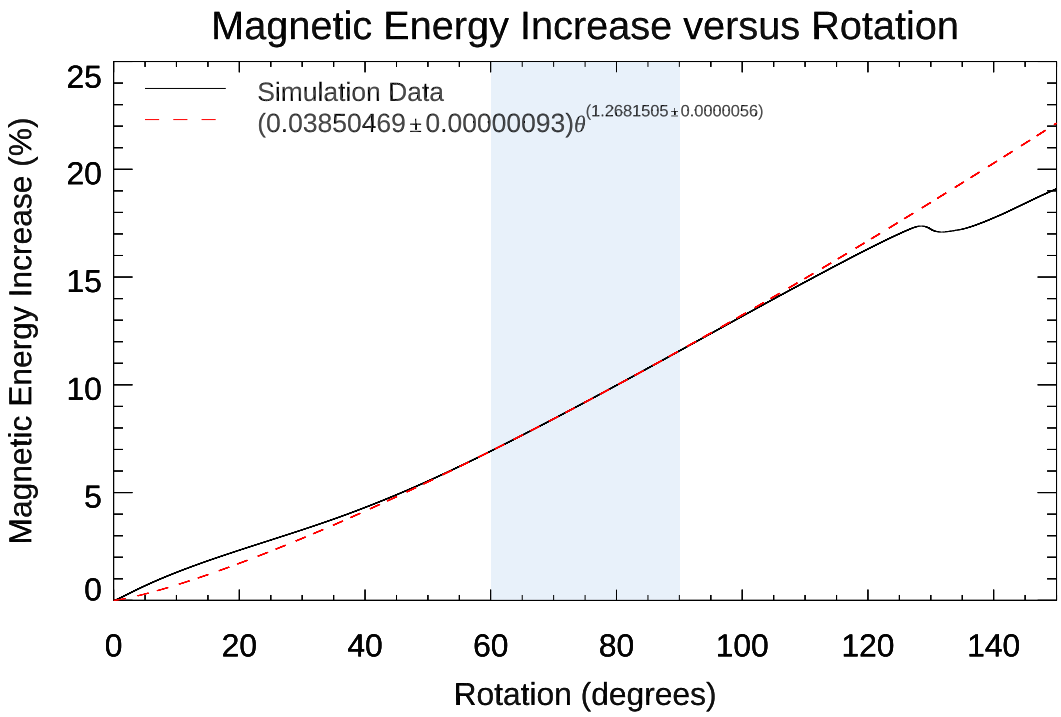

Figure B.6: This figure shows the power-law fit for simulation number 8.

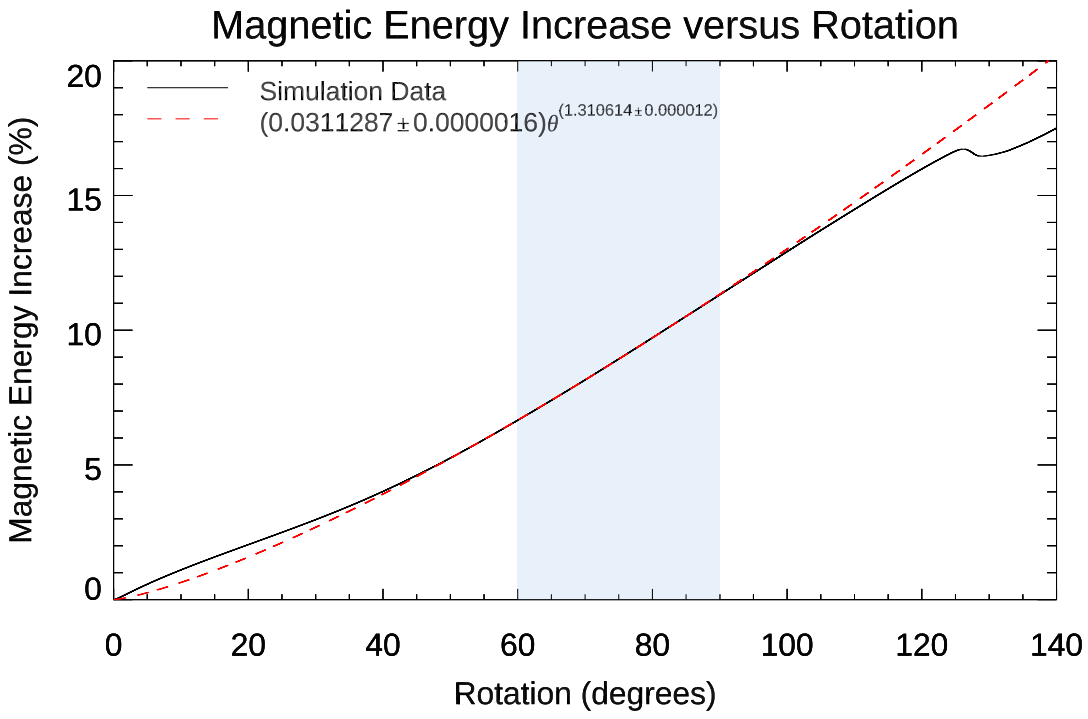

Figure B.7: This figure shows the power-law fit for simulation number 9.

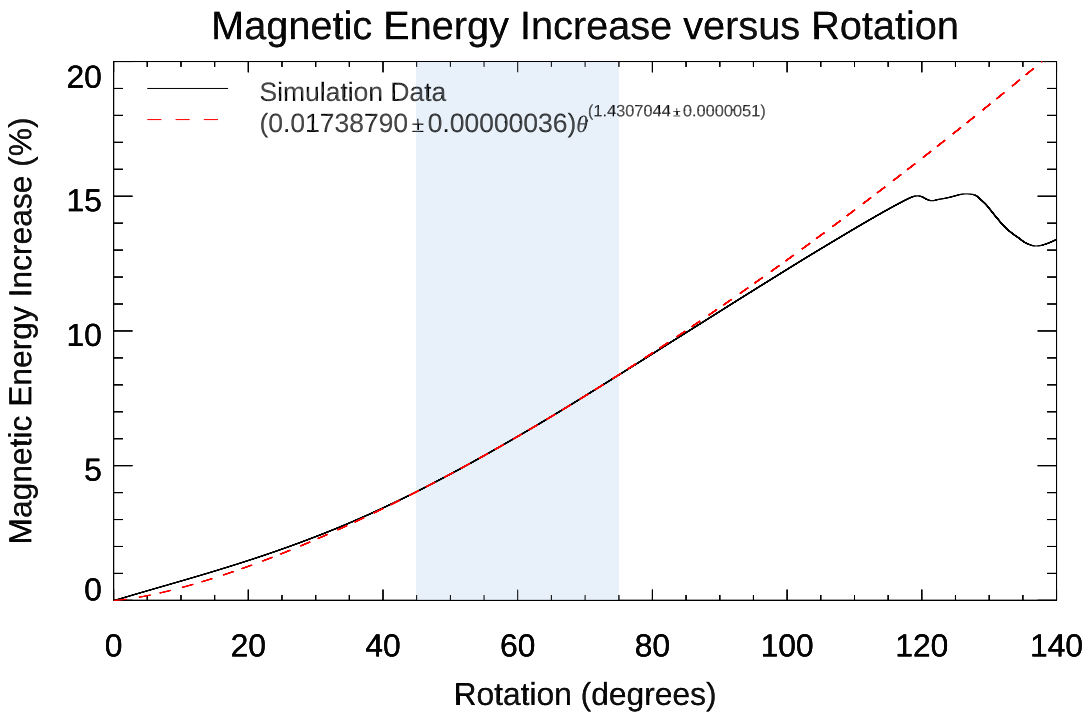

Figure B.8: This figure shows the power-law fit for simulation number 10.

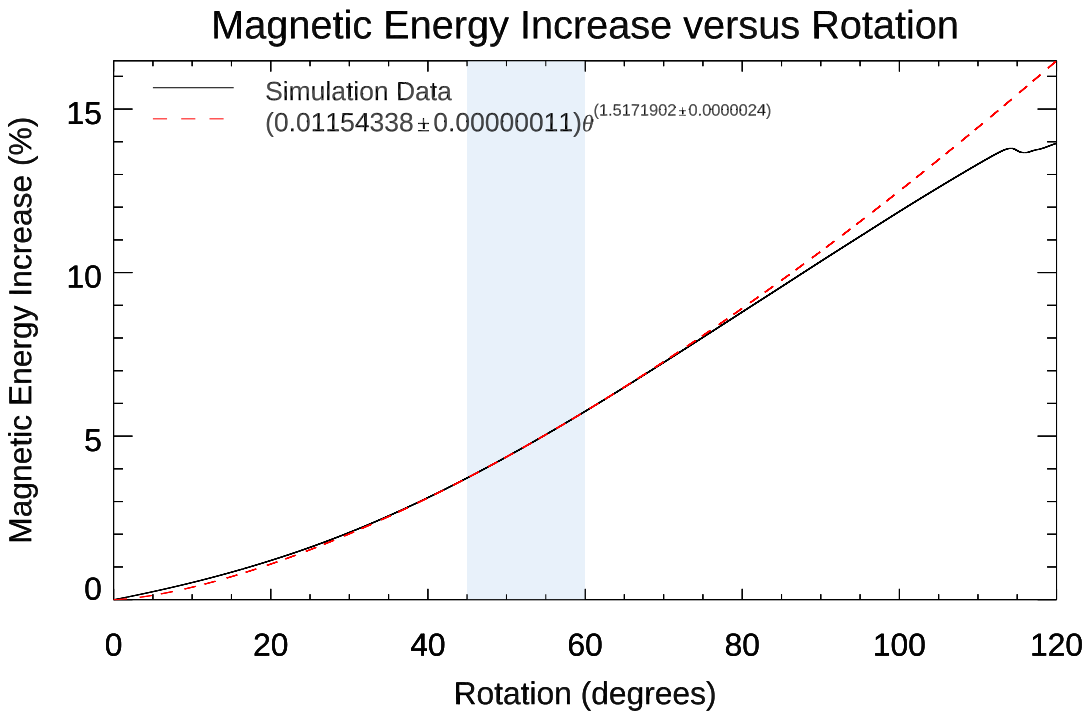

Figure B.9: This figure shows the power-law fit for simulation number 11.

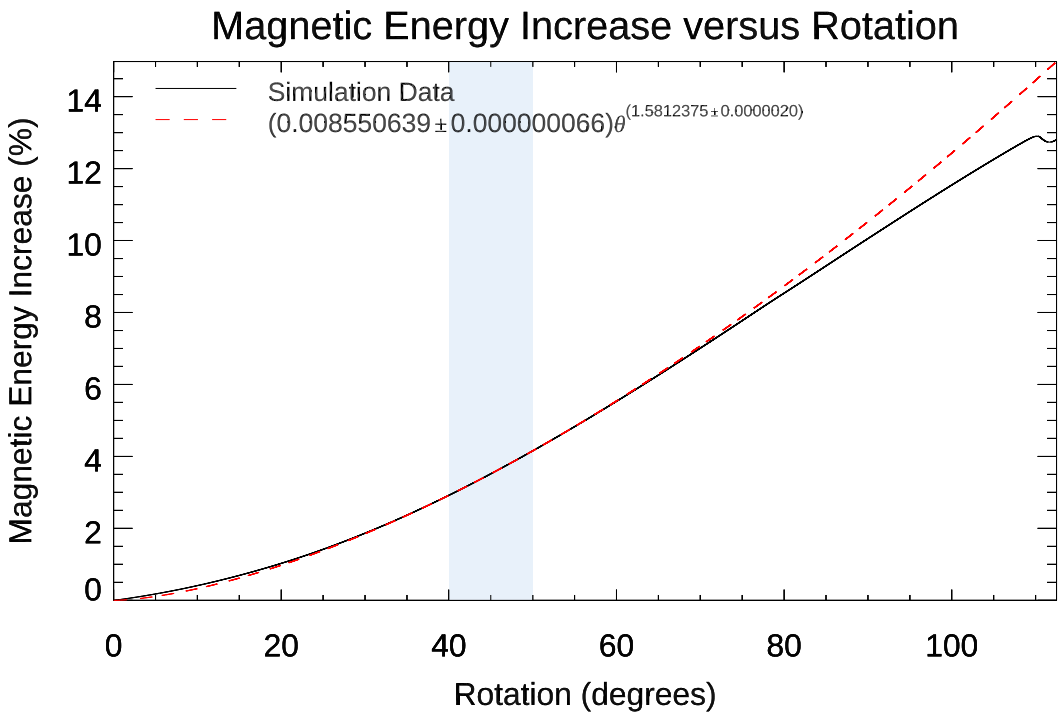

Figure B.10: This figure shows the power-law fit for simulation number 12.

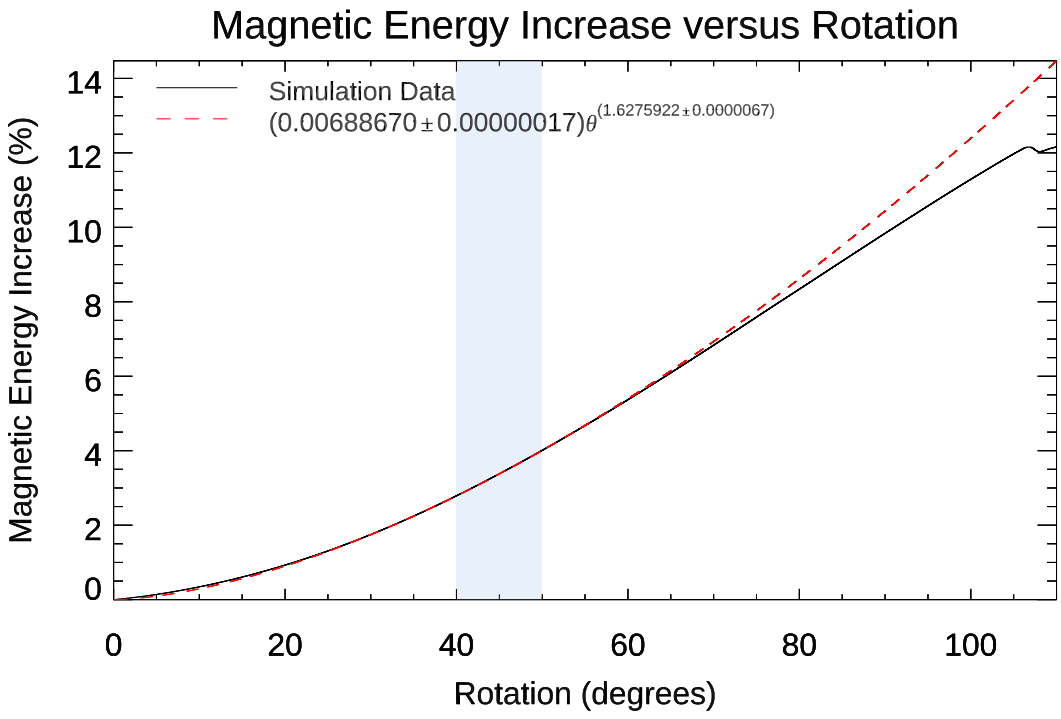

Figure B.11: This figure shows the power-law fit for simulation number 13.

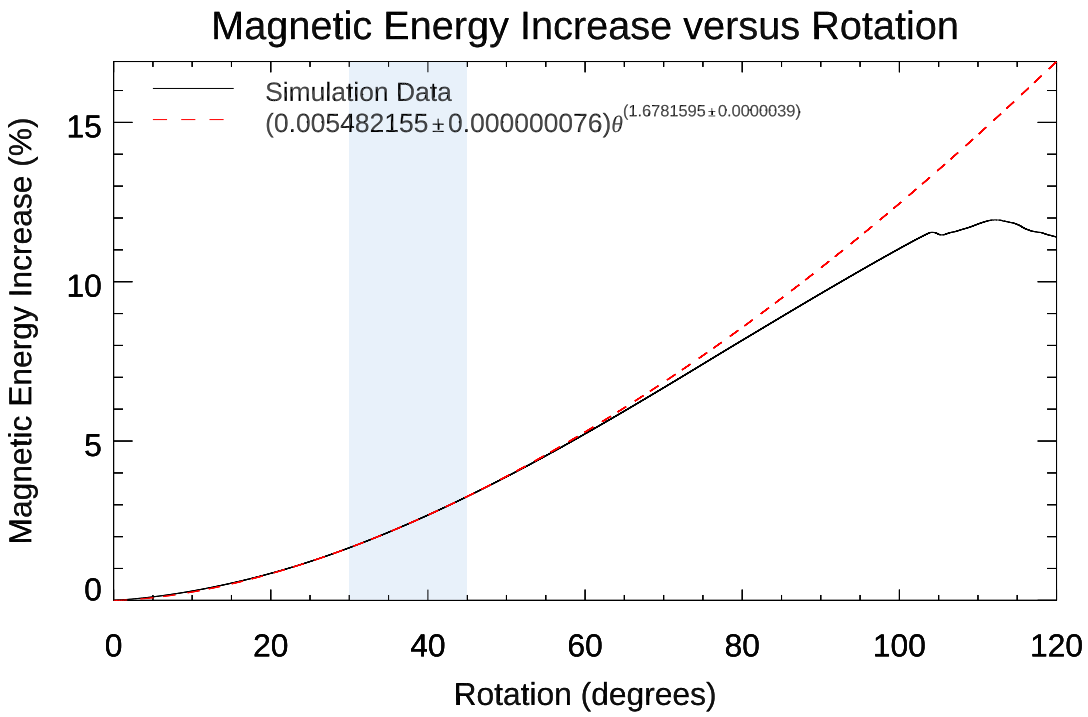

Figure B.12: This figure shows the power-law fit for simulation number 14.

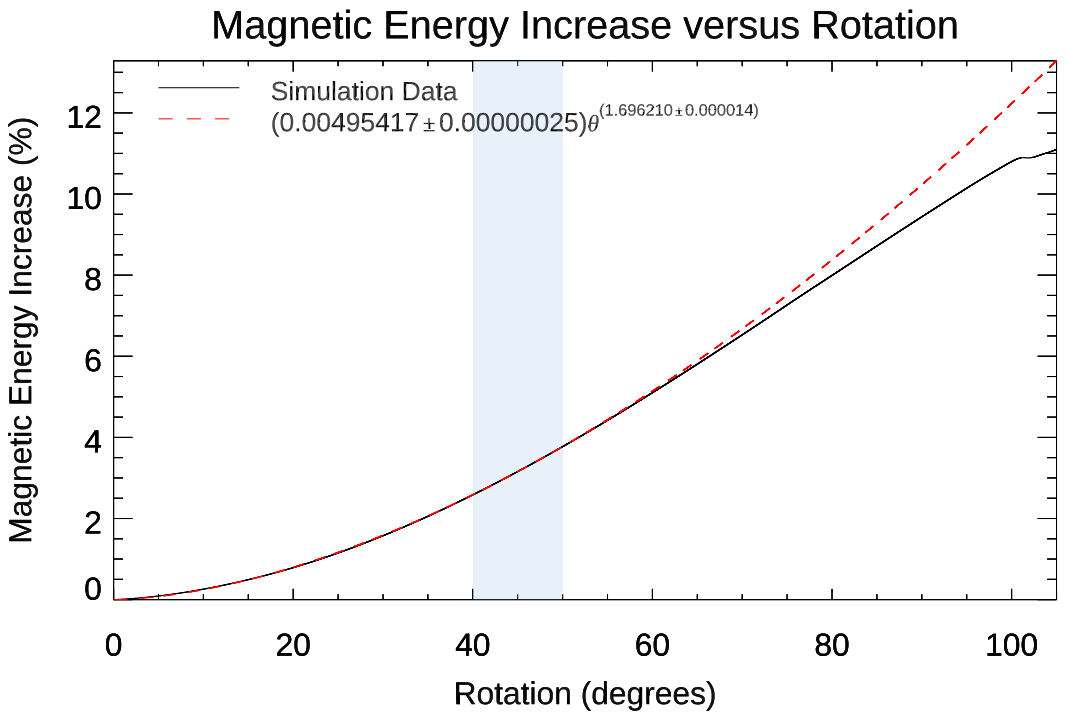

Figure B.13: This figure shows the power-law fit for simulation number 15.

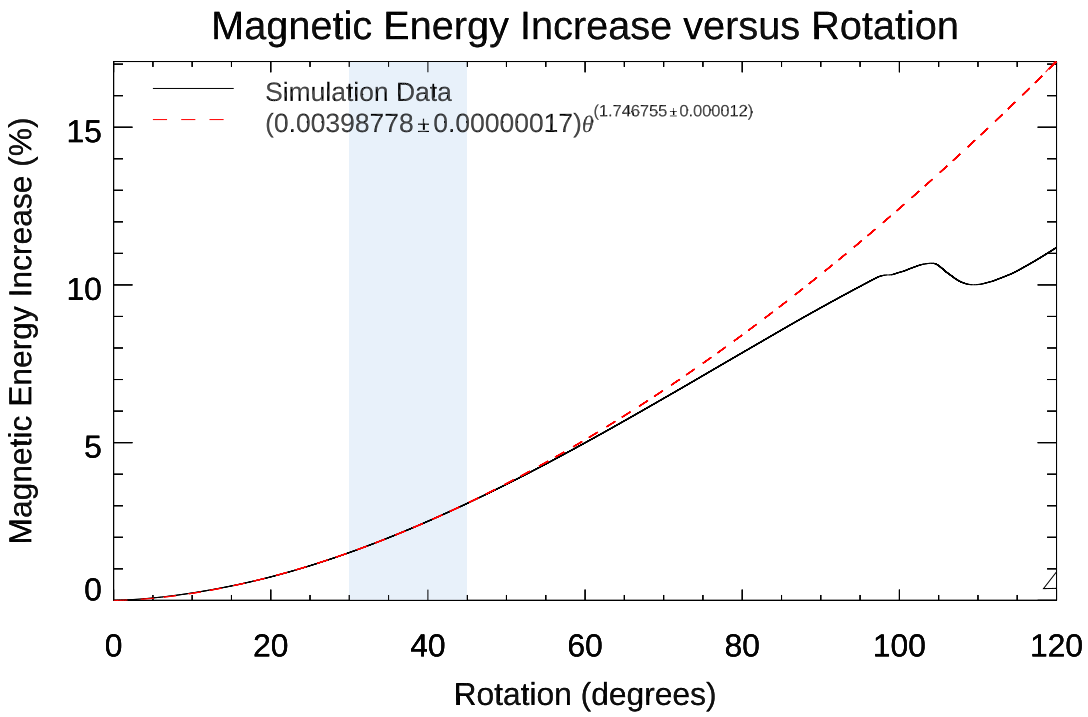

Figure B.14: This figure shows the power-law fit for simulation number 16.

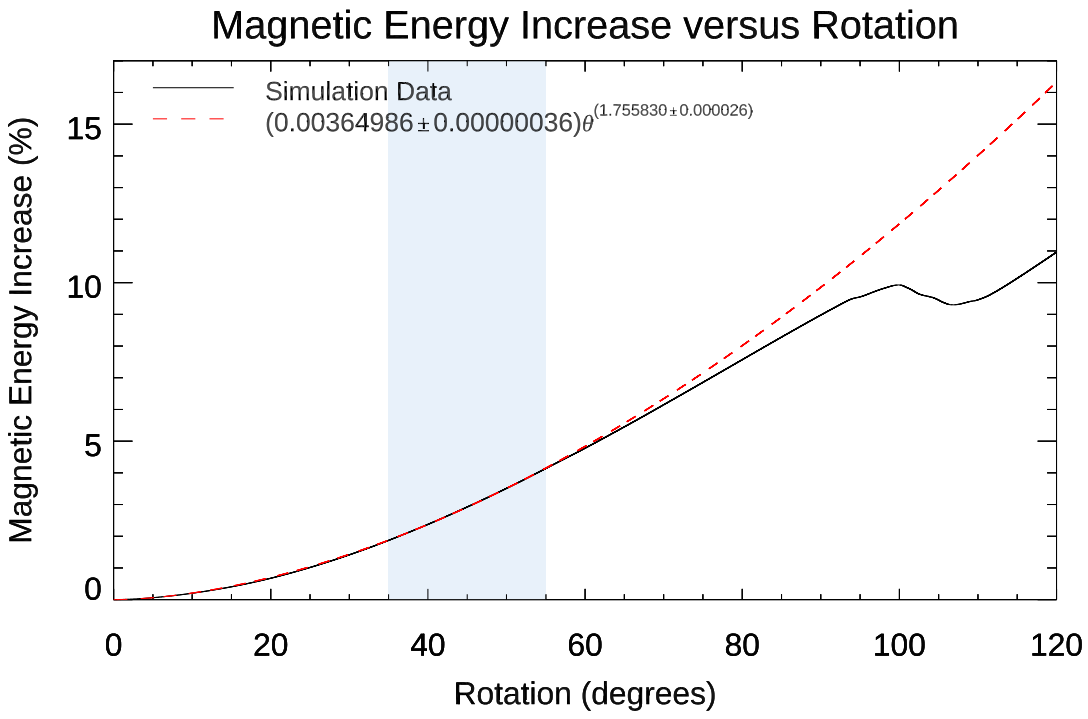

Figure B.15: This figure shows the power-law fit for simulation number 17.

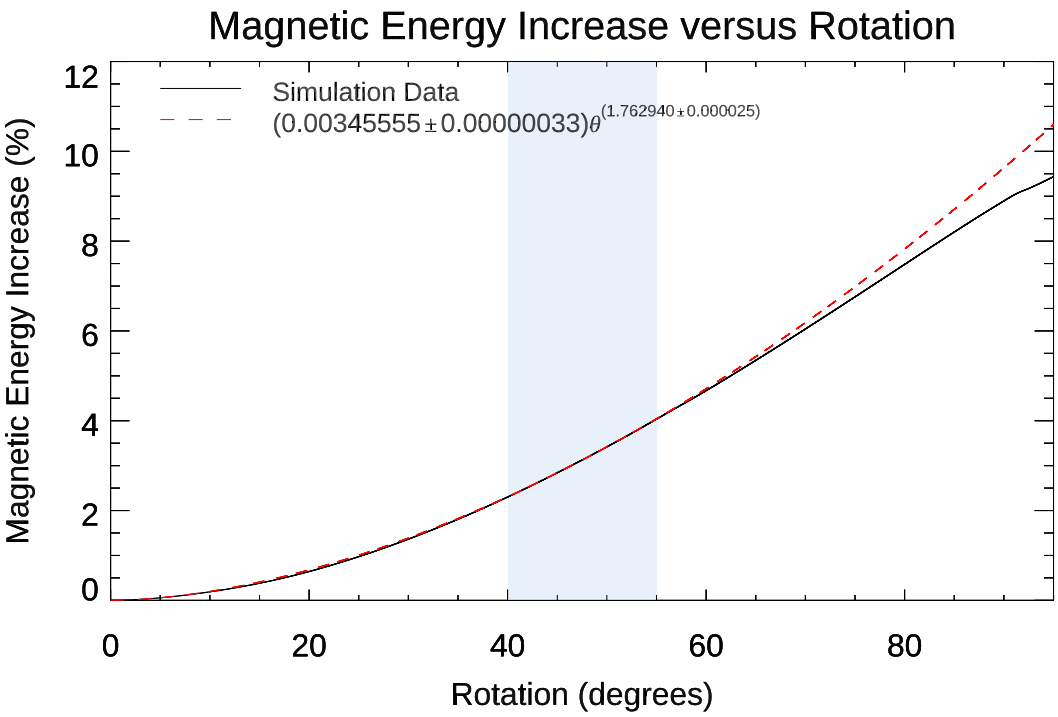

Figure B.16: This figure shows the power-law fit for simulation number 18.

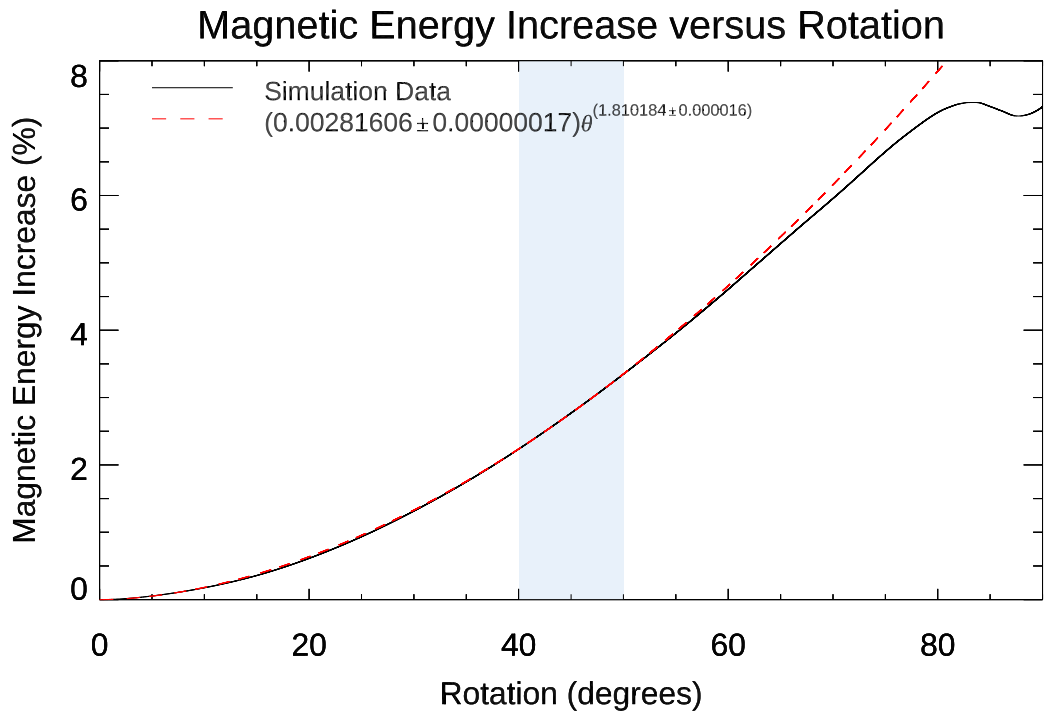

Figure B.17: This figure shows the power-law fit for simulation number 19.

Appendix C

Radii Ratio - ψ

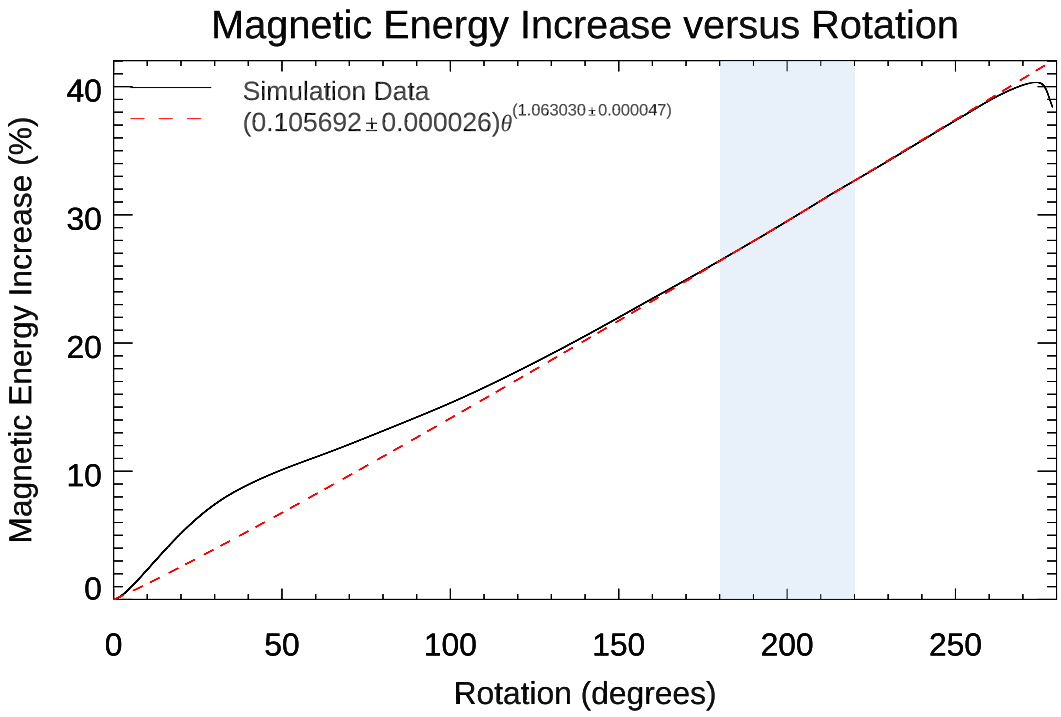

Figure C.1: This figure shows the power-law fit for simulation number 33.

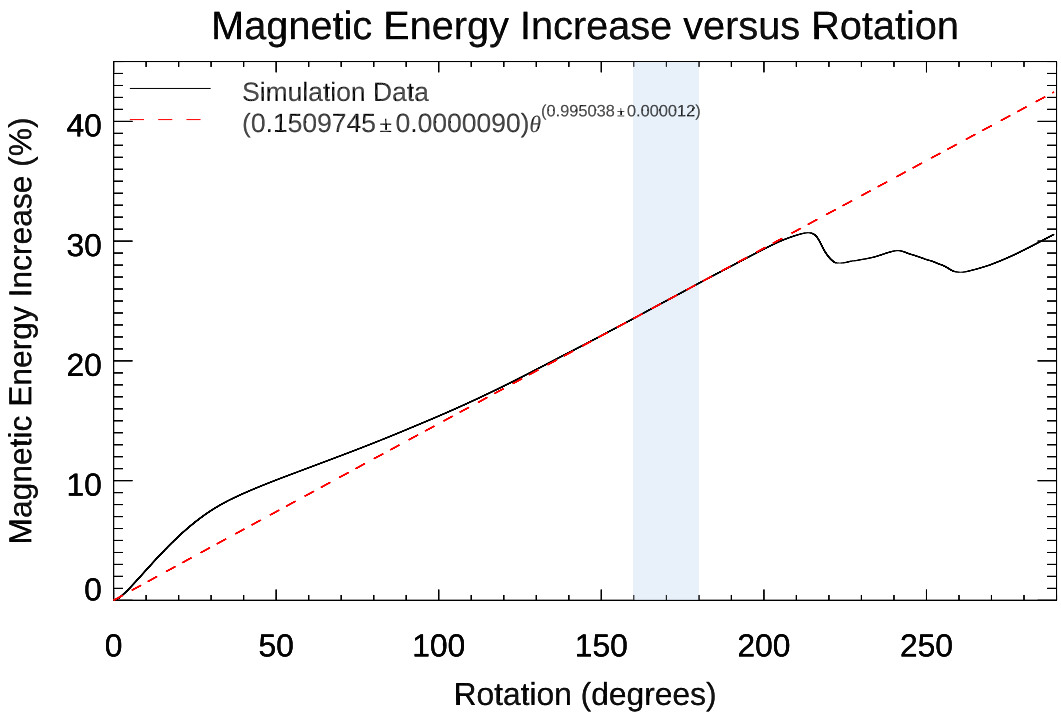

Figure C.2: This figure shows the power-law fit for simulation number 34.

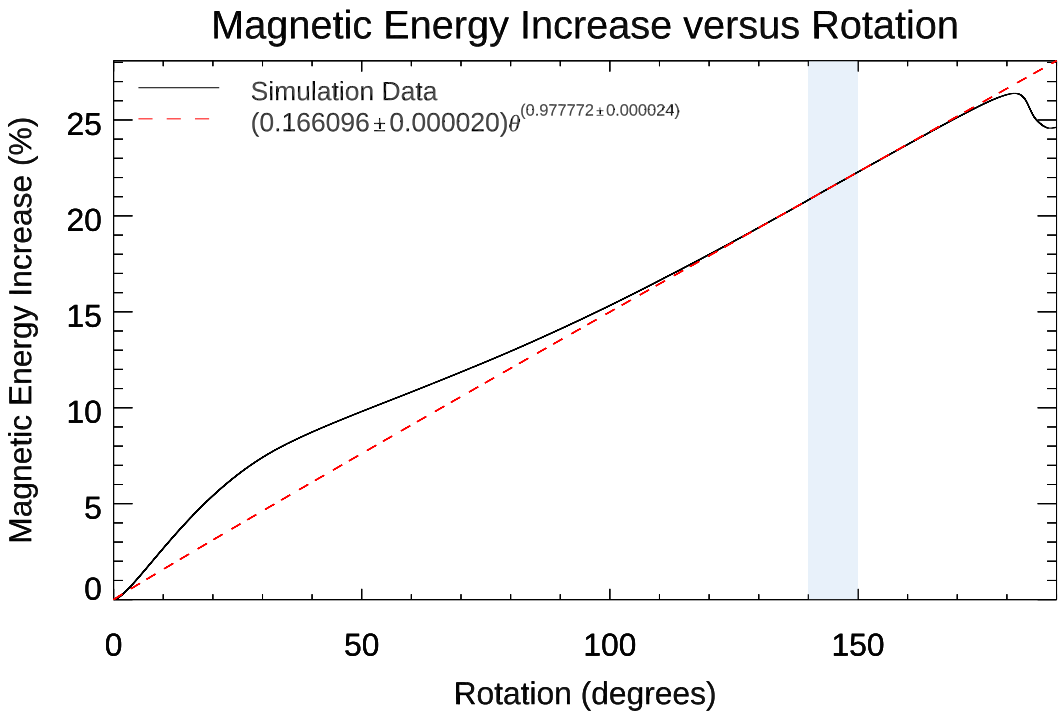

Figure C.3: This figure shows the power-law fit for simulation number 35.

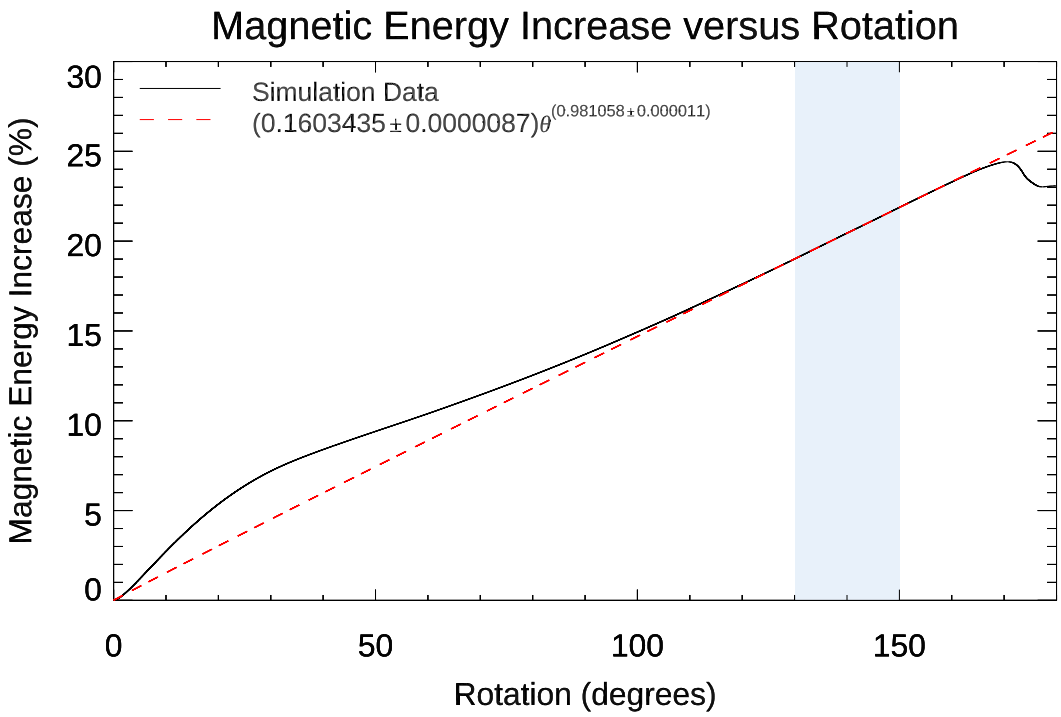

Figure C.4: This figure shows the power-law fit for simulation number 36.

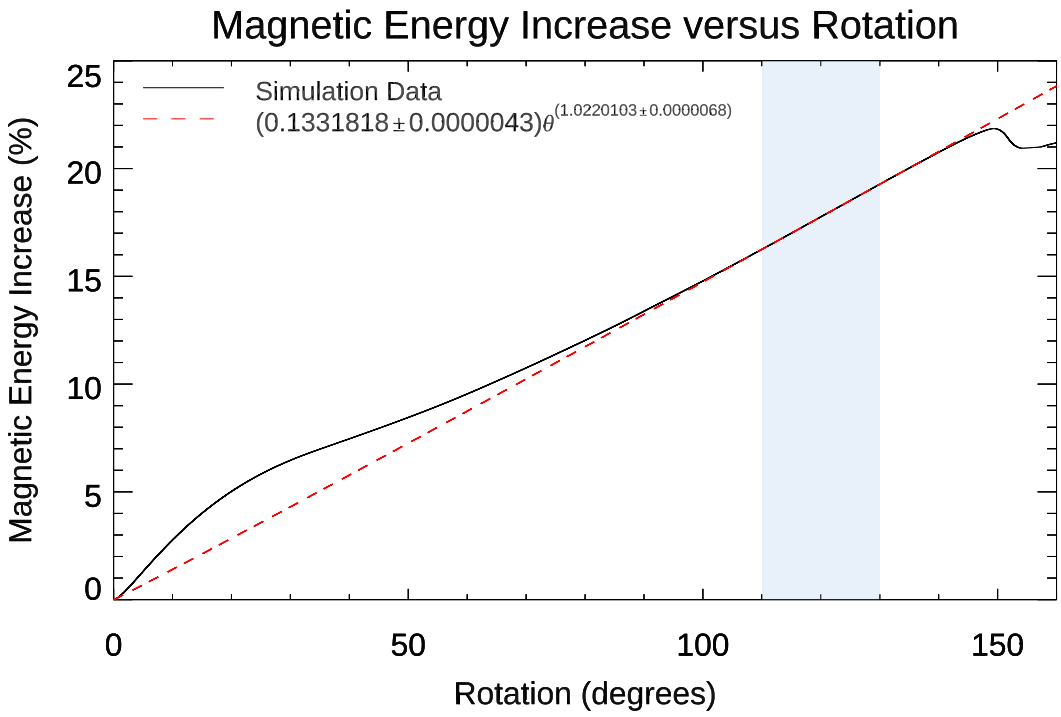

Figure C.5: This figure shows the power-law fit for simulation number 37.

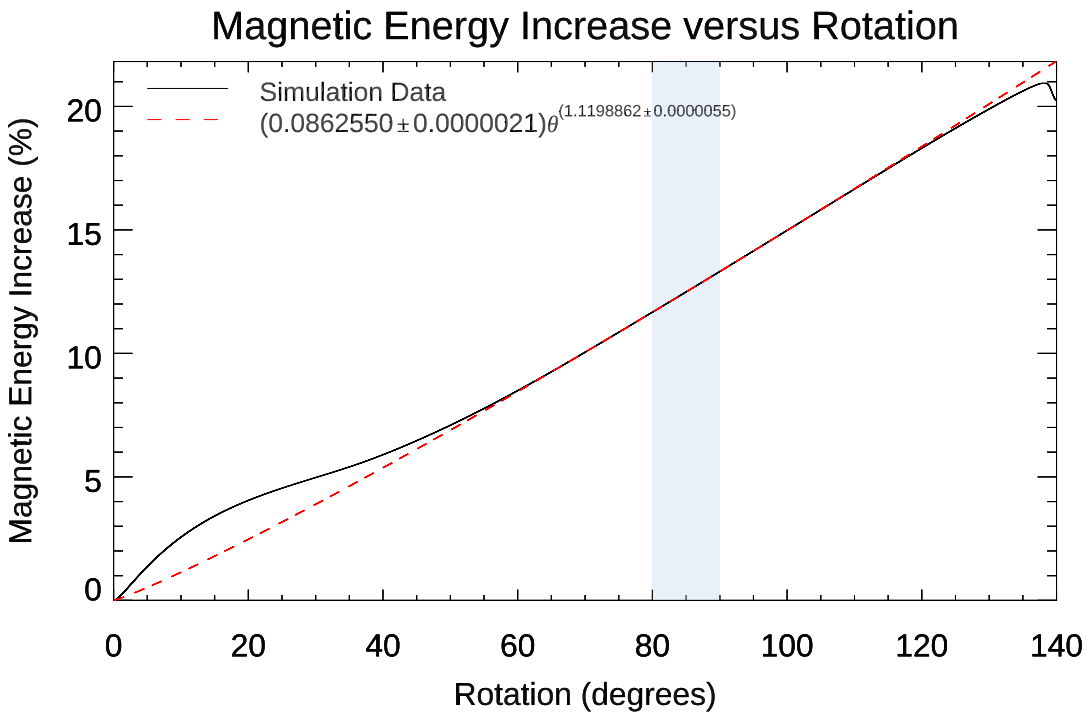

Figure C.6: This figure shows the power-law fit for simulation number 38.

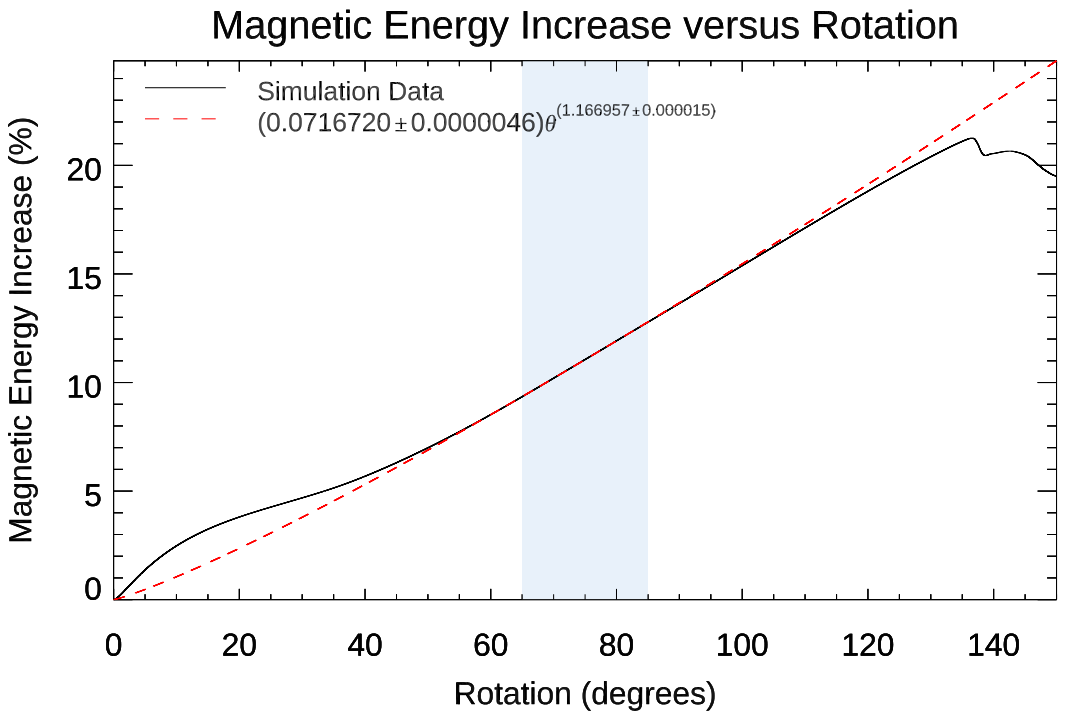

Figure C.7: This figure shows the power-law fit for simulation number 39.

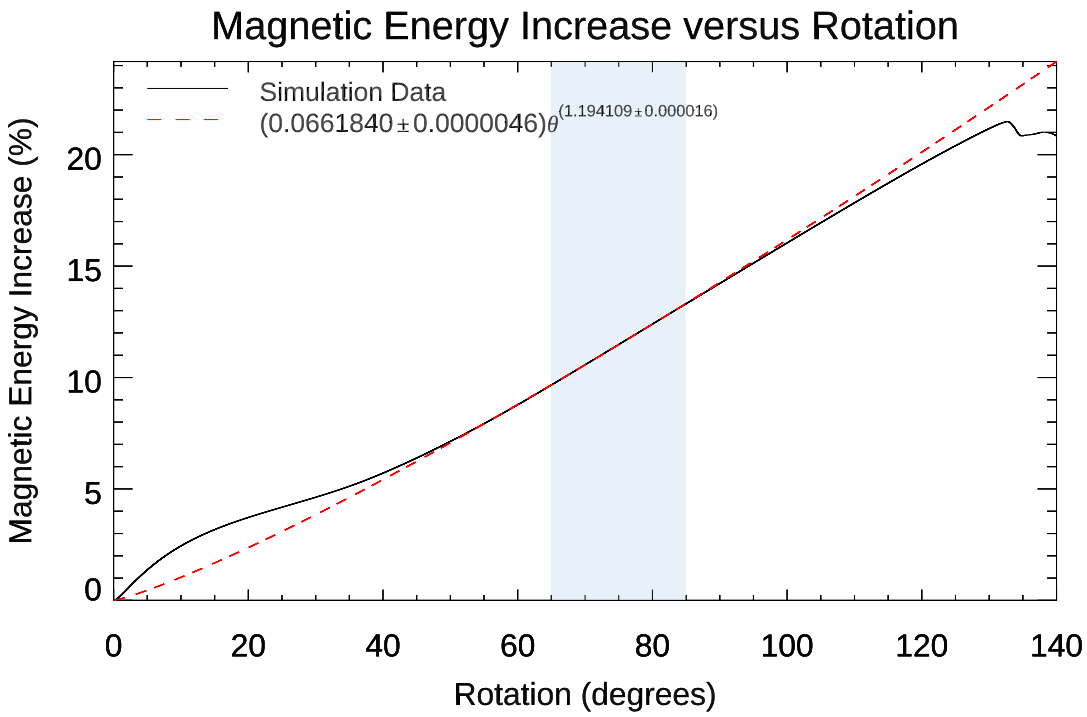

Figure C.8: This figure shows the power-law fit for simulation number 40.

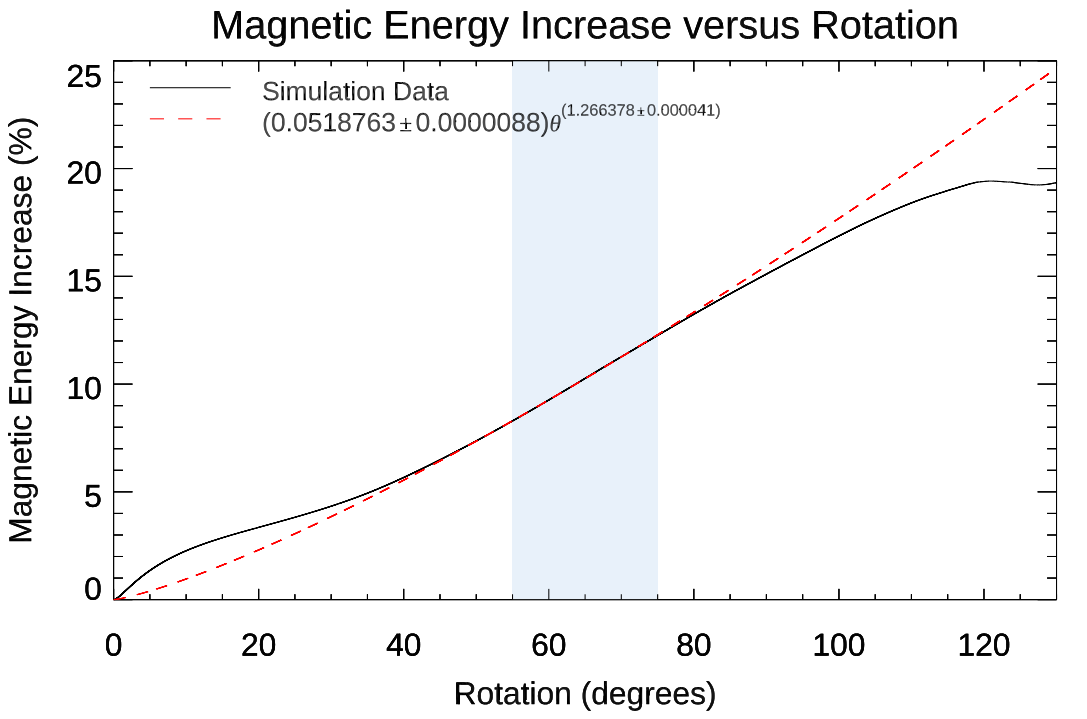

Figure C.9: This figure shows the power-law fit for simulation number 41.

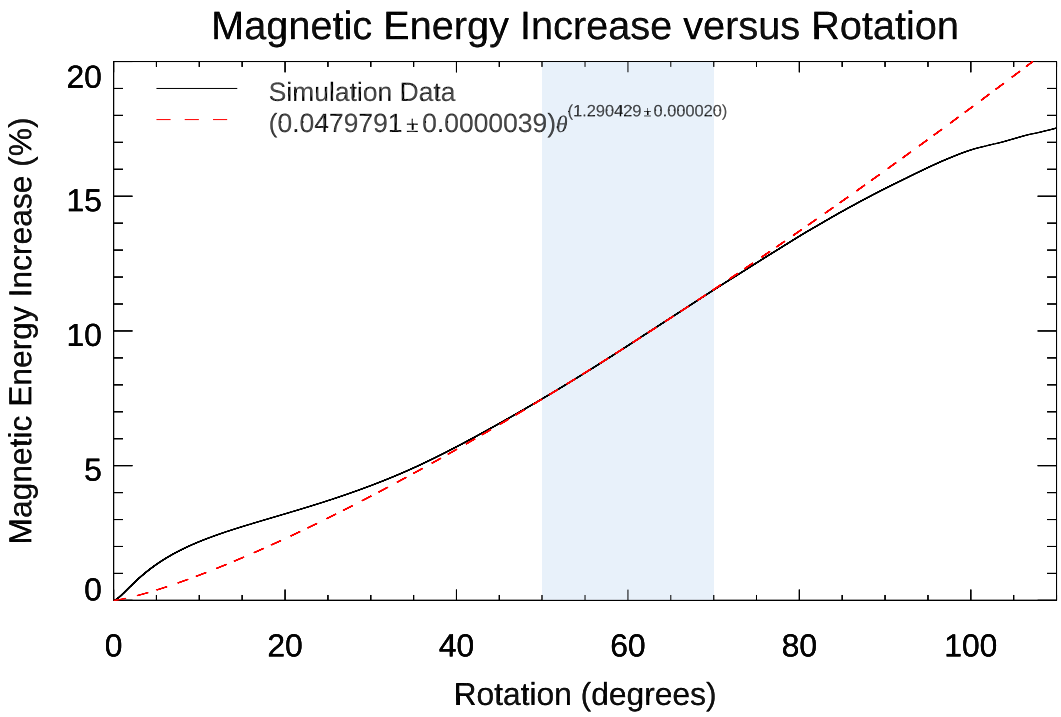

Figure C.10: This figure shows the power-law fit for simulation number 42.

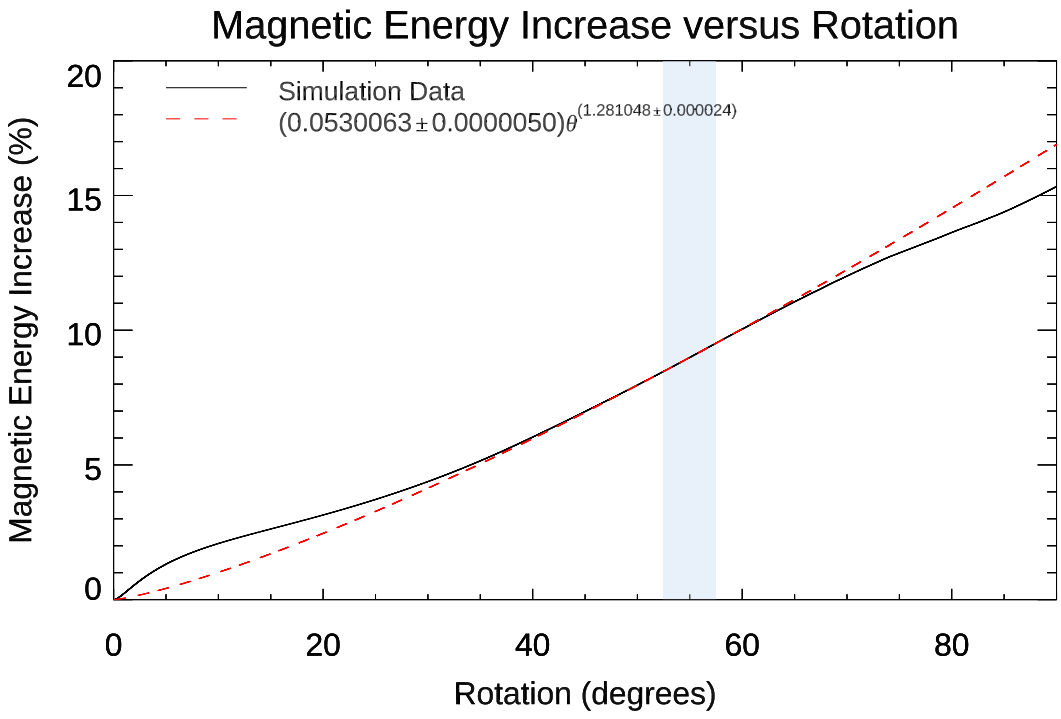

Figure C.11: This figure shows the power-law fit for simulation number 43.

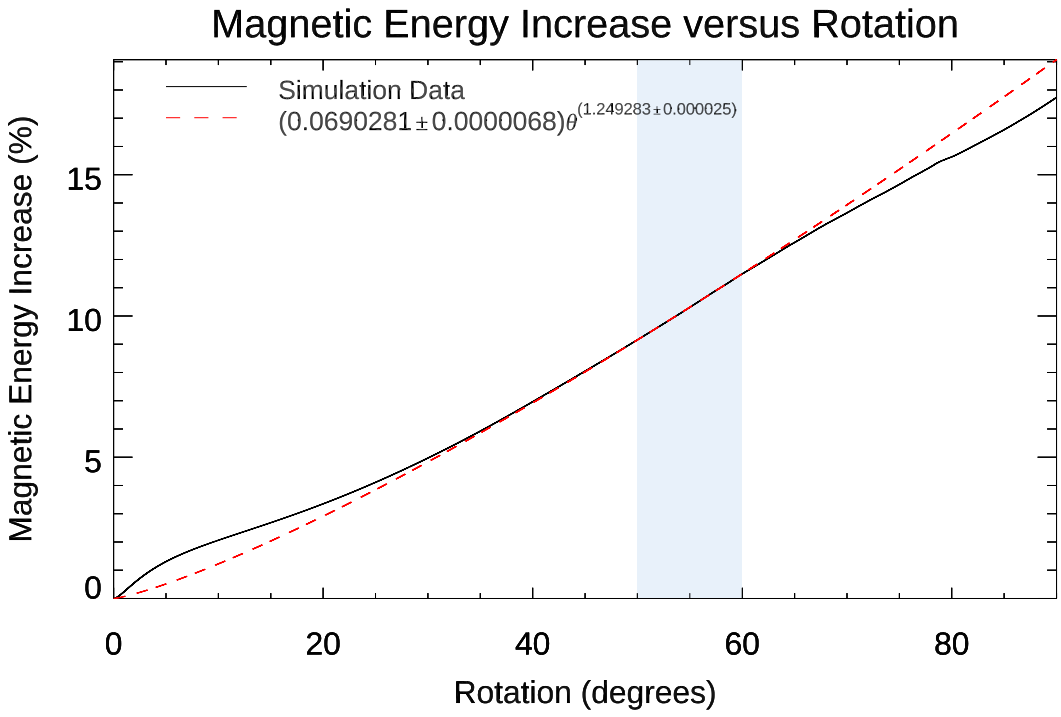

Figure C.12: This figure shows the power-law fit for simulation number 44.

Appendix D

Sunspot Size - P_r

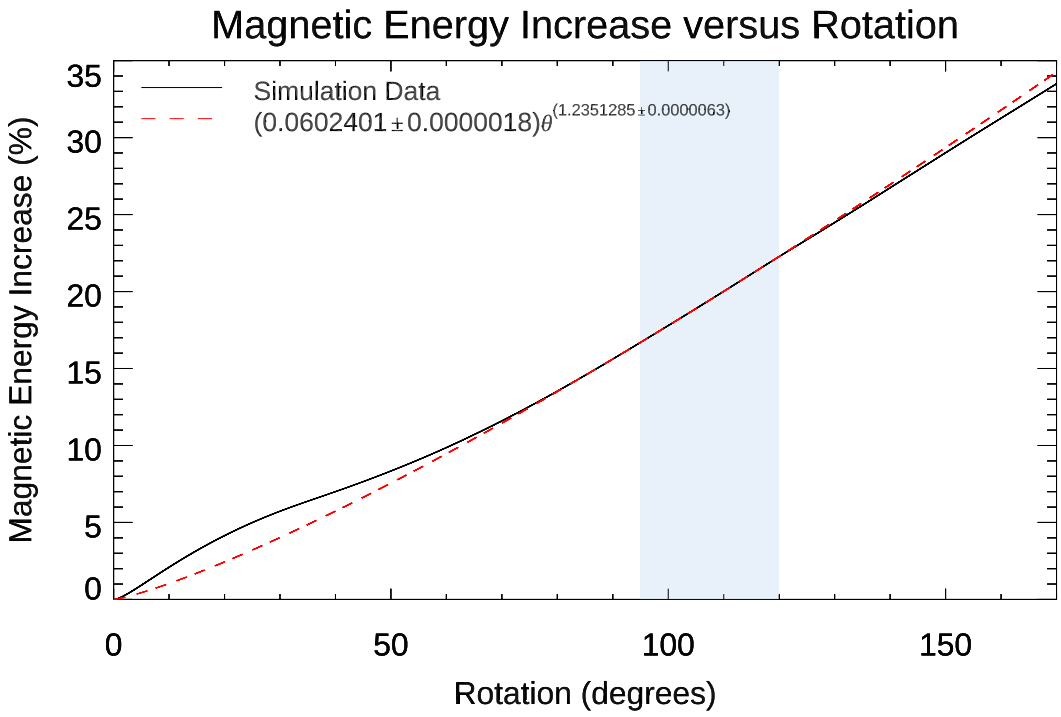

Figure D.1: This figure shows the power-law fit for simulation number 20.

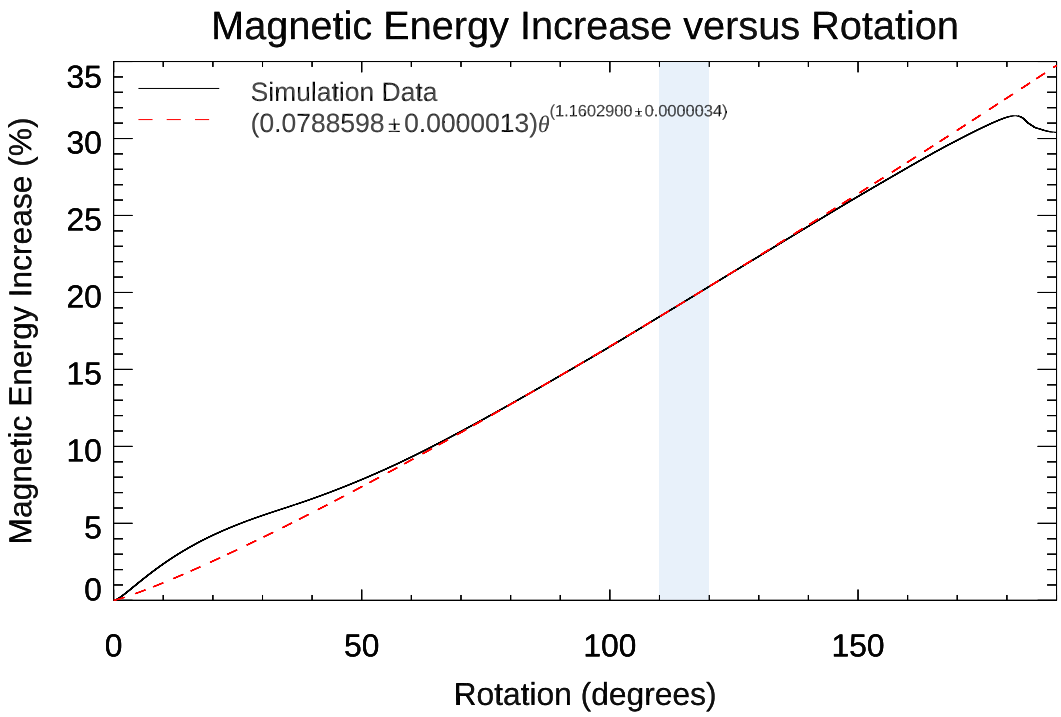

Figure D.2: This figure shows the power-law fit for simulation number 21.

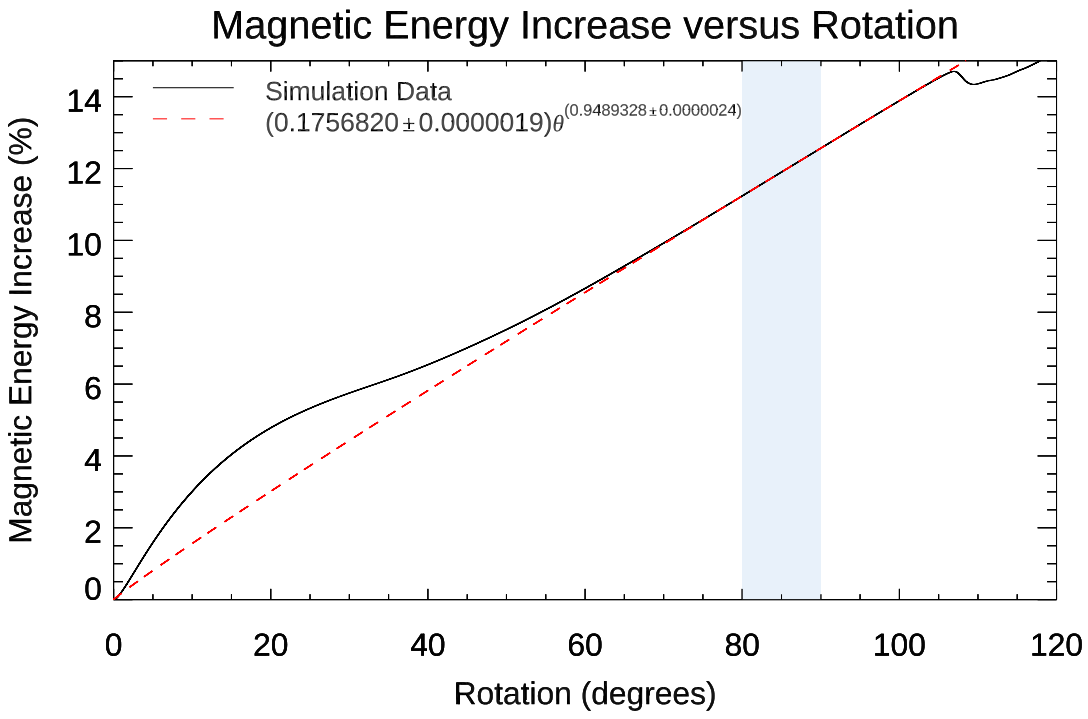

Figure D.3: This figure shows the power-law fit for simulation number 22.

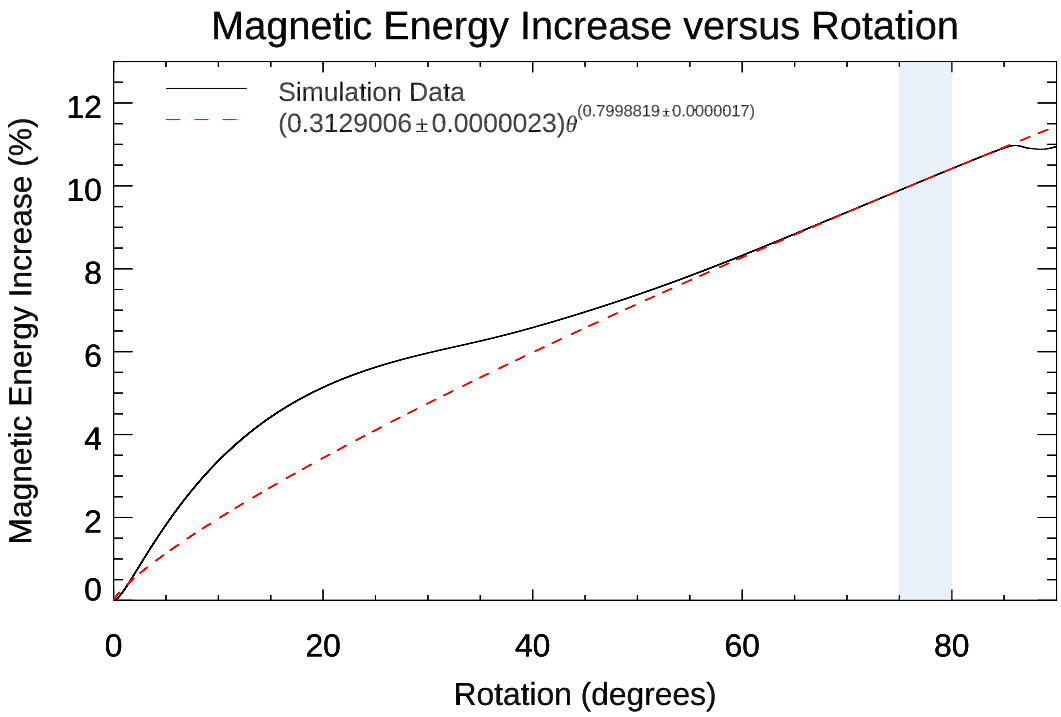

Figure D.4: This figure shows the power-law fit for simulation number 23.

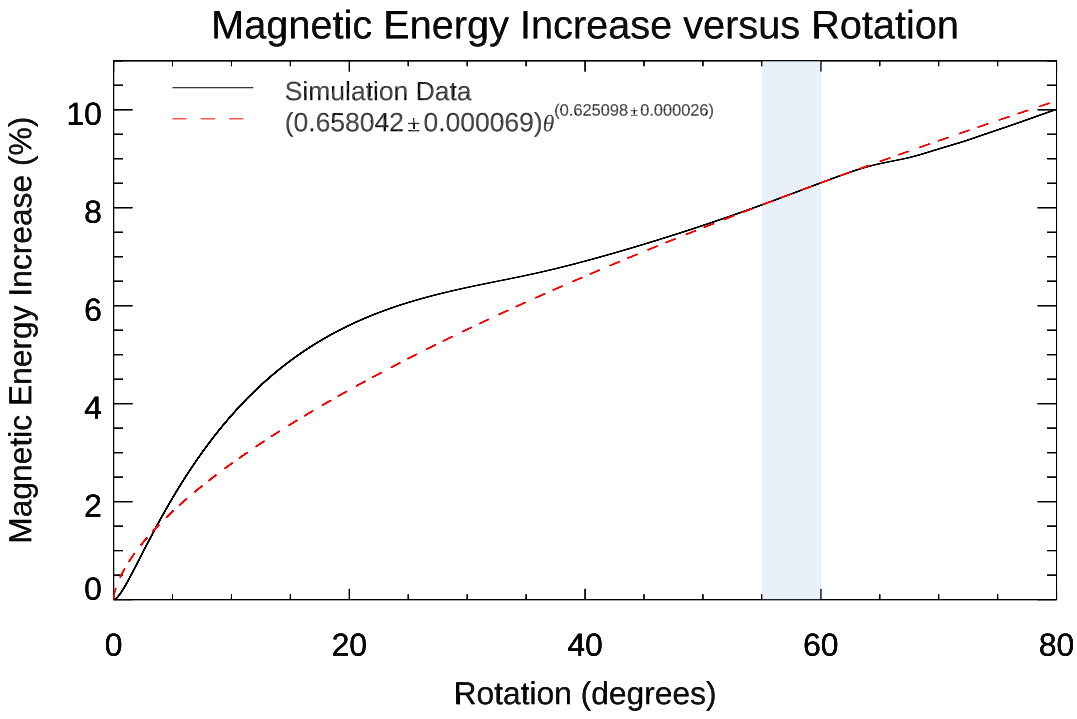

Figure D.5: This figure shows the power-law fit for simulation number 24.

Appendix E

Peak Penumbral Field Strength - μ

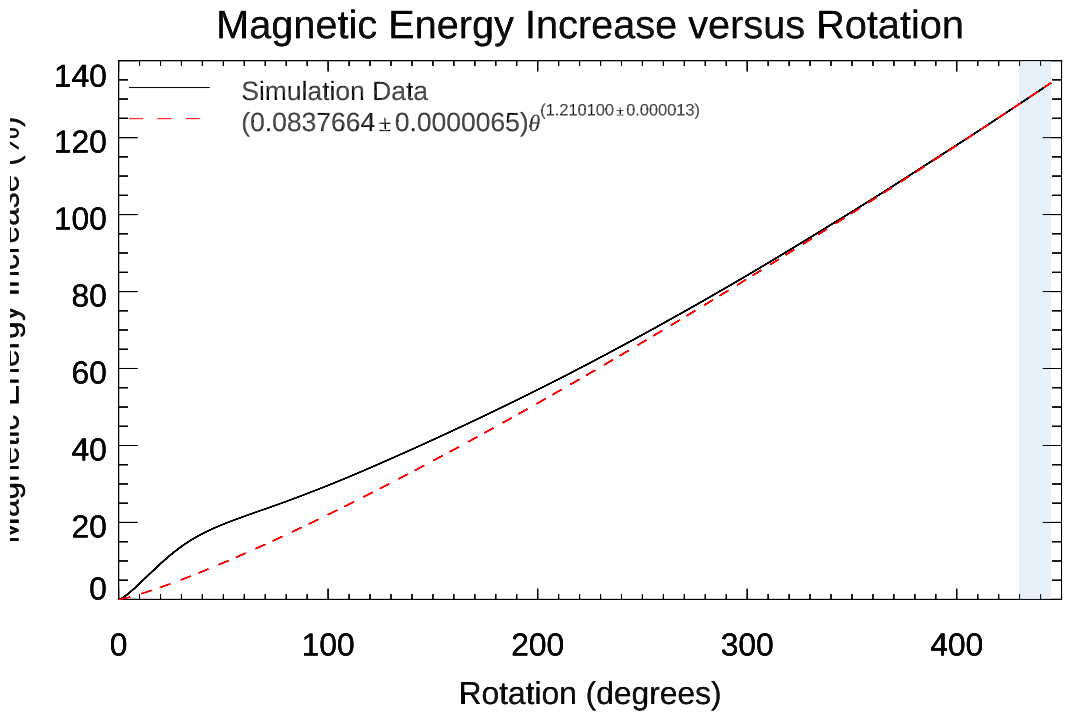

Figure E.1: This figure shows the power-law fit for simulation number 45.

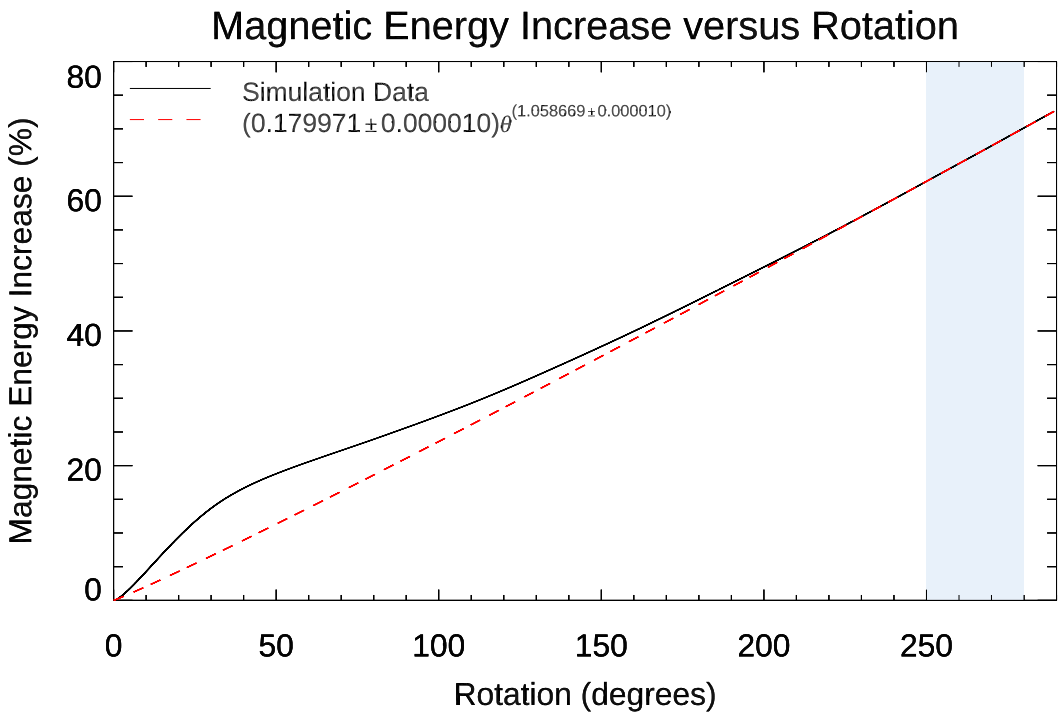

Figure E.2: This figure shows the power-law fit for simulation number 46.

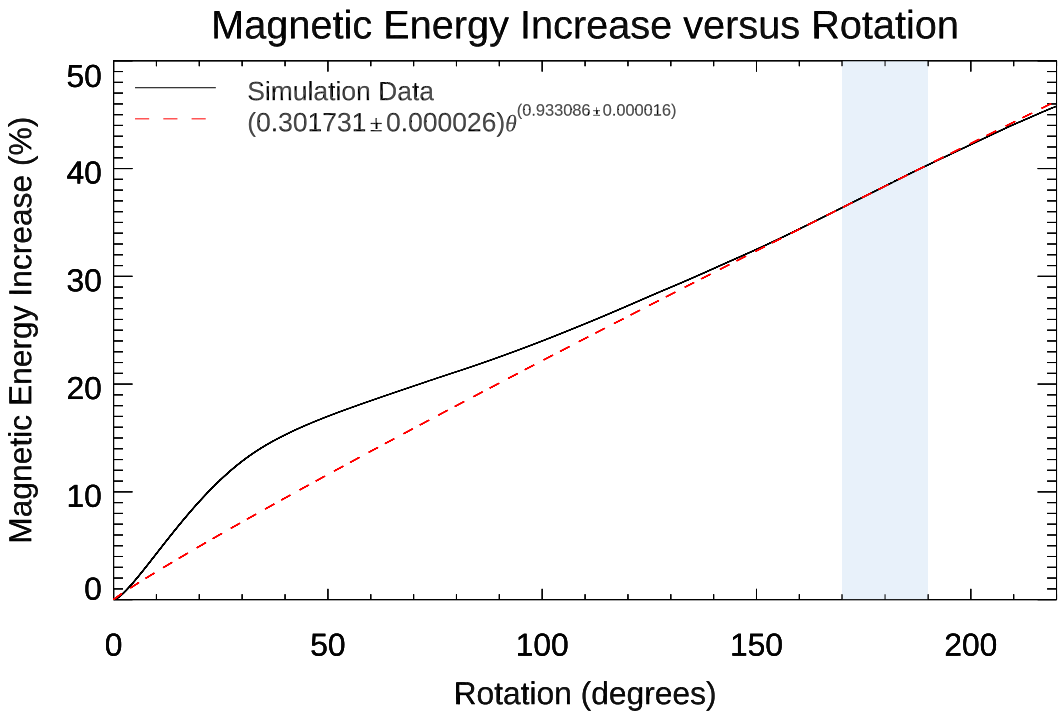

Figure E.3: This figure shows the power-law fit for simulation number 47.

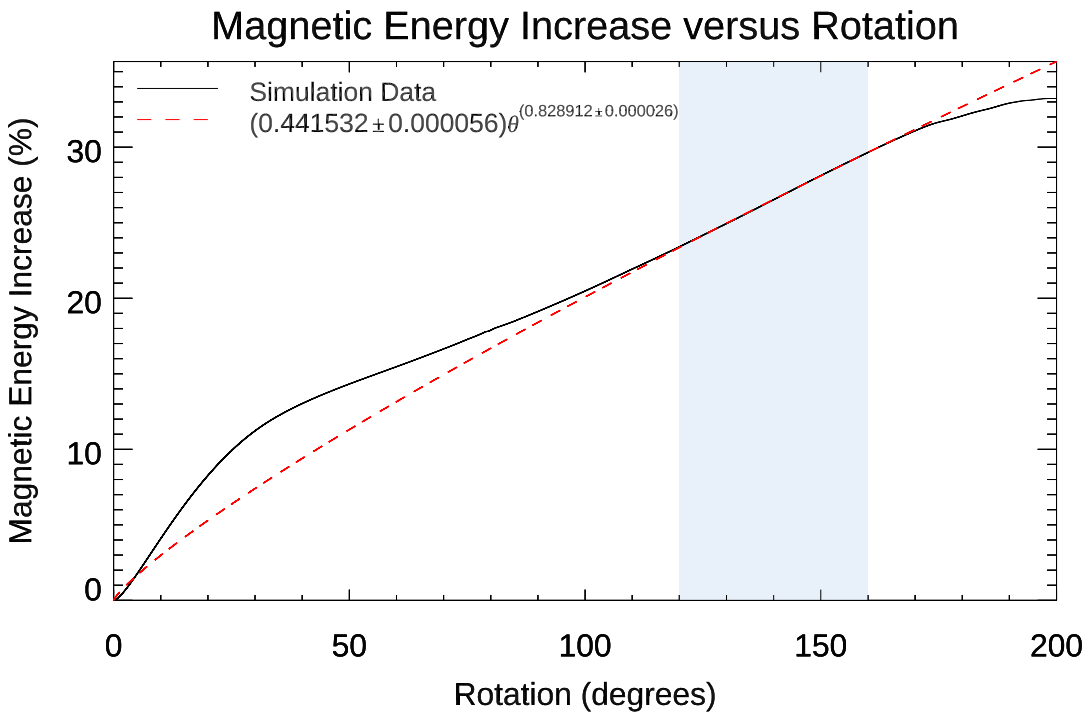

Figure E.4: This figure shows the power-law fit for simulation number 48.

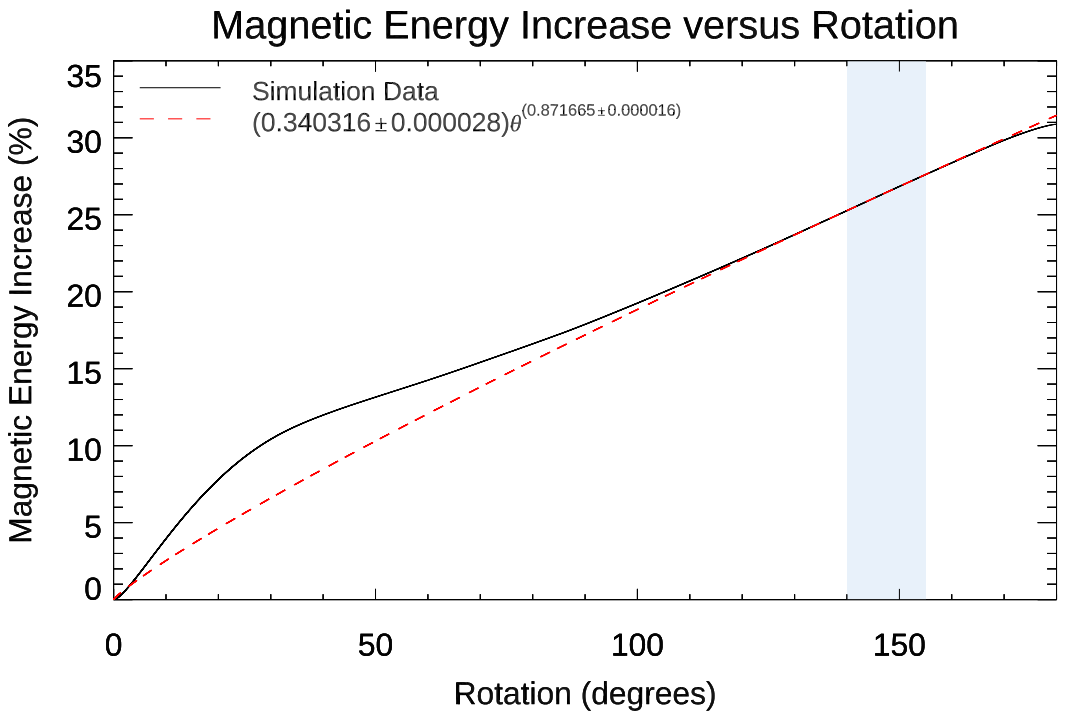

Figure E.5: This figure shows the power-law fit for simulation number 49.

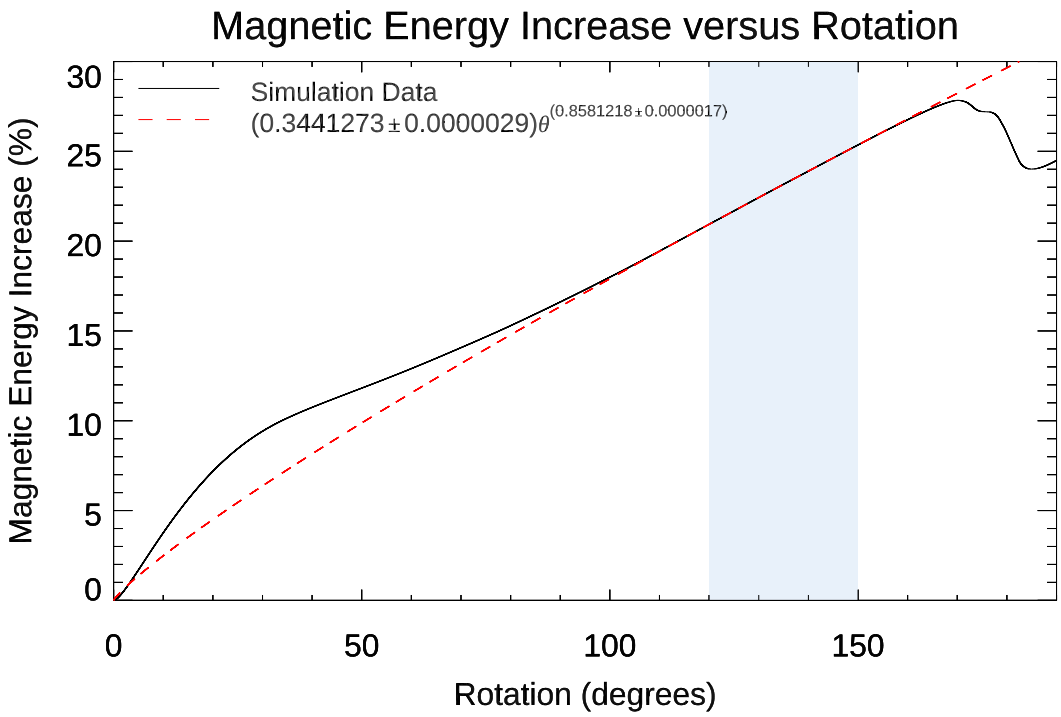

Figure E.6: This figure shows the power-law fit for simulation number 50.

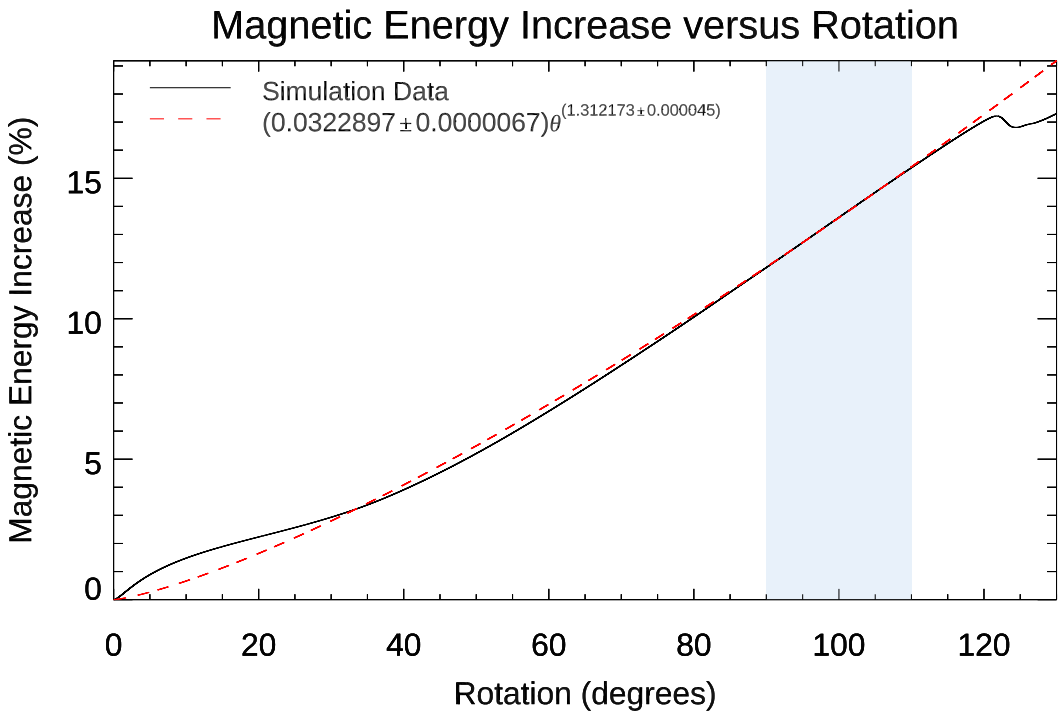

Figure E.7: This figure shows the power-law fit for simulation number 51.

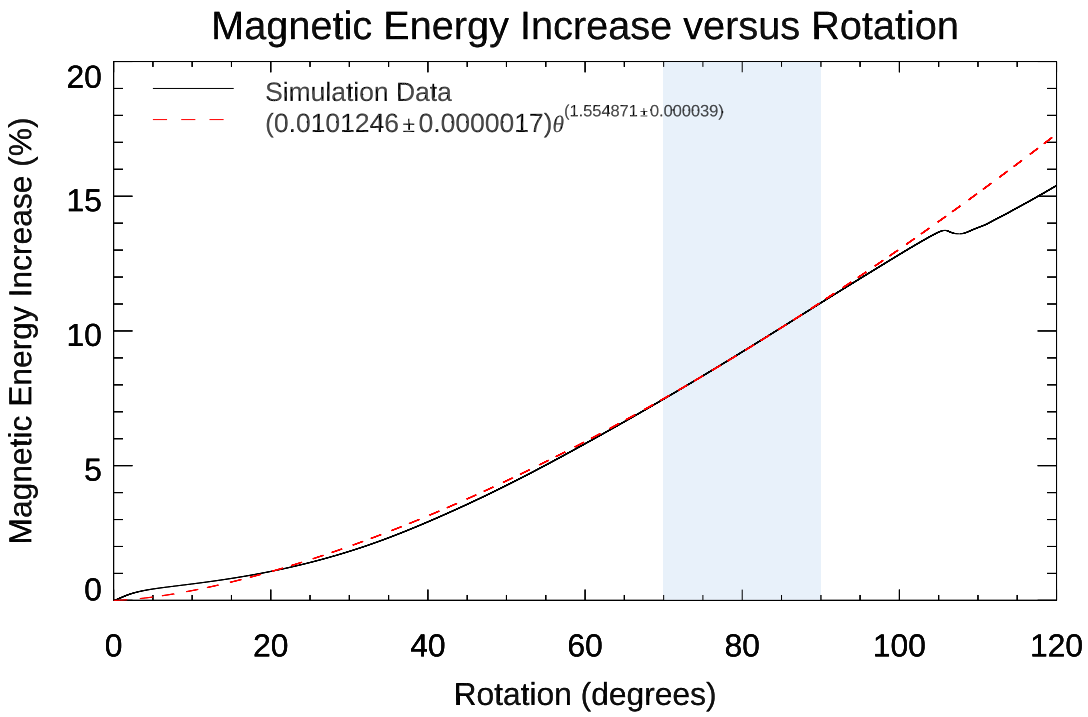

Figure E.8: This figure shows the power-law fit for simulation number 52.

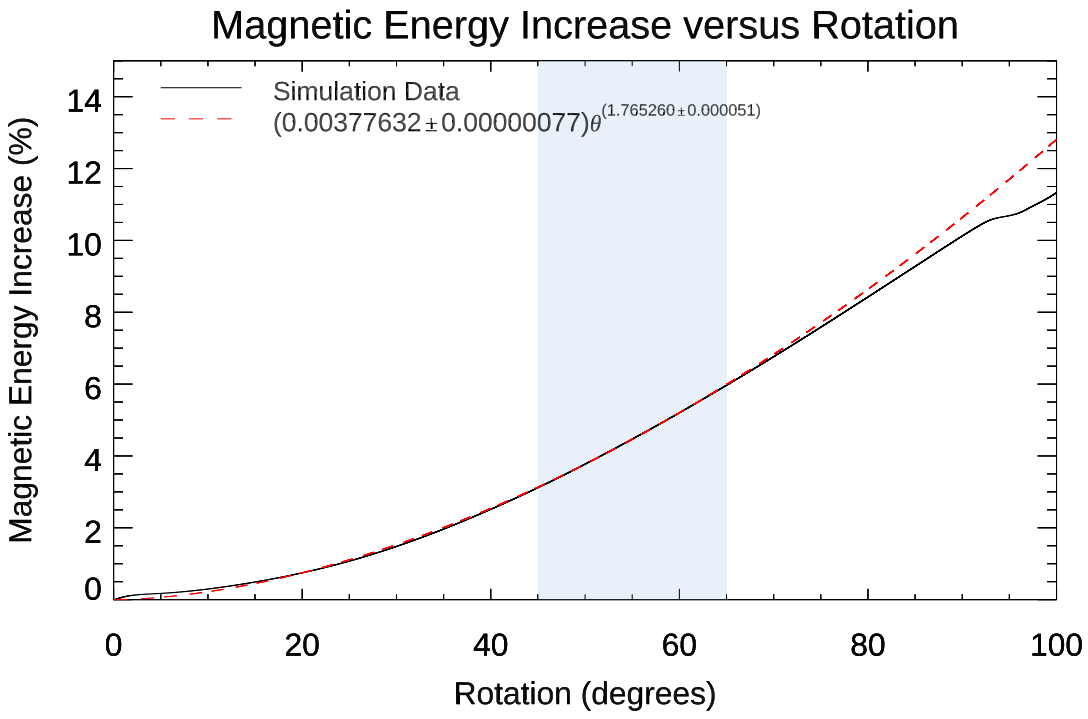

Figure E.9: This figure shows the power-law fit for simulation number 53.

Appendix F

Rotation Rate - ω

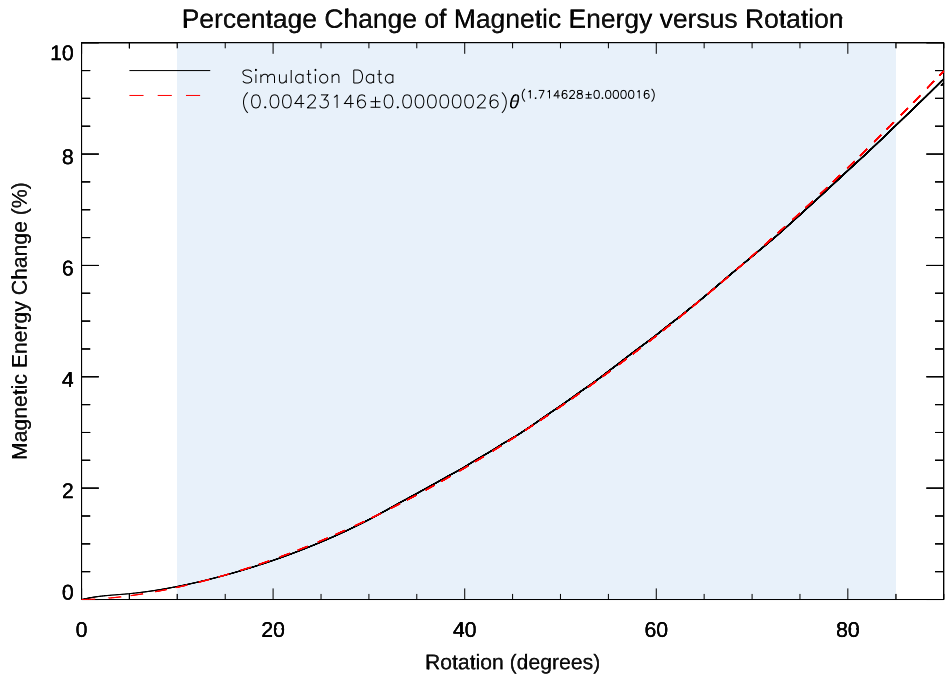

Figure F.1: This figure shows the power-law fit for simulation number 25.

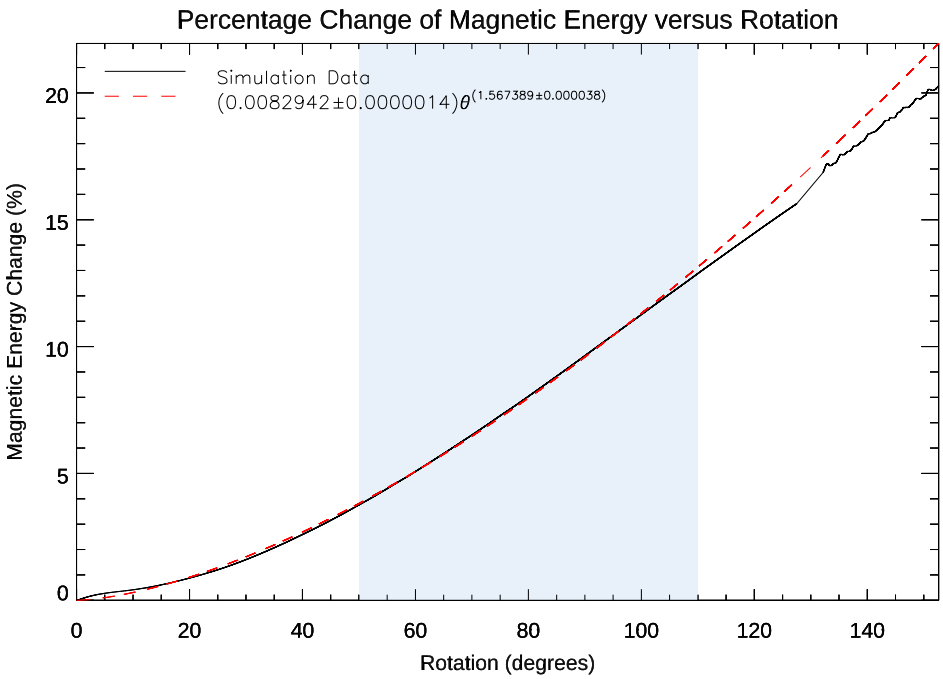

Figure F.2: This figure shows the power-law fit for simulation number 26.

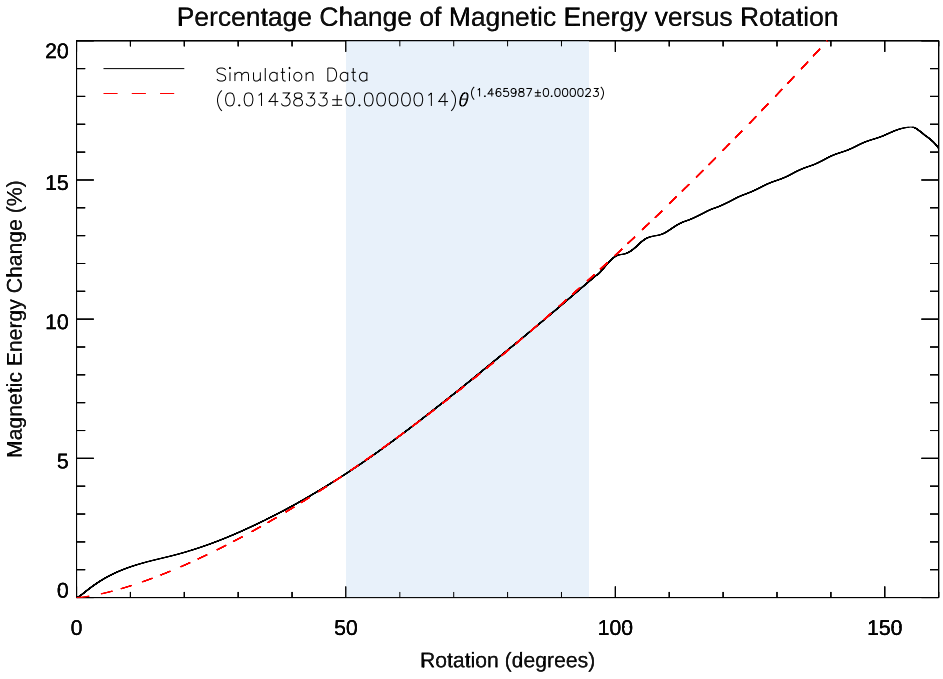

Figure F.3: This figure shows the power-law fit for simulation number 27.

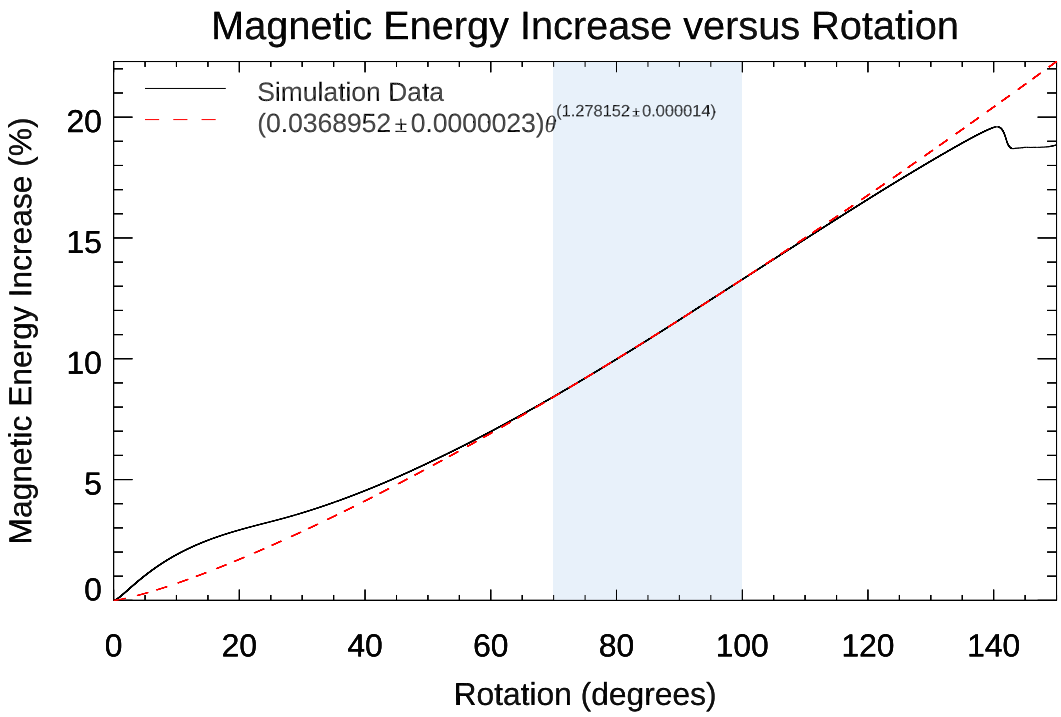

Figure F.4: This figure shows the power-law fit for simulation number 28.

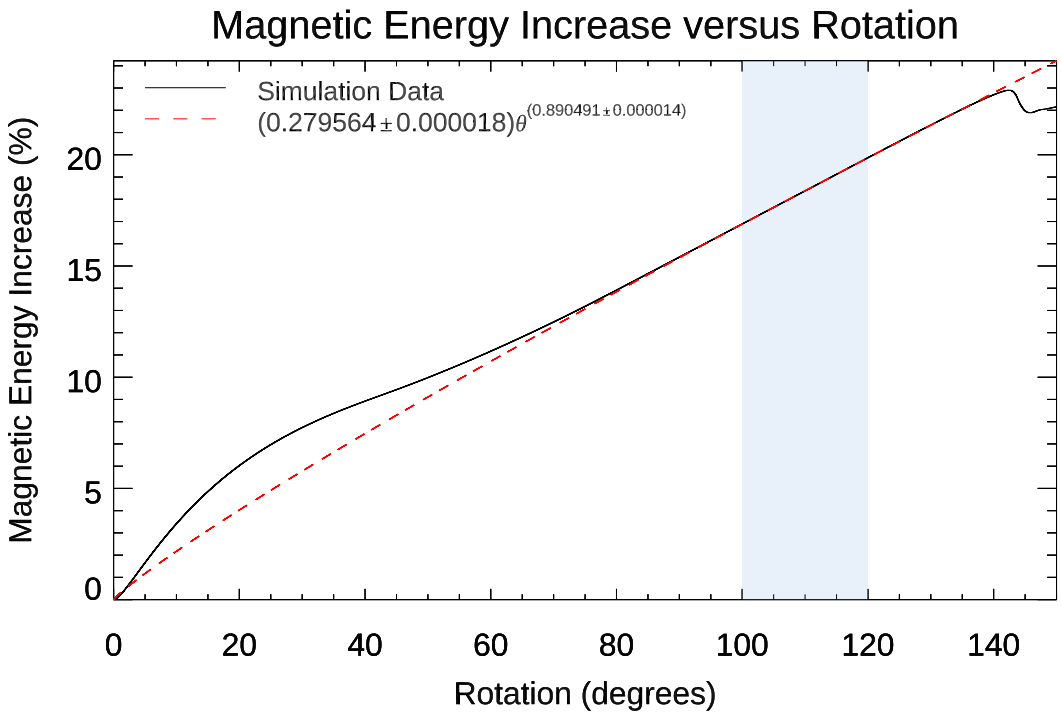

Figure F.5: This figure shows the power-law fit for simulation number 29.

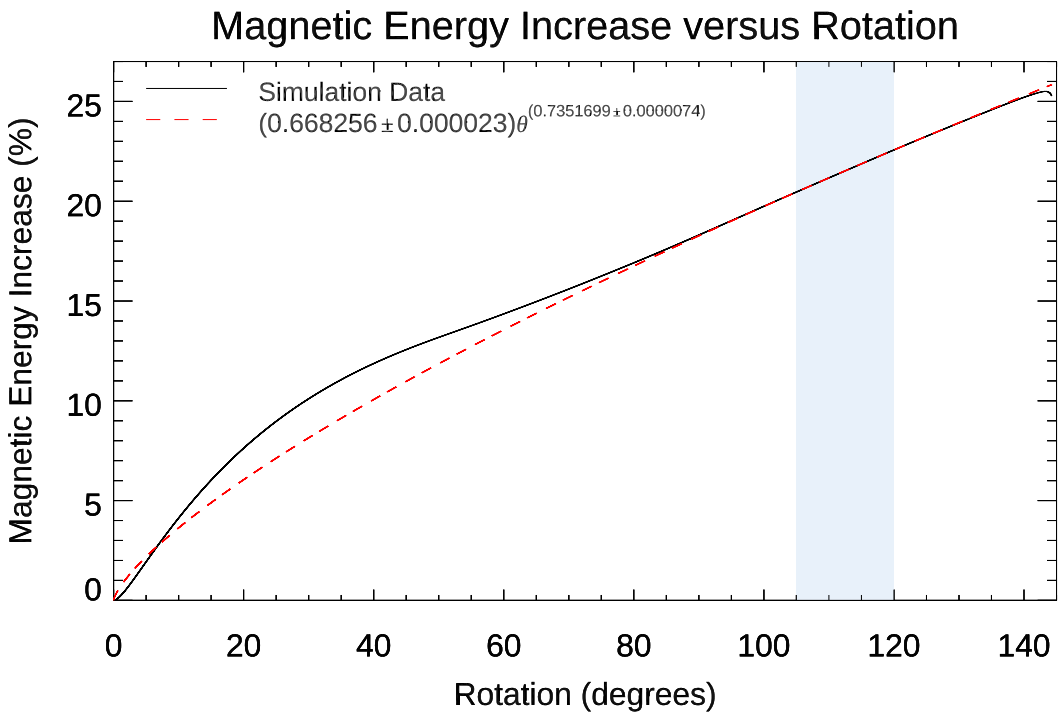

Figure F.6: This figure shows the power-law fit for simulation number 30.

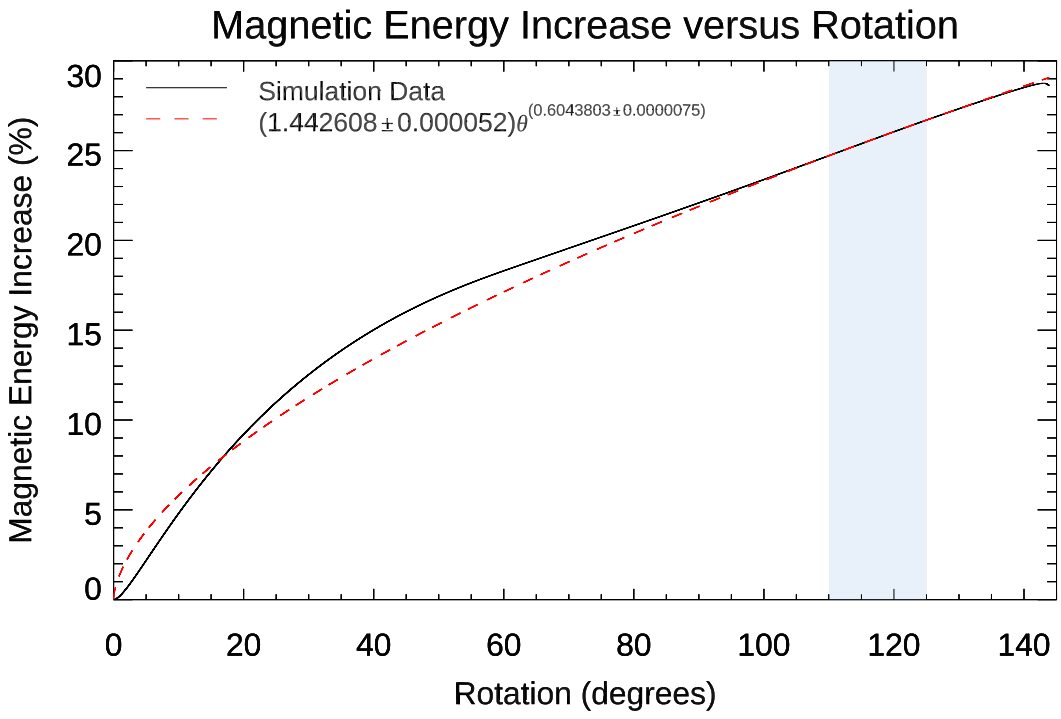

Figure F.7: This figure shows the power-law fit for simulation number 31.

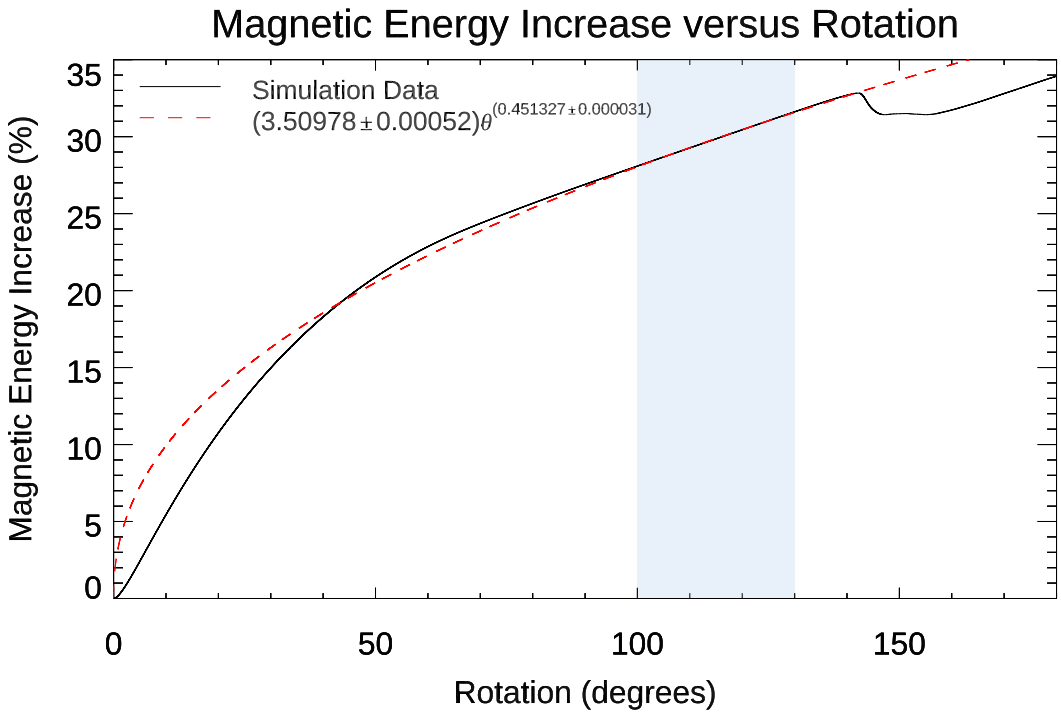

Figure F.8: This figure shows the power-law fit for simulation number 32.

Appendix G

Gamma -γ

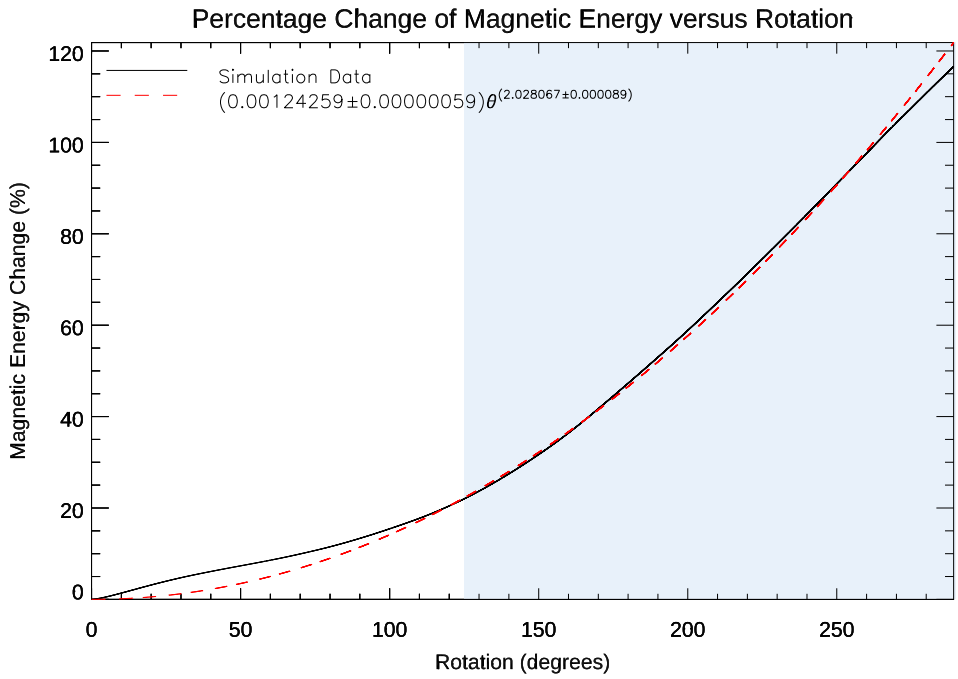

Figure G.1: This figure shows the power-law fit for simulation number 54.

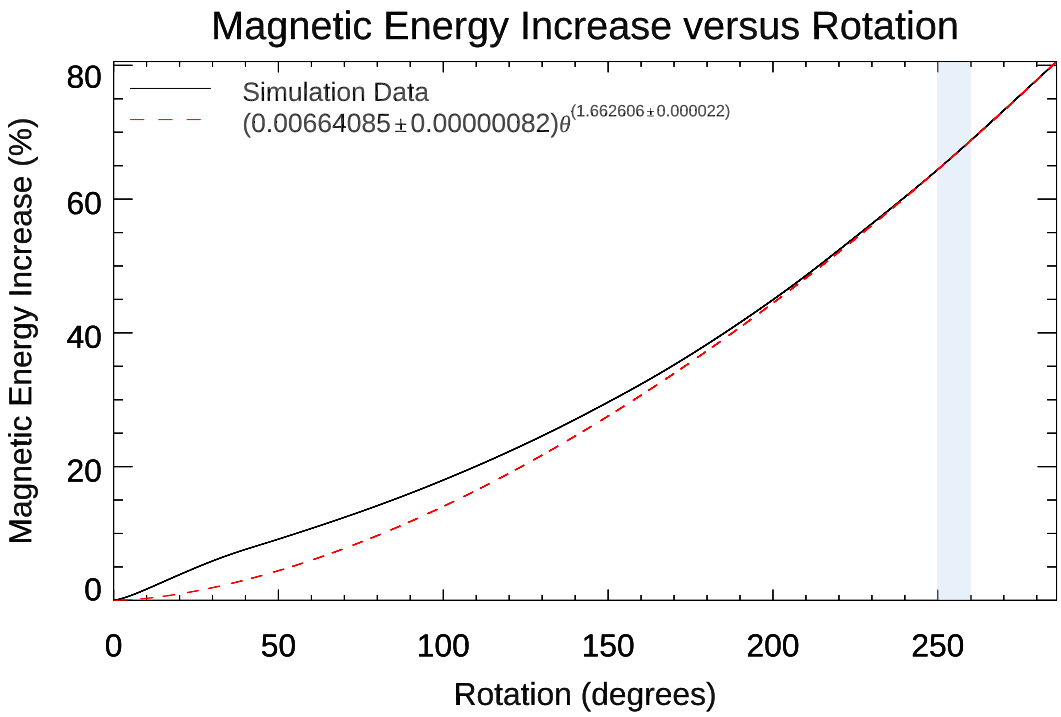

Figure G.2: This figure shows the power-law fit for simulation number 55.

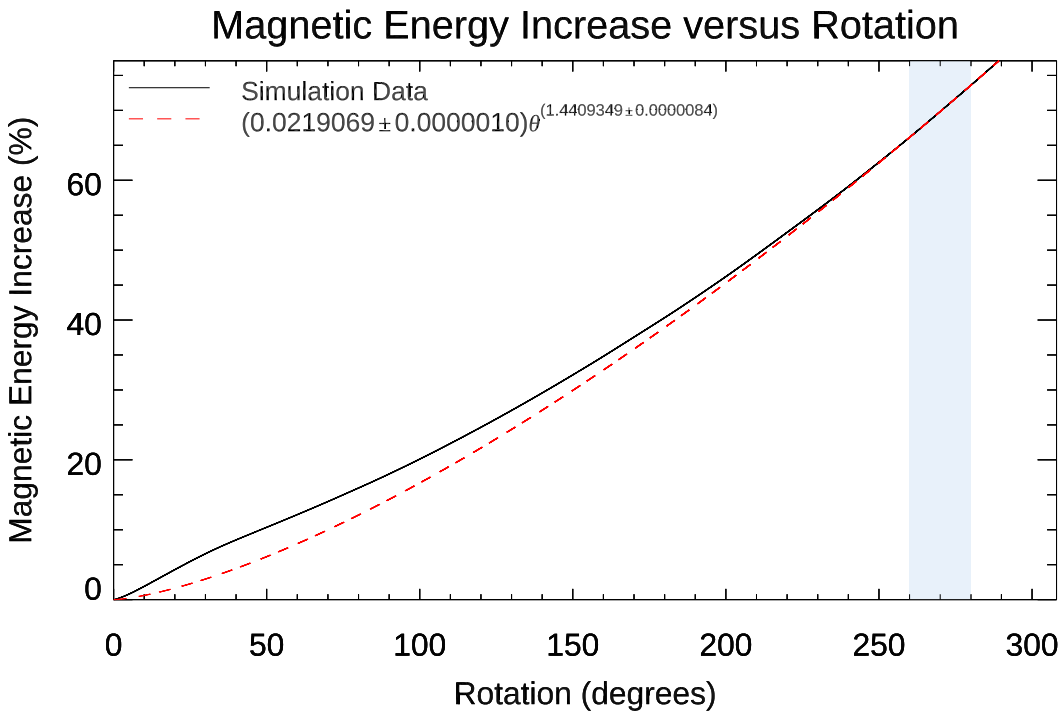

Figure G.3: This figure shows the power-law fit for simulation number 56.

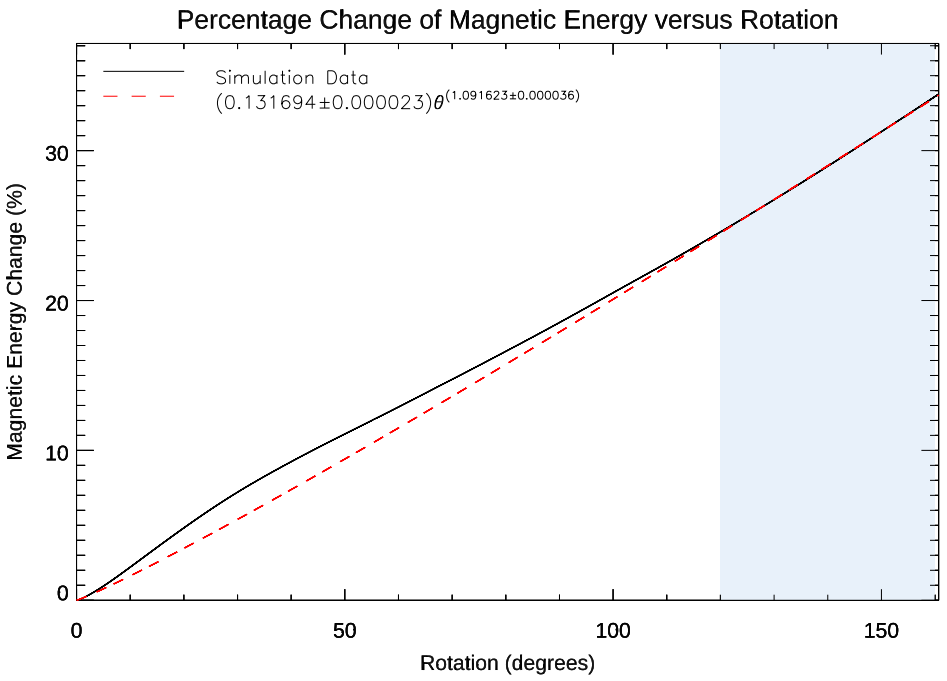

Figure G.4: This figure shows the power-law fit for simulation number 57.

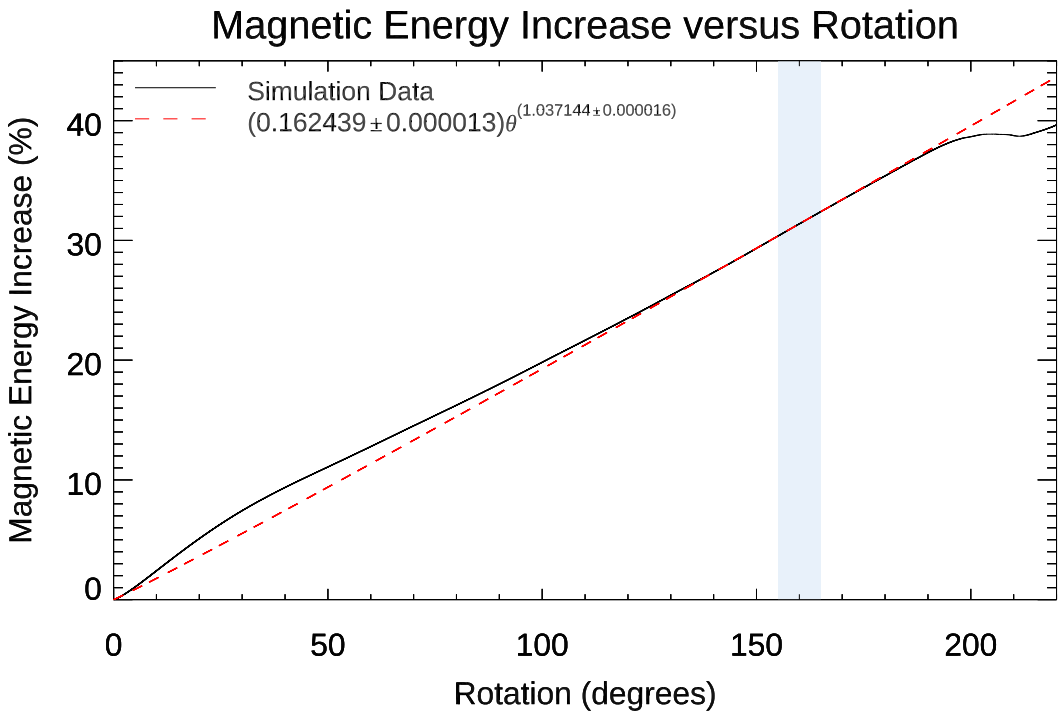

Figure G.5: This figure shows the power-law fit for simulation number 58.

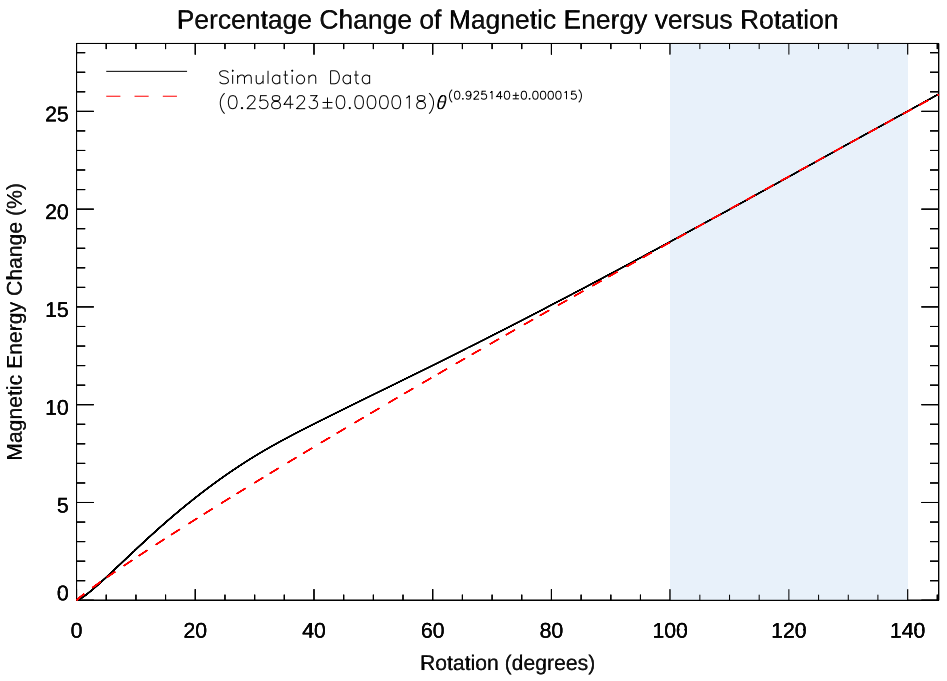

Figure G.6: This figure shows the power-law fit for simulation number 59.

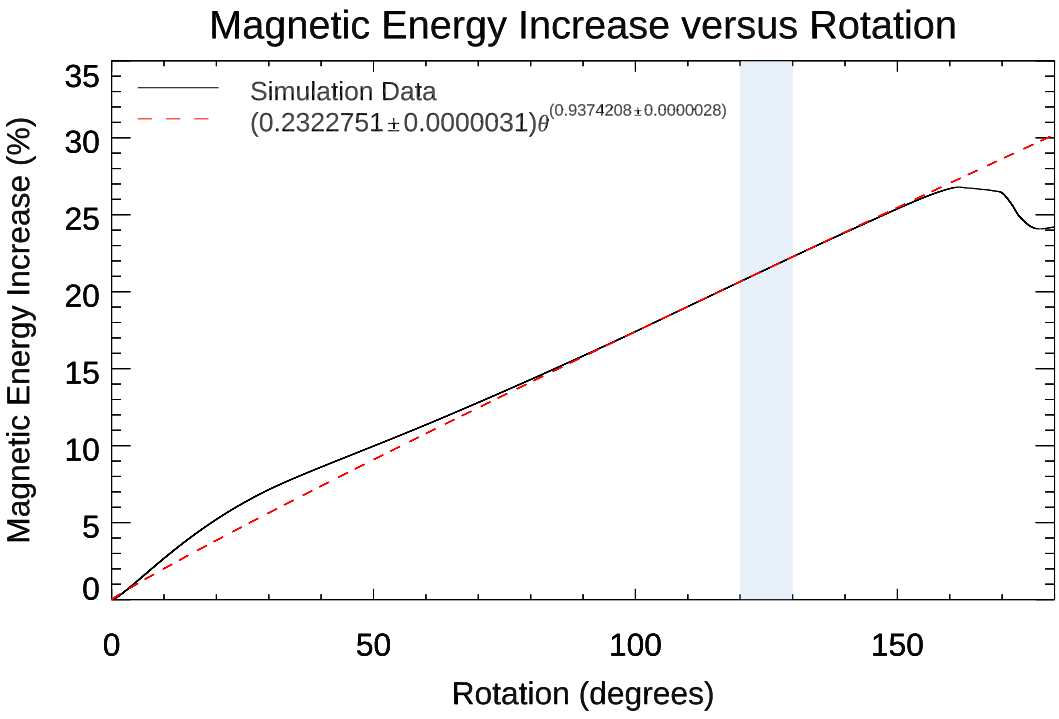

Figure G.7: This figure shows the power-law fit for simulation number 60.

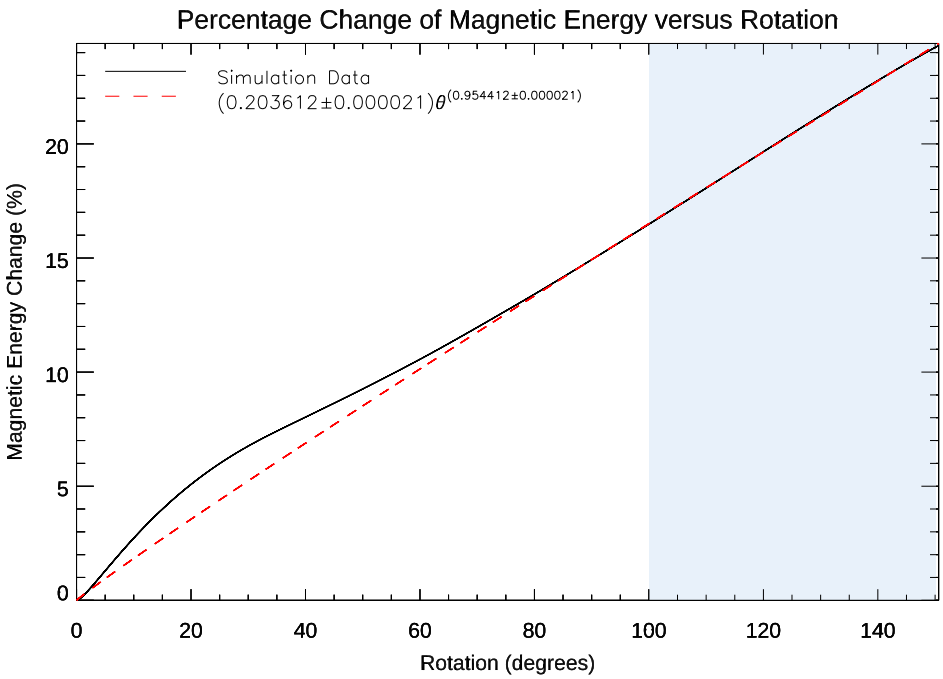

Figure G.8: This figure shows the power-law fit for simulation number 61.

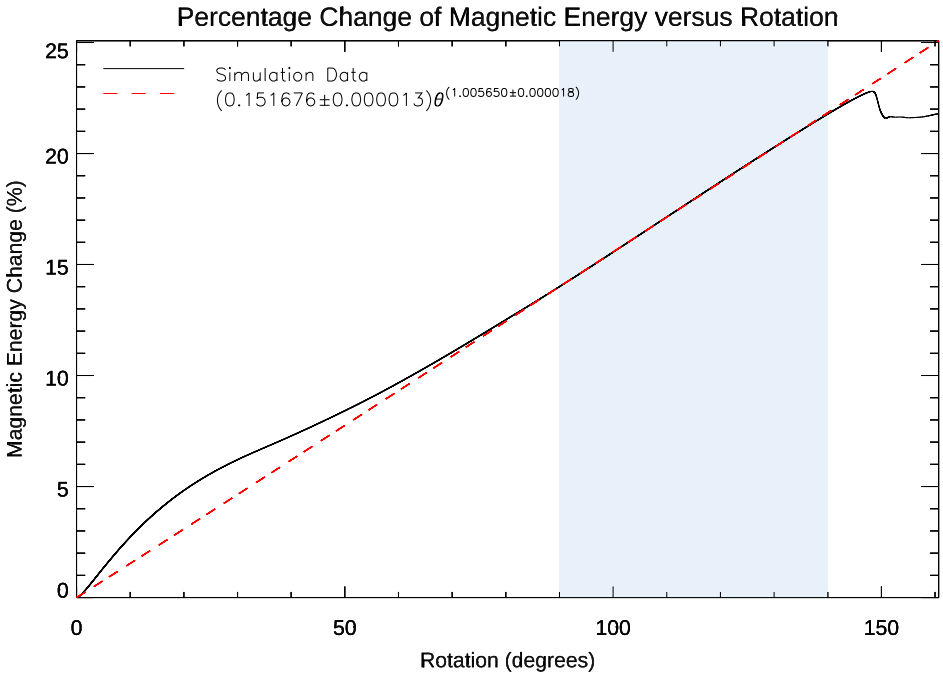

Figure G.9: This figure shows the power-law fit for simulation number 62.

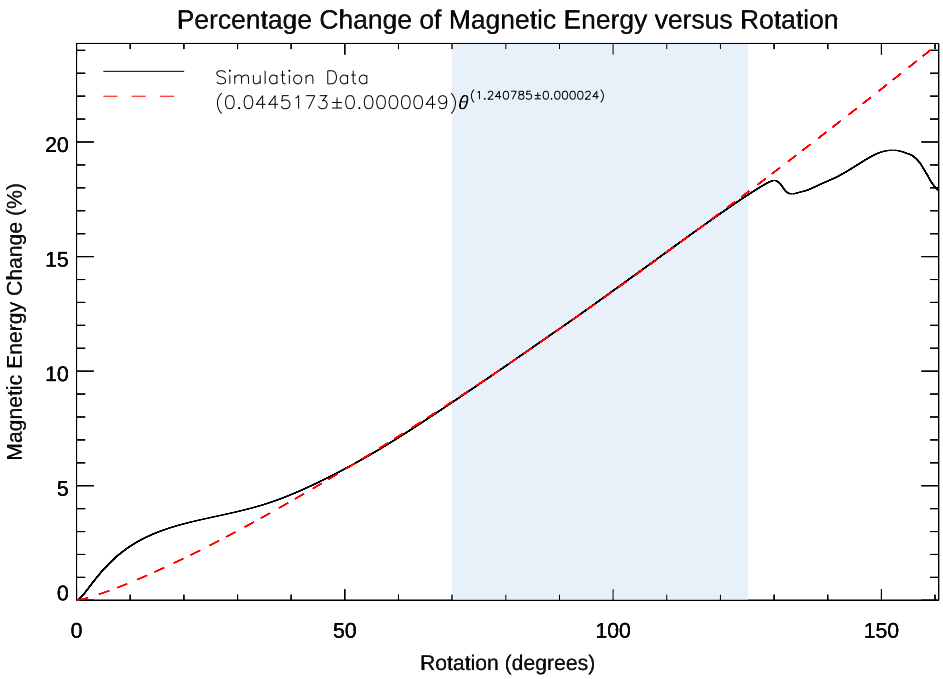

Figure G.10: This figure shows the power-law fit for simulation number 63.

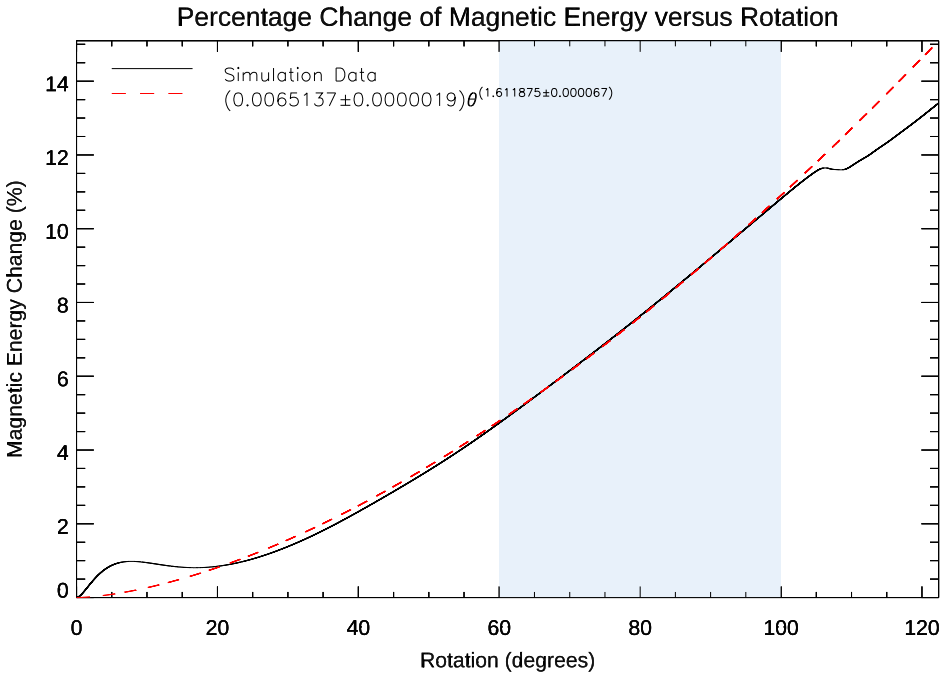

Figure G.11: This figure shows the power-law fit for simulation number 64.

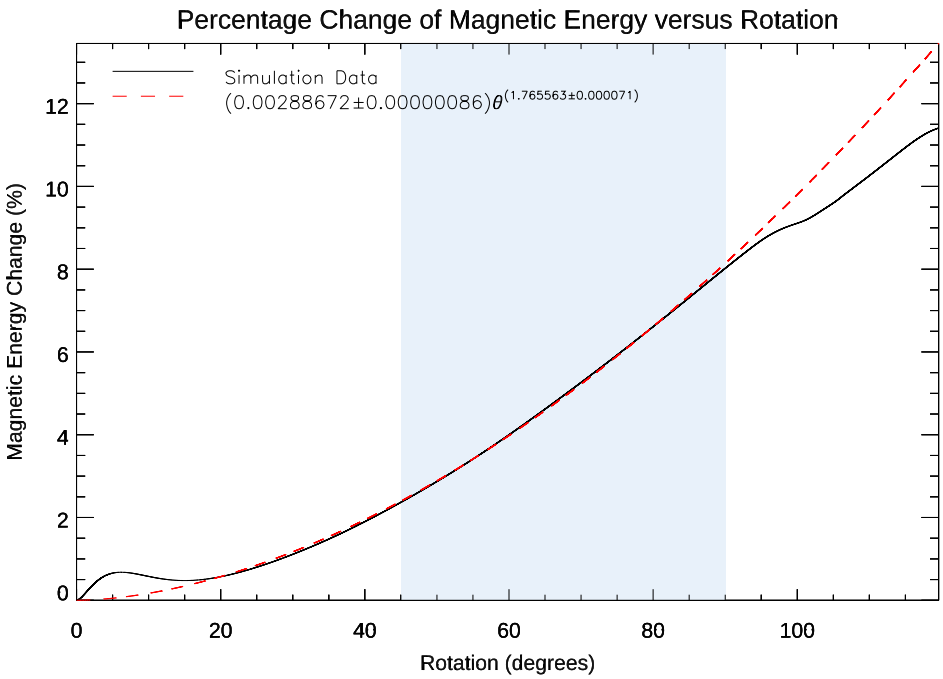

Figure G.12: This figure shows the power-law fit for simulation number 65.

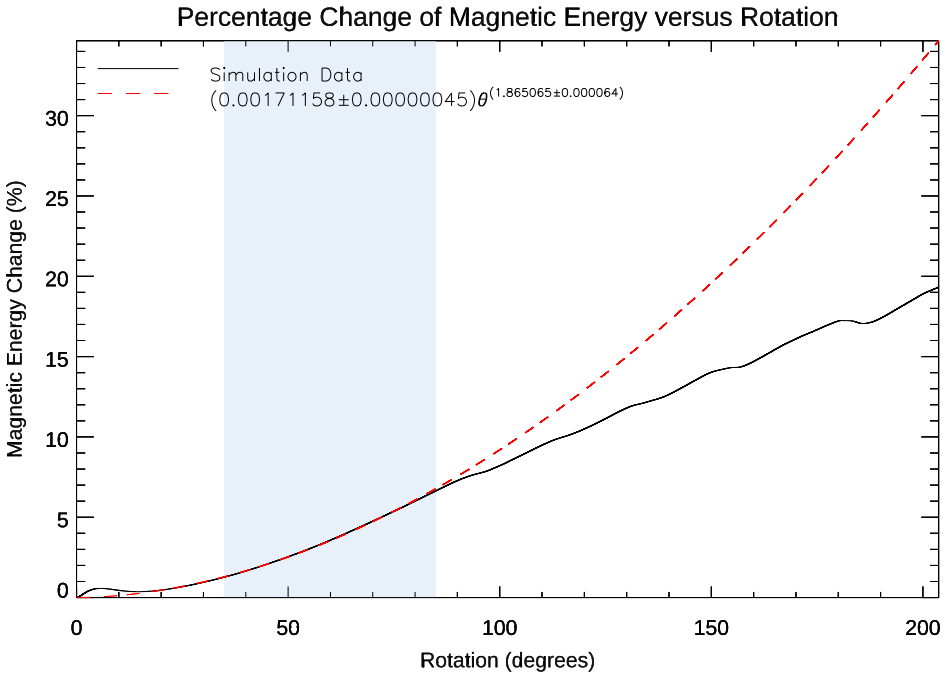

Figure G.13: This figure shows the power-law fit for simulation number 66.

Appendix H

Lare3D Time-step

```
1  !*******************************************************
2  ! Sets CFL limited step
3  !*******************************************************
4  SUBROUTINE set_dt
5
6   ! Assumes all variables are defined at the same point. Be
    careful with
7   ! setting 'dt_multiplier' if you expect massive changes across
    cells.
8
9   REAL(num) :: vxbm, vxbp, avxm, avxp, dvx, ax
10  REAL(num) :: vybm, vybp, avym, avyp, dvy, ay
11  REAL(num) :: vzbm, vzbp, avzm, avzp, dvz, az
12  REAL(num) :: cs2, c_visc2, volume, rho0, length
13  REAL(num) :: dxlocal, dt_local, dtr_local, dt1, dt2, dt3
14  REAL(num) :: dt_locals(2), dt_min(2)
15  LOGICAL, SAVE :: first = .TRUE.
16
17  IF (first) THEN
18     first = .FALSE.
19     IF (restart) THEN
```

```
20          dt = dt_from_restart
21          RETURN
22        END IF
23      END IF
24
25      dt_local = largest_number
26      dtr_local = largest_number
27
28      gamma_boris(:,:,:) = 1.0_num
29
30      DO iz = 0, nz
31        izm = iz - 1
32        DO iy = 0, ny
33          iym = iy - 1
34          DO ix = 0, nx
35            ixm = ix - 1
36
37            ! Fix dt for Lagrangian step
38            w1 = bx(ix,iy,iz)**2 + by(ix,iy,iz)**2 + bz(ix,iy,iz)**2
39            ! Sound speed squared
40            rho0 = MAX(rho(ix, iy, iz), none_zero)
41            w2 = w1 / rho0
42            IF (boris .AND. (w2 .GE. va_max2)) THEN
43              gamma_boris(ix,iy,iz) = 1.0_num / (1.0_num + w2 /
    va_max2)
44            END IF
45            cs2 = gamma_boris(ix,iy,iz) * (gamma * pressure(ix,iy,iz)
     + w1) / rho0
46
47            !effective speed from viscous pressure
48            c_visc2 = gamma_boris(ix,iy,iz) * p_visc(ix,iy,iz) / rho0
49
50            ! length estimates - could be smoother as in DYNA3D
```

```
51            length = MIN(dxb(ix), dyb(iy), dzb(iz))
52
53            ! Find ideal MHD CFL limit for Lagrangian step
54            dt1 = length / (SQRT(c_visc2) + SQRT(cs2 + c_visc2))
55            dt_local = MIN(dt_local, dt1)
56
57            ! Now find dt for remap step
58            ax = 0.25_num * dyb(iy) * dzb(iz)
59            ay = 0.25_num * dxb(ix) * dzb(iz)
60            az = 0.25_num * dxb(ix) * dyb(iy)
61            vxbm = (vx(ixm,iy ,iz ) + vx(ixm,iym,iz ) &
62                +   vx(ixm,iy ,izm) + vx(ixm,iym,izm)) * ax
63            vxbp = (vx(ix ,iy ,iz ) + vx(ix ,iym,iz ) &
64                +   vx(ix ,iy ,izm) + vx(ix ,iym,izm)) * ax
65            vybm = (vy(ix ,iym,iz ) + vy(ixm,iym,iz ) &
66                +   vy(ix ,iym,izm) + vy(ixm,iym,izm)) * ay
67            vybp = (vy(ix ,iy ,iz ) + vy(ixm,iy ,iz ) &
68                +   vy(ix ,iy ,izm) + vy(ixm,iy ,izm)) * ay
69            vzbm = (vz(ix ,iy ,izm) + vz(ixm,iy ,izm) &
70                +   vz(ix ,iym,izm) + vz(ixm,iym,izm)) * az
71            vzbp = (vz(ix ,iy ,iz ) + vz(ixm,iy ,iz ) &
72                +   vz(ix ,iym,iz ) + vz(ixm,iym,iz )) * az
73
74            dvx = ABS(vxbp - vxbm)
75            dvy = ABS(vybp - vybm)
76            dvz = ABS(vzbp - vzbm)
77            avxm = ABS(vxbm)
78            avxp = ABS(vxbp)
79            avym = ABS(vybm)
80            avyp = ABS(vybp)
81            avzm = ABS(vzbm)
82            avzp = ABS(vzbp)
83
```

```
84          volume = ax * dxb(ix)
85          dt1 = volume / MAX(avxm, avxp, dvx, 1.e-10_num * volume)
86          dt2 = volume / MAX(avym, avyp, dvy, 1.e-10_num * volume)
87          dt3 = volume / MAX(avzm, avzp, dvz, 1.e-10_num * volume)
88
89          ! Fix dt for remap step
90          dt_local = MIN(dt_local, dt1, dt2, dt3)
91
92          ! Note resistive limits assumes uniform resistivity hence
     cautious
93          ! factor 0.2
94          dxlocal = 1.0_num / (1.0_num / dxb(ix)**2 &
95              + 1.0_num / dyb(iy)**2 + 1.0_num / dzb(iz)**2)
96
97          IF (cowling_resistivity) THEN
98           dt1 = 0.2_num * dxlocal &
99               / MAX(MAX(eta(ix,iy,iz), eta_perp(ix,iy,iz)),
    none_zero)
100         ELSE
101          dt1 = 0.2_num * dxlocal / MAX(eta(ix,iy,iz), none_zero)
102         END IF
103
104         ! Adjust to accomodate resistive effects
105         dtr_local = MIN(dtr_local, dt1)
106       END DO
107     END DO
108   END DO
109
110   dt_locals(1) = dt_local
111   dt_locals(2) = dtr_local
112
113   CALL MPI_ALLREDUCE(dt_locals, dt_min, 2, mpireal, MPI_MIN, comm,
     errcode)
```

```
114
115     dt  = dt_multiplier * dt_min(1)
116     dtr = dt_multiplier * dt_min(2)
117
118     time = time + dt
119
120   END SUBROUTINE set_dt
121
122
123
```

Listing H.1: The Lare3D time-step subroutine that sets the imposes the CFL condition on the code's time-step taken directly from the Lare3D code (Arber et al., 2001).

Bibliography

Alfven, H. (1942). Existence of Electromagnetic-Hydrodynamic Waves. *Nature*, 150(3805):405–406.

Alfven, H. and Carlqvist, P. (1967). Currents in the solar atmosphere and a theory of solar flares. *Solar Physics*, 1(2):220–228.

Aly, J. J. (1991). How much energy can be stored in a three-dimensional force-free magnetic field? *The Astrophysical Journal*, 375:L61.

Amari, T., Boulmezaoud, T. Z., and Mikic, Z. (1999). An iterative method for the reconstruction of the solar coronal magnetic field I. Method for regular solutions. *ASTRONOMY AND ASTROPHYSICS*, 350:1051–1059.

Antalova, A. (1971). The ratio of penumbral to umbral areas of sun-spots in the 11-year solar activity cycle. *Bulletin of the Astronomical Institutes of Czechoslovakia*, 22:352.

Arber, T., Longbottom, A., Gerrard, C., and Milne, A. (2001). A Staggered Grid, LagrangianEulerian Remap Code for 3-D MHD Simulations. *Journal of Computational Physics*, 171(1):151–181.

Arber, T. D., Haynes, M., and Leake, J. E. (2007). Emergence of a Flux Tube through a Partially Ionized Solar Atmosphere. *The Astrophysical Journal*, 666(1):541–546.

Archontis, V. and Hood, A. W. (2012a). Magnetic flux emergence: a precursor of solar plasma expulsion. *Astronomy & Astrophysics*, 537:A62.

Archontis, V. and Hood, A. W. (2012b). Magnetic flux emergence: a precursor of solar plasma expulsion. *Astronomy & Astrophysics*, 537:A62.

Avrett, E. H. and Loeser, R. (2008). Models of the Solar Chromosphere and Transition Region from SUMER and HRTS Observations: Formation of the ExtremeUltraviolet Spectrum of Hydrogen, Carbon, and Oxygen. *The Astrophysical Journal Supplement Series*, 175(1):229–276.

Barnes, C. W. and Sturrock, P. A. (1972). Force-Free Magnetic-Field Structures and Their Role in Solar Activity. *The Astrophysical Journal*, 174(11):659.

Bi, Y., Jiang, Y., Yang, J., Hong, J., Li, H., Yang, B., and Xu, Z. (2016). Observation of a reversal of rotation in a sunspot during a solar flare. *Nature Communications*, 7(1):13798.

Blackman, E. G. (2015). Magnetic Helicity and Large Scale Magnetic Fields: A Primer. *Space Science Reviews*, 188(1-4):59–91.

Bogdan, T. J., Gilman, P. A., Lerche, I., and Howard, R. (1988). Distribution of sunspot umbral areas - 1917-1982. *The Astrophysical Journal*, 327(2):451.

Borrero, J. M. and Ichimoto, K. (2011). Magnetic Structure of Sunspots. *Living Rev. Solar Phys*, 8:4.

Botha, G. J. J., Busse, F. H., Hurlburt, N. E., and Rucklidge, A. M. (2008). Numerical simulations of rotating axisymmetric sunspots. *Monthly Notices of the Royal Astronomical Society*, 387(4):1445–1462.

Botha, G. J. J., Rucklidge, A. M., Busse, F., Botha, G. J. J., Rucklidge, A. M., Busse, F. H., and Hurlburt, N. E. (2014). Numerical simulations of rotating

sunspots Fluid mechanics View project Chromospheric Seismology View project NUMERICAL SIMULATIONS OF ROTATING SUNSPOTS.

Bourdin, P.-A. (2017). Plasma Beta Stratification in the Solar Atmosphere: A Possible Explanation for the Penumbra Formation. *The Astrophysical Journal*, 850(2):L29.

Boyd, T. J. M. and Sanderson, J. J. (1969). *Plasma Dynamics*. Thomas Nelson and Sons Ltd, London, first edition.

Brown, D. and Walker, A. (2021). A Semi-Automatic Method to Measure the Rotation of Sunspots. *Solar Physics*, 296(3):48.

Brown, D. S., Nightingale, R. W., Alexander, D., Schrijver, C. J., Metcalf, T. R., Shine, R. A., Title, A. M., and Wolfson, C. J. (2003). Observations of rotating sunspots from TRACE. *Solar Physics*, 216(1-2):79–108.

Burden, R. and Faires, J. D. (2010). *Numerical Analysis, International Edition*. Brooks Cole, 9th edition.

Byrne, J. P. (2012). The Kinematics and Morphology of Solar Coronal Mass Ejections.

Byrne, J. P. (2015). Investigating the kinematics of coronal mass ejections with the automated CORIMP catalog. *Journal of Space Weather and Space Climate*, 5:A19.

Byrne, J. P., Gallagher, P. T., McAteer, R. T. J., and Young, C. A. (2009). The kinematics of coronal mass ejections using multiscale methods. *Astronomy & Astrophysics*, 495(1):325–334.

Carrington, R. C. (1858). On the Distribution of the Solar Spots in Latitude since

the Beginning of the Year 1854; with a Map. *Monthly Notices of the Royal Astronomical Society*, 19(1):1–3.

Chae, J. and Sakurai, T. (2008). A Test of Three Optical Flow TechniquesLCT, DAVE, and NAVE. *The Astrophysical Journal*, 689(1):593–612.

Chen, F. F. (2016). *Introduction to Plasma Physics and Controlled Fusion*. Springer International Publishing, Heidelberg, third edition.

Cheung, M. C. M. and Isobe, H. (2014). Flux Emergence (Theory). *Living Reviews in Solar Physics*, 11.

Courant, R., Friedrichs, K., and Lewy, H. (1928). Uber die partiellen Differenzengleichungen der mathematischen Physik. *Mathematische Annalen*, 100(1):32–74.

Domingo, V., Fleck, B., and Poland, A. I. (1995). The SOHO mission: An overview. *Solar Physics*, 162(1-2):1–37.

Eastwood, J. P., Biffis, E., Hapgood, M. A., Green, L., Bisi, M. M., Bentley, R. D., Wicks, R., McKinnell, L.-A., Gibbs, M., and Burnett, C. (2017). The Economic Impact of Space Weather: Where Do We Stand? *Risk Analysis*, 37(2):206–218.

Evershed, J. (1909). Radial movement in sun-spots. *Monthly Notices of the Royal Astronomical Society*, 69(5):454–458.

Fan, Y. (2001). The Emergence of a Twisted {$Ω$}-Tube into the Solar Atmosphere. *The Astrophysical Journal*, 554(1):L111–L114.

Franz, M. (2012). On the surface structure of sunspots. *Astronomische Nachrichten*, 333(10):1009–1012.

Garcia, A. L. (2015). *Numerical Methods for Physics*. CreateSpace Independent Publishing Platform, second edition.

Gerrard, C. L., Arber, T. D., Hood, A. W., and R. A. M. Van der Linden (2001). Numerical simulations of kink instability in line-tied coronal Loops. *Astronomy & Astrophysics*, 373(3):1089–1098.

Gerrard, C. L., Brown, D. S., Mellor, C., Arber, T. D., and Hood, A. W. (2003). MHD simulations of sunspot rotation and the coronal consequences. *Solar Physics*, 213(1):39–54.

Golub, L. and Pasachoff, J. M. (2010). *The Solar Corona*. Cambridge University Press, Cambridge, second edition.

Gonzalez, W. D., Tsurutani, B. T., and Gonzalez, A. L. C. d. (1999). Interplanetary Origin of Geomagnetic Storms. *Space Science Reviews*, 88(3-4):529–562.

Gopalswamy, N., Mikić, Z., Maia, D., Alexander, D., Cremades, H., Kaufmann, P., Tripathi, D., and Wang, Y.-M. (2006). The Pre-CME Sun. *Space Science Reviews*, 123(1-3):303–339.

Gopalswamy, N., Yashiro, S., Michalek, G., Stenborg, G., Vourlidas, A., Freeland, S., and Howard, R. (2009). The SOHO/LASCO CME Catalog. *Earth, Moon, and Planets*, 104(1-4):295–313.

Gordovskyy, M., Browning, P. K., Kontar, E. P., and Bian, N. H. (2014). Particle acceleration and transport in reconnecting twisted loops in a stratified atmosphere. *Astronomy & Astrophysics*, 561(1-2):A72.

Grad, H. and Rubin, H. (1958). Hydromagnetic equilibria and force-free fields. *Journal of Nuclear Energy (1954)*, 7(3-4):284–285.

Griffiths, D. J. (2014). *Introduction to Electrodynamics*. Pearson Education Limited, Essex, fourth edition.

Grimes, R. and Pintér, B. (2022). Sunspot Rotation in High- and Low-Flaring Active Regions. *solphys*, 297(8):109.

Grimes, R., Pintér, B., and Morgan, H. (2020). Observation of Differential Rotation Within a Sunspot Umbra During an X-Class Flare. *Solar Physics*, 295(6):87.

Gurnett, D. A. and Bhattacharjee, A. (2005). *Introduction to Plasma Physics With Space and Laboratory Applications*. Cambridge University Press, Cambridge, first edition.

Hale, G. E. (1908). On the Probable Existence of a Magnetic Field in Sun-Spots. *The Astrophysical Journal*, 28:315.

Hale, G. E., Ellerman, F., Nicholson, S. B., and Joy, A. H. (1919). The Magnetic Polarity of Sun-Spots. *The Astrophysical Journal*, 49:153.

Harrison, R. A. and Bewsher, D. (2007). A benchmark event sequence for mass ejection onset studies. *Astronomy & Astrophysics*, 461(3):1155–1162.

Harrison, R. A., Davies, J. A., Barnes, D., Byrne, J. P., Perry, C. H., Bothmer, V., Eastwood, J. P., Gallagher, P. T., Kilpua, E. K. J., Möstl, C., Rodriguez, L., Rouillard, A. P., and Odstrcil, D. (2018). CMEs in the Heliosphere: I. A Statistical Analysis of the Observational Properties of CMEs Detected in the Heliosphere from 2007 to 2017 by STEREO/HI-1. *Solar Physics*.

Haynes, M., Arber, T. D., and Verwichte, E. (2008). Coronal loop slow mode oscillations driven by the kink instability. *Astronomy and Astrophysics*, 479(1):235–239.

Hood, A. W., Browning, P. K., and Van der Linden, R. A. M. (2009). Coronal heating by magnetic reconnection in loops with zero net current. *Astronomy & Astrophysics*, 506(2):913–925.

Horn, B. K. and Schunck, B. G. (1981). Determining optical flow. *Artificial Intelligence*, 17(1-3):185–203.

Howard, T. (2011). *Coronal Mass Ejections*, volume 376 of *Astrophysics and Space Science Library*. Springer New York, New York, NY.

Howard, T. A. and Tappin, S. J. (2009). Interplanetary Coronal Mass Ejections Observed in the Heliosphere: 1. Review of Theory. *Space Science Reviews*, 147(1-2):31–54.

Hudson, H. S. (2011). Global Properties of Solar Flares. *Space Science Reviews*, 158(1):5–41.

Hutton, J. and Morgan, H. (2017). Automated detection of coronal mass ejections in three-dimensions using multi-viewpoint observations. *Astronomy & Astrophysics*, 599:A68.

Inhester, B. and Wiegelmann, T. (2006). Nonlinear force-free magnetic field extrapolations: Comparison of the Grad Rubin and Wheatland Sturrock Roumeliotis algorithm. *Solar Physics*, 235(1-2):201–221.

Jackson, J. D. (1975). *Classical Electrodynamics*. John Wiley & Sons, Ltd, second edition.

Jin, C. L., Qu, Z. Q., Xu, C. L., Zhang, X. Y., and Sun, M. G. (2006). The Relationships of Sunspot Magnetic Field Strength with Sunspot Area, Umbral Area and Penumbra-Umbra Radius Ratio. *Astrophysics and Space Science*, 306(1-2):23–27.

Joshi, J., Lagg, A., Hirzberger, J., and Solanki, S. K. (2017). Three-dimensional magnetic structure of a sunspot: Comparison of the photosphere and upper chromosphere. *Astronomy & Astrophysics*, 604:A98.

Jurčák, J., Rezaei, R., Bello González, N., Schlichenmaier, R., and Vomlel, J. (2018). The magnetic nature of umbrapenumbra boundary in sunspots. *Astronomy & Astrophysics*, 611:L4.

Kazachenko, M. D., Canfield, R. C., Longcope, D. W., and Qiu, J. (2010). SUNSPOT ROTATION, FLARE ENERGETICS, AND FLUX ROPE HELICITY: THE HALLOWEEN FLARE ON 2003 OCTOBER 28. *The Astrophysical Journal*, 722(2):1539–1546.

Keppens, R. and Martinez Pillet, V. (1996). The magnetic structure of pores and sunspots derived from Advanced Stokes Polarimeter data. *Astronomy and Astrophysics*, 316:229–242.

Leake, J. E. (2005). Numerical modelling of flux emergence in the solar atmosphere: Effects of partial ionisation. *European Space Agency, (Special Publication) ESA SP*, 2(600):557–562.

Leake, J. E. and Arber, T. D. (2006). The emergence of magnetic flux through a partially ionised solar atmosphere. *Astronomy & Astrophysics*, 450(2):805–818.

Lemen, J. R., Title, A. M., Akin, D. J., Boerner, P. F., Chou, C., Drake, J. F., Duncan, D. W., Edwards, C. G., Friedlaender, F. M., Heyman, G. F., Hurlburt, N. E., Katz, N. L., Kushner, G. D., Levay, M., Lindgren, R. W., Mathur, D. P., McFeaters, E. L., Mitchell, S., Rehse, R. A., Schrijver, C. J., Springer, L. A., Stern, R. A., Tarbell, T. D., Wuelser, J.-P., Wolfson, C. J., Yanari, C., Bookbinder, J. A., Cheimets, P. N., Caldwell, D., Deluca, E. E., Gates, R., Golub, L., Park, S., Podgorski, W. A., Bush, R. I., Scherrer, P. H., Gummin, M. A., Smith, P., Auker, G., Jerram, P., Pool, P., Soufli, R., Windt, D. L., Beardsley, S., Clapp, M., Lang, J., and Waltham, N. (2012). The Atmospheric Imaging Assembly (AIA) on the Solar Dynamics Observatory (SDO). *Solar Physics*, 275(1-2):17–40.

Li, A. and Liu, Y. (2015). Sunspot Rotation and the M-Class Flare in Solar Active Region NOAA 11158. *Solar Physics*, 290(8):2199–2209.

Li, W., Ai, C., and Wang, H. (2001a). A Survey of the Size-flux Relation for Pores and Spots. In Brekke, P., Fleck, B., and Gurman, J. B., editors, *Recent Insights into the Physics of the Sun and Heliosphere: Highlights from SOHO and Other Space Missions*, volume 203, page 291.

Li, W., Ai, C., and Wang, H. (2001b). Recent Insights into the Physics of the Sun and Heliosphere: Highlights from SOHO and Other Space Missions. In *IAU Symposium, Vol. 203*.

Liu, C., Xu, Y., Cao, W., Deng, N., Lee, J., Hudson, H. S., Gary, D. E., Wang, J., Jing, J., and Wang, H. (2016). Flare differentially rotates sunspot on Suns surface. *Nature Communications*, 7(1):13104.

Livingston, W., Harvey, J. W., Malanushenko, O. V., and Webster, L. (2006). Sunspots with the Strongest Magnetic Fields. *Solar Physics*, 239(1-2):41–68.

Maltby, P., Avrett, E. H., Carlsson, M., Kjeldseth-Moe, O., Kurucz, R. L., and Loeser, R. (1986). A new sunspot umbral model and its variation with the solar cycle. *The Astrophysical Journal*, 306(1908):284.

Materassi, M., Ciraolo, L., Consolini, G., and Smith, N. (2011). Predictive Space Weather: An information theory approach. *Advances in Space Research*, 47(5):877–885.

Morton, K. W. and Mayers, D. F. (2005). *Numerical Solution of Partial Differential Equations*. Cambridge University Press, second edition.

Nagovitsyn, Y. A., Pevtsov, A. A., Osipova, A. A., Tlatov, A. G., Miletskii, E. V., and Nagovitsyna, E. Y. (2016). Two populations of sunspots and secular variations of their characteristics. *Astronomy Letters*, 42(10):703–712.

Nandy, D., Hahn, M., Canfield, R. C., and Longcope, D. W. (2003). Detection of a Taylor-like Plasma Relaxation Process in the Sun. *The Astrophysical Journal*, 597(1):L73–L76.

Newton, H. W. (1955). The lineage of the great sunspots. *Vistas in Astronomy*, 1(1):666–674.

Okamoto, T. J. and Sakurai, T. (2018). Super-strong Magnetic Field in Sunspots. *The Astrophysical Journal*, 852(1):L16.

Orozco Suarez, D., Lagg, A., and Solanki, S. K. (2005). Photospheric and Chromospheric Magnetic Structure of a Sunspot. In Innes, D. E., Lagg, A., and Solanki, S. A., editors, *Chromospheric and Coronal Magnetic Fields*, volume 596 of *ESA Special Publication*, page 59.1.

Osherovich, V. and Flaa, T. (1983). Sunspot models with twisted magnetic field. *Solar Physics*, 88(1-2):3155–3162.

Osherovich, V. A. (1980). A New Magneto-Hydrostatic Theory of Sunspots. In *Bulletin of the American Astronomical Society*, volume 12, page 897.

Osherovich, V. A. and Garcia, H. A. (1989). The relationship of sunspot magnetic fields to umbral sizes in return flux theory. *The Astrophysical Journal*, 336(1969):468.

Parker, E. N. (1955). The Formation of Sunspots from the Solar Toroidal Field. *The Astrophysical Journal*, 121:491.

Penn, M. J. and MacDonald, R. K. D. (2007). Solar Cycle Changes in Sunspot Umbral Intensity. *The Astrophysical Journal*, 662(2):L123–L126.

Pérez-Suárez, D., Higgins, P. A., Bloomfield, D. S., McAteer, R. J., Krista, L. D., Byrne, J. P., and Gallagher, P. T. (2011). Automated Solar Feature Detection

for Space Weather Applications. In *Applied Signal and Image Processing*, pages 207–225. IGI Global.

Pesnell, W. D., Thompson, B. J., and Chamberlin, P. C. (2012). The Solar Dynamics Observatory (SDO). *Solar Physics*, 275(1-2):3–15.

Pevtsov, A. A. (2008). What helicity can tell us about solar magnetic fields. *Journal of Astrophysics and Astronomy*, 29(1-2):49–56.

Phillips, K. J. H. (1992). *Guide to the Sun*. Cambridge University Press, 1st edition.

Priest, E. (2014). *Magnetohydrodynamics of the Sun*. Cambridge University Press, Cambridge.

Priest, E. and Forbes, T. (2000). *Magnetic Reconnection*. Cambridge University Press, Cambridge, first edition.

Régnier, S. (2013). Magnetic Field Extrapolations into the Corona: Success and Future Improvements. *Solar Physics*, 288(2):481–505.

Régnier, S. and Canfield, R. C. (2006). Evolution of magnetic fields and energetics of flares in active region 8210. *Astronomy & Astrophysics*, 451(1):319–330.

Régnier, S. and Priest, E. R. (2007a). Free Magnetic Energy in Solar Active Regions above the Minimum-Energy Relaxed State. *The Astrophysical Journal*, 669(1):L53–L56.

Régnier, S. and Priest, E. R. (2007b). Nonlinear force-free models for the solar corona I. Two active regions with very different structure. *Astronomy and Astrophysics*, 468(2):701–709.

Rempel, M. (2010). 3D numerical MHD modeling of sunspots with radiation transport. *Proceedings of the International Astronomical Union*, 6(S273):8–14.

Rempel, M. (2011). PENUMBRAL FINE STRUCTURE AND DRIVING MECHANISMS OF LARGE-SCALE FLOWS IN SIMULATED SUNSPOTS. *The Astrophysical Journal*, 729(1):5.

Rempel, M. (2012). Numerical sunspot models: Robustness of photospheric velocity and magnetic field structure. *Astrophysical Journal*, 750(1).

Rempel, M., Schüssler, M., and Knölker, M. (2009). RADIATIVE MAGNETOHYDRODYNAMIC SIMULATION OF SUNSPOT STRUCTURE. *The Astrophysical Journal*, 691(1):640–649.

Ringnes, T. S. and Jensen, E. (1960). On the relation between magnetic fields and areas of sunspots in the interval 1917-56. *Astrophysica Norvegica*, 7:99.

Ruiz Cobo, B. and Puschmann, K. G. (2012). TWIST, WRITHE, AND HELICITY IN THE INNER PENUMBRA OF A SUNSPOT. *The Astrophysical Journal*, 745(2):141.

Saad, Y. (2003). *Iterative Methods for Sparse Linear Systems*. Society for Industrial and Applied Mathematics, second edition.

Sadykov, V. M., Kosovichev, A. G., Oria, V., and Nita, G. M. (2017). An Interactive Multi-instrument Database of Solar Flares. *The Astrophysical Journal Supplement Series*, 231(1):6.

Santos, J. C., Büchner, J., and Otto, A. (2011). 3D MHD simulations of electric current development in a rotating sunspot: active region NOAA 8210. *Astronomy & Astrophysics*, 535:A111.

Scherrer, P. H., Schou, J., Bush, R. I., Kosovichev, A. G., Bogart, R. S., Hoeksema, J. T., Liu, Y., Duvall, T. L., Zhao, J., Title, A. M., Schrijver, C. J., Tarbell, T. D., and Tomczyk, S. (2012). The Helioseismic and Magnetic Imager (HMI)

Investigation for the Solar Dynamics Observatory (SDO). *Solar Physics*, 275(1-2):207–227.

Schou, J., Scherrer, P. H., Bush, R. I., Wachter, R., Couvidat, S., Rabello-Soares, M. C., Bogart, R. S., Hoeksema, J. T., Liu, Y., Duvall, T. L., Akin, D. J., Allard, B. A., Miles, J. W., Rairden, R., Shine, R. A., Tarbell, T. D., Title, A. M., Wolfson, C. J., Elmore, D. F., Norton, A. A., and Tomczyk, S. (2012). Design and Ground Calibration of the Helioseismic and Magnetic Imager (HMI) Instrument on the Solar Dynamics Observatory (SDO). *Solar Physics*, 275(1-2):229–259.

Schrijver, C. J. (2009). Driving major solar flares and eruptions: A review. *Advances in Space Research*, 43(5):739–755.

Schuck, P. W. (2008). Tracking Vector Magnetograms with the Magnetic Induction Equation. *The Astrophysical Journal*, 683(2):1134–1152.

Schwabe, H. (1844). Sonnen Beobachtungen im Jahre 1843. *Astronomische Nachrichten*, 21(15):234–235.

Solanki, S. (2002). The magnetic structure of sunspots and starspots. *Astronomische Nachrichten*, 323(3-4):165–177.

Solanki, S. K. (2003). Sunspots: An overview. *Astronomy and Astrophysics Review*, 11(2-3):153–286.

Somov, B. V., Kosugi, T., Hudson, H. S., Sakao, T., and Masuda, S. (2002). Magnetic Reconnection Scenario of the Bastille Day 2000 Flare. *The Astrophysical Journal*, 579(2):863–873.

Stenflo, J. O. (1969). A mechanism for the build-up of flare energy. *Solar Physics*, 8(1):115–118.

STFC (2019). STFC Science Challenges.

Stix, M. (2002). *The Sun An Introduction*. Astronomy and Astrophysics Library. Springer Berlin Heidelberg, Berlin, Heidelberg.

Strang, G. (2021). *Introduction to Linear Algebra*. Wellesley-Cambridge Press, Wellesley, fifth edit edition.

Sturrock, P. A. (1991). Maximum energy of semi-infinite magnetic field configurations. *The Astrophysical Journal*, 380:655.

Sturrock, Z. (2016). *Numerical simulations of sunspot rotation driven by magnetic flux emergence*. PhD thesis, St Andrews.

Sturrock, Z. and Hood, A. W. (2016). Sunspot rotation. II. Effects of varying the field strength and twist of an emerging flux tube. *Astronomy & Astrophysics*, 593:A63.

Sturrock, Z., Hood, A. W., Archontis, V., and McNeill, C. M. (2015a). Sunspot rotation. *Astronomy & Astrophysics*, 582:A76.

Sturrock, Z., Hood, A. W., Archontis, V., and McNeill, C. M. (2015b). Sunspot rotation. I. A consequence of flux emergence. *Astronomy & Astrophysics*, 582:A76.

Thomas, J. H. and Weiss, N. O. (2004). Fine Structure in Sunspots. *Annual Review of Astronomy and Astrophysics*, 42(1):517–548.

Thomas, J. H. and Weiss, N. O. (2008). *Sunspots and Starspots*. Cambridge University Press.

Tian, L. and Alexander, D. (2006). Role of Sunspot and Sunspot-Group Rotation in Driving Sigmoidal Active Region Eruptions. *Solar Physics*, 233(1):29–43.

Tlatov, A., Riehokainen, A., and Tlatova, K. (2019). The Characteristic Sizes of the Sunspots and Pores in Solar Cycle 24. *Solar Physics*, 294(4):45.

Tlatov, A. G. and Pevtsov, A. A. (2014). Bimodal Distribution of Magnetic Fields and Areas of Sunspots. *Solar Physics*, 289(4):1143–1152.

Török, T., Temmer, M., Valori, G., Veronig, A. M., van Driel-Gesztelyi, L., and Vršnak, B. (2013). Initiation of Coronal Mass Ejections by Sunspot Rotation. *Solar Physics*, 286(2):453–477.

Usoskin, I. G. (2017). A history of solar activity over millennia. *Living Reviews in Solar Physics*, 14(1):3.

Valori, G., Pariat, E., Anfinogentov, S., Chen, F., Georgoulis, M. K., Guo, Y., Liu, Y., Moraitis, K., Thalmann, J. K., and Yang, S. (2016). Magnetic Helicity Estimations in Models and Observations of the Solar Magnetic Field. Part I: Finite Volume Methods. *Space Science Reviews*, 201(1-4):147–200.

Vemareddy, P. (2017). Successive Homologous Coronal Mass Ejections Driven by Shearing and Converging Motions in Solar Active Region NOAA 12371. *The Astrophysical Journal*, 845(1):59.

Vemareddy, P., Ambastha, A., and Maurya, R. A. (2012). ON THE ROLE OF ROTATING SUNSPOTS IN THE ACTIVITY OF SOLAR ACTIVE REGION NOAA 11158. *The Astrophysical Journal*, 761(1):60.

Vemareddy, P., Cheng, X., and Ravindra, B. (2016a). Sunspot Rotation as a Driver of Major Solar Eruptions in NOAA Active Region 12158. *The Astrophysical Journal*, 829(1):24.

Vemareddy, P., Cheng, X., and Ravindra, B. (2016b). SUNSPOT ROTATION AS A DRIVER OF MAJOR SOLAR ERUPTIONS IN THE NOAA ACTIVE REGION 12158. *The Astrophysical Journal*, 829(1):24.

Walker, A. (2018). *The Impact of Sunspot Rotation on Solar Flares*. PhD thesis, University of Central Lancashire.

Wang, R., Liu, Y. D., Hoeksema, J. T., Zimovets, I. V., and Liu, Y. (2018). Roles of photospheric motions and flux emergence in the major solar eruption on 2017 September 6.

Wang, X., Jiang, C., Feng, X., Duan, A., and Bian, X. (2022). MHD Simulation of Homologous Eruptions from Solar Active Region 10930 Caused by Sunspot Rotation. (2000).

Watson, F. T., Fletcher, L., and Marshall, S. (2011). Evolution of sunspot properties during solar cycle 23. *Astronomy & Astrophysics*, 533:A14.

Wiegelmann, T. and Sakurai, T. (2012). Solar Force-free Magnetic Fields. *Living Reviews in Solar Physics*, 9.

Wiegelmann, T., Thalmann, J. K., and Solanki, S. K. (2014). The magnetic field in the solar atmosphere. *The Astronomy and Astrophysics Review*, 22(1):78.

Withbroe, G. L. and Noyes, R. W. (1977). Mass and Energy Flow in the Solar Chromosphere and Corona. *Annual Review of Astronomy and Astrophysics*, 15(1):363–387.

Woltjer, L. (1958). A THEOREM ON FORCE-FREE MAGNETIC FIELDS. *Proceedings of the National Academy of Sciences*, 44(6):489–491.

Yalim, M. S., Prasad, A., Pogorelov, N. V., Zank, G. P., and Hu, Q. (2020). Effects of Cowling Resistivity in the Weakly Ionized Chromosphere. *The Astrophysical Journal*, 899(1):L4.

Yan, X.-L., Qu, Z.-Q., and Kong, D.-F. (2008). Relationship between rotating sunspots and flare productivity. *Monthly Notices of the Royal Astronomical Society*, 391(4):1887–1892.

Yan, X. L., Qu, Z. Q., Kong, D. F., and Xu, C. L. (2012). SUNSPOT ROTATION, SIGMOIDAL FILAMENT, FLARE, AND CORONAL MASS EJECTION: THE EVENT ON 2000 FEBRUARY 10. *The Astrophysical Journal*, 754(1):16.

Yan, X. L., Wang, J. C., Pan, G. M., Kong, D. F., Xue, Z. K., Yang, L. H., Li, Q. L., and Feng, X. S. (2018). Successive X-class Flares and Coronal Mass Ejections Driven by Shearing Motion and Sunspot Rotation in Active Region NOAA 12673. *The Astrophysical Journal*, 856(1):79.

Yang, S. (2019). Trigger mechanisms of the major solar flares. *Proceedings of the International Astronomical Union*, 15(S354):392–406.

Young, D. (1954). Iterative methods for solving partial difference equations of elliptic type. *Transactions of the American Mathematical Society*, 76(1):92–111.

Zhang, J., Li, L., and Song, Q. (2007). Interaction between a Fast Rotating Sunspot and Ephemeral Regions as the Origin of the Major Solar Event on 2006 December 13. *The Astrophysical Journal*, 662(1):L35–L38.

Zheng, J., Yang, Z., Guo, K., Wang, H., and Wang, S. (2016). ON THE ROTATION OF SUNSPOTS AND THEIR MAGNETIC POLARITY. *The Astrophysical Journal*, 826(1):6.

Zhu, C., Alexander, D., and Tian, L. (2012). Velocity Characteristics of Rotating Sunspots. *Solar Physics*, 278(1):121–136.